The Swelling Behaviour of Polyelectrolyte Networks

Dissertation
zur Erlangung des Grades
"Doktor der Naturwissenschaften"

am Fachbereich Physik
der Johannes Gutenberg–Universität
in Mainz

vorgelegt von
Bernward A. F. Mann
geb. in Münster (Westf.)

Max-Planck-Institut für Polymerforschung
Max Planck Institute for Polymer Research

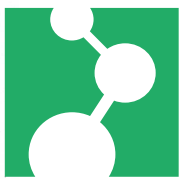

Zusammenfassung

Als Basis zahlreicher Produkte des täglichen Lebens mit der daraus resultierenden erheblichen industriellen Bedeutung wie auch als Bausteine für Biomaterialien stellen geladene Hydrogele auch nach Jahrzehnten des praktischen Einsatzes und intensivster Forschung Wissenschaftler der verschiedensten Fachrichtungen vor immer neue Herausforderungen. Trotz eines relativ einfach zu beschreibenden Aufbaus erschweren vor allem ihre internen Wechselwirkungsmechanismen aufgrund der einzigartigen Kombination von kurz- und langreichweitigen Kräften wissenschaftliche Untersuchungen ihrer charakteristischen Eigenschaften. Daher ist es wohl kaum verwunderlich, daß auf diesem Gebiet schon früh Computersimulationen als Bindeglied zwischen analytischer Theorie und empirischen Experimenten zum Einsatz kamen, um so die Lücke zwischen den vereinfachenden Annahmen der Modelle und der Komplexität realer Messungen schrittweise zu schließen. Aufgrund des selbst für Höchstleistungsrechenanlagen immensen numerischen Aufwands mußten die betrachteten Systemgrößen und Zeitskalen jedoch lange verhältnismäßig klein sein; erst heute sind die technischen Möglichkeiten vorhanden, welche es erlauben, auch ein Netzwerk geladener Polyelektrolyte numerisch zu modellieren. Dies ist Gegenstand der vorliegenden Doktorarbeit, welche sich mit einem der fundamentalen und zugleich äußerst faszinierenden Phänomenen der Polymerforschung beschäftigt:
Dem Quellverhalten von Hydrogelen.

Hierzu wurde ein erweiterbares Simulationspaket für Untersuchungen weicher Materie, Kurzform: ESPResSo, geschaffen, das insbesondere das mesoskopische Kugel-Feder-Standardmakromolekül zu komplexen Systemen zusammengesetzt zu berechnen versteht. Hocheffiziente Algorithmen und massive Parallelisierung verkürzen darin die erforderliche Rechenzeit zur Lösung der Bewegungsgleichungen selbst im Falle der langreichweitigen Elektrostatik und für hohe Teilchenzahlen, so dass selbst numerisch aufwendige Anwendungen realisierbar werden. Dabei ist dieses Programm dennoch modular und einfach strukturiert, um so steten Ausbau durch neue Wechselwirkungsmechanismen, Freiheitsgrade, Ensemble und Integratoren zu ermöglichen, zugleich aber einsteigerfreundlich dank Trennung in ein die Simulation steuerndes Tcl-Skript und den die Numerik ausführenden, rechenintensiven C-Teil gehalten. Eine Vielzahl verschiedener Analyseroutinen erlaubt zudem die Untersuchung extensiver wie intensiver Observablen.

Auch wenn sich in den letzten Jahren analytische Theorien weitgehend auf eine

Modellbildung geeinigt hatten, zeigen die im Rahmen dieses Forschungsprojektes durchgeführten numerischen MD-Simulationen, dass selbst im Falle einfacher Modellsysteme bereits grundlegende Annahmen der Theorien außer für einen engen Parameterbereich nicht mehr zutreffen und somit nicht länger in der Lage sind, wichtige Observable korrekt vorherzusagen. Dank "mikroskopischer" Analyse der isolierten Beiträge einzelner Systemkomponenten, dies eine besondere Stärke von Computersimulationen, gelang es aber dennoch, das Verhalten geladener Polymernetzwerke im Quellgleichgewicht in gutem Lösungsmittel und in der Nähe des θ-Punktes durch entscheidende Modellmodifikationen erfolgreich beschreiben zu können.

Ermöglicht wurde dies durch die konsequente Erweiterung bekannter einfacher Skalenargumente um in unserer detailierten Studie zuvor als ausschlaggebend identifizierte Mechanismen, welche sich dann zu einem generalisierten Modell zusammenfügen ließen. Mit diesem gelang es dann erstmals das finale Systemvolumen gequollener Polyelektrolytgele über den gesamten untersuchten Parameterbereich, für verschiedene Netzwerkgrößen, Ladungsanteile und Wechselwirkungsstärken mit Ergebnissen der Computersimulationen in Übereinstimmung zu bringen. Zudem wurde mit der Idee einer "Zelle unter Zugspannung" ein selbstregulierender Ansatz vorgestellt, der eine Vorhersage des Quellgrades allein auf Basis der verwendeten Systemparameter erlaubt. Ohne Rückgriff auf implizite oder effektive Observable kann so aus der Minimierung der freien Energie das Gleichgewichtsverhalten bestimmt werden.

In schlechter Lösung verändert sich das Aussehen der Netzwerkketten grundlegend, da nun deren Hydrophobizität entgegen der Abstoßung gleichgeladener Monomere den Kollaps der Polyelektrolyte betreibt. Je nach gewählten Parametern kann sich so ein fragiles Gleichgewicht ausbilden, das faszinierenden geometrischen Strukturen Vorschub leistet wie beispielsweise sogenannten Perlenketten. Dieses von einzelnen Polyelektrolyten unter ähnlichen Umgebungsbedingungen bekannte Verhalten war theoretisch vorhergesagt, konnte aber in unseren Simulationen nicht nur erstmalig nachgewiesen werden, sondern erlaubte auch anhand der Analyse totaler Strukturfaktoren erste Indizien für eine Existenz solcher Strukturen in experimentellen Ergebnissen erfolgreich zu bestätigen.

Summary

Being basic ingredients of numerous daily-life products with significant industrial importance as well as basic building blocks for biomaterials, charged hydrogels continue to pose a series of unanswered challenges for scientists even after decades of practical applications and intensive research efforts. Despite a rather simple internal structure it is mainly the unique combination of short- and long-range forces which render scientific investigations of their characteristic properties to be quite difficult. Hence early on computer simulations were used to link analytical theory and empirical experiments, bridging the gap between the simplifying assumptions of the models and the complexity of real world measurements. Due to the immense numerical effort, even for high performance supercomputers, system sizes and time scales were rather restricted until recently, whereas it only now has become possible to also simulate a network of charged macromolecules. This is the topic of the presented thesis which investigates one of the fundamental and at the same time highly fascinating phenomenon of polymer research: The swelling behaviour of polyelectrolyte networks.

For this an extensible simulation package for the research on soft matter systems, ESPResSo for short, was created which puts a particular emphasis on mesoscopic bead-spring-models of complex systems. Highly efficient algorithms and a consistent parallelization reduced the necessary computation time for solving equations of motion even in case of long-ranged electrostatics and large number of particles, allowing to tackle even expensive calculations and applications. Nevertheless, the program has a modular and simple structure, enabling a continuous process of adding new potentials, interactions, degrees of freedom, ensembles, and integrators, while staying easily accessible for newcomers due to a Tcl-script steering level controlling the C-implemented simulation core. Numerous analysis routines provide means to investigate system properties and observables on-the-fly.

Even though analytical theories agreed on the modeling of networks in the past years, our numerical MD-simulations show that even in case of simple model systems fundamental theoretical assumptions no longer apply except for a small parameter regime, prohibiting correct predictions of observables. Applying a "microscopic" analysis of the isolated contributions of individual system components, one of the particular strengths of computer simulations, it was then possible to describe the behaviour of charged polymer networks at swelling equilibrium in good solvent and

close to the θ-point by introducing appropriate model modifications.

This became possible by enhancing known simple scaling arguments with components deemed crucial in our detailed study, through which a generalized model could be constructed. Herewith an agreement of the final system volume of swollen polyelectrolyte gels with results of computer simulations could be shown successfully over the entire investigated range of parameters, for different network sizes, charge fractions, and interaction strengths. In addition, the "cell under tension" was presented as a self-regulating approach for predicting the amount of swelling based on the used system parameters only. Without the need for measured observables as input, minimizing the free energy alone already allows to determine the the equilibrium behaviour.

In poor solvent the shape of the network chains changes considerably, as now their hydrophobicity counteracts the repulsion of like-wise charged monomers and pursues collapsing the polyelectrolytes. Depending on the chosen parameters a fragile balance emerges, giving rise to fascinating geometrical structures such as the so-called pearl-necklaces. This behaviour, known from single chain polyelectrolytes under similar environmental conditions and also theoretically predicted, could be detected for the first time for networks as well. An analysis of the total structure factors confirmed first evidences for the existence of such structures found in experimental results.

Contents

Introduction

One of the most prominent features of a polyelectrolyte network can be observed when immersing a dry sample in solution: This hydrogel is then able to absorb large amounts of the solvent molecules, up to several hundred times its dry mass, while swelling to an enormous size. It will also respond to variations of the external conditions by rather drastic volume changes. Such remarkable properties allow numerous industrial applications, *e.g.* as superabsorbants (hygiene products, health care, water treatment, environmental cleanup operations), in drug delivery, cosmetics, pharmaceuticals, agriculture, in everyday products like rubber and compact discs, or as actuators in microfluidic devices [3–8]. With hygiene products alone being a billion-dollar-market [9], not only their economical importance ensured investigations into

Figure I.1.: Polyelectrolyte networks and their wide range of usability.
Left: Pharmaceutical application – this hydrogel is self-regulating, *i.e.* it releases moisture into dry wounds or absorbs excessive exudate from sezernising wounds up to twice its own weight, to ensure an optimal healing environment (see [1]).
Right: Agricultural application – while the two plants on the left hand side already perish after eight days without water supply, one tea spoon of hydrogel, immersed into the top two inches of the sandy-loam soil in which all four *cosmos sulphureus* are grown, sufficed to ensure the survival of both plants to the right for over 17 days under otherwise equal environmental conditions (picture taken on eighth day [2]).

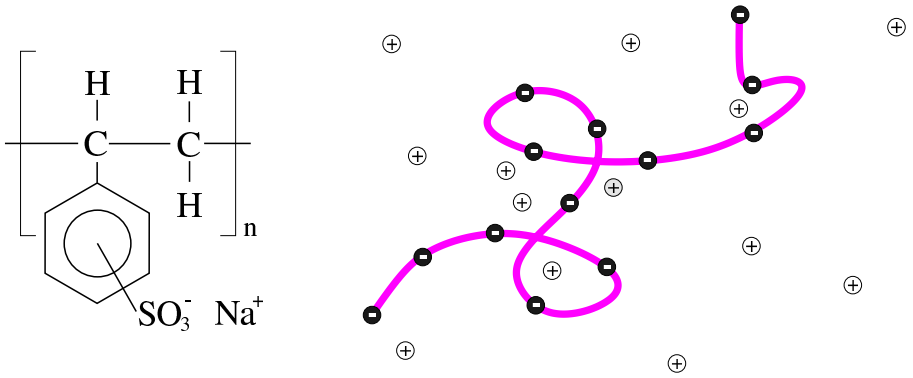

Figure I.2.: Example of a flexible polyelectrolyte, contrasting the constitution formula for sulfonated polystyrene and its sodium counterions (*left*) with the coarse-grained depiction of a physicist (*right*) who models the counterions in the solution as well as the relatively stiff monomer units on the chain as simple (charged) spheres, any chemical bonds between them as *e.g.* harmonic springs (taken from [11]).

the chemical processes required for their synthesis and application, but the general usefulness of the hydrogels' many trademark features as well. Despite the broad range of scientific questions provoked thereby, the underlying physical mechanisms however have not been receiving the same attention; simple theoretical models exist, but their validity cannot easily be verified against the experimental work due to the multitude of different effects overlaying each other. Containing macromolecular properties as well as long-range electrostatic interactions, they result in an impressive (and mostly cross-correlated) variety of phenomena and fundamental questions, *i.e.* [7] regarding the influence of molecular weight, intrinsic stiffness, solvent quality or ionic strength on the size of the polyelectrolytes, the characterizability of observables by coarse-grained quantities (such as a linear charge density) versus the necessity of considering full chemical details, the relation of dynamic quantities such as viscosity or electrophoretic mobility to static properties. Their fundamental understanding is also crucial in *e.g.* biochemistry or molecular biology with most proteins, including DNA itself, essentially being charged polymers. Nevertheless, mechanisms of their interactions with the cell membranes remain largely unknown [10], their mutual attraction surprising at first – why should *not* two likely charged objects repel each other?

Chemically, charged hydrogels are composed of cross-linked polyelectrolytes, polymer chains which dissociate ions in polar solvents [12]. Due to the macroscopic requirement of electro-neutrality the counterions released from the chains are hereby confined inside the gel and exert an osmotic pressure which leads to the swelling of the network against the elastic response of the network strands. The increase of the counterion entropy caused by the larger volume available to the ions in the

swollen state is thought to be the driving force behind the large swelling capacity of charged gels, neglecting long-range electrostatics, short-range hydrophobic interactions, and deviations from ideal behaviour. It is their delicate balance which renders the magnitude of the swelling and the phase behaviour of polyelectrolyte networks hard to predict [13]. In real systems, the composition of the gel and its surrounding solvent plays also an important role, though usually only the relative amount of cross-linkers can be well-controlled experimentally. The topology is much harder to control, and almost impossible to determine, leaving the distribution and type of strand lengths, entanglements, dangling ends, *etc.*, unknown and/or fluctuating. Despite recent progress in that respect, allowing to synthesize well-defined model polyelectrolyte networks based on the photodimerization of monodisperse star polymers from Poly(*tert*-butyl methacrylate) (P*t*BMA) star precursor polymers with subsequent photocrosslinking [14], equilibrium properties in general do depend on the preparation process of the gel (*e.g.* active ends, n-functional crosslinking agents). In contrast, the characteristics of the solution are relatively easy to control, with the addition of salt [15], multivalent ions, and oppositely charged surfactants [16,17] effectively reducing the gel volume.

Over the past decades, the attention polyelectrolyte networks attracted from both science and industry increased profoundly. While the latter used the gels' unprecedentedly high swelling capacity and their behaviour under external stimuli, the former's interest focuses on the complex interplay of short- and long-range effects which determine the equilibrium swelling properties [13]. Experimentally those have been extensively studied for a long time [19–21], where initial work concentrated on the swelling behaviour in solutions of simple salt [22,23]. More recent studies also addressed, among others, the influence of oppositely charged surfactants [24–28] and microgel particles [29,30].

Aside the experimental works, both single chain polyelectrolytes and neutral polymer gels have also been thoroughly examined by analytical [12,31–33] and numerical investigations [34–38] for a long time now. *Charged* networks or hydrogels on the other hand have been subjected to much less analytical or computational studies, which is why, from a fundamental point of view, polyelectrolyte gels are therefore less understood than neutral ones. This is largely due to the fact that uncharged polymer networks can benefit to a great extent from the powerful scaling description developed for single neutral chains and solutions, as one considers a semi-dilute polymer solution at the overlap concentration (c^*-picture) to be similar to a neutral gel without trapped entanglements and heterogeneities at swelling equilibrium. For a (charged) hydrogel no such strong analogy to polyelectrolyte solutions exists; even if for sufficiently large pressures $p > 0$ both systems display comparable behaviour, the underlying physical mechanisms remain different. Over the last years, theoretical approaches therefore concentrated on thermodynamic arguments, developing rather simple models for the equilibrium states of charged gels [39–41], studying the swelling of polyelectrolyte and polyampholyte networks in pure solvent, in the

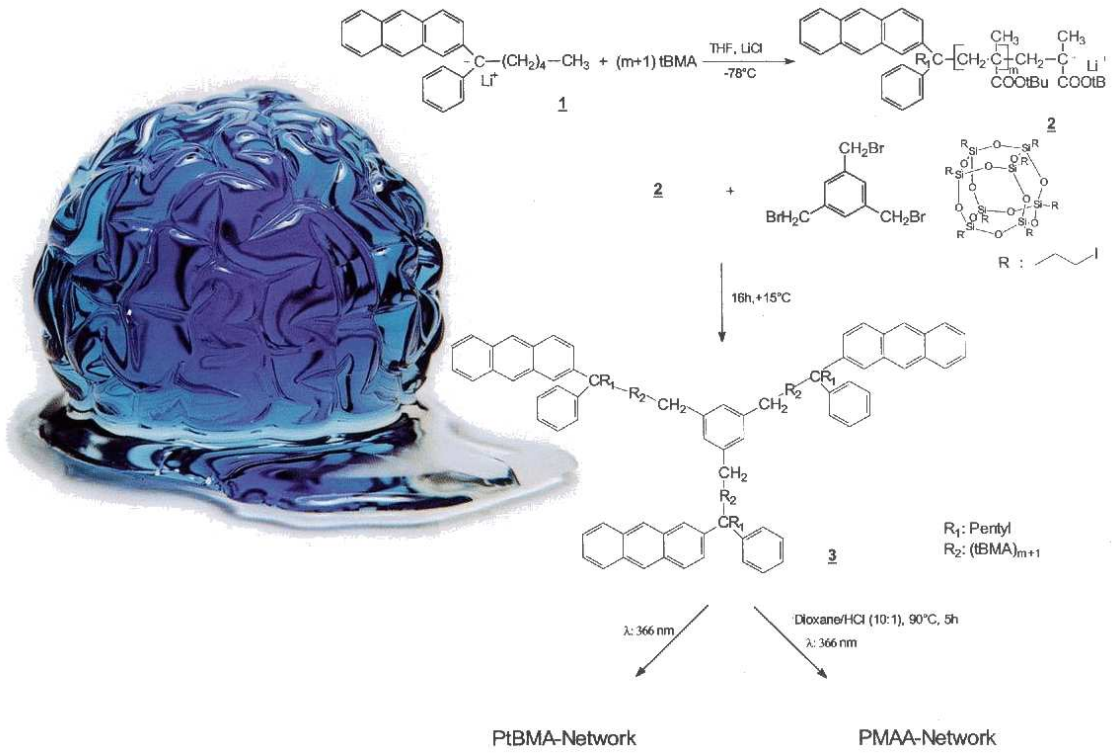

Figure I.3.: One of the famous polyelectrolyte networks T. Tanaka's group built (*left*). Roughly 10 cm in diameter, it is capable of absorbing water up to a thousand times its dry volume, since the solvent causes the ionizable groups on the macromolecular chains to dissociate counterions into solution; these remain confined to within the gel-like structure due to the global requirement of electro-neutrality, such that their osmotic pressure initiates the swelling process of the hydrogel during which its increasing volume draws more and more solvent into the network. The irregular pattern on its surface remains a mystery up to now; it seems to depend on the chemical substances used and the synthesis process employed, but no suitable explanation for its occurrence, shape, and geometry could yet be found (taken from [18]). On the *right* hand side the synthesis of P*t*BMA star precursor polymers is given which are subsequently photo-crosslinked by UV-radiation activating their end-groups to form a regular model network (from [14]). This method, developed at our institute, represents one of many possibilities to experimentally construct a polyelectrolyte *network*, here with special focus on the uniformity of the sample which allows increased control over the parameters and thus far better comparability with the idealized systems simulation and theory have to restrict themselves to (also see section 2.1). Chemical details are given in table 2.1, underlining the regularity of the created tri-, tetra-, and penta-functional stars with $N_m = 14, \ldots, 165$ monomers per arm, but still maintaining a very sharp molecular weight distribution, which indicates very small fluctuations in the arm's length. Due to the photocrosslinking, the chains can only bind at their ends, and provide an excellent model network for quantitative studies.

presence of salt, in mixed solvents, and in the presence of other macroions, *e.g.* surfactant micelles [13]. They usually calculated the free energy of the gel as sum of contributions from the elasticity of the strands, the solvent interaction of the network, the free motion of the counterions (entropy term), and the electrostatics in the system; such a treatment assumes the validity of the Flory-Rehner-Hypothesis (FRH) [42] which suggests that the elastic part of the free energy and the part from the interactions may simply be added, a procedure which is believed to fail in general [43, 44], then leading to a modified description [45, 46]. Unfortunately, due to the tremendous chemo-physical effort required for physically analyzable experimental investigations, no definite conclusion can be drawn from them regarding the validity or even applicability of the theories or their assumptions. On the one hand, this is caused by a vast number of hardly avoidable side effects in system and setup, on the other hand by the metrological necessity to always measure averages over large numbers of imperfect polymers, all deviating from ideal model behaviour in an individual manner, which may greatly obstruct accuracy and reproducibility of the results obtained.

This is where computer simulations come into play. They allow for well-defined systems (no impurities, parasitic drag, ...) which can be thoroughly evaluated and analyzed without much problems, since all real-world observables are available from the direct access to any microscopical details of the "experiment". That also allows control over individual effects by systematicly manipulating environmental or particle parameters to study their impact on the entire ensemble, giving valuable insight into what the leading contributions and mechanisms are that govern the macroscopic behaviour of the sample. Ideally, the results then enable experimentalists to focus their efforts on optimizing only predominantly important ingredients in their setup, control primary sources of error, and develop measurement methods for isolating the main effects, while theoreticians are given some means to evaluate the proposed models, whether their predictions can be confirmed quantitatively or at least qualitatively, and the validity of the underlying assumptions, whether these apply to the considered parameter regimes or need to be adjusted or revised. Here, another advantage of computer simulations becomes obvious: Being simplified descriptions of reality themselves, they can be based on the very same assumptions the theoretical models imposed, consequently revealing how the latter would behave as real world systems but representing an idealized realization of the experimental system at the same time. This bridges the gap between theory and experiment by determining how the systems *would* behave experimentally if all the theoretical model assumptions and simplifications were correct; any deviations found can then be traced rather easily[1] to imperfections in the underlying description of reality, be

[1] At least compared to the effort it would take the experimentalists to improve on their measurements, trying to separate interacting effects and to isolate microscopic details in a macroscopic sample, or to the problems theoreticians would have to face if they had to relinquish several of their (well-justified) presumptions about the system.

it that some of the simplifications were unjustified or too extensive, that important aspects or contributions were wrongfully neglected, or that the modeling itself failed to depict the leading mechanisms correctly. Next, whatever changes are proposed can directly be executed within the simulation environment, introducing new or modifying existing constraints, adding extended functionality or degrees of freedom if necessary (*e.g.* dipolar moments or rotational orientations, which are both commonly neglected), or simply evaluating the different model components separately to determine if their significance was properly addressed by the theory. Particularly the latter usually leads to the most valuable insights computer simulations can offer: While the analytical treatment concentrates on the description of certain aspects of the system and aims for explicit predictions of selected observables, the simulation derives the full behaviour of (a simplified version of) the setup and obtains complete particle trajectories and their spatio-temporal evolution (which themselves need to be analyzed as any experimental data has to be); but because both are based on the same model assumptions, comparing forecast and observation, then investigating how deviations change when manipulating model mechanisms in the simulation allows specific statements about their theoretical treatment and any changes necessary therein. Although it will always depend on the verification through "real" experiments and to no lesser extend on the input and guidance by analytical studies, the methodology of computational investigations has proved its worth over the years particularly in such complex and challenging applications as the many-body macromolecular systems in polymer physics with their different time and length scales, layers of intertwined interactions and coarse-grained behaviour based on microscopic details.

One commonly chosen approach thereby employs *Molecular Dynamics* (MD) simulations [47–51] which treats the polymer not atomisticly or even on a quantum level, but rather coarse-grained towards a simpler depiction, as hinted to in figure I.2 and elaborated on in figure I.4. The basic idea behind it originates in the argument that compared to the macroscopic length scales each molecular repeat unit can essentially be considered a solid object of constant size, with the overall shape of the polymer being determined by the relative orientation of these monomers to each other. Interconnected by chemical bonds along the carbon backbone, the distance between neighbouring monomeric center-of-masses behaves similarly to the elongation of a spring affixed accordingly, while the internal structure within the repeat units remains relatively unchanged. Usually, they are rotated around the polymer's contour axis, depending on the local charge distribution and other chemical effects, hence determining the overall shape of the macromolecule. The *bead-spring-model* now replaces each monomer by a simple sphere (charged, if appropriate) which is connected with an artificial spring to its neighbours; their respective radii are chosen such that the combination of excluded volume interactions and spring potential has the resulting bead-bead-separation ("*bond length*") correspond to the aforementioned center-of-mass distance.

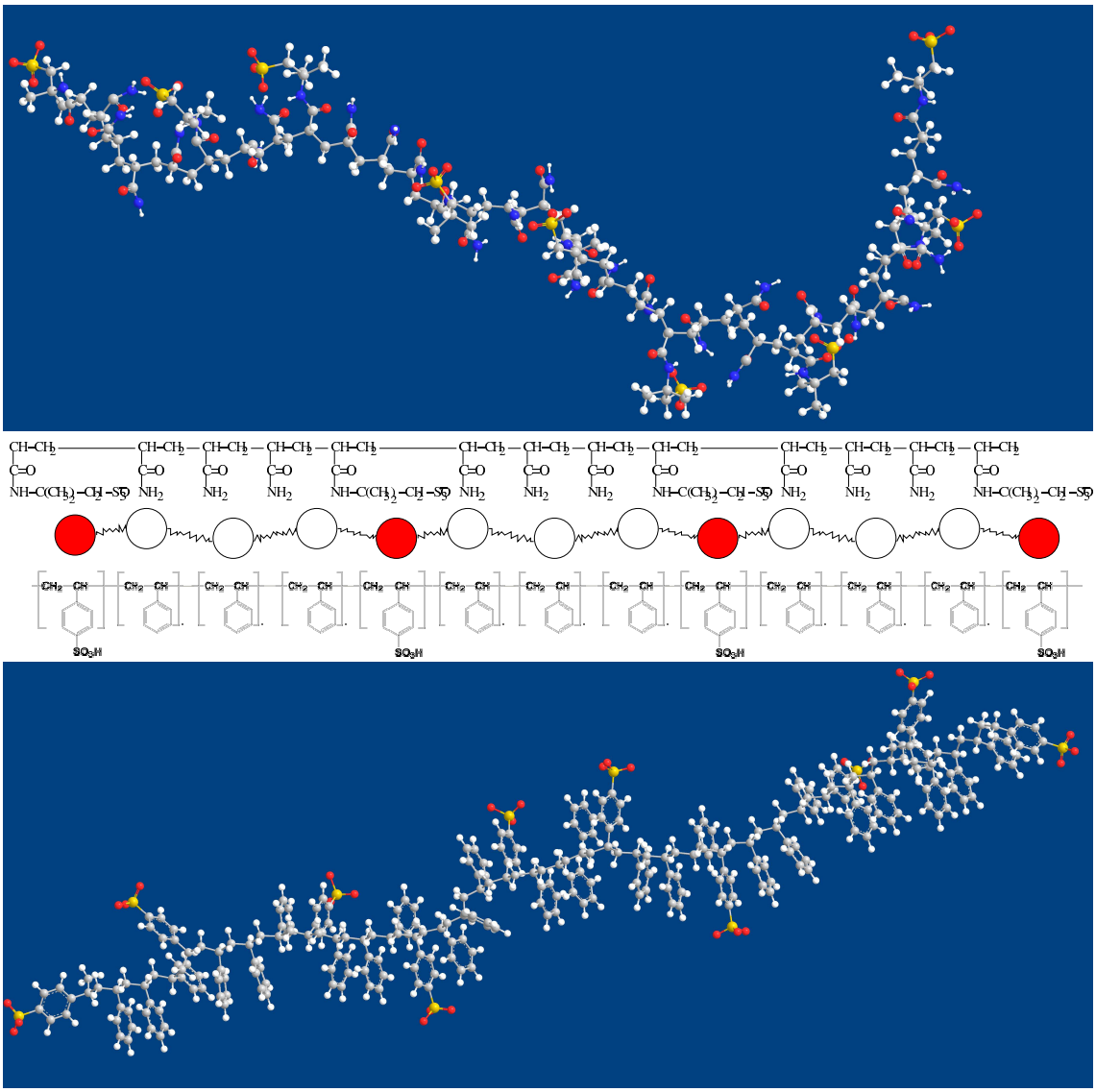

Figure I.4.: Illustration of the coarse-graining employed to map the highly complex chemical structures polyelectrolyte networks consist of onto the simpler bead-spring-model used in this computer simulation study. As examples AMAMPS (*top*) and PSS (*bottom*) have been chosen, whose possible steric conformations are displayed on the molecular level in the outer graphic panels. The corresponding chemical structure equations, given towards the center of the figure, translate to the 3D-depiction using the same colour coding for carbon (*gray*), hydrogen (*white*), sulfone (*yellow*), oxygen (*red*), and nitrogen (*blue*) atoms in both pictures. Every fourth monomer is charged (at the SO_3^--group) in case of AMAMPS as well as for PSS, the other three repeat units are electrostaticly neutral. In the middle the coarse-grained representation is given, replacing each monomer repeat unit in its entirety by a single sphere (which is coloured in red and assigned the appropriate charge of $-1e$ if it stands for a charged repeat unit), connected via a spring-like potential to its neighbours; it is the same for both polyelectrolytes (for further details see text).

Figure I.4 displays this exemplary for the two polyelectrolytes poly(acrylamide-co-sodium-2-acrylamido-2-methylpropane sulfonate) (AMAMPS) and poly(styrene-co-styrene sulfonate) (PSS), the former having a *hydrophilic* backbone, meaning that in aqueous solution it tries to increase its contact surface with the surrounding solvent, while the latter's *hydrophobic* backbone would generally lead towards the collapse of the macromolecule into a globular state, hence minimizing its contact surface with the solvent[2]. The carbon backbone of both macromolecules, to which their monomer groups are connected, is marking the principal axis of the polymer, around which the repeat units may freely rotate to minimize their steric energy. The regular fraction f of charged monomers has been chosen as $f = 0.25$ with the idealization that every repeat unit bearing the SO_3^--group responsible for the monomer's charge of $q = -1e$ is periodically followed by three neutral ones for illustration purposes (in reality it would not be possible to create such a regular structure, and f would rather reflect the ensemble average with the charged groups randomly distributed along the chain). Particularly if now looking at their respective chemical structure equations in figure I.4, a good illustration of the coarse-graining process can be obtained: Each of their monomer repeat units is replaced in its entirety by a sphere, and connected via a spring-like potential to its neighbours; charges q are assigned to these spheres according to the valency of the underlying molecules (with $q = -1e$ for the red-coloured ones in our example). Although this *ad-hoc* approach waives the specifics in the configuration, it is nevertheless a good approximation for their conformation. As it turns out, the resulting bead-spring-model is the same for both AMAMPS and PSS, despite the differences between the two polyelectrolytes in chemical composition as well as chemo-physical properties. This will be addressed by *how* the potentials are defined which model the bonds and the excluded volume of the spheres, since *e.g.* using for the latter a purely repulsive potential would mimic hydrophilic behaviour, while adding an attractive part on larger length scales leads towards increasing hydrophobicity within the same coarse-grained representation. It is also possible to include additional effects such as torsion or steric hindrance through further interactions or by employing bond angle or multi-body potentials in place of the simple spring bonds, these refinements will however not be considered in this work.

Although the example in figure I.4 presents single chain polyelectrolytes, the extension towards a network is straight forward and also mimics the common chemical

[2] In general this is only true for neutral polymers. In case of polyelectrolytes the picture becomes more complicated, since the likewise charged monomers along the chain repel each other electrostaticly, hence counteracting the collapsing tendency. Eventually, a delicate balance emerges and the chain may assume a pearl-necklace-like structure [52–54] where globular parts (due to the hydrophobicity) are connected by straight elongated segments (due to the electrostatic repulsion). Found for single polyelectrolytes in computer simulations and preliminarily observed in experiments *e.g.* at our institute [55], similar behaviour is theoretically predicted for hydrophobic hydrogels as well [40]; however, this will be detailed in chapter 5.

creation process: Once the polymers are set up, additional bonds are introduced between monomers on different chains once they are sufficiently close to each other; because the length of these *crosslinks* is typically not larger than the intra-chain bond lengths, this either requires a high enough density in the system to work or another mechanism to attract potential binding sites towards each other. In the experiments, one of several possibilities to realize this consists of using chemically active ends which will form a covalent bond if close to any other monomer, resulting in a *randomly end-crosslinked network* where entanglements between and loops around neighbouring chains may (even frequently) occur. Since such hydrogels do no longer have one common chain length[3] but rather a distribution of probable values, the *end-to-end crosslinked networks* are more suitable candidates for representing the very simple theoretical models; with their active ends only able to link to other end groups (or to specific n-functional crosslinking agents added to the system), the single chain observables retain their meaning, and eventual entanglements are left as source of impurities. Figure I.5 contrasts these two approaches, also visualizing the different density regimes where the respective network formations take place.

Following the strategies detailed in the previous paragraphs, the coarse-grained modeling of crosslinked PSS or P*t*BMA would consequently result in a depiction similar to the left resp. right panel in figure I.5, and could therefore be used as a starting point for MD computer simulations. Despite the profound experience of the theory group at the Max-Planck-Institute for Polymer Research, where the presented research was conducted, in single chain polyelectrolytes and neutral polymer networks, charged hydrogels had never been dealt with before in a numerical investigation, hence no ready-to-use solution existed in the beginning. Instead of writing an entirely new program or modifying existing code towards that aim, ending up with a highly specialized program from which once again future projects could only benefit if they were treating very similar systems, it was decided early on to create a more flexible, modular, and extensible simulation package which would be capable of handling all different kinds of coarse-grained setups in soft matter systems. In cooperation with Axel Arnold and Hans-Jörg Limbach we therefore developed ESPResSo[4] where all available algorithms and special expertises the group had accumulated over the years were merged into, and which soon lived up to its promise by quickly replacing all other programs previously being used in the group, enabling new users to start off with their computer experiments almost immediately and without the need for software development, stimulating them to enter their specific knowledge through small enhancements (new interaction potentials, new analysis routines, *etc.*) later on. Due to this, the capabilities of ESPResSo grew tremendously since its first official release in April of 2003, now covering one of the widest ranges of

[3] In a network, "chain length" refers to the number of monomers between nearest neighbouring nodes, an analogy which extends to all other single chain properties as well, *e.g.* "end-to-end distance" R_{E}, here describing the separation of nearest neighbouring nodes.

[4] Abbreviates **E**xtensible **S**imulation **P**ackage for **Res**earch on **So**ft Matter Systems.

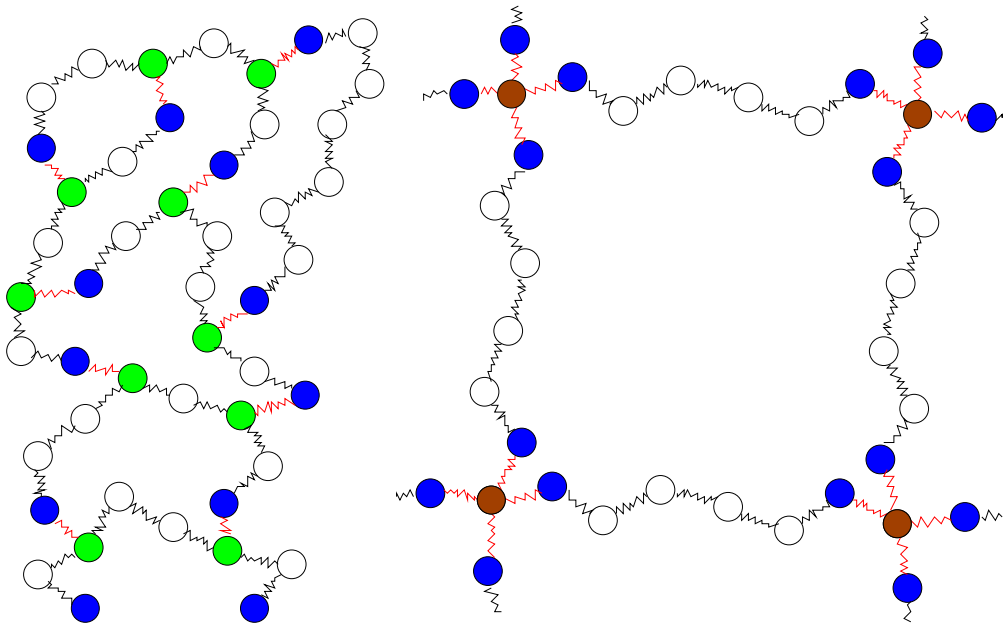

Figure I.5.: Coarse-grained polymer network formation. *Left:* A randomly end-crosslinked network composed of single chains with $N_\mathrm{m} = 8$ monomers each, where the active ends (*blue* spheres) establish crosslinks (*red* bonds) to close enough monomers of other chains, forming tetra-functional nodes (*green* spheres) in this example. *Right:* An end-to-end crosslinked network built from shorter $N_\mathrm{m} = 6$-chains in a system where tetra-functional crosslinking agents (*brown* spheres) had been added to which the active ends bounded. Note the significantly lower density of this network to the previous one (the lack of entanglements is due to the 2D representation where they cannot occur).

techniques developed for MD simulations, and still being one of the fastest programs available due to its usage of some of the most efficient algorithms and its parallelized structures for multi processor environments. It has not only become the default simulation tool at our institute, but it is also used by an increasing number of scientific groups in Germany, Europe, and worldwide, as well as industrial researchers at *e.g.* Freudenberg, BASF, and Nestlé. Awarded at the annual Heinz-Billing-Competition 2003 for the Advancement of Scientific Computation [56, 57], ESPResSo remains an open source project free of charge for public use. More informations and a detailed overview of its current capabilities will be given in chapter 1.

It was not before the beginning of this Ph. D. project, that simulation techniques and computational resources allowed for numerical studies of polyelectrolyte networks [58–63] because of the vast effort required when dealing with electrostatic systems under periodic boundary conditions and because of the understanding of the single chain behaviour which had only just previously reached a sufficiently satisfying degree. The cited works usually examined an end-to-end crosslinked gel with ideal diamond configuration in a (N, V, T)-ensemble at various network packing

fractions and different sets of parameters [58,60,61] or in cubic symmetry and with explicit solvent [59] in very small systems, confirming the tremendous swelling as compared to uncharged systems [58,61] and claiming a discontinuous volume transition at very high electrostatic coupling [60], but without investigating the connection of the measured data to the theoretical predictions mentioned before. Their findings will be summarized at the beginning of chapter 4 and chapter 5 as far as they are relevant for this work.

Here, it is our aim to investigate the physical foundations of the swelling behaviour of polyelectrolyte networks. Chapter 2 will therefore introduce important concepts in polymer physics which are a prerequisite for the theoretical treatment of chapter 3, where we develop and discuss suitable approaches to the prediction of macroscopic properties based on input parameters only.

Using computer simulations and employing a similar model system as the one previously described, we then thoroughly examine the validity of simple scaling arguments for a wide range of multiple parameters, focusing on a detailed analysis of the different contributions entering the theoretical models. From there we are able to determine their limits and possible corrections to the assumed mechanisms behind the swelling equilibrium. In chapter 4 we will thereby focus on hydrophilic hydrogels similar to the AMAMPS in the upper half of figure I.4, for which an aqueous solution is a *good solvent*. Since the solubility also depends on system properties such as the pH-level or the temperature, changing *e.g.* the latter may cause a crossover from hydrophilic to hydrophobic behaviour at a specific temperature which has historically been termed θ. In that state monomers do not seem to have an excluded volume any longer, and (neutral) polymers behave as ideal chains with a Gaussian distribution describing the chain conformations, which now look like a Random Walk of stepsize N_{m}. Nevertheless, it turns out that at this *θ-point* the theoretical predictions remain basically the same, at least on the *scaling level* where prefactors are neglected, and that the only distinction resides in an universal exponent ν which is slightly larger for the good solvent regime ($\nu = 0.588$) than at the θ-point ($\nu = 0.5$). Consequently, to prevent repetitions we integrated the results of θ-like hydrogels into chapter 4 as well, pointing out whenever there are differences between both systems.

Regarding hydrophobic hydrogels such as the PSS in the lower section of figure I.4 for which water is a *poor solvent*, we report our findings in chapter 5. There, fundamental changes occur compared to hydrophilic or θ-systems, as now the energetic trend to minimize the contact surface with the solvent overcomes the entropy, causing a neutral polymer to collapse and fall out of solution; a polyelectrolyte, however, will enter a delicate balance as its charges repel each other and thus counteract the collapsing tendencies, which may lead to a good solvent-like elongated shape (if there are many effective charges on the chain), to a slower collapse (if only few effective charges remain), or to a compromise in the shape of *e.g.* a pearl-necklace-like structure. In case of hydrogels, the network structure introduces another constraint, now

acting as an "external" force on the strands. Nevertheless, for sufficiently long chains similar structures are expected [40] and can be confirmed by our simulations. Here we also perform a thorough comparison to the single polyelectrolyte results found in our group [52–54] to evaluate the assumed mechanisms behind the equilibrium swelling behaviour of polyelectrolyte networks in poor solvents.

While the ESPResSo core program was originally developed by Axel Arnold, Hans-Jörg Limbach, and myself, the project itself has now become a group effort with various people contributing extensions, modifications, and bug fixes. The actual simulation scripts as well as conducting, analyzing, and evaluating the numerical experiments towards this Ph. D. thesis were however my sole responsibility.

Parts of this thesis have already been published, accepted for publication, or submitted for (re-)review, *i.e.* in [56, 57, 64] (chapter 1), [62, 63, 65] (chapters 2-4), and [66] (chapter 5).

1. ESPResSo –
An Extensible Simulation Package for the Research on Soft Matter Systems

The computer code concept this work is based upon is introduced. Design aspects and abilities are listed. Special features and implementation details are discussed. The parallel performance presented shows favorable scaling and competitive computation speed limited only by hardware constraints.

Real-world experiments have nature as driving force determining observations and outcome, computer simulations require software to create the same in a virtual environment. While the choice of possible setups is unlimited in reality (given unlimited resources and time), the usability of a simulation is limited to the capabilites of the underlying algorithms. Consequently, it is important to ensure that the code engine of a simulation is powerful, versatile and flexible enough to address all aspects of the system under investigation.

On the coarse-grained level we are interested in, long years of methodological research offer a wide range of suitable algorithms to tackle not only our depiction of polyelectrolyte networks, but all sorts of coarse-grained soft matter systems such as membranes, DNA, ferrofluids, polyampholytes, and much more. The basic idea thereby is the application of Newton's laws of motion [67] to the (consequently classical) treatment of a many-body system of simple, interacting particles, whose force potentials superpose such that the resulting net force $\vec{\mathsf{f}}_i$ on each individual object i induces an acceleration $\vec{a}_i = \vec{\mathsf{f}}_i/m_i$ which will move the particle. This *Molecular Dynamics* (MD) approach will be detailed a bit further in section 4.1 regarding its employment in the framework of our computer simulations. The great advantage lies in the obvious ability to actually follow particle trajectories through phase space, depicting a somewhat "realistic" temporal evolution of a given system. Another ansatz arriving at thermodynamic equilibrium much faster, initially at the expense of only representing possible snapshots or equilibrium conformations without a temporal connection between them, is called *Monte Carlo*-technique (MC). Here, the total energy of the system is calculated based on the current particle positions and their mutual interactions with each other, before arbitrary (but system compliant) changes are applied to the setup, *e.g.* random re-positioning of particles or polymers, re-sizing of the simulation box, insertion/deletion of particles. The new state is accepted as next iteration if its energy is now lower, otherwise it is discarded with a certain probability increasing with the expected energy gain.

A good introduction to these and other important standard techniques can be found in [47, 51]. In the following we will focus on a more general description of

the program package we developed with Axel Arnold and Hans-Jörg Limbach that is designed to perform numerical MD-/MC-simulations for a broad class of soft matter systems in a parallel computing environment. Our main concept during its development was to provide a user friendly and fast simulation tool which serves at the same time as a research platform capable of rapidly incorporating the latest algorithmic achievements in the field of soft matter sciences; that is reflected in its name, **E**xtensible **S**imulation **P**ackage for **Res**earch on **So**ft Matter Systems, or ESPResSo for short.

It is unique with respect to the efficient treatment of long-range interactions for various geometries using modern algorithms like P^3M, MMM2D, MMM1D and ELC. Already equipped with a broad variety of interaction potentials, thermostats, and integrators, it offers the usage of constraints, masses and rotational degrees of freedom, and allows to move between different ensembles on-the-fly. Should the need arise for new features, a clear program structure enables even average users to enhance ESPResSo to everyone's desired custom level. An efficient MPI parallelization encourages usage of multi-processor architectures, while strict employment of ANSI-C for the core functions and the Tcl-script driven user interface make ESPResSo platform independent. This also ensures easily modifiable interfaces to communicate with other MD-/MC-packages, real-time visualization tools, and other programs. ESPResSo is an open source project and is therefore giving others full and up-to-date access to new developments, with the goal to stimulate researchers all over the world to contribute to the package by incorporating their special (*i.e.* algorithmic) expertise into the core distribution of the program.

1.1. Soft Matter Simulations

Soft matter is a term[1] for materials in states that are neither simple liquids nor hard solids (crystals,...) but rather macromolecular assemblies, *e.g.* polymers, colloids, liquid crystals, and dipolar fluids. Many such materials are familiar from everyday life – glues, paints, soaps, baby diapers – while others are important in industrial processes, such as polymer melts that are molded and extruded to form plastics [68], or polymer networks for the development of rubber [69]. Biological components are mainly made out of soft matter as well, *i.e.* DNA, membranes, filaments and other proteins, and even most of the food we digest belongs to this class.

Common for all these materials is the importance of a wide range of length and time scales for both their microscopic behaviour and their macroscopic properties. Since typical energies between different structures are similar to thermal energies, Brownian motion of thermal fluctuations plays a prominent role. Another key feature, the propensity of soft matter systems to self-assemble, often results in complex

[1] With many soft matter systems being highly complex in their composition and their interactions, they are also called *complex fluids*.

phase behaviours yielding a rich variety of accessible structures; most of the biological systems are not even in equilibrium usually but evolve along switchable steady states. Much of today's insight into their underlying mechanisms has thereby been gained through computer simulations of these systems at either the full atomistic or on a coarse-grained, so called *mesoscopic*, level.

In the past, charged polymers (polyelectrolytes) and colloids have been a key center of interest in the research activities at our institute. Serving as important substances for many of the technical applications mentioned so far, charged systems also occur in biological environments [70] and are already involved when modeling explicit water, hereby entering through the partial charges. Simulating these systems is not straightforward and very time consuming [35, 71, 72], since the effort scales at best linearly with the number of charges, thus the production of single data points could take weeks or even months for complex biomolecular problems [73]. Consequently, a number of algorithms have been improved or developed in our group which yield fast expressions for the energy and forces of fully or partially periodic systems [74–78], pending a suitable simulation environment to be applied to. Another research focus in our group, besides considering charged systems in various geometries, *e.g.* films or porous media, and with different topologies ranging from linear to branched to networks [62, 63], considers systematically coarse-graining atomistic models such that one can access mesoscopic time and length scales with computer simulations [79–81], necessary for *quantitatively* predicting dynamic properties or surface interactions for complex materials which depend on local chemical interactions and local packing. For the coarse-graining procedure it is required to switch back and forth between an atomistic and a coarse-grained description, implying complicated steering schemes for a simulation; therefore, a high flexibility of the steering level and an easy way to interact with other programs is needed as well as extensibility to easily implement and test new methods and algorithms, because such tasks usually involve changes in the core part of a program.

What else should a suitable program be able to do? It should be easy to use, but scientifically sound; it should grant experts access to state-of-the-art techniques, but enable beginners to investigate scientific problems easily and at the same time not limit them to run the program as a "black box"; it should be general and flexible, but still fast; it should be easily extensible, but remain at the same time reliable and keep continuity with older versions. Looking at other available simulation packages, *e.g.* BALL [82], GISMOS [83], GROMOS [84], GROMACS [85], LAMMPS [86], NAMD [87, 88], polyMD [89], Amber [90], NWChem [91], DL_Poly [92], and OCTA [93], none of these were fit to meet all the desired (and required) capabilites.

This led us to create a newly structured program for this field of science, which we called ESPResSo [56, 57, 64]. (In the meantime, another project called Quantum-Espresso [94] has been established, which is a package for Car-Parinello MD simulations and is independent of our approach.) Our program is designed to study soft matter model systems via Molecular Dynamics (MD) algorithms, with partic-

ular emphasis on extensibility for new, highly complex force/energy algorithms. It is parallelizable and fast and thus able to compete in speed with any of the above mentioned programs (see section 1.6). On the steering level it is far more flexible than any other simulation tool with a similar scope that we have seen; still, the clear program structure together with the documentation enables new users to run their own simulations after a very short time, contributing new features soon thereafter.

In this chapter, the current version of the ESPResSo-package is presented, which as of this writing continues to be expanded with new features and capabilities, undergoing thorough testing before being officially announced. Downloads, updates and more documentation can be found on the project's webpage http://www.espresso.mpg.de/. The distribution of the source code adheres to the open source standards under the GPL-License [95]. By this we hope to ignite the further development of our code into a valuable research tool for the soft matter community, beyond the already participating groups, scientific institutes, and researchers at industrial companies.

The description of ESPResSo starts with a general outline of the design ideas that guided the development (section 1.2), before giving an overview of the capabilities and algorithms included in section 1.3. Followed by a discussion of some implementation details in section 1.4, benchmarks for sample systems are presented in section 1.6 and the speed to other simulation programs is compared. This chapter is rounded off by conclusions and an outlook about features that will be incorporated in the near future.

1.2. Program Design

This section lists the main design goals and their implementation in ESPResSo during the process of development. They are given in order of precedence, since as usual there has to be a certain trade-off between competing design goals, and they are certainly influenced by the special needs of our work group, where we use coarse-grained descriptions of soft matter systems, mainly bead-spring models, as enhancements of the fully atomistic treatment. However, it had also become evident in the past that applying a program to different scientific scenarios can only be successful if its code is easily adjustable to the specific challenges each new project contains. In achieving this requirement even some performance loss on runtime is absolutely acceptable, as it will be overcompensated by the reduced preparation period needed to initiate the actual simulation.

1.2.1. Goals and Principles

Extensibility: It is the nature of fundamental research projects that objectives can change, system complexities expand, and often new challenges arise – a simulation package must enable the user to add custom code, otherwise it will only be useful

for a very restricted group of people. ESPResSo addresses these concerns by having an entirely modular integration and communication core around which all other routines are structured. This allows the exploration of a wide range of models with a vast variety of properties, and gives at the same time solid support for algorithm development. The extensibility of ESPResSo, its routines and its data structures, has been proven during the incorporation of new algorithmic techniques like the Maggs algorithm (see section 1.3.3) and the lattice Boltzmann algorithm (see section 1.7) which both required changes in the core of the program. This makes us confident that the given program structure is well suited for further not yet foreseen changes and additional features.

Readability: Unless the structure and coding style are kept simple, extensibility would remain a theoretical issue. That is why ESPResSo puts much emphasis on a clear structure and thorough documentation, to ensure that programmers with various degree of programming skills are able to gain access to the different coding layers that form the simulation engine. Naturally, beginners would want to start off with smaller tasks such as implementing a new potential (maybe following the *How To*-Guide in the documentation) before attempting to alter core sections of ESPResSo, since the latter's complexity naturally requires an increased experience from the user.

Flexibility: ESPResSo's scope of general applicability discourages the usage of highly specialized and optimized functions. Flexibility requires looking at each functionality or data structure from multiple directions to ensure that it is useful to a large variety of problems. Even if most enhancements probably originate from a very concrete application, the aim is to always extend them towards a more universal applicability before they are released. Examples for this flexibility are the usage of a very general Lennard-Jones potential which enables the simulation of colloidal particles and the implementation of a particle structure which allows also the treatment of anisotropic particles.

But this is only one part of ESPResSo's flexibility. The employment of Tcl as the steering level opens vast opportunities for the design and course of intended computer experiments. Moreover it opens the opportunity to implement new requirements on a script language level at the same time still being in close linkage to the program core. Practiced *e.g.* for hybrid Monte-Carlo-/MD-simulations, this approach saved a huge amount of human development time, at the expense that the resulting program will be somewhat slower than a highly optimized and specialized one – acceptable for the aforementioned reasons.

Correctness: ESPResSo is not only a multi-user, but more importantly a multi-developer program where the full source code is accessible to everyone. This has the advantage that whoever is a specialist in a certain (algorithmic) field will be implementing the desired functions with expert knowledge. However, every individual contributor to the ESPResSo-project must be enabled to run a thorough check on the added code fragments to ensure that the numerical and physical correctness of

the package as a whole remains intact even after the changes were applied.

For this purpose, ESPResSo includes a testsuite of various cases which quickly evaluates if the most important features are still functioning properly; since this check takes only a few minutes, the inhibition threshold for developers to use it is low. In addition, there are also more elaborate test scenarios and sample scripts that contain well known physical problems and systems solved some time ago. These will provide a very thorough review of ESPResSo's overall integrity by comparing the computed results to the published reference data; although these tests take longer, they help to avoid programming bugs. Despite the automatic control features already ensuring a high degree of reliability of the package's consistency, for any major release we check the correctness of added or changed features and code sections manually as well.

Efficiency: Last, but surely not least, the applied algorithms should naturally be the most modern ones available, to ensure a fast execution time of the simulation. For this purpose ESPResSo incorporates state-of-the-art electrostatic routines such as P^3M or ELC, provides multiple cell systems for choosing a particle storage organization optimized for the investigated systems, and constantly adds new algorithms (*e.g.* a recent suggestion for treating electrostatics locally [96,97]) providing new features. However, all these attempts must still fulfill the previous design criteria, particularly *readability* and *flexibility* – *i.e.*, no hardcoded assembler loops or platform dependent computation tricks will be implemented, because the achievable speedup through this would most likely render further attempts of enhancing the program much harder, if not impossible, also sacrificing platform independency along the way.

These wide specifications and conflicting design goals enforced a thorough thinking about the program architecture, data structures and general programming guidelines for the development of ESPResSo. Since ESPResSo is a team project where basic concepts evolve in a discussion process, further adjustments may be implemented, always having feasibility and applicability in mind. In the end, everything will be documented in an understandable and usable way to ensure coherence and compliance for future releases (see section 1.5).

1.2.2. Basic Program Structure

ESPResSo is organized in two hierarchical program levels, each suited to optimize some of the main targets in mind: the *steering level* for large flexibility, usability and extensibility, the *simulation engine level* for efficiency, readability and again extensibility.

Steering Level: The steering of ESPResSo is done on a script language level, namely Tcl/Tk [98]. All tasks are implemented as C-functions enhancing the Tcl-interpreter and acting as new Tcl-script commands. This includes input and output of data, setting of particle properties, interactions, and parameters, and performing

the integration and analysis of a given system. All commands interacting with the simulation are by construction able to both set and retrieve informations similar to the Tcl-syntax, *e.g.*

```
thermostat set langevin 1.0 1.0
```

will active the Langevin thermostat with a reduced temperature $T^* = 1.0$ and a friction coefficient $\Gamma = 1.0\tau^{-1}$, whereas executing `thermostat` alone would output

```
{ set langevin 1.0 1.0 }
```

i.e. all currently activated thermostats with their parameters.

But steering a simulation in ESPResSo is much more than setting up system parameters. From the steering level one can interact with the actual simulation in a very flexible way. That means one can change the system properties during the simulation in any desired way, may this be the insertion or deletion of particles, a change of interaction parameters, a switch from one to another thermodynamic ensemble, a change of parameters for the integrator or the thermostat – just to name a few possibilities. This allows *e.g.* to conduct simulated annealing by modulating the temperature, or to perform a thermodynamic integration by gradually changing the Hamiltonian of the system.

However, in the equilibration of most systems, this feature is also frequently used: For the simulation of dense, charged polymer melts, as another example, one could start the equilibration without electrostatics, add polymers and some neutral spheres (the latter to become counterions later on) at the correct density; temporarily capping the excluded volume interactions would then allow to carefully push overlapping particles apart, always supervised by the Tcl-script which could use analysis routines to monitor the minimum distance of all particles until they are separated. Afterwards, the spatial positions of the monomers could be fixed before the electrostatic interactions are activated, to prevent locally unbalanced charges to rupture the polymer's bonds, allowing the counterions to equilibrate. Releasing the chains is then the last step towards the physical system setup of a poor solvent polyelectrolyte melt (see chapter 5 for further details).

All steps described above are typically part of the Tcl-script that steers the simulation. Even more complex tasks can easily be formulated with the Tcl language. It is also possible to conduct a wide range of data analysis during runtime of the simulation, which is not only convenient but also allows to feedback analysis results into the steering of the simulation flow, *e.g.* to implement cross checks surveying the kinetic temperature in an isothermal ensemble or the instantaneous pressure in (N, p, T), to initiate system configuration swaps, something needed to use *parallel tempering* [99], or to change the coarse-graining level of the physical system. This can involve replacing explicit particles with a larger and appropriately heavier center-of-mass representation, and vice versa.

With all these possibilities available, the user is never constrained to a specific system, ensemble, or configuration. One can, in principle, modify all of the initially chosen properties during runtime. Of course, instead of using the slower, but more flexible Tcl interface, the user always has the option of adding features to the engine level of ESPResSo. As already mentioned in section 1.2.1 the steering level enables the user to carry out a huge part of the programming work required for solving new problems on the script language level rather than being forced into laborious C-programming. Even though for standard simulations the script can be very simple, the given possibilities can yield quite complex simulation scripts, which perform not only the steering of the simulation, but also analyze the data on the fly, report regularly the observables of interest, and directly export graphs of their mutual interplay. The steering level also allows to manipulate the simulation from a graphical user interface (Tk) or via input from external programs.

Simulation Engine Level: In contrast to the steering level, which uses the Tcl-script language for easy usability, the simulation engine has to be as efficient as possible, therefore being implemented in ANSI-C. The engine is responsible for storing the particle and interaction data on any number of processors, but it also performs the integration of Newton's equation of motion as well as the necessary calculations of basic quantities like forces, energies and pressures.

The simulation engine code has been organized to be as modular as possible, separating clearly different tasks like *e.g.* particle organization, interaction organization, integration, or force calculation. Some advanced algorithms, especially for the calculation of the electrostatic interactions, require deep knowledge about the particle organization, making complex interfacing necessary. Basic functions can be accessed using well-defined lean interfaces, hiding the details of the complex numerical algorithms, and important informations such as the particle data can always be accessed through a defined set of functions and variables, although internally very different particle organization schemes can be applied (see section 1.4).

Another example is the implementation of new potentials, which is possible without touching the integrator code, while in turn the integrator can be modified without touching the potential implementations. In this way it is much easier to implement a new type of interaction, a new integrator, or a new thermostat. It is also much easier for a beginner to understand what the program is doing during the simulation, which is important in light of our belief that it is not useful to perform scientific research with a simulation tool that appears mainly as a "black-box" to the scientist utilizing it.

Besides Tcl/Tk, ESPResSo relies on another open source package, namely the FFTW [100] in the P^3M method for the electrostatic interaction, providing the "fastest Fourier transform in the west" (according to the acronym used). For the parallelization MPI routines are used; on platforms running Linux and Darwin ESPResSo employs the LAM/MPI [101] implementation, offering the option to choose other packages such as MPICH [102] instead.

1.3. Capability and Algorithms

Although ESPResSo is highly extensible, it is of course favorable to find the desired features already implemented in the program. Therefore, this section will give a short overview of algorithms and capabilities available in ESPResSo as of this writing, ranging from different integrators and thermostats over particle interactions and potentials up to data analysis routines. During the start of our program most of the implemented algorithms had been devoted to (charged) polymers, rod-like objects, or membranes [56, 57], while today ESPResSo is not limited to these applications anymore. Many features have been added in the meantime, including the possibility to perform atomistic simulations and to employ various coarse-graining techniques. Since ESPResSo is constantly being extended by the users at our institute, at all the other collaborating scientific places, and at the associated industrial workgroups, the features presented in the following are in the continuous process of being amended, complemented and expanded. Therefore, an up-to-date listing can always be found in the `RELEASE_NOTES`-file of the distribution and on our webpage (`http://www.espresso.mpg.de`).

1.3.1. System Setup

The Tcl-script level of ESPResSo allows for an easy and variable setup of the starting configurations together with the simulation parameters, as well as choosing the desired algorithms. From placing particles and charges, defining potentials and interactions, assigning bonds and constraints, applying external forces and customized boundary conditions, to reading in existing configurations in ESPResSo's native blockfiles (see 1.3.5) and other formats, everything can be easily executed using few simple commands within the Tcl-script. It is also possible to rely on pre-defined setup routines and sample topologies such as polymer chains, networks, fullerenes, counterion- and salt-distributions which are provided as shortcut-like conveniences of commonly employed systems, and which the user may adjust to any custom needs arising.

For an impression of the scripting interface some simple sample segments now show how to *e.g.* create a simple Lennard-Jones fluid by putting particles at random positions in the simulation box, which is possible to do directly within a single loop:

```
set box_x [lindex [setmd box_l] 0]
set box_y [lindex [setmd box_l] 1]
set box_z [lindex [setmd box_l] 2]
for {set i 0} { $i < $n_part } {incr i} {
    part $i pos [expr $box_x*[t_random]] \
                [expr $box_y*[t_random]] \
                [expr $box_z*[t_random]]
           type 0
```

```
}
```

Here, the first three lines extracted the current length of the simulation box in all three dimensions, relying on the aforementioned mechanisms that any Tcl- and ESPResSo-command returns its current settings automatically (conversely, the box can be set up using `setmd box_l $box_x $box_y $box_z` once the Tcl-variables `box_x`, `box_y`, and `box_z` have been assigned proper values). The following loop iterated over all `set n_part [setmd n_part]` particles known to ESPResSo at that point, setting their respective positions to a random fraction of the box length (with `[t_random]` returning random numbers on the unit interval) and their particle type to `0` for latter reference (*e.g.* when defining interactions which should only act on certain kind of objects).

Next, the setup of a somewhat more complex system is demonstrated, namely a bead spring model of a polymer melt, consisting of 100 chains carrying 200 monomers each [34], thereby using the `polymer`- command as an example of a pre-defined setup routine which reduces this entire task to a single line:

```
polymer 100 200 1.0 mode SAW
```

It fills the simulation box with the corresponding number of self-avoiding walks (SAW) of step size 1.0σ (the bond length), once the excluded volume interactions and the bond potentials have been defined. To obtain correct statistics, whenever the placement of a monomer fails due to its intended position being too close to already existing particles, the entire chain is removed and its creation process restarted. Although it would be tempting for performance reasons[2] to think of rather replacing only the obstructed monomer, which would very quickly lead to a start-up system with correct minimal distances between all monomers, the resulting polymer conformation distribution would differ from SAW statistics such that an additional warm-up process being sufficiently long[3] would be required to allow relaxation of all chains, overcompensating the initial speed-up in the setup for high densities.

Using optional arguments (*e.g.* `charge +1`) turns the polymers into polyelectrolytes, with

```
counterions [expr 100*200] charge -1
salt [expr 100*50] [expr 100*150] charges +3 -1
```

adding the appropriate amount of oppositely charged counterions and some trivalent salt to the system (note the usage of Tcl for calculating the necessary numbers).

Creating a (single-stranded) DNA-helix instead is just as simple, using

```
polymer 1 10000 1.0 angle [expr [PI]/4.] [expr [PI]/6.] \
          charge -1 distance 2
```

[2] It is quite obvious that the deletion of the entire polymer leads to a diverging probability of being able to create a suitable start-up system *at all* if the density becomes very high.

[3] Herein lies the central problem as the required relaxation time diverges for high densities, being on the order of typical time scales for an entire project.

to have every other monomer along the coiled backbone carry one negative unit charge.

If one needs to constrain single particles, `part ... fix` fixes their spatial coordinates, for example if one wants to investigate the force acting on them as a function of the (imposed) distance, or if one wants to model immobile surfaces.

The user's influence is not limited to geometrical or topological issues. Besides specifying the particles' interactions, choosing thermostats, or the ensemble (*e.g.* constant volume or constant pressure), all other aspects of the simulation remain fully customizable in the course of the whole simulation. All parameters may be freely adjusted depending on whatever criterion chosen. This is useful in system equilibration, where interaction can be capped temporarily, or during the integration, *e.g.* to perform simulated annealing, or to add/remove/manipulate particles for grand canonical ensembles or multiscale approaches.

1.3.2. Integrators and Thermostats

ESPResSo uses as default the *Velocity Verlet Molecular Dynamics* integration scheme [51, 103] for rotationally invariant particles, which is robust enough for most applications. If a simulation incorporates particles with rotationally degrees of freedom like dipoles or cigar shaped Lennard–Jones particles, the rotational degrees of freedom are represented by quaternions, and an extension of the velocity Verlet algorithm for rigid body motion is used [104]. Mass and inertia moments are fully implemented, but may be replaced by the default reduced mass $m^* = 1$ for performance reasons if no distinction of different masses is desired (as is the case for our entire investigations in the following chapters). For the simulation of dynamic experiments like a simple shear flow, ESPResSo uses *Non Equilibrium Molecular Dynamics* (NEMD) [105, 106]. In addition to the intrinsic (N, V, E)-ensemble, the velocity Verlet integration scheme can be combined with one of the implemented thermostats to obtain integrators for the (N, V, T)-ensemble. At the moment these include a *Langevin thermostat*, a *Berendsen thermostat* [107] and a *dissipative particle dynamics thermostat* (DPD) [106, 108]. The type and the temperature of the thermostat can be changed during the simulation on the script level, allowing *e.g.* simulated annealing. The DPD thermostat implements the friction and noise as a particle pair force rather than a global one, and thus maintains momentum conservation, which is important for yielding correct hydrodynamic interactions for equilibrium and non-equilibrium simulations [106].

Apart from (N, V, E)- and (N, V, T)-ensembles, ESPResSo is also able to keep the pressure constant during the particle propagation, *i.e.* to simulate the (N, p, T)-*ensemble* [109]. This is implemented by introducing an artificial piston mass which acts on the simulation box and rescales its dimensions isotropically. With the Langevin-type equations of motion for this new degree of freedom one arrives at a stochastic MD integration scheme, enhancing the MD approach by Andersen,

Nosé, and Hoover with stochastic dynamics (SD), and follows the momentum of the piston such that its derivative corresponds to the difference between the currently measured "instantaneous" pressure and the given external one. There is also a corresponding isotropic thermostat available which adds friction and noise. In addition to the implementation given in [109], our algorithm allows for using a constant tension ensemble as well, where only the pressure in one or two dimensions is considered, the rescaling adjusted to respond accordingly; this is useful when studying *e.g.* membranes under tension [110].

Details on these algorithms, their implementation in ESPResSo, and their application to our systems are given in sections 4.1 and 5.3.1, where they will also be compared to alternative approaches.

1.3.3. Force Calculation Strategies

ESPResSo distinguishes three kinds of forces: long-ranged forces, short-ranged forces, and bonded interactions. Short-ranged interactions have to be calculated only for particles within a small interaction range. To avoid unnecessary operations, information from the cell structure can be used for eliminating particle pairs that are far away from each other. Therefore, each cell structure comes with an optimized force calculation routine for the short-ranged forces. For example, when the particles are sorted by the *domain decomposition* cell structure (see section 1.4.1), the *linked cell* concept chooses the size of the space-filling cells corresponding to the maximum range of the short-range interactions, such that only particles in adjacent cells can interact with each other; this naturally reduces drastically the number of particle pairs that have to be considered. Additionally, ESPResSo keeps a record of the particles currently interacting in so-called *Verlet lists* to decrease the computational work by another factor of around 8, since the lists have to be updated only every few time steps as long as the movement of the particles is small compared to the cell sizes. The optimal choice of this "*skin*" (defining the threshold for a "small movement") also depends on the cell layout, because as usually the box length will not be a multiple of the aforementioned maximum range of the short-range interactions, the smallest possible space-filling cell layout will have to have larger cell sizes, such that each of them will unavoidably contain some non-interacting particles. As larger cells allow for larger skins reducing the need for Verlet-updates but increasing the time every update requires, ESPResSo contains an automatic tuning routine which will take care of optimizing this balance by finding an appropriate choice for the parameters.

The bonded interactions are treated together with the short-ranged interactions. There is no limitation on the number of bond partners, *i.e.* many-body bonded interactions are already implemented in ESPResSo. The efficient treatment of long-range forces is only possible using highly sophisticated algorithms. Those will be discussed in section 1.3.3.

Short-ranged non–bonded Potentials

ESPResSo features the following non–bonded short-ranged potentials:

- *Lennard–Jones potential.* In our implementation the cut-off radius of this potential can be shifted to obtain a purely repulsive interaction (so-called WCA potential [111]), or one can add an additional hard-core offset radius. The Lennard–Jones can be capped during the warm-up phase of the simulation, such that even overlapping particles feel only a finite repulsive force. This allows for an easy random placing of particles in an initial configuration, and will be used in our simulations as well (see sections 4.1 and 5.3.1).

- *Combined Lennard–Jones–cosine potential.* If the Lennard–Jones potential is not cut-off in its minimum, *e.g.* if one needs the attractive tail, the forces are discontinuous. This potential adds a monotonous part of the cosine function to ensure that the force are continuous everywhere [112].

- *Buckingham potential* [113]. This is another potential mimicking a van-der-Waals type interaction between particles. It is a widely used force field in atomistic simulations.

- *Gay–Berne potential* [114]. Essentially the anisotropic version of the Lennard–Jones potential, *i.e.*for cigar shaped objects, it has to be used in conjunction with an integrator for rigid bodies.

- *Debye–Hückel potential* [115]. This potential describes a *screened* Coulomb interaction, which is short ranged by itself. In the limit of a screening length $\kappa^{-1} \to \infty$, the pure Coulomb potential is obtained. Note, however, that in this special case the integration loop is of order $\mathcal{O}(N^2)$ in the number of particles N.

- *Tabulated potentials.* ESPResSo can handle any number of tabulated potentials, where the force and the energy is described as a piecewise linear function of the distance with finite support. A very useful feature if one either has very complex particle interactions (*e.g.* based on an only numerically solvable formula), wants to compare the simulation to an experimentally obtained force field, or looks for a simple way to try out new potentials without directly implementing them as a well-defined new feature.

There are special model systems such as phantom networks, in which there are no nonbonded interactions between particles of the same chain. This behaviour can be implemented using different particle types, which however is extremely inefficient if several thousand chains are to be considered. ESPResSo offers exclusions as an alternative, allowing to specify particle pairs for which the nonbonded interactions are not calculated, *e.g.* interactions along the backbone of specific chains. While

these exclusions can be set manually, in standard atomistic simulations one typically excludes the interactions of each particle with its neighbours within the molecule, which can be done automatically by the `part auto_exclude` command.

Bonded Potentials

The bonded potentials are:

- *Pair forces.* Two particles can be bound by FENE (finite extensible nonlinear elastic) [112] and harmonic bonds. As an alternative to the exclusion mechanism, ESPResSo features a two-particle Lennard-Jones subtraction potential, which is simply a bonded version of the Lennard-Jones potential with inverted sign. The exclusion code adds some additional overhead to the nonbonded force calculation, since one needs to check for each pair of particles whether they interact or do not. If only a few interactions have to be left out, it may be more efficient to calculate the nonbonded interactions the usual way, subtracting the interaction of non-wanted particle pairs.

- *Three-body forces.* Three particles can be bound by a bond-angle potential. ESPResSo implements three different kinds of bond-angle potentials. First, a *harmonic potential* around the optimal angle ϕ_0, *i.e.* $1/2k(\phi - \phi_0)^2$, then a *cosine potential* $k(1 - \cos(\phi - \phi_0))$, and finally a *harmonic cosine potential* $(1/2)k(\cos(\phi) - \cos(\phi_0))^2$.

- *Four body forces.* Four particles can be bound by a dihedral angle potential. The implemented form is $k(1 + \delta\cos(n\theta))$, where θ is the dihedral angle, $n = 1, 2, ..., 6$ is the multiplicity and $\delta = \pm 1$ is a phase factor. With this potential one can also mimic force fields which use $\sum_i k_i \cos(\theta)^i$ as the functional form for the dihedral interactions.

- In addition to the potentials above, bonded potentials can be given in a *tabulated form* as well, where the energy and the force are given as piecewise linear functions of the distance (two particles), the bond angle (three particles), or the dihedral angle (four particles); see section 1.3.3.

Long-range Potentials

While the implementation of the short-ranged potential normally consists only of two short routines, namely the force and energy calculations, the treatment of long-ranged interactions requires much more care due to the large number of possible interaction partners. The algorithms for long-range interactions are highly sophisticated [71] and normally have their own parallelization strategies, separate from the one applied to all other parts of the program. This enormous effort is justified by the fact that a simulation with electrostatic interactions might spend more than

two thirds of the computation time only for the calculation of the long-range interactions. While ESPResSo currently handles Coulomb interactions only, since this is the dominant force for soft matter problems, fast algorithms for dipolar interactions are already being implemented at the moment.

For any finite geometry without periodic boundary conditions a simple loop over all N charged particles is used, resulting in an algorithm of order $\mathcal{O}(N^2)$ in the particle number N, as it was the case for the Debye-Hückel potential in the limit of $\kappa^{-1} \to \infty$. For 3D periodic boundary conditions the standard Ewald method still has a complexity of $\mathcal{O}(N^{3/2})$ in its optimal implementation, which is why ESPResSo contains the P^{3}M algorithm of Hockney and Eastwood [116] in the version of [74], where the computational effort now scales with $\mathcal{O}(N \log N)$. This method is the optimal choice for FFT-based "particle mesh Ewald" algorithms since it uses the lattice Green's function optimized for minimal pair-force errors, being superior to other variants by construction [117,118]. Additionally, robust error estimates exist [75] to ensure the best trade-off between speed and accuracy. The implementation in ESPResSo handles arbitrary dielectric constants at the boundary, while it uses the FFTW for the necessary Fourier transformations, which exists for various platforms and is self-confidently dubbed "**F**astest **F**ourier **T**ransform in the **W**est" by its developers [100]. As the maximal number of usable processors is usually required to be equal to the mesh size in the parallel multidimensional FFT employed in the FFTW, ESPResSo uses a combination of MPI and the only one-dimensional version of the FFTW for its more flexible parallel implementation.

For systems with periodicity only in 2 or 1 dimensions, ESPResSo features the MMM2D [76,119] and MMM1D algorithms [120] which stand for "**M**ultiple **M**esh **M**ethod" in 2D or 1D periodic systems, respectively. They are based on a convergence factor approach to evaluate the Coulomb sum. These algorithms are implemented for arbitrary box shapes, but have scalings of $\mathcal{O}(N^{5/3})$ (2D) and $\mathcal{O}(N^2)$ (1D). They also feature robust error estimates, and one of their advantages is that high numerical precision is not computationally costly, being faster and more robust than the 1D and 2D standard Ewald methods, or Lekner sums [121]. For a more complete discussion see [76,119,122,123].

MMM2D's scaling of $\mathcal{O}(N^{5/3})$ normally allows for not more than 1000 particles to be treated in a simulation. Dense electrostatically interacting systems in *e.g.* biomolecular applications require higher particle numbers or lower precision, for which ESPResSo contains an "**El**ectrostatic **L**ayer **C**orrection" (ELC) to be combined with any arbitrary algorithm for fully periodic boundary conditions (preferably one with a favorable scaling, P^{3}M for example), only replicating two of the three dimensions [77,78,123]. The summation order is made slabwise by a simple change in the dipole term [124], computing the unwanted interactions of particles with their images in the non-periodic dimension analytically (ELC-term) to be subsequently subtracted through the ELC-term. Since its calculation is linear in the number of charges, the favorable scaling of *e.g.* the P^{3}M method is preserved, improving quite

impressively on MMM2D.

All the methods described so far allow pre-setting a user defined accuracy based on which the remaining parameters are optimized automatically, taking the employed computer hardware into account as well. To the best of our knowledge, this ability of choosing the accuracy and having an automated tuning facility for long-range algorithms is unique to ESPResSo and not contained in other simulation packages.

In addition to the methods already described, ESPResSo also possesses a local electrostatic solver introduced by T. Maggs [96, 125] in the version of Pasichnyk and Dünweg [97], developed for MD simulations. The essential philosophy of this approach is to view electrostatics as the quasi-static limit of a dynamic field theory, in this case Maxwell electrodynamics, and to explicitly simulate the dynamics of the field degrees of freedom. The speed of light c appears as an adjustable parameter and realistic dynamics occurs for particle velocities $v \ll c$. The Maxwell equations are discretized on a simple-cubic lattice, with scalars on the sites, electric fields on the links, and magnetic fields on the plaquettes. The method is rather simple to implement and to parallelize, and appears to be quite competitive with respect to efficiency. In principle, it should allow for a locally varying dielectric constant [125], although this feature has not yet been implemented.

1.3.4. Constraints and External Forces

For a non-bulk simulation, the particles usually have to be constrained to some finite region of the space. In ESPResSo these constraints are implemented as soft immobile objects, *i.e.* they interact with the particles through one of the short-ranged potentials. ESPResSo features basic constraints such as walls, cylinders or spheres, which can be arbitrarily combined to form the desired simulation region. Walls and cylinders with infinite extension, *i.e.* in periodic boundary conditions, are able to carry a charge for simulations of charged surfaces. More exotic constraints are available, too, such as a two-dimensional array of spherical cavities interconnected by circular holes, a geometry used by Nykypanchuk *et al.* [126] to study Brownian motion of DNA.

Other type of constraints are positional constraints and external forces. While the former simply makes a particle immobile in some or all of the spatial coordinates, allowing *e.g.* pulling at a molecule fixed to a surface, the latter exerts a constant force on specific particles as if they were in an external field. This can be used to *e.g.* determine the potential of mean force between two macromolecules by fixing their center-of-mass distance through the `comfixed`-constraint, which allows to explore the configurational phase space as a function of the center-of-mass separation.

1.3.5. File Input/Output

Though Tcl provides built-in support for reading and writing (text-)files, ESPResSo introduces a unified file format for saving and (automatically) restoring its computer simulation data to allow easy exchange between users. Based on the structure of Tcl-lists, this *blockfile format* subdivides all informations on the current state of the program into categories (*blocks*). For each block type routines exist to write the block to a blockfile and to read its data back into the running simulation. ESPResSo handles many block types by default, such as `variable` (contains global parameters such as simulation box length, skin, processor node grid, cell grid, chosen periodicity), `tclvariable` (contains Tcl-variables, such as important constants or observables in the simulation script), `interactions` (contains a list of all the employed bonded, non-bonded, and electrostatic potentials with their parameters), `integrator`, `thermostat` (both contain parameters for the respective integrators and thermostats), `particle` (contains informations on the particles, *e.g.* positions, velocities, forces, and charges), `bonds` (contains the bonding topology of the system), `random` (contains the state of the random number generators) and `configs` (contains the particle trajectories of past, user-defined timesteps for online analysis purposes).

In addition to these standard blocks, ESPResSo allows to add arbitrary blocks written in Tcl. As a matter of fact, the default block types are implemented as Tcl routines, too. To add a new block type, one has to define only two Tcl procedures, one which is used to write the block data and one to parse it. This is quite easy to do because most ESPResSo-commands are able to output their parameters in a format that allows to be directly used as input, already demonstrated in section 1.2.2 where

```
eval thermostat [thermostat]
```

would expand to the `thermostat set langevin 1.0 1.0` employed there. This feature can also be used to conveniently write and parse observables.

For each of the categories a block is defined and transferred to or from the file, its head providing unique identification of the content. Consequently, parsing of a blockfile is a simple task, allowing ESPResSo to not only read in the informations given therein, but to directly apply all settings to the simulation engine level appropriately, hence preparing the simulation environment for further immediate usage.

As with all aspects of ESPResSo, the amount of informations to be included may be chosen entirely by the user. Some shortcut commands exist as well, *e.g.* to create a simulation system snapshot which includes everything necessary for starting or resuming an integration. The output will be saved in plain text (ASCII) format ensuring great flexibility, portability, and (more importantly) platform independence compared to proprietary, system dependent binary formats; the unavoidable size disadvantage is easily compensated when compressing the resulting files (which can be done on-the-fly) using external programs such as gzip.

```
{variable
        {box_l 316.950192362 316.950192362 316.950192362}
        {periodicity 1 1 1}
        {node_grid 1 1 1}
        {time 5200}
        {time_step 0.0125}
}
{interactions
        {0 FENE 7.0 2.0}
        {0 0 lennard-jones 1.75 1.0 2.5 0.004079222784 0.0 0.0 }
}
{integrate
        { set nvt }
}
{thermostat
        { langevin 1.0 1.0 }
}
{particles {id pos type q}
        {0 -0.933410431074 -4.396367828 4.07839266194 0 1.0}
        {1 80.6308288023 73.5960975815 74.5619693121 0 1.0}
...
        {3583 28.8582652959 75.2256394353 412.044956716 2 -1.0}
}
{bonds
        {0  { } }                    ...
        {206  { {0 205} {0 1} } }    ...
}
{tclvariable  {V1 31840000.0} }
```

Figure 1.1.: Example sketch of an ESPResSo-compatible blockfile (excerpt), displaying some of the different categories as described in the text. Taken from an actual simulation, it contains informations on the simulation box (box length, boundary conditions), the parallelization (from the node grid it follows that this was a single CPU job), and the temporal status ($t = 5200\tau$ with $\Delta t = 0.0125\tau$) in the first block. A bonded FENE- and a nonbonded LJ-potential are defined next, followed by settings for the integrator (standard velocity Verlet, (N, V, T)-ensemble) and the thermostat (Langevin, with reduced temperature $T^* = 1.0$ and friction $\Gamma = \tau^{-1}$). Afterwards, unique identifier, 3D position, type number, and charge (in multiples of the electron charge e_0) are given for all particles in the system, including their bonding information in the next block (showing that no bond is stored with the zero*th* particle, while the 206*th* is connected to particle 205 and particle 1). Finally, the value of a user-defined Tcl-variable `V1` is included, which could *e.g.* represent an observable. Points (...) indicate wherever the output was abridged.

Most architectures ESPResSo supports excel through high availability. Nevertheless, apart from job execution interruptions by simple system maintenance or restricted resources of CPU time, it may also be useful for later offline analysis of particle trajectories or merely for sound scientific documentation that it is easily possible to create *checkpoints* regularly on course of the computer experiment's run that can be used to restart the system in a well defined state. For this matter, invocation of

```
checkpoint_set custom_name.$i.gz
```

from the Tcl-script will create a blockfile `custom_name.$i.gz` which will be compressed automatically, and which stores all available information about the currently executed simulation. This file represents the *i-th* entry to the list of checkpoints. Its filename will be appended to `custom_name.chk`, allowing to keep track of the series of checkpoints built so far. Whenever it is necessary or desired to resume the program,

```
checkpoint_read custom_name.chk
```

will successively rebuild the stored trajectory, continuing the simulation *exactly* at the data status of the last checkpoint.

In addition to reading its own data format, ESPResSo is also able to read or write other file formats, such as pdb/psf-files which are used by visualization software such as VMD [127] and file formats of simulation packages previously used in our work group; there is also an ongoing project to include import and export of GROMOS and GROMACS files. Due to the use of the Tcl-script language, adding new text file formats is particularly easy, which is often necessary if data from self-written simulation codes should be imported to ESPResSo.

1.3.6. Data Analysis

ESPResSo does not only supply the simulation kernel, but provides tools for analyzing the data as well. The analysis can be done both after the simulation is complete and while it is running ("on-the-fly" or "*online*") and the trajectory is still being built. This can be used to implement some simple plausibility checks, *e.g.* for following energy conservation or the temporal evolution of selected observables, allowing to abort the simulation in the case of abnormal values. On the other hand it might be necessary to perform an additional analysis later ("*off-line*") that one did not think of when writing the simulation, so an off-line analysis of stored configurations is also important. Typical derived observables range from the forces exerted on specific particles, the energy or pressure, particle distributions, to typical properties of chain molecules. The pressure can hereby be calculated both tensorial and isotropic.

Radial distribution functions can be computed for specific particle types, allowing for *e.g.* the calculation of the distribution of counterions around a macromolecule.

Implemented observables for chain molecules are the average end-to-end distance R_{E}, the radius of gyration R_{G}, the hydrodynamic radius R_{H}, the average bond length $\langle b \rangle$, the internal distance distribution, and the mean square displacements g_1 of the particles, g_2 of chain particles relative to the chain's center-of-mass, and the center-of-mass displacement g_3 itself. For comparison with scattering experiments, *structure factors*, both as spatially averaged single-chain form factors for polymers, as well as as total structure factors for selected particle species or the entire system, can be calculated (see *e.g.* (4.9) and (5.9) resp. (5.10) later on). For membrane systems, ESPResSo can perform a fluctuation mode analysis [128].

Most of the data analysis does not only average over the current sample, but is also able to optionally average over an entire series of past timesteps stored in memory. For this feature, ESPResSo allows to keep specific configurations loaded, building up an entire trajectory for online analysis; of course, this trajectory can also be saved to disk for later re-usage employing the blockfile format (*i.e.* the `configs`-block).

For a simple error analysis of the averaged observables, the standard deviation of the measured values is computed. The derivation of more abstract error estimates is supported by a simple linear regression, or, for correlated observables, the `uwerr`-command, which calculates the errors of values derived by, in general, nonlinear functions from observables with known correlated errors [129].

1.3.7. Additional Features

In addition to the built-in analysis procedures, there is a fast growing number of Tcl procedures for mathematical treatments, analysis, and general data manipulation. The extensibility of ESPResSo also brought up some more unusual features: ESPResSo can make use of the Tcl extension Tk, which allows for the creation of graphical interfaces. This is useful primarily for writing scripts for visual simulation demonstrations. To this aim, ESPResSo also has an IMD interface that can send configurations during the simulation to the visualization package VMD [127] which can provide animated movies of the simulation trajectories. ESPResSo can automatically generate postscript graphics of graphs using *gnuplot* for direct plotting of any arbitrary combination and functional expressions of measured observables.

1.3.8. Testsuite

Due to the scope and sheer size of ESPResSo it is an important task on its own to ensure the physical correctness of the entire package, its reliability, and backwards compatibility – despite the easy access of all users to all parts of the program. To this aim, each of the major features in ESPResSo (*e.g.* each potential, each integrator, the thermostats, common data analysis routines, specialties such as constraints, partial periodic boundary conditions, external forces, etc.) have their own little testcase which quickly compares the output of the current version of the program to an earlier

reference state, thereby detecting any deviations (maybe inadvertently) introduced in between.

Before submitting modifications to the CVS-repository for future releases of ESPResSo, each developer is required to ensure an error- and warning-free compilation on *all* the officially supported hardware platforms, checking for each architecture whether the testsuite runs through without any problems. The testsuite is build into the project's makefile for the compilation; hence, it can be executed with the single command `gmake test`. By construction all the testcases add up to only a few minutes of computation time to encourage developers to use it as often as possible.

In addition, larger checks testing physical properties of "real" systems provide simple means to also trace more subtle bugs only occurring for specific scenarios or unique combinations of features or circumstances. Being based on previous research projects or "classic" simulation scenarios (*e.g.* the Kremer-Grest study of a polymer melt [34]), these may take considerable longer time to complete. The comparison of the output of the current program version to the published data, however, allows for an excellent test of the overall correctness of ESPResSo. Done on a regular basis, all these verification scenarios are executed and need to be fulfilled when releasing a new version of the code. In this way we hope to keep the number of newly created errors in updated releases bound to a minimum, and to enhance stability of our program package.

1.4. Implementation Details

After having described the overall structure, capabilities, and included algorithms of ESPResSo this section will now focus on details of the implementation, especially of the particle data organization optimized for highly efficient computations in parallel environments.

1.4.1. Data Structures for Parallel Computation

The data ESPResSo needs during the integration are mainly particles, interactions, and constraints. While the number of interactions and constraints is normally small, and simple lists are efficient enough for their storage, the particle data needs some more elaborate organization. as the particle itself is represented by a structure consisting of several substructures, which in turn represent basic physical properties such as position, velocity, force, mass (if enabled), or charge. The particles are organized in one or more particle lists on each node, the *cells*, which in turn are arranged again in one of several possible layouts, the *cell systems*. Each of these defines how the particles are stored in ESPResSo, *i.e.* how they are distributed onto the processor nodes and how they are organized there. The program currently supports three cell

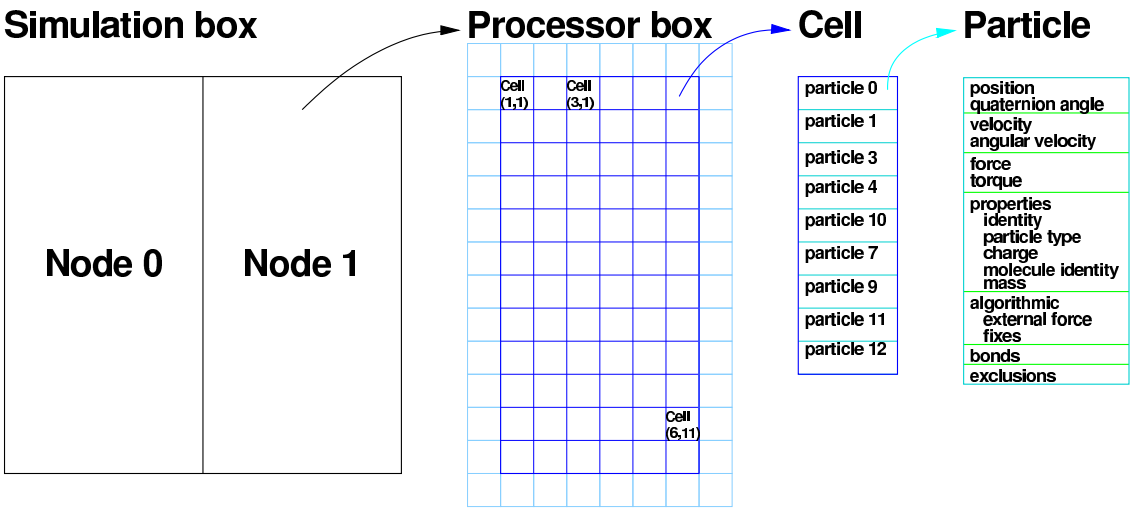

Figure 1.2.: Schematic description of the particle data organization using the domain decomposition cell system within ESPResSo. The simulation box is split up into equally sized regions, each assigned to a single processor and subsequently split up spatially into cells (dark blue squares); around the cells, a shell of additional cells is wrapped that will contain data of the particles from neighbouring processors (light blue squares). The cells are simple arrays of particles, which finally consist of several substructures containing the position, force and other particle data. Depending on the type of simulations, the detailed contents of the substructures can vary (taken from [64, 123]).

systems, namely an N^2-model, a *layered* model, and a *domain decomposition* model. For most simulations (including our own) the last model is used, which is shown schematically in figure 1.2.

Technically, a cell is organized as a dynamically growing array, not as a list, ensuring that the data of all particles in a cell is stored contiguously in the memory. It is accessed transparently through a set of methods common to all cell systems, which allocate the cells, add new particles, retrieve particle information and are responsible for communicating the particle data between the nodes. Therefore, most parts of the code can access informations on the particles safely without direct knowledge of the currently used cell system. Only the force, energy and pressure loops are implemented separately for each cell model, because their calculation is able to benefit directly from the particle organization by *e.g.* deriving the pair forces in linear computation time using the domain decomposition method.

Many pairwise interactions, such as the Lennard-Jones potential, are short-ranged, *i.e.* their value becomes negligible at distances much smaller than the size of the simulated system. As a consequence, only interactions with particles close to each other have to be calculated, and a potential cut-off r_{cut} may be introduced allowing to simply ignore the interaction for distances $r_{ij} > r_{\text{cut}}$. Although already saving quite

an amount of unnecessary potential evaluations, because of the required derivation of the respective particle-particle separation r_{ij} this would still remain an algorithm with a computation time scaling of $\mathcal{O}(N^2)$, *i.e.* the number of necessary operations growing quadratically with the number of particles. The *link cell algorithm* [47, 130, 131], on which the *domain decomposition cell system* in ESPResSo is based upon, therefore introduces additional *cells* at the beginning of the simulation which fill the entire box volume and contain *links* to all the particles in their spatial domain (thus "link cells" as their name), with their size chosen slightly larger than the maximal interaction range r_{cut}. In the force calculation only interactions between particles in adjacent cells have then to be calculated, because by construction the distance r_{ij} between any particle i in a given cell to any particle j in the next-nearest cell is larger than r_{cut}, the lower limit for the width of the cell in between. Instead of looking at all possible particle pair combinations, one now has to only loop over the 27 neighbours of each cell (in three dimensions), reducing the computational effort to $\mathcal{O}(N)$ at constant density and interaction ranges (which keep the number of particles in a cell constant), as this algorithm looks at each cell (*i.e.* each particle) only once.

Parallelization of the force calculation within the domain decomposition cell system is straightforward, too. The simulation box is split up into a number of smaller sections corresponding to the amount of processors available, aiming for equal section sizes but not necessarily for isotropy (*i.e.* distributing a cubic box onto two processors results in non-cubic sections with $(L/2, L, L)$ as subbox lengths). The particles are then assigned to the processor that is responsible for the subbox they are located in, before each subbox is subsequently divided up into the domain decomposition cells previously discussed. Since for the force calculation mentioned there the particles in *all* neighbouring boxes are needed, the cells adjacent to each subbox are required as well to be able to compute the interaction of objects in the outermost layer of cells on the processor to those on the next one. To this aim, that layer is replicated as *ghost shell* on all neighbours, with the particle copies contained therein being the *ghosts* [89], see the sketch in figure 1.2. While all the other particles are only needed on the processor possessing their cell, ghosts need to be communicated between nodes once every timestep; as a consequence, this parallelization scheme is useful for *short*-range (*i.e.* r_{cut} small) interactions and homogeneous systems because in that regime the amount of communication required for transferring the ghosts between nodes is much smaller than the time spent on actually computing forces between the particles *on* the node. (As mentioned in section 1.3.3, "real" long-range interactions, *i.e.* those without a potential cut-off, have an entirely different parallelization scheme, independent of the cell system employed.)

Each of the integration schemes (see section 1.3.2) uses equations of motion temporally discretized to propagate the entire system. Every timestep might thereby move particles out of their cell, which would require updating the link cells, even causing costly particle transfers between nodes in a multiprocessor environment. To

reduce the amount of updates, it is possible to exploit the cell size being constructed slightly larger than the maximal interaction range r_{cut}, with their difference r_{skin} acting as a *skin* for the particles. As long as none of them moved further than $r_{\text{skin}}/2$, the distance of two particles did not increase by more than r_{skin}, such that adjacent cells still contain all interacting particle pairs, and the link cells do not have to be updated. Storing its spatial position $\vec{r}_{\text{old}}$ during the creation of the current set of cells, finding one particle at $\vec{r}$ with $|\vec{r} - \vec{r}_{\text{old}}| > r_{\text{skin}}$ will then trigger the re-creation of the link cells (and overwriting of $\vec{r}_{\text{old}}$ with $\vec{r}$). In actual simulations, the skin can become as large as $20 - 40\%$ of the maximum interaction range, while the particle lists turn out to be updated *e.g.* every $15 - 35$ timesteps when running ESPResSo on an average AMD Linux-PC. To safely cover a wide range of simulation conditions, the distance criterion is checked after *every* integration step, in contrast to many other programs.

Contrary to the original version, the domain decomposition cell system implemented in ESPResSo does not use links to the particles but has the cells contain their data directly. Although this creates considerable overhead once the lists have to be rebuilt, since now the entire physical particle information needs to be moved to its new location instead of simple re-setting a pointer, it also avoids a lot of indirect particle accesses through the link cell pointers, actually accelerating access to the data now stored in larger contiguous blocks. This is advantageous especially on modern computers, where not only random memory access is quite slow while continuous transfers circumvent most of the addressing issues, but clever prefetching algorithms already load data they think to be required next while the current calculation is still executed – and during the processing of a contiguous memory block these guesses are rarely wrong. To support this, looking at a double data rate RAM module at 200 MHz, less than 50 words per microseconds may be read from random positions, while a contiguous block of memory will be fetched at a rate of more than 250 words per microseconds, corresponding to 1 GB/s instead of 200 MB/s. In contrast, an AMD Opteron processor can multiply 500 double precision floating point numbers per microsecond, clearly identifying main memory as the bottleneck of our computer simulations. It can be partially bypassed by the processor cache which is small but operates at the full processor clock speed, corresponding to more than 700 words per microsecond; its size, however, is only sufficient for about 1000 particles. In the benchmark section 1.6 this effect will be demonstrated, *e.g.* timing simulation runs with an increasing number of particles which will clearly exhibit a significant slowdown once the cache size is no longer able to hold all their data.

The optimal value for the skin is hardware-dependent because it reflects a trade-off between larger cells (for larger r_{skin}), causing more particles to be part of the distance and force calculation loop, and smaller r_{skin}, enforcing more frequent list updates; while the former is favored by systems with low memory bandwidth, as it reduces the frequency of particle data reorganization, the latter is preferred by memory systems with a high throughput compared to the floating point performance,

because it minimizes the computational effort. As it is also a question of whether the architecture is more efficient in accessing the memory or shifting particles between nodes or prefetching desired data into its caches, no general statement can be made; ESPResSo however contains an automated tuning routine which invokes several integrations at different skin values for the user's current system, choosing the parameter set running the least amount of time. Due to its different memory organization, the optimal skin values of ESPResSo are slightly larger than the values typically used in other programs, which simply reflects that the particle reorganization is more, while the interaction calculation is less costly.

In a simulation box with an *e.g.* cubic geometry of length $L = 20\sigma$ and 2 processors, each will be responsible for the particles within a non-cubic subbox of $(10\sigma, 20\sigma, 20\sigma)$. If the maximal interaction range is 1.2σ, the minimal possible cell size is 1.25σ for 8 cells along the first spatial coordinate, allowing for a small skin of 0.05σ, while it increases to 0.467σ for only 6 cells assigned to the first coordinate. Assuming the cells to be cubic (the subbox is not!), the latter would be organized by ESPResSo on each node in a $6 \times 12 \times 12$ cell grid embedded at the center of a $8 \times 14 \times 14$ grid, where the additional cells represent the ghost shell in which the information of the ghost particles from the neighbouring nodes is stored. This has the particle information to reside in 1568 particle lists per node, with 864 of these actually containing particles assigned to that processor, while the remainder consists of ghosts from other nodes.

The other two cell systems, namely the N^2-cell system and the layered cell system, are not as efficient as the domain decomposition and are only used in conjuction with certain potentials. The *N^2-cell system* derives the interactions for all particle pairs, as is necessary *e.g.* for MMM1D, a method for the calculation of the electrostatic interaction in one dimensionally periodic systems, or for the computation of the electrostatic interaction with no periodic boundary conditions at all, *e.g.* in a simple cell model that possesses hard or open boundaries. Since both examples require all interactions to be calculated anyway, a domain decomposition is unnecessary, and its organizational overhead would only decrease the (already poor) performance further; the only optimization applied therefore restricts to the particles being load balanced at the beginning of the simulation, *i.e.* the particle number does not differ by more than one from the average particle number on each node, without resorting them during the simulation.

The *layered cell system* is specificly designed for MMM2D, a method for the calculation of the electrostatic interaction in two dimensionally periodic systems, although it may be used for other algorithms, too. Being a combination of the domain decomposition and the N^2-method, it splits the system into cells or layers only along the z-coordinate, treating interactions with particles in adjacent layers only.

The concept of having multiple cell systems allows for quite different data organization schemes, enabling ESPResSo to provide whatever framework some state-of-the-art algorithms require, and is also quite unique for a simulation package of this

scope. It renders the program code to be somewhat easier to read, making the addition of new cell systems rather simple if a new algorithm should require a different particle organization. As a consequence, it nicely reflects the design goals we set out to fulfill in section 1.2.

1.4.2. Topology Information in ESPResSo

The topology of a simulation system is what distinguishes *e.g.* a simple LJ-liquid from a polymer melt from a rubber-like network. Being both global and local property, different concepts on how to implement, store, and process bonds and connections seem suitable depending on the desired application.

For the integrator, only informations related to the calculation of interaction forces are required. It is therefore sufficient to store only reduced topology informations, *i.e.* a bond list containing the bond type and the unique identifier of all bond partners, locally at each particle, which is then always present where needed. This also allows the user to specify whatever topology desired on the script level, connecting individual particles using

```
part <ID> bond { <bond_type> <bond_partner1> ... }
```

or relying on some of the predefined geometries such as the `polymer`-command already discussed in section 1.3.1. It additionally grants the ability to change the topology at all times during the simulation run, adding/removing/modifying bonds, bond partners, or bond potential parameters. Usually, this is sufficient for the integrator, rendering any additional topological concepts such as molecules, polymer chains or residues in a protein unnecessary, and thereby avoids ambiguity *e.g.* in a random network where "molecule" would loose most of its unique meaning. For some applications it is nevertheless advantageous to distinguish inter- and intramolecular interactions, *e.g.* in a phantom model [132, 133] where the chains entangle and interact with each other, but not with itself. In addition to the particle type, determining non-bonded interactions, each particle therefore has a *molecule identity* as well which can be used in the potential derivation.

In contrast to the integrator, data analysis usually requires knowledge of the global topology to be effective, as otherwise *e.g.* for the derivation of the end-to-end distance in a polymer melt the algorithm would have to loop through *all* particles, trying to reconstruct which particles are actually joint on the same chain and identifying the end monomers before being able to start the actual calculation of the observable; in a network, where the node-node separation takes the place of the end-to-end distance, the pattern recognition would be even more difficult (and time consuming). Thus, the topology in the analysis routines of ESPResSo is stored as a list of molecules, each containing a sorted sequence of particle identities, such that the aforementioned example would simply have to look at the first and last entry in each molecule's list to access the particle positions of the end monomers.

As illustrated in figure 1.3, the three topology concepts are by default independent from each other, with separate interfaces connecting them to the simulation script. If desired, it is however possible to synchronize all three such that they describe the same structure. Within this concept, any topology containing n-body interactions can be handled; the number of bond partners is merely restricted by the potentials implemented.

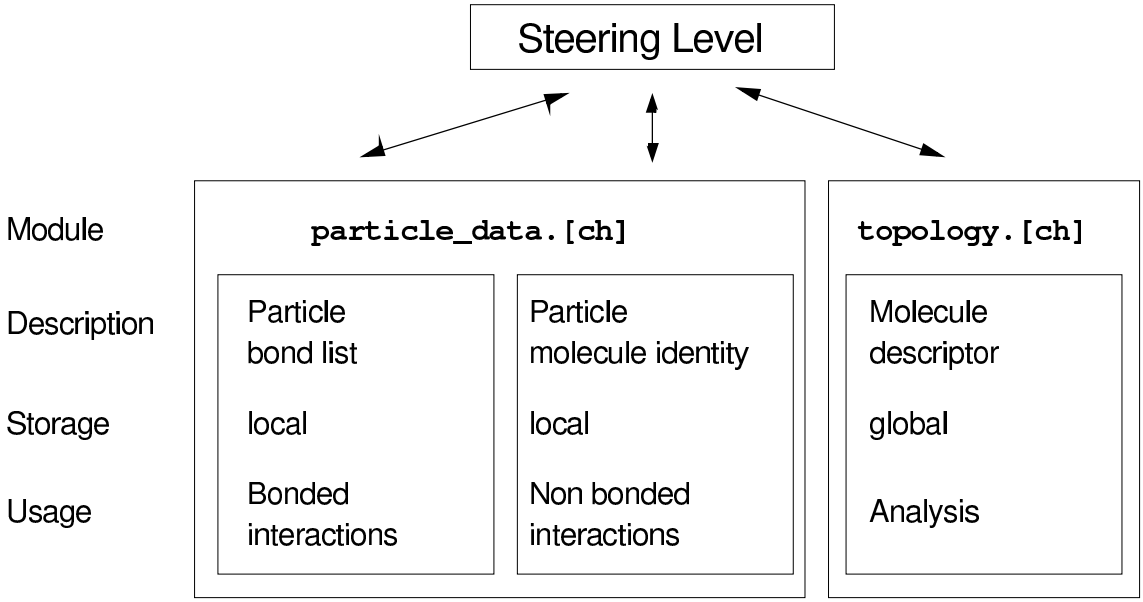

Figure 1.3.: The three different topology concepts in ESPResSo. Shown are the location in the program package, the type of data storage, and their main usage (taken from [64]).

1.4.3. Internal Program Flow

The Tcl-simulation script is processed by a Tcl-interpreter on a single node, the *master node* or *node* 0, while all other nodes (*slaves*) are standing by and wait for commands to be issued from the master node. For any non-Tcl-statement the interpreter encounters, the Tcl-connection built into the code upon compilation will allow to find and invoke the appropriate C-procedure in ESPResSo, which by convention has the same name as the calling command, *i.e.* `setmd` will call the C-procedure "`setmd()`", with the variable name and value as (string) parameters. The C-procedure then parses the input and performs the desired operations, *e.g.* setting or retrieving the value of a global variable. In a multiprocessor environment, most commands cause changes in the entire system (a modified global parameter, for example, must be known to all other nodes, too), which is why the C-function on the master node will issue a communication request in such cases, transferring the necessary informations

to the slaves and invoking an appropriate procedure there, *e.g.* updating the value of the local copy corresponding to the global variable in question. Since the amount and sequence of commands coming from the master node during this process is *a priori* unknown, the communication is asynchronous.

ESPResSo allows to change anything accessible from the script at any time, even on course of the simulation run. This requires special efforts to ensure continued consistency within the system, as a change in the processor grid, for example, might change the association of the particles to the different nodes which would have to call for a rebuilt of the internal particle structures. Similarly, if the Bjerrum length is changed, the currently used method for the calculation of the electrostatic interaction has to be reinitialized; moreover, if this happens during the simulation, the forces stored in the particles for the current configuration are invalid and have to be recalculated. Due to the large number of algorithms implemented in ESPResSo, such dependencies are actually even more complex, which is why the sample scripts are so important in tracing possible conflicts of this kind (see section 1.3.8). They are to be resolved by handler procedures, dealing with common events such as changes in a global parameter (calls `on_parameter_change()`) or in one of the electrostatic methods (calls `on_coulomb_change()`, is also called by `on_parameter_change()`); these are covering a rather general range of steps to be taken to keep the state of the simulation consistent, even if that implies *e.g.* reinitializing more parts of the code than absolutely necessary. While it does not affect the actual speed on the simulation engine level because such changes are usually invoked from the Tcl-script[4] where efficiency is not as important, it greatly increases the robustness of the code which by itself would already justify any minor drawbacks in computational speed.

One of the asynchronous commands (usually `integrate`) starts the propagation of the system in time, the integration. During the integration, ESPResSo uses synchronous communication as do all other simulation programs for efficiency reasons, *i.e.* every node has to know without prior request which MPI communication follows. This is less robust than the asynchronous communication scheme, but the request–answer structure creates too big of an overhead, and is not needed in the integration, if everything is implemented properly.

1.4.4. Error Handling

The Tcl-command extensions of ESPResSo use the standard Tcl-error return mechanism to report erroneous execution. If the error is not caught, this mechanism will terminate script execution and output a script backtrace, which, together with comprehensible error messages, allows to easily identify the source of the error.

[4] There are exceptions such as the (N, p, T)-integrator which are modifying global system properties (*i.e.* the box length) at every single timestep which would be unfeasably slow if `on_parameter_change` was to be executed everytime; in those cases only the necessary adjustments were isolated and are now separately called by this functions.

However, as the Tcl-interpreter exists only on the master node, ESPResSo implements its own error reporting scheme for the other nodes. Moreover, an immediate error reporting during the synchronous phase, *i.e.* integration, would be ineffective. Instead of terminating erroneous conditions, only an error message is placed in an error buffer, and the parameters are adjusted such that execution can temporarily continue. During the integration loop and just before completing any Tcl-command execution, the master node then checks regularly for errors from the slaves, creating a regular Tcl-error if an error condition is found. Such *background errors* are reported in addition to regular Tcl-errors as a string like

```
background_errors 0 {<error>} {<error>}...
        1 {<error>} {<error>}...
```

Following the `background_errors` keyword, the error messages are listed, preceded by the number of the node that raised the error. If all nodes report the same error, for example, an unset timestep, then instead of repeating the error messages, a simple `<consent>` is output for each node except the master. A typical example is

```
background_errors 0 {010 time_step not set} {011 skin not set}
        {012 thermostat not initialized} 1 <consent>
```

which is the result if the integrator is started without setting up anything. Typical examples, where the messages are different from node to node, are broken bonds, which look like

```
background_errors 0 {083 bond broken between particles 1 and 0}
        1 {083 bond broken between particles 22 and 23}}
```

Each error message is assigned a unique three–digit code to support automated parsing of error messages. There are various applications of this feature, for example testing simulation parameters for validity during tuning, or speeding up warmup up by using larger timesteps. If a bond breaks, one can simply return to an earlier timestep, simulate more carefully for some time, and then raise the timestep again. For polymer networks, this allows to reduce the warmup time considerably, while it is an almost mandatory feature for employing the (N, p, T)-algorithm to charged hydrogels where the box fluctuations may become so large that they rupture the bonds of the network strands; as in the latter example the simulation remains physically sound, reverting to a previous timestep and simply increasing the piston mass Q ensures further survival of the experiment (see section 4.1 for details).

1.5. Documentation

ESPResSo is not intended to be a black-box-like package. Users are encouraged to try to understand its algorithms and routines, and developers are strongly advised

to do so before extending it. In order to preserve the knowledge about algorithms and their physical/chemical background, it is important to provide and maintain a well structured documentation.

The hierarchical program design is reflected once more by its organization. The first information for the user is a separated documentation of the Tcl-extensions to steer the simulation, to organize the data in- and output, and to analyze the resulting observables; examples are the `part` command that modifies the particle data, or the `analyze` command that performs data analysis. It also contains documentation of Tcl-procedures that serve to abbreviate common programming tasks on the script level, for example setting up a polymer chain. In the meantime, we have also realized a thorough documentation of the program flow, the integration schemes, and the basic data structures to give new users an introduction to the general program design and an overview of the connection between the different modules.

The largest part of the documentation is done within the program code itself and will be automatically extracted, processed and linked to the above described parts with help of the `doxygen` program [134]. The result is a cross-referencing HTML documentation or a pdf-user manual. It is important to note that also the documentation of the Tcl-commands and the underlying physical principals and algorithms is directly linked to the corresponding source code documentation.

Changes and extensions made during the development process are documented via the log function of the CVS-environment (concurrent version system [135]) where the project resides in. To make important changes more visible to both users and developers, the `RELEASE_NOTES`-file contains information about all new features, relevant changes, and important bug fixes in a condensed and easily accessible way.

1.6. Benchmarks and Comparison

While the general aim in the development process of ESPResSo had been directed towards the flexibility and extensibility of a simulation package and its portability to a wide range of commonly used scientific computation platforms and architectures, ESPResSo is also comparable in performance with other state-of-the-art simulation codes in both single CPU and multi-processor environments. ESPResSo does not use platform-dependent optimizations, but the clever particle organization (see section 1.4.1) together with algorithms like P^3M or ELC nevertheless results in a high-performance code. With Moore's Law still valid and the continuous plunging of costs for faster and more powerful computers, it is no longer economically expedient to invest human resources into developing hardware-related algorithms: Often the achievable speed-up becomes more than overcompensated by technological advancements during the time frame of the implementation, particularly since switching to different platforms or different scientific problems usually renders these optimizations useless. In this section, the performance of ESPResSo will be demonstrated

using several benchmarking scenarios on various hardware platforms (systems).

We begin by demonstrating the scaling of the computation time with the number of particles on a single AMD Opteron 246 processor. The benchmark scenarios are:

b1 a simple Lennard-Jones (LJ) liquid:

The scenario consists of N particles in a cubic simulation box at a density of $\rho = 0.8442\sigma^{-3}$, with a purely repulsive Lennard-Jones potential as the only interactions between them. Simulating a (N, V, E)-ensemble, the timestep was chosen to be $\Delta t = 0.00462\tau$.
This scenario only uses the short-ranged nonbonded interactions of ESPResSo. It is relatively dense, leading to a large number of simple interactions to be calculated; therefore, this benchmark stresses especially the memory architecture of the used hardware platform.

b2 a dilute electrostatic scenario:

The scenario consists of N unit charges in a cubic simulation box at a density of $\rho = 10^{-3}\sigma^{-3}$. Half of the particles are positively charged, the other half is negative. The Bjerrum length, characterizing the strength of the electrostatic interactions, is set to $\ell_B = \frac{e^2}{4\pi\epsilon_0\epsilon_s k_B T} = 2\sigma$, and again the particles also interact via a purely repulsive Lennard-Jones potential. The temperature is now set to $T = 1\epsilon$, which is maintained using the Langevin thermostat with a friction coefficient of $\Gamma = \tau^{-1}$, and a timestep of $\Delta t = 0.001\tau$. For the calculation of the electrostatic interactions the P^3M algorithm is used, tuned to a force error smaller than $10^{-2}\epsilon/\sigma$.
Here, the calculation of the long-ranged electrostatic interactions dominates the computation time, while memory bandwidth only plays a minor role compared to the floating point performance of the used CPU architecture.

b3 Kremer-Grest polymer melt:

The scenario consists of N particles in a cubic simulation box at a density of $\rho = 0.85\sigma^{-3}$ grouped into polymer chains of 100 monomers each; in addition to a purely repulsive Lennard-Jones interaction between beads, their bonds are constructed by a FENE-spring-potential with $k_F = 30\frac{k_B T}{\sigma^2}$ and $r_F = 1.5\sigma$ (parameters taken from [34]); a timestep of $\Delta t = 0.006\tau$ with $T = 1\epsilon$ and $\Gamma = 0.5\tau^{-1}$ was chosen.
It tests the ability of ESPResSo to deal with bonded interactions, and allows to compare this additional effort to the plain Lennard-Jones liquid *b1* at a similarly dense density.

b4 (N, p, T) constant pressure thermostat:

The scenario is identical to the simple Lennard-Jones scenario, but uses the (N, p, T)-integrator of ESPResSo to maintain a constant pressure of $2\epsilon/\sigma^{-2}$. The (N, p, T)-algorithm prohibits the use of Verlet lists, therefore this test shows the efficiency of the plain link cell implementation.
It also displays a typical performance difference when using ESPResSo's extensibility to modify or rewrite its core integration routine, since the (N, p, T)-algorithm is implemented as (optional) addition to the standard velocity Verlet integration scheme.

The time measurements are performed using a Tcl control script to ensure realistic numbers representing an entire integration cycle, rather than only measuring the execution times of specific parts of the simulation code. For each benchmark case, five independent pre-equilibrated configurations were integrated for 1000 MD steps each, and the computation time per particle and timestep was measured. Prior to this, the cell size ($\rightarrow r_{\text{skin}}$, see section 1.4.1) and, for the electrostatics scenario, the P^3M parameters were automatically tuned using the built-in tuning functions. For all benchmarks only minimal ESPResSo components were compiled in (*e.g.* no electrostatics for the neutral cases *b1*, *b3* and *b4*), and compiler flags for platform-dependent optimization were used where available. Throughout this section computation times are given as wall times, as measured by the Tcl-command `time`.

Figure 1.4 shows the resulting computation times. As expected, the electrostatic scenario *b2* is the slowest scenario, compared to the simple Lennard-Jones liquid it is slower by a factor of ≈ 3.5. The computation time for this scenario shows a typical festoon shape, which is generated by the interplay of the constant FFT computation time at fixed mesh size and an increasing real space computation time. Whenever the real space computation becomes too costly, the optimal mesh size increases, creating a larger constant offset.

For all other scenarios, the computation time per particle decreases slightly for up to 1000 particles. This simply reflects that the computation time scales proportional with the number of the particles plus a small constant overhead, which becomes negligible with increasing number of particles. The data of more than 500 to 1000 particles and the necessary organizational data no longer fit into the 1MB L2 cache of the Opteron, and more and more data has to be fetched and put back to the slower main memory. When finally the entire particle data has to be read from main memory, the computation time is around 70% larger compared to the calculation that completely uses the cache. This drop is easily understood from the fact that even linear main memory accesses are three times slower than cache accesses, see section 1.4.1. Nevertheless, 1.4μ s per particle and timestep is still a very good performance and comparable to other simulation codes. The cache effect is not visible in the electrostatics scenarios, since the slowdown through the grid discretization is much stronger.

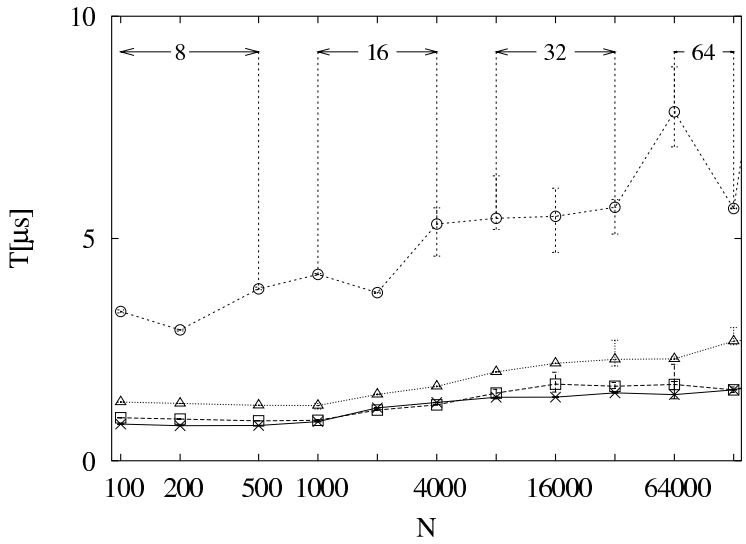

Figure 1.4.: Computation time T in microseconds per particle and timestep of ESPResSo for various benchmark scenarios with different numbers of particles N, each run on a single AMD Opteron 246 processor. The symbols stand for the scenario *b1* (crosses), *b2* (circles), *b3* (squares) and *b4* (triangles). The arrows denote the P^3M mesh size used, *e.g.* 8 for up to 500 particles, 16 for up to 4000 particles and so on. For details on the scenarios, see text.

It is remarkable that the additional computation of the bonded interactions in the Kremer-Grest scenarios does not lead to a significant increase in the computation time. This shows that, once the organizational part of the integration is done and the particle data is loaded into the fast L1 cache of the CPU, the computation time spent in the actual force calculation is almost negligible, not least due to the computationally cheap choice of the bond potential [34] having only a logarithm in the FENE formula (4.1) instead of the usual square root of the harmonic (Gaussian) one.

The approximately constant offset between *b4* and the two fastest scenarios (*b1* and *b3*) originates in the (N, p, T)-algorithm itself, which requires an additional amount of operations for each particle (*i.e.* pressure evaluations, coordinate rescaling, and thermostat application) without further accesses to stored data; consequently, the computation time increases compared to *b1* and *b3* while displaying the same cache-related behaviour on the amount of particles N in the simulation. Efficient bookkeeping tricks such as the employment of Verlet-lists cannot be used for the (N, p, T)-algorithm because in the environment of a fluctuating simulation box with a continuously rescaled coordinate system it is not possible to define a suitable distance criterion, which signals whenever particles from a cell have moved "too far" such that the Verlet-lists would have to be updated, as long as there is not distinction possible between "real" particle movement based on the force

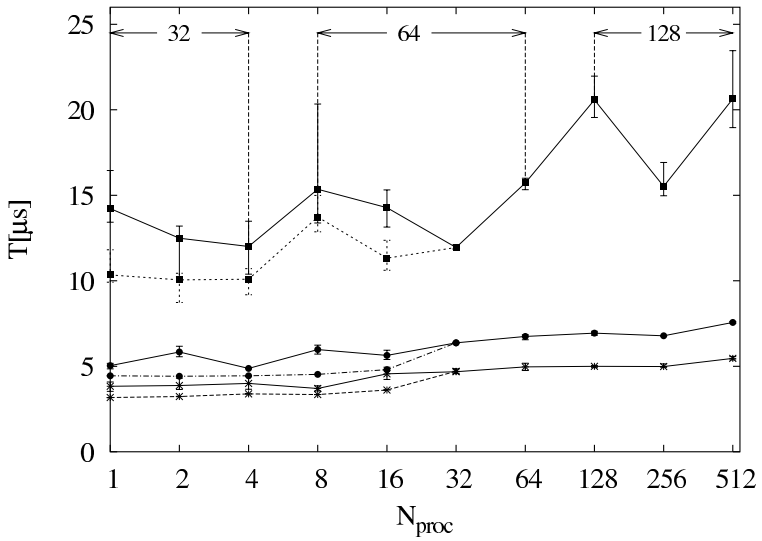

Figure 1.5.: Computation time T in microseconds per particle and timestep of ESPResSo for the benchmark scenarios *b1* (stars), *b2* (squares), *b4* (circles) on an IBM Regatta system of up to 16 pSeries 690 with different numbers of processors N_{proc} and 4000 particles per processor. For each scenario, the dotted, lower lines denote results for an otherwise unloaded 32 processor machine, while the solid, upper lines represent data for a fully loaded machine.

fields and "virtual" displacement due to changes in the box volume[5]. Without the Verlet-lists, *b4* encounters an N-dependent slowdown due to the need to assess all $\frac{27}{2} \cdot (\#\text{ of cells})\frac{1}{2}(\#\text{ of particles per cell})^2 \sim N$ interactions per cell (as the number of cells scales with the number of particles) and the additional operations required to calculate the pressure (which is done on-the-fly during the integration, *i.e.* consisting of a constant number of operations per particle), plus the administrative overhead for adjusting the box dimensions (negligible, as it is only required once per timestep), *i.e.* the offset exhibited in figure 1.4 depending on the amount of particles N alone.

For a parallel simulation code the scaling with the number of processors is as important as the scaling with the number of particles. In figure 1.5 we demonstrate the scaling of ESPResSo for the simple Lennard-Jones liquid scenario *b1*, the electrostatics scenario *b2*, and the (N, p, T) scenario *b4* on an IBM Regatta system consisting of up to 16 pSeries 690 system with 32 Power4 CPUs running at 1.3 GHz each. The Kremer-Grest scenario *b3* was not repeated on the multiprocessor system, as it is very similar to the Lennard-Jones scenario (see figure 1.4). The number of particles was chosen proportional to the number of processors, namely 4000 particles per pro-

[5] It would be possible of course to track all particles accordingly to obtain this information, however the administrative and computational cost would simply be too high.

cessor. For less than 32 processors, a single machine was used for two runs, one on an otherwise unloaded machine and one on a fully loaded machine (which is the more realistic scenario, but naturally generates larger error bars and may increase the computation time if memory access is the bottleneck). For more than 32 processors, we always used entire 32 processor machines, interconnected by an IBM federation switch.

From the computation times given in Fig. 1.5, it is easy to calculate the speedup factors for ESPResSo which are defined depending on the number N_p of employed processors as the computation time used on a single CPU divided by the computation time for N_p processors. For testsystem *b1*, the factor is between 95% and 105% for 1 to 16 processors, 85% for 32 processors, and slowly drops to 70% for 512 processors, which is comparable to *e.g.* the benchmarks known from LAMMPS [136].

Both *b1* and *b4* scale extremely well with the number of processors. For the *b2* scenario ESPResSo shows the typical festoon behaviour, which was already observed in the single CPU benchmarks, and which is due to the complex interplay of FFT time and real space calculation time. It should be noted that ESPResSo scales extremely well up to 512 processors or 2 million particles, even for the electrostatic scenario, and there is no fundamental reason that ESPResSo should not able to run on even larger supercomputers.

In the *b2* scenario, the Regatta system switches faster to higher grid sizes, which simply reflects that the Regatta FFTW implementation performs extremely well. Again, the additional computational effort required for the (N, p, T) is responsible for a constant (*i.e.* N-dependent) decrease of that scenario's performance compared to the LJ-liquid's case. For the *b1* and *b4* scenario, there is a noticeable computation time difference between a fully loaded and an unloaded machine. This is a result of the shared memory architecture of the Regatta system: The CPUs are organized in dual core units with a small shared L2 cache of only 1.44MB. Four of these dual core units form a processor board with a total of eight processors, which share an additional L3 cache of 32MB. If all 32 processors are loaded, the L2 cache per CPU is 768kB, which is not enough for 4000 particles, and the CPU has to resort to the L3 cache. However, if only one processor per dual core is active (as is the case for $N_{proc} \leq 16$ on an otherwise unloaded machine), then it can use the full 1.44MB L2 cache, which is sufficient for the data of 4000 particles. Since in a production environment normally all 32 CPUs will be loaded, the numbers for the loaded system are more realistic regarding *e.g.* estimation of required CPU time for a given project, although the unloaded machine illustrates the theoretical performance of ESPResSo as determined by its algorithms and program design.

In contrast to the memory organization of the Regatta system, the federation switch shows a high performance and does not seem to add a noticeable additional performance loss for less than 16 machines; even for 16 machines, the impact is only small. Therefore, it should be possible to simulate scenarios of several million charged (!) particles using ESPResSo on a sufficiently large IBM Regatta system.

Now that we have shown the scaling of ESPResSo for some of the built-in algorithms on a single CPU and a multiprocessor system, we finally want to compare results from different architectures, *i.e.*

s1 dual AMD Opteron 246, 2 GB RAM, S.u.S.E.-Linux 9.1, gcc 3.3 [137]

s2 single AMD Athlon64 3200+, 1 GB RAM, S.u.S.E.-Linux 9.1, gcc 3.3

s3 dual AMD AthlonMP 2000+, 1 GB RAM, S.u.S.E.-Linux 9.0, gcc 3.1

s4 dual Intel Xeon 2.8 GHz, 3 GB RAM, RedHat 9.0, icc v8.0 [138]

s5 dual Apple G5 2.0 GHz, 1 GB RAM, MacOS X (Darwin 7.4.0), gcc 3.3

s6 IBM pSeries 690 Turbo, 32-way Power4 1.3GHz, 64 GB RAM, AIX 5.2, IBM xlc V6

s7 IBM pSeries 655, 8-way Power4 1.7GHz, 16 GB RAM, AIX 5.2, IBM xlc v6

s8 dual Alpha 21264 833MHz, 3 GB RAM, Tru64 V5.1A, Compaq C V6.4

Again, the benchmarking scenarios *b1* and *b2* were run five times with 4000 and 16000 particles on each architecture, measuring the computation time per particle and timestep, as well as the used number of cells N_{cells} and mesh points per dimension. The majority of the systems are multi processor systems with varying numbers of processors, however for comparability all scenarios were done on only *one* of the CPUs. All other CPUs were loaded with other simulations as in a typical production environment. Although this perturbs the measured computation times a little bit (for systems with shared access to the memory banks, *e.g. s3* or *s6*, but *not* for systems such as *s1* which have a n-way connection between CPU and RAM), it gives the best picture of what one can expect when running ESPResSo for production. The results are shown in table 1.1, giving an overview of the efficiency of ESPResSo on the various platforms.

For scenario *b1* and 4000 particles, the maximal possible number of cells is 14, for scenario *b2* 8 cells with a FFT mesh size of 16 and a charge assignment order of 3, and 15 cells for a mesh size of 32 and order 3. The optimal grid sizes for the scenarios are slightly smaller, and correspond to skin sizes of $0.3 - 0.5\sigma$. For 16000 particles, the maximal number of cells is 23, and the chosen cell sizes correspond to skin sizes of $0.3 - 0.6\sigma$. Despite the fact that the number of cells is chosen automatically by a simple golden section search, the resulting cell sizes correspond to skins which are only slightly larger than the values typically used by other simulation codes, ranging from 0.2σ to 0.4σ. The reason for this is the link cell implementation of ESPResSo requiring more memory operations during the particle reorganization, making it slower compared to other implementations, while the building of the Verlet list and

system	$T_{b1}[\mu s]$	N_{cells}	$T_{b2}[\mu s]$	N_{cells}	mesh
s1	1.31 (1.31,1.31)	10	5.32 (4.60,5.69)	8	16
s2	1.58 (1.57,1.59)	10	4.87 (4.85,4.89)	8	16
s3	3.35 (3.34,3.35)	10	11.36 (10.50,12.72)	7.6 (6,8)	16
s4	2.18 (1.99,2.48)	10.4 (10,11)	7.55 (5.66,10.24)	7.4 (7,8)	16
s5	2.27 (2.26,2.27)	10	8.69 (7.39,10.64)	7.6 (7,8)	16
s6	3.83 (3.54,4.08)	10.7 (10,11)	14.23 (13.43,16.45)	11.8 (7,14)	28.0 (16,32)
s7	2.37 (2.37,2.38)	11.2 (11,12)	7.58 (7.28,8.66)	13.6 (11,15)	32
s8	2.26 (2.23,2.29)	10.8 (10,11)	9.75 (9.70,9.82)	8	16
s1	1.53 (1.41,1.83)	15.9 (15,16)	4.77 (4.72,4.91)	14	32
s2	1.63 (1.63,1.64)	16	5.79 (5.76,5.81)	14	32
s3	4.11 (3.47,5.44)	15.6 (15,16)	15.88 (15.21,16.51)	13.6 (12,14)	32
s4	3.14 (3.06,3.17)	15	10.19 (7.58,12.05)	13.4 (13,14)	32
s5	3.05 (2.82,3.36)	15.8 (15,17)	9.27 (8.48,11.32)	13 (10,14)	32
s6	5.52 (4.26,6.64)	18.3 (15,17)	18.84 (14.06,22.47)	11.6 (11,13)	32
s7	2.60 (2.56,2.63)	17.8 (17,18)	7.16 (7.07,7.39)	14	32
s8	3.01 (2.93,3.07)	16.8 (16,17)	11.48 (11.34,11.60)	14	32

Table 1.1.: Computation time T in microseconds per particle and timestep for the *b1* and *b2* scenarios with 4000 (top) and 16000 (bottom) particles on the platforms described in the text. N_{cells} denotes the used cell grid sizes (due to the symmetry of the scenarios, the cell grid is always cubic, *i.e.* $N_{cells} \times N_{cells} \times N_{cells}$). For the *b2* scenario, the Coulomb mesh size is shown as well. The numbers are given as *average*(*min*,*max*) of the five runs performed for each system. If minimum and maximum are not given, all five measurements produced the same value.

the force calculation are somewhat faster. The larger skin sizes that are optimal for ESPResSo reflect this, since a larger skin means less frequent particle reorganization steps (see section 1.4.1).

Systems *s1* through *s5* favor smaller cell grids compared to systems *s6* through *s8*, especially for 16000 particles. Since the cell grid size represents a trade-off between an increased number of particle moves for large numbers of cells, and an increased number of particle distance calculations for smaller grids, this means that memory operations are fast compared to floating point operations on the latter systems. This is an effect of the different cache sizes of the used systems: Systems *s1* through *s5* have L2 cache sizes of at most 1MB, and only system *s4* has an additional L3 cache of 2MB per CPU; thus, only for system *s4* 4000 particles fit into the L3 cache. In contrast, systems *s6* and *s7* have 1.44MB L2 cache per two CPUs and 32MB L3 cache per eight CPUs, and system *s8* even has an 8MB L2 cache, allowing the latter systems to easily fit the data of 16000 particles into their caches, increasing the memory performance dramatically.

The outstanding performance of the AMD 64-bit systems *s1* and *s2* is due to their large memory bandwidth and the additional 64-bit registers, which can host floating point numbers and consequently speed up the force calculation. In contrast to this, the performance of the IBM pSeries 690 system is rather weak. The much better performance of the pSeries 655, which has a faster memory bus, as well as the multiprocessor results for the unloaded machines suggest that the primary reason for this lies in the memory performance of the pSeries architecture, despite the

large caches. For the electrostatic scenario *b2*, the efficiency of the FFTW routine is important, which on the Regatta is much better than the performance of the other ESPResSo components.

Compared to high performance MD simulation codes like GROMACS or LAMMPS, ESPResSo excels through its parallelization where it is much faster than *e.g.* GROMACS, although under certain conditions it may also be somewhat slower, depending on the used hardware and the benchmark scenario employed. The main reason for such a performance drop in those cases is the flexibility of the cell systems. Unlike the other simulation codes, which use specialized force loops for each interaction, this is not viable in ESPResSo, since it would require a separate implementation not only for each reasonable combination of potentials, but in addition for each cell system as well. Therefore, ESPResSo uses unified force calculation interfaces, rendering new potentials simple to implement for all cell systems – at the expense of some overhead which is mainly due to the inability of current compilers to keep array values in registers. However, looking at the aforementioned unavoidable hardware restrictions, the impact of compiler optimization and the continuing improvements expected therein, and the competitive performance of ESPResSo even for modified and customized scenarios, our design goals from section 1.2 seem once again confirmed.

1.7. Conclusion and Outlook

Several publications have already appeared that used ESPResSo for data production [62, 63, 97, 110, 139–143]. As of this writing, the ESPResSo-package continues to undergo significant enlargement. A dipolar Ewald sum [144] is currently being implemented, with a dipolar P^3M version to be added soon, which will enhance the capabilities to simulate ferrofluids or dipolar fluids like simple water models.

For the dynamics of soft matter systems it is often necessary to include hydrodynamic interactions. Since in practice one cannot consider all molecular details of the systems, this can be achieved on a coarse-grained level by coupling the solvent degrees of freedom to the simulated particles. The implementation of an advanced lattice Boltzmann algorithm [145] is almost finished, having already proven its usefulness in polymer dynamics simulations [146] and electrophoresis simulations of charged colloids [147, 148].

Clever Monte Carlo strategies are lacking so far. Although easily implementable on the Tcl-level [62], where for example a hybrid Monte Carlo technique has been successfully employed [149, 150], other, more efficient sampling methods, are planned for the future.

Other features like the `rattle` algorithm for constraint dynamics, and more potentials suited for atomistic force fields are already in progress and will continue towards enabling ESPResSo to handle atomistic simulations. The ultimate goal is to

implement multiscale simulation strategies which will allow probing different length and time scales within one single simulation run of the program.

There are many more improvements planned for the years to come, and hopefully the capabilities of ESPResSo will grow even further once more researchers take up its idea and contribute to the package by using, customizing, and extending it. The hope is to attract further developers that can contribute to the project, while keeping the anticipated program structure simple, extensible, well documented, and easy to use. We realize that this is a challenging goal to achieve, although the past two years, in which ESPResSo left its alpha stage and first external collaborations have started, encouraged us that this challenge can be mastered.

2. Polymer Physics Prerequisites

Basic concepts in polymer physics are introduced and important definitions detailed. The coarse-graining concept is explained. The freely jointed chain (FJC) and the worm-like chain (WJC) models are used to describe ideal chains under tension, and the force-extension-relation is given for both cases. For real chains excluded volume effects are added and scaling laws derived based on the famous Flory estimate. The blob picture is introduced as well and applied to both neutral and charged polymers, i.e. polyelectrolytes.

Research on polymeric macromolecules, which had used to be a chemically dominated field of science for quite some time, moved to the center of interest in statistical physics as well due to some groundbreaking achievements on the theoretical level, such as the works of S.F. Edwards [151] and P.G. deGennes [32]. With some of their techniques dating back to the first half of the 20^{th} century, it became possible to approach the complex processes involved on a physical level. Employing increasingly detailed models and modern analytical methods such as path integrals, scaling concepts, and field-theoretical approaches, basic questions like the shape of a polymer chain in solution could be formulated and solved systematically. Once the usage of supercomputers was no longer restricted to military applications and their speed became exponentially faster, computer simulations were added to the methodic toolbox as the one bridging element which connects theory and experiments with each other.

This chapter should provide an introduction to the terminology and concepts used in polymer physics. While section 2.1 will focus on basic definitions and experimental observables, section 2.2 will present the coarse-grained approach to incorporate only the important chemical features on a simplified scale; after some initial derivations of basic geometric properties for ideal chains, free energies and forces will be studied in the subsequent section 2.3, before the generalization towards real chains and real solvents is done in section 2.4. There, the important Flory arguments are introduced as well as the blob model, both quite useful tools to estimate the spatial extension of a polymer chain which will be used throughout this work. Finally, the influence of charged subgroups on the macromolecule are considered in section 2.5, rounding off this chapter by applying the blob picture to those polyelectrolytes. We hereby follow [152–156] to some extent.

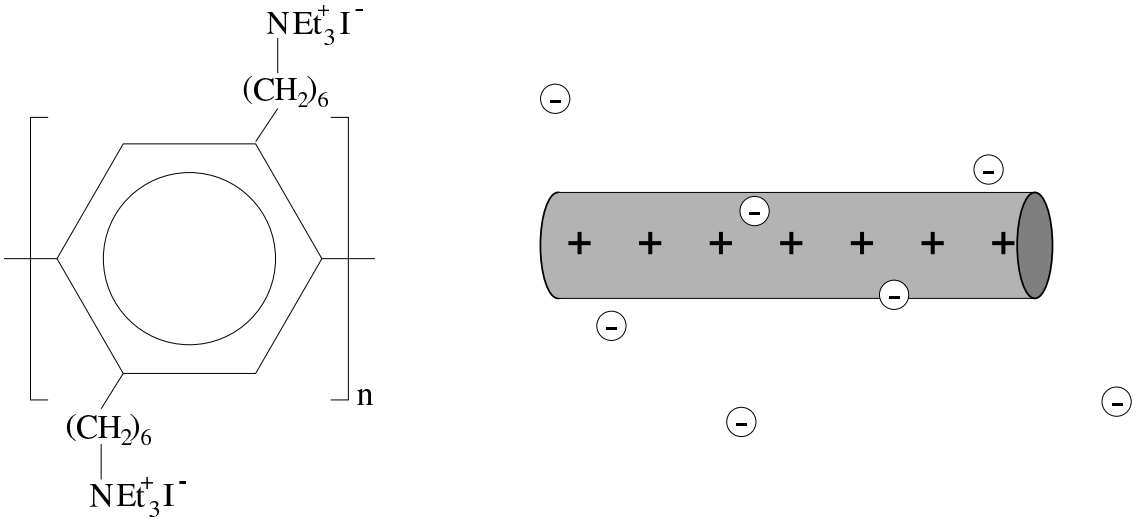

Figure 2.1.: Some polyelectrolytes, such as poly(paraphenylene) with iodine counterions, are relatively stiff and can therefore be treated similar to a charged rod (taken from [157]).

2.1. Terminology and Definitions

In soft matter physics, the term *polymer* denominates a macromolecule consisting of $N_\mathrm{m} > 1$ monomers which are connected by covalent bonds; an *oligomer* is a polymer with $2 \leq N_\mathrm{m} \lesssim 10$ monomers. The *monomer* itself is a molecule carrying one or more polymerizable groups whose count is given by the *functionality* f_f of the monomer [154]. As figure I.4 depicted, a polymer may have a coiled or worm-like shape, but stiff extensions similar to rods are also common (*e.g.* poly(paraphenylene) whose constitution formula figure 2.1 compares to a rod-like model depiction). Typical chains may be composed of just a few, several hundreds, or even 10^9 monomers; DNA for example is composed of up to 10^7 nucleotides. The monomers are hereby usually (chemically) identical, with only one kind of molecule repeating itself, as was visualized by the structure equations in figure I.4. Other possible conformations exist, figure 2.2 illustrating a few, the polymers considered in this study, however, fulfill that requirement strictly, being built from just two subgroups (a charged and a neutral one).

Usually, polymers do not possess an exactly determined molar mass but rather a mass distribution as sketched in figure 2.2. This allows different averages to be taken, such as the *number average molecular weight*

$$\overline{M}_n = \frac{\Sigma N_{N_\mathrm{m}} M_{N_\mathrm{m}}}{\Sigma N_{N_\mathrm{m}}} \tag{2.1}$$

which relates the number of molecules N_{N_m} with length N_m and molecular mass

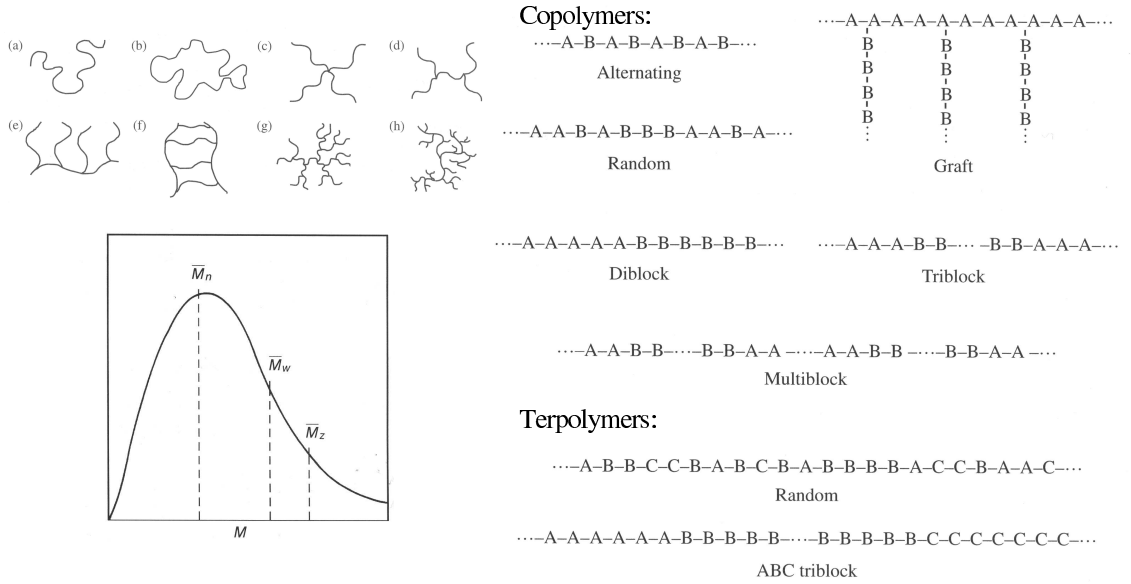

Figure 2.2.: Examples of polymer architectures (*upper left*), *i.e.* (a) linear, (b) ring, (c) star, (d) H, (e) comb, (f) ladder, (g) dendrimer, (h) randomly branched, and different types of copolymers and terpolymers (*right*). The *lower left* sketches a molar mass distribution of a polydisperse polymer, comparing the different averages $\overline{M}_n$, $\overline{M}_w$ and $\overline{M}_z$ (taken from [154,156]).

M_{N_m} to the total number of polymers, or the *weight average molecular weight*

$$\overline{M}_w = \frac{\Sigma N_{N_\mathrm{m}} M_{N_\mathrm{m}}^2}{\Sigma N_{N_\mathrm{m}} M_{N_\mathrm{m}}} > \overline{M}_n \tag{2.2}$$

using the total mass of the sample as the reference value. Their ratio $\overline{M}_w/\overline{M}_n$ is called the *polydispersity index* which indicates the width of the distribution in figure 2.2, *i.e.* the "purity" of the sample in terms of deviations from the averages. If it was unity, the underlying polymers would be *monodisperse* and would all have the same chain length $N_\mathrm{m} = \langle N_\mathrm{m} \rangle$; more common are ratios $\overline{M}_w/\overline{M}_n \sim 2$, though model systems such as the photocrosslinkable star polymers in figure I.3 are capable of reaching almost monodisperse distributions (see table 2.1). The *degree of polymerization*

$$P_\mathrm{n} = \frac{\overline{M}_n}{M_0} \tag{2.3}$$

finally gives a measure for the chain length N_m by relating the molecular weight of the macromolecule to the original weight M_0 of the monomer the polymer was built of; the corresponding $P_w = \overline{M}_w/M_0$ exists as well, but is less common. Sometimes, higher moments are considered as well, *e.g.* $\overline{M}_z$ as the ratio of the third to the second moments of the number fraction distribution, emphasizing the high molar mass

tail of the molar mass distribution (see figure 2.2); molecular theories of polymer dynamics predict these higher-order averages to be important, but currently available characterization methods for measuring them have insufficient precision to be useful [154,156].

polymer's name	terminating agent	precursor $\overline{M}_n$	precursor $\overline{M}_w/\overline{M}_n$	f_f	P_n	polymer $\overline{M}_n$
St_3–PtBMA$_1$4	TBMB	6.3	1.08	3	14	3.8
St_3–PtBMA$_6$0	TBMB	25.3	1.06	3	30	7.9
St_3–PtBMA$_7$5	TBMB	32.5	1.08	3	60	15.3
St_3–PtBMA$_9$0	TBMB	37.9	1.07	3	75	20.0
St_3–PtBMA$_1$65	TBMB	74.9	1.11	3	90	23.0
St_{4-5}–PtBMA$_2$0	T_8-(prop-J)$_8$	13.3	1.15	4-5	18-23	7.9

Table 2.1.: Characteristic data of PtBMA star polymers, the polyelectrolyte model networks whose synthesis was shown in figure I.3. $\overline{M}_n$ is given in g/mol, P_n refers to one of the arms which are connected through the terminating agent (the tri-functional 1,3,5-trisbromomethylbenzene, or octa[(3-iodopropyl)-silsesquioxane] with an eightfold functionality), before being hydrolyzed to PMAA star polymers and photo-crosslinked by UV light ($\lambda = 366$ nm) irradiation, or vice versa (from [14]).

If more than one single macromolecule is under consideration, their respective inter-chain interactions might have to be taken into account, too. Two types of such *polymer liquids* are common, namely *polymer melts* and *polymer solutions*. While the former are "neat polymeric liquids" [156] above their glass transition and melting temperatures, with macroscopic pieces remembering their shape and having elasticity on short time scales, but exhibiting liquid flow (with a high viscosity) at long times, the latter can be obtained by *e.g.* dissolving a polymer in a solvent. Polymer solutions are classified as dilute or semidilute (see figure 2.3) depending on the polymer *mass concentration* c, defined as the ratio of the total mass of polymer dissolved in a solution and the volume of the solution. Alternatively, the *volume fraction*

$$\phi = \frac{c}{\rho} \tag{2.4}$$

relates the concentration to the polymer density ρ, measuring the ratio of occupied volume of the polymer in the solution and the volume of the solution.

The *pervaded volume* V is the volume of solution spanned by the polymer chain of size R_E, which are roughly related by

$$V \approx R_\mathrm{E}^3 \tag{2.5}$$

if numerical prefactors are ignored[1]. This volume is typically orders of magnitude larger than the occupied volume of the chain, most of the pervaded volume will be

[1] That is a very important concept which will be essential throughout this work: As they remain

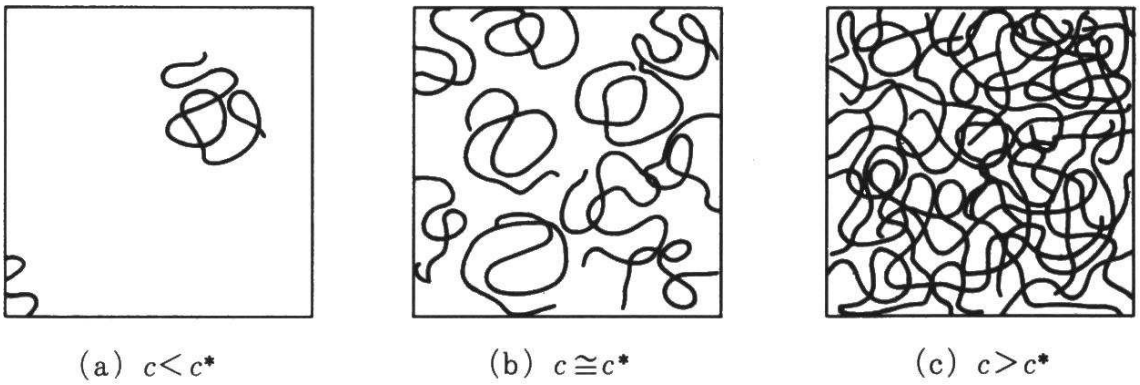

Figure 2.3.: Solution regimes of flexible polymers: (a) dilute, (b) at the overlap concentration c^*, (c) semidilute (taken from [158]).

filled with solvent or other chains. The volume fraction of a single macromolecule inside its pervaded volume is called the *overlap volume fraction* ϕ^* or the corresponding *overlap concentration* c^*, as obtained from (2.4). This definition allows to classify different regimes of polymer solutions: If the volume fraction ϕ of the polymer solution is equal to the overlap volume fraction ϕ^*, the pervaded volumes of macromolecules densely fill space, and the chains are just at overlap with each other ($c = c^*$, see figure 2.3). If it is below the overlap volume fraction (or $c < c^*$), the solution is called *dilute*, and the average distance between chains will be larger than their size R_E. Therefore, polymer coils in dilute solutions are far from each other, inter-chain interactions are negligible, and most of their properties are very similar to pure solvent with small modifications due to the presence of the polymer. In *semi-dilute* polymer solutions (with $c > c^*$) however, the polymer coils overlap and dominate most of the physical properties of the solvent, despite the fact that actual values of the volume fractions are still usually quite low ($\phi \ll 1$), and most of the volume is occupied by the solvent. Thus, adding a very small amount of polymer to a solvent can create a liquid with drastically different properties than the solvent.

2.2. Coarse-Graining Concepts

To allow an effective yet sufficient treatment of polymer physics problems, figure I.4 already introduced the concept of *coarse-graining* the chemical details on the macromolecule towards a simpler *bead-spring-model*. Using the periodicity of its repeat units, the polymer is pictured as a linear chain of n interconnected spheres, characterized by a *bond length* ℓ_i (measuring the distance between two neighbouring

constant for different R_E as long as the physics stays the same, prefactors of order unity are considered to not change the qualitative behaviour (*e.g.* critical exponents) and are therefore ignored.

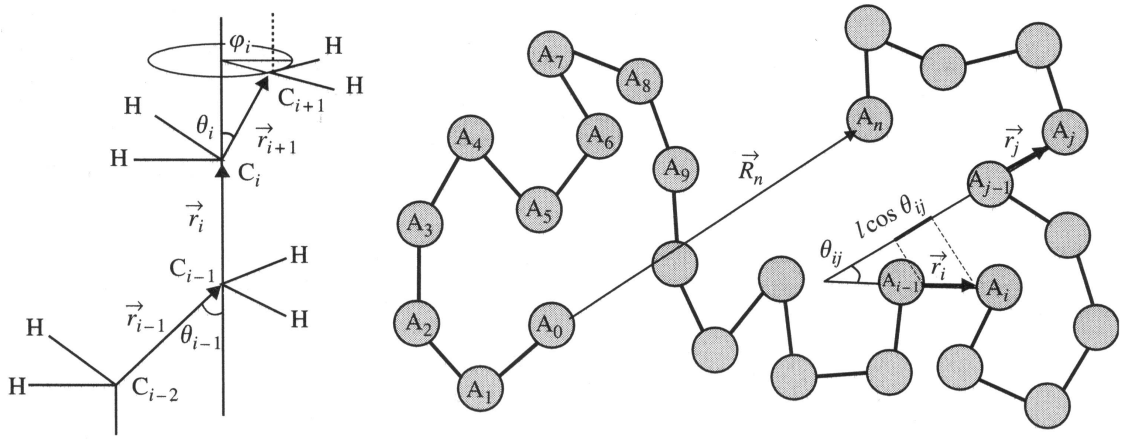

Figure 2.4.: Illustration of the notation regarding monomer-monomer vector $\vec{r}_i = \vec{\ell}_i$, bond angle θ_i, and torsion angle φ_i for a sequence of three main-chain bonds (*left*) and a conformation of a flexible polymer (*right*) with end-to-end vector $\vec{R}_n = \vec{R}_\mathrm{E}$ (taken from [156]).

center-of-masses) and an angle θ_i (comparing the direction of neighbouring bond vectors) for each of the monomer pairs $(i, i+1)$. As shown in figure 2.4, a random conformation of the polymer can then be described in terms of the bond vectors $\vec{\ell}_i$, such that the end-to-end distance $\vec{r}_\mathrm{E}$ and its square r_E^2 follow as

$$r_\mathrm{E}^2 = (\vec{r}_\mathrm{E})^2 = \left(\sum_{i=1}^{n} \vec{\ell}_i\right)^2 = n\ell^2 + 2\sum_{j>i} \vec{\ell}_i \cdot \vec{\ell}_j \tag{2.6}$$

In its current form, (2.6) is even valid for a single polymer with non-local interactions and additional effects, although in the following we will drop that generality. As with many macromolecular systems, it is now feasible to employ a statistical description of the entire ensemble of chains, accounting for the inner degrees of freedom of the chain molecules and their respective interactions; in fact, due to the unavoidable thermal fluctuations it is even mandatory to do so, which is why in the following sections we will always refer to statistical averages when discussing observables from the simulations (even if not using $\langle . \rangle$) unless explicitely stated otherwise. Here, $\langle \ell_i \rangle = \ell$ and

$$R_\mathrm{E}^2 = \langle r_\mathrm{E}^2 \rangle = n\ell^2 + \sum_{j>i} \left\langle \vec{\ell}_i \cdot \vec{\ell}_j \right\rangle = n\ell^2 + \ell^2 \langle \cos\theta \rangle = n\ell^2 \tag{2.7}$$

following from (2.6) and from the expectation value $\langle \cos\theta \rangle = 0$ for the bond angles, the latter originating in the assumption that all bonds $\vec{\ell}_i$ are randomly oriented, rendering all conformations $\left\{\vec{\ell}_i\right\}_i$ of the polymers to be uniformly distributed. That now leads to

$$\langle r_\mathrm{E} \rangle = 0 \tag{2.8}$$

essentially rendering that observable useless, and at the same time the reason for choosing R_{E}^2 (or $R_{\mathrm{E}} = \sqrt{R_{\mathrm{E}}^2} \neq \langle r_{\mathrm{E}} \rangle$) as the quantity to look at. Consequently, the probability of finding a chain with end-to-end vector $\vec{r}_{\mathrm{E}}$ follows a Gaussian distribution

$$P(\vec{r}_{\mathrm{E}}, n) = \left(\frac{3}{2\pi n \ell^2} \right)^{\frac{3}{2}} \cdot \exp\left(-\frac{3 r_{\mathrm{E}}^2}{2 n \ell^2} \right) \quad \text{for } n \gg 1 \tag{2.9}$$

as would a *Random Walk* of n steps of (average) length ℓ, with the polymer as possible depiction of the taken path.

Flexible polymers have many universal properties that are independent of local chemical structure. A simple unified description of all ideal polymers is provided by an *equivalent freely jointed chain*: It has by definition the same mean-square end-to-end distance $\langle R_{\mathrm{E}}^2 \rangle$ and the same maximum end-to-end distance $R_{\max}$ as the actual polymer, but instead of any more chemical details it simply consists of N_{m} freely jointed effective bonds of length b, called the *Kuhn length*. Then, the *contour length* of this equivalent freely jointed chain is

$$N_{\mathrm{m}} b = R_{\max} \tag{2.10}$$

and its mean-square end-to-end distance is

$$\langle R_{\mathrm{E}}^2 \rangle = N_{\mathrm{m}} b^2 = b R_{\max} \tag{2.11}$$

as in (2.7), describing a simple random walk. This allows an alternative definition of the sphere size for the bead-spring model depiction, particularly if the optimal mapping of the chemical details to the coarse-grained level is not yet known[2].

While the (equivalent) *freely jointed chain* (FJC) model[3] merely assumed a constant bond length b and no correlations between the directions of different bond vectors, *i.e.* $\langle \cos\theta_i j \rangle = 0$ for $i \neq j$, the *freely rotating chain model* (FRC) only ignores differences between the probabilities of different torsion angles, assuming all $-\pi \leq \varphi_i \leq \pi$ to be equally likely and independent of each other, but takes all bond lengths b and bond angles θ to be fixed at constant values. The mean-square end-to-end distance of the freely rotating chain is then a simple function of the number N_{m} of bonds in the backbone, the length b of each backbone bond, and the bond angle θ:

$$\langle R_{\mathrm{E}}^2 \rangle = n\ell^2 + 2n\ell^2 \frac{\cos\theta}{1-\cos\theta} = n\ell^2 \frac{1+\cos\theta}{1-\cos\theta} \tag{2.12}$$

[2] On a more general level, it also allows to treat any macromolecule with n repeat units connected by bond vectors $\vec{\ell}_i$ in a similar fashion, mapping it as explained onto an equivalent freely jointed chain of N_{m} Kuhn segments (monomers) with bond lengths $b = \frac{\langle R_{\mathrm{E}}^2 \rangle}{R_{\max}}$, removing another layer of chemical details from the scene. In this work, however, we always assume the Kuhn segments to correspond to the repeat units, *i.e.* we use the assumption $\ell \approx b$.

[3] Without "equivalent" it uses n and $\vec{\ell}_i$, otherwise N_{m} and $\vec{b}_i$; as mentioned in the preceeding footnote, we are not differentiating between the two models here.

Polymers with carbon single bonds making up their backbone, such as those in figure I.4, have a bond angle of $\theta = 68°$ [156], would turn the prefactor in (2.12) to be ≈ 2. However, real chains are never as flexible as the freely rotating chain model predicts, since the most flexible polymers (those with $\theta = 68°$) rather have a prefactor of $\gtrsim 4$, because there is steric hindrance to bond rotation in all polymers.

The *worm-like chain model* (WLC) is a special case of a freely rotating chain for very small values of the bond angle. It is a good model for *stiff polymers*, such as double stranded DNA for which the flexibility is due to fluctuations of the contour of the chain from a straight line rather than due to bond rotations. Regarding the number s_p of main-chain bonds in a persistence segments, which is the scale at which local correlations between bond vectors decay, the FRC result

$$s_p = -\frac{1}{\ln(\cos\theta)} \tag{2.13}$$

can be expanded for small values of the bond angle $\theta \ll 1$, and with $\cos\theta \cong 1 - \frac{\theta^2}{2}$ and $\ln(1-x) \cong -x$ (for small x) it becomes

$$s_p \cong \frac{2}{\theta^2} \tag{2.14}$$

for a worm-like chain. Since θ is small, the persistence segment contains a large number of main-chain bonds, and the *persistence length*

$$l_p = s_p \ell = \ell \frac{2}{\theta^2} \tag{2.15}$$

renders the prefactor in (2.12) to be similarly large, namely $\approx \frac{4}{\theta^2}$. The corresponding Kuhn length b is twice the persistence length, $b = 2l_p$, which in case of the aforementioned double-helical DNA translates to $l_p \approx 50$ nm and $b \approx 100$ nm.

Up to now, the size of the polymers was characterized by their mean-square end-to-end distance R_E. However, for more complex macromolecules like branched or ring polymers or networks this quantity is not well defined, because those either have too many ends or no ends at all[4] This is overcome by employing the square *radius of gyration* R_G^2, which is defined as the average square distance between monomers in a given conformation $\vec{R}_i$ and the polymer's center of mass[5] $\vec{R}_\mathrm{CM} = \frac{1}{N_\mathrm{m}} \sum_{i=1}^{N_\mathrm{m}} \vec{R}_i$ along

$$\vec{R}_\mathrm{G}^2 = \frac{1}{2N_\mathrm{m}^2} \sum_{i=1}^{N_\mathrm{m}} \sum_{j=1}^{N_\mathrm{m}} \left\langle \left(\vec{R}_i - \vec{R}_j \right)^2 \right\rangle = \frac{1}{N_\mathrm{m}} \sum_{i=1}^{N_\mathrm{m}} \left\langle \left(\vec{R}_i - \vec{R}_\mathrm{CM} \right)^2 \right\rangle \tag{2.16}$$

[4] Although for networks one can simply define the distance between nearest crosslinks as R_E, which overcomes the ambiguity particularly in our case of model networks.

[5] Note that this definition does not actually contain a "mass", as we assume throughout this study that all monomers have equal masses, which can be scaled out. This is also justifiable since we do not distinguish between different types of monomers, even counterions are treated similarly to one repeat unit.

using $\vec{R}_{i+1} - \vec{R}_i = \vec{b}_i \; \forall i = 1, \ldots, N_\mathrm{m}$. It can not only characterize the size of polymers of any architecture, but it is also measurable experimentally by static scattering experiments (*e.g.* SANS or SAXS). For an ideal linear chain, using continuous coordinates (instead of the discrete repeat units) allows to derive [156]

$$\begin{aligned}
\langle R_\mathrm{G}^2 \rangle &= \frac{1}{N_\mathrm{m}^2} \int_0^{N_\mathrm{m}} \int_u^{N_\mathrm{m}} \langle (\vec{R}(u) - \vec{R}(v))^2 \rangle \mathrm{d}v\mathrm{d}u = \frac{b^2}{N_\mathrm{m}^2} \int_0^{N_\mathrm{m}} \int_u^{N_\mathrm{m}} (v-u) \mathrm{d}v\mathrm{d}u \\
&= \frac{b^2}{N_\mathrm{m}^2} \int_0^{N_\mathrm{m}} \int_0^{N_\mathrm{m}-u} v' \mathrm{d}v' \mathrm{d}u = \frac{b^2}{N_\mathrm{m}^2} \int_0^{N_\mathrm{m}} \frac{(N_\mathrm{m}-u)^2}{2} \mathrm{d}u = \frac{b^2}{2N_\mathrm{m}^2} \int_0^{N_\mathrm{m}} (u')^2 \mathrm{d}u' \\
&= \frac{b^2}{2N_\mathrm{m}^2} \frac{N_\mathrm{m}^3}{3} = \frac{N_\mathrm{m} b^2}{6} = \frac{\langle R_\mathrm{E}^2 \rangle}{6}
\end{aligned} \tag{2.17}$$

using (2.7) once more in the last step. Similarly, the radius of gyration of other shapes of flexible ideal chains can be calculated (see table 2.2). For a rod-like polymer the end-to-end distance becomes $R_\mathrm{E} = R_\mathrm{max} = N_\mathrm{m} b = L$, from where the original definition (2.16) leads to

$$\begin{aligned}
\langle R_\mathrm{G}^2 \rangle &= \frac{b^2}{N_\mathrm{m}} \int_0^{N_\mathrm{m}} \left(u - \frac{N_\mathrm{m}}{2} \right)^2 \mathrm{d}u = \frac{b^2}{N_\mathrm{m}} \int_{-\frac{N_\mathrm{m}}{2}}^{\frac{N_\mathrm{m}}{2}} x^2 \mathrm{d}x \\
&= \frac{N_\mathrm{m}^2 b^2}{12} = \frac{\langle R_\mathrm{E}^2 \rangle}{12}
\end{aligned} \tag{2.18}$$

which is noticeably different from (2.17) for a linear chain. Again, other rigid objects can be derived similarly, results are given in table 2.2.

linear:	$\frac{N_\mathrm{m} b^2}{6}$	ring:	$\frac{N_\mathrm{m} b^2}{12}$	f_f-arm star:	$\frac{N_\mathrm{m}}{f_\mathrm{f}} \frac{b^2}{6} (3 - \frac{2}{f_\mathrm{f}})$	H-polymer:	$\frac{N_\mathrm{m} b^2}{6} \frac{89}{625}$
disk:	$\frac{R^2}{2}$	sphere:	$\frac{3R^2}{5}$	rod:	$\frac{L^2}{12}$	cylinder:	$\frac{R^2}{2} + \frac{L^2}{12}$

Table 2.2.: Mean-square radii of gyration R_G^2 of ideal polymers with N_m Kuhn monomers of length b: ideal chains (*top*), *i.e.* linear chain, f_f-arm star with each arm containing $N_\mathrm{m}/f_\mathrm{f}$ Kuhn monomers, and H-polymer with all linear sections containing $N_\mathrm{m}/5$ Kuhn monomers; rigid objects (*bottom*), namely uniform thin disc of radius R, uniform sphere of radius R, thin rod of length L, and uniform right cylinder of radius R and length L (from [156]).

Particularly for polyelectrolytes, a third observable related to the size of a polymer chain becomes important, the *hydrodynamic radius*

$$R_\mathrm{H} = \left(\frac{1}{N_\mathrm{m}^2} \sum_{i \neq j} \left\langle \frac{1}{\vec{R}_i - \vec{R}_j} \right\rangle \right)^{-1} \tag{2.19}$$

which can be obtained from *e.g.* measuring the diffusion constant [151]

$$D \approx \frac{k_\mathrm{B} T}{6\pi\eta} \langle \frac{1}{R_\mathrm{H}} \rangle \tag{2.20}$$

in the experiment.

With these findings it is now also possible to characterize non-ideal polymers by measuring their $R_{\mathrm{E}}^2/R_{\mathrm{G}}^2$-ratio: If it is close to 6, one observes a macromolecule exhibiting features of a Random Walk, close to 12 will be the outcome for a strongly stretched polymer. Even higher ratios are possible, if the chain becomes highly anisotropic by *e.g.* having a rather large accumulation of monomers close to its center-of-mass.

2.3. Free Energies and Forces

With $\Omega(N_{\mathrm{m}}, \vec{R}_{\mathrm{E}})$ as the number of conformations of a freely jointed chain of N_{m} monomers with end-to-end vector $\vec{R}_{\mathrm{E}}$, the *entropy*

$$S(N_{\mathrm{m}}, \vec{R}_{\mathrm{E}}) = k_{\mathrm{B}} \ln \Omega(N_{\mathrm{m}}, \vec{R}_{\mathrm{E}}) \tag{2.21}$$

is the product of the Boltzmann constant k_{B} and the logarithm of the number of states Ω, and it is then also a function of N_{m} and $\vec{R}_{\mathrm{E}}$. The probability distribution, since (2.9) known to be Gaussian for ideal chains in the FJC-model, is in general the fraction of all conformations that actually have an end-to-end vector $\vec{R}_{\mathrm{E}}$ between $\vec{R}_{\mathrm{E}}$ and $\vec{R}_{\mathrm{E}} + \mathrm{d}\vec{R}_{\mathrm{E}}$, namely

$$P(N_{\mathrm{m}}, \vec{R}_{\mathrm{E}}) = \frac{\Omega(N_{\mathrm{m}}, \vec{R}_{\mathrm{E}})}{\int \Omega(N_{\mathrm{m}}, \vec{R}_{\mathrm{E}}) \mathrm{d}\vec{R}_{\mathrm{E}}} \tag{2.22}$$

Using (2.22) and (2.9) in (2.21), gives

$$\begin{aligned} S(N_{\mathrm{m}}, \vec{R}_{\mathrm{E}}) &= k_{\mathrm{B}} \ln P(N_{\mathrm{m}}, \vec{R}_{\mathrm{E}}) + k_{\mathrm{B}} \ln \left[\int \Omega(N_{\mathrm{m}}, \vec{R}_{\mathrm{E}}) \mathrm{d}\vec{R}_{\mathrm{E}} \right] \\ &= -\frac{3}{2} k_{\mathrm{B}} \frac{\vec{R}_{\mathrm{E}}^2}{N_{\mathrm{m}} b^2} + \frac{3}{2} k_{\mathrm{B}} \ln \left(\frac{3}{2\pi N_{\mathrm{m}} b^2} \right) + k_{\mathrm{B}} \ln \left[\int \Omega(N_{\mathrm{m}}, \vec{R}_{\mathrm{E}}) \mathrm{d}\vec{R}_{\mathrm{E}} \right] \\ &= -\frac{3}{2} k_{\mathrm{B}} \frac{\vec{R}_{\mathrm{E}}^2}{N_{\mathrm{m}} b^2} + S(N_{\mathrm{m}}, 0) \end{aligned} \tag{2.23}$$

where the terms independent of $\vec{R}_{\mathrm{E}}$ have been denoted by $S(N_{\mathrm{m}}, 0)$.

Since the monomers of an ideal chain have no interaction energy[6], the energy $U(N_{\mathrm{m}}, \vec{R}_{\mathrm{E}})$ of an ideal chain is also independent of the end-to-end vector $\vec{R}_{\mathrm{E}}$, and the *Helmholtz free energy* $\mathcal{F}(N_{\mathrm{m}}, \vec{R}_{\mathrm{E}})$ then becomes

$$\mathcal{F}(N_{\mathrm{m}}, \vec{R}_{\mathrm{E}}) = U(N_{\mathrm{m}}, \vec{R}_{\mathrm{E}}) - TS(N_{\mathrm{m}}, \vec{R}_{\mathrm{E}}) = \frac{3}{2} k_{\mathrm{B}} T \frac{\vec{R}_{\mathrm{E}}^2}{N_{\mathrm{m}} b^2} + \mathcal{F}(N_{\mathrm{m}}, 0) \tag{2.24}$$

[6] The ideal chain never has long-range interactions, though short-range interactions are possible.

where $\mathcal{F}(N_\mathrm{m},0)$ is the free energy of the chain with both ends at the same point. The largest number of chain conformations correspond to $\vec{R}_\mathrm{E}=0$ [156]; that number decreases with increasing end-to-end vector, leading to the decrease of polymer entropy and increase of its free energy, the latter quadratically with the magnitude of $\vec{R}_\mathrm{E}$. This implies that the entropic elasticity of an ideal chain satisfies Hooke's law: To hold the chain at a fixed end-to-end vector $\vec{R}_\mathrm{E}$ would therefore require equal and opposite forces $\vec{\mathsf{f}}_\mathrm{E}$ acting on the chain ends, proportional to $\vec{R}_\mathrm{E}$

$$\vec{\mathsf{f}}_\mathrm{E}=\nabla\mathcal{F}=\frac{3k_\mathrm{B}T}{N_\mathrm{m}b^2}\vec{R}_\mathrm{E} \tag{2.25}$$

like a simple elastic spring. Note that the prefactor in (2.25), the *entropic spring constant*, is proportional to the temperature, which is a signature of entropic elasticity and distinguishes polymers from other materials such as metals or ceramics which become softer as temperature is raised because their deformation requires displacing atoms from their preferred positions, while for larger end-to-end distances of a polymer the restoring force increases because there are fewer possible conformations available. The linear dependence in (2.25) is due to the Gaussian approximation, valid only for $R_\mathrm{E}\ll R_\mathrm{max}=N_\mathrm{m}b$; for larger extensions the dependence has to become strongly non-linear, with the force f_E diverging at $R_\mathrm{E}=R_\mathrm{max}$, due to the finite extensibility of real chains as will be discussed later on.

Since most of the conformational entropy of the chain arises from local conformational freedom on the smallest length scales, the random walks that happen to have end-to-end distances $R_\mathrm{E}>N_\mathrm{m}^{1/2}b$ can be regarded as a sequential array of smaller sections sized ξ that are essentially unperturbed by the stretch, as shown in the left part of figure 2.5. Then, the mean-square projection of the end-to-end vector of these sections onto $\vec{R}_\mathrm{x}$ obeys (2.7),

$$\xi^2\approx b^2g \tag{2.26}$$

when g denotes the number of monomers per section, while on larger length scales than ξ the external tension $\vec{\mathsf{f}}_\mathrm{x}$ changes the polymer conformation from that of a random walk to that of an elongated chain, which is why the sections are also called *tension blobs*. The physical reason for the chain to only be extended on its largest length scale lies again in the resulting maximization of the chain's conformational entropy through this phenomenon. As there are now N_m/g such sections, it is assumed that they arrange sequentially, such that

$$R_\mathrm{x}\approx\xi\frac{N_\mathrm{m}}{g}\approx\frac{N_\mathrm{m}b^2}{\xi} \tag{2.27}$$

Stretching the chain forces each tension blob to follow a particular direction (*i.e.* $\vec{R}_\mathrm{x}$), therefore one degree of freedom is restricted per section, and from the equipartition

theorem it follows that the free energy of the chain increases by $k_{\mathrm{B}}T$ per blob:

$$\mathcal{F}(N_{\mathrm{m}}, \vec{R}_{\mathrm{E}}) \approx k_{\mathrm{B}}T \frac{N_{\mathrm{m}}}{g} \approx k_{\mathrm{B}}T \frac{\vec{R}_{\mathrm{E}}^2}{N_{\mathrm{m}} b^2} \tag{2.28}$$

Comparing (2.28) and (2.24), it turns out that this crude approximation nevertheless gets the correct result within a prefactor of order unity. This is the character of all *scaling predictions* as they provide a simple means to extract the essential physics, but fail to determine numerical coefficients. Regarding all the assumptions which already went into the coarse-grained models of the macromolecule (see *e.g.* figure I.4 and section 2.2) that however seems like a good trade-off; it is also very acceptable, as it is the general physical understanding we are interested in.

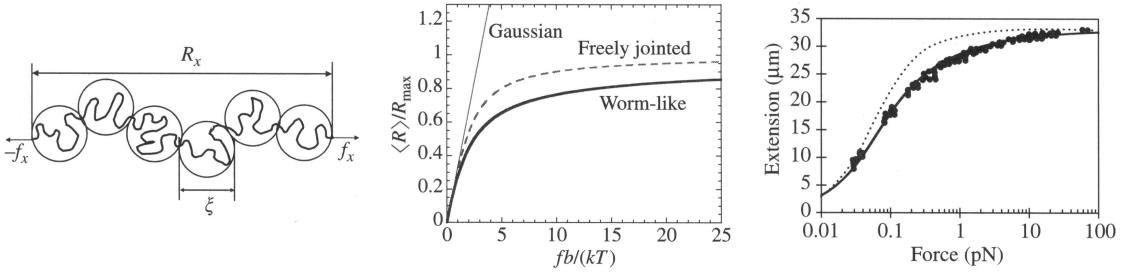

Figure 2.5.: Blob depiction of an ideal polymer, elongated by opposing forces $\pm\vec{\mathrm{f}}_{\mathrm{x}}$ to an end-to-end distance $\vec{R}_{\mathrm{x}}$. The chain is only stretched on its largest length scales, while inside the tension blobs of diameter ξ the conformation of the chain remains essentially unperturbed (*left*). The *center* panel displays the average end-to-end distance as a function of stretching force for a Gaussian chain (see (2.25), *thin line*), a freely jointed chain (Langevin function (2.31), *dashed line*), and a worm-like chain (according to (2.34), *thick line*). On the *right* hand side a comparison of experimental forces measured for 97 kilobase λ-DNA dimers with the worm-like chain model is shown, using (2.34) with $R_{\max} = 33$ μm and $b = 100$ nm as parameters; the dotted curve corresponds to the Langevin function (2.31) of the freely jointed chain model (taken from [156]).

If one now considers a freely jointed chain of N_{m} bonds in place of the ideal Gaussian model, the effect of the finite extensibility of real chains can be estimated. Again stretching it by a force $\vec{\mathrm{f}}_{\mathrm{x}}$ towards an elongation $\vec{R}_{\mathrm{x}}$ gives rise to the energy $U = -\vec{\mathrm{f}}_{\mathrm{x}} \cdot \vec{R}_{\mathrm{x}}$ of the chain. Different chain conformations will then have different statistical Boltzmann factors $\exp(-U/k_{\mathrm{B}}T)$, whose sum over all possible conformations leads to the *partition function* Z. Equivalent to this approach is taking the integral over all possible orientations of all bond vectors of the chain, and representing the x-component of the end-to-end vector as the sum of the projections of all bond vectors onto the x-axis:

$$Z = \sum_{\text{states}} \exp\left(-\frac{U}{k_{\mathrm{B}}T}\right) = \sum_{\text{states}} \exp\left(-\frac{\vec{\mathrm{f}}_{\mathrm{x}} \cdot \vec{R}_{\mathrm{x}}}{k_{\mathrm{B}}T}\right)$$

$$
\begin{aligned}
&= \int \exp\left(-\frac{\mathsf{f}_\mathrm{x} R_\mathrm{x}}{k_\mathrm{B}T}\right) \prod_{i=1}^{N_\mathrm{m}} \sin\theta_i \mathrm{d}\theta_i \mathrm{d}\varphi_i \\
&= \int \exp\left(-\frac{\mathsf{f}_\mathrm{x}}{k_\mathrm{B}T} b \sum_{i=1}^{N_\mathrm{m}} \cos\theta_i\right) \prod_{i=1}^{N_\mathrm{m}} \sin\theta_i \mathrm{d}\theta_i \mathrm{d}\varphi_i \\
&= \left[\int_0^\pi 2\pi \sin\theta_i \exp\left(\frac{\mathsf{f}_\mathrm{x} b}{k_\mathrm{B}T}\cos\theta_i\right) \mathrm{d}\theta_i\right]^{N_\mathrm{m}} \\
&= \left[\frac{2\pi}{\frac{\mathsf{f}_\mathrm{x} b}{k_\mathrm{B}T}}\left[\exp\left(\frac{\mathsf{f}_\mathrm{x} b}{k_\mathrm{B}T}\right) - \exp\left(-\frac{\mathsf{f}_\mathrm{x} b}{k_\mathrm{B}T}\right)\right]\right]^{N_\mathrm{m}} \\
&= \left[\frac{4\pi \sinh\left(\frac{\mathsf{f}_\mathrm{x} b}{k_\mathrm{B}T}\right)}{\frac{\mathsf{f}_\mathrm{x} b}{k_\mathrm{B}T}}\right]^{N_\mathrm{m}}
\end{aligned}
\tag{2.29}
$$

From (2.29), the *Gibbs free energy* $\mathcal{G}$ can be directly calculated as [155]

$$
\mathcal{G} = -k_\mathrm{B}T \ln Z = -k_\mathrm{B}T\left[\ln\left(4\pi \sinh\left(\frac{\mathsf{f}_\mathrm{x} b}{k_\mathrm{B}T}\right)\right) - \ln\left(\frac{\mathsf{f}_\mathrm{x} b}{k_\mathrm{B}T}\right)\right] \tag{2.30}
$$

Similarly to (2.25), the divergent restoring force f_x follows implicitly as a function of R_x

$$
\begin{aligned}
\langle R_\mathrm{x}\rangle &= -\frac{\partial \mathcal{G}}{\partial \mathsf{f}_\mathrm{x}} = b N_\mathrm{m}\left[\coth\left(\frac{\mathsf{f}_\mathrm{x} b}{k_\mathrm{B}T}\right) - \frac{1}{\frac{\mathsf{f}_\mathrm{x} b}{k_\mathrm{B}T}}\right] \\
\Rightarrow \frac{\langle R_\mathrm{x}\rangle}{R_\mathrm{max}} &= \mathcal{L}\left(\frac{\mathsf{f}_\mathrm{x} b}{k_\mathrm{B}T}\right)
\end{aligned}
\tag{2.31}
$$

using the *Langevin function*

$$
\mathcal{L}(\beta) = \coth(\beta) - \frac{1}{\beta} \tag{2.32}
$$

as an abbreviation for the expression in the square brackets.

The center part of figure 2.5 now illustrates how the Langevin function in (2.31) relates the average chain elongation to the normalized extensional force for a freely jointed chain by comparing this to the Gaussian case from (2.25). It can be observed that for small relative elongations, *i.e.* $\langle R_\mathrm{x}\rangle \ll R_\mathrm{max}$, both curves coincide approximately, as $\mathcal{L}(\beta) \cong \frac{\beta}{3}$ for $\beta \ll 1$ makes (2.31) following Hooke's law (2.25) in that regime. For larger relative elongations, the Langevin function significantly deviates from linear dependence and saturates at unity, approaching another simple limit for $\mathsf{f}_\mathrm{x} \gg \frac{k_\mathrm{B}T}{b}$, namely $\mathcal{L}(\beta) \cong 1 - \frac{1}{\beta}$ for $\beta \gg 1$. Consequently, for strong stretching (2.31) becomes

$$
\frac{\mathsf{f}_\mathrm{x} b}{k_\mathrm{B}T} \cong \frac{1}{1 - \frac{\langle R_\mathrm{x}\rangle}{R_\mathrm{max}}} \qquad \text{for } \langle R_\mathrm{x}\rangle \to R_\mathrm{max} \tag{2.33}
$$

having the restoring force f_x diverge reciprocally proportional to $R_\mathrm{max} - \langle R_\mathrm{x} \rangle$.

There is no similarly simple analytical solution for the worm-like chain model at all extensions [156], but again approximations exist for both small and large relative extensions:

$$\frac{\mathsf{f}_\mathrm{x} b}{k_\mathrm{B} T} \cong 2\frac{\langle R_\mathrm{x} \rangle}{R_\mathrm{max}} + \frac{1}{2}\left(\frac{1}{1 - \frac{\langle R_\mathrm{x} \rangle}{R_\mathrm{max}}}\right)^2 - \frac{1}{2} \tag{2.34}$$

While in the first case worm-like chains behave as Hookean springs, just as the freely jointed chains did, the second case has the extensional force diverge reciprocally to the *square* of $R_\mathrm{max} - \langle R_\mathrm{x} \rangle$ along

$$\frac{\mathsf{f}_\mathrm{x} b}{k_\mathrm{B} T} \cong \frac{1}{2}\left(\frac{1}{1 - \frac{\langle R_\mathrm{x} \rangle}{R_\mathrm{max}}}\right)^2 = \frac{1}{2\left(1 - \frac{\langle R_\mathrm{x} \rangle}{R_\mathrm{max}}\right)^2} \qquad \text{for } \langle R_\mathrm{x} \rangle \to R_\mathrm{max} \tag{2.35}$$

These different divergences of the force near the maximum chain extension in (2.35) and (2.33) are due to bending modes on length scales shorter than the Kuhn length b. These modes do not exist in freely jointed chains because sections of length b are assumed to be absolutely rigid in FJC, but not in WLC.

Figure 2.5 now contrasts this difference (center panel) once more, but it also shows an experimental force-extension-relation for double-stranded DNA (on the right hand side), clearly favoring the worm-like chain model as being in excellent agreement with the experimental data.

2.4. Real Chains and Real Solvents

While in the previous subsections the conformations of an ideal chain were studied that ignored interactions between monomers separated by many bonds along the chain, in the following their impact on the polymer's behaviour should be considered. Regarding the energy cost $U(r)$ of bringing two monomers from ∞ to within a distance r of each other in a solvent, it will contain a repulsive hard-core barrier that corresponds to the energy cost of steric repulsion of two overlapping repeat units, implying $U(r \to 0) \to \infty$. Depending on the affinity of the monomers to each other compared to the solvent, $U(r)$ will have an attractive well around finite distances for *hydrophobic* groups which prefer contact with other monomers over contact with solvent molecules (see left panel in figure 2.6), while *hydrophilic* ones might see a purely repulsive potential $U(r)$. If the monomers are chemically identical to the solvent and there is no energy difference between their interactions, the energy $U(r)$ will contain only the hard-core repulsion; that is the case for an *athermal solvent*.

The probability of finding two monomers separated by a distance r in a solvent at temperature T is now proportional to the Boltzmann factor $\exp\left[-\frac{U(r)}{k_\mathrm{B} T}\right]$ (see

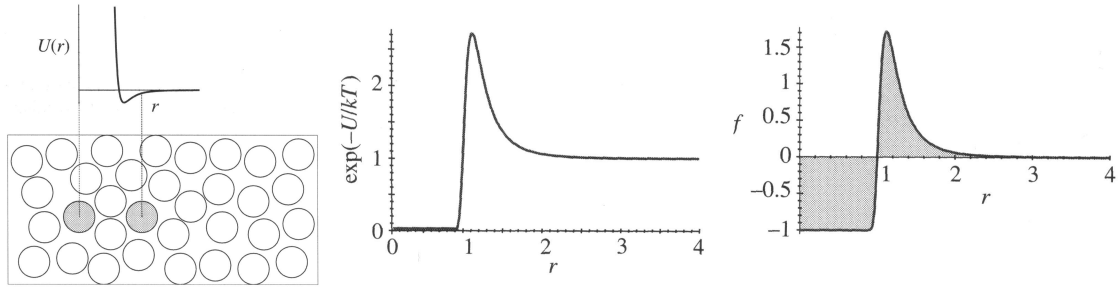

Figure 2.6.: Effective interaction potential between two monomers in a solution of other molecules (*left*). Relative probability of finding a second monomer at distance r from a given monomer (*center*). The Mayer f-function and its integration (shaded region) to determine excluded volume (*right*, taken from [156]).

center panel of figure 2.6). With the help of the *Mayer f-function*, taken to be the difference between the Boltzmann factor for two monomers at distance r and that for the case of no interaction (*i.e.* $r = \infty$),

$$f(r) = \exp\left[-\frac{U(r)}{k_{\mathrm{B}}T}\right] - 1 \tag{2.36}$$

an *excluded volume* v_{ex} can be defined as

$$v_{\mathrm{ex}} = -\int f(r)\mathrm{d}^3r = \int \left(1 - \exp\left[-\frac{U(r)}{k_{\mathrm{B}}T}\right]\right)\mathrm{d}^3r \tag{2.37}$$

to summarize the *net* two-body interaction between monomers. As shown on the right hand side of figure 2.6, the hard-core repulsion for $r < 1$ makes a negative contribution to the integration of the Mayer f-function and a positive contribution to excluded volume, while the opposite is true for the attractive part $U(r > 1)$. In this example, attraction and repulsion largely offset each other, rendering the net excluded volume quite small; net attraction would however be registered by this definition through a negative excluded volume $v_{\mathrm{ex}} < 0$, while net repulsion would have $v_{\mathrm{ex}} > 0$. Note however, that the simple calculation in (2.37) is only valid for spherical monomers, to which we restrict ourself in this study anyway.

Using v_{ex}, one now has a criterion to distinguish the different solvent regimes:

(a) *Athermal solvents:* In the high temperature limit, the Mayer f-function (2.36) has a contribution only from hard-core repulsion, making the excluded volume independent of temperature (hence "athermal").

$$v_{\mathrm{ex}} \approx b^3 \tag{2.38}$$

An example is polystyrene in ethyl benzene.

(b) *Good solvents:* In the athermal limit, the monomer makes no energetic distinction between other monomers and solvent molecules, contrary to typical solvents where the monomer-monomer attraction is slightly stronger than the monomer-solvent attraction because dispersion forces usually favor identical species. This net attraction creates a small attractive well $U(r) < 0$ which leads to a lower excluded volume than the athermal value.

$$0 < v_{\text{ex}} < b^3 \tag{2.39}$$

An example is polystyrene immersed in benzene.

(c) *Theta solvents:* As the temperature is lowered, the excluded volume is reduced further, until it reaches

$$v_{\text{ex}} = 0 \tag{2.40}$$

at the *θ-temperature*, where the contribution from the attractive well exactly cancels the hard-core repulsion. Then, the chains have nearly ideal conformations[7] because there is no penalty for monomer-monomer contact.
An example is polystyrene in cyclohexane at $\theta \cong 34.5°\text{C}$.

(d) *Poor solvents:* For $T < \theta$, the attractive well dominates the interactions, and it is more likely to find monomers close together due to the net attraction, which is also signified by a negative excluded volume.

$$-b^3 < v_{\text{ex}} < 0 \tag{2.41}$$

An example is polystyrene in ethanol.

(e) *"Non-solvents":* This is the limiting case of the poor solvent, where the strong attraction leads the polymer to prefer its own monomers over all solvent molecules, nearly excluding the latter from being within the forming coil.

$$-b^3 \approx v_{\text{ex}} \tag{2.42}$$

An example is polystyrene in water[8].

Note that these definitions are based on a mean-field approximation of the system, taking only two-body interactions into account. Going to three or more body potentials lowers the given thresholds, such that the case of $v_{\text{ex}} \approx b^3$ may be considered to be the "real" good solvent, while $v_{\text{ex}} = 0$ would still be on the good side, shifting the θ-point slightly into the regime of $v_{\text{ex}} < 0$.

The conformations of a real chain in an athermal or good solvent are determined by the balance of the effective repulsion energy between monomers that tends to swell the chain and the entropy loss due to such deformation. Though surprising at first regarding its simplicity, one of the most successful simple models that captures

[7] Up to logarithmic corrections.
[8] This is also the reason why styrofoam coffee cups are made from polystyrene.

the essence of this balance remains the *Flory theory* [31] which makes rough estimates of both the energetic and the entropic contributions to the free energy. It considers a polymer of N_m repeat units, swollen to size $R_\mathrm{E} > R_\mathrm{Gauß} = bN_\mathrm{m}^{1/2}$ (see the prediction of (2.7) for ideal chains whose end-to-end vectors $\vec{R}_\mathrm{E}$ follow a Gaussian distribution), and assumes that these monomers are uniformly distributed within the volume R_E^3 with no correlations between them. The probability of a second monomer being within the excluded volume v_ex of a given first monomer then follows as $v_\mathrm{ex} \cdot N_\mathrm{m} R_\mathrm{E}^{-3}$, where $N_\mathrm{m} R_\mathrm{E}^{-3}$ is the number density of monomers in the pervaded volume of the chain. The energetic cost of being excluded from this volume, *i.e.* the energy of excluded volume interaction, is $k_\mathrm{B}T$ per exclusion, or $k_\mathrm{B}T \cdot v_\mathrm{ex} \cdot N_\mathrm{m} R_\mathrm{E}^{-3}$ per monomer. For all N_m repeat units on the chain, this energy is simply N_m times larger, namely

$$\mathcal{F}_\mathrm{int} \approx k_\mathrm{B}T \cdot v_\mathrm{ex} \cdot \frac{N_\mathrm{m}^2}{R_\mathrm{E}^3} \tag{2.43}$$

which already roughly corresponds to the beginning of the virial expansion of the free interaction energy. The Flory estimate of the entropic contribution to the free energy of a real chain is the energy required to stretch an ideal chain to end-to-end distance R_E,

$$\mathcal{F}_\mathrm{ent} \approx k_\mathrm{B}T \frac{R_\mathrm{E}^2}{N_\mathrm{m} b^2} \tag{2.44}$$

as was already derived for the ideal chains in a similar manner in (2.24) and (2.28); it may be re-used here because it is argued that the difference between ideal and real chains (the interactivity of the chain monomers) does not influence the response of the (harmonic) bonds. Then, the total free energy of a real chain in the Flory approximation is the sum of the energetic interaction (2.43) and the entropic contributions (2.44), adding up to

$$\mathcal{F}_\mathrm{tot} = \mathcal{F}_\mathrm{int} + \mathcal{F}_\mathrm{ent} \approx k_\mathrm{B}T \left(v_\mathrm{ex} \frac{N_\mathrm{m}^2}{R_\mathrm{E}^3} + \frac{R_\mathrm{E}^2}{N_\mathrm{m} b^2} \right) \tag{2.45}$$

The optimum size of the real chain, the *Flory radius* R_F, is determined through the minimum free energy of the chain:

$$\begin{aligned} \frac{\partial \mathcal{F}_\mathrm{tot}}{\partial R_\mathrm{E}} &\stackrel{!}{=} 0 = k_\mathrm{B}T \left(-3 v_\mathrm{ex} \frac{N_\mathrm{m}^2}{R_\mathrm{F}^4} + 2 \frac{R_\mathrm{F}^2}{N_\mathrm{m} b^2} \right) \\ \Rightarrow R_\mathrm{F} &\approx v_\mathrm{ex}^{1/5} b^{2/5} N_\mathrm{m}^{3/5} \end{aligned} \tag{2.46}$$

Long real chains are consequently predicted to be much larger than ideal chains with the same number of monomers N_m, as also depicted by figure 2.7.

Looking at (2.46), it displays a universal power law dependence of the polymer size R_E on the number of monomers N_m, namely

$$R_\mathrm{E} \sim N_\mathrm{m}^\nu \tag{2.47}$$

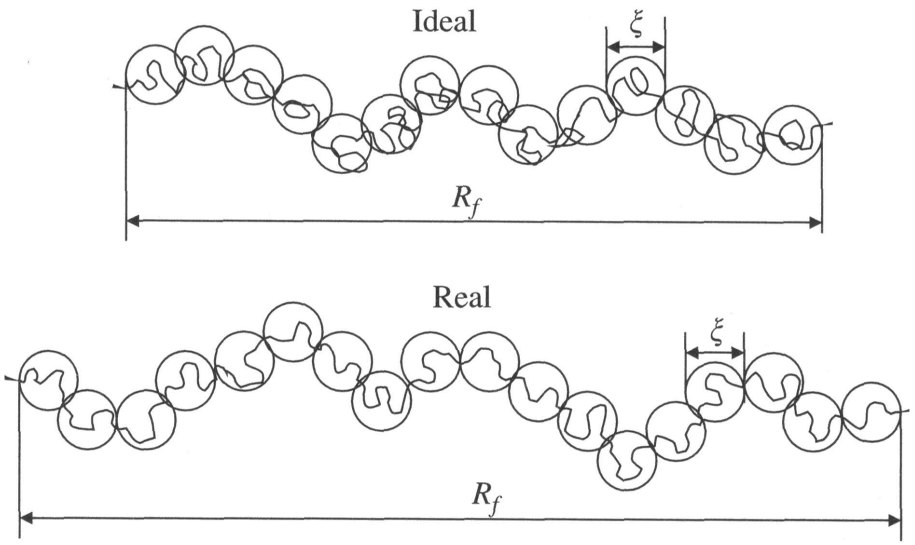

Figure 2.7.: Comparison of an ideal (*top*) and a real chain (*bottom*) of the same contour length $R_{\max} = N_{\mathrm{m}} b$ stretched by the same force $\vec{\mathrm{f}}_{\mathrm{x}}$ (taken from [156]).

which does not only contain (2.46) for $\nu = 3/5$, but it also describes the result of an ideal chain (2.7) for $\nu = 1/2$ on the scaling level (*i.e.* neglecting numerical prefactors). This analogy continues regarding the random walk conformation of ideal chains as the real chain's monomers cannot occupy the same position in space due to their excluded volume, rendering its conformation similar to that of a *self-avoiding (random) walk* (SAW). Dimensional arguments [31, 153, 159] generalize this good solvent result to d dimensions, the so-called *Flory estimate*

$$\nu = \frac{3}{2+d} \tag{2.48}$$

which is exact for $d = 2$ and $d = 4$, while being close to the more exact value of $\nu = 0.588(1)$ [153, 160, 161] for $d = 3$.

Note that though the predictions of the Flory theory are in good agreement with experiments, computer simulations, and more sophisticated theories, it is nevertheless due to a fortuitous cancellation of errors: The repulsion energy is overestimated because the correlations between monomers along the chain are omitted, while the elastic energy is also overestimated since the ideal chain conformational entropy is assumed. However, the Flory theory remains useful because it is simple and provides a reasonably good estimation. In the same spirit, mean-field estimates of the energetic part of the free energy, ignoring correlations between monomers, are often used with entropy estimates based on ideal chain statistics, referring to such simple calculations as "Flory(-type) theory", too, while also hoping that the errors will cancel again.

Next in the comparison between ideal and real chains is their behaviour under tension. Continuing the arguments from section 2.3, a θ-solvent with nearly ideal chain statistics and a good solvent with excluded volume $v_{\mathrm{ex}} \approx b^3$ is considered. If both polymers are put under tension by the same force $\vec{\mathsf{f}}_{\mathrm{x}}$, the tension blob depiction of figure 2.5 changes to that of figure 2.7 because of the larger space $R_{\mathrm{F}} = bN_{\mathrm{m}}^{3/5}$ a real chain requires compared to the $R_{\mathrm{Gauß}} = bN_{\mathrm{m}}^{1/2}$ of Gaussian chain; this difference in the end-to-end distance will however diminish for $\mathsf{f}_{\mathrm{x}} \to \infty$ as local repulsion will play an increasingly negligible role for overstretched chains. The size of one tension blob now changes from the $\xi \approx bg^{1/2}$ in (2.26) to

$$\xi \approx bg^{3/5} \tag{2.49}$$

once again arguing that on local scales within a blob the behaviour of the g monomers is unperturbed by the global tension, which in turn only extends the N_{m}/g blobs along the direction of $\vec{\mathsf{f}}_{\mathrm{x}}$. Therefore, (2.27) or $R_{\mathrm{x}} \approx R_{\mathrm{Gauß}}^2/\xi$ becomes

$$R_{\mathrm{x}} \approx \xi \frac{N_{\mathrm{m}}}{g} \approx \frac{N_{\mathrm{m}} b^{5/3}}{\xi^{2/3}} \approx \frac{R_{\mathrm{F}}^{5/3}}{\xi^{2/3}} \tag{2.50}$$

The free energy cost for stretching the chains, on the order of $k_{\mathrm{B}}T$ per tension blob, changes $\mathcal{F} \approx k_{\mathrm{B}}T\,(R_{\mathrm{x}}/R_{\mathrm{Gauß}})^2$ from (2.28) to

$$\mathcal{F} \approx k_{\mathrm{B}}T \left(\frac{R_{\mathrm{x}}}{R_{\mathrm{F}}}\right)^{5/2} \tag{2.51}$$

from where the force f_{x} necessary to stretch the chain to an end-to-end distance R_{x} can be derived as

$$\mathsf{f}_{\mathrm{x}} = \frac{\partial \mathcal{F}}{\partial R_{\mathrm{x}}} = k_{\mathrm{B}}T \frac{5}{2} \left(\frac{R_{\mathrm{x}}}{R_{\mathrm{F}}}\right)^{3/2} \tag{2.52}$$

instead of the linear Hooke's law (2.25). This non-linear dependence of f_{x} on an elongation R_{x} for real chains in (2.52) was first derived by Pincus [162] which is why the tension blobs are also called *Pincus blobs*. The divergence of the force near maximal extension $R_{\mathrm{x}} \to R_{\mathrm{max}}$ is not described by this scaling approach. For ideal chains given in (2.31), in case of real polymers it is not a textbook topic and will be derived in section 3.2.6.

2.5. Polyelectrolyte Chains in Solution

Up to now, only neutral systems have been considered. The general ideas and scaling concepts can however be applied in case of weakly charged chains as well, if the electrostatic interaction along the backbone with charge fraction f is smaller than the thermal energy, *i.e.* if

$$k_{\mathrm{B}}T \frac{\ell_{\mathrm{B}} f^2}{b} \ll k_{\mathrm{B}}T \tag{2.53}$$

(where the *Bjerrum length* $\ell_B = e_0^2/(4\pi\epsilon_0\epsilon_S k_B T)$ indicates the strength of the electrostatic coupling by representing the distance two elementary charges e_0 have when their interaction energy is $k_B T$).

Then, for sufficient dilution a single chain may be treated while neglecting its counterions, because the coulombic coupling between them and the monomers is smaller than the counterions' entropy. The repulsion between the monomers comes into play, and the chain conformation is determined by the competition between the chain entropy and the electrostatic repulsion of the charged beads. For large length scales, electrostatics dominates and leads to a rodlike shape, while for small scales entropy dictates Gaussian statistics. The resulting blob picture [12,33,163] is similar to the one previously discussed for neutral systems, except that now the coulombic coupling determines the formation of the string of electrostatic blobs of size ξ_{PE} with g_{PE} monomers each. Hence, each blob balances electrostatic and thermal energy to

$$k_B T \frac{\ell_B \left(f g_{PE}\right)^2}{\xi_{PE}} \approx k_B T \tag{2.54}$$

while within lengths smaller ξ_{PE} obeying Gaussian chain statistics because there the coulombic interaction energy is smaller than $k_B T$.

In the θ-regime this translates to

$$\xi_{PE} \approx b g_{PE}^{1/2} \tag{2.55}$$

from where ξ_{PE} and g_{PE} can be derived by using (2.54) with (2.55) to arrive at

$$\xi_{PE} \approx b^{4/3} \ell_B^{-1/3} f^{-2/3} \tag{2.56}$$

$$g_{PE} \approx b^{2/3} \ell_B^{-2/3} f^{-4/3} \tag{2.57}$$

Since there are N_m/g_{PE} blobs of that size, the total extension $R_E = (N_m/g_{PE})\xi_{PE}$ of the chain follows as

$$R_E = N_m b \left(\frac{\ell_B f^2}{b}\right)^{\frac{1}{3}} \tag{2.58}$$

if N_m monomers are present.

Good solvent conditions, high temperatures, strong(er) electrostatics cause this picture to break down, and a rich phase diagram as a function of the solvent quality and the Bjerrum length is discovered [33,164]. These and similar considerations can then be transferred to the network regime, which will be done in section 3.2.3.

2.6. Conclusions and Outlook

This chapter introduced the basic concepts in polymer physics upon which the considerations in the following chapters are based. It clarified elementary definitions

and discussed the coarse-graining idea used by theoreticians and computer experimentalists alike to tame the complex macromolecular mechanisms. It contrasted the different ideal chain models, particularly the (equivalent) freely jointed chain (FJC) and the worm-like chain (WLC) which will play an important role when we will try to characterize the force-elongation-relation of the network strands later on. Changes in the free energy and the response to an externally applied pulling force were also detailed for both models. Theoretically favorable as well as experimentally accessible definitions for the chain conformation size were given, where the end-to-end distance R_{E} will be one of the main observables we will be investigating, without neglecting the radius of gyration R_{G} and the hydrodynamic radius R_{H} useful for real world comparison. Moving from ideal to real solvent environments, good and θ-like and poor solvents were contrasted, introducing the excluded volume concept and the very important Flory arguments for obtaining a scaling relation between chain length N_{m} and chain extension R_{E} up to omitted prefactors of order unity. The blob picture contained therein was subsequently applied to charged polymers, the polyelectrolytes, too, and will reappear in the following chapter when predictions for the macroscopic swelling behaviour of a polyelectrolyte network will be made.

3. Theoretical Treatment of Good Solvent Hydrogels

Advanced concepts in polymer physics are introduced and applied to macromolecular networks. The c^*-picture is detailed by discussing the c^*-gel upon which most known theories are based. Simple models are sufficient to describe the swelling equilibrium of polyelectrolyte networks in the limit of weak electrostatics. Higher charge fractions and/or stronger coulombic coupling cause deviations, requiring a number of corrections to account for neglected but increasingly important mechanisms in that regime. A blob picture based scaling approach is shown to be able to take all these into account, and successfully matches results from computer simulations over the entire parameter range. Alternatively, the "cell under tension"-model is introduced which allows for a self-consistent way to do the same, but without any additional assumptions on the system.

For describing a polymer network theoretically, the single chain concepts from the previous chapter 2 become very useful. The reason lies in the c^*-picture, which will be introduced in section 3.1, because it allows to derive network properties from the behaviour of a single chain. Even if the c^*-theorem, explained in that section as well, is not applicable in the case of our charged hydrogels, the construct of a c^*-gel and many other techniques developed for the single chain or neutral network treatment may be re-used.

This quickly leads to first, simple estimates on their equilibrium extension in a θ-solvent environment (section 3.2.1) and in a good solvent (section 3.2.2), which will be enhanced further by considering the polyelectrolyte blobs from section 2.5 (section 3.2.3), the effect of counterion condensation (section 3.2.4), screening effects (section 3.2.5), and the finite extensibility of the chains (section 3.2.6). Such additional layers of complexity are necessary because the simpler models naturally neglect a number of mechanisms which might modify the gel's behaviour in certain parameter regimes; we will therefore investigate how their predictions compare to the outcome of our computer simulations from chapter 4 and what deviations remain. This will inevitably lead back to the question of the counterion distribution, which can be addressed in a more systematic way in the framework of the cylindrical cell model (section 3.2.7), where the solution of the Poisson-Boltzmann equation gives both their osmotic pressure and number density in the system. Discussing different

definitions for the effective charge fraction and adding the intra-chain charge repulsion in section 3.2.8 completes the extensions to the simple scaling approach. As final result we will be able to predict the equilibrium behaviour of charged hydrogels on the scaling level, which will be double-checked for finite size effects in section 3.2.9 and employed to predict $p(V)$-relations as well, rounding off section 3.2.

Next, in section 3.3 we will develop a self-consistent model depiction of the swelling of polyelectrolyte networks in good solvent by introducing the "cell under tension"-model of a self-regulating cell system. The focus will thereby be on incorporating all the mechanisms previously identified as important into the framework, without using anything but system parameters as model input. A comparison with the simple scaling arguments to determine which approach yields the more promising perspective to justify further investigations rounds off this chapter.

3.1. Comments on the c^*-picture

In the following sections we are going to make extensive use of the construct of a c^*-gel for describing the basic behaviour of our networks. Hence, this section should provide a bit of background on the c^*-picture usually used for neutral systems.

In a good solvent polymers are swollen due to excluded volume effects. The *c^*-theorem* states, that for crosslinking in solution a gel automatically maintains a concentration close to the overlap concentration of the corresponding semi-dilute solution of non-crosslinked chains. As a consequence, the network strands exhibit single chain behaviour and act as non-linear entropic springs. The elastic properties of a network of such springs can be estimated within the usual approximations. This phenomenon is well understood for individual chains, but it is less clear what happens in the case of polymer networks which were prepared by cross-linking a dense melt of linear precursor chains. Recent computer simulations [37] suggest a surprising scenario: the network strands are more strongly swollen than single chains and exhibit a fractal structure characterized by a new exponent $\nu = 7/10$.

There is a fundamental difference between having a c^*-gel and using the c^*-theorem. While a *c^*-gel* in essence is nothing more than a polymer network which happens to have the same concentration $c = N_{\mathrm{tot}}/V$ as a corresponding polymer solution at its overlap concentration $c^* := N_{\mathrm{m}}/R_{\mathrm{E}}^3 = c$ (except for numerical prefactors correcting for the implied spherical symmetry), the c^*-theorem assumes this to be true in general, which would allow to treat the swelling process of a (neutral) network by always considering single chain effects at $c = c^*$. However, it can be shown [37] that this would rather quickly lead to serious contradictions.

As an example, if one starts with a (neutral) c^*-gel in the swollen state, then $R_{\mathrm{E}} = R_{\mathrm{F}} = bN_{\mathrm{m}}^{\nu}$ with R_{F} being the Flory radius, and from the concentration $c^* = N_{\mathrm{m}}/R_{\mathrm{E}}^3$ the volume fraction would follow to be $\Phi = b^3 c^* = b^3 N_{\mathrm{m}}/R_{\mathrm{F}}^3 = N_{\mathrm{m}}^{1-3\nu}$. Compressing this towards the melt state (where $\Phi = 1$) by scaling $V \to V/\lambda^3$

requires $\lambda = \Phi^{-1/3}$ to achieve $\Phi \to \Phi\lambda^3 = 1$, which in turn leads to $R_\mathrm{E} \to R_\mathrm{E}/\lambda = R_\mathrm{F}\Phi^{1/3} = bN_\mathrm{m}^\nu \cdot N_\mathrm{m}^{1/3-\nu} = bN_\mathrm{m}^{1/3}$ – but this would be a globular (collapsed) state, contradicting our assumption to compress to the melt state!

Similarly, problems also arise when starting with a polymer melt, forming the network there. Even if one now assumed the network strands to be of equal length N_m, all excluded volume interactions would be entirely screened such that $R_\mathrm{E} = R_\mathrm{Gauß} = bN_\mathrm{m}^{1/2}$. This would leave two choices for extending the network back to the swollen state discussed before: First, one could stretch the chains until their extension reaches R_F, requiring $R_\mathrm{E} \to R_\mathrm{E}\lambda$ with $\lambda = R_\mathrm{F}/R_\mathrm{Gauß}$, decreasing the volume fraction to $\Phi \to \Phi/\lambda^3 = 1/(R_\mathrm{F}/R_\mathrm{Gauß})^3 = N_\mathrm{m}^{3/2-3\nu}$, instead of the $N_\mathrm{m}^{1-3\nu}$ derived before (remember that $\Phi = 1$ in the melt state). Second, one could directly aim for that volume fraction by setting $\lambda = (N_\mathrm{m}^{1-3\nu})^{-1/3} = N_\mathrm{m}^{-1/3+\nu}$, which would then extend the chains towards $R_\mathrm{E} \to R_\mathrm{E}\lambda = bN_\mathrm{m}^{1/2} \cdot N_\mathrm{m}^{-1/3+\nu} = bN_\mathrm{m}^{1/6+\nu}$ instead of $R_\mathrm{F} = bN_\mathrm{m}^\nu$. Furthermore, if applying the c^*-theorem to the melt the volume fraction would become $\Phi = b^3 N_\mathrm{m}/R_\mathrm{Gauß}^3 = N_\mathrm{m}^{-1/2} \neq 1$, such that it had to be interpreted as $N_\mathrm{m}^{1/2}$ interpenetrating networks to arrive at the required $\Phi = 1$; this would in turn lead back to the two aforementioned choices of $\lambda = R_\mathrm{F}/R_\mathrm{Gauß}$ or $\lambda = N_\mathrm{m}^{-1/3+\nu}$ and their corresponding failure to describe the network's swelling process towards a c^*-gel.

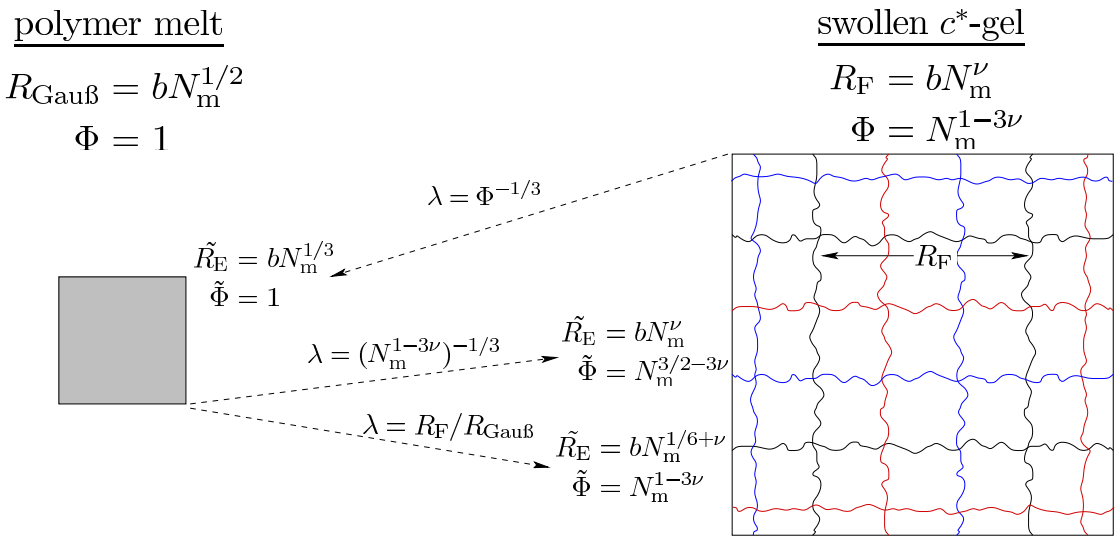

Figure 3.1.: Illustrating the failure of the c^*-theorem for describing the swelling process of networks by considering different (de-)swelling factors λ between a dry melt and a gel resp. interpenetrating networks (for details see text).

Considering that we even neglected impurities all randomly formed networks will inevitably have, *i.e.* the existence of entanglements when the formation occurred in the melt state, which in a first approximation would replace N_m by a distribution

of chain lengths, a rather random topology depending on the connectivity of nodes and network monomers, and maybe even dangling ends, it is safe to conclude that the c^*-theorem is not applicable for gels crosslinked in a melt, as could be seen in the example of the interpenetrating regular networks. Randomly crosslinked c^*-gels are produced from crosslinking in dilute solution, albeit mechanically they are relatively instable. Non-interpenetrating and non-entangled regular networks, however, do have equilibrium concentrations on the order of c^* as well, which is why it is more than justified to describe the swollen networks in our system as a c^*-gel, *i.e.* using $c = N_{\mathrm{tot}}/V \propto N_{\mathrm{m}}/R_{\mathrm{E}}^3$.

3.2. The Swelling Equilibrium of Polyelectrolyte Networks

This section will construct a theoretical model which will be able to describe the swelling equilibrium of charged hydrogels on the scaling level, *i.e.* up to numerical prefactors on the order of unity. To do so, we will first start with commonly accepted simple models for *e.g.* ideal neutral networks and charged model gels, which however quickly turn out to fail beyond the limit of weak electrostatics; the reason for this and the connection to their underlying assumptions will be thoroughly investigated in the next chapter 4 where we will focus on the discrepancy between the behaviour of model and simulation systems. This section then continues to build upon the simple models' basic ideas, expanding them by incorporating the neglected additional effects responsible for their original failure, until we reach satisfactory agreement with the simulations over the entire range of system parameters.

In a polyelectrolyte network the interplay of monomers and counterions, their charged, bonded and excluded volume interactions all lead to a multitude of pressure components $\mathcal{P}_i$, most of which are separable within the simulated environment, while few are independent of each other. Swelling equilibrium is reached when they all balance one another, and $\mathcal{P} = \Sigma_i \mathcal{P}_i = 0$, *i.e.* no effective forces are acting on the simulation box, neither outwards ($\mathcal{P} > 0$) nor inwards ($\mathcal{P} < 0$), to change its volume. Microscopically, the $\mathcal{P}_i$ can be categorized by *e.g.* sorting all mechanical and network-related contributions into $\mathcal{P}_{\mathrm{gel}}$, the ideal gas-like pressure and possible excluded volume effects of the counterions into $\mathcal{P}^{\mathrm{CI}}$, leaving the unparticularizable $\mathcal{P}_{\ell_{\mathrm{B}}}^{\mathrm{tot}} = \frac{1}{3V}\langle E_{\mathrm{C}} \rangle$ on its own[1].

Note however that although the pressure components itself are additive, the assumption of *e.g.* having all direct electrostatic contributions collected in $\mathcal{P}_{\ell_{\mathrm{B}}}^{\mathrm{tot}}$ is by itself already assuming the validity of the Flory-Rehner-Hypothesis (FRH; see section 4.3), the reason being that in principle one could find *e.g.* electrostatic effects

[1] More on the $\mathcal{P}_i$ and their categorization can be found in the simulation sections, *e.g.* in sections 4.1 and 4.2.3.

in other components as well, where the coulombic coupling changes for example the counterion distribution which in turn affects their excluded volume interactions and therefore $\mathcal{P}_{\mathrm{LJ}}^{\mathrm{CI}}$. Such cross-correlation would essentially prevent any modeling attempt, whereas the FRH restricts considerations to the superposition of independent contributions.

On a qualitative level, the swelling equilibrium can then be described by incorporating the following layers of complexity into one model:

- c^*-gel of point-like monomers swollen by an ideal gas of neutral "counterions"
- excluded volume effects on the chains $\rightarrow$ *tension* or *Pincus blobs*
- electrostatic effects $\rightarrow$ *polyelectrolyte blobs*
- counterion condensation for strongly charged systems
  $\rightarrow$ effective charge fraction f_{eff} and number of effective charges Q_{eff}
- screening of coulombic interactions $\rightarrow$ Debye screening length κ^{-1}
- finite extensibility of the chains
- counterion density in the cell model $\rightarrow \Pi_{\mathrm{C}}^{\mathrm{PB}}$
- charge renormalization and counterion distributions
- intra-chain repulsion of charged monomers

This will be done in the subsequent subsections. Note however, that the given list is by no means comprehensive, since it focuses on the effects predominant in our systems and parameter regimes; other influences, such as *e.g.* the impact of the valency on the shape of the network, which in the case of multivalent counterions will see them rather collapse the network than condense onto the chains if electrostatic interactions are strong, are deliberately omitted if irrelevant here (everything is monovalent in our study).

3.2.1. θ-solvent

Assuming the validity of FRH, the swelling equilibrium of a charged gel should mainly result from the elastic response of the chains' inner bonds balancing the osmotic pressure of the counterions trapped inside the network by the macroscopic electro-neutrality requirement.

Neglecting explicit electrostatic effects and treating all objects to be point-like, the N_{CI} counterions in the simulation box volume V thereby behave as an ideal gas-like cloud surrounding the N_{p} network chains, and elongate each to an average end-to-end distance R_{E}. Their osmotic pressure $\Pi_{\mathrm{C}} = \rho k_{\mathrm{B}} T$ consequently follows as

$$\Pi_{\mathrm{C}} = k_{\mathrm{B}} T \frac{N_{\mathrm{CI}}}{V} \propto k_{\mathrm{B}} T \frac{f N_{\mathrm{m}}}{R_{\mathrm{E}}^3} \tag{3.1}$$

if using the depiction of a c^*-gel (see section 3.1) with N_{nodes} tetra-functional nodes and N_{m} monomers per strand, of which a fraction f is oppositely charged to the monovalent counterions. Evidently, this can only be an accurate description as long as the coulombic contribution $\Pi_{\ell_{\mathrm{B}}}$ to the pressure remains negligible, *i.e.* the N_{m} monomers per strand are not too strongly charged, the fraction $(1-f)$ of neutral ones is not too small, and the electrostatic interactions are not too large.

For harmonic chains with Gaussian statistics the elastic response Π_{E} of the bonds of length b connecting the monomers is given by

$$\Pi_{\mathrm{E}} = -\frac{k_{\mathrm{B}}T}{N_{\mathrm{m}}b^2 \cdot R_{\mathrm{E}}} \tag{3.2}$$

which makes it possible to derive a simple prediction for the node-node-separation R_{E}, therefore describing the network's equilibrium extension, by balancing both terms in (3.1) and (3.2) to mimic the swelling equilibrium.

From there, $\Pi_{\mathrm{C}} + \Pi_{\mathrm{E}} = 0$ gives [39–41]

$$R_{\mathrm{E}} = f^{1/2} N_{\mathrm{m}} b \quad \Rightarrow \quad \alpha_\theta = \frac{R_{\mathrm{E}}^2}{R_\theta^2} = (fN_{\mathrm{m}})^1 \tag{3.3}$$

for the end-to-end extension of the network strands, and the swelling ratio α_θ relating R_{E} to the neutral single chain case where $R_\theta = bN_{\mathrm{m}}^{1/2}$.

3.2.2. Good Solvent

Drawing further on the analogy to single chains, excluded volume effects can be taken into account by employing the classical tension blob model [31,32] developed for ideal polymers (section 2.3) and modified for good solvent (section 2.4).

It allows the network chains to be treated as a sequence of $\frac{N_{\mathrm{m}}}{g_{\mathrm{T}}}$ blobs of size $\xi_{\mathrm{T}} = bg_{\mathrm{T}}^{\nu}$ containing g_{T} monomers of size b each, and having $R_{\mathrm{E}} = \xi_{\mathrm{T}} \cdot \frac{N_{\mathrm{m}}}{g_{\mathrm{T}}}$ as the chain extension.This implies the network strands to have unperturbated single chain characteristics on local scales of length ξ_{T}, *i.e.* inside the *tension* or *Pincus blobs* [162]. Since ξ_{T} is chosen such that one blob has the energy $k_{\mathrm{B}}T = \mathsf{f}_{\mathrm{E}} \cdot \xi_{\mathrm{T}}$, the presence of fN_{m} counterions per strand stretches each chain as if a force f_{E} was acting on the ends, elongating it to an end-to-end distance R_{E}, which puts the elastic pressure at

$$\Pi_{\mathrm{E}} = -\frac{\mathsf{f}_{\mathrm{E}} \cdot R_{\mathrm{E}}}{R_{\mathrm{E}}^3} = -\frac{k_{\mathrm{B}}T}{R_{\mathrm{E}}^3} \cdot \frac{N_{\mathrm{m}}}{g_{\mathrm{T}}} \tag{3.4}$$

As before in section 3.2.1, this is supposed to balance the osmotic pressure Π_{C} of the counterions given by (3.1),

$$0 = \Pi_{\mathrm{C}} + \Pi_{\mathrm{E}} = \left(k_{\mathrm{B}}T \frac{fN_{\mathrm{m}}}{R_{\mathrm{E}}^3}\right) + \left(-\frac{k_{\mathrm{B}}T}{R_{\mathrm{E}}^3} \cdot \frac{N_{\mathrm{m}}}{g_{\mathrm{T}}}\right)$$

from where the number of monomers per blob follows as

$$g_{\mathrm{T}} = \frac{1}{f} \tag{3.5}$$

The scaling prediction [39,62,63] for the network strands then yields

$$R_{\mathrm{E}} = f^{1-\nu} N_{\mathrm{m}} b \quad \Rightarrow \quad \alpha_\nu = \frac{R_{\mathrm{E}}^2}{R_\nu^2} = (f N_{\mathrm{m}})^{2(1-\nu)} \tag{3.6}$$

using the single chain description $R_\nu = b N_{\mathrm{m}}^\nu$ for uncharged systems in the swelling ratio α_ν.

For Gaussian chains (θ-solvent, $\nu = \frac{1}{2}$) the very same result has been obtained in (3.3), so that the blob picture turns out to be an equivalent description; in a good solvent, however, $\nu = \frac{3}{5}$ [31] or $\nu = 0.588$ [153,160,161], hence the dependency of R_{E} on f is expected to be more pronounced than for the θ-case (note that $0 < f \leq 1$).

3.2.3. Polyelectrolyte Blobs

An alternative scenario considers the swelling of the gel to be a single-chain effect due to repulsive electrostatic interactions between the monomers on the network strands (see section 2.5). So far, these interactions have been neglected, all mechanisms discussed have been of a purely mechanical nature. That is no longer valid once the coulombic energy exceeds the tension one from the previous section 3.2.2 because in that case the size of a blob, *i.e.* the length scale on which the interaction energy between monomers reaches $k_{\mathrm{B}}T$, is set by $\xi_{\mathrm{PE}} < \xi_{\mathrm{T}}$ along [163]

$$k_{\mathrm{B}}T = k_{\mathrm{B}}T \cdot \ell_{\mathrm{B}} \frac{(f g_{\mathrm{PE}})^2}{\xi_{\mathrm{PE}}} > \mathsf{f}_{\mathrm{E}} \cdot \xi_{\mathrm{T}} \tag{3.7}$$

with $g_{\mathrm{PE}} < g_{\mathrm{T}}$ denoting again the number of monomers per blob (*"the smaller blob wins"*). From (3.7) and the definition of a blob, namely that within one the unperturbated ideal chain behaviour $\xi_{\mathrm{PE}} = b g_{\mathrm{PE}}^\nu$ is valid, g_{PE} follows as

$$g_{\mathrm{PE}} = \left(\frac{f^2 \ell_{\mathrm{B}}}{b} \right)^{-\frac{1}{2-\nu}} \tag{3.8}$$

Comparing (3.8) to the tension blob result (3.5) allows to distinguish both regimes:

$$\begin{aligned} g_{\mathrm{PE}} &< g_{\mathrm{T}} \\ \Rightarrow \left(\frac{f^2 \ell_{\mathrm{B}}}{b} \right)^{-\frac{1}{2-\nu}} &< \frac{1}{f} \\ \Rightarrow f &> \left(\frac{\ell_{\mathrm{B}}}{b} \right)^{-\frac{1}{\nu}} \end{aligned} \tag{3.9}$$

Hence, with (3.9) one has a qualitative criterion for the applicability of the two blob models presented, intuitively predicting that for larger f (higher fraction of charged monomers, more important electrostatics) coulombic interactions will become stronger than the tension, leading to the Pincus blobs being replaced by the polyelectrolyte blob regime (see figure 3.3).

3.2.4. Counterion Condensation

Increasing the strength of the electrostatic interactions further will also invalidate the description of the counterions as an ideal gas-like cloud acting as an osmotic pressure exerting but otherwise uniform charged background. Ions close to the chains will become increasingly attracted towards them, until eventually a defined number will be systematically trapped in their vicinity due to the coulombic attraction overcompensating the entropic penalty. For the special case of an infinitely stiff, entirely straight polymer (or its model, a charged rod) it has been found [165], that for a Manning parameter $\xi_\mathrm{M} = \frac{\ell_\mathrm{B}}{a} \geq \frac{1}{v_\mathrm{CI}}$ (a being the charge separation on the rod, v_CI being the valency of the counterions) a fraction of $(1 - \frac{1}{\xi_\mathrm{M}})$ counterions will "condense" onto the rod, *i.e.* will be confined to a small cylindrical volume around it, thereby renormalizing f towards an *effective* charge fraction f_eff; for $\xi_\mathrm{M} > 1$ all counterions added to the system will condense as well, rendering any $f > f_\mathrm{max}$ to not increase the amount of free counterions contributing to Π_C and keeping the effective charge f_eff to one charge per Bjerrum length. Consequently, it is given by

$$f_\mathrm{eff} = \begin{cases} f & \text{for } \frac{\ell_\mathrm{B}}{a} < \frac{1}{v_\mathrm{CI}} \Rightarrow f < f_\mathrm{max}, \\ f_\mathrm{max} = f\frac{a/v_\mathrm{CI}}{\ell_\mathrm{B}} & \text{for } \frac{\ell_\mathrm{B}}{a} \geq \frac{1}{v_\mathrm{CI}} \Rightarrow f \geq f_\mathrm{max}, \end{cases} \tag{3.10}$$

allowing a simple argument for the inherently complex situation of having firmly trapped, partially attracted, and entirely undisturbed counterions to be accounted for[2].

Although only considering monovalent systems here ($v_\mathrm{CI} = 1$), applying the Manning picture to real polymers leaves the problem of determining the distance a between neighbouring charges. As depicted in figure 3.2, the definition $a = \frac{\text{length}}{\#\text{ charges}}$ becomes ambiguous when used with only rod-*like* polymers: Depending on whether one measures the charge separation along the chain's contour length or projects that distance onto a line of length R_E, gives with $a = b/f$ and $a = R_\mathrm{E}/(fN_\mathrm{m})$, respectively, two results dissimilar even for highly extended polymers with *e.g.* $\langle R_\mathrm{E}^2\rangle/\langle R_\mathrm{G}^2\rangle = 12$. Within the blob picture any criterion is to be applied locally to each blob, leading to $a = \xi/(fg)$ for ξ, g corresponding to either $\xi_\mathrm{T}, g_\mathrm{T}$ from the Pincus model, or $\xi_\mathrm{PE}, g_\mathrm{PE}$ in case of polyelectrolyte blobs. To illustrate this dilemma, in the following both the rod's $f_\mathrm{max}^\mathrm{rod} = (\ell_\mathrm{B}/b)^{-1}$ (using $a = b/f$) and $f_\mathrm{max}^\mathrm{blob} = \xi/(g\ell_\mathrm{B})$ (from the blob picture's $a = \xi/(fg)$) will be applied to the results from the previous sections.

[2] Note that this definition (3.10) is more general than the one previously used in (4.11).

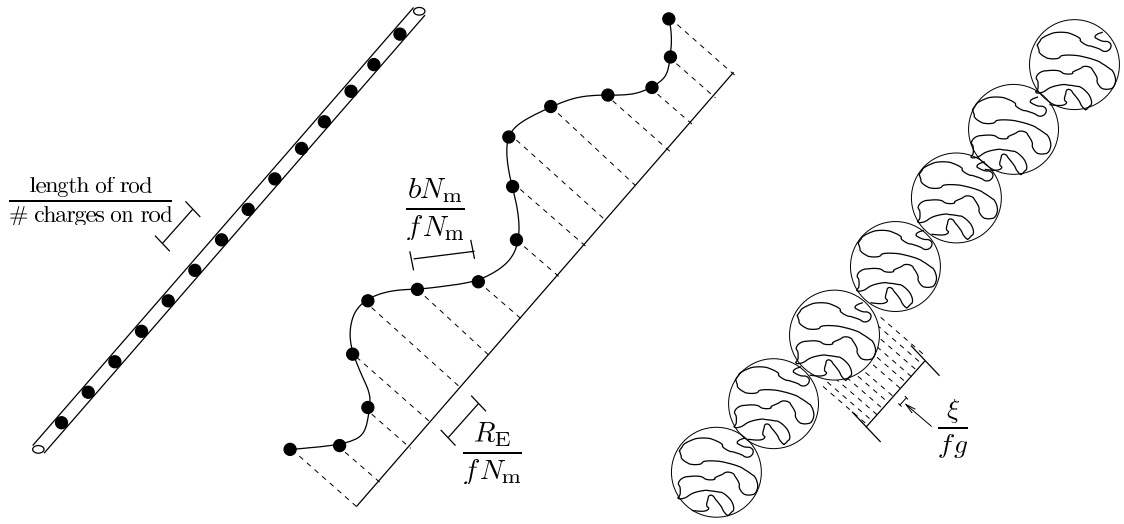

Figure 3.2.: Illustrating the problem of finding an appropriate description for the charge separation a in the Manning criterion: Defined for a rod (*left*), in case of a real polymer (*center*) using the separation b/f along the contour length bN_m is different from projecting the charges onto R_E/fN_m, while for the blob model (*right*) the projection occurs separately within each blob.

Since $\xi = bg^\nu$, the requirement $f \leq f_{max}^{blob}$ becomes $f \leq g^{\nu-1}b/\ell_B$, which in the tension blob regime (3.5) translates to

$$\begin{aligned} f &\leq \left(\frac{1}{f}\right)^{\nu-1} \frac{b}{\ell_B} \\ \Rightarrow f &\leq \left(\frac{b}{\ell_B}\right)^{-\frac{1}{\nu}} \end{aligned} \tag{3.11}$$

For polyelectrolyte blobs (3.8) we find

$$\begin{aligned} f &\leq \left(\frac{f^2\ell_B}{b}\right)^{-\frac{1}{2-\nu}\cdot(\nu-1)} \frac{b}{\ell_B} = f^{2(1-\frac{1}{2-\nu})} \left(\frac{\ell_B}{b}\right)^{-\frac{1}{2-\nu}} \\ \Rightarrow f &\leq \left(\frac{b}{\ell_B}\right)^{(\frac{2-\nu}{\nu})\cdot(-\frac{1}{2-\nu})} = \left(\frac{b}{\ell_B}\right)^{-\frac{1}{\nu}} \end{aligned} \tag{3.12}$$

Comparing (3.11), (3.12) to the crossover criterion (3.9) between the Pincus ($g = g_T$) and the polyelectrolyte blob ($g = g_{PE}$) regime, it is noteworthy that they all coincide, *i.e.* as soon as $\ell_B/b \geq f^{-\nu}$ and the electrostatic interactions begin to dominate the chain conformation, counterion condensation immediately sets in, too. Since this fixes f in g_{PE} at f_{max}^{blob}, re-inserting $f = f_{max}^{blob}$ into (3.8) shows that further increasing

electrostatics will rather squeeze more monomers into one blob along

$$g_{\mathrm{PE}}^{\mathrm{blob}} = \left(\frac{\ell_{\mathrm{B}}}{b}\right)^{\frac{1}{\nu}} \tag{3.13}$$

causing $R_{\mathrm{E}} = \xi \cdot \frac{N_{\mathrm{m}}}{g} = g^{\nu-1} b N_{\mathrm{m}}$ to shrink. As is illustrated in figure 3.3, considering g as a function of ℓ_{B}/b has it consequently cross over from $g = g_{\mathrm{T}}$ directly to $g = g_{\mathrm{PE}}^{\mathrm{blob}}$ at $\ell_{\mathrm{B}}/b = f^{-\nu}$ and

$$g(\frac{1}{f^{\nu}}) = g_{\mathrm{T}}(\frac{1}{f^{\nu}}) = g_{\mathrm{PE}}(\frac{1}{f^{\nu}}) = g_{\mathrm{PE}}^{\mathrm{blob}}(\frac{1}{f^{\nu}}) = \frac{1}{f} \tag{3.14}$$

without even entering the region where $g = g_{\mathrm{PE}}$ would be applicable.

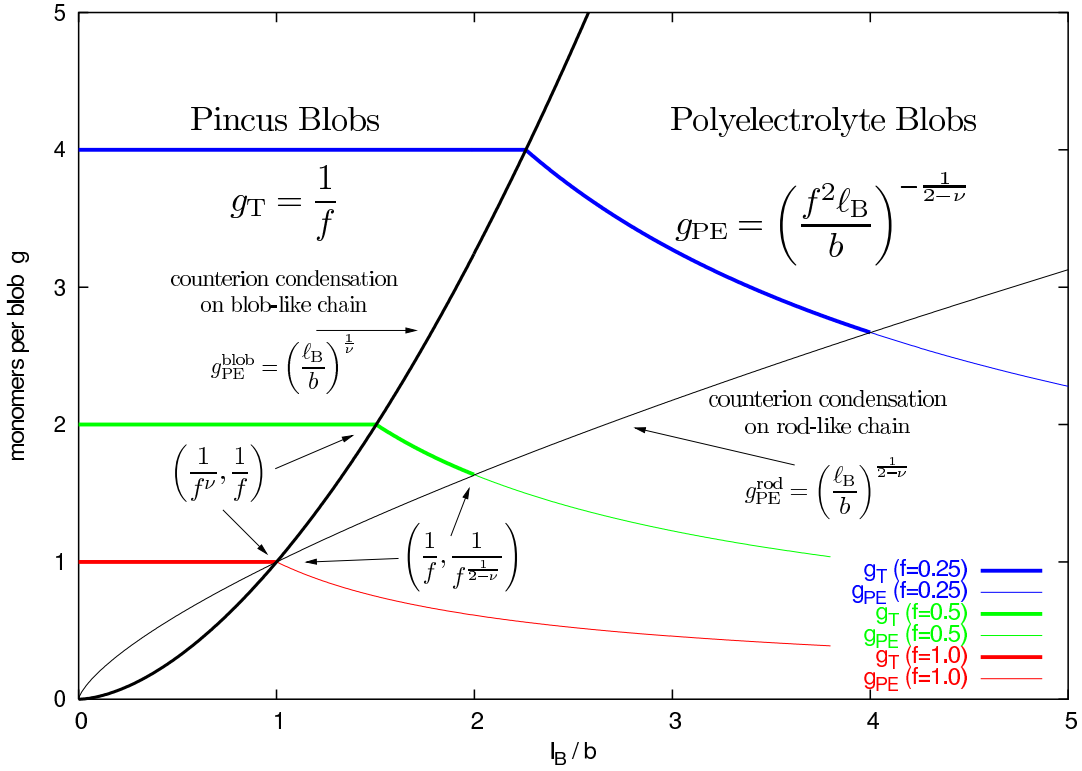

Figure 3.3.: The number g of monomers in a blob, given for constant f as a function of ℓ_{B}/b, the strength of the electrostatic interactions. While for $\ell_{\mathrm{B}}/b < f^{-\nu}$ it follows the tension blob description $g = g_{\mathrm{T}}$, the behaviour for stronger coulombic interactions depends on the model chosen to specify the distance a between two neighbouring charges on the chains, having g to either directly enter the Manning regime by diverging along $g = g_{\mathrm{PE}}^{\mathrm{blob}}$, or having it display the polyelectrolyte blob behaviour $g = g_{\mathrm{PE}}$ first, before then diverging slower with $g = g_{\mathrm{PE}}^{\mathrm{rod}}$ at $\ell_{\mathrm{B}}/b > f^{-1}$ (for full details see text).

Using the rod-like description $f \leq f_{\max}^{\mathrm{rod}} = (\ell_{\mathrm{B}}/b)^{-1}$ instead shifts the onset of counterion condensation towards stronger coulombic interactions, since due to $0 < f \leq 1$ for the charge fraction $f_{\max}^{\mathrm{rod}} \leq 1 \Rightarrow b \leq \ell_{\mathrm{B}}$ and thence $(\ell_{\mathrm{B}}/b)^{-1/\nu} \leq (\ell_{\mathrm{B}}/b)^{-1}$ follows (as $\nu < 1$). Contrary to the previous case, this implies an intermediate regime where the number of monomers g behaves as g_{PE} *before* the Manning condensation begins to set in at $f > f_{\max}^{\mathrm{rod}}$. Again, inserting this then fixed charge fraction into g_{PE} allows to derive

$$g_{\mathrm{PE}}^{\mathrm{rod}} = \left(\frac{\ell_{\mathrm{B}}}{b}\right)^{\frac{1}{2-\nu}} \tag{3.15}$$

now exhibiting a slower divergence than in the case of $g_{\mathrm{PE}}^{\mathrm{blob}}$, indicating an also slower decrease in R_{E}. Regarding the intersection of this second transition, looking at $\ell_{\mathrm{B}}/b = f^{-1}$ in (3.8) and (3.15) gives

$$g(\frac{1}{f}) = g_{\mathrm{PE}}(\frac{1}{f}) = g_{\mathrm{PE}}^{\mathrm{rod}}(\frac{1}{f}) = \frac{1}{f^{\frac{1}{2-\nu}}} \tag{3.16}$$

i.e. a lower value than in the case of $g_{\mathrm{PE}}^{\mathrm{blob}}$.

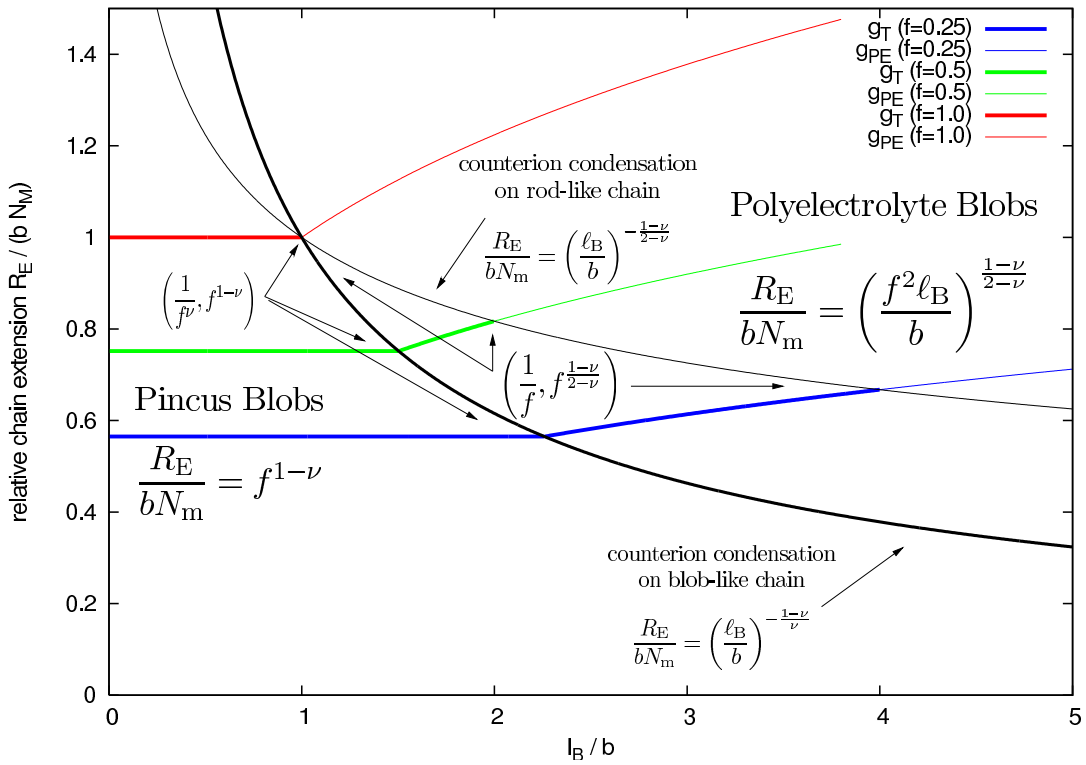

Figure 3.4.: Using $R_{\mathrm{E}} = g^{\nu-1} b N_{\mathrm{m}}$, this plot translates the number g of monomers in a blob from figure 3.3 to the relative chain extension $R_{\mathrm{E}}/(bN_{\mathrm{m}})$, again for constant f as a function of ℓ_{B}/b (for full details see text).

As a consequence, depending on the chosen model the onset of counterion condensation displays qualitatively different behaviour: In case of the blob-like description the chain collapses as soon as the Manning criterion is fulfilled, whereas figure 3.4 shows for the rod-like depiction that in an intermediate regime the strands actually reach a local maximum, even larger than their tension blob value. In the following we therefore have to bear in mind that the choice of model already leads to a certain physical behaviour, and further findings, *e.g.* from our simulation study, are required to decide which approach is more likely to match reality.

This disadvantage can be avoided if one employs the following simple argument to merely estimate the effective charge on a charged hydrogels' network chain: Obviously, its line charge density depends on the amount of swelling in the system, with the projected distance a along $\vec{R}_\mathrm{E}$ between neighbouring charges being bound by $a \geq \ell_\mathrm{B}$ from below because of the Manning condensation preventing anything closer. Re-using the blob picture, a will be given locally as $a = \xi/(fg)$ with blob size ξ and g monomers per blob, such that an amount of effective charges Q_eff would essentially follow

$$Q_\mathrm{eff} = \frac{R_\mathrm{E}}{a} = \frac{R_\mathrm{E}}{\ell_\mathrm{B} + \frac{\xi}{fg}} \tag{3.17}$$

Though (3.17) is only an estimate based on suitable limiting behaviour, it will nevertheless be sufficient on the scaling level, as we will see in the next sections.

3.2.5. Screening Effects

For any coulombic coupling strength, proximity of the counterions to oppositely charged monomers on the chains leads to a partial screening of electrostatic effects on length scales characterized by the Debye screening length κ^{-1}. Within the context of describing the network strands as a linear sequence of blobs, this allows to consider an overall neutralized volume κ^{-3} around each chain, containing a charge concentration

$$c = \frac{fN_\mathrm{m}}{(\frac{N_\mathrm{m}}{g} \cdot \xi)^3} \tag{3.18}$$

of ions and monomers in N_m/g blobs of diameter ξ. In analogy to the polyelectrolyte blobs (3.7), the criterion $k_\mathrm{B}T = k_\mathrm{B}T \cdot \ell_\mathrm{B}(c \cdot \kappa^{-3})/\kappa^{-1}$ then gives $\kappa^2 = \ell_\mathrm{B} \cdot c$ for the square of the inverse screening length, from which a Debye-Hückel type pressure Π_DH can be derived to

$$\Pi_\mathrm{DH} = k_\mathrm{B}T\kappa^3 = k_\mathrm{B}T \left(\ell_\mathrm{B} \frac{fN_\mathrm{m}}{(\frac{N_\mathrm{m}}{g} \cdot \xi)^3} \right)^{\frac{3}{2}} \propto \frac{1}{N_\mathrm{m}^3} \tag{3.19}$$

using that g and $\xi = bg^\nu$ have no explicit dependency on N_m, as could be seen *e.g.* in (3.5) and (3.8). From here, the force f_DH acting on the end of each chain follows

as

$$\mathsf{f}_{\mathrm{DH}} = \Pi_{\mathrm{DH}} \cdot \left(\frac{N_{\mathrm{m}}}{g} \cdot \xi\right)^2 = k_{\mathrm{B}}T \frac{(\ell_{\mathrm{B}} \cdot f N_{\mathrm{m}})^{3/2}}{\left(\frac{N_{\mathrm{m}}}{g} \cdot \xi\right)^{5/2}} \tag{3.20}$$

which has the pressure contributions of the screening effects being negligible if $\mathsf{f}_{\mathrm{DH}} < k_{\mathrm{B}}T/\xi$, leading to

$$\begin{aligned} \frac{(\ell_{\mathrm{B}} \cdot f N_{\mathrm{m}})^{3/2}}{\xi^{3/2} \cdot \left(\frac{N_{\mathrm{m}}}{g}\right)^{5/2}} &= \frac{(\ell_{\mathrm{B}} \cdot f)^{3/2}}{N_{\mathrm{m}} \cdot b^{3/2} \cdot g^{\frac{3\nu}{2}-\frac{5}{2}}} < 1 \\ \Rightarrow \frac{\left(\frac{\ell_{\mathrm{B}}}{b}\right)^{3/2} f^{3/2}}{N_{\mathrm{m}}} &< g^{\frac{3\nu-5}{2}} \end{aligned} \tag{3.21}$$

This means, that the impact of Π_{DH} on the total pressure balance in the system can always be made negligible for sufficiently large N_{m}, *i.e.* similar to the influence of the charge accumulation around the nodes this is a physical finite size effect.

To assert the significance of this statement, inserting $g = g_{\mathrm{T}}$ from (3.5) and $g = g_{\mathrm{PE}}$ from (3.8), respectively, into (3.21) gives

$$\begin{aligned} \left(\frac{1}{f}\right)^{\frac{3\nu-5}{2}} &> \frac{\left(\frac{\ell_{\mathrm{B}}}{b}\right)^{3/2} f^{3/2}}{N_{\mathrm{m}}} \\ \Rightarrow N_{\mathrm{m}} &> \left(\frac{\ell_{\mathrm{B}}}{b}\right)^{\frac{3}{2}} f^{\frac{3\nu-2}{2}} \end{aligned} \tag{3.22}$$

in the regime of Pincus blobs, and

$$\begin{aligned} \left(\frac{f^2 \ell_{\mathrm{B}}}{b}\right)^{-\frac{1}{2-\nu}\cdot\frac{3\nu-5}{2}} &> \frac{\left(\frac{\ell_{\mathrm{B}}}{b}\right)^{3/2} f^{3/2}}{N_{\mathrm{m}}} \\ \Rightarrow N_{\mathrm{m}} &> \left(\frac{\ell_{\mathrm{B}}}{b}\right)^{-\frac{1}{2\nu-4}} f^{-\frac{3\nu-4}{2\nu-4}} \end{aligned} \tag{3.23}$$

where polyelectrolyte blobs apply. Since we are interested in knowing if our chains have a large enough N_{m} are already large enough to neglect Π_{DH}, we only need an upper bound. Therefore, applying (3.9) in the tension blob regime as $(\ell_{\mathrm{B}}/b)^{-\nu} > f$ to (3.22) gives

$$\left(\frac{\ell_{\mathrm{B}}}{b}\right)^{\frac{1}{\nu}} > \left(\frac{\ell_{\mathrm{B}}}{b}\right)^{\frac{3}{2}} f^{\frac{3\nu-2}{2}} \tag{3.24}$$

and using it as $f^{\nu} > (\ell_{\mathrm{B}}/b)^{-1}$ in (3.23) for polyelectrolyte blobs leads to

$$\frac{1}{f} > \left(\frac{\ell_{\mathrm{B}}}{b}\right)^{-\frac{1}{2\nu-4}} f^{-\frac{3\nu-4}{2\nu-4}} \tag{3.25}$$

which both allow to draw the conclusion from (3.21) that for "normal" parameter regimes such as our $0 \leq \ell_B \leq 5\sigma$, $b \approx 1\sigma$, $0 < f \leq 1$ a network chain length of $N_m \geq 39$ monomers is more than sufficient to safely neglect additional pressure components originating in electrostatic screening effects.

Similarly, the electrostatic persistence length

$$\frac{\ell_P}{\xi} = \left(\frac{1}{\kappa\xi}\right)^2 \tag{3.26}$$

does then not represent one of the leading contributions to the swelling equilibrium either, as the same line of arguments also lead to a N_m^{-1}-dependency sufficiently decreased for our parameters, independent of the blob representation.

With Π_{DH} made negligible, however, electrostatics would become negligible as a whole in such a Debye-Hückel approach. Obviously, this cannot be true, as stronger coulombic couplings causing counterion condensation must have a significant electrostatic contribution $\mathcal{P}_{\ell_B}^{tot}$ to the pressure (which our simulations will confirm, see *e.g.* the data in table 4.3). Hence, it can only be concluded that this Debye-Hückel picture cannot be applied to these systems.

3.2.6. Finite Extensibility

Following the trivial observation that for $f \to \frac{1}{N_m}$ (the obvious lower boundary for the charge fraction of a polyelectrolyte chain) the scaling in (3.6) becomes that of a single neutral chain R_ν, the other extreme of strong elongation should now be addressed. Real chains cannot extend beyond $R_{max} = bN_m$ without breaking. From (3.6) it follows that therefore the charge fraction, more precisely $f^{1-\nu}$, has to be significantly smaller than 1, *i.e.* that the chains may not be too strongly charged for the scaling law to be applicable. Although the charge renormalization from section 3.2.4 allows to treat systems with very strong electrostatics in that limit, too, because their heavy counterion condensation will eventually lead to a small enough f_{eff}, the intermediate regime depicted in figure 3.3 remains which is more pronounced for a large amount of counterions $fN_m \approx N_m$ per chain but low electrostatics ($\xi_M \approx 1$). Here, the finite extensibility of real network chains causes the restoring force f_E of the bonds to strongly deviate from the harmonic behaviour implied in Π_E.

The polymer chains in our simulation are modeled as bead spring chains with the FENE (Finite Extension Nonlinear Elastic) potential

$$\begin{aligned} U_{FENE}(r' < r_F) &= -\frac{1}{2}k_F r_F^2 \ln\left[1 - \left(\frac{r'}{r_F}\right)^2\right] \\ U_{FENE}(r < R_{max}) &= \frac{k_F}{2}R_{max}^2 \ln\left[\frac{1}{1 - \left(\frac{r}{R_{max}}\right)^2}\right] \end{aligned} \tag{3.27}$$

representing bonds and cross-links, similar to the (4.1) we will use for the simulation model (see section 4.1). While for small elongations r it corresponds to the harmonic

$$U_{\text{Gauß}}(r) = \frac{3}{2}\frac{r^2}{\langle R_\theta^2 \rangle} = \frac{3}{2}\frac{r^2}{b^2 N_\text{m}} \tag{3.28}$$

which itself allows for arbitrarily long chain extension, U_{FENE} diverges at $r \to R_{\max}$ to infinity, hence enforcing bonds to always have $0 < b < r_\text{F}$, with the equilibrium bond length also depending on the chosen representation of the excluded volume interactions.

Using the blob depiction again, we now want to incorporate those excluded volume interactions on a general level first into $U_{\text{Gauß}}$, having the emerging U_{SAW} describe harmonic bonds on a self-avoiding walk-like polymer, to then be able to deduce from there how to modify U_{FENE} to end up with an interaction potential U_{FESAW} representing finite extensible nonlinear elastic bonds between monomers with excluded volume interactions.

Similar to the derivation of (3.4) a good starting point is the blob definition $k_\text{B}T = \mathsf{f}_\text{E} \cdot \xi$. From there, with $\xi = bg^\nu$, the requirement of unperturbated behaviour within a blob, follows $\mathsf{f}_\text{E} \cdot (bg^\nu) = k_\text{B}T$ and $g^\nu = k_\text{B}T/(\mathsf{f}_\text{E} \cdot b)$. Since $R_\text{E} = N_\text{m}/g \cdot \xi = N_\text{m} b g^{\nu-1}$, one finds (with $R_\text{F} = N_\text{m}^\nu b$ from (2.46) being the Flory radius)

$$\begin{aligned}
\frac{R_\text{E}}{R_\text{F}} &= \frac{N_\text{m} b \cdot g^{\nu-1}}{N_\text{m}^\nu b} \\
&= \frac{N_\text{m} b \cdot \left(\frac{k_\text{B}T}{\mathsf{f}_\text{E} \cdot b}\right)^{\frac{\nu-1}{\nu}}}{N_\text{m}^\nu b} \\
&= \left(\frac{N_\text{m}}{\left(\frac{k_\text{B}T}{\mathsf{f}_\text{E} \cdot b}\right)^{\frac{1}{\nu}}}\right)^{1-\nu} \\
\Rightarrow \left(\frac{R_\text{E}}{R_\text{F}}\right)^{\frac{1}{1-\nu}} &= \left(\frac{\mathsf{f}_\text{E} \cdot b N_\text{m}^\nu}{k_\text{B}T}\right)^{\frac{1}{\nu}} \\
&= \left(\frac{R_\text{E}}{R_\text{F}}\right)^{-\frac{1}{\nu}} \cdot \left(\frac{\mathsf{f}_\text{E} \cdot R_\text{E}}{k_\text{B}T}\right)^{\frac{1}{\nu}} \\
\Rightarrow \left(\frac{R_\text{E}}{R_\text{F}}\right)^{\frac{1}{1-\nu}} &= \frac{\mathsf{f}_\text{E} \cdot R_\text{E}}{k_\text{B}T}
\end{aligned}$$

such that an appropriate description for U_{SAW} is given by

$$U_{\text{SAW}}(r) = k_\text{B}T \left(\frac{r}{R_\text{F}}\right)^{\frac{1}{1-\nu}} \tag{3.29}$$

using $U(r) = \int \partial U(r) = -\int F \partial r$.

Incorporating the structure of (3.29) into U_{FENE} from (3.27) leads to the desired

$$\begin{aligned} U_{\mathrm{FESAW}}(r) &= k_{\mathrm{B}}T \left(\frac{R_{\max}}{R_{\mathrm{F}}}\right)^{\frac{1}{1-\nu}} \ln\left[\frac{1}{1-\left(\frac{r}{R_{\max}}\right)^{\frac{1}{1-\nu}}}\right] \\ &= k_{\mathrm{B}}T N_{\mathrm{m}} \ln\left[\frac{1}{1-\left(\frac{r}{R_{\max}}\right)^{\frac{1}{1-\nu}}}\right] \end{aligned} \tag{3.30}$$

with the corresponding restoring force

$$\begin{aligned} \mathsf{f}_{\mathrm{FESAW}} &= -\frac{\partial U_{\mathrm{FESAW}}}{\partial r} \\ &= -\frac{N_{\mathrm{m}}}{r} \cdot \frac{k_{\mathrm{B}}T}{(1-\nu)\cdot\left[\left(\frac{r}{R_{\max}}\right)^{\frac{1}{\nu-1}} - 1\right]} \end{aligned} \tag{3.31}$$

For small relative extensions $\epsilon = (r/R_{\max})^{1/(1-\nu)} \ll 1$ the logarithm in (3.30) can be expanded to

$$\ln\left[\frac{1}{1-\epsilon}\right] = \epsilon + \frac{\epsilon^2}{2} + \mathcal{O}(\epsilon^3) \tag{3.32}$$

showing that $U_{\mathrm{FESAW}} \xrightarrow{r \ll R_{\max}} U_{\mathrm{SAW}}$ as intended.

Now that (3.30) provides a description for excluded volume chains connected by finite extensible bonds, we can replace the harmonic restoring force f_{E} in the derivation of (3.4) by $\mathsf{f}_{\mathrm{FESAW}}$, which allows to extend the scaling prediction (3.6) for R_{E} to the regime of overstretched chains. From the equilibrium swelling condition for the pressure balance

$$\begin{aligned} 0 &= \Pi_{\mathrm{C}} + \Pi_{\mathrm{E}}^{\mathrm{FESAW}} \\ &= \rho k_{\mathrm{B}}T + \frac{\mathsf{f}_{\mathrm{FESAW}} \cdot R_{\mathrm{E}}}{R_{\mathrm{E}}^3} \\ &= \frac{f N_{\mathrm{m}}}{R_{\mathrm{E}}^3} - \alpha \frac{N_{\mathrm{m}}}{R_{\mathrm{E}}^3} \cdot \frac{k_{\mathrm{B}}T}{(1-\nu)\cdot\left[\left(\frac{R_{\mathrm{E}}}{bN_{\mathrm{m}}}\right)^{\frac{1}{\nu-1}} - 1\right]} \end{aligned} \tag{3.33}$$

the end-to-end distance is now found to scale as

$$R_{\mathrm{E}} = bN_{\mathrm{m}} \left(\frac{f}{f + \frac{\alpha}{1-\nu}}\right)^{1-\nu} \tag{3.34}$$

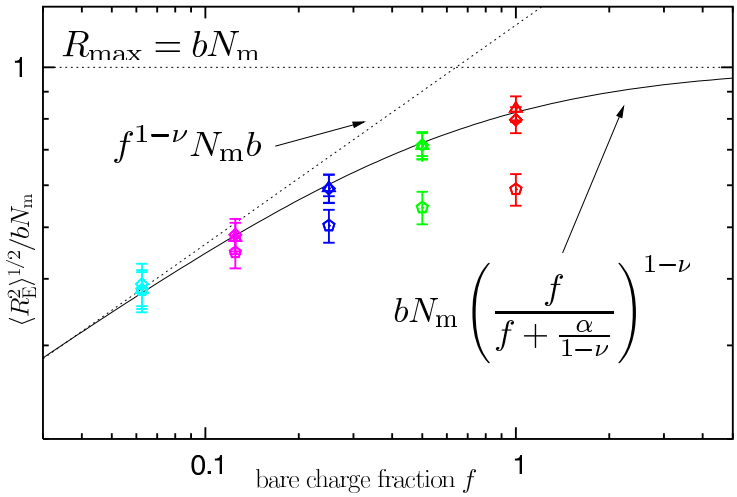

Figure 3.5.: Comparison of the simulation data for a chain length of $N_{\mathrm{m}} = 239$ monomers (see next chapter for details) to the scaling prediction (3.34) which includes the finite extensibility of the network strands (*curved solid line*); also given are the maximum elongation $R_{\max} = bN_{\mathrm{m}}$ (*dotted horizontal line*) and the ideal behaviour (3.6) of a harmonic chain in good solvent (*dotted diagonal line*). The colour coding scheme for the simulation parameters follows table S.1, using same symbols for same Bjerrum length ℓ_{B}, and same colours for same bare charge fraction f on the chains.

with α being a (constant) placeholder for omitted numerical prefactors.

This scaling prediction now provides a smooth crossover from the blob behaviour (3.6) towards the maximum elongation $R_{\max} = bN_{\mathrm{m}}$ of a chain of N_{m} monomers, as shown in figure 3.5 for an $\alpha = 1/4$. Compared to the simulation data also given therein (see next chapter 4 for details on them), the general trend is already captured correctly, which comes as not too much of an surprise since the divergence in the elastic restoring force was modeled based on the potential utilized for the bonded interactions in the computer experiment. There are, however, some clear and some subtle deviations which deserve additional attention in the following.

Most noticeable are the much smaller relative chain extensions for the systems with strong electrostatic interactions (*i.e.* $\ell_{\mathrm{B}} = 5\sigma$). Here, the counterion condensation (see also section 3.2.4) is too large to allow for the ideal gas assumption used in (3.33) for the derivation of (3.34) to be applicable, as due to $\xi_{\mathrm{M}} \lesssim 5$ up to 80 % of the originally fN_{m} mobile charges per strand are now confined to a small volume around it, such that the remaining osmotic pressure $\Pi_{\mathrm{C}}^{\mathrm{eff}}$ effectively acting on the chains and swelling the network is much smaller. Section 3.2.4 presented a way to incorporate this effect into the harmonic blob pictures by replacing the amount of bare charges fN_{m} in the ansatz (3.1) for the ideal gas pressure Π_{C} by an effective number $Q_{\mathrm{eff}} = f_{\mathrm{eff}} N_{\mathrm{m}}$ as in (3.17). Combining that idea with the blob picture as in subsection 3.2.2, where a network chain was considered to be composed of

blobs with diameter ξ containing g monomers each, the self-consistency condition $k_\mathrm{B}T \stackrel{!}{=} \mathsf{f}_\mathrm{E}{\cdot}\xi \Rightarrow \mathsf{f}_\mathrm{E} \stackrel{!}{=} k_\mathrm{B}T/\xi$ for a stretching force f_E acting on the blob can be fulfilled with $\mathsf{f}_\mathrm{E} \propto \Pi_\mathrm{C} R_\mathrm{E}^2$ being generated by the remaining (effective) ions in the gel. Hence,

$$\begin{aligned} \mathsf{f}_\mathrm{E} \quad &\propto \quad \Pi_\mathrm{C} R_\mathrm{E}^2 \propto \left(k_\mathrm{B}T \frac{f_\mathrm{eff} N_\mathrm{m}}{R_\mathrm{E}^3} \right) R_\mathrm{E}^2 = k_\mathrm{B}T \frac{Q_\mathrm{eff}}{R_\mathrm{E}} \\ &\overset{(3.17)}{=} \quad \frac{k_\mathrm{B}T}{\ell_\mathrm{B} + \frac{\xi}{fg}} \stackrel{!}{=} \frac{k_\mathrm{B}T}{\xi} \end{aligned} \tag{3.35}$$

provides a possibility to find the equilibrium swelling behaviour of a charged hydrogel based on only local observables, here still for fully harmonic (*i.e.* infinitely extensible) network chains, but already with an effective amount of charge to take condensation effects into account. For practical reasons one would now use

$$\xi \propto b g^\nu \tag{3.36}$$

(valid for linear chains even under tension) to reduce (3.35) from two to one unknown, ending at

$$b g^\nu \left(1 - \frac{1}{fg} \right) \stackrel{!}{=} \ell_\mathrm{B} \tag{3.37}$$

for the amount of monomers g per blob in equilibrium, which can then be used to obtain the end-to-end distance $R_\mathrm{E} = (N_\mathrm{m}/g)\xi \propto g^{\nu-1} b N_\mathrm{m}$. Although due to the scaling nature of the derivation this introduces two numerical prefactors of order unity, c_id in the expression for Π_C, and c_blob in the blob relation between ξ and g, (3.37) provides a convenient way to include counterion condensation without the problems addressed in section 3.2.4 regarding renormalization and definitions.

Even the finite extensibility of real network chains can now be easily added on this level by re-using once more the self-consistency condition $k_\mathrm{B}T \stackrel{!}{=} \mathsf{f}_\mathrm{E}{\cdot}\xi \Rightarrow \xi \stackrel{!}{=} k_\mathrm{B}T/\mathsf{f}_\mathrm{E}$, this time with $\mathsf{f}_\mathrm{E} = \mathsf{f}_\mathrm{FESAW}$ from (3.31) as the now non-linear restoring force. With $N_\mathrm{m}/R_\mathrm{E} = g/\xi$ and $R_\mathrm{E}/R_\mathrm{max} = R_\mathrm{E}/(bN_\mathrm{m}) \propto \xi/(bg)$ this leads $k_\mathrm{B}T/\xi = \mathsf{f}_\mathrm{FESAW}(r = R_\mathrm{E})$ to become

$$g \propto \left(\frac{\xi}{bg} \right)^{\frac{1}{\nu-1}} - 1 \tag{3.38}$$

which now replaces the previous $\xi \propto b g^\nu$ from the linear regime and therefore (3.37) by the equation system consisting of (3.35) and (3.38). Unfortunately, this cannot be solved explicitely, numerical solutions are however easily obtainable.

The plots in figure 3.6 now demonstrate both by picking up the representation of the previous figure 3.5 to compare condition (3.35) to the simulation data, for the case of linear chains (*left* plot) as well as for the finite extensible strands (*right* plot). The connection to figure 3.5 does not end at using the same axes and data, but it also allows a simple consistency check by comparing both $\ell_\mathrm{B} = 0\sigma$-cases in

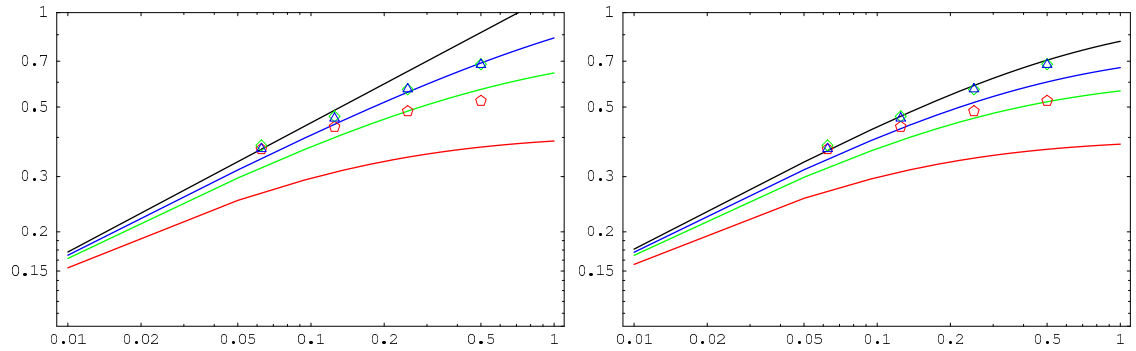

Figure 3.6.: Similar to figure 3.5 the scaling prediction (3.35) is compared to the same simulation data therein, again plotting the relative chain extension $R_{\mathrm{E}}/R_{\max} = R_{\mathrm{E}}/(bN_{\mathrm{m}}) \propto \xi/(bg)$ as a function of the bare charge fraction f on the x-axis. For technical reasons, the colouring had to be changed, such that it now represents the Bjerrum length (with *black* corresponding to $\ell_{\mathrm{B}} = 0\sigma$, *blue* to $\ell_{\mathrm{B}} = 1\sigma$, *green* to $\ell_{\mathrm{B}} = 2\sigma$ and *red* to $\ell_{\mathrm{B}} = 5\sigma$); the symbol shape however retains its meaning. The plot for (3.37) on the *left* extends the basic picture by introducing an effective charge Q_{eff}, the one for the equation system of (3.37) and (3.38) on the *right* also adds finite extensibility of the network chains.

figure 3.6 (the *black lines*) to figure 3.5, where the *dotted diagonal line* represented the ideal behaviour (3.6) of a harmonic chain in good solvent, *i.e.* linear extensibility as on the *left* of the current figure, and the *solid curved line* plotted the scaling law (3.34) for non-linear and finite extensible chains, corresponding to the *right* side of the current figure. As we did not have explicitely dependent terms on the electrostatics in both former cases, they should match the limit $\ell_{\mathrm{B}} = 0\sigma$ in our new models, which can be nicely checked by looking at the corresponding plots. At the same time figure 3.6 shows the impact of the coulombic coupling to the ideal gas distribution of counterions alone, because each value of ℓ_{B} now has its own distinct curvature. These however underestimate the relative extension of the chains as stronger electrostatics gets; consequently we either underestimated the amount Q_{eff} of remaining charges responsible for swelling the gel, *i.e.* overestimated the degree of swelling, or another electrostaticly-based mechanism influencing the equilibrium behaviour is still neglected.

We leave it to the following subsection 3.2.7 to investigate if a more sophisticated treatment for the condensing counterions will improve the result; there we will choose a more rigorous approach by resorting to Poisson-Boltzmann theory to determine a more appropriate counterion pressure $\Pi_{\mathrm{C}}^{\mathrm{PB}}$ which will then update the pressure balance (3.33) in the current picture of finite extensibility.

The other possibility of an additional effect will then be discussed in section 3.2.8, where we will identify the repulsion of the like-wise charge monomers on the chains as main source for the deviations, being able to correct the current result.

3.2.7. Counterions in the Cell Model

A very well developed theory (see *e.g.* [157,166,167]) to tackle the intrinsically complex many-body problem of a system with essentially rod-like (*i.e.* $\langle R_\mathrm{E}^2\rangle/\langle R_\mathrm{G}^2\rangle \approx 12$) polyelectrolytes at low densities and associated counterions is the cylindrical cell model with its effective one-particle treatment. Embedding each chain in a fictitious cylinder, whose length L_cyl by definition corresponds to that of the polyelectrolyte, and whose radius R_cyl is chosen such that its volume equals the volume per chain in the system, maps the monomer density to the cell model, while requiring equal distribution of the counterions between these cylinders ensures the electrostatic decoupling of the cells, rendering each electrostaticly neutral:

$$L_\mathrm{cyl} \stackrel{!}{=} R_\mathrm{E} \tag{3.39a}$$

$$\frac{V}{N_\mathrm{p}} \propto R_\mathrm{E}^3 \stackrel{!}{=} \pi R_\mathrm{cyl}^2 \cdot L_\mathrm{cyl} \Rightarrow R_\mathrm{cyl} = \frac{R_\mathrm{E}}{\sqrt{\pi}} \tag{3.39b}$$

If end-effects are neglected, *i.e.* $L_\mathrm{cyl} \to \infty$ is considered, the problem acquires cylindrical symmetry. Within this picture, one can now rely on the nonlinear Poisson-Boltzmann (PB) theory: The individual counterions are replaced by a cylindrical counterion density $n(r)$, where r denotes the radial distance from the cylinder axis, assuming it to have cylindrical symmetry, too. From there, the derivation of the osmotic pressure $\Pi_\mathrm{C}^\mathrm{PB}$ of the counterions under the influence of the charges on the rod is then in principle possible due to the exact result [167,168] that $\Pi_\mathrm{C}^\mathrm{PB}$ corresponds to the counterion density $n(R_\mathrm{cyl})$ at the outer cell boundary along

$$\Pi_\mathrm{C}^\mathrm{PB} = k_\mathrm{B}T \cdot n(R_\mathrm{cyl}) \tag{3.40}$$

leaving the task of determining $n(R_\mathrm{cyl})$. Unfortunately, for this to succeed one now has to solve the entire symmetrized problem.

Starting off at the Poisson equation

$$\left(\frac{\mathrm{d}^2}{\mathrm{d}r^2} + \frac{1}{r}\frac{\mathrm{d}}{\mathrm{d}r}\right)\psi(r) = \frac{e_0}{\epsilon}\, n(r) \tag{3.41}$$

for the electrostatic potential $\psi(r)$, the dielectric constant ϵ outside the cylinder, and the unit charge e_0, the counterion density is assumed to be influenced by the potential through the Boltzmann factor

$$n(r) = n(R_\mathrm{cyl})\, \exp\left[-\frac{e_0\psi(r)}{k_\mathrm{B}T}\right] \tag{3.42}$$

implying the normalization $\psi(R_\mathrm{cyl}) = 0$. The Poisson-Boltzmann equation itself is then obtained by simply combining (3.41) and (3.42).

It is more convenient to rewrite this in terms of the Bjerrum length ℓ_B, the Manning parameter ξ_M, and a reduced electrostatic potential $y(r)$ and screening constant $\kappa > 0$ defined along

$$y(r) := \frac{e_0}{k_\mathrm{B}T}\psi(r) \tag{3.43}$$

$$\kappa^2 := 4\pi\ell_\mathrm{B} \cdot n(R_\mathrm{cyl}) \tag{3.44}$$

leading to the nonlinear differential equation

$$y'' + \frac{y'}{r} = \kappa^2 \mathrm{e}^y \tag{3.45}$$

with boundary conditions

$$y'(r_0) = -\frac{2\xi_\mathrm{M}}{r_0} \qquad \text{and} \qquad y'(R_\mathrm{cyl}) = 0 \qquad \text{and} \qquad y(R_\mathrm{cyl}) = 0 \tag{3.46}$$

on the rod ($r = r_0$) and at the cell's surface ($r = R_\mathrm{cyl}$). First solved by Fuoss *et al.* [169] and Alfrey *et al.* [170], the solution to (3.45) under the constraints of (3.46) reads

$$y(r) = -2 \ln \left[\frac{r}{R_\mathrm{cyl}} \sqrt{1 + \gamma_\mathrm{PB}^{-2}} \cos\left(\gamma_\mathrm{PB} \ln \frac{r}{R_\mathrm{M}} \right) \right] \tag{3.47}$$

with the following two coupled transcendental equations

$$\gamma_\mathrm{PB} \ln \frac{r_0}{R_\mathrm{M}} = \arctan \frac{1 - \xi_\mathrm{M}}{\gamma_\mathrm{PB}} \tag{3.48a}$$

$$\gamma_\mathrm{PB} \ln \frac{R_\mathrm{cyl}}{R_\mathrm{M}} = \arctan \frac{1}{\gamma_\mathrm{PB}} \tag{3.48b}$$

for the integration constants γ_PB and R_M, which can be reduced to one by subtracting (3.48a) from (3.48b) towards

$$\gamma_\mathrm{PB} \ln \frac{R_\mathrm{cyl}}{r_0} = \arctan \frac{1}{\gamma_\mathrm{PB}} + \arctan \frac{\xi_\mathrm{M} - 1}{\gamma_\mathrm{PB}} \tag{3.49}$$

thus eliminating R_M. Since γ_PB is related to κ via

$$\kappa^2 R_\mathrm{cyl}^2 = 2\,(1 + \gamma_\mathrm{PB}^2) \tag{3.50}$$

the derivation of the osmotic pressure $\Pi_\mathrm{C}^\mathrm{PB}$ of the counterions through (3.40) is now achievable by using (3.44) and (3.50) to substitute $n(R_\mathrm{cyl})$, obtaining

$$\Pi_\mathrm{C}^\mathrm{PB} = k_\mathrm{B}T \cdot \frac{2(1 + \gamma_\mathrm{PB}^2)}{4\pi\ell_\mathrm{B} \cdot R_\mathrm{cyl}^2} \tag{3.51}$$

in which the γ_{PB} is determined through (3.49).

Unfortunately, the latter equation cannot be solved explicitely. Even more, it only has a real solution for γ_{PB} if ξ_{M} is larger than some $\xi_{\mathrm{M}}^{\mathrm{min}}$ (which would need to be determined as well); for smaller charge densities it becomes imaginary (which does not hurt $\Pi_{\mathrm{C}}^{\mathrm{PB}}$ as in (3.51) only the square of γ_{PB} enters) requiring an analytical continuation of (3.49). Hence, in the following three regimes will be considered:

Regime $\xi_{\mathrm{M}} > 1$**.** Here, the right hand side of (3.49) can be expanded to

$$\pi - \frac{\xi_{\mathrm{M}}}{\xi_{\mathrm{M}} - 1}\gamma_{\mathrm{PB}} + \frac{1}{3}\left(1 + \frac{1}{(\xi_{\mathrm{M}} - 1)^3}\right)\gamma_{\mathrm{PB}}^3 + \mathcal{O}(\gamma_{\mathrm{PB}}^5) \tag{3.52}$$

allowing to take the zeroth and the first order Taylor expansion as the upper resp. lower bound for the left hand side $\gamma_{\mathrm{PB}} \ln(R_{\mathrm{cyl}}/r_0)$ in (3.49), which leads to

$$\begin{aligned} \pi \geq \quad & \gamma_{\mathrm{PB}} \ln \tfrac{R_{\mathrm{cyl}}}{r_0} \quad \geq \pi - \frac{\xi_{\mathrm{M}}}{\xi_{\mathrm{M}} - 1}\gamma_{\mathrm{PB}} \\ \Rightarrow \frac{\pi}{\ln \frac{R_{\mathrm{cyl}}}{r_0}} \geq \quad & \gamma_{\mathrm{PB}} \quad \geq \frac{\pi}{\ln \frac{R_{\mathrm{cyl}}}{r_0} + \frac{\xi_{\mathrm{M}}}{\xi_{\mathrm{M}} - 1}} \end{aligned} \tag{3.53}$$

and brackets γ_{PB} with logarithmically slowly coinciding bounds. Figure 3.7 illustrates its dependency on ξ_{M} by plotting both left hand side and right hand side of (3.49)whose intersections mark the respective solutions to be numerically obtained.

Special case $\xi_{\mathrm{M}} = 1$**.** This renders expansion (3.52) invalid, and

$$\frac{\pi}{2} - \gamma_{\mathrm{PB}} + \frac{1}{3} + \gamma_{\mathrm{PB}}^3 + \mathcal{O}(\gamma_{\mathrm{PB}}^5) \tag{3.54}$$

can be used instead. Consequently, the bracketing bounds become

$$\begin{aligned} \frac{\pi}{2} \geq \quad & \gamma_{\mathrm{PB}} \ln \tfrac{R_{\mathrm{cyl}}}{r_0} \quad \geq \pi - \gamma_{\mathrm{PB}} \\ \Rightarrow \frac{\pi/2}{\ln \frac{R_{\mathrm{cyl}}}{r_0}} \geq \quad & \gamma_{\mathrm{PB}} \quad \geq \frac{\pi}{\ln \frac{R_{\mathrm{cyl}}}{r_0} + 1} \end{aligned} \tag{3.55}$$

which, as figure 3.7 shows, may function as new upper limit for even smaller ξ_{M}.

Regime $1 > \xi_{\mathrm{M}} > \xi_{\mathrm{M}}^{\mathrm{min}}$**.** The expansion of the right hand side of (3.49) now changes to

$$\frac{\xi_{\mathrm{M}}}{1 - \xi_{\mathrm{M}}}\gamma_{\mathrm{PB}} - \frac{1}{3}\left(\frac{1}{(1 - \xi_{\mathrm{M}})^3} - 1\right)\gamma_{\mathrm{PB}}^3 + \mathcal{O}(\gamma_{\mathrm{PB}}^5) \tag{3.56}$$

which allows to determine $\xi_{\mathrm{M}}^{\min}$ from the first order Taylor expansion:

$$\begin{aligned} \frac{\xi_{\mathrm{M}}}{1-\xi_{\mathrm{M}}}\gamma_{\mathrm{PB}} &> \gamma_{\mathrm{PB}} \ln \frac{R_{\mathrm{cyl}}}{r_0} \\ \Rightarrow \xi_{\mathrm{M}} &> \xi_{\mathrm{M}}^{\min} = \frac{\ln \frac{R_{\mathrm{cyl}}}{r_0}}{1+\ln \frac{R_{\mathrm{cyl}}}{r_0}} \end{aligned} \tag{3.57}$$

While π still is a valid upper bound here due to the two arctan-functions in (3.49), it was shown in (3.55) that $\pi/2$ can also be used as it limits the entire r.h.s. for $\xi_{\mathrm{M}} = 1$ which in turn bounds all $1 > \xi_{\mathrm{M}} > \xi_{\mathrm{M}}^{\min}$ from above. The lower bound 0, obtained from using only the first order Taylor expansion again, can also be improved by taking the next, *i.e.* third order term as well, leading to

$$\begin{aligned} \pi \geq \gamma_{\mathrm{PB}} \ln \frac{R_{\mathrm{cyl}}}{r_0} &\geq \frac{\xi_{\mathrm{M}}}{1-\xi_{\mathrm{M}}}\gamma_{\mathrm{PB}} - \frac{1}{3}\left(\frac{1}{(1-\xi_{\mathrm{M}})^3}-1\right)\gamma_{\mathrm{PB}}^3 \\ \Rightarrow \frac{\pi}{\ln \frac{R_{\mathrm{cyl}}}{r_0}} \geq \gamma_{\mathrm{PB}} &\geq \sqrt{3\cdot \frac{\ln \frac{R_{\mathrm{cyl}}}{r_0} - \frac{\xi_{\mathrm{M}}}{1-\xi_{\mathrm{M}}}}{1-\frac{1}{(1-\xi_{\mathrm{M}})^3}}} \end{aligned} \tag{3.58}$$

which now allows to approach γ_{PB} from below.

Special case $\xi_{\mathrm{M}} = \xi_{\mathrm{M}}^{\min}$. Note that for $\xi_{\mathrm{M}} \to \xi_{\mathrm{M}}^{\min}$ the lower boundary in (3.58) will go to zero, implying $\gamma_{\mathrm{PB}}(\xi_{\mathrm{M}} \to \xi_{\mathrm{M}}^{\min}) \to 0$, too. As depicted in figure 3.7, from there γ_{PB} will cease to posses a real solution for even smaller ξ_{M}.

Regime $\xi_{\mathrm{M}}^{\min} > \xi_{\mathrm{M}} > 0$. Now that no more real solutions for (3.49) exist and γ_{PB} becomes imaginary, the analytical continuation $\gamma_{\mathrm{PB}} \to -\mathrm{i}\gamma_{\mathrm{PB}} =: \tilde{\gamma}_{\mathrm{PB}}$ replaces (3.49) with

$$\tilde{\gamma}_{\mathrm{PB}} \ln \frac{R_{\mathrm{cyl}}}{r_0} = -\left(\operatorname{arccoth}\frac{1}{\tilde{\gamma}_{\mathrm{PB}}} + \operatorname{arccoth}\frac{\xi_{\mathrm{M}}-1}{\tilde{\gamma}_{\mathrm{PB}}}\right) \tag{3.59}$$

whose right hand side expands to

$$\left(\frac{1}{1-\xi_{\mathrm{M}}}-1\right)\tilde{\gamma}_{\mathrm{PB}} + \frac{1}{3}\left(\frac{1}{(1-\xi_{\mathrm{M}})^3}-1\right)\tilde{\gamma}_{\mathrm{PB}}^3 + \mathcal{O}(\tilde{\gamma}_{\mathrm{PB}}^5) \tag{3.60}$$

for the now real $\tilde{\gamma}_{\mathrm{PB}}$. While $\operatorname{arccoth} x = \operatorname{arctanh}(1/x)$ has a non-imaginary solution for $|x| > 1$, $\operatorname{arctanh} x$ for $|x| < 1$, their sum in (3.59) is consequently real if $|\tilde{\gamma}_{\mathrm{PB}}| < 1$ and if $|(\xi_{\mathrm{M}}-1)/\tilde{\gamma}_{\mathrm{PB}}| > 1 \Rightarrow \tilde{\gamma}_{\mathrm{PB}} < 1-\xi_{\mathrm{M}}$ (note that $\xi_{\mathrm{M}} < \xi_{\mathrm{M}}^{\min} < 1$ and $0 < \tilde{\gamma}_{\mathrm{PB}}$). Since the left hand side $\tilde{\gamma}_{\mathrm{PB}} \ln(R_{\mathrm{cyl}}/r_0)$ is always positive, while $\operatorname{arccoth}(1/\tilde{\gamma}_{\mathrm{PB}}) >$

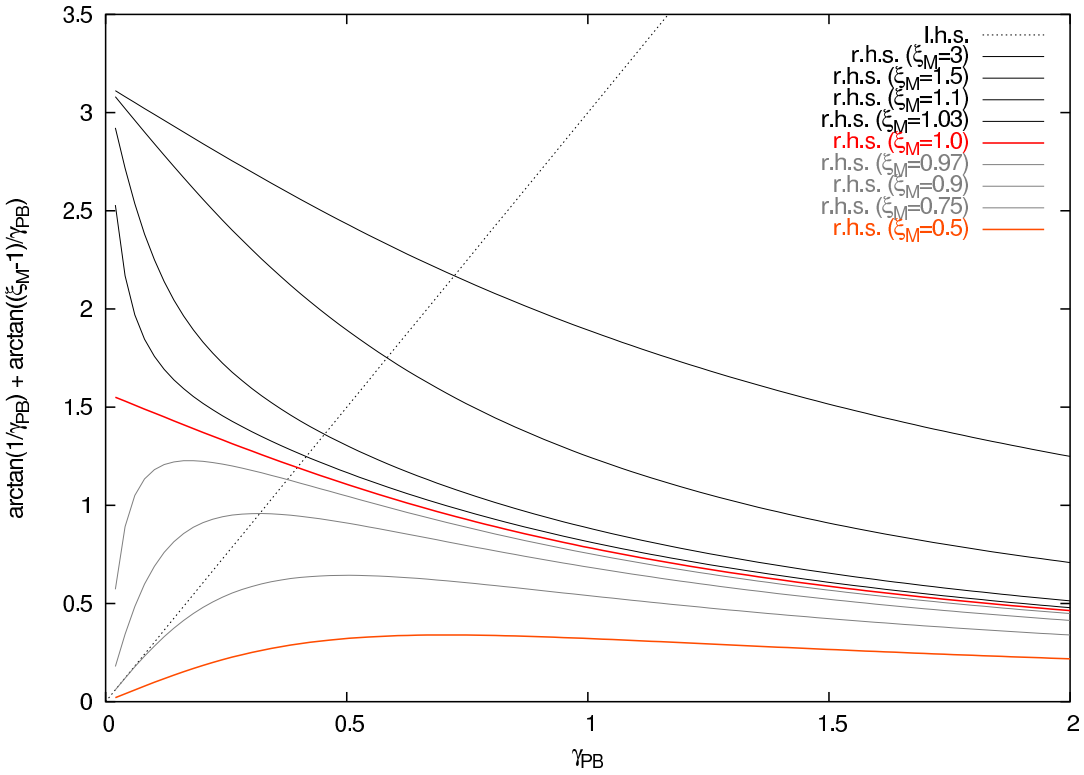

Figure 3.7.: Illustration of (3.49) and its solution for γ_{PB}. While the dashed straight line depicts the left hand side $\gamma_{\mathrm{PB}} \ln(R_{\mathrm{cyl}}/r_0)$ for the choice of $\ln(R_{\mathrm{cyl}}/r_0) = 3$, the other curves plot the right hand side for the exemplary values of ξ_{M} given in the legend (corresponding to the lines in order from top to bottom), distinguishing between the first regime ($\xi_{\mathrm{M}} > 1$, *black lines*) and its expansion (3.52) starting at π, and the second regime ($1 > \xi_{\mathrm{M}} > \xi_{\mathrm{M}}^{\mathrm{min}}$, *gray lines*) coming from zero. Note particularly, that, as predicted by (3.57), for $\xi_{\mathrm{M}} < \xi_{\mathrm{M}}^{\mathrm{min}} = 0.75$ no real solution (*i.e.* intersection with $\gamma_{\mathrm{PB}} \ln(R_{\mathrm{cyl}}/r_0)$) for γ_{PB} can be found.

$\mathrm{arccoth}((\xi_{\mathrm{M}} - 1)/\tilde{\gamma}_{\mathrm{PB}}) > 0$ renders the right hand side negative for all valid arguments, the solution is to be found for $0 < \tilde{\gamma}_{\mathrm{PB}} < 1$ only. Figure 3.8 corroborates this by plotting both sides of (3.59), showing not only the one solution (*i.e.* intersection) for $\tilde{\gamma}_{\mathrm{PB}}$, but also illustrating the increasingly strong divergence of the right hand side for smaller ξ_{M}, posing a serious challenge if intermediates for $\tilde{\gamma}_{\mathrm{PB}}(\xi_{\mathrm{M}} \to 0) \to 1$ should be numerically determined. Similar to (3.58), the bounds necessary for that are obtained from the expansion (3.60), which is taken up to its third order term. As illustrated in figure 3.8, it is then possible to arrive at an approximate lower boundary and therefore narrowing the rough estimate

$1 > \tilde{\gamma}_{\mathrm{PB}} > 0$ found so far to

$$1 - \xi_{\mathrm{M}} > \tilde{\gamma}_{\mathrm{PB}} \quad \geq \quad \sqrt{\frac{\ln\left(\frac{R_{\mathrm{cyl}}}{r_0}\right) - \left(\frac{1}{1-\xi_{\mathrm{M}}} - 1\right)}{\frac{1}{3}\left(\frac{1}{(1-\xi_{\mathrm{M}})^3} - 1\right)}} \tag{3.61}$$

which particularly in case of the upper bound is unfortunately a hard limit (“>” instead of the ”≥” found before).

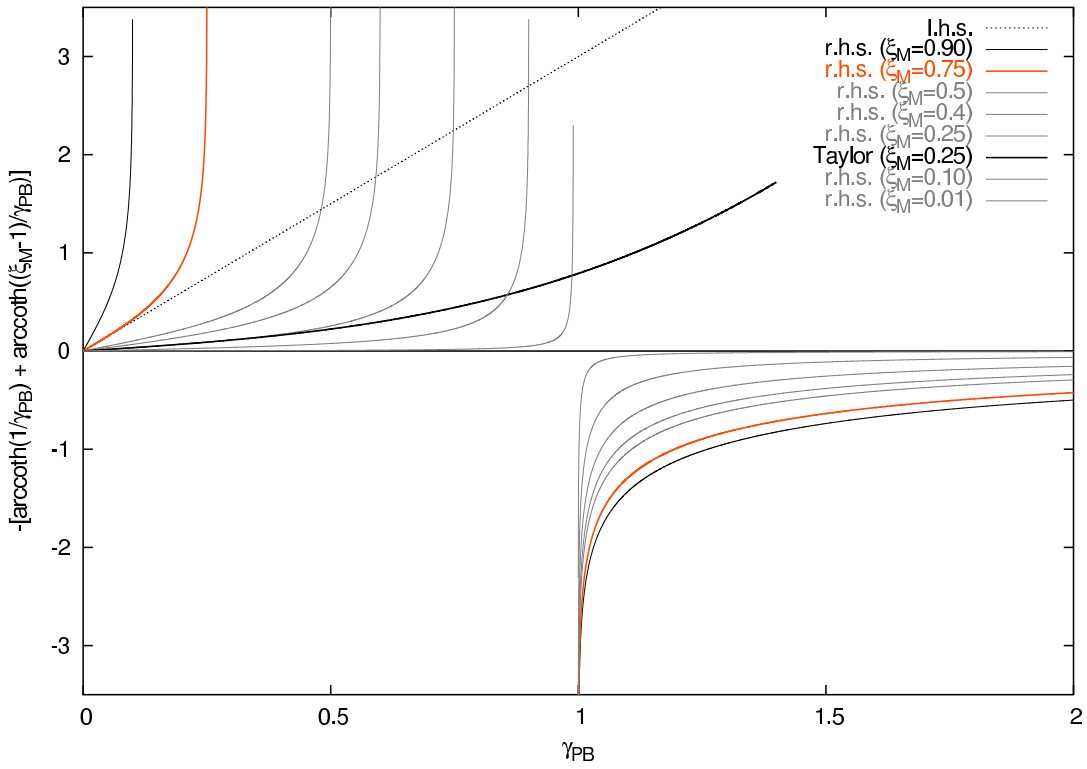

Figure 3.8.: Illustration of (3.59) and its solution for $\tilde{\gamma}_{\mathrm{PB}}$. Similar to figure 3.7, the dashed straight line depicts the left hand side $\tilde{\gamma}_{\mathrm{PB}} \ln(R_{\mathrm{cyl}}/r_0)$, again for the choice of $\ln(R_{\mathrm{cyl}}/r_0) = 3$, the other curves plot the right hand side for the exemplary values of $\xi_{\mathrm{M}} < \xi_{\mathrm{M}}^{\mathrm{min}}$ given in the legend (corresponding to the lines in order from top to bottom for $\tilde{\gamma}_{\mathrm{PB}} < 1$). As discussed in the text, no intersection between $\gamma_{\mathrm{PB}} \ln(R_{\mathrm{cyl}}/r_0)$ and the curves exists for $\tilde{\gamma}_{\mathrm{PB}} > 1$ because the right hand side of (3.59), being negative there, goes to zero. While the uppermost line reprises one representative ($\xi_{\mathrm{M}} = 0.90$) of the previously discussed regimes, now obviously not being solved by the analytical continuation, the *red line* depicts the border $\xi_{\mathrm{M}} = \xi_{\mathrm{M}}^{\mathrm{min}} = 0.75$ between the second and this third regime. Also given is the third order Taylor expansion (3.60) for $\xi_{\mathrm{M}} = 0.25$ (without the imaginary zeroth term), illustrating the difficulties of finding an usable upper bound for bracketing the solution $\tilde{\gamma}_{\mathrm{PB}}$.

The sharp divergence in figure 3.8, increasingly pronounced for $\xi_{\mathrm{M}} \to 0$, does on the one hand complicate the process of finding a numerical solution to (3.59); on the other hand, it also offers a convenient way to approximate $\tilde{\gamma}_{\mathrm{PB}}$ by simply setting it to its upper bound $\tilde{\gamma}_{\mathrm{PB}} \approx 1 - \xi_{\mathrm{M}}$, making a relatively small error which even diminishes further as $\xi_{\mathrm{M}} \to 0$ amplifies the singularity (see figure 3.8). This allows to determine the limit of vanishing electrostatics for (3.51) as well, in which with $\xi_{\mathrm{M}} = \ell_{\mathrm{B}}/a$ from section 3.2.4 the aforementioned $\xi_{\mathrm{M}} \to 0$ translates to

$$\lim_{\ell_{\mathrm{B}} \to 0} \Pi_{\mathrm{C}}^{\mathrm{PB}} = \lim_{\ell_{\mathrm{B}} \to 0} k_{\mathrm{B}}T \frac{2(1 + [-\mathrm{i}(1 - \frac{\ell_{\mathrm{B}}}{a})]^2)}{4\pi\ell_{\mathrm{B}} \cdot R_{\mathrm{cyl}}^2} = \frac{k_{\mathrm{B}}T}{a\pi R_{\mathrm{cyl}}^2} \tag{3.62}$$

Recalling the discussion in that section on the difference between modeling the charge distance a within a rod-like ($a = b/f$) or blob-like

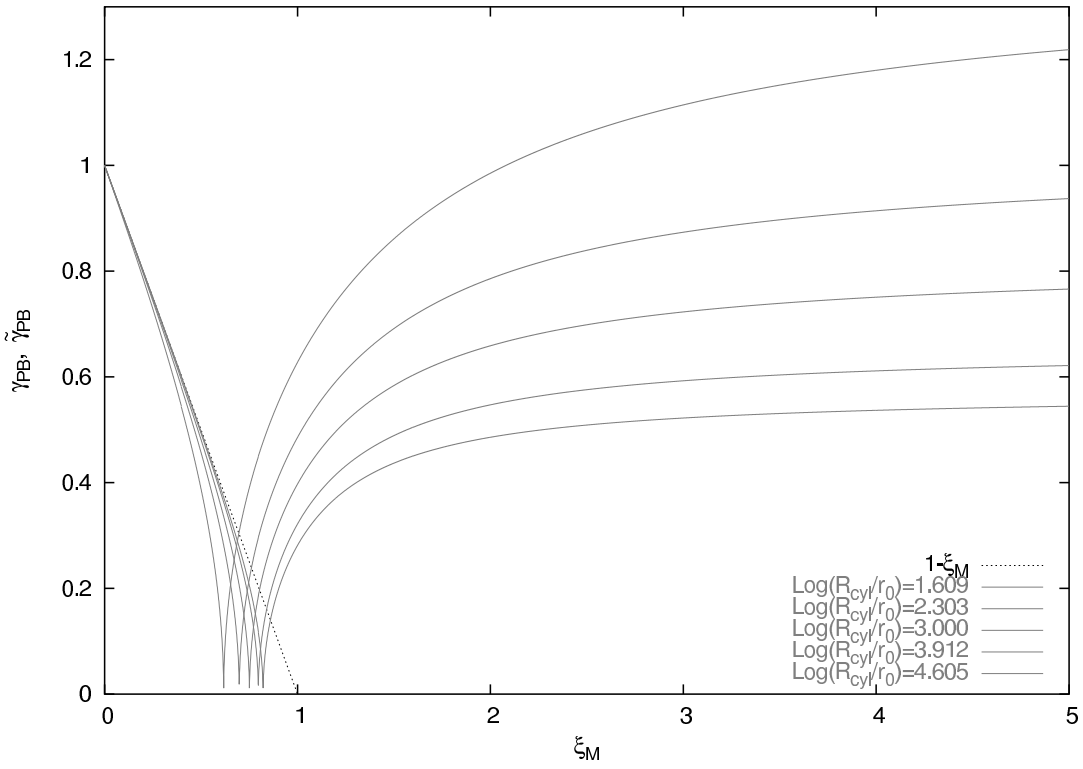

Figure 3.9.: Numerical solution of the real γ_{PB} from (3.49) and its analytical continuation $\tilde{\gamma}_{\mathrm{PB}} = -\mathrm{i}\gamma_{\mathrm{PB}}$ from (3.59) as a function of the Manning parameter ξ_{M}, given for different $R_{\mathrm{cyl}} \in \{5, 10, \mathrm{e}^3, 50, 100\}\sigma$ (from top to bottom) and $r_0 = \sigma$. The dashed line represents the limit $1 - \xi_{\mathrm{M}}$ to which $\tilde{\gamma}_{\mathrm{PB}}$ goes for $\xi_{\mathrm{M}} \to 0$; the position of the minimum corresponds to $\xi_{\mathrm{M}}^{\mathrm{min}} = \ln(R_{\mathrm{cyl}}/r_0)/(1 + \ln(R_{\mathrm{cyl}}/r_0))$. Note that for $\xi_{\mathrm{M}} < \xi_{\mathrm{M}}^{\mathrm{min}}$ the plotted $\tilde{\gamma}_{\mathrm{PB}}$ represents the complex solution of (3.49).

($a = R_\mathrm{E}/(fN_\mathrm{m})$) description, also summarized in figure 3.2, the limit in (3.62) becomes

$$\lim_{\ell_\mathrm{B}\to 0} \frac{\Pi_\mathrm{C}^\mathrm{PB}}{k_\mathrm{B}T} = \begin{cases} \frac{f}{b\pi R_\mathrm{cyl}^2} = \frac{fN_\mathrm{m}}{R_\mathrm{max}^3} & \text{for } a = \frac{b}{f}, \\ \frac{fN_\mathrm{m}}{R_\mathrm{E}\pi R_\mathrm{cyl}^2} = \frac{fN_\mathrm{m}}{R_\mathrm{E}^3} & \text{for } a = \frac{R_\mathrm{E}}{fN_\mathrm{m}} \end{cases} \tag{3.63}$$

using the definition for R_cyl from (3.39b). Hereby it is particularly noteworthy that within the blob-like description the osmotic pressure of the counterions from the cell model matches the ideal gas pressure $\Pi_\mathrm{C} = k_\mathrm{B}TfN_\mathrm{m}/R_\mathrm{E}^3$ for vanishing electrostatic interactions perfectly [3].

Figure 3.9 summarizes this discussion by presenting the numerical solution of (3.49) for γ_PB, including the analytical continuation $\tilde{\gamma}_\mathrm{PB} = -\mathbb{i}\gamma_\mathrm{PB}$ from (3.59) for small Manning parameters $\xi_\mathrm{M} < \xi_\mathrm{M}^\mathrm{min} = \ln(R_\mathrm{cyl}/r_0)/(1 + \ln(R_\mathrm{cyl}/r_0))$ into the picture. Though the chosen parameter range does not allow to evaluate the limit of very strong electrostatics $\gamma_\mathrm{PB}(\xi_\mathrm{M} \to \infty) \to \pi$, it already becomes clear that this upper bound from (3.53) will be reached logarithmically slow. All other limits are however present, including the discussed $\gamma_\mathrm{PB}(\xi_\mathrm{M} \to 0) \to -\mathbb{i}(1 - \xi_\mathrm{M})$ for vanishing electrostatics (hence confirming (3.63) as well), and the crossover between real and complex solution at $\gamma_\mathrm{PB}(\xi_\mathrm{M} \to \xi_\mathrm{M}^\mathrm{min}) \to 0$.

Therefore, it is now finally possible to return to (3.51) and the (numerical) derivation of the osmotic pressure $\Pi_\mathrm{C}^\mathrm{PB}$ of the counterions within the framework of the cell model. As announced, we solve (3.49) for each set of ξ_M (see section 3.2.4), R_cyl (as in (3.63) choose (3.39b) such that it matches the rod-like or blob-like description used for ξ_M), and $r_0 = \sigma$, and enter the result into (3.51). Figure 3.10 shows this accordingly achieved solution for the rod-like representation, adding the $\gamma_\mathrm{PB} = \gamma_\mathrm{PB}(\xi_\mathrm{M}, R_\mathrm{cyl}, r_0)$-values for our simulation parameters. While the rather strong sensitivity to the bond length b is quite remarkable (using $b = 1.00\sigma$ instead of $b = 1.05\sigma$ pushes all lines up by $\sim 20\%$), and the dependency of $\Pi_\mathrm{C}^\mathrm{PB}$ on ξ_M and fN_m also changes significantly if the blob-like description is used instead, the graph also underlines the error made by taking Π_C to represent an ideal gas-like distribution of counterions for the pressure balance in *e.g.* (3.33).

Nevertheless, the question remains if all this effort is really necessary when looking at our systems. On the one hand, the cell model is a much more accurate description of rod-like systems than the very simple model of an (even partially condensed) ideal gas around some strands; on the other hand, we already know that some aspects cannot be captured on the Poisson-Boltzmann level nonetheless, such as the precise form of the interactions between condensing/condensed counterion within a curled

[3] This is also true for the rod-like case if $R_\mathrm{E} = R_\mathrm{max}$ is used there.

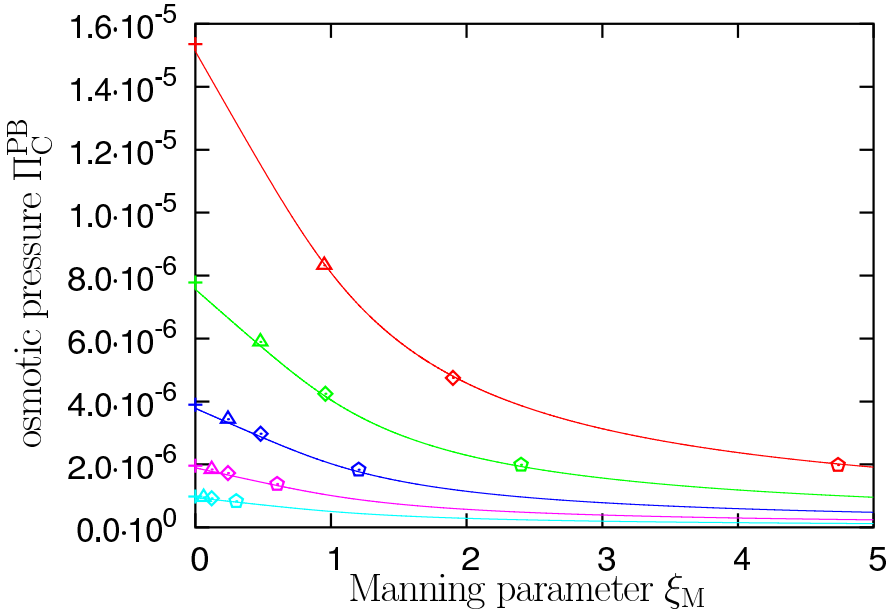

Figure 3.10.: The osmotic pressure Π_C^{PB} of the fN_m counterions around a rod-like polyelectrolyte of N_m monomers within the cylindrical cell of radius R_{cyl} as a function of the Manning parameter ξ_M, given for $N_m = 239$ but different charge fractions f and Bjerrum lengths ℓ_B. Obtained from (3.51), the required $\gamma_{PB} = \gamma_{PB}(\xi_M, R_{cyl}, r_0)$ was found numerically from (3.49), as is depicted in figure 3.9. Also given are the solutions for our simulation parameters, using (3.39) to map them onto $\xi_M = \ell_B/(b/f)$ and $R_{cyl} = bN_m/\sqrt{\pi}$. Their discrepancy to the straight lines is solely due to the bond length b which is set to $b = 1.05\sigma$ there while taken from the measured averaged equilibrium value here (colour coding scheme as in table S.1).

segment of the charged chains, allowing ions to "enter" the central cylinder hence experiencing partially shielded countercharges. While we will postpone all these details to the next section 3.3, where the "cell under tension"-model is introduced which will be specifically designed to address those questions, and where the Poisson-Boltzmann results will become important once more, on the current scaling level we will rather continue with the more simple expression of Q_{eff} for the effective charges.

Figure 3.11 therefore compares the osmotic pressure Π_C of the counterions based on Q_{eff} (coloured lines) to Π_C^{PB} including the solution of the Poisson-Boltzmann equation (coloured symbols connected by gray lines to guide the eye). While both approaches return pressures on the same order of magnitude, their limiting behaviour is different: For vanishing electrostatics the cell model predicts higher osmotic pressures than the effective Π_C, and vice versa for strong coulombic coupling where the charge number Q_{eff} saturates because of the lower limit ℓ_B in the distance of neighbouring charges.

Using Π_C^{PB} instead of Π_C as the driving force behind the swelling of our hydrogels

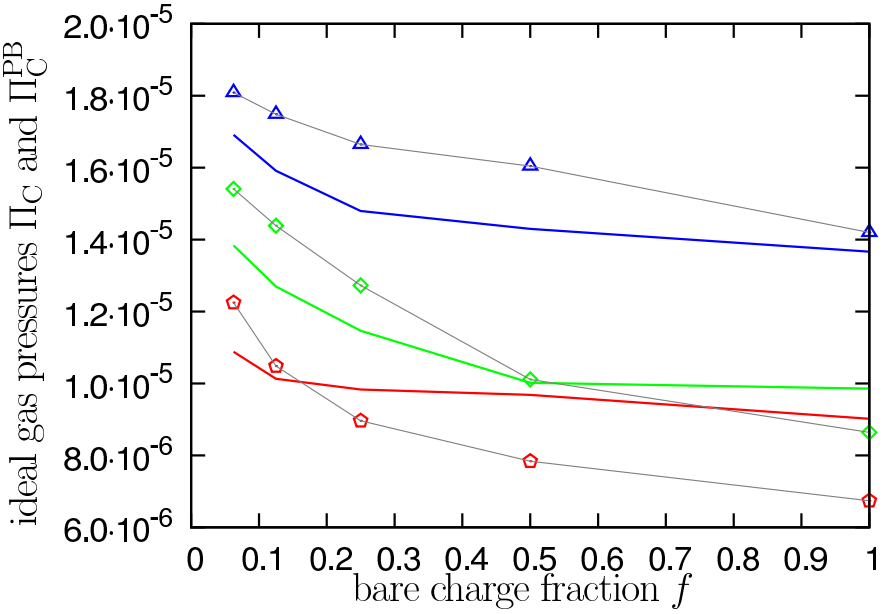

Figure 3.11.: Comparing the ideal gas pressure Π_C of a cloud of Q_{eff} effective counterions around polyelectrolyte network strands to the osmotic pressure Π_C^{PB} of the fN_m counterions around a blob-like polyelectrolyte of N_m monomers within the cylindrical cell of radius R_{cyl} as a function of the Manning parameter ξ_M, given for $N_m = 239$ but different charge fractions f and Bjerrum lengths ℓ_B. While the former is given as coloured lines as in figure 3.6, the latter uses the same colour coding but mere data points connected by gray lines to guide the eye (for the symbols see table S.1).

should consequently change the scaling prediction (3.34) for the end-to-end distance of the network strands particularly for strong electrostatic interactions (large ℓ_B, large ξ_M, strong counterion condensation), since the deviation from the ideal gas-like behaviour previously assumed is strongest there. Hence, replacing Π_C in (3.33) with Π_C^{PB} from (3.51) leads to

$$\begin{aligned} 0 &= \Pi_C^{PB} + \Pi_E^{FESAW} \\ &= k_B T \frac{2(1+\gamma_{PB}^2)}{4\pi\ell_B \cdot R_{cyl}^2} - \alpha \frac{N_m}{R_E^3} \cdot \frac{k_B T/(1-\nu)}{\left[\left(\frac{R_E}{bN_m}\right)^{\frac{1}{\nu-1}} - 1\right]} \\ &= \frac{R_E}{bN_m} - \left(\alpha \frac{2\pi\ell_B}{1+\gamma_{PB}^2} \frac{N_m}{1-\nu} \frac{R_{cyl}^2}{R_E^3} + 1\right)^{\nu-1} \end{aligned} \tag{3.64}$$

which by itself cannot be solved explicitely, too, because even when replacing R_{cyl} through (3.39) the middle term will still contain a factor of $1/R_E$. Due to the occurrence of γ_{PB} this is not too much of a drawback as the latter had to be determined numerically anyway, particularly since in the blob-like description of the

network strands R_{cyl} and the Manning parameter ξ_{M} become R_{E}-dependent, rendering $\gamma_{\mathrm{PB}}(\xi_{\mathrm{M}}, R_{\mathrm{cyl}}, r_0)$ to be an *implicit* function of R_{E}, principally prohibiting an analytical solution to (3.64).

Effective Charge Fraction

The Poisson-Boltzmann equation (3.45) provides a full description of rod-like systems within the cell model framework. Particularly, it also contains the interplay between monomer charges and counterions, their increasing interaction for stronger electrostatics, and the crossover from the initial ideal gas-like distribution throughout the cell towards the phenomenon of counterion condensation, with which the confinement of a fraction of $(1-1/\xi_{\mathrm{M}})$ counterions to the cylindrical volume $\pi R_{\mathrm{M}}^2 \cdot L_{\mathrm{cyl}}$ around the rod-like central charge occurring for $\xi_{\mathrm{M}} > 1$ is denoted. This enforced and permanent proximity of opposite charges cancels part of the coulombic interactions from the system due to screening effects between rod and condensate which needs to be taken into account when modeling electrostatic effects.

While we already considered the influence of charged interactions on the counterion distribution by using $\Pi_{\mathrm{C}}^{\mathrm{PB}}$ instead of the simple ideal gas pressure Π_{C}, it turns out that the description of the equilibrium swelling condition $\mathcal{P} = \Sigma_i \Pi_i = 0$ for the pressure also requires a contribution $\Pi_{\ell_{\mathrm{B}}}$ from the intra-chain repulsion between the like-charged monomers. This effect however directly depends on the number of *effective* charges, *i.e.* if part of the fN_{m} interacting beads have their electrostatic potential screened through nearby condensed counterions the overall repulsion will naturally be less pronounced than without any opposite charges. The charge fraction f consequently drops to f_{eff} for $\xi_{\mathrm{M}} > 1$, given once again within the framework of the cell model as $f_{\mathrm{eff}} = (1/\xi_{\mathrm{M}}) \cdot f$ (see section 3.2.4 and (3.10) for details), reducing the amount of free charges to Q_{eff}.

Even though the different possible definitions for such a measure of effective coulombic interactions, all based on the rather primitive model of a charged rod or linearly extended polyelectrolyte chain contained in an isolated cylindrical cell, already provided relatively satisfying agreement, the remaining deviations still exhibit a dependency on the chain length N_{m} which could not be captured so far. This is not really surprising, as specific features of a hydrogel such as the crosslinking nodes with their charge accumulation, counteracting both the idea of isolatable strands and negligible end effects, have not been considered so far. One promising approach towards their inclusion could be the analyzation of the integrated counterion distribution as measured in our computer experiments, since the inflection point criterion [166] allows to extract from them another f_{eff} which should be more closely related to the actual amount of condensation, *i.e.* the true renormalization of electrostatic interactions (at least as far as this is subsumable into one single parameter).

An extensive analysis of all integrated counterion distributions for all parameters

we investigated, given and discussed in appendix B, shows a clear correlation to the f_{eff} required for the scaling laws to hold, although evenly clear non-negligible deviations still exist. However, on course of our analysis we also found another striking observation by indicating the four different effective charge fractions discussed so far (namely $f_x(\xi_{\text{M}}^{\text{Rod}})$ and $f_x(\xi_{\text{M}}^{\text{Blob}})$ for the f_{eff} from (3.10) with $f_{\text{max}}^{\text{rod}}$ and $f_{\text{max}}^{\text{blob}}$, respectively, and $f_x(\gamma_{\text{PB}}^{\text{Rod}})$ and $f_x(\gamma_{\text{PB}}^{\text{Blob}})$ from the scaling laws with the rod-like or blob-like description entering the derivation of γ_{PB} in (3.49) through r_0, R_{cyl} and ξ_{M}) in the plots of the integrated counterion distributions, relating them to the charge fraction f_x at the manually determined point of inflection: While $f_x(\gamma_{\text{PB}}^{\text{Blob}})$ and f_x do not always "agree" on the same amount of counterion condensation, it is nevertheless remarkable that $f_x(\gamma_{\text{PB}}^{\text{Blob}})$ always indicates the very same point on the distribution functions, namely the point of smallest concave radius (point of inflection of the derivative). Recalling that the inflection criterion leading to f_x originates from the treatment of infinitely long stiff rods and is only valid as a rigid threshold in that infinite limit anyway, an agreement with $f_x(\gamma_{\text{PB}}^{\text{Blob}})$ could not be expected exactly; it is even uncertain if drawing the analogy to a polyelectrolyte network could work on a conceptual level due to the lack of a clear definition. Furthermore, comparing the counterion distributions around the chains to those around the nodes (again, see appendix B for the plots), the latter almost always display ideal gas-like behaviour even in the strong condensation limit because they cannot differentiate between looking at a distance r along a chain or into the space between them; consequently, that ensures further N_{m}-dependent effects in the plots which would not be there for the infinitely long rod model. While the analogy to the Manning depiction therefore breaks down on the quantitative level, the qualitative findings, especially regarding $f_x(\gamma_{\text{PB}}^{\text{Blob}})$, tie the free parameter in (3.68) to the effective charge renormalization due to the counterion condensation, once again confirming the rough estimate we already did on the scaling level for (4.25).

Having procured that information, the length scales to be found in the integrated counterion distributions are also noteworthy: For one, the spatial distance $|r|$ from a chain corresponding to its average length $\langle R_{\text{E}}^2 \rangle^{1/2}$ is indicated as well as the model representations $R_{\text{cyl}}^{\text{Blob}}$ and $R_{\text{cyl}}^{\text{Rod}}$, the latter providing the idealized length of a network strand in the blob-like and rod-like representation of the cylindrical cell model, respectively. Since $R_{\text{cyl}}^{\text{Blob}}$ is essentially a projection of the network strand on the node-node-axis, $R_{\text{cyl}}^{\text{Rod}}$ follows the contour line of the chain (assuming it to be sufficiently stiff); hence, the rod-like description implies larger charge distances a, and $R_{\text{cyl}}^{\text{Blob}} < R_{\text{cyl}}^{\text{Rod}}$ is expected as sketched in figure 3.2. This can also be observed in the given plots of the counterion distributions, where $R_{\text{cyl}}^{\text{Blob}}$ is identified as too short a distance for the network's mesh size, because for $|r| = R_{\text{cyl}}^{\text{Blob}} < R_{\text{E}}$ not all counterions have been found (*i.e.* the functional value is significantly smaller than 100%). $R_{\text{cyl}}^{\text{Rod}}$ and the measured end-to-end distance R_{E} on the other hand display a more complicated connection: While for $f = 0.25$, $\ell_{\text{B}} \in \{1\sigma, 2\sigma\}$ and $f = 1.0$, $\ell_{\text{B}} = 5\sigma$ they coincide,

for strong electrostatics the rod-like description tends to overestimate the chain size, and vice versa for weaker coulombic interactions. Nevertheless, $R_{\mathrm{cyl}}^{\mathrm{Blob}}$ does indicate an important length scale, namely the one where "far" counterions enter the realm of the next network chain. This can be most easily seen if looking at the distributions around the nodes, because they exhibit ideal gas-like behaviour for $|r| \leq R_{\mathrm{cyl}}^{\mathrm{Blob}}$, which changes dramatically once that threshold is surpassed; not quite as obvious but still noticeable, the same holds true for the chain-centered distributions which also abandon their convex shape at the same $|r|$-value. In a way, this refers back to the cell model which would have that convex trend continued until a fraction of 1.0 is reached, because of its assumption of vanishing potential $\psi(r)$ at its boundaries.

3.2.8. Intra-Chain Charge Repulsion

While the leading effect of the swelling of polyelectrolyte networks is to be found in the osmotic pressure of the counterions being balanced by the elastic response of the chains, in section 3.2.4 we already identified the regime of polyelectrolyte blobs where the coulombic interaction became dominant on local scales. Particularly for strong electrostatics there has to be an additional pressure component $\Pi_{\ell_{\mathrm{B}}}$ entering the equilibrium balance which represents the local repulsion of the charged monomers, consequently depending on the Bjerrum length ℓ_{B} (as representation of the coulombic strength) and the effective charge distance a (for a discussion on the difference between rod-like and blob-like treatment see section 3.2.4).

Based on the Coulomb law between each of the fN_{m} neighbouring charges per chain we can therefore derive the electrostatic potential $U_{\ell_{\mathrm{B}}}$ for one network strand

$$U_{\ell_{\mathrm{B}}}(r) = \frac{1}{2} k_{\mathrm{B}} T \ell_{\mathrm{B}} \frac{(fN_{\mathrm{m}})^2}{r} \tag{3.65}$$

from which, as in (3.31), the repulsion force $\mathsf{f}_{\ell_{\mathrm{B}}}$ between the charged monomers follows

$$\begin{aligned} \mathsf{f}_{\ell_{\mathrm{B}}} &= -\frac{\partial U_{\ell_{\mathrm{B}}}}{\partial r} \\ &= k_{\mathrm{B}} T \ell_{\mathrm{B}} \frac{(fN_{\mathrm{m}})^2}{r^2} \end{aligned} \tag{3.66}$$

both up to logarithmical corrections in $\ln(r/r_0)$, as discussed later in section 3.3.3. Similar to (3.33), the electrostatic contribution to the pressure is consequently given by

$$\Pi_{\ell_{\mathrm{B}}} = \frac{\mathsf{f}_{\ell_{\mathrm{B}}} \cdot R_{\mathrm{E}}}{3R_{\mathrm{E}}^3} = k_{\mathrm{B}} T \ell_{\mathrm{B}} \frac{(fN_{\mathrm{m}})^2}{3R_{\mathrm{E}}^4} \tag{3.67}$$

generalizing the balance from (3.64) towards

$$0 = \Pi_{\mathrm{C}}^{\mathrm{PB}} + \Pi_{\ell_{\mathrm{B}}} + \Pi_{\mathrm{E}}^{\mathrm{FESAW}}$$

$$
\begin{aligned}
&= k_{\mathrm{B}}T\frac{2(1+\gamma_{\mathrm{PB}}^2)}{4\pi\ell_{\mathrm{B}}\cdot R_{\mathrm{cyl}}^2} + k_{\mathrm{B}}T\ell_{\mathrm{B}}\frac{(fN_{\mathrm{m}})^2}{3R_{\mathrm{E}}^4} \\
&- \alpha\frac{N_{\mathrm{m}}}{R_{\mathrm{E}}^3}\cdot\frac{k_{\mathrm{B}}T/(1-\nu)}{\left[\left(\frac{R_{\mathrm{E}}}{bN_{\mathrm{m}}}\right)^{\frac{1}{\nu-1}}-1\right]} \\
&= \frac{R_{\mathrm{E}}}{bN_{\mathrm{m}}} - \left(\alpha\frac{N_{\mathrm{m}}}{R_{\mathrm{E}}^3}\frac{\frac{1}{1-\nu}}{\frac{1+\gamma_{\mathrm{PB}}^2}{2\pi\ell_{\mathrm{B}}\cdot R_{\mathrm{cyl}}^2}+\ell_{\mathrm{B}}\frac{(fN_{\mathrm{m}})^2}{3R_{\mathrm{E}}^4}}+1\right)^{\nu-1}
\end{aligned}
\tag{3.68}
$$

Again, this expression cannot be solved explicitely for R_{E}, for structural reasons and because of the implicitly R_{E}-dependent integration constant γ_{PB} which needs to be derived from (3.49). As before in subsection 3.2.6, we can enter the blob picture to apply the same idea of locally repelling charges there. Using the electrostatic self-energy

$$U_{\mathrm{PE}} = k_{\mathrm{B}}T\ell_{\mathrm{B}}\frac{Q_{\mathrm{eff}}^2}{R_{\mathrm{E}}} \tag{3.69}$$

of a blob chain with an effective amount of Q_{eff} charges remaining, and the corresponding force

$$\mathsf{f}_{\mathrm{PE}} = -\left.\frac{\partial U_{\mathrm{PE}}}{\partial r}\right|_{r=R_{\mathrm{E}}} = k_{\mathrm{B}}T\ell_{\mathrm{B}}\frac{Q_{\mathrm{eff}}^2}{R_{\mathrm{E}}^2} \tag{3.70}$$

allows this effect to be simply added to the osmotic pressure of the counterions, *i.e.* to write the self-consistency condition (3.35) for the stretching force on a blob chain as

$$\mathsf{f}_{\mathrm{E}} \propto \Pi_{\mathrm{C}}R_{\mathrm{E}}^2 + \mathsf{f}_{\mathrm{PE}} \propto \frac{k_{\mathrm{B}}T}{\ell_{\mathrm{B}}+\frac{\xi}{fg}} + \ell_{\mathrm{B}}\frac{k_{\mathrm{B}}T}{\left(\ell_{\mathrm{B}}+\frac{\xi}{fg}\right)^2} \stackrel{!}{=} \frac{k_{\mathrm{B}}T}{\xi} \tag{3.71}$$

which introduces a third numerical prefactor c_{PE}.

Figure 3.12 demonstrates how the inclusion of the intrachain electrostatic repulsion dramatically improves the match between scaling law prediction and computer simulation study findings. Even for the case of assuming linear chains, the *left* plot here shows much higher relative chain lengths than the corresponding one on the *left* side of figure 3.6, even overcompensating the latter's lack of sufficient swelling. Also taking the finite extensibility into account (the *right* plots in both figures) finally shifts the curves right onto the simulation data, indicating that we have now accounted for all leading contributions to the swelling behaviour of polyelectrolyte networks, *i.e.* an osmotic pressure of an effective amount of non-condensed counterions acting in unison with locally repelling charges on the network chains against the nonlinearly diverging elastic restoring force of the strands.

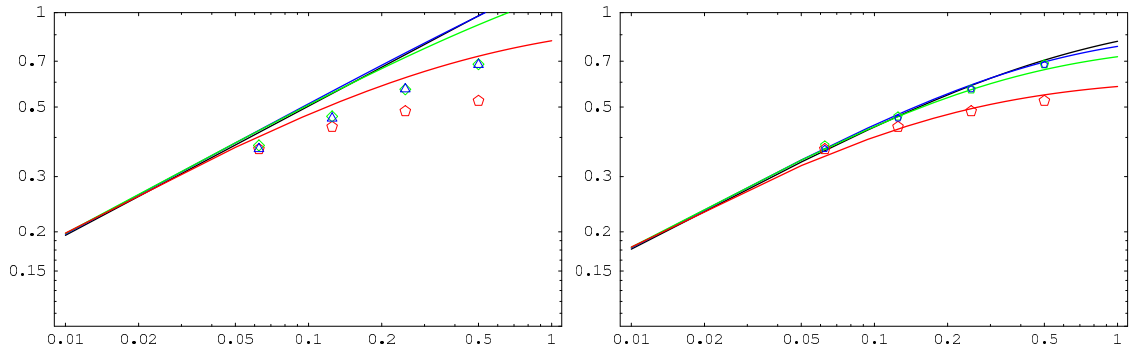

Figure 3.12.: Mimicking figure 3.6, the scaling prediction (3.71) is compared to the computer simulation data, using the same axes (plotting the relative chain extension $R_E/R_{max} = R_E/(bN_m) \propto \xi/(bg)$ as a function of the bare charge fraction f on the x-axis) and colour coding (*black* corresponds to $\ell_B = 0\sigma$, *blue* to $\ell_B = 1\sigma$, *green* to $\ell_B = 2\sigma$ and *red* to $\ell_B = 5\sigma$). The *left* graph assumes linear chains, while the *right* one considers the strands' finite extensibility, thereby matching the simulation data satisfactorily.

3.2.9. Finite Size Effects & (N, V, T)-Behaviour

Before we can consider the combination of (3.71) and (3.38) a successful scaling relation for charged hydrogels, we need to check the dependence of the result on the amount of monomers N_m per chain, because the employed blob picture usually assumes infinitely long strands, which naturally is not the case in our computer simulations. Hence, figure 3.13 takes the *right* plot of the previous figure 3.12 and adds the relative chain extension for $N_m = 79$ and $N_m = 159$ to the $N_m = 239$ already displayed earlier.

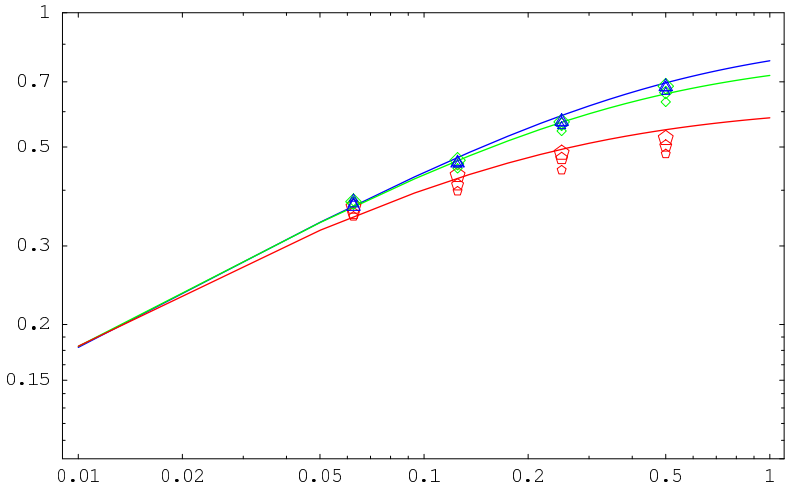

Figure 3.13.: Taking the *right* plot of figure 3.12, the simulation data for network strands with $N_m = 79$ and $N_m = 159$ is added to the ones for $N_m = 239$ already displayed there, to be able to assess finite size effects in the scaling prediction (3.71); hereby, smaller symbols correspond to shorter chains.

While for weak electrostatics there is almost no difference between the results for N_m, in particular if one remembers the size of the error bars of the simulation data

as given in figure 3.5, even strong coulombic coupling does not exhibit serious finite size effects but rather a direct convergence of the deviating data onto the predicted scaling curves. It can therefore be safely concluded that our longer systems with $N_\mathrm{m} = 239$ are already close enough to the desired limit of $N_\mathrm{m} \to \infty$ that no special care is required (once again, this is particularly true if the error bars are taken into account as well).

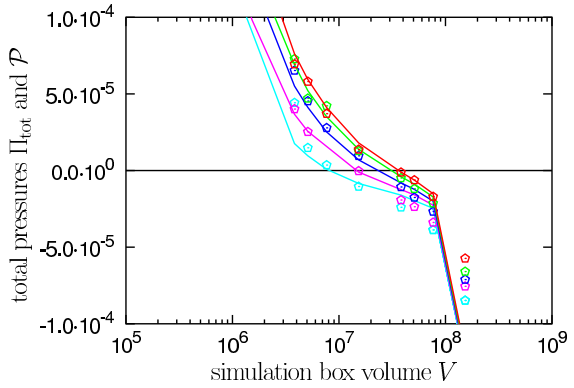

Figure 3.14.: Volume dependency of the total theoretical pressure Π_tot as predicted by the scaling relation (3.71) compared to the (N,V,T)-data $\mathcal{P}(V)$ measured in the computer simulations for $N_\mathrm{m} = 239$, a Bjerrum length of $\ell_\mathrm{B} = 5\sigma$, and varying charge fractions $f \in \{0.0625, 0.125, 0.25, 0.5, 1.0\}$ (colour coded as explained in table S.1).

Figure 3.14 takes the scaling prediction (3.71), derived for the system volume $V = V_\mathrm{eq}$ at swelling equilibrium where $\Pi_\mathrm{tot} = 0$, and assumes its validity in the vicinity of V_eq as well, arguing that

$$\begin{aligned} \mathsf{f}_\mathrm{E}^\mathrm{tot} &= \mathsf{f}_\mathrm{E} + \Delta\mathsf{f}_\mathrm{E} \propto \Pi_\mathrm{tot} R_\mathrm{E}^2 \propto \frac{k_\mathrm{B}T}{\ell_\mathrm{B} + \frac{\xi}{fg}} + \ell_\mathrm{B} \frac{k_\mathrm{B}T}{\left(\ell_\mathrm{B} + \frac{\xi}{fg}\right)^2} - \frac{k_\mathrm{B}T}{\xi} \quad \Rightarrow \\ \Pi_\mathrm{tot} &= \frac{c_\mathrm{id}}{R_\mathrm{E}^2 \left(\ell_\mathrm{B} + \frac{R_\mathrm{E}}{fN_\mathrm{m}}\right)} + \frac{\ell_\mathrm{B}}{R_\mathrm{E}^2} \frac{c_\mathrm{PE}}{\left(\ell_\mathrm{B} + \frac{R_\mathrm{E}}{fN_\mathrm{m}}\right)^2} - \frac{N_\mathrm{m}/R_\mathrm{E}^3}{c_\mathrm{blob}\left(\left(\frac{R_\mathrm{E}}{bN_\mathrm{m}}\right)^{\frac{1}{\nu-1}} - 1\right)} \end{aligned} \tag{3.72}$$

will hold for not too large $\Pi_\mathrm{tot} \neq 0$, too. Plotting the resulting $\Pi(V)$-graphs as *solid lines*, we can then compare that accuracy to the pressures $\mathcal{P}(V)$ measured by computer simulations in the (N,V,T)-ensemble. We find good agreement for over almost two decades in the volume, which is quite remarkable considering the approximations we used.

Though it might seem surprising to see such a simple scaling ansatz succeed in capturing the essential physics behind a rather complex macromolecular system with all its many interactions and correlations, it is one of the reasons why scaling theories are so common in polymer physics. It should nevertheless be noted that this approach is only exact up to the numerical prefactors of order unity we had to introduce, making *a priori* predictions of entirely unknown systems rather difficult. For that reason, the next section 3.3 will present an attempt to extend the considerations towards a rigorously self-consistent approach, a self-regulating model construct without the need for additional system input or prefactors.

3.3. The "Cell under Tension"-Model

The previous section 3.2 introduced the cell model as a framework for solving the Poisson-Boltzmann equation. While very successful in describing real rode-like systems, it failed to capture the specifics of a polyelectrolyte network on a more than qualitative level[4]. This should now be rectified by developing a unique combination of the "chain under tension" approach for ideal (section 2.3), real (section 2.4), and network chains (section 3.2.2), with the said cell model for infinitely long and infinitely stiff polyelectrolytes (section 3.2.7).

From there, we want to derive a free energy expression for the behaviour of charged counterions within such a construct, combining it with the expressions (3.30) and (3.65) for elastic response and electrostatic self-energy, respectively, to obtain a new framework for the treatment of polyelectrolyte networks.

3.3.1. Self-Stretching Cells

The first task is to replace the four different definitions for the cell dimensions, entering the length L_{cyl} of the cell in (3.39a), its outer radius R_{cyl} in (3.39b), and its inner one r_0, with a unified approach which takes the specifics of the polyelectrolyte networks equally well into account as the definition of the basic cell model itself.

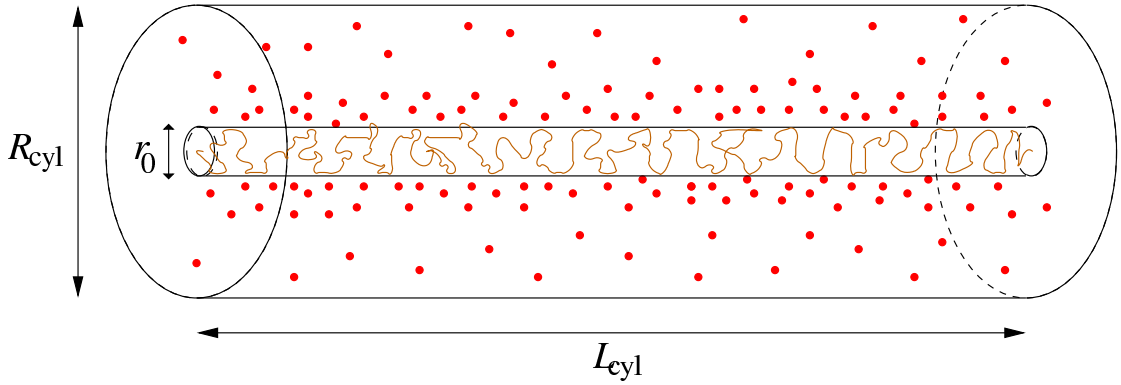

Figure 3.15.: Sketch of the cell geometry around each network strand (neglecting the nodes and crosslinks), illustrating the definition of L_{cyl}, R_{cyl}, and r_0; the latter encloses the entire polymer, assuming that none of the counterions enter that excluded volume.

Instead of distinguishing rod-like and blob-like polymers, we consider the network strands to be smeared out within the inner cylinder of radius r_0, as depicted in figure 3.15. That allows to define an excluded volume $\pi r_0^2 \cdot L_{\mathrm{cyl}}$ where none of the

[4] That was the reason why we rather continued using the scaling arguments in the previous section.

counterions enter, but without actually destroying the electrostatic interactions between them and the monomers, because since the latter are assumed to be on the (inner) surface of the inner cylinder, the counterions are still able to approach them as close as desired. It also has the advantage that most of the definitions become now straightforward: As seen in figure 3.15, L_{cyl} undoubtedly corresponds to the chain's end-to-end distance R_{E}, while the Manning parameter $\xi_{\mathrm{M}} = \ell_{\mathrm{B}}/a$ must take the form

$$\xi_{\mathrm{M}}^{\mathrm{CuT}} = \frac{\ell_{\mathrm{B}}}{\frac{R_{\mathrm{E}}}{fN_{\mathrm{m}}}} = \ell_{\mathrm{B}} \frac{fN_{\mathrm{m}}}{R_{\mathrm{E}}} \tag{3.73}$$

because of the fN_{m} smeared monomer charges along the cylinder of length $L_{\mathrm{cyl}} = R_{\mathrm{E}}$ which lead to the definition of the charge distance $a = \text{length}/\#\text{ charges}$ in (3.10) to be uniquely fulfilled by $a = L_{\mathrm{cyl}}/(fN_{\mathrm{m}})$. The outer cell radius R_{cyl} is once again given by the requirement of equal total volume between the $N_{\mathrm{p}} = 16$ cells and the entire simulation box, such that the average counterion number density $\bar{n}_{\mathrm{avg}}$ is the same in the cell model and the simulation reality. Due to the diamond-like structure of the cubic unit cell with its edge length a_{sim}, it is even possible to derive the desired relation *including* numerical prefactors, because the system setup ensures $R_{\mathrm{E}} = (\sqrt{3}/4)a_{\mathrm{sim}}$, as figure 4.2 already showed:

$$\begin{aligned}
N_{\mathrm{p}} \cdot \left(\pi R_{\mathrm{cyl}}^2 \cdot L_{\mathrm{cyl}}\right) &\stackrel{!}{=} V = a_{\mathrm{sim}}^3 \\
\Rightarrow \quad N_{\mathrm{p}} \cdot \left(\pi R_{\mathrm{cyl}}^2 \cdot R_{\mathrm{E}}\right) &\stackrel{!}{=} \left(\frac{R_{\mathrm{E}}}{\sqrt{3}/4}\right)^3 \\
\Rightarrow \quad R_{\mathrm{cyl}}^2 &\stackrel{!}{=} \frac{4^3}{3^{3/2}\pi N_{\mathrm{p}}} R_{\mathrm{E}}^2 \\
\Rightarrow \quad R_{\mathrm{cyl}} &\stackrel{!}{=} \frac{2}{3^{3/4}\sqrt{\pi}} R_{\mathrm{E}}
\end{aligned} \tag{3.74}$$

If one excludes the counterions from the inner cylinder with radius r_0, that volume must also be deducted from the cell's volume to ensure the same $\bar{n}_{\mathrm{avg}}$:

$$\begin{aligned}
N_{\mathrm{p}} \cdot \left(\pi R_{\mathrm{cyl}}^2 \cdot L_{\mathrm{cyl}} - \pi r_0^2 \cdot L_{\mathrm{cyl}}\right) &\stackrel{!}{=} V = a_{\mathrm{sim}}^3 \\
\Rightarrow \quad N_{\mathrm{p}} \cdot \left(\pi (R_{\mathrm{cyl}}^2 - r_0^2) \cdot R_{\mathrm{E}}\right) &\stackrel{!}{=} \left(\frac{R_{\mathrm{E}}}{\sqrt{3}/4}\right)^3 \\
\Rightarrow \quad R_{\mathrm{cyl}} &\stackrel{!}{=} \sqrt{\frac{4^3}{3^{3/2}\pi N_{\mathrm{p}}} R_{\mathrm{E}}^2 + r_0^2}
\end{aligned} \tag{3.75}$$

The radius r_0 of the inner cell cylinder can now be determined from the blob picture, as the idea behind this approach is to allow the network chains to minimize their energy (*i.e.* balance the blobs) while having the resulting length scale ξ determine $r_0 \sim \frac{1}{2}\xi$. The ratio R_{max}/l_g of the contour length of the entire chain to the contour

length l_g per blob size ξ is going to replace N_m/g because in the limit of strongly stretched chains when $g < 1$ it no longer makes sense to interpret g as "monomers per blob". Then, the blobs are no longer spherical, and we need to determine the perpendicular dimension $\xi_\perp$ (while the parallel one $\xi_\parallel$ still corresponds to the known ξ). In analogy to section 3.2.2 we can therefore write:

$$\left.\begin{array}{rcl} R_\mathrm{E} & = & \xi_\parallel \cdot \frac{R_\mathrm{max}}{l_g} \\ k_\mathrm{B}T & = & \mathsf{f}_\mathrm{E} \cdot \xi \end{array}\right\} \quad \Rightarrow \quad l_g = \frac{\xi_\parallel R_\mathrm{max}}{R_\mathrm{E}} = \frac{k_\mathrm{B}T R_\mathrm{max}}{\mathsf{f}_\mathrm{E} \cdot R_\mathrm{E}} \tag{3.76}$$

Now using (3.30) and (3.31) replaces f_E by $\mathsf{f}_\mathrm{FESAW}$ and (3.76) by

$$l_g = R_\mathrm{max} \left(\frac{R_\mathrm{F}}{R_\mathrm{max}}\right)^{\frac{1}{1-\nu}} (1-\nu) \left[\left(\frac{R_\mathrm{E}}{R_\mathrm{max}}\right)^{\frac{1}{\nu-1}} - 1\right] \tag{3.77}$$

Since from (2.46) and (2.15) it is known that $R_\mathrm{F}/R_\mathrm{max}^{3/5} = \ell_\mathrm{P}^{1/5} d^{1/5}$, the vertical extension $\xi_\perp$ of the blob chain under tension follows from (3.76) as

$$\xi_\perp \sim \frac{R_\mathrm{F}}{R_\mathrm{max}^\nu} \left(l_g - \xi_\parallel\right)^\nu \tag{3.78}$$

with $\xi_\parallel = l_g \frac{R_\mathrm{E}}{R_\mathrm{max}}$. We have to prevent that the inner cell cylinder becomes smaller than 1σ because that is the minimum separation a monomer must always have from any counterion, hence we find for r_0 the requirement

$$r_0 \sim 1\sigma + \frac{R_\mathrm{F}}{R_\mathrm{max}^\nu} \left(l_g \left(1 - \frac{R_\mathrm{E}}{R_\mathrm{F}}\right)\right)^\nu \tag{3.79}$$

with l_g given by (3.77).

In summary, we introduce a cell model as sketched in figure 3.15 whose parameters are given by the condition of equal counterion number density $\bar{n}_\mathrm{avg}$ with the simulation box and therefore have to fulfill

$$\xi_\mathrm{M}^\mathrm{CuT} = \ell_\mathrm{B} \frac{f N_\mathrm{m}}{R_\mathrm{E}} \tag{3.80a}$$

$$L_\mathrm{cyl} \stackrel{!}{=} R_\mathrm{E} \tag{3.80b}$$

$$R_\mathrm{cyl} \stackrel{!}{=} \sqrt{\frac{4^3}{3^{3/2}\pi N_\mathrm{p}} R_\mathrm{E}^2 + r_0^2} \tag{3.80c}$$

$$r_0 \stackrel{!}{\sim} 1\sigma + \frac{R_\mathrm{F}}{R_\mathrm{max}^\nu} \left(l_g \left(1 - \frac{R_\mathrm{E}}{R_\mathrm{F}}\right)\right)^\nu \tag{3.80d}$$

which due to its explicit dependence on the chain's blob conformation represents a stretched *cell under tension*.

3.3.2. Solving the Poisson-Boltzmann Equation

Recalling the definitions of section 3.2.7 for the cylindrical cell model, we considered the electrostatic potential $\psi(r)$ at a distance r from the cylinder axis in cylindrical symmetry. Introducing the counterion density $n(r)$ and a reduced electrostatic potential $y(r)$ defined as

$$n(r) = n(R_{\mathrm{cyl}}) \exp\left[-\frac{e_0\psi(r)}{k_{\mathrm{B}}T}\right] \tag{3.42}$$

$$y(r) = -\frac{e_0}{k_{\mathrm{B}}T}\psi(r) \tag{3.43}$$

we presented the solution (3.47) to the Poisson-Boltzmann equation

$$y'' + \frac{y'}{r} = \kappa^2 \mathrm{e}^y \tag{3.45}$$

under the boundary conditions

$$y'(r_0) = -\frac{2\xi_{\mathrm{M}}}{r_0} \qquad \text{and} \qquad y'(R_{\mathrm{cyl}}) = 0 \qquad \text{and} \qquad y(R_{\mathrm{cyl}}) = 0 \tag{3.46}$$

and derived the numerical solution for one of the two integration constants, γ_{PB}, from (3.49) over the entire range of validity of the Manning parameter $\xi_{\mathrm{M}} \geq 0$. As γ_{PB} became purely imaginary for $\xi_{\mathrm{M}} < \xi_{\mathrm{M}}^{\mathrm{min}}$, an analytical continuation of (3.49) in that regime was required which we restricted to γ_{PB} because for the remainder of section 3.2 we were only interested in the osmotic pressure $\Pi_{\mathrm{C}}^{\mathrm{PB}}$, a function of only γ_{PB} according to (3.51).

Now, however, we need the full solution for $y(r)$ and the second integration constant R_{M} as well, because the simplest ansatz for the free energy $\mathcal{F}_{\mathrm{PB}}$ of the cylindrical cell model, restricting to the electrostatic part of the energy and the entropy, reads [171,172]

$$\mathcal{F}_{\mathrm{PB}} = L_{\mathrm{cyl}} \int_{r_0}^{R_{\mathrm{cyl}}} 2\pi r \left[\frac{\epsilon_0\epsilon_{\mathrm{S}}}{2}\left(\nabla\psi(r)\right)^2 + k_{\mathrm{B}}T\, n(r) \ln\frac{n(r)}{\bar{n}_{\mathrm{avg}}}\right] \mathrm{d}r \tag{3.81}$$

requiring knowledge of $y(r)$ for all ξ_{M} (since $n(r)$, $\psi(r)$ and $\mathcal{F}_{\mathrm{PB}}$ then follow from (3.42), (3.43) and (3.81), respectively). Unfortunately, the known relation (3.47) for $y(r)$ contains with R_{M} a second integration constant for which the transcendental equations in (3.48) only provide a solution if $\xi_{\mathrm{M}} > \xi_{\mathrm{M}}^{\mathrm{min}}$. If that is not the case, R_{M} becomes complex (just as γ_{PB} does) and (3.47) is no longer valid; since there is no such simple analogon to the analytical continuation for γ_{PB}, we have to re-solve the Poisson-Boltzmann equation to be able to use $\mathcal{F}_{\mathrm{PB}}$ for $\xi_{\mathrm{M}} \leq \xi_{\mathrm{M}}^{\mathrm{min}}$, too.

A constructive solution for the non-linear differential equation(3.45) may *e.g.* follow [157,166,169,170,173] by substituting r and $y(r)$ according to

$$u(r) \;:=\; \ln(\kappa r) \tag{3.82a}$$

$$f(u) \;:=\; y\left(r\left(u\right)\right) + 2u \tag{3.82b}$$

which implies

$$r \;=\; \frac{1}{\kappa}\mathrm{e}^{u} \quad \Rightarrow \quad \mathrm{e}^{2u} = \kappa^2 r^2 \tag{3.83a}$$

$$\frac{\mathrm{d}u}{\mathrm{d}r} \;=\; \frac{1}{r} \tag{3.83b}$$

$$\frac{\mathrm{d}^2u}{\mathrm{d}r^2} \;=\; -\frac{1}{r^2} \tag{3.83c}$$

With these substitutions the electrostatic potential $y(r)$ becomes

$$y(r) \;=\; f(u(r)) - 2u(r) \tag{3.84a}$$

$$y'(r) \;=\; \frac{\mathrm{d}f}{\mathrm{d}u}\cdot\frac{\mathrm{d}u}{\mathrm{d}r} - 2\frac{\mathrm{d}u}{\mathrm{d}r} = \left(\frac{\mathrm{d}f}{\mathrm{d}u} - 2\right)\frac{\mathrm{d}u}{\mathrm{d}r} \tag{3.84b}$$

$$y''(r) \;=\; \left(\frac{\mathrm{d}^2f}{\mathrm{d}u^2}\cdot\frac{\mathrm{d}u}{\mathrm{d}r}\right)\frac{\mathrm{d}u}{\mathrm{d}r} + \left(\frac{\mathrm{d}f}{\mathrm{d}u} - 2\right)\frac{\mathrm{d}^2u}{\mathrm{d}r^2} \tag{3.84c}$$

which transform the Poisson-Boltzmann equation, using (3.83), towards

$$\begin{aligned}
\left[\left(f''\frac{1}{r}\right)\frac{1}{r} - \left(f'-2\right)\frac{1}{r^2}\right] + \frac{\left(f'-2\right)\frac{1}{r}}{r} \;&=\; \kappa^2\mathrm{e}^{f-2u} = \kappa^2\frac{\mathrm{e}^f}{\mathrm{e}^{2u}} = \kappa^2\frac{\mathrm{e}^f}{\kappa^2 r^2} \\
\left[\frac{f'' - \left(f'-2\right)}{r^2}\right] + \frac{\left(f'-2\right)}{r^2} \;&=\; \frac{\mathrm{e}^f}{r^2} \\
f'' \;&=\; \mathrm{e}^f
\end{aligned} \tag{3.85}$$

The boundary conditions (3.46) become

$$y'(r_0) = -2\frac{\xi_\mathrm{M}}{r_0} \;\rightarrow\; \left(f'\left(u(r_0)\right) - 2\right)\frac{1}{r_0} = -2\frac{\xi_\mathrm{M}}{r_0} \;\Rightarrow\; f'(u(r_0)) = 2(1-\xi_\mathrm{M}) \tag{3.86a}$$

$$y'(R_\mathrm{cyl}) = 0 \;\rightarrow\; \left(f'\left(u(R_\mathrm{cyl})\right) - 2\right)\frac{1}{R_\mathrm{cyl}} = 0 \;\Rightarrow\; f'(u(R_\mathrm{cyl})) = 2 \tag{3.86b}$$

$$y(R_\mathrm{cyl}) = 0 \;\rightarrow\; f\left(u(R_\mathrm{cyl})\right) = 2u(R_\mathrm{cyl}) \;\Rightarrow\; f(u(R_\mathrm{cyl})) = 2\ln\left(\kappa R_\mathrm{cyl}\right) \tag{3.86c}$$

Multiplying (3.85) by f' and integrating over u gives

$$\begin{aligned}
\int f'f''\mathrm{d}u \;&=\; \int f'\mathrm{e}^f\mathrm{d}u \\
\frac{1}{2}\left(f'\right)^2 \;&=\; \mathrm{e}^f + \mathrm{const}_1 \\
\left(f'\right)^2 \;&=\; 2\mathrm{e}^f - 4\gamma_\mathrm{PB}^2
\end{aligned} \tag{3.87}$$

with the integration constant $\text{const}_1 := -2\gamma_{\text{PB}}^2$ following from (3.86b), (3.87), and (3.86c) as

$$\begin{aligned} 4 = \left(f'\right)^2\Big|_{r=R_{\text{cyl}}} &= \left(2\mathrm{e}^f - 4\gamma_{\text{PB}}^2\right)\big|_{r=R_{\text{cyl}}} = 2\mathrm{e}^{2\ln\left(\kappa R_{\text{cyl}}\right)} - 4\gamma_{\text{PB}}^2 \\ 4 + 4\gamma_{\text{PB}}^2 &= 2\left(\mathrm{e}^{\ln\left(\kappa R_{\text{cyl}}\right)}\right)^2 = 2\left(\kappa R_{\text{cyl}}\right)^2 \\ 2\left(1+\gamma_{\text{PB}}^2\right) &= \kappa^2 R_{\text{cyl}}^2 \end{aligned} \tag{3.50}$$

Integrating (3.87) again by separating variables leads to

$$\begin{aligned} \left(f'\right)^2 &= 2\mathrm{e}^f - 4\gamma_{\text{PB}}^2 \\ \frac{\mathrm{d}f}{\mathrm{d}u} = f' &= \pm\sqrt{2\mathrm{e}^f - 4\gamma_{\text{PB}}^2} \\ \frac{\mathrm{d}f}{\pm\sqrt{2\mathrm{e}^f - 4\gamma_{\text{PB}}^2}} &= \mathrm{d}u \\ \pm\int \mathrm{d}f \left(2\mathrm{e}^f - 4\gamma_{\text{PB}}^2\right)^{-1/2} &= \int \mathrm{d}u \\ \pm\frac{1}{\gamma_{\text{PB}}} \arctan\left(\frac{\sqrt{2\mathrm{e}^f - 4\gamma_{\text{PB}}^2}}{\sqrt{4\gamma_{\text{PB}}^2}}\right) &= u + \text{const}_2 = \ln\left(\kappa r\right) + \text{const}_2 \end{aligned} \tag{3.88}$$

with the definition for u from (3.82a), and a second integration constant $\text{const}_2 := -\ln\left(\kappa R_{\text{M}}\right)$. Re-inserting f from (3.82b) as well as using (3.50) then turns (3.88) for $\gamma_{\text{PB}} \in \mathbb{R}$ into

$$\begin{aligned} \ln\left(\kappa r\right) - \ln\left(\kappa R_{\text{M}}\right) &= \pm\frac{1}{\gamma_{\text{PB}}} \arctan\left(\frac{\sqrt{2\mathrm{e}^{y+2\ln(\kappa r)} - 4\gamma_{\text{PB}}^2}}{\sqrt{4\gamma_{\text{PB}}^2}}\right) \\ y(r) &= \ln\left[2\gamma_{\text{PB}}^2 \frac{1 + \tan^2\left[\gamma_{\text{PB}}\left(-\ln\left(\kappa R_{\text{M}}\right) \pm \ln\left(\kappa r\right)\right)\right]}{\kappa^2 r^2}\right] \\ y(r) &= -\ln\left[\frac{r^2}{R_{\text{cyl}}^2} \frac{\kappa^2 R_{\text{cyl}}^2}{2\gamma_{\text{PB}}^2\left(1 + \tan^2\left[\gamma_{\text{PB}} \ln\left(\frac{r}{R_{\text{M}}}\right)\right]\right)}\right] \\ y(r) &= -\ln\left[\frac{r^2}{R_{\text{cyl}}^2} \frac{2\left(1+\gamma_{\text{PB}}^2\right)}{2\gamma_{\text{PB}}^2\left(1 + \tan^2\left[\gamma_{\text{PB}} \ln\left(\frac{r}{R_{\text{M}}}\right)\right]\right)}\right] \\ y(r) &= -\ln\left[\frac{r^2}{R_{\text{cyl}}^2}\left(1+\gamma_{\text{PB}}^{-2}\right)\cos^2\left[\gamma_{\text{PB}} \ln\left(\frac{r}{R_{\text{M}}}\right)\right]\right] \\ y(r) &= -2\ln\left[\frac{r}{R_{\text{cyl}}}\sqrt{1+\gamma_{\text{PB}}^{-2}}\cos\left(\gamma_{\text{PB}} \ln\frac{r}{R_{\text{M}}}\right)\right] \end{aligned} \tag{3.47}$$

The boundary conditions (3.46) consequently result in

$$\begin{aligned} y'(r_0) &= -\frac{2\xi_\mathrm{M}}{r_0} \\ \ln(\kappa R_\mathrm{M}) &= \left[\ln(\kappa r) - \frac{1}{\gamma_\mathrm{PB}} \arctan\frac{r_0 - r\xi_\mathrm{M}}{r_0\gamma_\mathrm{PB}}\right]\Bigg|_{r=r_0} \\ \gamma_\mathrm{PB} \ln\frac{r_0}{R_\mathrm{M}} &= \arctan\frac{1-\xi_\mathrm{M}}{\gamma_\mathrm{PB}} \end{aligned} \tag{3.48a}$$

and

$$\begin{aligned} y'(R_\mathrm{cyl}) &= 0 \\ \ln(\kappa R_\mathrm{M}) &= \left[\ln(\kappa r) - \frac{1}{\gamma_\mathrm{PB}} \arctan\frac{1}{\gamma_\mathrm{PB}}\right]\Bigg|_{r=R_\mathrm{cyl}} \\ \gamma_\mathrm{PB} \ln\frac{R_\mathrm{cyl}}{R_\mathrm{M}} &= \arctan\frac{1}{\gamma_\mathrm{PB}} \end{aligned} \tag{3.48b}$$

which can be combined by subtracting (3.48a) from (3.48b) to obtain the equation

$$\gamma_\mathrm{PB} \ln\frac{R_\mathrm{cyl}}{r_0} = \arctan\frac{1}{\gamma_\mathrm{PB}} + \arctan\frac{\xi_\mathrm{M}-1}{\gamma_\mathrm{PB}} \tag{3.49}$$

for γ_PB. How (3.49) can be solved for the different regimes of ξ_M was discussed in depth in section 3.2.7; here, we are interested only in the regime $\xi_\mathrm{M} < \xi_\mathrm{M}^\mathrm{min}$ where γ_PB becomes purely imaginary and (3.47), (3.48), and (3.49) are no longer valid. Using the analytical continuation $\gamma_\mathrm{PB} \to -\mathrm{i}\gamma_\mathrm{PB} =: \tilde{\gamma}_\mathrm{PB}$ allowed to find a suitable replacement for (3.49) in section 3.2.7, which is why this idea should now be extended to the other equations, too.

Restarting at (3.88), which was still valid for both real and imaginary γ_PB, we can follow the same line of arguments again while using $\tilde{\gamma}_\mathrm{PB} = -\mathrm{i}\gamma_\mathrm{PB} \in \mathbb{R}$ appropriately inserted. Instead of (3.47) we then find[5]

$$y(r) = -\ln\left[\frac{r}{R_\mathrm{cyl}}\sqrt{\tilde{\gamma}_\mathrm{PB}^{-2} - 1}\,\sinh\left(\tilde{\gamma}_\mathrm{PB}\ln\frac{r}{R_0}\right)\right]^2 \tag{3.89}$$

with the second integration constant from (3.88) modified to

$$R_0 = R_\mathrm{M}\exp\left(-\frac{\pi}{2\gamma_\mathrm{PB}}\right) \quad \text{or} \quad R_\mathrm{M} = R_0\exp\left(-\frac{\mathrm{i}\pi}{2\tilde{\gamma}_\mathrm{PB}}\right) \tag{3.90}$$

[5] Contrary to (3.47), in the low electrostatics limit of (3.89) we left the exponent within the natural logarithm because for $r < R_0 \Rightarrow \ln\frac{r}{R_0} < 0 \Rightarrow \sinh(.) < 0$ which renders the argument of the logarithm to be negative because of $\sinh(-x) = -\sinh(x)$; only the square around it then prevents $y(r)$ to become complex. For (3.47) this was not an issue because it contained a cosine instead, for which $\cos(-x) = \cos(x)$.

because as $\xi_M \to 0$ decreases below $\xi_M^{\min}$, γ_{PB} goes through 0 and becomes purely imaginary, while R_M goes through 0, too, but becomes complex afterwards; (3.90) then conveniently defines a $R_0 \in \mathbb{R}$ which keeps $y(r) \in \mathbb{R}$ as well. Once again applying the boundary conditions (3.46) replaces (3.48) for $\gamma_{PB} \in \mathbb{iR}$ by

$$\tilde{\gamma}_{PB} \ln \frac{r_0}{R_M} = -\operatorname{arccoth} \frac{1-\xi_M}{\tilde{\gamma}_{PB}} \tag{3.91a}$$

$$\tilde{\gamma}_{PB} \ln \frac{R_{cyl}}{R_M} = -\operatorname{arccoth} \frac{1}{\tilde{\gamma}_{PB}} \tag{3.91b}$$

which can be combined by subtracting (3.91a) from (3.91b) to obtain the equation

$$-\tilde{\gamma}_{PB} \ln \frac{R_{cyl}}{r_0} = \operatorname{arccoth} \frac{1}{\tilde{\gamma}_{PB}} + \operatorname{arccoth} \frac{\xi_M - 1}{\tilde{\gamma}_{PB}} \tag{3.59}$$

for $\tilde{\gamma}_{PB}$. While as in section 3.2.7 this allows to derive γ_{PB} numerically for all ξ_M via (3.49) and (3.59), it is now also possible to deduce R_M resp. R_0 from (3.48) and (3.91) even for $\xi_M < \xi_M^{\min}$, which finally enables us to determine the electrostatic potential $y(r)$ within the framework of the cylindrical cell model and the Poisson-Boltzmann description over the entire parameter range of $\xi_M = \xi_M(f, \ell_B)$, *i.e.* by inserting γ_{PB}, R_M into (3.47) and $\tilde{\gamma}_{PB}$, R_0 into (3.89).

Figure 3.16 now displays the resulting $y(r)$ for $f \in \{0.0625, 0.125, 0.25, 0.5, 1.0\}$ and $\ell_B \in \{1\sigma, 2\sigma, 5\sigma\}$, using the equilibrium swelling value of R_E measured in our simulations (see table 4.1). Similar to a $1/r$-potential, the graphs drop monotonically from larger numbers close the inner rod towards zero, reaching the boundary condition $y(R_{cyl}) = 0$ from (3.46) at different values of r for the various parameters because of $R_{cyl} = R_{cyl}(R_E)$ depending on the measured R_E we entered into its definition (3.80c). Higher charge fractions f or increased electrostatics (larger ℓ_B) are followed by a shift of the potential towards larger $y(r)$ at all spatial distances r.

The counterion density $n(r)$ is also given in figure 3.16 (*right column*) as it easily follows from the electrostatic potential once $n(R_{cyl})$ is derived from (3.44) and (3.50), and is combined with the definition (3.43) into the Boltzmann factor of (3.42), obtaining

$$n(r) = \left(\frac{2\,(1+\gamma_{PB}^2)}{R_{cyl}^2 \cdot 4\pi\ell_B} \right) \exp\left[-y(r)\right] \tag{3.92}$$

Here, the shape of the functions no longer shifts monotonically for increasing parameters f and/or ℓ_B; instead, they all approach their corresponding average counterion density

$$\bar{n}_{avg} = \frac{f N_m}{\pi\,(R_{cyl}^2 - r_0^2) \cdot R_E} \tag{3.93}$$

(also given in figure 3.16 using the same line style as for the respective $n(r)$ itself) for vanishing electrostatics. This also allows a simple safeguard calculations to verify

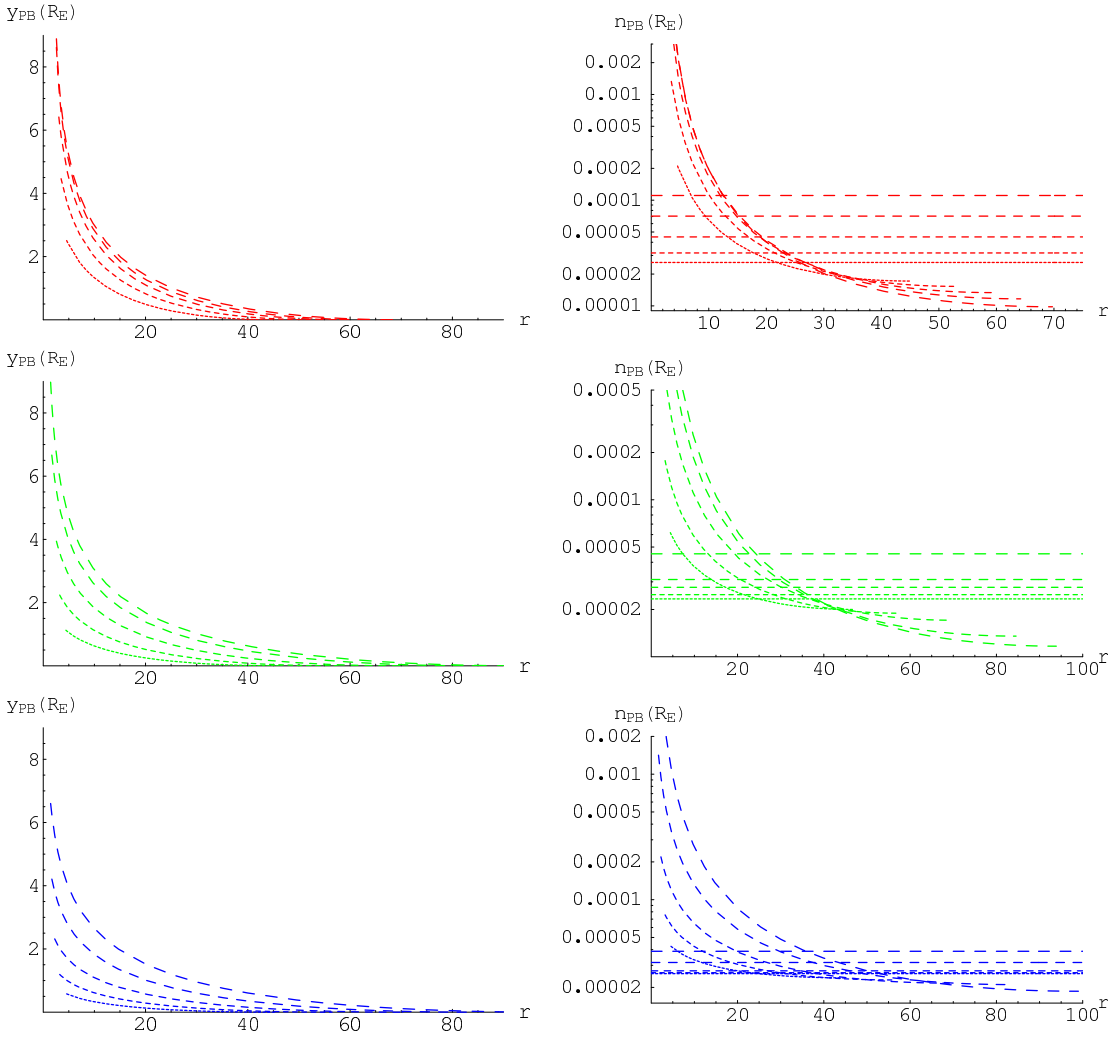

Figure 3.16.: Plots of the electrostatic potential $y(r)$ (*left column*) and the counterion density $n(r)$ (*right column*) within the framework of the "cell under tension"-model, using the experimental values from table 4.1 for R_{E}, decreasing Bjerrum length $\ell_{\mathrm{B}} = 5\sigma$ (*red lines*), $\ell_{\mathrm{B}} = 2\sigma$ (*green lines*), $\ell_{\mathrm{B}} = 1\sigma$ (*blue lines*), and all charge fractions $f \in \{0.0625, 0.125, 0.25, 0.5, 1.0\}$ (indicated by increasing dashing); the plots of $n(r)$ also contain the corresponding $\bar{n}_{\mathrm{avg}}$ as a *straight line* in the appropriate line style.

the results we achieved so far by checking if

$$\int \mathrm{d}^3 r\, n(\vec{r}) = \int_{r_0}^{R_{\mathrm{cyl}}} 2\pi r\, L_{\mathrm{cyl}}\, \mathrm{d}r\, n(r) \stackrel{!}{=} f N_{\mathrm{m}}$$

is fulfilled by all derived densities $n(r)$, *i.e.* all counterion charges are found in the cylindrical cell (as it turns out, this is the case).

3.3.3. Free Energies and Equilibrium

The thermodynamic equilibrium is characterized by the minimization of the free energy of the system. Corresponding to the balance in the pressure components, which themselves are derivatives of the respective free energy contributions, this opens a convenient way to determine the equilibrium swelling behaviour of the polyelectrolyte networks in the more elaborate setting of the "cell under tension"-model.

Instead of the simple ideal gas approach for the osmotic pressure of the counterions employed earlier, the free energy $\mathcal{F}_{\mathrm{PB}}$ of the cell can be used, which consists of an electrostatic part of the energy, the entropy, and a free volume contribution:

$$\mathcal{F}_{\mathrm{PB}} = \mathcal{F}_{\mathrm{PB-E}} + \mathcal{F}_{\mathrm{PB-S}} + \mathcal{F}_{\mathrm{PB-V}} \tag{3.94}$$

Various definitions for the individual components exist, *e.g.* [167,171,172]

$$\begin{aligned}
\mathcal{F}_{\mathrm{PB-E}} &= \frac{1}{2}\iint \mathrm{d}\vec{r}\mathrm{d}\vec{r}'\, n(\vec{r})n(\vec{r}')\, V(\vec{r}-\vec{r}') \;-\; (fN_{\mathrm{m}})\int \mathrm{d}\vec{r} n(\vec{r})\, V(\vec{r}) \\
&= \int \mathrm{d}^3 r\, e_0 n(\vec{r}) \left[\frac{1}{2}\psi(\vec{r}) + \psi_{\mathrm{f}}(\vec{r})\right] && (3.95a) \\
\mathcal{F}_{\mathrm{PB-S}} &= k_{\mathrm{B}}T \int \mathrm{d}^3 r\, n(\vec{r}) \left[\ln\left(\frac{n(\vec{r})}{\bar{n}_{\mathrm{avg}}}\right) - 1\right] \\
&= k_{\mathrm{B}}T \int \mathrm{d}\vec{r} n(\vec{r})\, \ln\left(n(\vec{r})\cdot v_0\right) && (3.95b) \\
\mathcal{F}_{\mathrm{PB-V}} &= -k_{\mathrm{B}}T \int \mathrm{d}^3 r\, n(\vec{r}) \ln\left(1 - \frac{n(\vec{r})}{\bar{n}_{\mathrm{max}}}\right) && (3.95c)
\end{aligned}$$

with the coulombic interaction potential $V(\vec{r}) = k_{\mathrm{B}}T\frac{\ell_{\mathrm{B}}}{|\vec{r}|}$, the electrostatic potentials $\psi(r)$ and $\psi_{\mathrm{f}}(r)$ generated by the free counterions resp. the "fixed" charges on the rod, the molecular volume v_0 of a counterion, the average resp. maximum counterion density $\bar{n}_{\mathrm{avg}}$ from (3.93) and $\bar{n}_{\mathrm{max}} = \frac{3}{2}\pi d^3$ where $d = 1.0\sigma$ is the diameter of the counterions.

While we found the excluded volume term $\mathcal{F}_{\mathrm{PB-V}}$ to be negligible for non-collapsed chains with $R_{\mathrm{E}}/R_{\mathrm{max}} \gtrsim 0.1$, the normalization of the counterion density in the entropic term $\mathcal{F}_{\mathrm{PB-S}}$ is not; for the minimization, however, constant contributions are of no consequence, which is why

$$\begin{aligned}
& k_{\mathrm{B}}T \int \mathrm{d}^3 r\, n(\vec{r}) \left[\ln\left(\frac{n(\vec{r})}{\bar{n}_{\mathrm{avg}}}\right) - 1\right] \\
= \;& k_{\mathrm{B}}T \int \mathrm{d}^3 r\, n(\vec{r}) \left[\ln\left(n(\vec{r})v_0 \cdot \frac{1}{v_0\bar{n}_{\mathrm{avg}}}\right) - 1\right] \\
= \;& k_{\mathrm{B}}T \int \mathrm{d}^3 r\, n(\vec{r}) \left[\ln\left(n(\vec{r})v_0\right) - \ln\left(v_0\bar{n}_{\mathrm{avg}}\right) - 1\right]
\end{aligned}$$

$$
\begin{aligned}
&= k_{\mathrm{B}}T \int \mathrm{d}\vec{r}\, n(\vec{r})\, \ln\left(n(\vec{r})\cdot v_0\right) - k_{\mathrm{B}}T\, \left[\ln\left(v_0 \bar{n}_{\mathrm{avg}}\right) - 1\right] \int \mathrm{d}^3 r\, n(\vec{r}) \\
&= k_{\mathrm{B}}T \int \mathrm{d}\vec{r}\, n(\vec{r})\, \ln\left(n(\vec{r})\cdot v_0\right) - k_{\mathrm{B}}T\, \left[\ln\left(v_0 \bar{n}_{\mathrm{avg}}\right) - 1\right]\, (fN_{\mathrm{m}})
\end{aligned}
$$

shows that both definitions in (3.95b) are equivalent.

Similarly for the electrostatic contribution $\mathcal{F}_{\mathrm{PB-E}}$: The first definition integrates the coulombic counterion-counterion and counterion-cylinder interactions over the entire space (assuming that there are fN_{m} fixed charges on a rod going through the origin), which can be re-written as

$$
\begin{aligned}
&\frac{1}{2} \iint \mathrm{d}\vec{r}\mathrm{d}\vec{r}'\, n(\vec{r}) n(\vec{r}')\, V(\vec{r}-\vec{r}') \;\; - \;\; (fN_{\mathrm{m}}) \int \mathrm{d}\vec{r}\, n(\vec{r})\, V(\vec{r}) \\
= \;& \frac{1}{2} \int \mathrm{d}^3 r\, n(\vec{r}) \int \mathrm{d}^3 r'\, n(\vec{r}')\, V(\vec{r}-\vec{r}') \;\; - \;\; (fN_{\mathrm{m}}) \int \mathrm{d}^3 r\, n(\vec{r})\, V(\vec{r}) \\
= \;& \int \mathrm{d}^3 r\, n(\vec{r}) \left[\frac{1}{2} \int \mathrm{d}^3 r'\, n(\vec{r}')\, V(\vec{r}-\vec{r}') \;\; - \;\; (fN_{\mathrm{m}}) V(\vec{r})\right] \\
= \;& \int \mathrm{d}^3 r\, e_0 n(\vec{r}) \left[\frac{1}{2}\psi(\vec{r}) + \psi_{\mathrm{f}}(\vec{r})\right]
\end{aligned}
$$

to arrive at (3.95a). It is also possible to relate $\mathcal{F}_{\mathrm{PB-E}}$ to the total electrostatic potential $\psi_{\mathrm{tot}}(r) = \psi(r) + \psi_{\mathrm{f}}(r)$ via

$$
\begin{aligned}
& \int \mathrm{d}^3 r\, e_0 n(\vec{r}) \left[\frac{1}{2}\psi(\vec{r}) + \psi_{\mathrm{f}}(\vec{r})\right] \\
= \;& \int \mathrm{d}^3 r\, e_0 n(\vec{r}) \left[\frac{1}{2}\left(\psi(\vec{r}) + \psi_{\mathrm{f}}(\vec{r})\right) + \frac{1}{2}\psi_{\mathrm{f}}(\vec{r})\right] \\
= \;& \frac{1}{2} \int \mathrm{d}^3 r\, e_0 n(\vec{r}) \left[\psi_{\mathrm{tot}}(\vec{r}) + \psi_{\mathrm{f}}(\vec{r})\right]
\end{aligned}
\tag{3.96}
$$

eliminating the need for determining $\psi(r)$, but now requiring $\psi_{\mathrm{tot}}(r)$ and $\psi_{\mathrm{f}}(r)$. The latter, however, can be derived on a textbook level [174, 175], as it stands for the electrostatic potential of a homogeneously charged cylinder with line charge density $\lambda = fN_{\mathrm{m}}/L_{\mathrm{cyl}}$; employing Gauss' Law we find for the radial component E_r of the electric field[6]:

$$
\begin{aligned}
\frac{fN_{\mathrm{m}}}{\epsilon_0} = \frac{\lambda L_{\mathrm{cyl}}}{\epsilon_0} \;\; &= \;\; \oint \vec{E}\cdot \mathrm{d}\vec{A} = E_r \oint \mathrm{d}A = E_r \cdot 2\pi r\, L_{\mathrm{cyl}} \\
\Rightarrow \qquad E_r \;\; &= \;\; \frac{1}{2\pi\epsilon_0}\frac{\lambda}{r} = \frac{fN_{\mathrm{m}}}{2\pi\epsilon_0\, L_{\mathrm{cyl}}}\frac{1}{r}
\end{aligned}
\tag{3.97}
$$

[6] In cylindrical coordinates, the other two components are zero.

From there, the potential $\psi_\mathrm{f}(r)$ follows as

$$
\begin{aligned}
-\nabla\psi_\mathrm{f} = \vec{E} \quad \Rightarrow \quad \psi_\mathrm{f}(r) &= -\int E_r \,\mathrm{d}r = -\int \left(\frac{1}{2\pi\epsilon_0}\frac{\lambda}{r}\right)\mathrm{d}r \\
\psi_\mathrm{f}(r) &= -\frac{\lambda}{2\pi\epsilon_0}\ln\left(\frac{r}{R_\mathrm{cyl}}\right) = -\frac{e_0^2}{4\pi\epsilon_0 k_\mathrm{B}T}\frac{2k_\mathrm{B}T\lambda}{e_0^2}\ln\left(\frac{r}{R_\mathrm{cyl}}\right) \\
\psi_\mathrm{f}(r) &= -\frac{2k_\mathrm{B}T}{e_0}\xi_\mathrm{M}\ln\left(\frac{r}{R_\mathrm{cyl}}\right) \qquad (3.98a) \\
\Rightarrow \quad y_\mathrm{f}(r) &= -2\,\xi_\mathrm{M}\ln\left(\frac{r}{R_\mathrm{cyl}}\right) \qquad (3.98b)
\end{aligned}
$$

where we chose $\psi_\mathrm{f}(R_\mathrm{cyl}) \stackrel{!}{=} 0$ as normalization for the integration constant, and used $\ell_\mathrm{B} = e_0^2/(4\pi\epsilon_0 k_\mathrm{B}T)$ and $\xi_\mathrm{M} = \lambda\ell_\mathrm{B}/e_0$ to replace the line charge density with the Manning parameter; the analogy to (3.43) then led to the reduced potential $y_\mathrm{f}(r)$.

Note that through $r_0 = r_0(R_\mathrm{E})$, $R_\mathrm{cyl} = R_\mathrm{cyl}(R_\mathrm{E})$, $L_\mathrm{cyl} = L_\mathrm{cyl}(R_\mathrm{E})$, and $\xi_\mathrm{M} = \xi_\mathrm{M}(R_\mathrm{E})$, all due to (3.80), functional minimization of $\mathcal{F}_\mathrm{PB}$ requires variation of R_E, from where then the cell model parameters are set, allowing γ_PB and R_M resp. R_0 to be computed, which in turn determines $y(r)$ and $n(R_\mathrm{cyl})$, leading to $\psi(r)$ and $n(r)$, with which one finally arrives at $\mathcal{F}_\mathrm{PB}$ – a procedure that needs to be repeated for every R_E until the minimum in the free energy is found.

$$
R_\mathrm{E} \to (3.80)\text{: } \left\{\begin{array}{c} \xi_\mathrm{M}(R_\mathrm{E}) \\ L_\mathrm{cyl}(R_\mathrm{E}) \\ R_\mathrm{cyl}(R_\mathrm{E}) \\ r_0(R_\mathrm{E}) \end{array}\right\} \to \left\{\begin{array}{c} \text{for } \xi_\mathrm{M} > \xi_\mathrm{M}^\mathrm{min}\text{:} \\ (3.49)\text{: } \gamma_\mathrm{PB} \to (3.48)\text{: } R_\mathrm{M} \to (3.47)\text{:} \\ \text{for } \xi_\mathrm{M} \le \xi_\mathrm{M}^\mathrm{min}\text{:} \\ (3.59)\text{: } \tilde{\gamma}_\mathrm{PB} \to (3.91)\text{: } R_0 \to (3.89)\text{:} \end{array}\right\} y(r)
$$

$$
y(r) \to (3.43)\text{: } \psi(r) \to \left\{\begin{array}{c} (3.50) \to (3.44)\text{: } n(R_\mathrm{cyl}) \\ \downarrow \\ (3.42)\text{: } n(r) \end{array}\right\} \to \left\{\begin{array}{l} (3.95a)\text{:} \\ (3.95b)\text{:} \end{array}\right\} \mathcal{F}_\mathrm{PB}
$$

Considering that (3.49) and (3.59) can only be solved numerically, the latter thereby requiring special algorithmic caution due to the steep divergence shown in figure 3.8, it will be understandable that the intrinsically simple idea of minimizing the free energies becomes quite an effort for the application to the cell model.

Electrostatic Self-Energy

In its current form, $\mathcal{F}_\mathrm{PB}$ still lacks an important contribution to the total free energy $\mathcal{F}_\mathrm{PB-tot}$ of all currently considered components, namely the self-energy $\mathcal{F}_\mathrm{se-rod}$ of the rod. That can be seen most easily when starting off with the definition of $\mathcal{F}_\mathrm{PB-tot}$, *i.e.* with

$$
\mathcal{F}_\mathrm{PB-tot} = \frac{1}{2}\int \mathrm{d}^3r\, e_0 n_\mathrm{tot}(\vec{r})\,\psi_\mathrm{tot}(\vec{r}) = \frac{1}{2}\int \mathrm{d}^3r\, e_0\,[n(\vec{r}) + n_\mathrm{f}(\vec{r})]\;[\psi(\vec{r}) + \psi_\mathrm{f}(\vec{r})]
$$

$$
\begin{aligned}
&= \frac{1}{2}\int \mathrm{d}^3r\, e_0 \left[n(\vec{r})\psi(\vec{r}) + n(\vec{r})\psi_\mathrm{f}(\vec{r}) + n_\mathrm{f}(\vec{r})\psi_\mathrm{f}(\vec{r})\right] \\
&= \int \mathrm{d}^3r\, e_0 n(\vec{r}) \left[\frac{1}{2}\psi(\vec{r}) + \psi_\mathrm{f}(\vec{r})\right] + \frac{1}{2}\int \mathrm{d}^3r\, e_0 n_\mathrm{f}(\vec{r})\psi_\mathrm{f}(\vec{r}) \\
&= \mathcal{F}_\mathrm{PB-E} + \mathcal{F}_\mathrm{se-rod}
\end{aligned}
\tag{3.99}
$$

and using $n(\vec{r})\psi_\mathrm{f}(\vec{r}) = n_\mathrm{f}(\vec{r})\psi(\vec{r})$ before introducing $\mathcal{F}_\mathrm{PB-E}$ from (3.95a) and identifying the second term as $\mathcal{F}_\mathrm{se-rod}$, which in turn can be derived by taking the surface charges for $n_\mathrm{f}(\vec{r})$ and the potential $\psi_\mathrm{f}(\vec{r})$ from (3.98a) to

$$
\begin{aligned}
\mathcal{F}_\mathrm{se-rod} &:= \frac{1}{2}\int \mathrm{d}^3r\, e_0 n_\mathrm{f}(\vec{r})\psi_\mathrm{f}(\vec{r}) \\
&= \frac{1}{2}\int_0^{L_\mathrm{cyl}} \mathrm{d}z \int_0^{2\pi} \mathrm{d}\varphi \int_{r_0}^{R_\mathrm{cyl}} r\,\mathrm{d}r\, e_0 \left[\frac{\lambda}{2\pi r_0}\,\delta\left(|\vec{r}| - r_0\right)\right] \left[-\frac{2k_\mathrm{B}T}{e_0}\xi_\mathrm{M} \ln\left(\frac{r}{R_\mathrm{cyl}}\right)\right] \\
&= -\frac{1}{2}\lambda\xi_\mathrm{M}k_\mathrm{B}TR_\mathrm{E} \ln\left(\frac{r_0}{R_\mathrm{cyl}}\right) \\
&= \frac{1}{2}k_\mathrm{B}T\ell_\mathrm{B}\frac{(fN_\mathrm{m})^2}{R_\mathrm{E}} \ln\left(\frac{R_\mathrm{cyl}}{r_0}\right)
\end{aligned}
\tag{3.100}
$$

again replacing $\lambda = fN_\mathrm{m}/R_\mathrm{E}$ and $\xi_\mathrm{M} = \ell_\mathrm{B}\, fN_\mathrm{m}/R_\mathrm{E}$ in the last step.

This result is a very nice confirmation for how we previously modeled the self-energy of a rod-like polyelectrolyte, because up to the logarithmic correction (3.100) corresponds both to the pressure component Π_{ℓ_B} we found in our simulation as difference $\mathring{\Delta}\mathcal{P}_\mathrm{gel}$ between charged and uncharged hydrogels at the same volume V_eq, as well as to the potential

$$
U_{\ell_\mathrm{B}}(r) = \frac{1}{2}k_\mathrm{B}T\ell_\mathrm{B}\frac{(fN_\mathrm{m})^2}{r} \tag{3.65}
$$

we based our theoretical investigation from section 3.2.8 upon. Comparing figures 3.17 and 3.18, where both $\mathcal{F}_\mathrm{se-rod}$ and U_{ℓ_B} are plotted, shows how the logarithmic correction depends on the choice of the model parameters r_0 and R_cyl, becoming negligible for large enough chain extensions.

Sticking more closely to the smeared out depiction of the network strands in our "cell under tension"-model, other descriptions for the self-energy of the monomers are available as well, *e.g.* that of a prolate ellipsoid with one large semiaxis a_1 and two identical small semiaxes a_2, and $x = a_1/a_2 \geq 1$ abbreviating the aspect ratio. If the ellipsoid is charged with a homogeneous charge density equaling the fN_m charges it should represent, then the electrostatic self-energy is given by [176, 177]

$$
U^{\ominus}_{\ell_\mathrm{B}} = \frac{3}{5}\frac{(fN_\mathrm{m})^2}{4\pi\epsilon_0\epsilon_\mathrm{S}a_1}\frac{\operatorname{arccosh} x}{\sqrt{1-x^{-2}}} \tag{3.101}
$$

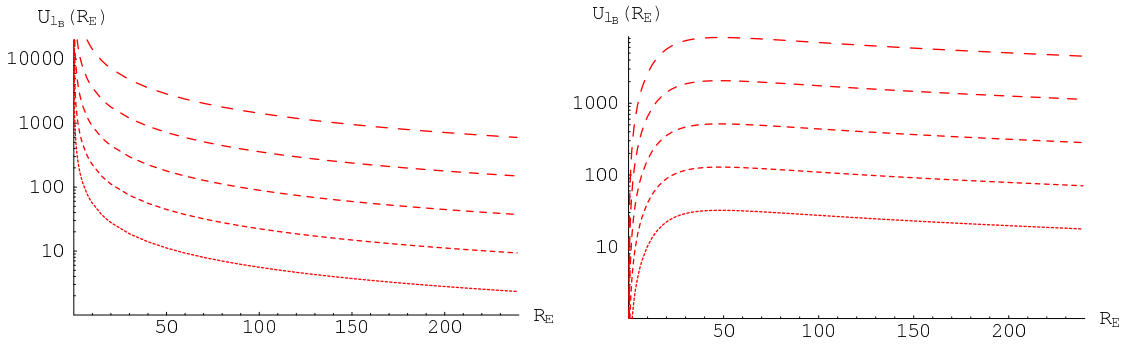

Figure 3.17.: Comparison of different electrostatic potentials, namely the U_{ℓ_B} from (3.65) on the *left* and $U^{\ominus}_{\ell_B}$ from (3.102) on the *right*, as function of the node-node separation R_E for a chain with $N_m = 239$; similar to *e.g.* figure 4.8, thinner dashing refers to smaller charge fraction $f \in \{0.0625, 0.125, 0.25, 0.5, 1.0\}$, while both plots are only displayed for $\ell_B = 5\sigma$ as a different ℓ_B would only rescale the y-axis.

Its volume $(4\pi/3)a_1a_2^2$ then has to be matched to the polymer cylinder from our model setup in figure 3.15, setting the semiaxes to

$$\begin{aligned} \frac{4\pi}{3}a_1a_2^2 &\stackrel{!}{=} \pi r_0^2 \cdot L_{\text{cyl}} \\ a_1 &\stackrel{!}{=} L_{\text{cyl}} = R_E \\ \Rightarrow \quad a_2 &= \frac{\sqrt{3}}{2}r_0 \end{aligned}$$

which, using $\epsilon_0\epsilon_S = e_0^2/(4\pi k_B T \ell_B)$ from the definition of the Bjerrum length ℓ_B, gives

$$U^{\ominus}_{\ell_B} = k_B T \frac{3}{5}\ell_B \frac{(fN_m)^2}{e_0^2 R_E} \frac{\operatorname{arccosh}\left(\frac{2}{\sqrt{3}}\frac{R_E}{r_0}\right)}{\sqrt{1-\left(\frac{2}{\sqrt{3}}\frac{R_E}{r_0}\right)^{-2}}} \tag{3.102}$$

as electrostatic self-energy of an ellipsoidal monomer distribution of matching volume in place of our cell cylinder.

Figure 3.17 shows how U_{ℓ_B} and $U^{\ominus}_{\ell_B}$ differ in their short-range behaviour for small R_E: While U_{ℓ_B} diverges, as one would expect when considering a charged polymer chain which is confined to smaller and smaller space, the elliptic potential exhibits a maximum after which it goes to zero. While U_{ℓ_B} is much larger for $R_E \leftarrow 0$, it quickly becomes smaller than *UlbNew* from the latter's maximum onwards, since with increasing R_E the polyelectrolyte assumes an increasingly linear shape which the coulombic potential considers but the elliptic one does not. As could already be inferred from their respective definitions (3.65) and (3.102), in both cases the charge fraction f enters quadratically (shown in figure 3.17 through more widely dashed

lines for larger f), the Bjerrum length ℓ_B linearly (which is why only the plots for $\ell_B = 5\sigma$ are given).

Varying Cell Radii

The definition (3.80d) for the inner cell radius r_0 is not necessarily undisputed, as we employed the tension blob model to estimate the impact of the chain extension R_E on the cylinder size, which will introduce small errors on the order of unity due to neglected prefactors[7]. Therefore, we want to investigate how the choice of the inner cell radius (which in turn also influences the outer one, see (3.80c) for the definition of R_{cyl}) influences the free energy components in $\mathcal{F}_{PB-tot}$.

Besides the obvious alternative of $\check{r}_0 = 1.0\sigma$, which simply allows the counterions to approach every monomer on the inner "rod" up to the excluded volume while neglecting the lateral extension of an eventually coiled polymer[8], we also compare an attempt of an improvement on the blob picture: Returning to (3.76), where the derivation of r_0 originated, we replace the elastic force f_E acting on each blob not by the theoretically obtained f_{FESAW} but rather by

$$\mathsf{f}_{FE/fit} = \frac{k_B T}{b}\left(3\left(\frac{R_E}{R_{max}}\right)^{\frac{\nu}{1-\nu}} \cdot \left(1 - \left(\frac{R_E}{R_{max}}\right)^{\beta}\right)^{-\gamma}\right) \tag{4.17}$$

with $\beta = 3.7$ and $\gamma = 2$ as exponents, shown in section 4.2.3 to fit the force-extension-relation measured in our computer simulations; this leads to another alternative set of cell parameters, *i.e.*

$$\tilde{l}_g = \frac{k_B T R_{max}}{\mathsf{f}_{FE/fit} \cdot R_E} \qquad \text{and} \qquad \tilde{r}_0 \sim 1\sigma + \frac{R_F}{R_{max}^{\nu}}\left(\tilde{l}_g\left(1 - \frac{R_E}{R_{max}}\right)\right)^{\nu} \tag{3.103}$$

which should pose a slightly better representation of our "cell under tension"-idea.

The *left* plot in figure 3.18 illustrates these three choices by plotting them as a function of the chain extension R_E. With $\check{r}_0$ and $\check{R}_{cyl} \propto R_E$ as their limits for large R_E, the other two definitions for inner and outer cell radius do not differ much from each other even for smaller chains, where their similar shapes both diverge while $\check{r}_0$ and $\check{R}_{cyl}$ approach the excluded volume limit 1.0σ. This also implies that unless the swelling equilibrium occurs at rather shortly extending strands[9], the different

[7] An example is the Flory radius $R_F \sim bN_m^{\nu}$ for which the alternative expression $R_F \sim v_{ex}^{1/5} b^{2/5} N_m^{3/5}$ may give the same numbers $b_1 = v_{ex}^{1/5} b_2^{2/5}$, depending on the system under consideration. Extensive computer simulations of single neutral chains found $b_1 \approx 1.1$ for parameters similar to the ones we employed, although in general scaling predictions might also neglect prefactors as large as ± 9 to be "on the order of unity".

[8] This pictures the polyelectrolyte to essentially shrink along its end-to-end vector.

[9] Since both (3.77) and (3.103) used the blob picture to estimate the lateral chain extension, the equilibrium must occur for $R_E \gg R_F$ anyway to not conflict with the assumptions employed therein; looking at our simulation data, where $R_E/R_F \gtrsim 3.5$ for all parameter sets, we certainly expect our theory to fulfill that requirement.

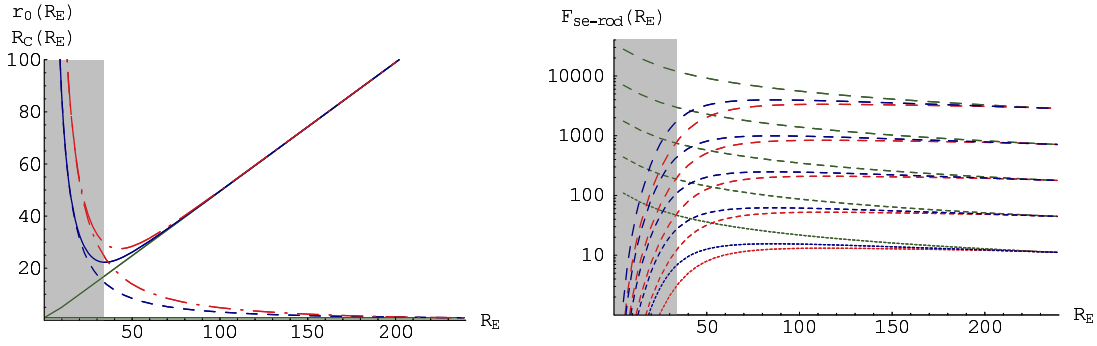

Figure 3.18.: *Left:* Comparison of different definitions for the cell radii from (3.80), *i.e.* the usual r_0 and R_{cyl}, printed in *Navy blue*, the similar $\tilde{r}_0$ and $\tilde{R}_{\mathrm{cyl}}$ in *Venetian red*, and $\check{r}_0 = 1.0\sigma$ as *olive lines*. *Right:* Their impact on the electrostatic self-energy $\mathcal{F}_{\mathrm{se-rod}}$ of the inner cylinder in the cell model, again only shown for $\ell_{\mathrm{B}} = 5\sigma$ as different ℓ_{B} merely rescale the y-axis; here, *Navy blue* lines refer to the usage of r_0 in the definition of $\mathcal{F}_{\mathrm{se-rod}}$, while *Venetian red* indicates employment of $\tilde{r}_0$, and *olive lines* of $\check{r}_0$ there. The shaded box indicates the regimes $R_{\mathrm{E}} < R_{\mathrm{F}}$ where the chain is shorter than the Flory radius, *i.e.* the blob picture no longer applies.

modeling of the cell parameters seems to be of secondary importance.

That assessment changes when evaluating its impact on the respective free energy components $\mathcal{F}_{\mathrm{PB-tot}}$ is composed of, choosing $\ell_{\mathrm{B}} = 5\sigma$ as exemplary parameter value to accompany the charge fractions $f \in \{0.0625, 0.125, 0.25, 0.5, 1.0\}$: The self-energy $\mathcal{F}_{\mathrm{se-rod}}$ of the rod, shown in the *right* plot of figure 3.18, *e.g.* exhibits an entirely different physical behaviour when using r_0 or $\tilde{r}_0$ in place of $\check{r}_0 = 1.0\sigma$, as the latter follows a simple $1/R_{\mathrm{E}}$-dependency, indicating that the system always tries to maximize the intra-charge distance on the rod by maximizing its total length, while the former also allow a collapsing chain to minimize the self-energy since for $R_{\mathrm{E}} \to 0$ the inner radius diverges, so does the cylinder's surface on which the constant fN_{m} charges are smeared out, enabling the likewise charged monomers to maximize their respective distance, too. For r_0 and $\tilde{r}_0$ the system therefore phase separates, favoring very large or very small conformations, whereas for $\check{r}_0$ only ever increasing extensions are preferred.

The energetic part $\mathcal{F}_{\mathrm{PB-E}}$ of the Poisson-Boltzmann free energy $\mathcal{F}_{\mathrm{PB}}$, as plotted on the *left* of figure 3.19, behaves very similar, except that the short-range extremum is shifted towards smaller R_{E} and the potential values are about five times larger; the slope of the $\check{r}_0$-limit is now also more strongly curved for smaller f, whereas in the previous case the curvature was seemingly constant for all charge fractions. Note however, that $\mathcal{F}_{\mathrm{PB-E}}$ has the opposite sign of the self-energy because it is dominated by the (attractive) interaction between ions and chain monomers, which is more pronounced than the repulsion between mostly gas-like counterions also contained therein. As a consequence, the energetic part of $\mathcal{F}_{\mathrm{PB}}$ favors *smaller* systems,

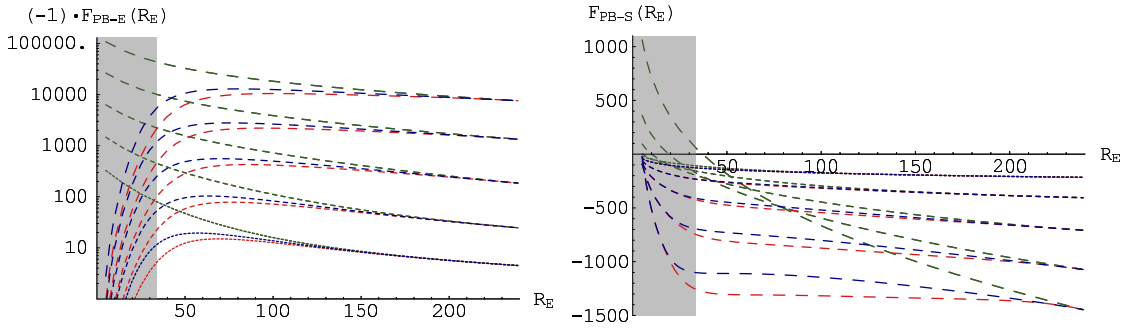

Figure 3.19.: Impact of the different definitions r_0 (*Navy blue*), $\tilde{r}_0$ (*Venetian red*), and $\check{r}_0$ (*olive lines*) for the cell radii on the components of $\mathcal{F}_{\mathrm{PB}}$, *i.e.* $(-1)\cdot\mathcal{F}_{\mathrm{PB-E}}$ (*left*) and $\mathcal{F}_{\mathrm{PB-S}}$ (*right*); line style, colours and shaded region as in figure 3.18.

indicating total collapse when using $\check{r}_0$, and even exhibiting a distinct minimum for r_0 and $\tilde{r}_0$ such that a stable state would be found if nothing but $\mathcal{F}_{\mathrm{PB-E}}$ was to decide. This is understandable because in the second case the suddenly increasing surface over which the monomers are smeared out for $R_{\mathrm{E}} \to 0$ also decreases the monomer-ion interaction, as compared to the case of $\check{r}_0$ where smaller R_{E} leads to much higher charge concentrations on the center cylinder resulting in *stronger* interactions; the counterions have the same decreasing volume available in both cases, making their repulsion eventually the dominant contribution under blob-like boundary conditions. Thus, the minimum in $\mathcal{F}_{\mathrm{PB-E}}$ essentially reflects the combination of surface monomer charge density $fN_{\mathrm{m}}/(2\pi r_0 R_{\mathrm{E}})$, as indicated by the behaviour of r_0 and $\tilde{r}_0$ in the *left plot* of figure 3.18, and counterion density $n(r = r_0)$, as in figure 3.16, there.

Even more dramatic appear the changes for the entropic component $\mathcal{F}_{\mathrm{PB-S}}$ (on the *right* in figure 3.19), where functions for r_0 and $\tilde{r}_0$ only coincide for very small or very large R_{E}, with their area of deviation (*i.e.* the range of R_{E} where and the amount by which their energy values differ) vanishing for small f. Although the *right* plot in figure 3.19 reveals no physical difference between the definitions this time, with all functions monotonically decreasing for increasing R_{E}, *i.e.* all counterions trying to maximize their occupied volume to gain entropy, the *olive lines* based on $\check{r}_0 = 1.0\sigma$ are still introducing a different weight into the free energy balance we are aiming at due to their much steeper descent; consequently, entropic effects will play a more pronounced role in systems using $\check{r}_0$ instead of r_0 or $\tilde{r}_0$, at least for higher charge fractions, as for smaller f all three definitions already coincide for R_{E} larger than a f-dependent, increasing threshold.

So, the proper choice of the inner cell radius obviously plays a rather significant role for the free energy equilibrium, with both kinds of definitions, *i.e.* blob picture leading to r_0 or $\tilde{r}_0$, and excluded volume approach resulting in $\check{r}_0 = 1.0\sigma$, being justifiable from a physical point of view. This is why we want to continue comparing

both choices in the following; we are, however, going to neglect $\tilde{r}_0$ as its difference to the results based on r_0 are not of a qualitative nature.

Elasticity and Energy Equilibrium

Knowing $\mathcal{F}_{\mathrm{PB}}$ is only one part of the bargain, as it merely includes the electrostatic and entropic contributions of the counterions to the system; even after adding with $\mathcal{F}_{\mathrm{se-rod}}$ the electrostatic self-energy of the rod, $\mathcal{F}_{\mathrm{PB-tot}}$ only describes the free energy of the intrinsic cylindrical cell model. For a proper connection to our network model, the elastic response of the chains to the swelling process must be included, too. This was already calculated earlier

$$U_{\mathrm{FESAW}}(r) = -k_{\mathrm{B}}T \left(\frac{R_{\max}}{R_{\mathrm{F}}}\right)^{\frac{1}{1-\nu}} \ln\left[1 - \left(\frac{r}{R_{\max}}\right)^{\frac{1}{1-\nu}}\right] \tag{3.30}$$

$$U_{\mathrm{FE/fit}}(r) = \int \mathrm{d}r\, \mathsf{f}_{\mathrm{FE/fit}}(r) = \int \mathrm{d}r\, \frac{k_{\mathrm{B}}T}{b} \left(3\left(\frac{R_{\mathrm{E}}}{R_{\max}}\right)^{\frac{\nu}{1-\nu}} \cdot \left(1 - \left(\frac{R_{\mathrm{E}}}{R_{\max}}\right)^{\beta}\right)^{-\gamma}\right) \tag{3.104}$$

such that the total free energy $\mathcal{F}_{\mathrm{tot}}$ of the hydrogels is given by

$$\mathcal{F}_{\mathrm{tot}} = \begin{cases} \mathcal{F}_{\mathrm{PB-tot}} + U_{\mathrm{FESAW}} = \mathcal{F}_{\mathrm{PB}} + \mathcal{F}_{\mathrm{se-rod}} + U_{\mathrm{FESAW}} \\ \mathcal{F}_{\mathrm{PB-tot}} + U_{\mathrm{FE/fit}} = \mathcal{F}_{\mathrm{PB}} + \mathcal{F}_{\mathrm{se-rod}} + U_{\mathrm{FE/fit}} \end{cases} \tag{3.105}$$

depending on the preferred choice of bond model, *i.e.* $\mathsf{f}_{\mathrm{FESAW}}$ from (3.31) or $\mathsf{f}_{\mathrm{FE/fit}}$ from (4.17) with its parameters $\beta = 3.7$ and $\gamma = 2$ fit to our simulation data in figure 4.11.

The difference between these two elasticity models becomes apparent when looking at the plots of figure 3.20: For smaller and intermediate chain extensions R_{E} both potentials coincide, as by construction they should correspond to the harmonic or Gaussian limit there. Their divergence, however, is different, with the potential of the finite extensible self-avoiding walk allowing longer chains which would already get a rather severe energetic penalty from the fitted force relation (compare their energy values *e.g.* with the numbers in figures 3.18 and 3.19), *i.e.* representing a stiffer polymer than U_{FESAW}. Keeping figure 4.11 in mind where $U_{\mathrm{FE/fit}}$ was successfully matched against our simulation data, and recalling that U_{FESAW} was not only constructed to correspond to the FENE-potential, used in the simulations to model chemical bonds, but also provided the improved scaling prediction (3.34) which matched our weakly charged data in figure 3.5 rather well, their difference may play an important role now because the elastic energy will be the main component counteracting the general trend from the counterions' entropic and the rod's energetic desire for as large as possible system sizes. Consequently, it will have a significant impact on the overall equilibrium how "soon" (in terms of increasing

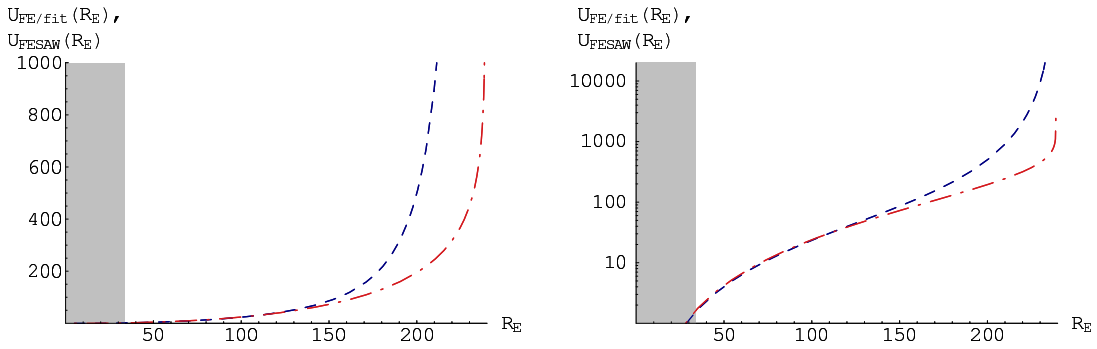

Figure 3.20.: Comparison of different definitions for the elastic energy, *i.e.* the $U_{\text{FE/fit}}$ from (3.104), printed in *Navy blue*, and U_{FESAW} from (3.30) in *Venetian red*; to visualize the magnitude of both potentials' divergence towards $R_{\max} = bN_{\text{m}} = 239\sigma$, the same graph is given on a linear (*left*) and logarithmic scale (*right*), albeit with a different range. The shaded box indicates the regimes $R_{\text{E}} < R_{\text{F}}$ where the chain is shorter than the Flory radius, *i.e.* the blob picture no longer applies.

R_{E}) the elasticity will be large compared to $\mathcal{F}_{\text{PB-tot}}$. Note in this context that both U_{FESAW} and $U_{\text{FE/fit}}$ only depend on R_{E} and particularly *not* on f or ℓ_{B} as the other contributions do; the aforementioned question therefore translates to investigating when $\mathcal{F}_{\text{PB-tot}}$ itself will be large enough to swell against the elastic energy.

Following these trends for the separate contributions to the total free energy $\mathcal{F}_{\text{tot}}$ of the "cell under tension" as a function of the chain extension R_{E} and the coulombic parameters f and ℓ_{B} leads to plots as in figure 3.21. There, $\mathcal{F}_{\text{PB-tot}}$ is detailed through the electrostatic $\mathcal{F}_{\text{PB-E}}$ (long dashed *orange* lines) and the entropic $\mathcal{F}_{\text{PB-S}}$ (short dashed *sandy brown* lines) part of the counterions, plus the self-energy $\mathcal{F}_{\text{se-rod}}$ (straight *brown* lines) of the smeared out monomeric charges on the rod, with the added elasticity entering through $U_{\text{FE/fit}}$ (dashed *blue* lines) or U_{FESAW} (dot-dashed *red* lines), respectively. Clearly, entropy and self-energy are the mechanisms trying to phase separate (*left column*, using r_0) or maximize (*right column*, using $\check{r}_0 = 1.0\sigma$) the system size against the combined efforts of elasticity and electrostatic energy, where it is the respective parameter set deciding on which terms are dominating. The emerging balance is then characterized by a minimum in the total free energy $\mathcal{F}_{\text{tot}}$, drawn as thick *blue* or *red* lines, depending on which of the elastic potentials $U_{\text{FE/fit}}$ or U_{FESAW} was used in (3.105).

First thing to notice when looking at the plots is the lack of such a minimum for systems with many counterions ($f = 1.0$) when using $\check{r}_0 = 1.0\sigma$ as inner boundary conditions (*upper* graphs in the *right column* of figure 3.21). There, the energetic contribution $\mathcal{F}_{\text{PB-E}}$ is so strong that its desire to collapse the network does not only overcome the electrostatic self-energy $\mathcal{F}_{\text{se-rod}}$ but the entropy of the counterions as well. Between $\ell_{\text{B}} = 5\sigma$ (*uppermost* plot) and $\ell_{\text{B}} = 1\sigma$, however, the pronounced decrease in the absolute values of all coulombic contributions already sets the trend

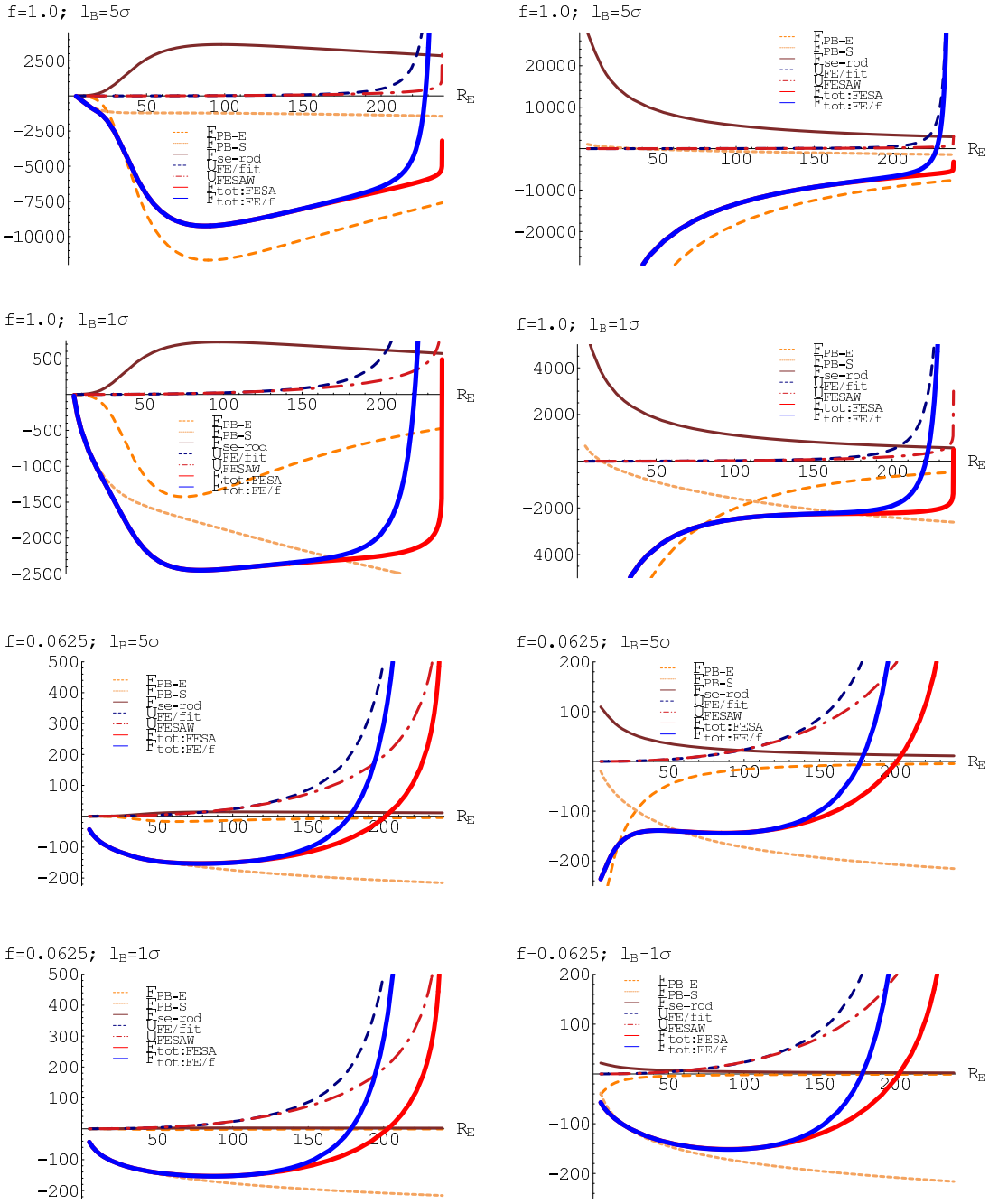

Figure 3.21.: $\mathcal{F}_{\rm tot}$ and its components, *i.e.* $\mathcal{F}_{\rm PB-E}$ (long dashed *orange* lines), $\mathcal{F}_{\rm PB-S}$ (short dashed *sandy brown* lines), and $\mathcal{F}_{\rm se-rod}$ (straight *brown* lines), balancing the elastic energies $U_{\rm FE/fit}$ (dashed *blue* lines; total sum: straight, thick *blue* lines) and $U_{\rm FESAW}$ (dot-dashed *red* lines; total sum: straight, thick *red* lines) based on the cell radius r_0 from (3.80d) for the *left column*, and on $\check{r}_0 = 1.0\sigma$ for the plots in the *right column*; shown are (from *top* to *bottom*) the charge parameters $\{f, \ell_{\rm B}\} = \{\frac{1}{1}, 5\sigma\}$, $\{\frac{1}{1}, 1\sigma\}$, $\{\frac{1}{16}, 5\sigma\}$, $\{\frac{1}{16}, 1\sigma\}$.

for further diminishing of the electrostatics' significance as the entropy term starts to become noticeable by slowing down the descent of $\mathcal{F}_{\mathrm{tot}}$ for smaller R_{E} considerably. This trend continues when fewer counterions are around ($f = 0.0625$, *lower* plots in the *right column*), and eventually entropy wins by introducing a minimum into the total free energy of the system. As a results, employment of purely cylindric boundary conditions (*i.e.* allowing the counterions to get as close to the monomers as excluded volume permits, but also accepting the charge density of the inner rod to become unrealisticly high for small R_{E}) with $\check{r}_0 = 1.0\sigma$ fails to find the swelling equilibrium once electrostatics becomes dominant, essentially rendering itself useless because for weak coulombic coupling we already showed much simpler approaches such as the pressure balance against an ideal gas to work sufficiently well.

The other case of a blob-like depiction for the inner cell cylinder (*left column* in figure 3.21) always exhibits a minimum in the total free energy $\mathcal{F}_{\mathrm{tot}}$, even for strong coulombic coupling where it is due to the short range trend of both electrostatic contributions $\mathcal{F}_{\mathrm{PB-E}}$ and $\mathcal{F}_{\mathrm{se-rod}}$ going to zero for $R_{\mathrm{E}} \to 0$ and $f = 1.0$ (instead of diverging to $\pm\infty$ as for $\check{r}_0 = 1.0\sigma$). The self-energy (3.100) thereby scales linearly with ℓ_{B}, *i.e.* decreasing by a factor of 5 between the *upper* two plots representing $f = 1.0$ and $\ell_{\mathrm{B}} = 5\sigma$ resp. $\ell_{\mathrm{B}} = 1\sigma$, but remains always absolutely smaller than the energetic part of $\mathcal{F}_{\mathrm{PB}}$ even for the former case of strong repulsion between the close, neighbouring, and likewise charged beads[10] on the polymer-cylinder. In the same regime, the much stronger counterion condensation causing their proximity to the oppositely charged monomers also has $\mathcal{F}_{\mathrm{PB-E}}$ to clearly dominate the energy balance while decreasing their entropic contribution as well, with ions confined to a small volume around the central chain clearly having less entropy than those few remaining free and mobile in the outer cell. That is also why the (absolute) drop in $\mathcal{F}_{\mathrm{PB-E}}$ between $\ell_{\mathrm{B}} = 5\sigma$ and $\ell_{\mathrm{B}} = 1\sigma$ is much more than the factor 5 seen in the self-energy, since most of the condensed counterions return into an unbound state, causing $\mathcal{F}_{\mathrm{PB-S}}$ to almost double its magnitude along the way towards weaker electrostatics. Consequently, it is the minimum in $\mathcal{F}_{\mathrm{PB-E}}$ *alone* which determines the swelling equilibrium in the limit of strong coulombic coupling, before the monotonic decrease in the (absolute) values of $\mathcal{F}_{\mathrm{PB-E}}$ and $\mathcal{F}_{\mathrm{se-rod}}$ allows the entropic term, growing for less condensation and shrinking for smaller charge fractions (*i.e.* less counterions), to influence the position of the minimum in $\mathcal{F}_{\mathrm{tot}}$. For vanishing electrostatics, both *lower* plots in the *left column* of figure 3.21 finally reflect the expected balance between an (almost) ideal gas-like "cloud" of counterions and the elastic response of the network, which we had already independently confirmed earlier. These graphs do not only visualize how negligible $\mathcal{F}_{\mathrm{PB-E}}$ and $\mathcal{F}_{\mathrm{se-rod}}$ really are with respect to $\mathcal{F}_{\mathrm{PB-S}}$ and U_{FESAW} or $U_{\mathrm{FE/fit}}$, even for the strong $\ell_{\mathrm{B}} = 5\sigma$ (as long

[10] In reality it is *effectively* screened, which is purposefully not included in $\mathcal{F}_{\mathrm{se-rod}}$ since we are interested in the *bare* effects here; the summed $\mathcal{F}_{\mathrm{PB-tot}}$ then contains with the superposition all effective adjustments as well.

as with $f = 0.0625$ only few charges are around) where the entropy of the mobile ions is nevertheless only barely affected, but they also demonstrate once more the physical difference in the choice of boundary conditions when comparing them to the corresponding plots in the *right column*.

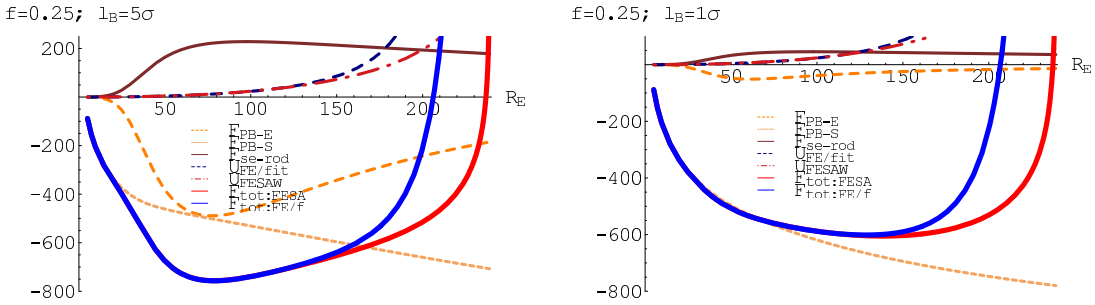

Figure 3.22.: $\mathcal{F}_{\text{tot}}$ and its components, drawn as in *left column*, of figure 3.21, *i.e.* based on the cell radius r_0 from (3.80d); shown are (from *left* to *right*) the charge parameters $\{f, \ell_{\text{B}}\} = \{\frac{1}{4}, 5\sigma\}$, $\{\frac{1}{4}, 1\sigma\}$.

Although for both strong and weak electrostatics the minimum in the total free energy seemed to be occurring around the same chain extension R_{E}, the trends we outlined for the individual contributions to $\mathcal{F}_{\text{tot}}$ would not necessarily indicate this to hold for all other parameter sets as well. Therefore, we are looking at an additional intermediate combination of $f = 0.25$ and $\ell_{\text{B}} = 5\sigma$ or $\ell_{\text{B}} = 1\sigma$ plotted on the *left* and *right* of figure 3.22, respectively. The former case of stronger electrostatics appears similar to the $f = 1.0$, $\ell_{\text{B}} = 1\sigma$ discussed previously, with the energetic $\mathcal{F}_{\text{PB-E}}$ determining the minimum which is slightly shifted by an always (absolutely) larger entropic $\mathcal{F}_{\text{PB-S}}$; since the magnitude of all contributions (except the elastic ones) is lower, $\mathcal{F}_{\text{tot}}$ is still platykurtic, albeit its width became smaller, the minimum more pronounced. The latter case of weaker electrostatics resembles $f = 0.0625$, $\ell_{\text{B}} = 5\sigma$ from the previous figure, with the exception of $\mathcal{F}_{\text{PB-E}}$ now being small but non-negligible enough to support the larger entropic contribution in balancing the elasticity at a much larger value of R_{E}. It is only now that the difference in the modeling of the elastic response begins to play a role, as U_{FESAW} produces a later divergence of $\mathcal{F}_{\text{tot}}$ than $U_{\text{FE/fit}}$; all previous plots had stayed within the regime where both representations coincided. Consequently, while for $\ell_{\text{B}} = 5\sigma$ the minimum in the total free energy remains at small chain extensions, for $\ell_{\text{B}} = 1\sigma$ it obviously depends on the interplay between entropy and elasticity (for small charge fractions) resp. electrostatic energy (for large f), moving the equilibrium value of R_{E} through a maximum at intermediate coulombic coupling.

Swelling Behaviour

The equilibrium swelling behaviour of the network strands' end-to-end distance R_E follows from minimizing the total free energy $\mathcal{F}_\mathrm{tot}$ in figure 3.21 which is again only possible to achieve numerically because of the $\psi(r)$ and $n(r)$ required for $\mathcal{F}_\mathrm{PB}$ coming from the solution of the Poisson-Boltzmann equation. While we already discussed the general trends to be expected for R_E as the underlying charge parameters f and ℓ_B are varied, the previous subsection focused on *how* the final balance emerged in terms of the respective contributions to the free energy for some exemplary parameters. Here, we now want to present the final outcome once all the intermediate steps are complete, relating the results to previous predictions and our simulation data.

Figure 3.23 therefore picks up the representation of figure 3.5, where the relative chain extension $R_\mathrm{E}/R_\mathrm{max}$ had been plotted as a function of the charge fraction f, using the Bjerrum length ℓ_B as parameter; added to that graph had been lines indicating the maximum extension $R_\mathrm{max} = bN_\mathrm{m}$ to which the chain diverges non-harmonically before bonds break, the simple scaling prediction $R_\mathrm{E} = f^{1-\nu}N_\mathrm{m}b$ from (3.6) valid for not too strong coulombic coupling and counterion condensation, and the modified scaling prediction

$$R_\mathrm{E} = bN_\mathrm{m}\left(\frac{f}{f+\frac{\alpha}{1-\nu}}\right)^{1-\nu} \tag{3.34}$$

we already applied earlier in section 3.2.6. Colour coded as usual, *i.e.* *blue*, *green*, and *red* corresponding to a Bjerrum length of $\ell_\mathrm{B} = 1\sigma$, 2σ, and 5σ, respectively, figure 3.23 compares the results of minimizing the total free energy $\mathcal{F}_\mathrm{tot}$ derived via (3.105) for the various parameter sets, given as *lines* obtained from interpolating the discrete data, to the simulation results from chapter 4, given as *points* as before.

After the investigation of the previous subsection into the interplay of the individual components in $\mathcal{F}_\mathrm{tot}$ revealed that the formation of the total free energy lacks a (local) minimum for strong electrostatics when the inner cell radius is set to $\check{r}_0 = 1.0\sigma$, we will focus on the results from the "cell under tension"-model alone, where for all parameter sets the swelling equilibrium could be found. Using U_FESAW as representation of the chain elasticity, we will omit the other bond potential because we have seen that they both coincide over almost the entire expected range of equilibrium chain extensions. Within this framework, the numerical solutions of the minimization of $\mathcal{F}_\mathrm{tot}$ are presented for a chain length of $N_\mathrm{m} = 239$, a Flory radius (2.46) of $R_\mathrm{F} = v_\mathrm{ex}^{1/5}b^{2/5}N_\mathrm{m}^{3/5}$ with bond length $b = 1.0\sigma$ and excluded volume v_ex derived via (2.37) from the Lennard-Jones parameters (4.2) used in our simulation.

For the case of weak electrostatics, *i.e.* $\ell_\mathrm{B} = 1\sigma$ and $f < 1.0$, or $\ell_\mathrm{B} = 2\sigma$ and $f < 0.5$, figure 3.23 shows that the interpolated minima of $\mathcal{F}_\mathrm{tot}$ now follow the modified scaling prediction (3.34) quite well. Actually, this is not too surprising since in those regimes our detailed analysis of the individual components showed

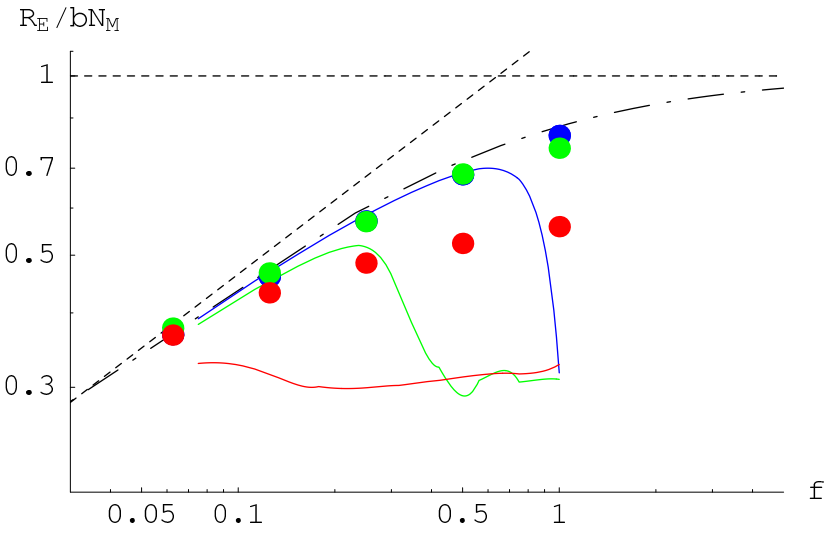

Figure 3.23.: The relative chain extension $R_\mathrm{E}/R_\mathrm{max}$ as a function of the charge fraction f for varying coulombic coupling $\ell_\mathrm{B} \in \{1\sigma, 2\sigma, 5\sigma\}$ and a polymer length $N_\mathrm{m} = 239$, obtained from minimizing $\mathcal{F}_\mathrm{tot}$ with r_0 as inner boundary condition and U_FESAW modeling the chain elasticity. The *dark lines* correspond to the limits and scaling predictions from figure 3.5, the *blue*, *green*, and *red lines* and *points* to the aforementioned Bjerrum lengths, respectively, where the *lines* interpolate the results of the free energy minimization (that interpolation is also responsible for the seemingly oscillatory overshoot for $\ell_\mathrm{B} = 2\sigma$), while the *points* indicate the equilibrium swelling data from our computer simulations.

only the entropy and elasticity to be of major importance, while electrostatics could either be neglected or only played a minor role – as (3.34) is based on the assumed balance between ideal gas-like and elastic pressure, both being the derivatives of the terms $\mathcal{F}_\mathrm{PB-S}$ and U_FESAW we employed here, a good agreement was to be expected and merely re-confirms the negligibility of coulombic interactions in those regimes.

Complying with our simulation data, stronger electrostatics now shift the equilibrium towards shorter chain extensions, because the repulsive increase in $\mathcal{F}_\mathrm{se-rod} \propto f^2\ell_\mathrm{B}$ and the entropy loss mobile ions experience is overcompensated by the energy gain of oppositely charged monomers and counterions getting closer, for which smaller system sizes are more favorable. As was observed before, the strongly charged hydrogels with $\ell_\mathrm{B} = 5\sigma$ even exhibit approximately constant node-node separations, because of the dominating $\mathcal{F}_\mathrm{PB-E}$ enforcing its minimum onto $\mathcal{F}_\mathrm{tot}$ and allowing only slight shifts due to $\mathcal{F}_\mathrm{PB-S}$, whose balance with the elasticity for small f occurs at the same $R_\mathrm{E}/R_\mathrm{max}$.

The magnitude, however, deviates dramatically from the experimental expectations, with data for $\ell_\mathrm{B} = 5\sigma$ appearing constant, for $\ell_\mathrm{B} \leq 2\sigma$ and larger charge fractions even suddenly dropping from following the modified scaling prediction onto the plateau the $\ell_\mathrm{B} = 5\sigma$-values form, as if a collapse-like crossover would be present,

from the "neutral" behaviour following (3.34) towards the "charged" plateau prepared by the data for very strong electrostatics, occurring in between $f = 0.25$ and $f = 0.5$ for $\ell_B = 2\sigma$, and for $0.5 \leq f \leq 1.0$ in case of $\ell_B = 1\sigma$. This transition mirrors the maximum in the chain extension R_E described while discussing figure 3.22 in the previous subsection, where the entropy increasing with f shifted the balance with the (constant, f-/ℓ_B-independent) elasticity towards longer node-node separations, until the onset of counterion condensation caused $\mathcal{F}_{PB-S}$ to start shrinking, while the electrostatic interaction between ions and chain monomers became the dominant term in $\mathcal{F}_{tot}$, implementing its own minimum as the global one – which is also why the system size after the transition is complete coincides for all ℓ_B, because the *location* of that minimum depends mainly on $r_0 = r_0(R_E)$ instead of other parameters (which in exchange decide on its magnitude).

Recalling the results of the previous subsection, particularly the *left column* of figure 3.21 where it was shown that the minimum of the total free energy $\mathcal{F}_{tot}$ for strong coulombic coupling mainly depends on the shape of the balance between the electrostatic term $\mathcal{F}_{PB-E}$ and the self-energy $\mathcal{F}_{se-rod}$ of the polyelectrolyte chain, it is there where possible improvements have to be applied. As it seems in figure 3.23, the effect of strong coulombic coupling is either overestimated or not sufficiently compensated by other contributions, such that the implications of counterion condensation (dominating that regime) need to be revised. Although the employment of the Poisson-Boltzmann theory for deriving the counterion density distribution $n(r)$ was intended to circumvent this, its original design for infinitely long stiff rods requires more complex modifications, which will be done in the following.

Penetrating the Central Cylinder

The electrostatic self-energy $\mathcal{F}_{se-rod}$ of the polyelectrolyte was derived from a cylinder with the charged monomers being smeared out over its surface, with the choice of r_0, $\tilde{r}_0$, or $\check{r}_0$ deciding whether it depicts a thin rod of diameter $2\check{r}_0$ with ever increasing line charge density for $R_E \to 0$, or whether it models a disk-like object whose surface charges maximize their respective distance in the same limit. Considering the polymer chain where all charges are at most at fixed separations b/f along the backbone, but possibly closer due to a coiled contour for $R_E \ll R_{max}$, the electrostatic repulsion has to always diverge for vanishing node-node separations; according to figure 3.18 this is only the case for an energy like (3.100) if its inner radius remains constant. On the other hand, because of the desired modeling of an increased eigenvolume a polymer occupies for decreasing chain extensions, also distributing the fN_m fixed charges more realisticly in space, the blob-like r_0 or $\tilde{r}_0$ are better suited as a framework for the terms in $\mathcal{F}_{PB}$, at the same time ensuring the total free energy to have a minimum over the entire parameter range.

Which of the boundary conditions $\check{r}_0$, r_0, or $\tilde{r}_0$ is therefore an appropriate choice for defining the central cylinder's boundaries? Is the assumed charge distribution of

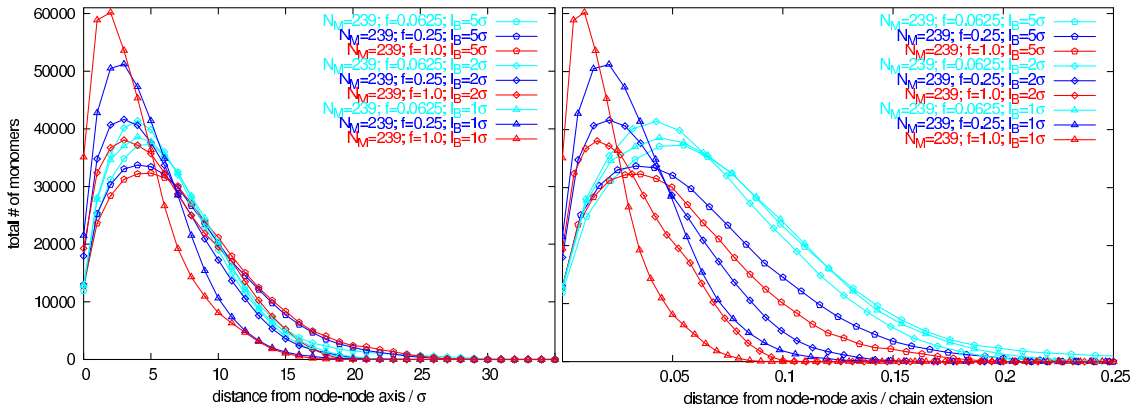

Figure 3.24.: The lateral extension of a network chain perpendicular to its node-node-axis $\vec{R}_{\mathrm{E}}$, averaged over all strands and equilibrium conformations of the corresponding parameter set. Given as a distribution of the individual distances the chain monomers have from $\vec{R}_{\mathrm{E}}$, the *left plot* compares the absolute values for selected parameters, while the *right* one rescales the spatial axis by the length of $\vec{R}_{\mathrm{E}}$ to assert relative effects (colours and symbols as in table S.1).

the monomers sitting on its surface a realistic description? This can be easily checked by looking at the simulation data, analyzing the lateral extension of a given network chain perpendicular to its node-node-axis $\vec{R}_{\mathrm{E}}$. Figure 3.24 displays the result as distribution of the individual distances each monomer has from $\vec{R}_{\mathrm{E}}$, averaged over all chains and equilibrium conformations. As it turns out, the co-ions do indeed exhibit a distinct maximum at a certain distance, although it depends on the given parameters, ranging between 2σ and 5σ instead of a constant $\check{r}_0 = 1\sigma$; in addition, its width is much broader than the δ-peak assumption implied by the depiction of an impenetrable central cylinder onto whose surface the monomers were assumed to be smeared out. All in all, it resembles more the projection of a 3D-Gaussian-like distribution around an axis $\vec{R}_{\mathrm{E}}$.

Looking at the individual graphs in detail (for better visibility not all parameters have been plotted), electrostatics seems to mainly determine the lateral extension of the chains, as for few ions (*i.e.* a small charge fraction f) the relative width of the distance distribution is widest and also independent of ℓ_{B}, while for larger f the Bjerrum length decides if the maximum peak is pronounced and close to the axis (small ℓ_{B}) or if it is wide and further away (large ℓ_{B}) towards the almost neutral cases with $f = 0.0625$. In absolute numbers, the peak position for $\ell_{\mathrm{B}} = 5\sigma$ corresponds to that for $f = 0.0625$ because of the very strong counterion condensation effectively neutralizing the chain locally; the tail of the distribution nevertheless extends further as there the intra-chain charge repulsion becomes effective. For decreasing ℓ_{B} this effect is reduced as now the counterions are no longer "bound" to the chain but rather accumulate close-by, such that their remaining osmotic pressure swells the system

and therefore stretches the chains, which in turn decreases their lateral extension. The onset of condensation is thereby visible when for $\ell_B = 1\sigma$ more counterions cause a higher peak (larger f means larger Π_C), whereas for $\ell_B \geq 2\sigma$ the tide turns (larger f means larger ξ_M means smaller f_{eff} means smaller Π_C^{eff}).

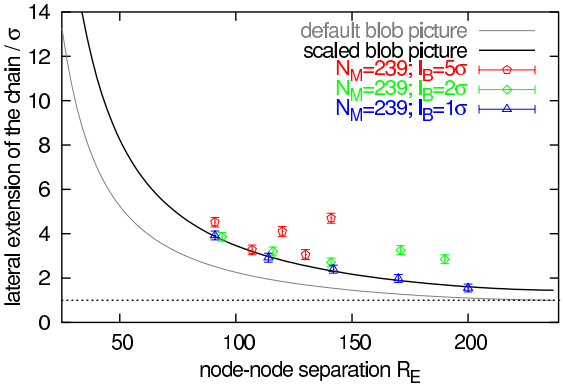

Figure 3.25.: Peak position of the lateral extension distribution in figure 3.24 as a function of the node-node separation R_E, plotting the simulation data for $\ell_B \in \{1\sigma, 2\sigma, 5\sigma\}$ as *blue*, *green*, and *red symbols*, respectively. Also given are the size estimates for the central cylinder's radius r_0, *i.e.* using (3.79) without (*gray line*) and with (*black line*) numerical prefactor, and the constant $r_0 = \check{r}_0 = 1\sigma$ (*dotted line*).

How is that reflected by our model? For starters, the peak position, corresponding to the central cylinder's size r_0, is obviously not constant but has to follow a length-dependent estimate such as *e.g.* (3.79). To assess its usefulness, from figure 3.24 we determined the respective value for all parameters, plotting the result in figure 3.25, and comparing it with the prediction of (3.79). Without condensation effects in the system, all data actually obeys our estimate qualitatively (*gray line*, (3.79) unchanged) as well as quantitatively (*black line*, also accounting for the numerical prefactor in the blob measure $\xi_\perp$ of section 3.3.1) rather nicely; we only see deviations for $f \geq 0.5$, $\ell_B = 2\sigma$ and $f \geq 0.25$, $\ell_B = 5\sigma$, *i.e.* for $\xi_M \geq 1$ where condensing counterions obstruct the lateral extension of the chains.

Thus, in general we find (3.79) to be a good description for the inner radius r_0 of the central cylinder – although figure 3.24 also shows that the assumption of the monomers to be smeared out only on its surface (*i.e.* behaving similar to a δ-distribution of charges) is not very accurate. Combined with the fact that the counterions are actually space-filling, it seems worth investigating how our results are affected if we allow the ions to penetrate the central cylinder of the cell model, while also attempting to use different distributions for the monomers there.

No analytical solutions are known for these kind of modifications because they both render most of the strategy for solving the Poisson-Boltzmann equation over the entire range of coulombic coupling rather useless. It is however possible, albeit computationally expensive, to construct a solution numerically. The basic idea is given in Technical Point 1.5 of [157], which we used to write a C-module for Mathematica; its findings were included into our previous calculation scheme, replacing (3.42), (3.44), and (3.43) with a new $n(r)$, $n(R_{cyl}) = n(r = R_{cyl})$, and $y(r) = \ln(n(r)/n(R_{cyl}))$, plus substituting the fixed charge quantities $n_f(r)$ and $y_f(r)$ with their new counterparts.

Figure 3.26 illustrates the resulting changes to the counterion density $n(r)$ and

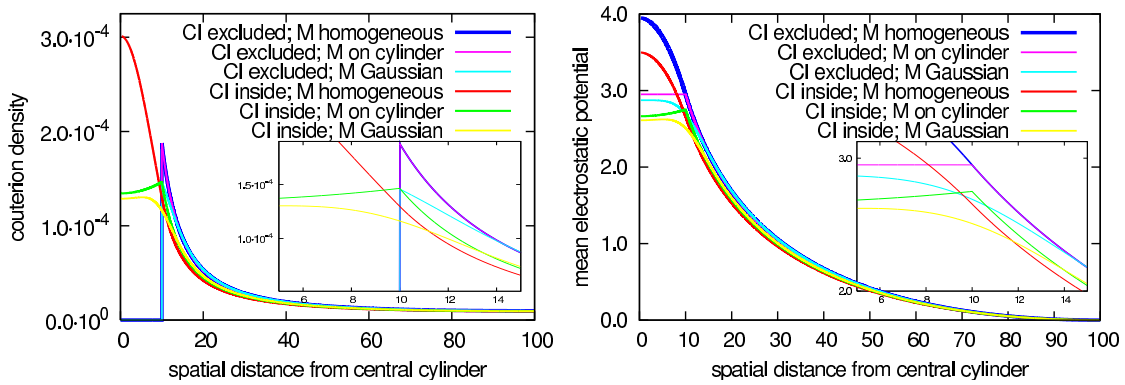

Figure 3.26.: Counterion density $n(r)$ (*left*) and resulting mean electrostatic potential (*right*) in the cylindrical cell model as determined by the Poisson-Boltzmann equation (3.45) for oppositely charged monomers smeared out over the central cylinder's surface (*magenta* and *green* lines), being homogeneously distributed within (*blue* and *red* lines), or following a Gaussian distribution with mean $\mu_{\text{Gauss}} = r_0$ and width $\sigma_{\text{Gauss}} = 3.0\sigma$ (*cyan* and *yellow* lines); the counterions are excluded from that inner volume (*blue*, *magenta*, and *cyan* lines) resp. are allowed to enter the central cylinder as well (*red*, *green*, and *yellow* lines). To magnify the differences between the four combinations, here the parameters $r_0 = 10\sigma$, $R_{\text{cyl}} = 100\sigma$, $N_{\text{CI}} = 10^4$ were used in addition to $\ell_{\text{B}} = 2\sigma$ and $\xi_{\text{M}} = 1$ for the coulombic coupling. The insets zoom in on the regime around $r = r_0$ where the differences between the different definitions are largest.

their electrostatic potential $y(r)$ if one allows the ions to penetrate the central cylinder and also modifies the monomers' charge distribution there. First to notice are the vanishing deviations for $r \to R_{\text{cyl}}$ in all cases although we purposefully chose the overexaggerated parameters $r_0 = 10\sigma$, $R_{\text{cyl}} = 100\sigma$, $N_{\text{CI}} = 10^4$ to magnify any aberrations. This is a very important observation, because the osmotic pressure $\Pi_{\text{C}}^{\text{PB}}$ responsible for swelling the polyelectrolyte network in the cell model is given by $\Pi_{\text{C}}^{\text{PB}} = k_{\text{B}}T \cdot n(R_{\text{cyl}})$ according to (3.40), *i.e.* solely depends on the counterion density at the outer cell boundary. However, as figure 3.26 shows, that value $n(R_{\text{cyl}})$ coincides despite the significant (physical!) differences between an impenetrable and a porous cylinder, or a homogeneous vs. a δ-distribution. For the parameter regime of weak electrostatics (which we were already able to predict quantitatively in figure 3.23 anyway), where the swelling equilibrium is mainly determined by the balance between osmotic pressure and elastic restoring force, no change is consequently expected, independent of the chosen combination of r_0 and $n_{\text{f}}(r)$.

This expectation changes if the regime of stronger coulombic coupling is considered, because there the minimum in the total free energy $\mathcal{F}_{\text{tot}}$ is mainly given by the slope of the electrostatic contributions $\mathcal{F}_{\text{PB-E}}$ and $\mathcal{F}_{\text{se-rod}}$ which both depend on the whole $n(r)$ resp. $n_{\text{f}}(r)$. Figure 3.26 shows how the former is affected if the counterions may enter the central cylinder: Then, $n(r)$ will describe a lower density, which

exhibits a maximum at $r = r_0$ and decreases for $r \to 0$ towards a non-zero $n(0)$ if the monomers remain on the cylinder's surface (*green line*), while for a homogeneous distribution $n(r \to 0)$ continues to increase below $r \leq r_0$ until it reaches a global maximum at $r = 0$ (*red line*). That there is no difference between both excluded cases (*blue* and *magenta line*) should not be surprising since the counterion density is essentially determined by Gauss' Law (3.97), *i.e.* by $Q_{\text{in}}/\epsilon_0 = \oint \vec{E} \cdot \mathrm{d}\vec{A}$ with the total charge Q_{in} enclosed by the considered volume segment, such that it does not matter how the monomers are distributed within if one only regards $r > r_0$.

In case of a Gaussian distribution $\mathcal{W}^{\mu_{\text{Gauss}}}_{\sigma_{\text{Gauss}}}(r)$ of the monomers around r_0 (using $\mu_{\text{Gauss}} = r_0$ and $\sigma_{\text{Gauss}} = 3.0\sigma$ as parameters for the mean and width, respectively) they also extend outside the central cylinder where $r > r_0$, such that their excluded case (*cyan line*) differs in the core's close vicinity from the other two corresponding cases. Allowed to enter the inner region, the counterion density $n(r)$ here (*yellow line*) shows a smooth crossover towards a global maximum at $r = 0$, thereby remaining smaller than the other two cases over the entire range $r \leq r_0$. Regarding the charge density $n_{\text{f}}(r)$ of the Gaussian-like distributed monomers, we can use $Q_{\text{Gauss}} := fN_{\text{m}} / \int_0^{R_{\text{cyl}}} \mathcal{W}^{\mu_{\text{Gauss}}}_{\sigma_{\text{Gauss}}}(r)\mathrm{d}r$ as charge prefactor in the normalization condition to ensure $\int_0^{R_{\text{cyl}}} 2\pi r\, L_{\text{cyl}}\, n_{\text{f}}(r)\, \mathrm{d}r \stackrel{!}{=} fN_{\text{m}}$ for $\mathcal{W}^{\mu_{\text{Gauss}}}_{\sigma_{\text{Gauss}}}(r)$ as well.

With the fixed charge density $n_{\text{f}}(r)$ of the monomers therefore becoming

$$n_{\text{f}}(r) = \begin{cases} \frac{fN_{\text{m}}}{2\pi r_0\, L_{\text{cyl}}} \delta\left(r - r_0\right) & \text{monomers on cylinder} \\ \begin{cases} \frac{fN_{\text{m}}}{\pi r_0^2\, L_{\text{cyl}}} & \text{if } r \leq r_0 \\ 0 & \text{if } r > r_0 \end{cases} & \text{monomers homogeneous} \\ \frac{1}{2\pi r\, L_{\text{cyl}}} \cdot Q_{\text{Gauss}} \cdot \mathcal{W}^{\mu_{\text{Gauss}}}_{\sigma_{\text{Gauss}}}(r) & \text{monomers Gaussian} \end{cases} \tag{3.106}$$

the corresponding potential $\psi_{\text{f}}(r)$ follows from integrating

$$E_r(r) = \begin{cases} \begin{cases} 0 & \text{if } r < r_0 \\ \frac{\lambda}{2\pi\epsilon_0 r} & \text{if } r \geq r_0 \end{cases} & \text{monomers on cylinder} \\ \begin{cases} \frac{\lambda}{2\pi\epsilon_0 r_0^2} r & \text{if } r < r_0 \\ \frac{\lambda}{2\pi\epsilon_0 r} & \text{if } r \geq r_0 \end{cases} & \text{monomers homogeneous} \\ 2\frac{k_{\text{B}}T}{e_0} \frac{\ell_{\text{B}}}{L_{\text{cyl}}} \frac{1}{r} \int_0^r 2\pi r'\, L_{\text{cyl}}\, n_{\text{f}}(r')\, \mathrm{d}r' & \text{monomers Gaussian} \end{cases} \tag{3.107}$$

as in (3.98a), such that $\psi_{\rm f}(r = R_{\rm cyl}) \stackrel{!}{=} 0$ and

$$\psi_{\rm f}(r) = \begin{cases} \begin{cases} -2\frac{k_{\rm B}T}{e_0}\xi_{\rm M} \ln\left(\frac{r_0}{R_{\rm cyl}}\right) & \text{if } r < r_0 \\ -2\frac{k_{\rm B}T}{e_0}\xi_{\rm M} \ln\left(\frac{r}{R_{\rm cyl}}\right) & \text{if } r \geq r_0 \end{cases} & \text{monomers on cylinder} \\ \begin{cases} -\frac{k_{\rm B}T}{e_0}\xi_{\rm M}\left[\frac{r^2}{r_0^2} - 1 + 2\ln\left(\frac{r_0}{R_{\rm cyl}}\right)\right] & \text{if } r < r_0 \\ -2\frac{k_{\rm B}T}{e_0}\xi_{\rm M} \ln\left(\frac{r}{R_{\rm cyl}}\right) & \text{if } r \geq r_0 \end{cases} & \text{monomers homogeneous} \\ -int_{R_{\rm cyl}}^{r} 2\frac{k_{\rm B}T}{e_0}\frac{\ell_{\rm B}}{L_{\rm cyl}}\frac{1}{r'}\left(\int_{R_{\rm cyl}}^{r'} 2\pi r'' \, L_{\rm cyl}\, n_{\rm f}(r'')\, {\rm d}r''\right) {\rm d}r' & \text{monomers Gaussian} \end{cases} \tag{3.108}$$

determine both potentials, $\psi_{\rm f}(r)$ and $y_{\rm f}(r) = \psi_{\rm f}(r) \cdot (e_0/k_{\rm B}T)$.

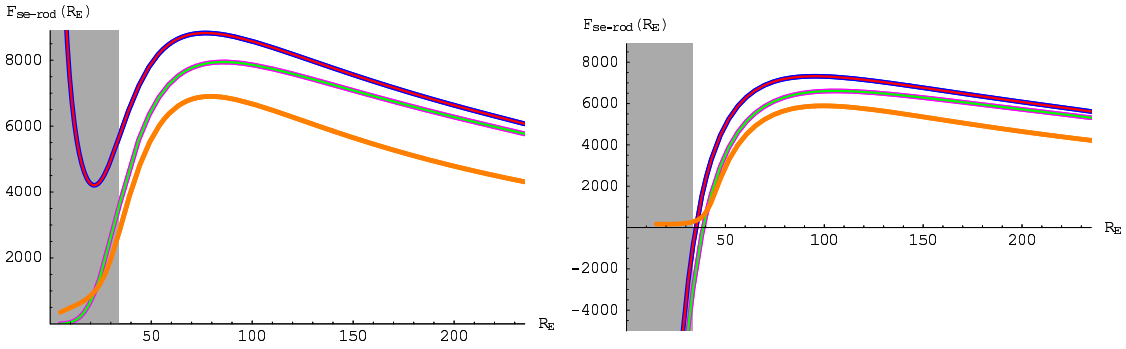

Figure 3.27.: Electrostatic self-energy $\mathcal{F}_{\rm se-rod}$ for a porous central cylinder and different monomer distributions. As on the *right* of figure 3.18, the shaded box indicates the regime $R_{\rm E} < R_{\rm F}$ where the chain is shorter than the Flory radius, *i.e.* the blob picture no longer applies; the colour coding follows figure 3.26 with *orange* representing both (coinciding) Gaussian cases. For the *left* plot, the outer radius $R_{\rm cyl}$ was given by (3.75), for the *right* one through (3.74) which reduced the cylindrical cell's volume there.

The electrostatic self-energy $\mathcal{F}_{\rm se-rod}$ of such a porous cylinder is then similar to (3.100) given through

$$\mathcal{F}_{\rm se-rod}(R_{\rm E}) = \begin{cases} -k_{\rm B}T\ell_{\rm B}\frac{(fN_{\rm m})^2}{R_{\rm E}} \ln\left(\frac{r_0}{R_{\rm cyl}}\right) & \text{monomers on cylinder} \\ +k_{\rm B}T\ell_{\rm B}\frac{(fN_{\rm m})^2}{R_{\rm E}}\left[\frac{1}{4} - \ln\left(\frac{r_0}{R_{\rm cyl}}\right)\right] & \text{monomers homogeneous} \\ \frac{1}{2}\int_0^{R_{\rm cyl}} 2\pi r \, L_{\rm cyl}\, e_0 \, [n_{\rm f}(r)\,\psi_{\rm f}(r)] \, {\rm d}r & \text{monomers Gaussian} \end{cases} \tag{3.109}$$

which is plotted in figure 3.27. There, compared to figure 3.18 the free energy also exhibits a minimum for small $R_{\rm E} < R_{\rm F}$ (*i.e.* outside of the range considered here) in case of the homogeneous charge distribution within the cylinder (*left plot*), whereas

the Gaussian-like monomers (now as *orange line*) mimic the homogeneous behaviour for $R_\mathrm{E} > R_\mathrm{F}$ shifted towards smaller absolute values. Since only the slope of these functions is of importance for the later minimization process in the total free energy, not much difference is therefore to be expected between the impact of $\mathcal{F}_\mathrm{se-rod}$ on $\mathcal{F}_\mathrm{tot}$ in these two cases, contrary to the δ-peak distribution (*green* and *magenta* lines) whose absolutely smaller slope indicates a minimum at shorter chain extensions. The independence of the counterion exclusion on all results is understandable because none of their properties explicitely enter into (3.109).

There is however an implicit influence they have if one remembers our original definition for the outer cell boundary R_cyl from (3.75) where we specifically took into account that the counterions cannot enter the central cylinder, compensating for the loss of free volume available to them. Now that the inner core has been made porous, such correction is no longer necessary, and we can return to the original definition (3.74) for R_cyl, effectively reducing the total cell size. While this does not affect $n_\mathrm{f}(r)$ or $\psi_\mathrm{f}(r)$, it changes observables such as $\mathcal{F}_\mathrm{se-rod}$ being integrated over the entire system space, as can be seen in the *right* plot of figure 3.27 where the absolute slope of the curves decreased significantly, pushing the self-energy towards even negative values for small R_E and non-Gaussian distributions. The more important relative behaviour between the three cases however remains similar: For large R_E homogeneous and Gaussian-like monomers contribute alike to the energy balance, while the absolute slope of the δ-peak distribution remains lower; for small chain extension this does no longer hold, as the *orange* curve flattens towards zero while the others continue towards $\mathcal{F}_\mathrm{se-rod}(R_\mathrm{E} \to 0) \to -\infty$.

While the changes in the charge distributions $n(r)$ and $n_\mathrm{f}(r)$ remain negligible for weak electrostatics because of the osmotic pressure $\Pi_\mathrm{C}^\mathrm{PB}$ of the counterions only depending on $n(r = R_\mathrm{cyl})$, which the *left* plot in figure 3.26 already showed to not be influenced by the monomers, they play a crucial part once the coulombic components $\mathcal{F}_\mathrm{PB-E}$ and $\mathcal{F}_\mathrm{se-rod}$ become dominant in the energy balance (3.105). Here, the different slopes directly enter the energy balance during the minimization of $\mathcal{F}_\mathrm{tot}$, and shift the equilibrium chain extension compared to figure 3.23 where the counterions were excluded from the central cylinder.

Using the uncompensated definition (3.74) for the outer cell boundary R_cyl, figure 3.28 presents the resulting swelling sizes of the polyelectrolyte network with monomers smeared out only on the central cylinder's surface (plot in the *upper left*), distributed evenly within (plot in the *upper right*), or placed Gaussian-like around r_0 (*lower* plot). We immediately see significant improvement over the previous minimization once the counterions are allowed to enter the monomer's regime $r < r_0$ as *e.g.* the relative chain extension $R_\mathrm{E}/R_\mathrm{max}$ no longer forms a plateau for $\ell_\mathrm{B} = 5\sigma$ but rather increases with f similarly to the simulation data. The predicted sizes are also much higher, whereby the Gaussian case comes closest to the end-to-end distance we measured in the numerical experiment. Unfortunately, it is still far from a match, with the prediction for $\ell_\mathrm{B} = 2\sigma$ being even *lower* than the

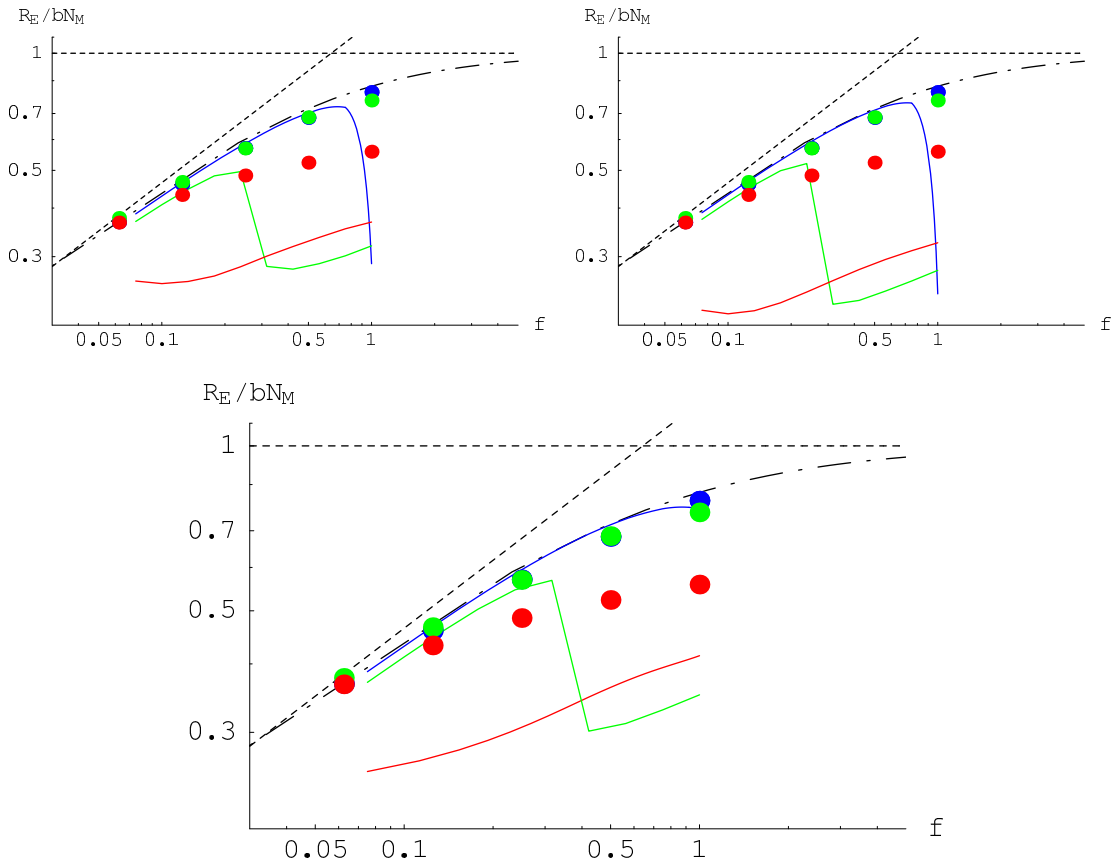

Figure 3.28.: The relative chain extension R_E/R_{max} as a function of the charge fraction f as in figure 3.23, but for counterions which are allowed to enter the central cylinder. Each plot depicts a different distribution of the network's monomers, assuming them to be on the cylinder's surface (*upper left*), homogeneously distributed within (*upper right*), or following a Gaussian distribution with mean $\mu_{Gauss} = r_0$ and width $\sigma_{Gauss} = 3.0\sigma$ (*lower* graph). As before, the *blue*, *green*, and *red* lines represent the results of minimizing $\mathcal{F}_{tot}$ from (3.105) for varying coulombic coupling $\ell_B \in \{1\sigma, 2\sigma, 5\sigma\}$, respectively, while the points give the equilibrium swelling data from our computer simulations in chapter 4.

$\ell_B = 5\sigma$-values. The sudden system collapse for higher electrostatics remains as well, although in the Gaussian case merely for the intermediate $\ell_B = 2\sigma$, while it vanishes for $\ell_B = 1\sigma$. This is encouraging because it shows that using $\mathcal{W}^{\mu_{Gauss}}_{\sigma_{Gauss}}(r)$ to model the monomer distribution around the network's backbones comes closest to the reference behaviour, such that at least qualitatively the data can be described in both regimes (of weak and of strong electrostatics).

From our analysis of the lateral chain extensions we know how the Gaussian profile should look like depending on the system parameters. As we have so far only adjusted $\mu_{Gauss} = r_0$ and kept $\sigma_{Gauss} = 3.0\sigma$ constant, this would consequently be the next logical step to consider: Figure 3.24 tells us that the width of the distribution

decreases for large amount of counterions but weak coulombic coupling, whereas for strong electrostatics it becomes wider than the (almost) neutral state of few free ions (*i.e.* $f = 0.0625$) which was independent of ℓ_B. Additionally, figure 3.25 shows that the profile's peak position deviates from $\mu_{Gauss} = r_0$ particularly for those parameters where the strong coulombic coupling leads to a final underestimate of the chain extension in figure 3.28. Hence, finding a suitably improved description for μ_{Gauss} and σ_{Gauss} beyond the initial choice employed here due to the time constraints, *e.g.* by applying the lateral blob description already used in the derivation of r_0 in (3.79), or by re-using the basic ideas behind the scaling arguments of the previous subsection 3.2, should therefore overcome the remaining issues at high electrostatics, allowing to use the "cell under tension"-model for the description of the swelling behaviour of polyelectrolyte networks over the entire parameter range.

3.4. Conclusions and Outlook

Combining both properties of single polyelectrolytes and polymer networks, charged hydrogels can benefit to a large extent from ideas and techniques developed for these systems over the last decades. In the beginning of this chapter, we therefore introduced the reader to the relevant results important for the line of argument later on, building upon the terminology and basic concepts used for theoretical models in polymer physics known from chapter 2.

These results were then related to a theoretical modeling of the swelling behaviour, starting at the simple scaling predictions based on the pressure balance between entropic degrees of freedom of the mobile counterions and the elastic response of the network chains. We quickly expanded on that picture, considering the polyelectrolyte and tension blob models as well as combining those approaches with the Poisson-Boltzmann theory within the framework of the cylindrical cell model. Arriving at a blob based scaling law, it was then possible to predict the relative chain extension of the charged hydrogels in equilibrium, matching the reference data from our computer simulations well within their error bars. Thereby identifying the leading contributions to the physics behind the macromolecular swelling, *i.e.* the osmotic pressure of uncondensed counterions, the electrostatic repulsion of the chain charges, and the elastic response of the network strands, we could even apply that scaling relation to the prediction of the $\mathcal{P}(V)$-behaviour in the vicinity of the equilibrium volume V_{eq}.

Next, we introduced the self-consistent "cell under tension"-model to avoid the undetermined numerical prefactors of order unity immanent in any scaling theory. It combined the cylindrical cell from the rod-like solution of the Poisson-Boltzmann equation with the constraint of a polyelectrolyte network, including all major components but the excluded volume effects of condensed counterions without any required input parameters but simple system setup ones. Deriving the total free energy of

such a construct and minimizing it afterwards allowed us to predict the node-node-separation of a charged hydrogel at swelling equilibrium. Although contrary to the previous scaling approach we achieved quantitative agreement with the data from the computer experiments only in the limit of not too strong electrostatics, based on the qualitative findings we could identify the necessary adjustments to the model which will allow it to be used over the entire parameter range as well. To this aim we developed means to solve the Poisson-Boltzmann equation in the cylindrical cell model for arbitrary distribution of fixed charges and non-excluded counterions, and studied the lateral extension of the network monomers around their node-node-axis, finding a Gaussian-type distribution with mean and width depending on the amount of counterions and the coulombic coupling.

Future directions would therefore start off at this point, fine-tuning the model on basis of the presented data by trying to find a suitable description for the radially non-uniform monomer distribution around the cell's inner cylinder, maybe even introducing the network topology by an additional z-dependency to reflect the higher charge accumulation at the nodes. More extensive rebuilds could include to replace the cylindrical symmetry with a more accurate double cone-shaped one, which would make the outer cell radius z-dependent, too, as well as to vary the strength of electrostatics the counterions experience when in the vicinity of the *outer* boundary, since in a diamond topology ions close to the cylinder's end faces are at the same time already approaching the next chain.

4. Polyelectrolyte Networks in θ-like and Good Solvent

The swelling equilibrium of a charged, diamond-like model network is investigated by means of MD computer simulations. Simple scaling laws are shown to hold for weak electrostatics, counterion condensation dominates for strong coulombic coupling; in between, the crosslinked chains are strongly stretched and enter the finite extensibility regime. An appropriate effective charge fraction allows to collapse all data onto a single master curve.

In this chapter, we will report on our findings regarding systems of hydrogels in good solvent and close to the θ-point. Section 4.1 will detail the simulation model employed, also discussing the setup, preparation, equilibration, and execution of the computer experiment. Afterwards, section 4.2 will expand on our initial work [62], which was the first to show the validity of simple scaling arguments in the limit of weak electrostatic interactions in a model hydrogel, and on our vastly extended study [63], investigating the detailed pressure components in the scaling treatment and their connection to the physical processes involved. From Molecular Dynamics (MD) simulations in the (N, p, T)-ensemble we obtain the equilibrium swelling properties of a charged defect-free network with much higher precision and for a wider range of system parameters than before, allowing a thorough examination of the different contributions entering the theoretical models. From there, we are also able to determine the validity of the Flory-Rehner-Hypothesis (FRH) by investigating the limits to that description [39–41], which will be done in section 4.3.

4.1. Model and Simulation Method

In our simulations, we employ a perfect and defect-free network of N_p polyelectrolyte chains connected at their ends to N_nodes tetra-functional cross-linking sites (nodes); this network topology is conserved at all times, *i.e.* neither formation nor breaking of bonds or crosslinks is allowed. Considering the multiple short and long-range interactions overlaying each other in a hydrogel, such a well-defined *model network* seems like a good starting point for an investigation, allowing to add more complex properties like entanglements, defects, or different preparation processes once the basic concepts have been understood. Particularly for a simulation study this is

additionally advantageous because here any effect can in principal be isolated and manually dis- or enabled; as figure I.3 already demonstrated, even in real life experiments synthesis procedures for simple model systems exist which exhibit similar(ly) well-defined properties.

The polymer chains are now modeled as bead spring chains of N_m Lennard-Jones (LJ) particles each with the FENE (Finite Extension Nonlinear Elastic) potential

$$U_\mathrm{FENE}(r) = \begin{cases} -\frac{1}{2} k_\mathrm{F} r_\mathrm{F}^2 \ln\left[1 - \left(\frac{r}{r_\mathrm{F}}\right)^2\right] & \text{for } r < r_\mathrm{F} \\ \infty \quad (\hat{=} \text{ broken bond}) & \text{for } r \geq r_\mathrm{F} \end{cases} \tag{4.1}$$

added for bonds and cross-links; the parameters are $k_\mathrm{F} = 10.0 \frac{k_\mathrm{B}T}{\sigma^2}$, $r_\mathrm{F} = 1.5\sigma$ [60], where σ is the monomer diameter (LJ unit). Note that, in contrast to the Gaussian chains from section 2.2, this potential (4.1) is not harmonic but diverges logarithmically for $r \to r_\mathrm{F}$ to mimic the finite extensibility of real chains (hence its name); therefore there are also differences to the divergences of the ideal freely jointed and worm-like chains in (2.33) and (2.35), respectively, because we do not restrict ourselves to these models. In section 3.2.6, however, a more general approach will generalize the ideas of section 2.2 to real chains with FENE-bonds, leading to the diverging restoring force $\mathbf{f}_\mathrm{FESAW}$ in (3.31).

The van der Waals interaction between chain beads is modeled by the standard LJ potential

$$U_\mathrm{LJ}(r) = \begin{cases} 4\,\epsilon_\mathrm{LJ}\left[\left(\frac{\sigma}{r}\right)^{12} - \left(\frac{\sigma}{r}\right)^{6} - c\right] & \text{for } r < r_\mathrm{cut} \\ 0 & \text{for } r \geq r_\mathrm{cut} \end{cases} \tag{4.2}$$

vanishing for distances $r \geq r_\mathrm{cut}$ (the potential cut-off); the constant

$$c = \left(\frac{\sigma}{r_\mathrm{cut}}\right)^{12} - \left(\frac{\sigma}{r_\mathrm{cut}}\right)^{6} \tag{4.3}$$

is chosen such that the potential value is zero and continuous in $r = r_\mathrm{cut}$. As introduced in section 2.4, such a short-range potential can be used to vary the excluded volume interaction not only between neighbouring beads but between all monomers, nodes, and counterions, allowing to seamlessly adjust their v_ex and consequently to mimic any solubility condition of the background environment, even without the need of adding explicit solvent molecules to the simulation. Here, good solvent is modeled by $r_\mathrm{cut} = 2^{1/6}\sigma$ and $\epsilon_\mathrm{LJ} = 1\,k_\mathrm{B}T$, leaving only the repulsive part of the interaction (4.2); this potential is also employed for the mutual bead-counterion and counterion-counterion excluded volume interaction. The θ-solvent is modeled by an attractive interaction between the beads, represented by the same LJ potential, now with a larger cut-off ($r_\mathrm{cut} = 2.5\sigma$) and $\epsilon_\mathrm{LJ} = 0.34\,k_\mathrm{B}T$ chosen to give θ-solvent properties [1].

[1] This value for ϵ_LJ was determined by U. Micka [178,179] for a slightly different bond potential

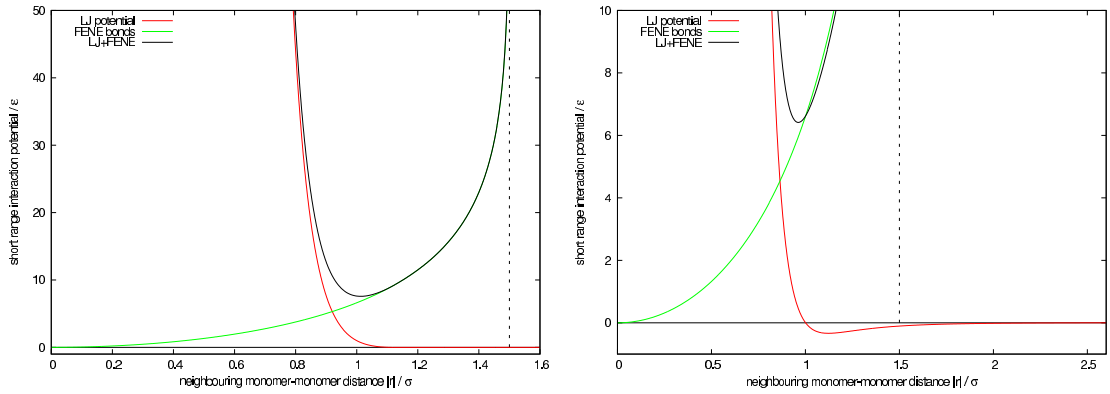

Figure 4.1.: The short-range interaction between neighbouring monomers consists of the excluded volume Lennard-Jones (4.2) and the attractive FENE (4.1) potential diverging for $r_F = 1.5\sigma$. While for the good solvent (*left*) the LJ is purely repulsive, cut off at its minimum $r_{cut} = 2^{1/6}\sigma$, the θ-solvent (*right*) also sees part of the attractive well up to r_{cut}, allowing next-nearest neighbour attraction, too.

All counterions, the N_{nodes} nodes, and a fraction f of the N_m monomers on each of the N_p chains bear $q_i = \pm 1$ unit charges e_0, interacting via the Coulomb energy $E_C(r_{ij}) = k_B T \ell_B q_i q_j / r_{ij}$ with other charged particles at distance r_{ij}, where the *Bjerrum length* $\ell_B = e_0^2/(4\pi\epsilon_0\epsilon_S k_B T)$ (e_0: unit charge, ϵ_0 and ϵ_S: permittivity of the vacuum and of the solvent, respectively) is defined as the distance at which two unit charges have an interaction energy of $k_B T$ (*e.g.* for water $\ell_B = 7.14$Å); consequently, ℓ_B is a convenient way to characterize the *strength* of the electrostatic interaction, while f represents a similar measure for the *amount* of charges in the system (since everything is monovalent anyway). In the simulation, the Coulomb interaction is calculated with the P^{3}M-algorithm [74,75], tuned to force accuracies well above the thermal noise level (see section 1.3.3).

The initial setup of the cubic simulation box with periodic boundary conditions has $N_p = 16$ polymer chains placed along the edges of a diamond lattice and connected at $N_{nodes} = 8$ tetra-functional nodes, a fraction of f monomers charged on each chain, and $N_{CI} = N_{nodes} + N_p \cdot f N_m$ counterions added to the system at random positions, ensuring overall electro-neutrality for the $N_{tot} = N_{nodes} + N_p \cdot N_m + N_{CI}$ particles (see figure 4.2).

Using ESPResSo for the computer simulation, preparing this setup on the steering level of the Tcl-script, as described in section 1.2.2, was rather easy once all necessary features were implemented in the simulation engine. So, having a script, *e.g.* `diamond.tcl`, which takes N_m, f, ℓ_B, and a solvent identifier as inputs, and adopting the syntax

with $k_F = 7\frac{k_B T}{\sigma^2}$, $r_F = 2\sigma$; within the accuracy of the determination of θ we do not expect any deviation.

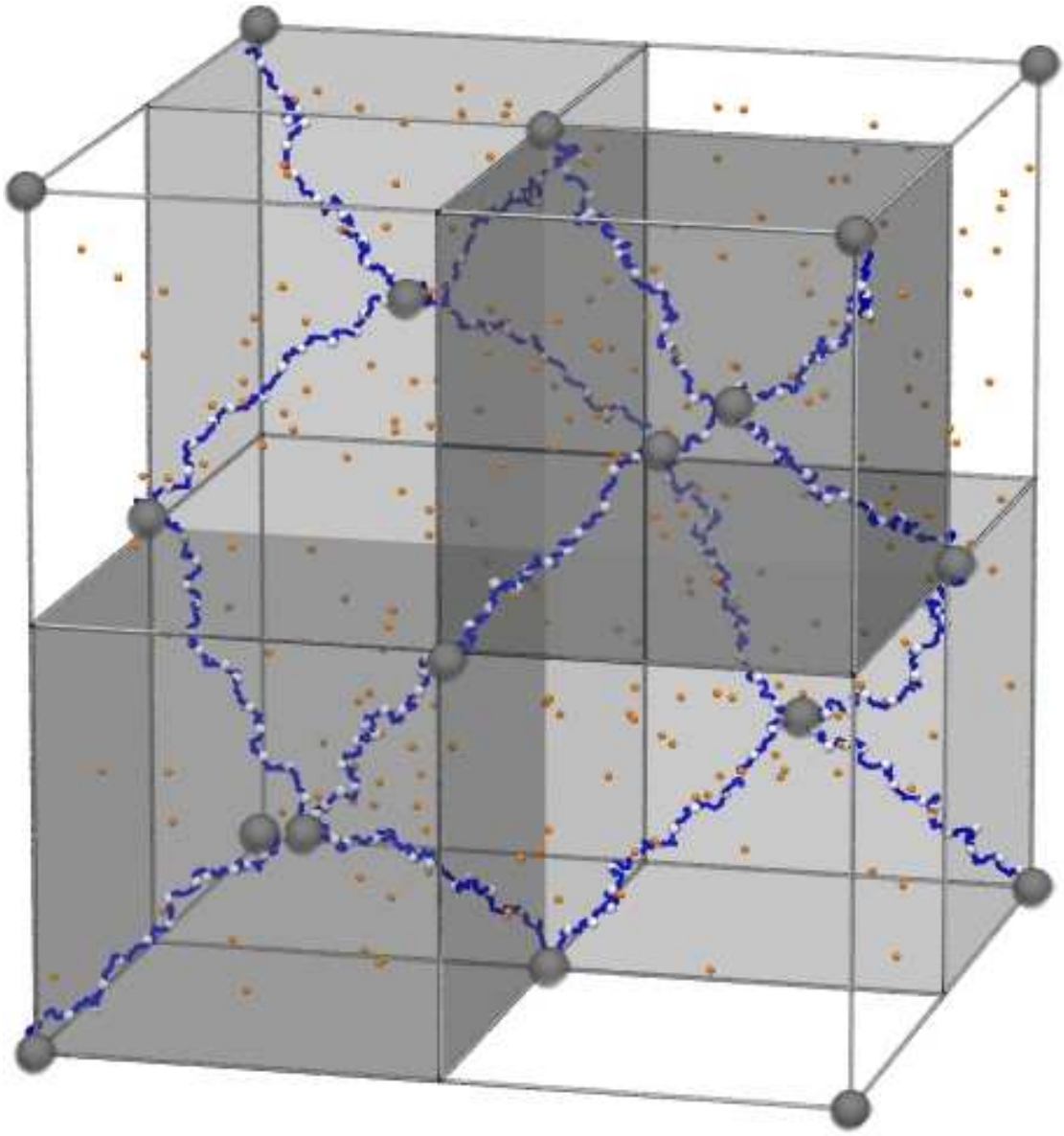

Figure 4.2.: Snapshot depicting the diamond lattice topology of the polyelectrolyte network. From the $N_{\mathrm{nodes}} = 8$ tetra-functional nodes and their periodic images (for illustration purposes both drawn as oversized gray spheres) $N_{\mathrm{p}} = 16$ polymer chains emerge, on each fN_{m} monomers charged (white spheres) and $(1-f)N_{\mathrm{m}}$ neutral (blue spheres). While the strands only occupy those four subboxes shaded in gray due to the periodicity (even though the nodes are *not* fixed to their lattice positions, merely placed there initially during setup), the N_{CI} counterions (orange spheres) move freely through the entire unit cell (other parameters: $N_{\mathrm{m}} = 239$, $f = 0.0625$, $\ell_{\mathrm{B}} = 1\sigma$; $N_{\mathrm{CI}} = 232$, $N_{\mathrm{tot}} = 4064$; initial box length $L = 545.3\sigma$; shown is the system in its thermodynamic equilibrium at $L = V_{\mathrm{eq}}^{1/3} = 211\sigma \pm 4\sigma$, see table 4.1).

```
<Espresso-binary> diamond.tcl <MPC> <charged> <bjerrum> { good | theta }
```

on the command line, the following lines of Tcl-code were used to create the simulation box in figure 4.2:

```
### Read in parameters from the command-line
# ('cM_dist' is the monomer distance between charged Monomers)
set MPC      [lindex $argv 0]
set charged  [lindex $argv 1]
set cM_dist  [expr $charged ? round(1./(1.*$charged)) : -1]
set bjerrum  [lindex $argv 2]
set q_solv   [lindex $argv 3]

### Set system parameters
# ('val_...' give the valency of nodes, charged Monomers, counterions)
set N_node   8
set N_P      16
set bond_l   1.0
set val_node [expr $charged ? +1. : 0.0]
set val_cM   [expr $charged ? +1. : 0.0]
set val_CI   [expr $charged ? -1. : 0.0]
set N_CI     [expr $charged ? round(($N_node*$val_node \
                + $N_P*int($charged*$MPC)*$val_cM) / (-1.0*$val_CI)) : 0]
set N_T      [expr $N_node + $N_P*$MPC + $N_CI]

### Set interaction parameters
if { $q_solv == "good" } {
    # Lennard Jones for a good solvent
    set lj1_eps   1.0
    set lj1_sig   1.0
    set lj1_cut   1.122462048309373
    set lj1_shift [expr -4.*$lj1_eps*(pow($lj1_cut,-12)-pow($lj1_cut,-6))]
} elseif { $q_solv == "theta" } {
    # Lennard Jones for a theta solvent
    set lj1_eps   0.34
    set lj1_sig   1.0
    set lj1_cut   2.5
    set lj1_shift [expr -4.*$lj1_eps*(pow($lj1_cut,-12)-pow($lj1_cut,-6))]
} else {
    puts "ERROR: Unknown solvent quality '$q_solv'!"; exit }
# repulsive Lennard Jones
    set lj2_eps   1.0
    set lj2_sig   1.0
    set lj2_cut   1.122462048309373
    set lj2_shift [expr -4.*$lj2_eps*(pow($lj2_cut,-12)-pow($lj2_cut,-6))]
```

```
# attractive FENE
    set bond      "FENE"
    set bond_k    10
    set bond_r    1.5
# accuracy to which electrostatics will be tuned to
    set accuracy  1.0e-02

### Particle & Interaction setup
# create simulation box
    set a_cube    [expr 4/sqrt(3.)*($MPC+1)*$bond_l]
    setmd box_l   $a_cube $a_cube $a_cube
# create interactions (except electrostatics)
    inter 0   $bond $bond_k  $bond_r
    inter 0 0 lennard-jones $lj1_eps $lj1_sig $lj1_cut $lj1_shift 0
    inter 0 1 lennard-jones $lj1_eps $lj1_sig $lj1_cut $lj1_shift 0
    inter 1 1 lennard-jones $lj1_eps $lj1_sig $lj1_cut $lj1_shift 0
    inter 0 2 lennard-jones $lj2_eps $lj2_sig $lj2_cut $lj2_shift 0
    inter 1 2 lennard-jones $lj2_eps $lj2_sig $lj2_cut $lj2_shift 0
    inter 2 2 lennard-jones $lj2_eps $lj2_sig $lj2_cut $lj2_shift 0
# create diamond network polymers of (initial) bond length $bond_l
# and with ($cM_dist-1) neutral monomers between charged ones
    diamond $a_cube $bond_l $MPC counterions $N_CI \
        charges $val_node $val_cM $val_CI distance $cM_dist
# activate electrostatics
    inter coulomb $bjerrum p3m tune accuracy $accuracy
```

As one might notice, only the last of the four paragraphs is actually setting up the system, the previous ones are merely processing the input and preparing variables in which the parameters are stored; hence, one could reduce that script down to five lines only (namely

```
setmd box_l 554.3 554.3 554.3
inter 0 FENE 10 1.5
for {set i 0} {$i<=2} {incr i} { for {set j 0} {$j<=2} {incr j} {
    inter $i $j lennard-jones 1.0 1.0 1.122462048309373 1.0 } }
diamond 554.3 1.0 239 counterions 3832 charges +1. +1. -1. distance 1.
inter coulomb 2 p3m tune accuracy 1.0e-02
```

for an assumed $N_\mathrm{m} = 239$, $f = 1.0$, $\ell_\mathrm{B} = 2\sigma$, and good solvent conditions), though it would also lessen the flexibility for *e.g.* changing system parameters.

Initially, the `diamond`-command creates the polymers directly along the edges of the diamond lattice, *i.e.* with $R_\mathrm{E} = bN_\mathrm{m} =: R_\mathrm{max}$ and a box length of $L = (4/\sqrt{3})(N_\mathrm{m}+1)b$. Though this allows for an initial bond length $b = 1.0\sigma$ very close to the equilibrium value $\langle b\rangle \approx 1.04\sigma$ (figure 4.1 shows that even such a small difference has quite an impact on the interaction potential), it is clear that such conformation is far from the desired thermodynamic equilibrium. In addition, the counterions were

created at random positions and may consequently find themselves in energetically unfavorable states, *e.g.* too close to another excluded volume or likewise charged object. Both are calling for an initial preparation of the simulation system by in a first step integrating the equations of motion without any electrostatic potentials, relaxing the excluded volume degrees of freedom, and in a second step equilibrating the Coulomb interactions.

Velocity-Verlet-Algorithm (VVA)

For computer simulations of coarse-grained systems on the bead-spring level one of the most successful algorithms is based on Newton's classical laws of motion [67]

$$\vec{\mathsf{f}}_i = \dot{\vec{p}}_i = m_i \dot{\vec{v}}_i \tag{4.4}$$

which connect forces $\vec{\mathsf{f}}_i = \vec{\mathsf{f}}_i(\{\vec{r}_i\}_i, \{\vec{p}_i\}_i)$ to the particle positions $\vec{r}_i$ and momenta $\vec{p}_i = m_i \vec{v}_i$ (with mass m_i to be scaled out in our case, since we assume all coarse-grained objects to have equal mass as previously discussed) for all $0 \leq i < N_{\text{tot}}$. This *Molecular Dynamics* (MD) approach is different from *Monte Carlo* (MC) algorithms which would derive the total energy of a given conformation, introducing trial changes to it, and accepting those with a certain probability (which depends on the Boltzmann factor $\exp(-\Delta E/k_{\text{B}}T)$) or if it lowered the energy (*i.e.* $\Delta E < 0$).

The velocity Verlet integration scheme now takes (4.4) and propagates a given set $(\{\vec{r}_i(t)\}_i, \vec{p}_i(t)\}_i)$ of initial positions and velocities along a discretized temporal coordinate t in equidistant timesteps Δt through

(VVA.1) $\vec{p}_i(t + \frac{\Delta t}{2}) = \vec{p}_i(t) + \frac{\Delta t}{2}\ \vec{\mathsf{f}}_i(t)$

(VVA.2) $\vec{r}_i(t + \Delta t) = \vec{r}_i(t) + \Delta t\ \vec{p}_i(t + \frac{\Delta t}{2})$

(VVA.3) Derive new forces $\vec{\mathsf{f}}_i(t + \Delta t)$ based on new positions $\vec{r}_i(t + \Delta t)$

(VVA.4) $\vec{p}_i(t + \Delta t) = \vec{p}_i(t + \frac{\Delta t}{2}) + \frac{\Delta t}{2}\ \vec{\mathsf{f}}_i(t + \Delta t)$

Although it is restricted to (N, V, E)- or (N, V, T)-ensemble of constant volume, constant energy resp. temperature, and fixed number of particles, its simplicity and speed made it a very good choice for calculations where classical equations of motion and velocity-independent forces are considered.

In terms of an efficient implementation it is possible to execute steps (VVA.1) and (VVA.2) successively within the same particle loop because both depend on the current particle i only, saving some (costly) read-/write-accesses to the main memory. Similarly, it is advantageous to actually use rescaled variables

$$\begin{aligned} \tilde{p} &:= \Delta t\ p \\ \tilde{\mathsf{f}} &:= \frac{(\Delta t)^2}{2}\ \mathsf{f} \end{aligned}$$

throughout the integration as it removes quite a number of N_{tot}-dependent mathematical operations from the algorithm.

Introducing friction and noise can be done with the *Langevin thermostat* which keeps a (N,V,T)-ensemble at a given temperature T through random "kicks" against the particles, which heat up the system, and friction Γ, which drains kinetic energy from it. The force derivation in the above algorithm is thereby replaced by

$$\text{(VVA.4)} \quad \vec{\mathsf{f}}_i \frac{\Delta t}{2} \quad \longmapsto \quad \vec{\mathsf{f}}_i \frac{\Delta t}{2} - \Gamma \frac{\vec{p}_i}{m_i} \frac{\Delta t}{2} + \sqrt{k_{\mathrm{B}} T \Gamma \Delta t}\, \vec{z}_i$$

with uncorrelated random numbers $\vec{z}_i = \sqrt{12}\,(u - 1/2)$ where u is uniformly distributed on the unit interval. Although this introduces a pseudo-dynamic to the given system, it also allows to reach the thermodynamic equilibrium considerably faster, depending on a reasonable choice for Γ. Since we are only interested in equilibrium properties anyway, the (potential) loss of dynamic information is less significant than the simulation speed-up.

Whenever we are referring to the (N,V,T)-ensemble in the following, it will therefore imply usage of a simulation system solved by MD and VVA with an added Langevin thermostat for the derivation.

Seeking Equilibrium in (N,V,T)

There are now several ways to determine the swelling equilibrium of a coarse-grained polyelectrolyte network with computer simulations. While by definition we are looking for the simulation box volume $V_{\mathrm{eq}} = L_{\mathrm{eq}}^3$ where the pressure vanishes, *i.e.* $P = 0$, we have to solve the question *how* this special volume can be found[2] In practice this is not a trivial question because in a MD simulation only (N,V,T)-ensemble are straight-forward to implement, whereas the obvious choice of a (N,p,T)-system requires some artifice (which shall be given in the next subsection).

A first approach would simply run a rather large number of individual (N,V,T)-simulations at a wide range of volumes V, obtaining the $P(V)$ *phase diagram* whose root(s) correspond(s) to the targeted $V = V_{\mathrm{eq}}$. However, in addition to the vast amount of computation time needed the grid points of the volume will most likely not be fine enough to have one of the simulations at the equilibrium volume; interpolation through all available data, extended to the observables as well, can overcome this problem, although the effort usually prevents larger scans in the parameter space. Due to the phase transitions and instabilities associated with the structural

[2] That it is $P = 0$ we are looking for originates in the periodicity we applied to the network; interpreted as "force per volume", a positive pressure then means that the system in its entirety wants to swell further, exerting an outward force on the simulation box, while a negative pressure points to overstretched network chains which are now mainly spanned by the periodic topology, but favoring a smaller volume. Consequently, a pressure $P = 0$ then refers to the state where none of the system components would prefer a change in the environment – equilibrium is reached.

changes, this method was nevertheless the only one suitable for the investigation of the charged hydrogels in poor solvent environments, presented in the next chapter 5.

Another attempt succeeds in employing *MC-induced volume changes*. Here, only one (N,V,T)-simulation is required during which random volume changes $V_j \mapsto V_{j+1}$ are attempted and accepted if they fulfill the Metropolis criterion, *i.e.* if either the difference in energy $\Delta E = P_{j+1}V_{j+1} - P_jV_j$ is negative or the Boltzmann factor $\exp(-\Delta E/k_\mathrm{B}T)$ is larger than an uncorrelated random number uniformly distributed on the unit interval. Though very promising at a first glance and quite successful, too, this ansatz has the methodic disadvantage that it has to rely on most accurate measurements of the pressure P which by themselves require sufficient timesteps to allow averaging over uncorrelated snapshots[3]. Additionally, the volume changes need to be rather large in the beginning to allow fast relaxation, without being too large as that would either tear the network bonds apart or push close objects into each others excluded volume, both leading to the eventual (unphysical) explosion of the system; for $V \approx V_\mathrm{eq}$, on the other hand, the adjustments to the volume should just be minimal because equilibrium is near, requiring a sufficiently adaptive volume adjustment procedure.

It is also possible to *estimate* the final volume V_eq from the ideal gas law statement that the energy PV is conserved for isothermal changes such as the adjustment of V if T remains constant due to the thermostat. Also requiring one (N,V,T)-simulation only, we measured an external pressure P_ext through an initial volume change from (P_α, V_α) to (P_β, V_β) as

$$(P_\alpha + P_\mathrm{ext}) \cdot V_\alpha = (P_\beta + P_\mathrm{ext}) \cdot V_\beta \quad \Rightarrow \quad P_\mathrm{ext} = \frac{P_\beta V_\beta - P_\alpha V_\alpha}{V_\alpha - V_\beta}$$

which allows to derive the targeted volume V_{j+1} (where $P_{j+1} = 0$ is assumed) from

$$(P_j + P_\mathrm{ext}) \cdot V_j = (0 + P_\mathrm{ext}) \cdot V_{j+1} \quad \Rightarrow \quad V_{j+1} = \frac{P_j + P_\mathrm{ext}}{P_\mathrm{ext}} \cdot V_j$$

While this once again requires most accurate determination of the pressures involved, with P_ext entering all subsequent calculations here even more critical than before, it is nevertheless the fastest (N,V,T)-based method to find V_eq. Some improvements are also possible, *e.g.* moving from V_j to V_{j+1} in several smaller steps, which prevents the aforementioned danger of ruptured bonds or exploding systems, and re-calculating P_ext along the volume iterations[4].

Another option, in a sense combining previous ideas, is conducting a *Golden Section Search* in $P(V)$ until a volume with $P(V) \approx 0$ is found, in whose vicinity several (N,V,T)-simulations with a very fine grid in V are conducted, allowing to

[3] For MC it is also possible to use the instantaneous pressure values, although that introduces unwanted box fluctuations which will be dealt with in the next subsection.

[4] The latter, however, turns out to amplify roundoff errors in V_j and V_{j+1} dramatically.

interpolate $P(V_{\mathrm{eq}}) = 0$ with a much higher precision than before. Unfortunately, as figure 4.3 shows, the very high requirements for pressure measurements will once again prevent an accurate determination of the equilibrium volume.

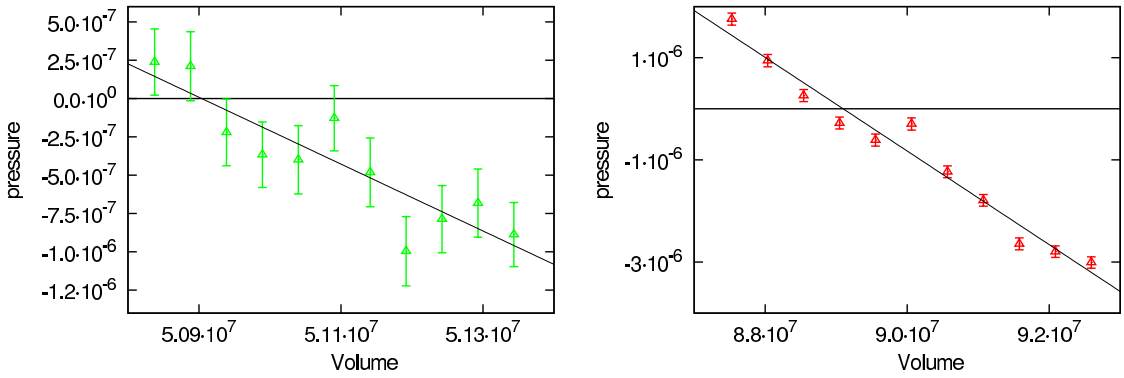

Figure 4.3.: Illustration of the Golden Section Search method for finding the swelling equilibrium volume V_{eq} in a polyelectrolyte network with $N_{\mathrm{m}} = 239$ monomers per chain, a charge fraction of $f = 0.5$ (*left*) or $f = 1.0$ (*right*), Bjerrum length $\ell_{\mathrm{B}} = 1\sigma$, and linear fit to the data (*gray line*).

So, while several promising procedures are available, the nature of the charged hydrogels with their high compressibility close to V_{eq} due to the lack of intrinsic stiffness or entanglements renders the equilibration process to be a tedious enterprise. The (N, p, T)-ensemble, considered next, introduces some relief, though the difficulty of persistent pressure determination remains (albeit less severe).

Constant Pressure Algorithm (N, p, T)

Contrary to our first investigation [62] which employed the aforementioned MC-induced volume changes to determine the equilibrium swelling volume V_{eq}, in the subsequent extended study [63] we used a stochastic MD integration scheme for isothermal-isobaric (N, p, T)-ensembles, based on Langevin-type equations of motion for the particle coordinates and a "piston" degree of freedom [109]. This algorithm, enhancing the MD approach by Andersen, Nosé, and Hoover with stochastic dynamics (SD), follows the canonically conjugate momentum $\Pi_V = Q\dot{V}$ of an artifical piston of mass Q acting on the simulation box volume V such that the difference between the currently measured "instantaneous" pressure [109, 157]

$$\mathcal{P} = \rho k_{\mathrm{B}} T - \frac{1}{3V} \sum_{i<j} \langle \vec{r}_{ij} \vec{\mathrm{f}}^{\,\mathrm{sr}}_{ij} \rangle + \frac{1}{3V} \langle E_{\mathrm{C}} \rangle \tag{4.5}$$

(with $\vec{\mathrm{f}}^{\,\mathrm{sr}}_{ij}$ being all short-range forces) and the desired "external" pressure P reads $\dot{\Pi} = \mathcal{P} - P$. This is also one striking advantage of this method over the previously

described ones: We do not need the absolute or real pressure of the system here (it is supposed to be $P = 0$ anyway), the instantaneous $\mathcal{P}$ is sufficient since the volume changes are not only immediately applied, hence counteracting even random fluctuations, but a memory of $V(t)$ is kept as well, ensuring a sustained trend towards V_{eq}. It leads to an updating scheme propagating the momentum $\vec{p}_i = m_i\vec{v}_i$ and the position $\vec{r}_i$ of each particle $i = 0, \ldots, (N_{\mathrm{tot}} - 1)$ according to:

(NpT.1) $\vec{p}_i' = \vec{p}_i(t) + \vec{\mathsf{f}}_i(t)\frac{\Delta t}{2}$

(NpT.2) Measure instantaneous pressure $\mathcal{P} = \mathcal{P}((\vec{r}_i, V, \vec{\mathsf{f}}_i)(t), \vec{p}_i')$
$\Pi_V(t + \frac{\Delta t}{2}) = \Pi_V(t) + (\mathcal{P}((\vec{r}_i, V, \vec{\mathsf{f}}_i)(t), \vec{p}_i') - P)\frac{\Delta t}{2}$

(NpT.3) $V(t + \frac{\Delta t}{2}) = V(t) + Q^{-1}\Pi_V(t + \frac{\Delta t}{2})\frac{\Delta t}{2}$

(NpT.4) $\vec{r}_i' = \vec{r}_i(t) + \frac{L^2(t)}{L^2(t+\frac{\Delta t}{2})}\frac{\vec{p}_i'}{m_i}\Delta t$

(NpT.5) $V(t + \Delta t) = V(t + \frac{\Delta t}{2}) + Q^{-1}\Pi_V(t + \frac{\Delta t}{2})\frac{\Delta t}{2}$
$\vec{r}_i(t + \Delta t) = \frac{L(t+\Delta t)}{L(t)}\vec{r}_i'$
$\vec{p}_i'' = \frac{L(t)}{L(t+\Delta t)}\vec{p}_i'$

(NpT.6) Derive new forces $\vec{\mathsf{f}}_i(t + \Delta t)$ based on new positions $\vec{r}_i(t + \Delta t)$
Measure instantaneous pressure $\mathcal{P} = \mathcal{P}((\vec{r}_i, V, \vec{\mathsf{f}}_i)(t + \Delta t), \vec{p}_i'')$
$\Pi_V(t + \Delta t) = \Pi_V(t + \frac{\Delta t}{2}) + (\mathcal{P}((\vec{r}_i, V, \vec{\mathsf{f}}_i)(t + \Delta t), \vec{p}_i'') - P)\frac{\Delta t}{2}$

(NpT.7) $\vec{p}_i(t + \Delta t) = \vec{p}_i'' + \vec{\mathsf{f}}_i(t + \Delta t)\frac{\Delta t}{2}$

For an efficient implementation, we grouped the two pressure-/velocity-propagation steps (NpT.1)–(NpT.2) and (NpT.6)–(NpT.7) as well as the rescaling steps (NpT.3)–(NpT.5) together. That allowed us to derive the ideal gas part of (4.5) *while* executing (NpT.1) or (NpT.7), using the equipartition theorem

$$\frac{f_{\mathrm{DoF}}}{2}k_{\mathrm{B}}T = \sum_{i=0}^{N_{\mathrm{tot}}-1}\left(\frac{1}{2}m_i\vec{v}_i^2 + \ldots\right) \tag{4.6}$$

(with the $f_{\mathrm{DoF}} = 3$ degrees of freedom in our case, $f_{\mathrm{DoF}} = 6$ if also rotational energies are added to the right hand side of (4.6), and so on) to get $k_{\mathrm{B}}T$, because we could successively build the sum in (4.6) after resp. before each of the propagation steps for the momentum. In a similar spirit, the virial part of $\mathcal{P}$ could be measured *while* the forces were updated in (NpT.6) because after each contribution to $\vec{\mathsf{f}}_i(t + \Delta t) = \vec{\mathsf{f}}(\{\vec{r}(t + \Delta t)\}_j)$ was determined, both $\vec{\mathsf{f}}_{ij}$ and $\vec{r}_{ij}$ are available for entering the sum in (4.5). Additionally, this part of the instantaneous pressure is independent from the momenta because no velocity-dependent forces are allowed; it does not change

between (*NpT*.6) and step (*NpT*.2) of the next iteration and may therefore be re-used there. While the propagation of volume V and piston momentum Π_V in (*NpT*.3)–(*NpT*.5) is computationally negligible, the aforementioned adjustments reduce the required, and very expensive, particle loops from seven to just four (one per group, and an additional one for the force calculation). This is more than in the case of the VVA, because there the two loops for propagating momenta and positions could be merged, whereas here it is unavoidable due to the volume-dependent position rescaling in (*NpT*.4) which requires the momentum-dependent Π_V from (*NpT*.2). The implied slowdown has been investigated in the benchmark section 1.6 where particularly the comparison of benchmark scenarios *b1* (pure Lennard-Jones liquid, constant volume) and *b4* (same Lennard-Jones liquid, constant pressure) revealed an only N_{tot}-dependent offset in the computation times of about $20\% - 30\%$ (see figures 1.4 and 1.5) which is remarkable considered that efficient bookkeeping tricks such as the employment of Verlet lists cannot be used for this algorithm.

From the volume oscillations of the piston degree of freedom and hence of $\mathcal{P}$ around P with a frequency Ω_0 the criterion $\Omega_0^{-2} = QV\kappa_T$ can be found for relating Q to the system's isothermal compressibility κ_T. We have chosen the resonance coupling $\Omega_0 = \omega_0$ to the typical molecular frequency ω_0 of the system which ensures both sufficiently fast relaxation of V to the equilibrium $V_{\mathrm{eq}} = V(\mathcal{P} \approx P)$ as well as suppression of unwanted "box ringing" [109]. Adding friction and noise introduces two more parameters, namely the molecular, respectively piston, dampening γ_0 and γ_V, which are connected via $\gamma_0 \approx 2\omega_0$, resp. $\gamma_V \approx 2Q\Omega_0$, to the basic timescales. They are entering the updating scheme (*NpT*.1)–(*NpT*.7) by replacing $\vec{\mathsf{f}}_i\Delta t/2$ and $\dot{\Pi}_V = (\mathcal{P} - P)\Delta t/2$ according to

$$\left.\begin{matrix}(NpT.1)\\(NpT.7)\end{matrix}\right\}\ \vec{\mathsf{f}}_i\frac{\Delta t}{2} \quad\longmapsto\quad \vec{\mathsf{f}}_i\frac{\Delta t}{2} - \gamma_0\frac{\vec{p}_i}{m_i}\frac{\Delta t}{2} + \sqrt{k_{\mathrm{B}}T\gamma_0\Delta t}\,\vec{z}_i$$

$$\left.\begin{matrix}(NpT.2)\\(NpT.6)\end{matrix}\right\}\ (\mathcal{P} - P)\frac{\Delta t}{2} \quad\longmapsto\quad (\mathcal{P} - P)\frac{\Delta t}{2} - \gamma_V\frac{\Pi_V}{Q}\frac{\Delta t}{2} + \sqrt{k_{\mathrm{B}}T\gamma_V\frac{\Delta t}{2}}\,z_V$$

with uncorrelated random numbers $\vec{z}_i$ and z_V having zero mean and unit variance, *e.g.* $z = \sqrt{12}\,(u - 1/2)$ if u is uniformly distributed on the unit interval. Note that in case of $\vec{\mathsf{f}}_i$ this directly corresponds to the Langevin thermostat for the VVA, while the same becomes apparent for $\dot{\Pi}_V = (\mathcal{P} - P)$ if one follows the analogy of Π_V being the momentum of the piston with mass Q (where $\dot{\Pi}_V$ would then correspond to a force).

The optimal choice of Q, γ_0 and γ_V is essential for successfully reaching V_{eq} within reasonable computation time. Setting the molecular dampening to $\gamma_0 = \tau^{-1}$ (using τ, σ, and ϵ as standard LJ units for time, length, and energy) simplifies its piston counterpart to $\gamma_V \approx 2Q\Omega_0 = 2Q\omega_0 = Q\gamma_0$ because of the resonance coupling we chose. The piston mass Q follows from

$$\Omega_0^{-2} = QV\kappa_T \Rightarrow Q = 1/(\omega_0^2 V\kappa_T) \tag{4.7}$$

with ω_0 deducible from the intermolecular potentials [109]. The compressibility κ_T, which is unfortunately *a priori* unknown, can be obtained from measuring the volume fluctuations in the (N, p, T)-ensemble, using [109]

$$V\kappa_T = \frac{1}{k_\mathrm{B}T} \cdot \left(\langle V^2\rangle - \langle V\rangle^2\right) \tag{4.8}$$

as a direct measure of the factor in (4.7). During the equilibration process while $V \neq V_\mathrm{eq}$ this may be non-constant, which is why we employed an iterative process by starting with an initial guess $Q = 10^{-8}$, determining $V\kappa_T$ from (4.8) at runtime, and updated Q using (4.7) until the equilibrium was reached.

Following a short warm-up sequence, the full system was integrated with that scheme for typically $2.4 \cdot 10^4\tau, \ldots, 7.2 \cdot 10^5\tau$, using an adaptive timestep of $\Delta t \leq 0.012\tau$ until the volume V had finally converged towards V_eq with an accuracy in the osmotic coefficient $\mathcal{P}_\mathrm{osm} = \mathcal{P}/(k_\mathrm{B}TN_\mathrm{CI}/V)$ of $|\langle\mathcal{P}_\mathrm{osm}\rangle| < 0.05$, which is the achievable limit within the high compressibility of the given systems and the resulting high fluctuations at small densities.

In terms of the Tcl-script, the (N, p, T)-integrator and its corresponding thermostat are activated by

```
integrate set   npt_isotropic $p_ext $piston
thermostat set  npt_isotropic $temp $gamma_0 $gamma_v
```

before entering the warm-up sequence for the neutralized system. Here, we want to prevent excessively large excluded volume repulsion due to too closely created particles by initially capping the LJ-force at some value, which is quickly increased during the `warm_loop` cycles of `warm_step` timesteps, and removed thereafter.

```
for { set j $j_start } { $j < $warm_loop } { incr j } {
    integrate $warm_step; set tmp_dist [analyze mindist]
    if { ($tmp_dist >= $min_dist) && ($j > $min_loop) } { break }
    inter ljforcecap $tmp_cap; set tmp_cap [expr $tmp_cap + $warm_incr]
    if { $j % 10 == 0 } {
        polyBlockWriteAll "$name$ident.twm" { j cM_dist tmp_cap } }
}
inter ljforcecap 0
```

This sequence also analyzes the minimum distance between all particles, aborting the integration if they are at least `min_dist` apart from each other after more than `min_loop` integration cycles. The current state of the system is saved every 10 timesteps to allow later resume of the warm-up at `j_start`, *e.g.* in case the hardware malfunctions or the allocated CPU time is exceeded.

In the subsequent equilibration integration with full interactions (*i.e.*activating electrostatics as shown before) we can follow the same scheme except for the necessary measurements of the volume fluctuations required to adjust Q using (4.7) by monitoring $V\kappa_T$ with (4.8) at runtime.

```
for { set j $j_start } { $dsw_done < $min_dsw } { incr j } {
    integrate $dsw_step
    if { $j <= $min_dsw } {
        set avg [expr $j*1.0] } else { set avg [expr 1.0*$min_dsw]
        set p_io [lindex $p_oI 0]; set p_oI [lreplace $p_oI 0 0]
    set p_inst [setmd npt_p_inst]; set p_aI [expr $p_aI + $p_inst - $p_io]
    lappend p_oI $p_inst
    set V1 [expr pow([lindex [setmd box_l] 0],3)]; set rho [expr $N_T/$V1]
    set Vkappa [expr abs([analyze Vkappa])]; set Vkn [analyze Vkappa read]
    if { abs($p_aI/$avg/($rho*$temp)) < $min_osm } { incr dsw_done
    } else { set dsw_done 0 }
    if { ($j+$dsw_cycl-$dsw_updt) % $dsw_cycl == 0 } {
        modfy_piston $Vkappa; analyze Vkappa reset; analyze Vkappa }
    polyBlockWriteAll "$name_ident.tmp" { j dsw_done p_aI p_oI }
}
polyBlockWriteAll "$name_ident.dsw" { j piston gamma_0 gamma_v Vkappa }
```

With the history of the previous `min_dsw` timesteps for both the pressure (stored in `p_oI`) and the volume (in `V_oV`) available, a floating average is taken to allow even systems starting very far from equilibrium to be processed. While the ESPResSo-function `analyze Vkappa` iterates (4.8) with each call, keeping track of the temporal evolution of the volume until that memory is erased using `analyze Vkappa reset`, the Tcl-function `modfy_piston <Vkappa>` implements (4.7) to adjust the integration parameters accordingly. The integration loop runs until the osmotic coefficient $|\langle \mathcal{P}_{\mathrm{osm}} \rangle|$ has been smaller than `min_osm` for `min_dsw` subsequent cycles; in that case another checkpoint is created.

From there, the equilibrium properties of the swollen hydrogel were determined by switching to the $(N, V = V_{\mathrm{eq}}, T)$-ensemble and applying a standard velocity Verlet algorithm, coupled to a heat bath and background friction (Langevin thermostat; friction coefficient $\Gamma = \tau^{-1}$, $T^* = 1\,\epsilon/k_{\mathrm{B}}T$). After another equilibration phase in this new ensemble, where we measured the pressure to check if indeed the $V = V_{\mathrm{eq}}(\mathcal{P} \approx 0)$ had previously been found, we integrated the equations of motion for 2400τ with timestep $\Delta t = 0.012\tau$ [35,180]. This introduces two different kinds of errors into our data: First, the standard statistical fluctuations of the observables measured in the $(N, V = V_{\mathrm{eq}}, T)$-ensemble, which lead to the error bars depicted in the plots later on; second, deviations due to the equilibration process' accuracy in finding $V_{\mathrm{eq}} = V(\mathcal{P} = 0)$, since the volume of the simulation box directly determines the size of the conserved network topology, which is spanned by the periodic boundary conditions, and is hence indirectly entering (along with its error) all other observables. While a thorough equilibration process can minimize the occurrence of the latter, some systematic errors may remain in the data.

All in all, we investigated polyelectrolyte networks in good solvent and close to the θ-point, whose $N_{\mathrm{p}} = 16$ strands carried $N_{\mathrm{m}} = 39, \ldots, 259$ monomers each, a

fraction $f \in \{\frac{1}{16}, \frac{1}{8}, \frac{1}{4}, \frac{1}{2}, \frac{1}{1}\}$ of them charged, surrounded by $N_{\mathrm{CI}} = 72, \ldots, 4152$ counterions with an electrostatic interaction strength characterized by a Bjerrum length of $\ell_{\mathrm{B}} \in \{1\sigma, 2\sigma, 5\sigma\}$. In our study, special emphasis was put on evaluating the significance of the direct electrostatic contributions to the swelling equilibrium, since they are neglected in classical theories (see section 3.2.2). For this purpose, we measured how the observables of the swollen hydrogel change when all coulombic interactions are turned off, leaving full entropic degrees of freedom for the (now neutral) "counterions", and remaining at the volume $V = V_{\mathrm{eq}}$ determined as the swelling equilibrium value for the charged case. While such a simulation may result in a non-vanishing total pressure $\mathring{\mathcal{P}}$ (namely, if the electrostatic contribution to the overall pressure is *not* negligible), its observables will be marked with a superscript (*e.g.* $\mathring{x}$) to distinguish them from their swelling equilibrium counterparts (*e.g.* x), with a superscripted $\mathring{\Delta}$ denoting their difference (*e.g.* $\mathring{\Delta}x = x - \mathring{x}$).

In addition, we also applied the entire (N, p, T)-scheme to systems without any electrostatics, *i.e.* $\ell_{\mathrm{B}} = 0\sigma$, but f-dependent amount of neutral spheres which are corresponding to the counterions for $\ell_{\mathrm{B}} > 0$, expecting them to provide the best correspondence to the theoretical picture of the section 3.2.2. While $\mathcal{P} = 0$ here, for distinction purposes the aforementioned non-equilibrium measurements at $\mathring{\mathcal{P}}$ will be referred to as *e.g.* "neutral $\ell_{\mathrm{B}} = 1\sigma$" to stress that they reflect systems with a simulation box volume solely determined by the corresponding fully charged network with *e.g.* $\ell_{\mathrm{B}} = 1\sigma$.

As already indicated, the entire setup, simulation, and analysis was performed using ESPResSo, the molecular dynamics package we introduced in chapter 1.

4.2. Results and Discussion

Although we already showed in the previous chapter 3 that the solution of a self-consistency condition such as (3.71) for the stretching force acting on the network strands in the swelling equilibrium of a charged hydrogel is sufficient to describe the underlying physical mechanisms, in this section we want to follow a different path of analysis. Starting off at the previously commonly accepted simple scaling model (3.6), we aim to illustrate the microscopic findings we obtained from analyzing our simulation data in detail on basis of the oversimplified picture behind (3.6), demonstrating the challenges one has to overcome if it should be made working. In the end we will show that it is indeed possible, if the effective charge fraction f_{eff} used is adjusted accordingly to also reflect the additional contributions considered in our own scaling law (3.71), thereby essentially trading the latter's numerical prefactors against fitting a physical parameter. Nevertheless, our detailed study reveals the microscopic mechanisms behind our scaling laws additional contributions, and allows a closer examination of them, which in turn corroborates further our findings from the previous chapter.

4.2.1. Structural Properties

The swelling equilibrium of a charged gel is expected to mainly result from the elastic response of the chains' inner bonds balancing the osmotic pressure of the counterions trapped inside the network by the macroscopic electro-neutrality requirement. Assuming the validity of the Flory-Rehner-Hypothesis (FRH) and neglecting explicit electrostatic effects and treating all objects as point-like spheres, in section 3.2 the classical tension blob model was employed to arrive at the scaling prediction

$$R_{\mathrm{E}} = f^{1-\nu} N_{\mathrm{m}} b \quad \Rightarrow \quad \alpha_\nu = \frac{R_{\mathrm{E}}^2}{R_\nu^2} = (f N_{\mathrm{m}})^{2(1-\nu)} \tag{3.6}$$

for the network strands' node-node separation of a gel under θ-like ($\nu = \frac{1}{2}$, section 3.2.1) or good solvent ($\nu = \frac{3}{5}$ [31] or $\nu = 0.588$ [153, 160, 161], section 3.2.2) conditions.

In case of only weak electrostatics, we showed the general validity of (3.6) in [62], having the more detailed study [63] focus on deviations from the previously predicted behaviour and explore possible corrections to the assumed swelling mechanisms of the hydrogel. Table 4.1 assembles some equilibrium properties for the longest chain ($N_{\mathrm{m}} = 239$) we investigated for all charge fractions f; the complete data, for other $N_{\mathrm{m}} \neq 239$ as well, is given in appendix A. While shorter N_{m} only confirm the overall observations, fluctuations and finite size effects begin to play an increasing role particularly for very short chains, where *e.g.* the network nodes and the heightened charge concentration there introduce additional deviations not present for longer chains, which is why we restrict our detailed discussion to the latter.

In general, it can be observed that larger amounts of mobile counterions (larger f) in the network cause the size of the simulation box L_{eq} at $\mathcal{P} \approx 0$ to grow monotonically, which in turn imposes the same behaviour on the gel's geometrical observables, due to the periodic boundary conditions causing the box to effectively span the network. Particularly, when comparing the swelling ratio α_ν for different ℓ_{B} but constant f, it turns out that in case of weakly charged systems the respective values match relatively well, since in (3.6) they are independent of ℓ_{B}. For larger f, however, stronger electrostatics causes an increasingly pronounced *drop* in the swelling ratio; strongly charged systems are effectively becoming even *smaller* than gels with up to 75% less counterions (comparing *e.g.* $\ell_{\mathrm{B}} = 5\sigma$, $f = 1.0$ with $\ell_{\mathrm{B}} < 5\sigma$, $f = 0.25$ in good solvent).

The network strands seem strongly stretched and assume an appearance as rod-like objects, according to their aspect ratio $R_{\mathrm{E}}^2/R_{\mathrm{G}}^2 = 12$ for all but the most weakly charged case $f = 0.0625$ (which still exhibits a $R_{\mathrm{E}}^2/R_{\mathrm{G}}^2 \geq 11.4 \pm 0.2$). Considering the other possibilities in table 2.2, it is particularly noteworthy that despite our single chain treatment, they do not follow the aspect ratio of a random walk, where $R_{\mathrm{E}}^2/R_{\mathrm{G}}^2 = 6$, or a similar shape of an isolated polymer. The scaling arguments from section 3.2.2 remain valid nevertheless since they essentially treated the network as

ℓ_B	f	$L = V_{eq}^{1/3}$	$\langle R_E^2 \rangle^{1/2}$	α_ν	$\frac{R_E}{N_m b}$	$\langle R_G^2 \rangle^{1/2}$	$\frac{\langle R_E^2 \rangle}{\langle R_G^2 \rangle}$	R_H
1	0.0625	211±4	91±6	3.51	0.368	27±2	11.4±0.2	13.0±0.5
2	0.0625	216±4	94±7	3.59	0.377	27±2	11.6±0.3	13.2±0.5
5	0.0625	210±4	91±7	3.49	0.367	27±2	11.7±0.3	13.1±0.6
1	0.125	265±4	114±5	4.39	0.46	33±2	11.8±0.2	14.7±0.4
2	0.125	269±4	116±6	4.45	0.467	34±2	11.9±0.2	14.8±0.5
5	0.125	249±5	107±5	4.12	0.432	31±2	11.9±0.2	14.4±0.4
1	0.25	330±3	142±5	5.44	0.571	41±2	12.0±0.1	16.7±0.4
2	0.25	329±3	141±5	5.43	0.569	41±2	12.0±0.1	16.8±0.4
5	0.25	278±4	120±6	4.62	0.485	35±2	11.8±0.2	15.5±0.5
1	0.5	395±2	170±4	6.51	0.683	49±1	12.1±0.1	18.8±0.3
2	0.5	397±3	171±5	6.53	0.684	49±1	12.0±0.1	19.1±0.3
5	0.5	303±5	130±6	4.99	0.523	38±2	11.8±0.2	16.5±0.4
1	1.0	465±2	200±3	7.58	0.794	57±1	12.2±0.1	21.1±0.2
2	1.0	443±3	190±3	7.22	0.756	55±1	11.9±0.1	20.8±0.2
5	1.0	328±5	141±6	5.33	0.558	41±2	11.9±0.2	17.5±0.4

ℓ_B	f	$L = V_{eq}^{1/3}$	$\langle R_E^2 \rangle^{1/2}$	α_ν	$\frac{R_E}{N_m b}$	$\langle R_G^2 \rangle^{1/2}$	$\frac{\langle R_E^2 \rangle}{\langle R_G^2 \rangle}$	R_H
1	0.0625	172±4	75±7	4.86	0.316	22±2	11.5±0.3	10.9±0.6
2	0.0625	172±4	74±5	4.85	0.315	22±2	11.9±0.2	10.9±0.5
5	0.0625	161±5	70±7	4.58	0.298	21±2	11.4±0.3	10.8±0.6
1	0.125	229±3	99±4	6.42	0.416	29±1	11.8±0.2	12.8±0.4
2	0.125	232±4	100±5	6.52	0.422	29±2	11.9±0.2	13.1±0.4
5	0.125	208±5	90±6	5.86	0.38	26±2	11.7±0.2	12.4±0.5
1	0.25	296±3	127±6	8.28	0.536	36±2	12.2±0.2	15.1±0.5
2	0.25	299±3	129±5	8.38	0.543	37±1	12.0±0.1	15.4±0.4
5	0.25	250±5	108±6	7.02	0.455	32±2	11.7±0.2	14.1±0.5
1	0.5	369±2	159±4	10.3	0.665	45±1	12.2±0.1	17.6±0.3
2	0.5	370±3	159±4	10.3	0.666	46±1	12.0±0.1	17.9±0.3
5	0.5	274±4	118±7	7.66	0.496	35±2	11.7±0.2	15.2±0.5
1	1.0	449±2	193±3	12.3	0.797	55±1	12.2±0.1	20.4±0.2
2	1.0	418±3	180±5	11.5	0.742	52±1	11.9±0.1	19.7±0.3
5	1.0	309±5	133±8	8.45	0.548	39±2	11.7±0.2	16.7±0.5

Table 4.1.: Selected network properties for a system with $N_m = 239$ monomers per chain in good solvent (*top*) and close to the θ-point (*bottom*) for different values of Bjerrum length ℓ_B and charge fraction f, namely length L of the simulation box after reaching the equilibrium volume V_{eq}, the average chain extension R_E, its swelling ratio α_ν compared to a single neutral chain, its extension relative to the contour length $N_m b$, its radius of gyration R_G, its aspect ratio R_E^2/R_G^2, and its hydrodynamic radius R_H.

single chains under tension, an appropriate description regarding the counterions' pressure which obviously elongates the strands into the rod-like regime.

The impact of the solvent quality diminishes with growing coulombic contributions: The absolute measures close to the θ-point such as L or R_{E} approach their good solvent counterparts from below (reducing the difference from $\sim 21\sigma$ or $\sim 33\%$ to $\sim 7\sigma$ or $\sim 4\%$), while their swelling ratio remains significantly larger, both in agreement with the single chain behaviour, where a θ-solvent polymer would always have a smaller R_ν than in the good solvent case.

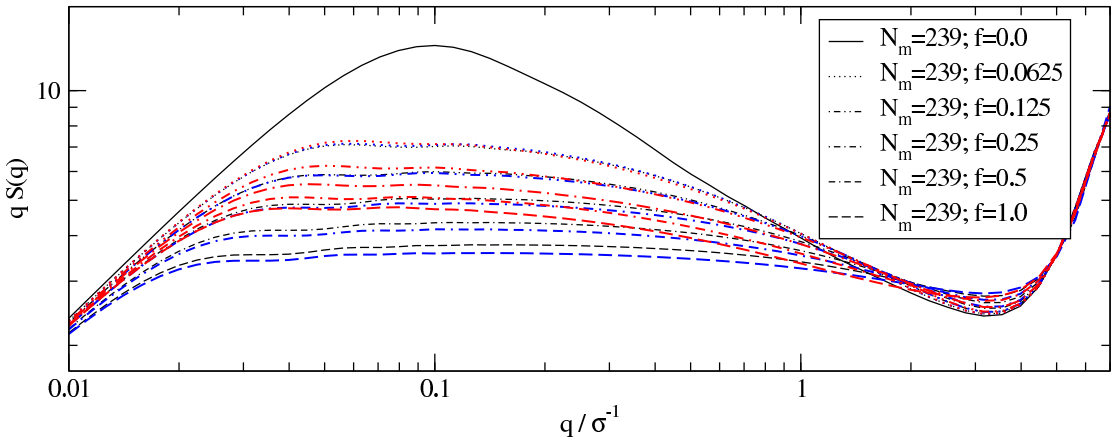

Figure 4.4.: Averaged form factor $S(q)$ of the network strands with $N_{\mathrm{m}} = 239$ monomers per chain, plotted for $\ell_{\mathrm{B}} = 0\sigma$ (*black lines*), $\ell_{\mathrm{B}} = 1\sigma$ (*blue lines*), and $\ell_{\mathrm{B}} = 5\sigma$ (*red lines*) in good solvent, rescaled by $S(q) \cdot q^{1/1}$; different line style corresponds to different charge fractions f (see legend).

Following the trivial observation that for $f \to \frac{1}{N_{\mathrm{m}}}$ (the obvious lower boundary for the charge fraction of a polyelectrolyte chain) the scaling in (3.6) becomes that of a single neutral chain R_ν, the spherically averaged form factor of the network strands

$$S(q) = \int_{|\vec{q}|=q} \mathrm{d}\vec{q}\, S(\vec{q}) = \frac{1}{4\pi N_{\mathrm{m}}} \sum_{i=1}^{N_{\mathrm{m}}} \sum_{j=1}^{N_{\mathrm{m}}} \frac{\sin(qr_{ij})}{qr_{ij}} \tag{4.9}$$

displayed in figure 4.4 for the same $N_{\mathrm{m}} = 239$ as in table 4.1 supports the general notion of the theoretical model to describe the swollen gel as crosslinked sequences of blobs. While the uncharged case of $f = 0.0$ (*solid line*), containing no counterions and therefore representing a neutral polymer network, has its strands behave like single neutral chains extending $R_\nu = bN_{\mathrm{m}}^\nu$ ($= R_{\mathrm{Gauß}}$ for θ-like, $= R_{\mathrm{F}}$ for good solvents), the presence of even few counterions introduces two regimes to the systems: On short length scales (large q) the segments of the network approximate the neutral behaviour $S(q) \sim q^{-1/\nu}$, for larger length scales (smaller q) the chains exhibit the anticipated straight conformation $S(q) \sim q^{-1/1}$ of the blobs which we just saw in the

rod-like aspect ratio $R_E^2/R_G^2 = 12$ as well. In case of weak electrostatics, the width of the elongated regime only depends on the amount of counterions within the gel, as figure 4.4 shows by comparing systems with $\ell_B = 0\sigma$ (*i.e.* uncharged ones) to $\ell_B = 1\sigma$ (*blue lines*); their form factors display very small deviations which entirely vanish for smaller charge fractions, at the same time asymptotically approaching the shape of the neutral network. Consequently, the crossover between the two regimes shifts towards smaller q (larger spatial distances) for decreasing f, not only reflecting the aforementioned trend towards less strongly swollen states (*i.e.* smaller R_E) contained in table 4.1, but also supporting $g \sim f^{-1} \Rightarrow \xi \sim bf^{-\nu}$ as obtained in section 3.2.2: For $f = 1.0$ each "blob" is predicted to consist of $g \sim 1$ monomer being $\xi \sim b$ wide in diameter (*i.e.* rendering the blob picture obsolete). This leads to the almost entirely stretched conformation, represented by the form factor in figure 4.4 for that charge fraction. For smaller values of f the regime in which $S(q)$ follows the neutral network behaviour becomes larger, *i.e.* more monomers can be considered to be part of a blob.

In the case of strong electrostatic interactions ($\ell_B = 5\sigma$, *red lines*) the relative dependency on the charge fraction remains the same, but it is shifted towards the form factors of $\ell_B = 1\sigma$ with *smaller* f, following the trend of the geometrical properties such as R_E in table 4.1 for corresponding Bjerrum lengths. This is due to counterion condensation taking place, renormalizing f towards an effective charge fraction f_{eff}, as will be discussed in the next section 4.2.2. While this explains why the form factors for $\ell_B = 5\sigma$, $f = 1.0$ and $f = 0.5$, with their $f_{\text{eff}} \approx 0.21$, behave similarly to the one of $\ell_B = 1\sigma$, $f = 0.25$ in the small q regime, on shorter length scales they approach their respective $f = 1.0$ and $f = 0.5$ counterparts with $\ell_B = 1\sigma$, since here the global charge renormalization is less significant than the local repulsion between neighbouring charged monomers.

Typical network conformations at swelling equilibrium are shown in figure 4.5, colour coded as in the simulation box model snapshot of figure 4.2, *i.e.* with *gray* spheres as network nodes, *blue* for uncharged and *white* for charged monomers, and *orange* spheres for the counterions. The chosen parameters represent two trends discussed so far: On the *left* the smallest ($R_E = 91\sigma$) and largest ($R_E = 200\sigma$) chain extensions are compared, where it is easily visualized that the counterions do behave gas-like and therefore increase the swelling significantly if added at not too strong coulombic coupling. Nevertheless, for $\ell_B = 1\sigma$ first deviations are already visible, which become particularly apparent when compared to the case of $f = 1.0$, $\ell_B = 5\sigma$ (*lower right*). There, most of the formerly free counterions are now condensed onto the network chains (note that both lower snapshots have the same amount N_{CI} present in the system) and obviously reduce the chain extension ($R_E = 141\sigma$) because of their lowered osmotic pressure. That reduction, however, now corresponds to a decrease of the charge fraction to $f = 0.25$ and of electrostatics to $\ell_B = 2\sigma$ according to the snapshot in the *upper right* where $R_E = 141\sigma$ as well. It is this delicate interplay between raw number of counterions in the system (given

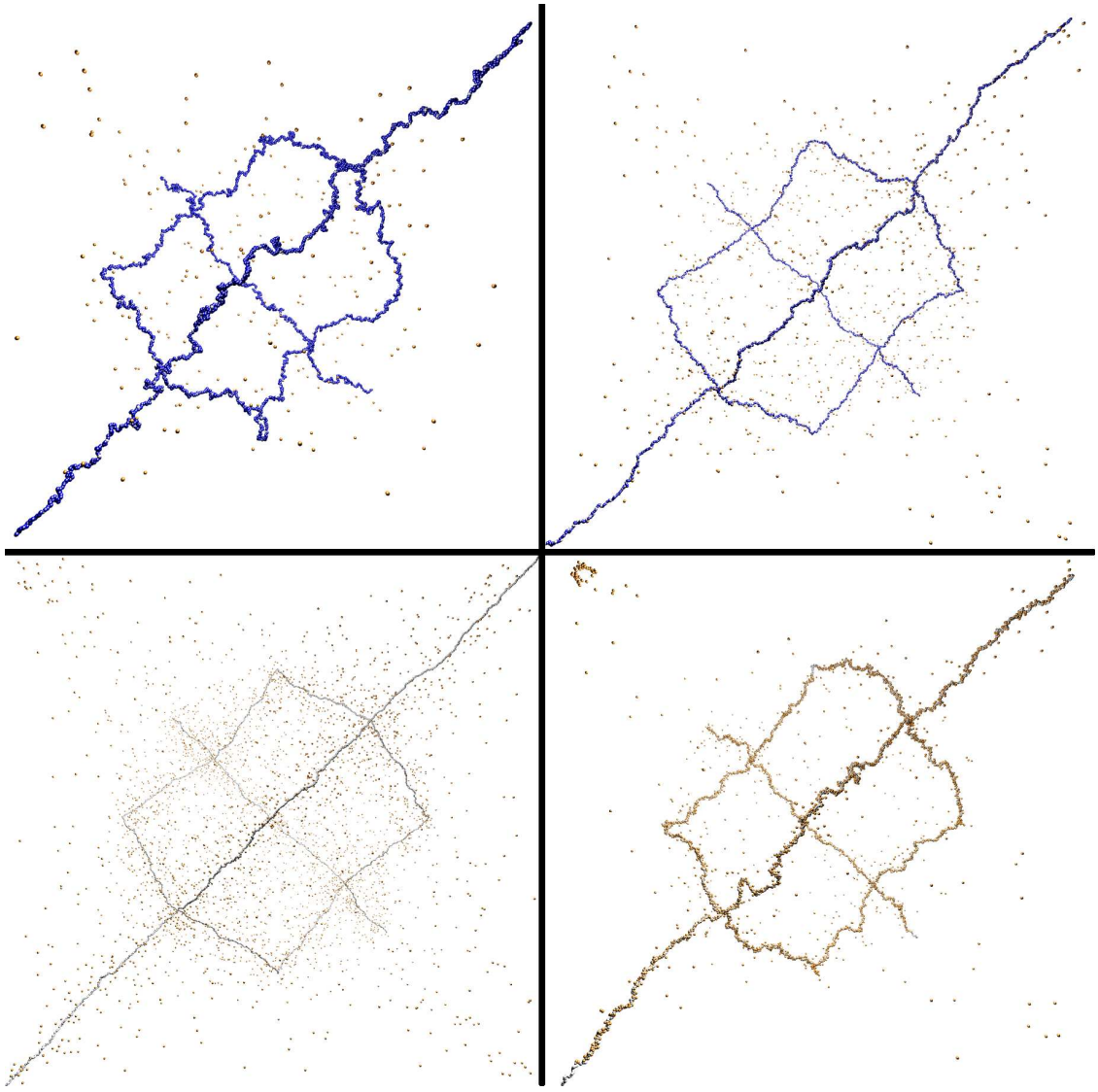

Figure 4.5.: Snapshots of network conformations at swelling equilibrium for $N_m = 239$ and $f = 0.0625$, $\ell_B = 1\sigma$ (*top left*), $f = 0.25$, $\ell_B = 2\sigma$ (*top right*), $f = 1.0$, $\ell_B = 1\sigma$ (*bottom left*), and $f = 1.0$, $\ell_B = 5\sigma$ (*bottom right*), each under good solvent conditions (colour coding as in figure 4.2).

by f), amount of free counterions contributing to the swelling (addressed in the next section 4.2.2), and coulombic coupling (given by ℓ_B) which will determine the discussion for the remainder of this chapter.

Looking at the form factors for other chain lengths $N_m = 39, \ldots, 259$ and all $\ell_B = 0\sigma, \ldots, 5\sigma$ (*i.e.* adding $\ell_B = 2\sigma$ as *green lines*) in good solvent (figure 4.6) and close to the θ-point (figure 4.7) confirms these findings in the limit of large N_m, but also shows the deviations for short chains: There, for weakly charged networks no

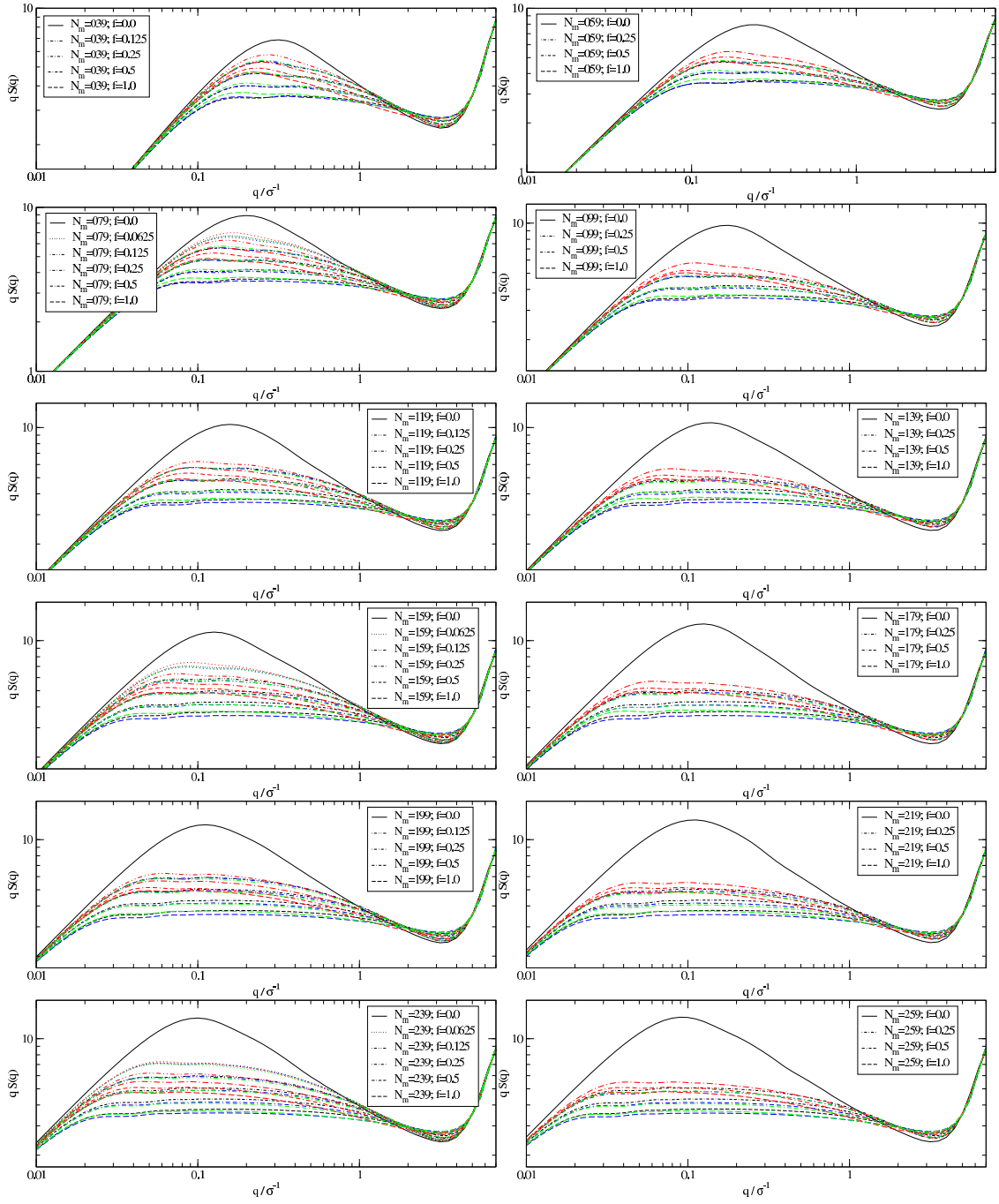

Figure 4.6.: Averaged form factor $S(q)$ of the network strands with $N_\mathrm{m} = 39, \ldots, 259$ monomers per chain (from *top left* to *bottom right*) in good solvent, plotted for $\ell_\mathrm{B} = 0\sigma$ (*black lines*), $\ell_\mathrm{B} = 1\sigma$ (*blue lines*), $\ell_\mathrm{B} = 2\sigma$ (*green lines*), and $\ell_\mathrm{B} = 5\sigma$ (*red lines*), and rescaled by $S(q) \cdot q^{1/1}$; different line style corresponds to different charge fractions f (see legend).

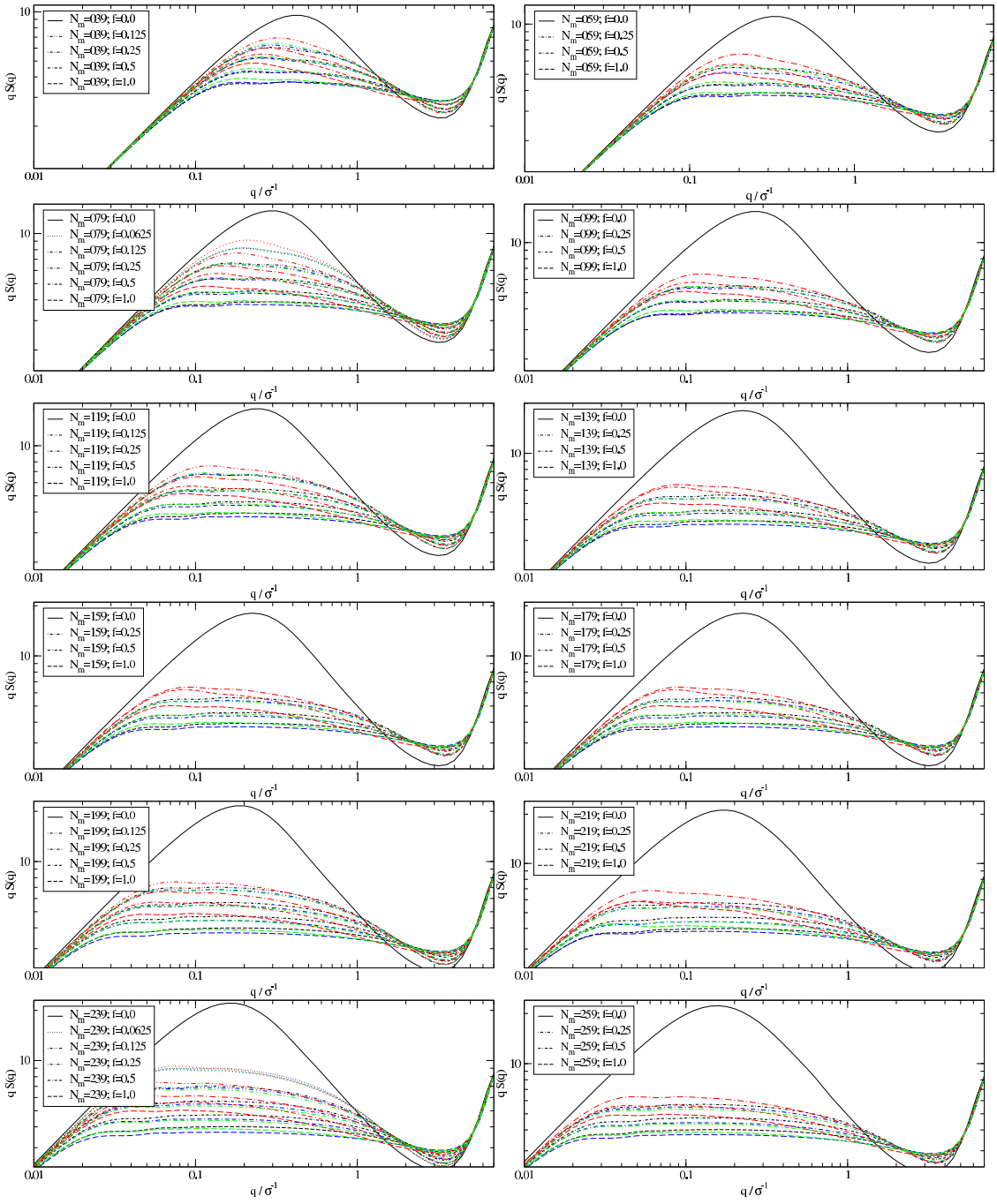

Figure 4.7.: Averaged form factor $S(q)$ of the network strands with $N_\mathrm{m} = 39, \ldots, 259$ monomers per chain (from *top left* to *bottom right*) close to the θ-point, plotted for $\ell_\mathrm{B} = 0\sigma$ (*black lines*), $\ell_\mathrm{B} = 1\sigma$ (*blue lines*), $\ell_\mathrm{B} = 2\sigma$ (*green lines*), and $\ell_\mathrm{B} = 5\sigma$ (*red lines*), and rescaled by $S(q) \cdot q^{1/1}$; different line style corresponds to different charge fractions f (see legend).

plateau of elongation on larger length scales (*i.e.* small q) can be formed, instead $S(q)$ mimics shape and maximum of the neutral system. Increasing the strength of electrostatics to $\ell_B = 5\sigma$ reveals another transitory effect with the form factor having only the $S(q) \sim q^{-1/\nu}$-regime but a significantly larger ν. A possible explanation is the increased stiffness of the network strands due to the strong condensation of counterions onto them which in turn prevent too much coiling, rendering the chains to appear more like a WLC. Upon closer inspection, this effect remains visible on short length scales (large q) even for $N_m \to 259$, as the two regimes of rod-like and single chain-like behaviour are not distinctly separated but experience a rather smooth crossover. That also implies a careful evaluation of the scaling prediction (3.6) as not only finite size effects are to be expected in form of N_m-dependent deviations, but adjustments to the exponent ν might be required, too.

Close to the θ-point the aberrations become more apparent, as the only slight shift in the exponent ν of the hydrogels of figure 4.7 increase the difference to the neutral case with its $S(q) \sim q^{-1/0.5}$, reducing the agreement with the scaling of the network strands to the limit of large q and small f. Again, it is the interference of the counterions which stiffen the chains, as in addition to condensation effects for strong electrostatics their excluded volume remains purely repulsive, whereas the monomers gained the attractive part of the Lennard-Jones interaction (4.2) as sketched in the right hand side of figure 4.1. Consequently, the impact of the Coulomb parameters f and ℓ_B on the shape of the polyelectrolyte networks is more significant than that of the solvent quality.

4.2.2. Counterion Condensation

The stretched conformations in figure 4.4 for large f or/and ℓ_B as well as the aspect ratio's $R_E^2/R_G^2 \approx 12$ in the data of table 4.1 suggest the comparison to charged rods. For these, *i.e.* infinitely long linear stiff rods, it is known [165] that for a *Manning parameter*

$$\xi_M = \frac{\ell_B}{b/f} > \frac{1}{v_{CI}} \tag{4.10}$$

(v_{CI} being the valency of the counterions, $v_{CI} = 1$ in our case) a fraction of $(1-1/\xi_M)$ counterions will "condense" onto the rod, *i.e.* will be confined to a small cylindrical volume around it. Since the arguments in section 3.2.2 support that the translational entropy of the free counterions is responsible for the swelling of the gel, condensation would fit into this picture by, in a first approximation, simply replacing f with an *effective* charge fraction f_{eff} defined by the Manning argument, according to which for $\xi_M > 1$ all counterions added to the system will condense and keep the effective charge of the system to one charge per Bjerrum length. Consequently, $\xi_M^{max} = \frac{\ell_B}{b/f_{max}} = \frac{1}{v_{CI}}$ would represent an upper bound for the charge fraction, rendering any $f > f_{max}$ to not increase the amount of free counterions contributing to Π_C,

hence not changing the scaling in (3.6) if using

$$f_{\mathrm{eff}} = \begin{cases} f & \text{for } \frac{\ell_{\mathrm{B}}}{b/f} < \frac{1}{\nu_{\mathrm{CI}}} \Rightarrow \quad f < f_{\max}, \\ f_{\max} = \frac{b}{\nu_{\mathrm{CI}}\ell_{\mathrm{B}}} & \text{for } \frac{\ell_{\mathrm{B}}}{b/f} \geq \frac{1}{\nu_{\mathrm{CI}}} \Rightarrow \quad f \geq f_{\max}. \end{cases} \tag{4.11}$$

instead of f there (most easily seen by using $\Pi_{\mathrm{C}}^{\mathrm{eff}} \propto k_{\mathrm{B}}T\frac{f_{\mathrm{eff}}N_{\mathrm{m}}}{R_{\mathrm{E}}^3}$ to balance Π_{E}).

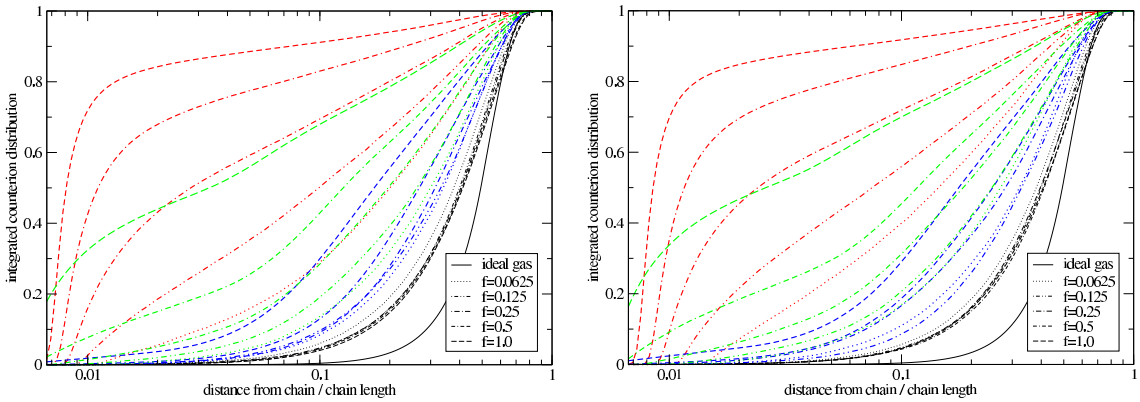

Figure 4.8.: Integrated counterion distribution for $N_{\mathrm{m}} = 239$, with $\ell_{\mathrm{B}} = 0\sigma$ (*black lines*), $\ell_{\mathrm{B}} = 1\sigma$ (*blue lines*), $\ell_{\mathrm{B}} = 2\sigma$ (*green lines*), and $\ell_{\mathrm{B}} = 5\sigma$ (*red lines*) in good solvent (*left*) and close to the θ-point (*right*), normalized by the end-to-end distance $\langle R_E^2\rangle^{1/2}$; different line style corresponds to different charge fractions f (see legend). For comparison, the corresponding ideal gas distribution for $\ell_{\mathrm{B}} = 5\sigma$ and $f = 1.0$ is given as well (*solid black line*). Note that each of the systems has its own V_{eq}, the graphs therefore reach the horizontal axis at different $1/R_{\mathrm{E}}$.

As can be inferred from figure 4.8, the assumption of an ideal gas-like distribution made in section 3.2.2 holds sufficiently well for weakly charged systems. Without electrostatics (*black lines*), all distributions coincide as expected after a successful equilibration of the systems, because then the number of neutral "counterions" should not be influential to their homogeneous spread throughout the network at a constant density; the excluded volume of the chains' monomers however introduces a constant shift from the shape of the pure ideal gas also given in the plot. While for $\ell_{\mathrm{B}} = 1\sigma$ (*blue lines*) and $f \leq 0.25$ there is not much deviation from the uncharged cases observable, stronger electrostatics perturb the "cloud" of counterions surrounding the network chains, increasingly attracting the former towards the charged monomers on the strands. With the integrated distribution functions taking on an (initially) concave shape up to an inflection point (R_{M}, f_x) which will be discussed later on, counterion condensation sets in. In the plots, this is the case for $\ell_{\mathrm{B}} = 5\sigma$ (*red lines*) and $f \geq 0.25$, although strong deviations from the ideal gas-like behaviour are already apparent for intermediate parameter regimes like $\ell_{\mathrm{B}} = 5\sigma$ and $f = 0.125$ where 40% of the counterions are within a distance of $|r| = L/10$ around

a network strand, illustrating the difficulty of defining something as continuous as this "condensation" effect which is obviously all but a sharp transition between two distinct phases or states.

		good solvent ($\nu = 0.588$)				θ-solvent ($\nu = 0.50$)			
ℓ_B	f	ξ_M	$1-\frac{1}{\xi_M}$	f_{eff}	f_x	ξ_M	$1-\frac{1}{\xi_M}$	f_{eff}	f_x
1	0.0625	0.0602	–	0.0625	–	0.0631	–	0.0625	–
2	0.0625	0.12	–	0.0625	–	0.126	–	0.0625	–
5	0.0625	0.301	–	0.0625	–	0.316	–	0.0625	–
1	0.125	0.12	–	0.125	–	0.126	–	0.125	–
2	0.125	0.241	–	0.125	–	0.252	–	0.125	–
5	0.125	0.602	–	0.125	–	0.631	–	0.125	–
1	0.25	0.241	–	0.25	–	0.252	–	0.25	–
2	0.25	0.481	–	0.25	–	0.503	–	0.25	–
5	0.25	1.2	0.169	0.208	0.69	1.26	0.206	0.198	0.74
1	0.5	0.48	–	0.5	–	0.501	–	0.5	–
2	0.5	0.959	–	0.5	–	1	0.00145	0.499	–
5	0.5	2.4	0.583	0.208	0.83	2.51	0.601	0.199	0.86
1	1.0	0.951	–	1	–	0.988	–	1	–
2	1.0	1.9	0.473	0.527	0.52	1.97	0.494	0.506	0.59
5	1.0	4.74	0.789	0.211	0.91	4.92	0.797	0.203	0.92

Table 4.2.: More network properties as in table 4.1, namely the Manning parameter ξ_M, the fraction of condensed counterions $1-\frac{1}{\xi_M}$, and the effective charge fraction f_{eff}, given for both good solvent (*left*) and close to the θ-point (*right*); a "–" for an entry signifies the absence of counterion condensation according to Manning, as the $\xi_M < 1$ in those cases renders $1-\frac{1}{\xi_M} < 0$ meaningless. The fraction of condensed counterions f_x is taken from the integrated counterion distributions (see appendix B) and given as a reference (for details see text).

The same condensation threshold is however predicted by the aforementioned Manning criterion as well, since only these parameters lead to $\xi_M > 1$ as laid out in table 4.2, therefore confirming the analogy drawn to stiff rods qualitatively. Quantitatively, however, the fraction of condensed counterions $1-\frac{1}{\xi_M}$, also given in table 4.2, is expected to be 0.17, 0.58, and 0.79 for the three charge fractions $f = 0.25$, 0.5, and 1.0, respectively, and is therefore underestimating the corresponding values obtained from the inflection point criterion [166], which relates the coordinates (R_M, f_x) where concave condensation curves change into the convex long-range behaviour to the Manning parameter ξ_M via $f_x = 1-\frac{1}{\xi_M}$. Although it is usually considered to be more accurate as it corresponds to an analytical solution in the limit of infinitely

long rods, it is at the same time not necessarily transferable to arbitrary geometries such as diamond-like network topologies. From there it follows that deriving f_{eff} from (4.11) does capture the correct trend for renormalizing Π_{C}, but might not correct (3.6) sufficiently for large coulombic couplings, *i.e.* too strong condensation effects.

This has been investigated in further detail in appendix B where for *all* parameters under consideration the integrated counterion distribution functions were analyzed and compared with the inflection point criterion, the Manning condensation charge renormalization, and the more refined criteria developed in section 3.2. As it turns out, the *spirit* of the inflection point criterion leads to the correct result, meaning that (R_{M}, f_x) itself does not reflect a suitable description for condensation effects, but it is a uniform mathematical argument, namely the point of maximum curvature, which indicates the y-value corresponding to the appropriate f_{eff}. This allows to continue this investigation using the simple charge renormalization argument to incorporate the effect of strong electrostatics in the following, leaving the exact value of f_{eff} rather ambiguous at the moment, with (4.11) nevertheless providing a good first approximation.

4.2.3. Balance in the pressure

One of the major advantages of computer simulations is the access to "microscopic" details of the investigated systems. Particularly in the case of far-reaching assumptions such as section 3.2.2 neglecting electrostatics entirely, it is beneficial to be able to actually compare the (theoretically) assumed behaviour to the (model) reality. Therefore, this section will investigate the contributions of counterions resp. gel to the overall pressure $\mathcal{P}$, starting with the assumption of the theory's validity, then carefully evaluating any discrepancies to its predictions from there. Since it is the balance in the pressure which essentially determines the swelling equilibrium of the hydrogel, a thorough understanding of how this balance is achieved and maintained will not only provide the necessary informations needed to arrive at a corrected theoretical description, but will also allow valuable insight into the actual physical mechanisms behind that process.

We will begin by introducing the respective components $\mathcal{P}$ is composed of, as by nature computer simulations cannot directly determine those macroscopic observables which in fact represent the result of multiple microscopic contributions; they are, however, capable to access precisely these microscopic details, allowing not only to construct the desired macroscopic quantity from there, but to investigate the underlying interplay between components, identifying leading contributions and evaluating possible cancellation taking place, as well. Measured according to (4.5), $\mathcal{P}$ contains the ideal components $\mathcal{P}_{\text{ideal}}^{\text{CI}}$ and $\mathcal{P}_{\text{ideal}}^{\text{monomers}}$ of counterions and monomers, respectively, their excluded volume interactions with themselves ($\mathcal{P}_{\text{LJ}}^{\text{CI}-\text{CI}}$ and $\mathcal{P}_{\text{LJ}}^{\text{monomers}}$) and with each other ($\mathcal{P}_{\text{LJ}}^{\text{CI}-\text{monomers}}$) from the Lennard-Jones interac-

tion (4.2), the total electrostatic pressure ($\mathcal{P}_{\ell_B}^{\mathrm{tot}}$) from the coulombic coupling, and the FENE-virial from the bonds ($\mathcal{P}_{\mathrm{FENE}}$) as in (4.1). Unfortunately, for principal reasons the long-ranged coulombic contribution $\mathcal{P}_{\ell_B}^{\mathrm{tot}}$ cannot be subdivided further into monomer-, counterion-, and crosscorrelated terms in a system with periodicity in all three dimensions without additional constraints. If the assumptions of section 3.2.2 are correct, this should not pose a problem, since then $\mathcal{P}_{\ell_B}^{\mathrm{tot}} \approx 0$, while from the ideal gas depiction for the counterions $\mathcal{P}_{\mathrm{LJ}}^{\mathrm{CI-CI}} \approx 0$ and $\mathcal{P}_{\mathrm{LJ}}^{\mathrm{CI-monomers}} \approx 0$ would follow[5]. Consequently, it seems reasonable to set $\mathcal{P}_{\mathrm{LJ}}^{\mathrm{CI}} = \mathcal{P}_{\mathrm{LJ}}^{\mathrm{CI-CI}} + \mathcal{P}_{\mathrm{LJ}}^{\mathrm{CI-monomers}}$, and to subdivide $\mathcal{P} = \mathcal{P}_{\mathrm{gas}} + \mathcal{P}_{\mathrm{gel}}$ along

$$\mathcal{P}_{\mathrm{gas}} = \mathcal{P}_{\mathrm{ideal}}^{\mathrm{CI}} + \mathcal{P}_{\mathrm{LJ}}^{\mathrm{CI}} + \mathcal{P}_{\ell_B}^{\mathrm{tot}} \tag{4.12a}$$

$$\mathcal{P}_{\mathrm{gel}} = \mathcal{P}_{\mathrm{ideal}}^{\mathrm{monomers}} + \mathcal{P}_{\mathrm{LJ}}^{\mathrm{monomers}} + \mathcal{P}_{\mathrm{FENE}} \tag{4.12b}$$

referring to $\mathcal{P}_{\mathrm{gas}}$ and $\mathcal{P}_{\mathrm{gel}}$ as "pressure of the gas" and "pressure of the gel".

Table 4.3 exemplifies this by providing the results of (4.5) for our simulation data at a chain length of $N_{\mathrm{m}} = 239$ monomers; the corresponding data for other $N_{\mathrm{m}} \neq 239$ is given in appendix A for comparison. Clearly, the leading contribution to $\mathcal{P}_{\mathrm{gas}}$ is the ideal pressure $\mathcal{P}_{\mathrm{ideal}}^{\mathrm{CI}}$ of the counterions which is up to three orders of magnitude larger than the other two components $\mathcal{P}_{\mathrm{LJ}}^{\mathrm{CI}}$ and $\mathcal{P}_{\ell_B}^{\mathrm{tot}}$. This however varies dramatically with the given parameters, as for increasing electrostatics the coulombic part of the pressure jumps up two orders of magnitude, even arriving at comparable numbers for *e.g.* $\ell_B = 1\sigma$ and $f = 1.0$ where $\mathcal{P}_{\mathrm{ideal}}^{\mathrm{CI}}$ is now only slightly larger than $\mathcal{P}_{\ell_B}^{\mathrm{tot}}$. Thereby, it might also seem surprising that the latter predominantly displays positive values, assuming $\mathcal{P}_{\ell_B}^{\mathrm{tot}} < 0$ only for the strong electrostatics limit of $\ell_B = 5\sigma$; one should bear in mind, though, that the Coulomb part of the pressure includes the contributions of *both* counterions *and* monomers, hence combining their mutual negative electrostatic interaction energy with the respective positive one from counterion-counterion and monomer-monomer repulsion can nevertheless lead to overall positive values. Particularly the latter has quite an impact on the overall result, as the charged monomers are forced into the energetically unfavorable constraint of a chain with a fixed maximum distance of b/f between neighbouring likewise charges, consequently providing a positive repelling "background" contribution which needs to be overcome by the negative attractive interaction energy between monomers and counterions. Our findings however indicate that the latter's significance overcomes the former's influence only for very strong electrostatics where system sizes are also smaller, as are mean distances between oppositely charged unit. This correlates with the onset of counterion condensation, which also leads to an increase in the excluded volume part $\mathcal{P}_{\mathrm{LJ}}^{\mathrm{CI}}$ of the pressure: Entirely negligible at first, with $\mathcal{P}_{\mathrm{ideal}}^{\mathrm{CI}}$ being 400 times larger for $\ell_B = 1\sigma$ and $f = 0.0625$, it eventually becomes *twice* as large as the ideal contribution for $\ell_B = 5\sigma$ and $f = 1.0$ when more than 80% of the counterions condense onto the network chains, dramatically increasing

[5] Since we want to check these assumptions, we are nevertheless considering the full contributions.

		$\mathcal{P}_{\text{gas}}$			$\mathcal{P}_{\text{gel}}$		
ℓ_B	f	$\mathcal{P}^{\text{CI}}_{\text{ideal}}$	$\mathcal{P}^{\text{CI}}_{\text{LJ}}$	$\mathcal{P}^{\text{tot}}_{\ell_B}$	$\mathcal{P}^{\text{monomers}}_{\text{ideal}}$	$\mathcal{P}^{\text{monomers}}_{\text{LJ}}$	$\mathcal{P}_{\text{FENE}}$
1	0.0625	$2.46{\cdot}10^{-5}$	$5.66{\cdot}10^{-8}$	$2.80{\cdot}10^{-7}$	$4.07{\cdot}10^{-4}$	$2.44{\cdot}10^{-3}$	$-2.89{\cdot}10^{-3}$
2	0.0625	$2.30{\cdot}10^{-5}$	$4.85{\cdot}10^{-8}$	$1.67{\cdot}10^{-6}$	$3.80{\cdot}10^{-4}$	$2.27{\cdot}10^{-3}$	$-2.70{\cdot}10^{-3}$
5	0.0625	$2.51{\cdot}10^{-5}$	$1.07{\cdot}10^{-6}$	$8.47{\cdot}10^{-7}$	$4.14{\cdot}10^{-4}$	$2.49{\cdot}10^{-3}$	$-2.94{\cdot}10^{-3}$
1	0.125	$2.55{\cdot}10^{-5}$	$2.58{\cdot}10^{-8}$	$1.96{\cdot}10^{-6}$	$2.07{\cdot}10^{-4}$	$1.23{\cdot}10^{-3}$	$-1.47{\cdot}10^{-3}$
2	0.125	$2.41{\cdot}10^{-5}$	$1.83{\cdot}10^{-7}$	$4.37{\cdot}10^{-6}$	$1.96{\cdot}10^{-4}$	$1.17{\cdot}10^{-3}$	$-1.39{\cdot}10^{-3}$
5	0.125	$3.06{\cdot}10^{-5}$	$3.72{\cdot}10^{-6}$	$-1.19{\cdot}10^{-6}$	$2.48{\cdot}10^{-4}$	$1.48{\cdot}10^{-3}$	$-1.76{\cdot}10^{-3}$
1	0.25	$2.65{\cdot}10^{-5}$	$1.73{\cdot}10^{-8}$	$3.41{\cdot}10^{-6}$	$1.07{\cdot}10^{-4}$	$6.25{\cdot}10^{-4}$	$-7.62{\cdot}10^{-4}$
2	0.25	$2.68{\cdot}10^{-5}$	$4.16{\cdot}10^{-7}$	$9.70{\cdot}10^{-6}$	$1.08{\cdot}10^{-4}$	$6.25{\cdot}10^{-4}$	$-7.70{\cdot}10^{-4}$
5	0.25	$4.43{\cdot}10^{-5}$	$1.55{\cdot}10^{-5}$	$-1.26{\cdot}10^{-5}$	$1.78{\cdot}10^{-4}$	$1.04{\cdot}10^{-3}$	$-1.27{\cdot}10^{-3}$
1	0.5	$3.09{\cdot}10^{-5}$	$5.20{\cdot}10^{-8}$	$1.07{\cdot}10^{-5}$	$6.19{\cdot}10^{-5}$	$3.41{\cdot}10^{-4}$	$-4.47{\cdot}10^{-4}$
2	0.5	$3.05{\cdot}10^{-5}$	$1.64{\cdot}10^{-6}$	$1.86{\cdot}10^{-5}$	$6.13{\cdot}10^{-5}$	$3.31{\cdot}10^{-4}$	$-4.45{\cdot}10^{-4}$
5	0.5	$6.90{\cdot}10^{-5}$	$6.10{\cdot}10^{-5}$	$-4.37{\cdot}10^{-5}$	$1.38{\cdot}10^{-4}$	$7.67{\cdot}10^{-4}$	$-9.96{\cdot}10^{-4}$
1	1.0	$3.80{\cdot}10^{-5}$	$3.94{\cdot}10^{-7}$	$3.04{\cdot}10^{-5}$	$3.80{\cdot}10^{-5}$	$1.78{\cdot}10^{-4}$	$-2.86{\cdot}10^{-4}$
2	1.0	$4.40{\cdot}10^{-5}$	$1.44{\cdot}10^{-5}$	$2.87{\cdot}10^{-5}$	$4.40{\cdot}10^{-5}$	$2.00{\cdot}10^{-4}$	$-3.34{\cdot}10^{-4}$
5	1.0	$1.09{\cdot}10^{-4}$	$2.17{\cdot}10^{-4}$	$-8.62{\cdot}10^{-5}$	$1.09{\cdot}10^{-4}$	$4.78{\cdot}10^{-4}$	$-8.30{\cdot}10^{-4}$

		$\mathcal{P}_{\text{gas}}$			$\mathcal{P}_{\text{gel}}$		
ℓ_B	f	$\mathcal{P}^{\text{CI}}_{\text{ideal}}$	$\mathcal{P}^{\text{CI}}_{\text{LJ}}$	$\mathcal{P}^{\text{tot}}_{\ell_B}$	$\mathcal{P}^{\text{monomers}}_{\text{ideal}}$	$\mathcal{P}^{\text{monomers}}_{\text{LJ}}$	$\mathcal{P}_{\text{FENE}}$
1	0.0625	$4.53{\cdot}10^{-5}$	$1.62{\cdot}10^{-7}$	$2.37{\cdot}10^{-6}$	$7.47{\cdot}10^{-4}$	$3.67{\cdot}10^{-3}$	$-4.48{\cdot}10^{-3}$
2	0.0625	$4.54{\cdot}10^{-5}$	$4.31{\cdot}10^{-7}$	$3.98{\cdot}10^{-6}$	$7.49{\cdot}10^{-4}$	$3.69{\cdot}10^{-3}$	$-4.49{\cdot}10^{-3}$
5	0.0625	$5.58{\cdot}10^{-5}$	$5.25{\cdot}10^{-6}$	$-4.41{\cdot}10^{-6}$	$9.23{\cdot}10^{-4}$	$4.54{\cdot}10^{-3}$	$-5.53{\cdot}10^{-3}$
1	0.125	$3.94{\cdot}10^{-5}$	$9.08{\cdot}10^{-8}$	$3.44{\cdot}10^{-6}$	$3.20{\cdot}10^{-4}$	$1.56{\cdot}10^{-3}$	$-1.92{\cdot}10^{-3}$
2	0.125	$3.76{\cdot}10^{-5}$	$2.72{\cdot}10^{-7}$	$8.23{\cdot}10^{-6}$	$3.05{\cdot}10^{-4}$	$1.48{\cdot}10^{-3}$	$-1.84{\cdot}10^{-3}$
5	0.125	$5.22{\cdot}10^{-5}$	$9.24{\cdot}10^{-6}$	$-6.95{\cdot}10^{-6}$	$4.23{\cdot}10^{-4}$	$2.06{\cdot}10^{-3}$	$-2.55{\cdot}10^{-3}$
1	0.25	$3.68{\cdot}10^{-5}$	$6.24{\cdot}10^{-8}$	$8.91{\cdot}10^{-6}$	$1.48{\cdot}10^{-4}$	$7.02{\cdot}10^{-4}$	$-8.97{\cdot}10^{-4}$
2	0.25	$3.56{\cdot}10^{-5}$	$7.06{\cdot}10^{-7}$	$1.40{\cdot}10^{-5}$	$1.43{\cdot}10^{-4}$	$6.74{\cdot}10^{-4}$	$-8.70{\cdot}10^{-4}$
5	0.25	$6.10{\cdot}10^{-5}$	$2.63{\cdot}10^{-5}$	$-2.13{\cdot}10^{-5}$	$2.46{\cdot}10^{-4}$	$1.17{\cdot}10^{-3}$	$-1.49{\cdot}10^{-3}$
1	0.5	$3.80{\cdot}10^{-5}$	$1.07{\cdot}10^{-7}$	$1.77{\cdot}10^{-5}$	$7.61{\cdot}10^{-5}$	$3.36{\cdot}10^{-4}$	$-4.69{\cdot}10^{-4}$
2	0.5	$3.77{\cdot}10^{-5}$	$2.97{\cdot}10^{-6}$	$2.27{\cdot}10^{-5}$	$7.56{\cdot}10^{-5}$	$3.27{\cdot}10^{-4}$	$-4.69{\cdot}10^{-4}$
5	0.5	$9.28{\cdot}10^{-5}$	$9.26{\cdot}10^{-5}$	$-6.19{\cdot}10^{-5}$	$1.86{\cdot}10^{-4}$	$8.30{\cdot}10^{-4}$	$-1.14{\cdot}10^{-3}$
1	1.0	$4.24{\cdot}10^{-5}$	$6.03{\cdot}10^{-7}$	$3.77{\cdot}10^{-5}$	$4.24{\cdot}10^{-5}$	$1.53{\cdot}10^{-4}$	$-2.78{\cdot}10^{-4}$
2	1.0	$5.23{\cdot}10^{-5}$	$1.97{\cdot}10^{-5}$	$3.28{\cdot}10^{-5}$	$5.23{\cdot}10^{-5}$	$1.85{\cdot}10^{-4}$	$-3.43{\cdot}10^{-4}$
5	1.0	$1.30{\cdot}10^{-4}$	$2.76{\cdot}10^{-4}$	$-1.01{\cdot}10^{-4}$	$1.30{\cdot}10^{-4}$	$4.28{\cdot}10^{-4}$	$-8.69{\cdot}10^{-4}$

Table 4.3.: Detailed pressure components for a system with $N_m = 239$ monomers per chain in good solvent (*top*) and close to the θ-point (*bottom*) for different values of Bjerrum length ℓ_B and charge fraction f, namely the contributions to the gas-like pressure $\mathcal{P}_{\text{gas}}$ (ideal part $\mathcal{P}^{\text{CI}}_{\text{ideal}}$, excluded volume $\mathcal{P}^{\text{CI}}_{\text{LJ}} = \mathcal{P}^{\text{CI-CI}}_{\text{LJ}} + \mathcal{P}^{\text{CI-monomers}}_{\text{LJ}}$, total electrostatic pressure $\mathcal{P}^{\text{tot}}_{\ell_B}$) and to the one of the gel $\mathcal{P}_{\text{gel}}$ (ideal part $\mathcal{P}^{\text{monomers}}_{\text{ideal}}$, excluded volume $\mathcal{P}^{\text{monomers}}_{\text{LJ}}$, bonded virial $\mathcal{P}_{\text{FENE}}$) for the fully charged gel at its swelling equilibrium volume V_{eq}.

the electrostaticly induced vicinity of counterions and monomers which is obviously merely balanced by the divergence in the Lennard-Jones potential for small spatial distances. This does not only impair the line of arguments in section 3.2.2 where neither electrostatics nor excluded volume was an issue, but it is also responsible for the deviation from ideal behaviour in the form factor $S(q)$ of figures 4.6 and 4.7 on short length scales (large q).

The elastic response of the network chains on the other hand, as expressed by the $\mathcal{P}_{\mathrm{FENE}}$-contribution to the pressure of the gel, appears as the undisputed leading term in $\mathcal{P}_{\mathrm{gel}}$, being 2.5 to 10 times larger than the ideal term $\mathcal{P}_{\mathrm{ideal}}^{\mathrm{monomers}}$, and keeping a smaller but distinct lead over the excluded volume contribution $\mathcal{P}_{\mathrm{LJ}}^{\mathrm{monomers}}$ between monomers. Its negative sign poses the main mechanism counteracting the swelling tendencies of the ideal and excluded volume terms, and even the electrostatic pressure component is balanced until the coulombic interaction becomes sufficiently strong. As a result, its behaviour mirrors that of $\mathcal{P}_{\ell_{\mathrm{B}}}^{\mathrm{tot}}$, *i.e.* $\mathcal{P}_{\mathrm{FENE}}$ gets larger with weaker electrostatics due to the influence of the osmotic pressure contribution $\mathcal{P}_{\mathrm{ideal}}^{\mathrm{CI}}$ of the counterions. Since a similar, albeit less pronounced, trend can be observed in $\mathcal{P}_{\mathrm{ideal}}^{\mathrm{monomers}}$, the effects of a smaller equilibrium volume V_{eq} and shorter chains R_{E}, which should both indicate less strongly stretched chains, are therefore overcompensated by the additional entropy of the monomers, resulting in more movement and increased stresses acting on the bonds. The matching behaviour of the excluded volume term $\mathcal{P}_{\mathrm{LJ}}^{\mathrm{monomers}}$ should thereby not come as a surprise, as figure 4.1 already depicted the very steep minimum in the next neighbour potential of bonded monomers for the chosen set of parameters; the usual fluctuations induced by the thermostat will consequently have each monomer contribute to both parts equally likely, until external effects come into play.

With full control over all aspects of the simulation system, its degrees of freedom with respect to the scaling arguments of section 3.2.2 can be reduced by deactivating electrostatics once the main investigations are complete, and re-running the $(N, V = V_{\mathrm{eq}}, T)$-ensemble in order to investigate the behaviour of a hydrogel under the same volume constraint but without the long-range coulombic interaction. Results are given in table 4.4, again for $N_{\mathrm{m}} = 239$ only, where $\mathring{\mathcal{P}}$ denotes the total pressure measured in such systems, and $\mathring{\Delta}\mathcal{P}_{\mathrm{gas}} = \mathcal{P}_{\mathrm{gas}} - \mathring{\mathcal{P}}_{\mathrm{gas}}$ and $\mathring{\Delta}\mathcal{P}_{\mathrm{gel}} = \mathcal{P}_{\mathrm{gel}} - \mathring{\mathcal{P}}_{\mathrm{gel}}$ give the difference between the gas-like resp. gel-like components of $\mathring{\mathcal{P}}$ to those from the same setup, but with electrostatics turned on (*i.e.* the $\mathcal{P}_{\mathrm{gas}}$ and $\mathcal{P}_{\mathrm{gel}}$ from table 4.3). The data confirms the arguments we have devised so far: In case of former weak electrostatics, switching them off results in a negligible non-zero total pressure $\mathring{\mathcal{P}}$ of as low as 10^{-8} which is already deep within the error bars. For charge fractions $f \geq 0.25$, $|\mathring{\mathcal{P}}|$ becomes significant, and we find the unexpected property that for $\ell_{\mathrm{B}} = 1\sigma$ and $\ell_{\mathrm{B}} = 2\sigma$ the hydrogel wants to *de*swell (since $\mathring{\mathcal{P}} < 0$) instead of indicating further volume increase through $\mathring{\mathcal{P}} > 0$ as in the case of $\ell_{\mathrm{B}} = 5\sigma$. This is remarkable because with the removal of electrostatic interactions the "counterions"

		good solvent ($\nu = 0.588$)			θ-solvent ($\nu = 0.50$)		
ℓ_B	f	$\mathring{\mathcal{P}}$	$\mathring{\Delta}\mathcal{P}_{gas}$	$\mathring{\Delta}\mathcal{P}_{gel}$	$\mathring{\mathcal{P}}$	$\mathring{\Delta}\mathcal{P}_{gas}$	$\mathring{\Delta}\mathcal{P}_{gel}$
1	0.0625	$1.84\cdot10^{-6}$	$3.21\cdot10^{-7}$	$-5.55\cdot10^{-6}$	$-2.02\cdot10^{-7}$	$2.47\cdot10^{-6}$	$-4.40\cdot10^{-6}$
2	0.0625	$6.00\cdot10^{-8}$	$1.71\cdot10^{-6}$	$-1.36\cdot10^{-5}$	$7.76\cdot10^{-6}$	$4.36\cdot10^{-6}$	$-2.12\cdot10^{-6}$
5	0.0625	$-1.84\cdot10^{-6}$	$1.85\cdot10^{-6}$	$1.84\cdot10^{-6}$	$8.92\cdot10^{-6}$	$7.00\cdot10^{-7}$	$-6.40\cdot10^{-6}$
1	0.125	$1.16\cdot10^{-6}$	$1.98\cdot10^{-6}$	$-6.76\cdot10^{-6}$	$2.72\cdot10^{-6}$	$3.51\cdot10^{-6}$	$-2.79\cdot10^{-6}$
2	0.125	$-2.56\cdot10^{-6}$	$4.54\cdot10^{-6}$	$6.36\cdot10^{-7}$	$-4.54\cdot10^{-6}$	$8.46\cdot10^{-6}$	$1.05\cdot10^{-7}$
5	0.125	$5.42\cdot10^{-6}$	$2.49\cdot10^{-6}$	$-4.46\cdot10^{-6}$	$1.04\cdot10^{-5}$	$2.10\cdot10^{-6}$	$-1.59\cdot10^{-5}$
1	0.25	$-4.97\cdot10^{-6}$	$3.42\cdot10^{-6}$	$3.33\cdot10^{-6}$	$-5.19\cdot10^{-6}$	$8.96\cdot10^{-6}$	$-1.78\cdot10^{-6}$
2	0.25	$-3.61\cdot10^{-6}$	$1.01\cdot10^{-5}$	$-5.04\cdot10^{-6}$	$-6.06\cdot10^{-6}$	$1.47\cdot10^{-5}$	$-8.67\cdot10^{-6}$
5	0.25	$1.83\cdot10^{-5}$	$2.73\cdot10^{-6}$	$-2.24\cdot10^{-5}$	$2.02\cdot10^{-5}$	$4.72\cdot10^{-6}$	$-2.19\cdot10^{-5}$
1	0.5	$-5.99\cdot10^{-6}$	$1.07\cdot10^{-5}$	$-5.92\cdot10^{-6}$	$-9.14\cdot10^{-6}$	$1.78\cdot10^{-5}$	$-8.31\cdot10^{-6}$
2	0.5	$-7.69\cdot10^{-6}$	$2.02\cdot10^{-5}$	$-1.27\cdot10^{-5}$	$-1.04\cdot10^{-5}$	$2.56\cdot10^{-5}$	$-1.59\cdot10^{-5}$
5	0.5	$3.70\cdot10^{-5}$	$1.66\cdot10^{-5}$	$-5.54\cdot10^{-5}$	$4.86\cdot10^{-5}$	$2.98\cdot10^{-5}$	$-7.80\cdot10^{-5}$
1	1.0	$-1.11\cdot10^{-5}$	$3.08\cdot10^{-5}$	$-2.04\cdot10^{-5}$	$-1.78\cdot10^{-5}$	$3.83\cdot10^{-5}$	$-2.09\cdot10^{-5}$
2	1.0	$-6.90\cdot10^{-7}$	$4.28\cdot10^{-5}$	$-4.37\cdot10^{-5}$	$-1.25\cdot10^{-6}$	$5.22\cdot10^{-5}$	$-5.12\cdot10^{-5}$
5	1.0	$7.80\cdot10^{-5}$	$1.29\cdot10^{-4}$	$-2.08\cdot10^{-4}$	$8.80\cdot10^{-5}$	$1.72\cdot10^{-4}$	$-2.63\cdot10^{-4}$

Table 4.4.: More detailed pressure components as in table 4.3 for the same system, but this time after switching off electrostatics, which changes the total pressure from zero to $\mathring{\mathcal{P}}$, and shifts $\mathcal{P}_{gas}$ and $\mathcal{P}_{gel}$ by $-\mathring{\Delta}\mathcal{P}_{gas}$ and $-\mathring{\Delta}\mathcal{P}_{gel}$, respectively, but keeping at the volume V_{eq} the charged gel had.

(now merely neutral spheres with excluded volume) will behave as the ideal gas the theory always assumed[6], which increases their osmotic pressure contribution if formerly condensed ions return into solution as $f_{eff} \mapsto f$; consequently, the shape of the hydrogel should either remain more or less unchanged (if electrostatics was weak and therefore negligible beforehand anyway) or its volume should respond to the additional osmotic pressure by *increasing* further. The systems with $\ell_B = 5\sigma$ and strong counterion condensation obey these arguments, while the intermediate cases of non-negligible but weak electrostatics appear to have an additional swelling mechanism which is caused by the coulombic interactions and stronger than the effective osmotic pressure of the counterions but independent of f_{eff}, as in the neutral case its disappearance weights stronger than the added entropy of the "counterions", causing the desired volume decrease; remembering that table 4.3 reported the similarly unusual $\mathcal{P}^{tot}_{\ell_B} > 0$ for the very same regime, which was only $2-3$ times smaller than $\mathcal{P}^{CI}_{ideal}$ (despite *including* the negative pressure contributions from the coulombic counterion-monomer-interaction), this mechanism is easily identified as

[6] The excluded volume of the neutral "counterions" is negligible regarding the low density, which is confirmed by the $\mathring{\mathcal{P}}^{CI}_{LJ}$ we measured.

the electrostatic self-energy of the chain, which repels likewise charged monomers, as we will demonstrate later on in (4.21).

Gas-like Contributions

Within the theoretical framework of sections 3.2.1 and 3.2.2 $\mathcal{P}_{\text{gas}}$ should equal Π_{C} from (3.1) (as well as $\mathcal{P}_{\text{gel}} \approx \Pi_{\text{E}}$ from (3.2) resp. (3.4) which will be analyzed in the next section 4.2.3). However, as the left part of figure 4.9 depicts, this cannot be confirmed even when renormalizing the effective amount of free counterions, substituting the f_{eff} from (4.11) as charge fraction into Π_{C}, *i.e.* using $\Pi_{\text{C}}^{\text{eff}}$. Not only that the Manning criterion predicts the wrong pressure, also using the value for f_{eff} obtained from the inflection point of the integrated counterion distribution in the simulations leads to strong deviations. While for all neutral systems the simple ideal gas term is (unsurprisingly) a very good description, the deviations of the actual $\mathcal{P}_{\text{gas}}$ from that picture become more pronounced for larger electrostatic interactions in the system.

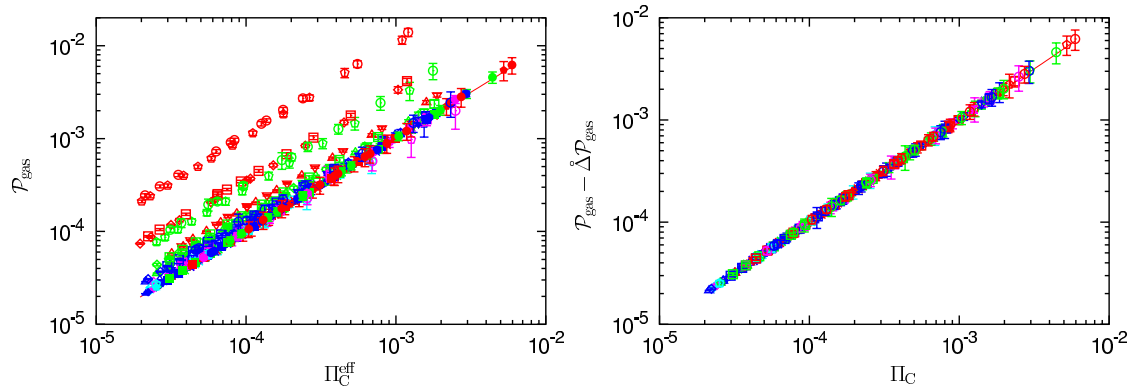

Figure 4.9.: Comparison of the pressure $\mathcal{P}_{\text{gas}}$ of the gas-like cloud of counterions to the assumed Π_{C} from the model in section 3.2.2. While the *left* plot displays significant deviations for larger f and ℓ_{B} although compensating for the occurrence of counterion condensation (see section 4.2.2) by using $\Pi_{\text{C}}^{\text{eff}}$, the *right* plot shows that those are entirely by the electrostatic effects contained in $\mathring{\Delta}\mathcal{P}_{\text{gas}}$, see text (same colour refers to same f, same symbol refers to same ℓ_{B}; for details see table S.1).

Without condensation this can almost entirely be attributed to the $\mathcal{P}_{\ell_{\text{B}}}^{\text{tot}}$-component, while on the other hand confined counterions significantly increase $\mathcal{P}_{\text{LJ}}^{\text{CI-monomers}}$, due to the contribution from excluded volume interaction *with* the monomers of the chains. The latter is thereby the dominating term in $\mathcal{P}_{\text{LJ}}^{\text{CI}}$ due to the low density of the networks in the swollen state which renders the remaining free counterions' $\mathcal{P}_{\text{LJ}}^{\text{CI-CI}}$ to be negligible, and allows an approximation like $\mathcal{P}_{\text{LJ}}^{\text{CI}} \approx \mathcal{P}_{\text{LJ}}^{\text{CI-monomers}} \gg \mathcal{P}_{\text{LJ}}^{\text{CI-CI}}$ which is confirmed by the left plot of figure 4.10

within the margin of error. Increasing up to three orders along the way (see table 4.3), $\mathcal{P}_{\mathrm{LJ}}^{\mathrm{CI}}$ eventually reaches the same order of magnitude as $\mathcal{P}_{\ell_{\mathrm{B}}}^{\mathrm{tot}}$ for strong coulombic coupling, where it it is even larger by a factor of 2. The right plot in figure 4.10 also shows that this is combined with some more finite size effects causing a rather dramatic increase of the ratio $\mathcal{P}_{\mathrm{LJ}}^{\mathrm{CI}}/\mathcal{P}_{\ell_{\mathrm{B}}}^{\mathrm{tot}}$ for intermediate electrostatics (*e.g.* $\ell_{\mathrm{B}} = 2\sigma$ and $f \geq 0.5$) and small chain lengths N_{m} where the excluded volume contribution becomes up to 4 times larger than the coulombic one, as shorter chains experience a stronger influence from the charge accumulation around the network nodes, having a much higher density with consequently more particle contacts. Since $\mathcal{P}_{\mathrm{LJ}}^{\mathrm{CI}}$ will always be positive, otherwise it would not represent *excluded* volume (see (2.37) and section 2.4), the sign of $\mathcal{P}_{\mathrm{LJ}}^{\mathrm{CI}}/\mathcal{P}_{\ell_{\mathrm{B}}}^{\mathrm{tot}}$ is given by the balance between repulsive and attractive coulombic contributions in $\mathcal{P}_{\ell_{\mathrm{B}}}^{\mathrm{tot}}$, which is why all the values for $\ell_{\mathrm{B}} = 5\sigma$ (and some very short and weakly charged chains) are plotted below zero.

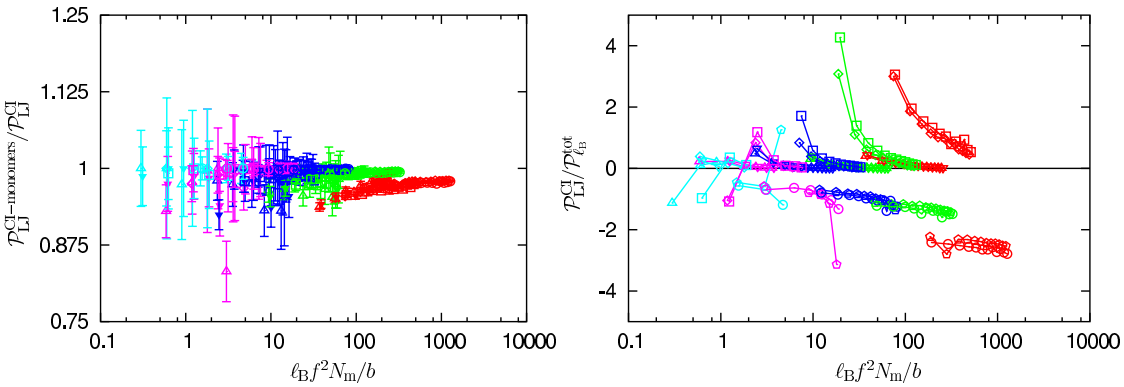

Figure 4.10.: Assessment of the leading pressure components in $\mathcal{P}_{\mathrm{gas}}$, namely $\mathcal{P}_{\mathrm{LJ}}^{\mathrm{CI}} \approx \mathcal{P}_{\mathrm{LJ}}^{\mathrm{CI-monomers}} \gg \mathcal{P}_{\mathrm{LJ}}^{\mathrm{CI-CI}}$ (*left*) and $\mathcal{P}_{\mathrm{LJ}}^{\mathrm{CI}}$ vs. $\mathcal{P}_{\ell_{\mathrm{B}}}^{\mathrm{tot}}$ (*right*); the lines are mere guides to the eye, connecting the data in the direction of increasing N_{m} (symbols as in figure 4.9).

Electrostatics consequently does play a non-negligible part in the swelling process of the hydrogel, more than simple charge renormalization can explain. Fortunately, all its direct and indirect contributions are by construction subsumed in $\mathring{\Delta}\mathcal{P}_{\mathrm{gas}}$, so that

$$\mathcal{P}_{\mathrm{gas}} - \mathring{\Delta}\mathcal{P}_{\mathrm{gas}} \approx \Pi_{\mathrm{C}} \tag{4.13}$$

provides a good starting point for nonetheless relating $\mathcal{P}_{\mathrm{gas}}$ to the ideal gas ansatz of the simple scaling theories. Shown to work in figure 4.9, this is at the same time confirming that such a simplified modeling of the counterions' effect is essentially only valid in a neutral (or likewise weakly charged) system.

What now remains to be found is of course an appropriate description for $\mathring{\Delta}\mathcal{P}_{\mathrm{gas}}$. As discussed, it is essentially dominated by the contributions from the electrostatics and (in case of condensation) the excluded volume interactions between counterions

and the chains,

$$\mathring{\Delta}\mathcal{P}_{\mathrm{gas}} \approx \mathcal{P}_{\ell_{\mathrm{B}}}^{\mathrm{tot}} + \mathcal{P}_{\mathrm{LJ}}^{\mathrm{CI-monomers}} > 0 \tag{4.14}$$

This pressure, according to (4.13) adding to the purely entropic Π_{C}, has to increase the strain on the network chains more than predicted for the neutral case, so that a similar $\mathring{\Delta}\mathcal{P}_{\mathrm{gel}} < 0$ is expected to be needed there for the comparison of $\mathcal{P}_{\mathrm{gel}}$ and Π_{E}; its interplay with $\mathring{\Delta}\mathcal{P}_{\mathrm{gas}}$ will be investigated in section 4.2.4.

Elastic Contributions

In section 3.2.2, the derivation of Π_{E} implied the validity of a Gaussian description for the force-elongation-relation between the extension R_{E} of a network chain and the resulting restoring force f_{E}, *i.e.* an only weak deformation of the tension blobs. Using the elastic free energy

$$\mathcal{F}_{\mathrm{E}} = 3(1-\nu)\left(\frac{R_{\mathrm{E}}}{N_{\mathrm{m}}^{\nu} b}\right)^{\frac{1}{1-\nu}} k_{\mathrm{B}}T = 3(1-\nu) N_{\mathrm{m}} k_{\mathrm{B}}T \left(\frac{R_{\mathrm{E}}}{R_{\max}}\right)^{\frac{1}{1-\nu}} \tag{4.15}$$

gives for that force and the corresponding pressure

$$\mathsf{f}_{\mathrm{E}} = \frac{\partial \mathcal{F}_{\mathrm{E}}}{\partial R_{\mathrm{E}}} \quad \Rightarrow \quad \frac{\mathsf{f}_{\mathrm{E}} b}{k_{\mathrm{B}}T} = 3\left(\frac{R_{\mathrm{E}}}{R_{\max}}\right)^{\frac{\nu}{1-\nu}} \tag{4.16a}$$

$$\Pi_{\mathrm{E}} = -\frac{\partial \mathcal{F}_{\mathrm{E}}}{\partial V} \quad \Rightarrow \quad \Pi_{\mathrm{E}} = -\frac{k_{\mathrm{B}}T}{R_{\mathrm{E}}^3}\left(\frac{R_{\mathrm{E}}}{N_{\mathrm{m}}^{\nu} b}\right)^{\frac{1}{1-\nu}} = -\frac{N_{\mathrm{m}}}{R_{\mathrm{E}}^3} k_{\mathrm{B}}T \left(\frac{R_{\mathrm{E}}}{R_{\max}}\right)^{\frac{1}{1-\nu}} \tag{4.16b}$$

with $R_{\max} = N_{\mathrm{m}} b$ and (4.16b) equaling the Π_{E} used in section 3.2.2.

Real chains cannot extend beyond $R_{\max}$ without breaking. From (3.6) it follows that therefore the charge fraction, more precisely $f^{1-\nu}$, has to be significantly smaller than 1, *i.e.* that the chains may not be too strongly charged for the scaling law to be applicable. Although the charge renormalization from section 4.2.2 allows to treat systems with very strong electrostatics in that limit, too, because their pronounced counterion condensation will lead to a small enough f_{eff}, an intermediate regime remains which is characterized by a large amount of counterions $fN_{\mathrm{m}} \approx N_{\mathrm{m}}$ per chain but low electrostatics ($\xi_{\mathrm{M}} < 1$). Here, the finite extensibility of the network chains causes the restoring force f_{E} to deviate from the ideal behaviour of (4.16a). Several models exist [156] to describe such a divergence, depending on the physical characteristics of the polymer: Introduced in section 2.2, the *freely jointed chain* (FJC) assumes, for example, that each bond between neighbouring monomers has the same length b, and no correlations between the directions of different bond vectors exist; while $R_{\max}$ is then the maximum end-to-end distance, more elongated conformations become less likely to occur, leading to the divergence in the restoring force f_{E} which was derived in section 2.3 and is given by (2.31) and (2.33) for large

$R_\mathrm{E} \to R_\mathrm{max}$, *i.e.*

$$\frac{\mathsf{f}_\mathrm{E} b}{k_\mathrm{B}T} = \mathcal{L}^{-1}\left(\frac{R_\mathrm{E}}{R_\mathrm{max}}\right) \sim \left(1 - \left(\frac{R_\mathrm{E}}{R_\mathrm{max}}\right)^1\right)^{-1}$$

with $\mathcal{L}^{-1}(\lambda)$ being the inverse of the Langevin function $\mathcal{L}(\lambda) = \coth(\lambda) - 1/\lambda$ from (2.32). The *worm-like chain* (WLC) additionally fixes all bond angles at very small values, hence being a good model for very stiff polymers; here the divergence in f_E shifts to

$$\frac{\mathsf{f}_\mathrm{E} b}{k_\mathrm{B}T} \sim \frac{1}{2}\left(1 - \left(\frac{R_\mathrm{E}}{R_\mathrm{max}}\right)^1\right)^{-2}$$

for $R_\mathrm{E} \to R_\mathrm{max}$, according to (2.35). A visualization of these divergences and their connection to a Gaussian chain was given in the center panel of figure 2.5, even though it was based on the behaviour of ideal chains.

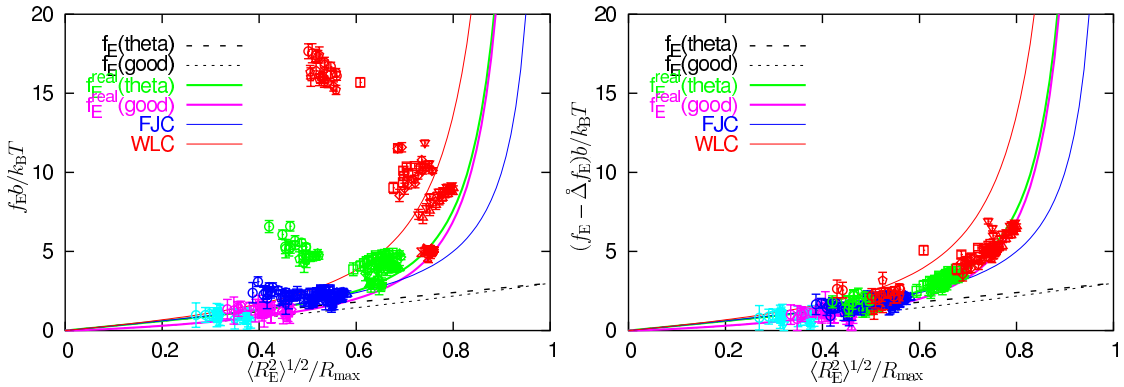

Figure 4.11.: Network restoring force f_E measured from the elastic contribution to the pressure, the excluded volume interaction between the monomers, and the ideal component, as a function of the average end-to-end-distance normalized by the maximum elongation R_max of a network chain; as reference the force-extension relation for Gaussian chains (f_E), for freely jointed chains (FJC) and for worm-like chains (WLC) are given as well as the model fit ($\mathsf{f}_\mathrm{E}^\mathrm{real}$). The *right* plot also compensates for the inner chain repulsion $\mathring{\Delta} f_\mathrm{E}$ due to the electrostatics, see text (same symbols as in figure 4.9).

Figure 4.11 now compares those models to the network restoring force $f_\mathrm{E} = -3R_\mathrm{E}^2 \mathcal{P}_\mathrm{gel}$ measured in the simulations, which consists of the elastic contribution of the bonds between the monomers, their respective excluded volume interaction, and the ideal pressure of the monomers, plotted as a function of the elongation of the chains relative to R_max. For small extensions, no deviation from (4.16a) is expected and observed, while longer chains clearly exhibit the announced divergence once the electrostaticly induced (absolute) pressure increase $\mathring{\Delta}\mathcal{P}_\mathrm{gel}$, leading to the additional force component $\mathring{\Delta} f_\mathrm{E} = f_\mathrm{E} - \mathring{f}_\mathrm{E}$, has been removed (right plot of figure 4.11); $\mathring{f}_\mathrm{E}$ is

thereby once again an observable measured without electrostatics in an otherwise unchanged system. Similarly to $\mathcal{P}_{\mathrm{gas}}$, there is a superposition of "neutral" effects also present without coulomb interactions, and "charged" ones to be investigated later on. Though neither the FJC nor the WLC lead to good agreement with the divergence behaviour of the hydrogel, which is not entirely unexpected since its network chains have neither complete rotational freedom (due to the excluded volume) as a FJC nor intrinsic stiffness as a WLC, we can use a similar functional form, the generalized finite extensibility divergence

$$\frac{\mathsf{f}_{\mathrm{E}} b}{k_{\mathrm{B}} T} \sim \left(1 - \left(\frac{R_{\mathrm{E}}}{R_{\max}}\right)^{\beta}\right)^{-\gamma} \tag{4.17}$$

with $\beta = 3.7$ and $\gamma = 2$ as exponents, and f_{E} given by (4.16a). As shown in figure 4.11, the measured f_{E} then corresponds nicely to usual force-extension-relations for real chains, and the "neutralized" pressure of the gel is therefore describable by

$$\mathcal{P}_{\mathrm{gel}} - \mathring{\Delta}\mathcal{P}_{\mathrm{gel}} \approx \Pi_{\mathrm{E}}^{\mathrm{real}} = \Pi_{\mathrm{E}} \cdot \left(1 - \left(\frac{R_{\mathrm{E}}}{R_{\max}}\right)^{\beta}\right)^{-\gamma} \tag{4.18}$$

and $\Pi_{\mathrm{E}} < 0$ given by (4.16b).

Again, electrostatics decreases this further by a $\mathring{\Delta}\mathcal{P}_{\mathrm{gel}} < 0$ getting more pronounced as the coulombic coupling is increased (see left part of figure 4.11), although technically $\mathcal{P}_{\mathrm{gel}}$ does not contain any direct charged contributions. Obviously, the (compared to a neutral network) additional pressure introduced into the system by $\mathring{\Delta}\mathcal{P}_{\mathrm{gas}} > 0$ leads to a likewise but opposite response from the gel, stretching the chains even further ($\mathcal{P}_{\mathrm{FENE}}$ goes down) without significant changes in the excluded volume ($\mathcal{P}_{\mathrm{LJ}}^{\mathrm{monomers}}$) or the ideal ($\mathcal{P}_{\mathrm{ideal}}^{\mathrm{monomers}}$) contribution. Why then the strong deviation of f_{E} from f_{E} in the first place, when we are relating the restoring force to the chains' elongation? This is due to the intra-chain repulsion of the charged monomers which increases their bond length b, causing a rather large increment in U_{FENE}, while models for f_{E}'s divergence usually assume the bond length itself to be unaffected by the force extending the chain to R_{E} (remember that for measuring f_{E} and $\mathring{f}_{\mathrm{E}}$ the volume V_{eq} and, due to the periodic boundary conditions, therefore R_{E} remains the same in both cases). Clearly having its foundation in the electrostatics, it should consequently balance $\mathring{\Delta}\mathcal{P}_{\mathrm{gas}}$, more complex effects such as counterion condensation notwithstanding.

4.2.4. Cancellation and Scaling

The results presented in the previous subsections 4.2.3 and 4.2.3 introduced the necessary adjustments to the simple model from section 3.2.2, which turned out to essentially hold for neutral(ized) systems only, while at the same time requiring

adjustment for the finite extensibility of the network chains not accounted for in the original Gaussian approach. It now remains to be investigated which mechanisms govern the electrostatic and electrostaticly induced changes $\mathring{\Delta}\mathcal{P}_{\mathrm{gas}}$ and $\mathring{\Delta}\mathcal{P}_{\mathrm{gel}}$ to the pressure of the (counterion) gas and the (polymer) gel, respectively.

Firstly, it is useful to note that by construction

$$\mathring{\Delta}\mathcal{P}_{\mathrm{gas}} + \mathring{\Delta}\mathcal{P}_{\mathrm{gel}} = (\mathcal{P}_{\mathrm{gas}} - \mathring{\mathcal{P}}_{\mathrm{gas}}) + (\mathcal{P}_{\mathrm{gel}} - \mathring{\mathcal{P}}_{\mathrm{gel}}) = -\mathring{\mathcal{P}} \tag{4.19}$$

because of the equilibrium condition $\mathcal{P}_{\mathrm{gas}} + \mathcal{P}_{\mathrm{gel}} = \mathcal{P} = 0$ ensured by our $(N, p = 0, T)$-algorithm[7]. For weakly charged systems one would expect electrostatic effects and therewith $\mathring{\mathcal{P}}$ to be negligible, which would in turn lead to a *cancellation* of the additional pressure components discussed before. For strongly charged systems where counterion condensation occurs one would expect $\mathring{\mathcal{P}}$ to reflect the amount of renormalized charges along *e.g.* $\mathring{\mathcal{P}} = k_{\mathrm{B}}T(f - f_{\mathrm{eff}})N_{\mathrm{m}}/R_{\mathrm{E}}^3$ because switching off coulombic interactions for measuring $\mathring{\mathcal{P}}$ should return the (now neutral) counterions into their "gaseous state" and thereby re-introducing additional osmotic pressure previously removed by the condensation; this presumes $\mathring{\mathcal{P}} > 0$, *i.e.* the corresponding $\ell_{\mathrm{B}} = 0\sigma$-system with the same number of counterions N_{CI} to reach a larger equilibrium swelling volume V_{eq}. In place of the Manning criterion (4.11), it is then possible to derive the effective charge fraction f_{eff} from $\mathring{\mathcal{P}}$ by

$$f_{\mathrm{eff}} = \frac{\left[(N_{\mathrm{CI}} - N_{\mathrm{nodes}}) - \frac{\mathring{\mathcal{P}}V_{\mathrm{eq}}}{k_{\mathrm{B}}T}\right]/N_{\mathrm{p}}}{N_{\mathrm{m}}} \tag{4.20}$$

which is plotted in figure 4.12 for the limit of strong electrostatics (where $\mathring{\mathcal{P}} > 0$, as discussed in section 4.2.3). Though certainly not a perfect match with Manning's prediction, which had been for an infinitely long real rod anyway, it is nevertheless a convincingly good agreement for $f \leq 0.125$ and, in case of sufficiently long chains, for $f \geq 0.5$ as well. The remaining $f = 0.25$ fails to agree with the predicted $f_{\mathrm{eff}} \approx 0.21$, but rather assumes values around 0.13, which agrees with the corresponding counterion distribution function in figure 4.8 which displayed more than the predicted $\sim 17\%$ of all counterions concentrated close to the chains.

For systems with a very small amount of counterions N_{CI} and weak or very strong electrostatic coupling, both aforementioned assessments of unperturbed behaviour in the former and Manning-like condensation in the latter case turn out to be verified by our data. There is, however, the aforementioned intermediate regime where $\mathring{\mathcal{P}} < 0$, *i.e.* the corresponding $\ell_{\mathrm{B}} = 0\sigma$-system is *smaller* than its charged counterpart, as can be exemplarily seen in table 4.4 particularly for the results of $\ell_{\mathrm{B}} = 1\sigma$ and $\ell_{\mathrm{B}} = 2\sigma$.

[7] Any deviation from (4.19), *e.g.* in the data of table 4.4, simply reflects an uncompensated $\mathcal{P}$ due to the fact that the random noise added to the (N, p, T)-algorithm systematically prevents the instantaneous pressure from (4.5) to ever be *exactly* zero; the proximity of $\mathcal{P}$ to the desired P is therefore an indication for the margin of error in V_{eq} (for details see section 4.1).

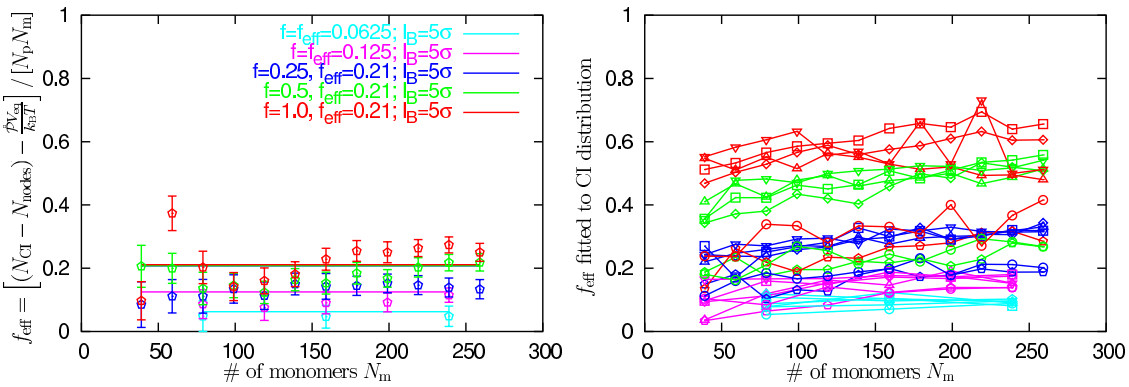

Figure 4.12.: The effective charge fraction f_{eff} as obtained via (4.20) from the pressure difference $\mathring{\mathcal{P}}$ for strong electrostatics (*left*), where the *straight lines* indicate the prediction of the Manning criterion (4.11), and from fitting f_{eff} to the integrated counterion distributions in appendix B (*right*), where the lines are once more mere guides to the eye, connecting the data in the direction of increasing N_{m} (colours and symbols as in figure 4.9; see table S.1).

Disabling electrostatics therefore leads to two possible effects: The (now neutral) system will either try to expand further (when $\mathring{\mathcal{P}} > 0$) or shrink in size (when $\mathring{\mathcal{P}} < 0$). Such a behaviour was not observed by Schneider and Linse [58] despite their $\ell_{\mathrm{B}} = 1.75241\sigma$ falling into the intermediate range, too, because they were only looking at very small systems with $N_{\mathrm{m}} = 20$ monomers per chain – and for these we also get $\mathring{\mathcal{P}} > 0$ (note again that table 4.3 only displays the data for $N_{\mathrm{m}} = 239$); this changes with increasing N_{m}, as the charge accumulation around the network nodes becomes less and less, the charge separation *on* the chains more and more influential.

Looking at the total electrostatic pressure $\mathcal{P}^{\mathrm{tot}}_{\ell_{\mathrm{B}}}$ as a function of the coulombic strength $\ell_{\mathrm{B}} f^2 N_{\mathrm{m}}/b$, plotted in figure 4.13 without and with rescaling by the ideal contribution $\mathcal{P}^{\mathrm{CI}}_{\mathrm{ideal}}$ of the counterions, the observation of a negative $\mathring{\mathcal{P}}$ becomes understandable, because for the parameter sets in question $\mathcal{P}^{\mathrm{tot}}_{\ell_{\mathrm{B}}}$ is actually *positive*, something one would not expect for *e.g.* a polyelectrolyte solution, while larger ℓ_{B} as well as smaller fN_{m} renders it negative again. The reason is to be found in the network topology under periodic boundary conditions: It forces the charges on the chains into energetically unfavorable positions and keeps them there, an effect more pronounced when many strongly interacting bare charges have only a small charge separation b/f (along the contour length) resp. $R_{\mathrm{E}}/(fN_{\mathrm{m}})$ (along the chain extension) to each other. Larger ℓ_{B}, *i.e.* stronger coulombic coupling, increases the charge correlations and also the amount of counterion condensation, which reduces the number of *effective* charges and increases their respective distance, all leading back to a $\mathcal{P}^{\mathrm{tot}}_{\ell_{\mathrm{B}}} < 0$. A smaller fN_{m} similarly separates the ionized monomers further, while fewer N_{m} lead to a stronger domination of the charge accumulation

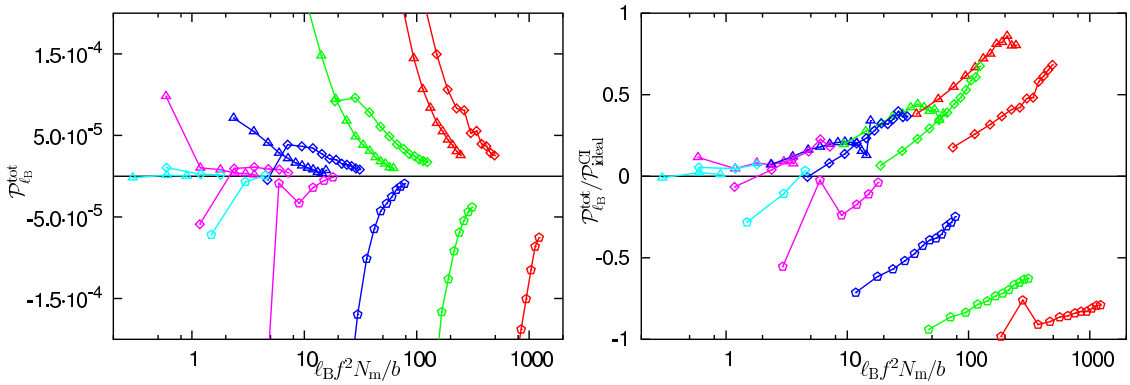

Figure 4.13.: The electrostatic contribution $\mathcal{P}^{\mathrm{tot}}_{\ell_\mathrm{B}}$ to the pressure, plotted around zero (*left*) and rescaled by $\mathcal{P}^{\mathrm{CI}}_{\mathrm{ideal}}$ (*right*), illustrating the competing effects in the pressure balance (see text). For simplicity, only the good solvent data is plotted, because no qualitative changes occur close to the θ-point. Again, the lines are mere guides to the eye, connecting the data in the direction of increasing N_m (symbols as in figure 4.9; see table S.1).

around the nodes, both ensuring $\mathcal{P}^{\mathrm{tot}}_{\ell_\mathrm{B}} < 0$ as well. In between there is a maximum in $\mathcal{P}^{\mathrm{tot}}_{\ell_\mathrm{B}}(\ell_\mathrm{B} f^2 N_\mathrm{m}/b)$ at positive values for large enough N_m, fN_m, and small enough ℓ_B. With $0 < \mathcal{P}^{\mathrm{CI-monomers}}_{\mathrm{LJ}} \lesssim -\mathring{\Delta}\mathcal{P}_{\mathrm{gel}}$ it follows from (4.14) and (4.19) that, unless $\mathring{\mathcal{P}} \approx 0$, for $\mathcal{P}^{\mathrm{tot}}_{\ell_\mathrm{B}} < 0$ the gas component $\mathring{\Delta}\mathcal{P}_{\mathrm{gas}}$ is smaller than $-\mathring{\Delta}\mathcal{P}_{\mathrm{gel}}$ ($\Rightarrow \mathring{\mathcal{P}} > 0$), and vice versa for $\mathcal{P}^{\mathrm{tot}}_{\ell_\mathrm{B}} > 0$ ($\Rightarrow \mathring{\mathcal{P}} < 0$). This explains why, depending on the chosen parameter regime, expansion or shrinking of the neutralized gel can be observed.

Considering the changes $\mathring{\Delta}\mathcal{P}_{\mathrm{gel}}$ in the pressure of the gel due to the coulombic interactions in the system, only effects on the network strands are measured, without any (direct) contributions from the counterions. It therefore has to correspond to the electrostatic self-energy [33]

$$\mathring{\Delta}\mathcal{P}_{\mathrm{gel}} \approx -\Pi_{\ell_\mathrm{B}} = -k_\mathrm{B}T\frac{\ell_\mathrm{B}(fN_\mathrm{m})^2}{3R_\mathrm{E}^4} \tag{4.21}$$

of a polyelectrolyte chain of the same length R_E, allowing to model $\mathcal{P}_{\mathrm{gel}}$ using (4.18) as

$$\mathcal{P}_{\mathrm{gel}} \approx \Pi_\mathrm{E}^{\mathrm{real}} - \Pi_{\ell_\mathrm{B}} \tag{4.22}$$

which is supported by the lower right inset of figure 4.14. Due to (4.19) this means in turn that from (4.13) and (4.21)

$$\mathcal{P}_{\mathrm{gas}} + \mathring{\mathcal{P}} \approx (\mathring{\Delta}\mathcal{P}_{\mathrm{gas}} + \Pi_\mathrm{C}) + (-\mathring{\Delta}\mathcal{P}_{\mathrm{gas}} - \mathring{\Delta}\mathcal{P}_{\mathrm{gel}}) = \Pi_\mathrm{C} - \mathring{\Delta}\mathcal{P}_{\mathrm{gel}} \approx \Pi_\mathrm{C} + \Pi_{\ell_\mathrm{B}}$$

follows, while the previous discussion of the interplay between the multiple electrostatically influenced components in $\mathcal{P}_{\mathrm{gas}}$ and $\mathcal{P}_{\mathrm{gel}}$, particularly regarding the charge

renormalization and the deviation from Gaussian behaviour of the overstretched network chains, leads to $\mathring{\mathcal{P}} \approx (\Pi_{\mathrm{C}} - \Pi_{\mathrm{C}}^{\mathrm{eff}}) - (\Pi_{\mathrm{E}} - \Pi_{\mathrm{E}}^{\mathrm{real}})$. Subsumed into one expression, the pressure of the gas can be written as

$$\mathcal{P}_{\mathrm{gas}} \approx (\Pi_{\mathrm{C}}^{\mathrm{eff}} + \Pi_{\ell_{\mathrm{B}}}) - (\Pi_{\mathrm{E}}^{\mathrm{real}} - \Pi_{\mathrm{E}}) \tag{4.23}$$

which is confirmed by the upper left inset of figure 4.14.

Once more reminding of our $(N, p = 0, T)$-algorithm, these partial pressure balances in (4.22) and (4.23) now provide access to the global equilibrium swelling behaviour of the hydrogel:

$$\begin{aligned} 0 = \mathcal{P} &= \mathcal{P}_{\mathrm{gas}} + \mathcal{P}_{\mathrm{gel}} \\ &\approx [(\Pi_{\mathrm{C}}^{\mathrm{eff}} + \Pi_{\ell_{\mathrm{B}}}) - (\Pi_{\mathrm{E}}^{\mathrm{real}} - \Pi_{\mathrm{E}})] + [\Pi_{\mathrm{E}}^{\mathrm{real}} - \Pi_{\ell_{\mathrm{B}}}] \\ &= \Pi_{\mathrm{C}}^{\mathrm{eff}} + \Pi_{\mathrm{E}} \end{aligned} \tag{4.24}$$

This does not only imply again the *cancellation* of the direct electrostatic effects behind $\Pi_{\ell_{\mathrm{B}}}$, but also the removal of the extensively discussed divergence in (4.18) from the total pressure of the system. In fact, it even brings us close to the original pressure balance, such that with the definitions of section 3.2.2 and (4.16b) the scaling prediction for R_{E} follows

$$\begin{aligned} 0 &= k_{\mathrm{B}}T \frac{f_{\mathrm{eff}} N_{\mathrm{m}}}{R_{\mathrm{E}}^3} - k_{\mathrm{B}}T \frac{N_{\mathrm{m}}}{R_{\mathrm{E}}^3} \left(\frac{R_{\mathrm{E}}}{R_{\mathrm{max}}} \right)^{\frac{1}{1-\nu}} \\ \Rightarrow R_{\mathrm{E}} &= N_{\mathrm{m}} b \cdot f_{\mathrm{eff}}^{1-\nu} \end{aligned} \tag{4.25}$$

with a good approximation for the effective charge fraction f_{eff} given by (4.11), as we have previously shown [62, 63].

Figure 4.14 finally summarizes our results by plotting (4.25) for all the investigated systems, including the neutral ones with $\ell_{\mathrm{B}} = 0\sigma$. From the good agreement between simulation data and theory also in the insets re-confirming the modeling of the gel-like pressure $\mathcal{P}_{\mathrm{gel}}$ and the gas-like $\mathcal{P}_{\mathrm{gas}}$ in (4.23) and (4.22), respectively, the developed scaling prediction seems to be correct despite its simpleness. Surprising at first, this explains why previous studies could safely assume coulombic interactions to be negligibly small – as we showed they are not, but since their components cancel each other out globally, the final shape of the network will not *explicitely* depend on electrostatic parameters (while still displaying an implicit dependency *i.e.* through the effective charge fraction f_{eff}). The individual network strands, however, do appear differently for real neutral systems (*i.e.* those with $\ell_{\mathrm{B}} = 0\sigma$) and charged ones, because all the aforementioned mechanisms will act here locally, pushing the charges on the chains apart, condensing the counterions such that a strong contact term arises ($\rightarrow \mathcal{P}_{\mathrm{LJ}}^{\mathrm{CI-monomers}}$).

The crucial factor in (4.25) remains the determination of the effective charge fraction f_{eff}. While the Manning criterion used for deriving (4.11) is a good starting

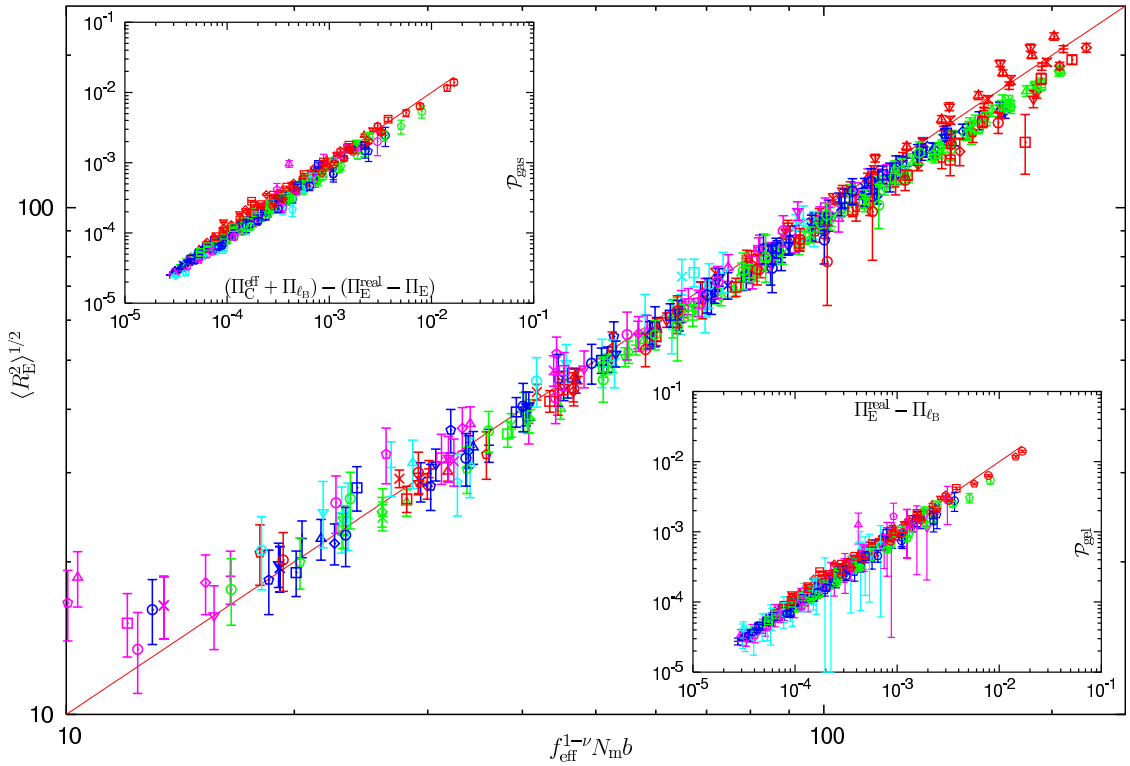

Figure 4.14.: The equilibrium swelling behaviour of salt-free polyelectrolyte networks in good solvent and close to the θ-point following the scaling law (4.25) successfully. The two insets provide confirmation for modeling the individual pressure components $\mathcal{P}_{\rm gel}$ (*lower right*) and $\mathcal{P}_{\rm gas}$ (*upper left*) by (4.23) and (4.22), respectively, leading to the pressure balance $\mathcal{P} = 0$ from where the scaling prediction is then derived (symbols as in figure 4.9).

point, it is far from being perfect, as the comparison with the inflection point criterion in section 4.2.2 and table 4.2 showed. The comparison with $\mathring{\mathcal{P}}$ from the neutral systems already yielded some improvement, as the left plot in figure 4.12 showed, besides not being very useful for practical applications (where one cannot easily "turn off electrostatics") it was however only applicable to the strong condensation regime where $\mathring{\mathcal{P}} > 0$. The right plot in figure 4.12 followed an alternative path of treating $f_{\rm eff}$ as a fitting parameter which resulted in reasonable values for $f_{\rm eff}$ over the entire range of parameters, and agreed with the counterions' distribution functions as well, although it would have been preferable if the amount of effective charges could have been directly determined from the system properties, too. Since it essentially comes down to precisely predicting the distributions of the counterions in the system, such as those in figure 4.8, we refer to the numerous literature on this challenging topic (see for example [166] and references therein). Continuing along this path, sections 3.2 and 3.3 explored possible approaches based on solving the

Poisson-Boltzmann equation for a simplified model system, developing techniques for tackling the charge renormalization in polyelectrolyte networks.

4.3. On the validity of FRH

In the introduction it was outlined that although most of the commonly accepted theories on the swelling of polyelectrolyte networks employ the FRH by simply adding the different parts of the free energy (resp. their corresponding pressure components) to obtain the equilibrium behaviour, this is not expected to be true in general, and cross terms between them have to exist. While we found in $\mathring{\Delta}\mathcal{P}_{\mathrm{gas}}$ and $\Pi_{\ell_{\mathrm{B}}}$ such contributions which were attributed to the interplay of charge repulsion on the chains and electrostatic interaction with the condensed counterions, it turned out that they canceled globally; even more, our derivation of the final scaling prediction (4.25) was despite all modifications essentially still based on the FRH.

To assess this seeming contradiction, it is plausible to compare our data to non-FRH theories. In [45] there was *e.g.* the average end-to-end distance of the chains connecting two neighbouring endlink-points in the network derived to

$$\langle R_{\mathrm{E}}^2 \rangle \propto \frac{N_{\mathrm{m}}^2 \ell_{\mathrm{B}}}{\kappa} \tag{4.26}$$

where $\kappa = \sqrt{4\pi\ell_{\mathrm{B}} f N_{\mathrm{m}}/R_{\mathrm{E}}^3}$ was the appropriate inverse Debye screening length; special emphasis was put on the fact that this prediction is made for the small κ-regime, *i.e.* neither the strong ($\kappa R_{\mathrm{E}} \gg 1$) nor the weak ($\kappa R_{\mathrm{E}} \ll 1$) screening limit – which is where our data was taken ($1 \lesssim \kappa R_{\mathrm{E}} \lesssim 12$, see left plot in figure 4.15), too. But the corresponding right plot in figure 4.15 shows significant and systematic differences from the data obtained in the simulations, without the possibility to relate those to condensation or effects of finite extensibility.

As a small remark it might be added that the independence of κR_{E} of the chain length N_{m}, displayed on the left side of figure 4.15, is not really surprising, since from the definition of the Debye screening length it follows that

$$\begin{aligned} \kappa R_{\mathrm{E}} &= \sqrt{4\pi\ell_{\mathrm{B}} \frac{f N_{\mathrm{m}}}{R_{\mathrm{E}}^3}} \cdot R_{\mathrm{E}} = \sqrt{4\pi\ell_{\mathrm{B}} \frac{f N_{\mathrm{m}}}{R_{\mathrm{E}}}} \\ &\cong \sqrt{4\pi\ell_{\mathrm{B}} \frac{f N_{\mathrm{m}}}{N_{\mathrm{m}} b \cdot f_{\mathrm{eff}}^{1-\nu}}} \\ &= \sqrt{4\pi \frac{\ell_{\mathrm{B}}}{b} \frac{f}{f_{\mathrm{eff}}^{1-\nu}}} \end{aligned}$$

will not contain N_{m} explicitely if the validity of (4.25) is used; it might however be employed as another measure to determine the effective charge fraction f_{eff}, as previously discussed.

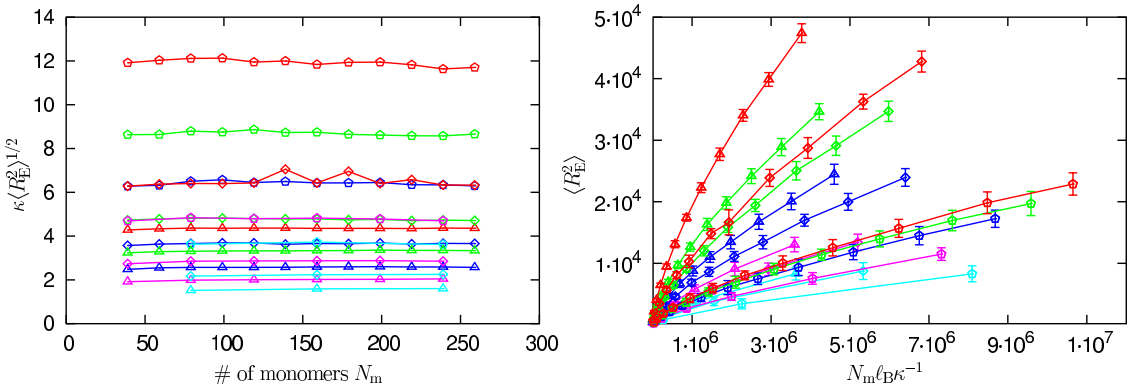

Figure 4.15.: *Left:* The product of screening length κ and end-to-end distance R_E as a function of the chain length N_m. *Right:* The non-FRH based scaling prediction (4.26) compared to the measured data, showing fundamental non-agreement even in the regime of low electrostatics and Gaussian elongation of the chain. Once again, the results close to the θ-point have been omitted from these plots as they show the same qualitative behaviour (same symbols as in figure 4.9; see table S.1 as a reference).

Without assessing systems in poor solvent or with added salt, it can therefore only be deduced that the violation of the FRH does not play a significant role in the description of salt-free model hydrogels and their behaviour at swelling equilibrium, at least not the way it was assumed in previous works [43–45, 181].

4.4. Conclusions and Outlook

Relating the theoretical considerations from chapter 3 to the numerical solution of an appropriate model, we investigated the results of large-scale MD computer simulations of a defect-free polyelectrolyte network without added salt in good solvent and close to the θ-point.

Initially, we detailed the coarse-grained system setup employed to measure the equilibrium swelling behaviour of the charged hydrogels under the given solvent conditions. We developed and compared several approaches to determine and reach that equilibrium characterized by a vanishing instantaneous pressure $\mathcal{P} = 0$. The swelling properties were subsequently obtained from MD computer experiments in the $(N, V = V_{eq}(\mathcal{P} = 0), T)$-ensemble, using the soft matter system simulation package ESPResSo we presented in chapter 1.

We investigated the results for a diamond-like network topology and a vast range of configurational, geometrical, and interaction parameters. While no direct violation of the FRH could be detected and corresponding predictions could not be confirmed, we developed a scaling relation for the end-to-end distance of the network strands which takes both the effects of counterion condensation as well as of finite extensibil-

ity of the chains into account, successfully testing it with our data. The analysis also showed rather strong components in the pressure which could be attributed to the inner-chain repulsion of the charged monomers and to the electrostatic interaction of the counterions with them; however, it was found that these contributions canceled out in the swelling equilibrium when using the appropriate effective charge fraction. The final shape of a hydrogel under the considered environmental conditions was therefore determined by the renormalized amount of charges on its network strands and their maximum elongation, while coulombic effects did only implicitly affect the outcome. This was true due to the effective charge fraction reflecting more than just the neutralization of condensed counterions in the vicinity of the network chains, as opposed to the more Manning-like usage employed in the previous chapter.

The detailed analysis of the microscopic mechanisms behind the equilibrium state of a charged hydrogel also revealed a closer look at the leading contributions assumed in our derivation of a universal scaling prediction in the previous chapter. It confirmed that the swelling is essentially driven by the osmotic pressure of mobile counterions and the electrostatic repulsion of the like-wise charged co-ions on the network chains, both acting against the elastic restoring force of the strands chemical bonds. In addition we found a very high excluded volume term for very strong coulombic coupling, indicating that in such a limit the condensing counterions are "bound" so strongly onto the chains that they add another swelling tendency to the system.

For future studies, one could follow the analogy to neutral network investigations by looking at *e.g.* randomly crosslinked chains, introducing entanglements, loops, or dangling ends into the system. Another road to explore would include expanding more on the coarse-graining aspect towards massively larger system sizes, eventually arriving at a level were unsolved questions such as to the nature of the curious surface patterns real world hydrogels like the one in figure I.3 exhibit could be solved.

5. Polyelectrolyte Networks in Poor Solvent

The simulation study is extended to poor solvent environments. There, regimes with different equilibrium conformations emerge. Pearl-necklace-like shapes are found, as theoretically predicted, but also other structures similar to those from an earlier single chain study. They are categorized in the parameter space, and their equilibrium properties compared.

A large number of polymers are based on a hydrocarbon backbone which is usually non-soluble in water. While quite often only the addition of charged side groups ensures solubility, the properties of such polyelectrolytes are fundamentally different than those of the macromolecules considered in the previous chapter 4. Since most polymers in biological environments, where the amount of water is usually high, virtually all proteins as well as the DNA are charged objects, the importance of this regime and its thorough understanding not only for biochemistry and molecular biology becomes apparent.

The sulfonated polystyrene (PSS) in the lower half of figure I.4 also has a *hydrophobic* hydrocarbon backbone, meaning that for this polyelectrolyte water is a *poor solvent*, causing the macromolecule to try and minimize its contact surface with the surrounding solution by attempting to collapse into a globular state. As was detailed in section 2.4, the same effect occurs if the system temperature T is lowered below a critical threshold, the *θ-temperature*; there, monomers are more likely to be found close together due to an effective net attraction, as expressed by the negative excluded volume in (2.41). An environment exhibiting such features is generally called a *poor solvent* because the macromolecule prefers contact with itself over the solvent molecules, and consequently falls out of solution eventually, if the system is neutral or the temperature too low.

Adding charges to the system now gives rise to a whole new set of structures, because the long-range interactions introduced, particularly the repulsion of likewise charged neighbouring monomers, are competing with the poor solvent attraction, and depending on the parameters entirely different conformations emerge. For the most intriguing one, a *pearl-necklace*-like shape of the chains, theoretical models for weakly [182–184] and strongly [33, 164, 185] charged chains exist which will be detailed in section 5.1. Although once more a single chain theory, similar shapes are

also expected for a polyelectrolyte gel [40] where the scaling predictions change due to the network topology.

Computer simulation studies [52–54,177–179] were successful in proving the existence of such shapes within single chain model systems, providing valuable insight into their basic properties. Section 5.2 will discuss some selected results, focusing on structural aspects and geometrical observables which are relevant for charged gels.

Based on those system parameters and same solvent conditions to achieve direct comparability, our numerical experiments of poor solvent polyelectrolyte networks will then be presented in section 5.3. They are the first to reveal pearl-necklace structures in charged hydrogels, as expected, and also corroborate findings from real-world experiments regarding scattering function observations which might indicate direct evidence for the existence of pearls in poor solvent polyelectrolytes.

5.1. Poor Solvent Theories

This section introduces the theoretical concepts for treating charged polymers under poor solvent conditions. Drawing further on the analogy to single chains, we first discuss the scaling picture for polyelectrolytes in dilute solution (section 5.1.1) and its predictions for the pearl-necklace structures, while later on we transfer these findings to the network regime (section 5.1.2).

5.1.1. The Scaling Behaviour of Poor Solvent Polyelectrolytes

In a solution with an effective excluded volume $v_{\mathrm{ex}} < 0$ the monomers are attracting each other. For a charged polymer, however, the repulsion of the likewise charged repeat units along the backbone introduces an additional effect counteracting the collapsing tendencies induced by the solvent, such that within certain parameter regimes a fragile balance can emerge, creating a sequence of locally collapsed structures (called *pearls*) interconnected by elongated *strings*, having the polyelectrolyte appear as a *pearl-necklace*.

This observation (an exemplary snapshot will be shown later in figure 5.2) can be treated as an emerging equilibrium between poor solvent attraction and the electrostatic repulsion. The former leads uncharged chains to form a globule whose density $\rho \approx \tau/b^3$ is given by the balance of two-body attraction ($BN_{\mathrm{m}}\rho$) and three-body repulsion ($b^6 N_{\mathrm{m}}\rho^2$) between the monomers of the chain, with second virial coefficient $B \approx -\tau b^3$, reduced temperature $\tau = (\theta - T)/\theta$ where θ is the temperature of the θ-point (equivalent definitions exist as well, *e.g.* $\tau = -(\epsilon^{\theta}_{\mathrm{LJ}} - \epsilon_{\mathrm{LJ}})/\epsilon^{\theta}_{\mathrm{LJ}}$ with $\epsilon^{\theta}_{\mathrm{LJ}} = 0.34\, k_{\mathrm{B}}T$ [178,179] as corresponding θ-value for our simulations, see sections 4.1 and 5.2), and bond length b; the size R of the globule is then given by [184]

$$R \approx \left(\frac{N_{\mathrm{m}}}{\rho}\right)^{1/3} \approx \xi_{\mathrm{T}} \left(\frac{N_{\mathrm{m}}}{g_{\mathrm{T}}}\right)^{1/3} \approx b\tau^{-1/3} N_{\mathrm{m}}^{1/3} \tag{5.1}$$

It contains an important length scale, namely the thermal blob size ξ_T, indicating the size of the density fluctuations. As in section 3.2.2, below ξ_T the chain statistics are unperturbed by the volume interactions, resembling a random walk of g_T monomers with $\xi_T \approx b g_T^{1/2}$; on length scales larger than ξ_T, the attraction between monomers is stronger, causing the thermal blobs in the globule to be space-filling with $\rho \approx g_T/\xi_T^3$. While the number of monomers in a thermal blob is $g_T \approx 1/\tau^2$ and its size is $\xi_T \approx b/\tau$, the surface tension γ of the globule is of the order of $k_B T$ per thermal blob at the globular surface, *i.e.* $\gamma \approx k_B T\, \xi_T^{-2}$.

The electrostatic interaction introduces coulombic blobs of size ξ_{PE} similar to the ones in section 3.2.3. However, contrary to the energy relation (3.7) there, they are determined by the balance between the electrostatic interactions within the blob and the surface tension $\gamma \cong k_B T \xi_T^{-2} \cong k_B T (\tau/b)^2$, given through

$$\ell_B \frac{(f g_{PE})^2}{\xi_{PE}} \cong \gamma\, \xi_{PE}^2 \tag{5.2}$$

Below length scales of ξ_{PE}, electrostatics is negligible, and the coulombic blob is composed of a dense packing of thermal blobs; for strong electrostatics, the poor solvent effects are negligible, and the polyelectrolyte appears as a linear sequence of coulombic blobs as in section 3.2.3. Starting *e.g.* at $N_m = 96$ in figure 5.2 and increasing the chain length consequently increases the size of the globule, until it is energetically more favorable for (5.2) to split into two smaller pearls, dramatically reducing the surface tension (where ξ_{PE} enters quadratically), but even more dramatically reducing the electrostatic repulsion (where, through $\xi_{PE} \cong b(g_{PE}/\tau)^{1/3}$, the blob size enters with ξ_{PE}^5).

Considering the shape of a *charged* globule turns out to be similar to the classical Rayleigh instability of a charged droplet [184, 186, 187] where it was shown that a spherical object with radius R and charge $Q > e(\gamma R^3/(k_B T \ell_B))^{1/2}$ is locally unstable and deforms spontaneously. Though its equilibrium state, a set of smaller droplets each charged lower than the critical value and placed at infinite distances, cannot be related to a polyelectrolyte due to the latter's chemical bonds of finite size between each monomer, the analogy still allows to conclude that the system can reduce its energy by splitting into a set of smaller charged globules connected by narrow strings – the pearl-necklace conformation.

Overall, a long polyelectrolyte chain in a poor solvent therefore adopts an elongated shape determined by the balance between surface tension and electrostatic self-energy. Minimizing the free energy of the respective contributions from the pearls and the strings (both consisting of their surface energy and the coulombic energy of the charges contained therein) and the total electrostatic energy of the pearl-necklace structure then leads to a chain extension [40, 188]

$$R_E \approx N_m b \left(\frac{\ell_B f^2}{b}\right)^{1/2} \tau^{-1/2} \tag{5.3}$$

which exhibits a different scaling exponent than the good solvent result from (2.58). At low charge fraction or/and very poor solvent, the surface energy is larger than the thermal energy, causing the counterions to be regulated by the pearls. The condensation of counterions inside the globules actually suppresses the Rayleigh instability, and even a large globule becomes stable against the necklace.

5.1.2. Treatment of Poor Solvent Gels

Not much can be said for the poor solvent behaviour of polyelectrolyte networks due to the many competing contributions, except for some simple scaling arguments [40]. Following the line of thoughts from sections 3.2.1 and 3.2.2, a c^*-gel is considered with disentangled meshes and in the absence of salt, where at equilibrium the total pressure in the system vanishes. Thus, the contributions arising from the counterions and from the strand elasticity cancel, and $\Pi = \Pi_\mathrm{C} + \Pi_\mathrm{E} = 0$.

Drawing further on the analogy to single chains, the elastic energy density in a poor solvent with $v_\mathrm{ex} = -\tau b^3 < 0$ is then proportional to the density of tensile blobs as derived in section 5.1.1, such that at the scaling level [40]

$$\Pi_\mathrm{E} = -k_\mathrm{B}T\frac{\tau}{R_\mathrm{E}^2 b} \tag{5.4}$$

This is compensated once more by the osmotic pressure of the counterions at the gel equilibrium concentration c, given through

$$\Pi_\mathrm{C} = k_\mathrm{B}T f c = k_\mathrm{B}T\frac{\tau^3}{(fN_\mathrm{m})^2 b^3} \tag{5.5}$$

Hence, the equilibrium mesh size follows as

$$R_\mathrm{E} = \frac{bfN_\mathrm{m}}{\tau} \tag{5.6}$$

With respect to a corresponding free necklace chain comprising N_m monomers, such a gel is consequently stretched. Also note that this description requires the necklace to be shorter than a string of thermal blobs as the pearl-necklace picture remains valid only if most monomers belong to the pearls, *i.e.* if $R_\mathrm{E} < N_\mathrm{m} b\tau$. Therefore, (5.6) holds for $\tau > f^{1/2}$, whereas closer to the θ-point the solvent quality becomes irrelevant and the structure is that of a θ-gel from section 3.2.1.

For very poor solvents the single chain results [40, 188] revealed the counterions to no longer be free and to condense onto the pearls. The same is expected for the network, where the gel then macroscopically collapses if $\tau > f^{1/3}$.

Concludingly, poor solvent conditions are irrelevant close to the θ-point for as long as $\tau < f^{1/2}$; the gel shrinks continuously for intermediate solvents $f^{1/2} < \tau < f^{1/3}$ and undergoes collapse at $\tau \sim f^{1/3}$ due to counterion condensation.

5.2. Single Chain Studies

Accessing the poor solvent regime within a coarse-grained simulation is quite simple from a technical point of view: Besides lowering the temperature T below the critical θ-temperature, one can alternatively adjust the short-range excluded volume interaction to exert an additional attraction by *e.g.* increasing the depth of the energy well in the Lennard-Jones potential (4.2) from the θ-value $\epsilon_{\mathrm{LJ}}^{\theta} = 0.34\,k_{\mathrm{B}}T$ [178, 179] to $\epsilon_{\mathrm{LJ}} = 1.75\,k_{\mathrm{B}}T$ while shifting the potential cut-off to $r_{\mathrm{cut}} = 2.5\sigma$. Introducing the reduced temperature $\tau = (\epsilon_{\mathrm{LJ}} - \epsilon_{\mathrm{LJ}}^{\theta})/\epsilon_{\mathrm{LJ}}^{\theta}$ from section 5.1, this leads to the negative excluded volume $v_{\mathrm{ex}} = -\tau b^3 < 0$ in (2.41) because of the attractive well dominating the interaction, making it more likely to find monomers close together[1]. It can be supported further by weakening the finite extensible bond potential from (4.1), decreasing the spring constant to $k_{\mathrm{F}} = 7\frac{k_{\mathrm{B}}T}{\sigma^2}$ and relaxing the maximum bond length towards $r_{\mathrm{F}} = 2.0\sigma$, which results in the effective pair interaction shown in figure 5.1. Note that other choices are possible, too, as long as the resulting, overall potential displays the necessary characteristics of an effectively attractive interaction beyond the θ-point, where the chain conformation would follow Gaussian statistics.

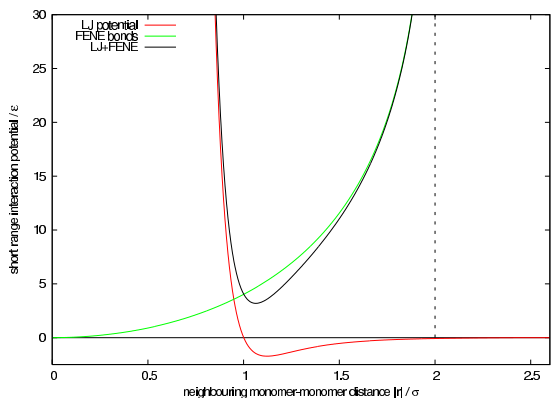

Figure 5.1.: The short-range interaction between neighbouring monomers in a poor solvent environment, consisting of the excluded volume Lennard-Jones (4.2) and the attractive FENE (4.1) potential. As in figure 4.1 for the case of good and θ-solvents, the effective interaction depends on the chosen parameters; here, the LJ includes part of its attractive well up to r_{cut}, extending even deeper with $\epsilon_{\mathrm{LJ}} = 1.75\,k_{\mathrm{B}}T$, while the finite extensible bond potential diverges softlier ($k_{\mathrm{F}} = 7\frac{k_{\mathrm{B}}T}{\sigma^2}$) and later ($r_{\mathrm{F}} = 2.0\sigma$).

The aforementioned parameters now correspond to those of a very detailed simulational study [54] conducted at our institute, investigating the structure of strongly charged polyelectrolytes in the dilute concentration regime of a poor solvent, in which the chain-chain interaction was found to be weak enough to be able to effectively deal with single-chain properties. Its model consisted of N_{p} flexible bead-spring chains with N_{m} monomers and an appropriate amount of N_{CI} counterions to ensure electroneutrality, all located in a cubic simulation box of length L under periodic boundary conditions. With a fraction f of the monomers monovalently charged, the

[1] Thus, instead of disliking the solvent molecules, which are only implicitly present in our model, the monomers are merely preferring contact with their own kind more; the resulting effects, however, are naturally the same.

plain monomer density $\rho_\mathrm{m} = N_\mathrm{p} N_\mathrm{m}/L^3$ was supplemented with the bulk charge density $\rho_\mathrm{c} = 2fN_\mathrm{p}N_\mathrm{m}/L^3 = 2N_\mathrm{CI}/L^3$ to render the system charge neutral. While the monomers interacted with the effective short-range potential from figure 5.1, the excluded volume of the counterions was modeled by the purely repulsive Lennard-Jones used in the good solvent regime, *i.e.* with $r_\mathrm{cut} = 2^{1/6}\sigma$. The Coulomb interaction between all charged objects was calculated with the P^{3}M-algorithm [74, 75] and force accuracies much higher than the thermal noise level. Overall, a velocity Verlet algorithm with a standard Langevin thermostat was used to integrate the equations of motion in the (N, V, T)-ensemble, using $\Gamma = \tau^{-1}$ as friction coefficient and a timestep of $\Delta t = 0.0125\tau$.

name	N_m	f	ℓ_B	ϵ_LJ	ρ_c
series A1	$48, \ldots, 478$	1/3	1.5σ	$1.75 k_\mathrm{B}T$	$1.0 \cdot 10^{-5}\sigma^{-3}$
series C1	200	1	$0\sigma, \ldots, 12.0\sigma$	$1.75 k_\mathrm{B}T$	$5.0 \cdot 10^{-5}\sigma^{-3}$
series C2	199	1/2	$0\sigma, \ldots, 6.0\sigma$	$1.75 k_\mathrm{B}T$	$5.0 \cdot 10^{-5}\sigma^{-3}$
series C3	199	1/3	$0\sigma, \ldots, 9.0\sigma$	$1.75 k_\mathrm{B}T$	$5.0 \cdot 10^{-5}\sigma^{-3}$

Table 5.1.: The parameters used in the single chain simulation study [54].

Of all the poor-solvent polyelectrolytes simulated in [54], mainly as a function of chain length N_m, solvent quality parameter ϵ_LJ, strength of the electrostatic interaction ℓ_B, and charge fraction f, we will focus on the so-called series A1 and C1 through C3 (see table 5.1), because they were covering most of the two-dimensional parameter space in the poor solvent regime we are interested in (which is why we will also base our network simulations in the next section 5.3 on their system parameters, allowing direct comparisons of the respective results as well). Series A1 thereby studied the chain-length dependence for systems with a fixed charge fraction of $f = 0.3333$, a Bjerrum length $\ell_\mathrm{B} = 1.5\sigma$, and a constant bulk charge density $\rho_\mathrm{c} = 1 \cdot 10^{-5}\sigma^{-3}$, varying $N_\mathrm{m} = 48, \ldots, 478$ in steps of 48 (with $N_\mathrm{m} = 48$ being the first, $N_\mathrm{m} = 46 + 48\mathbb{N}$ the subsequent iterations), while choosing $\epsilon_\mathrm{LJ} = 1.75\, k_\mathrm{B}T$ deep within the poor-solvent regime to receive relatively large and stable pearl-necklace conformations. At the same ϵ_LJ, series C1, C2, C3 studied the effect of the Coulomb interaction through changing the Bjerrum length between $\ell_\mathrm{B} = 0\sigma$ and 10σ; the charge fraction remained fixed at $f = 1.0$ (series C1), $f = 0.5$ (C2), and $f = 0.3333$ (C3), the bulk charge density at $\rho_\mathrm{c} = 5 \cdot 10^{-5}\sigma^{-3}$ although the actual number of counterions $N_\mathrm{CI} = N_\mathrm{p}\, f N_\mathrm{m}$ varied due to the different charge fraction.

A first impression of how different polyelectrolytes behave in a poor solvent environment is given by figure 5.2, where some snapshots from series A1 are shown. Clearly, the coiled but elongated shape found in good solvents, see *e.g.* our network snapshot in figure 4.2, is now replaced by a more complex conformation, reflecting the aforementioned competition between the attractive interactions due to the poor solubility of the backbone and the electrostatic repulsion of the polyelectrolyte's

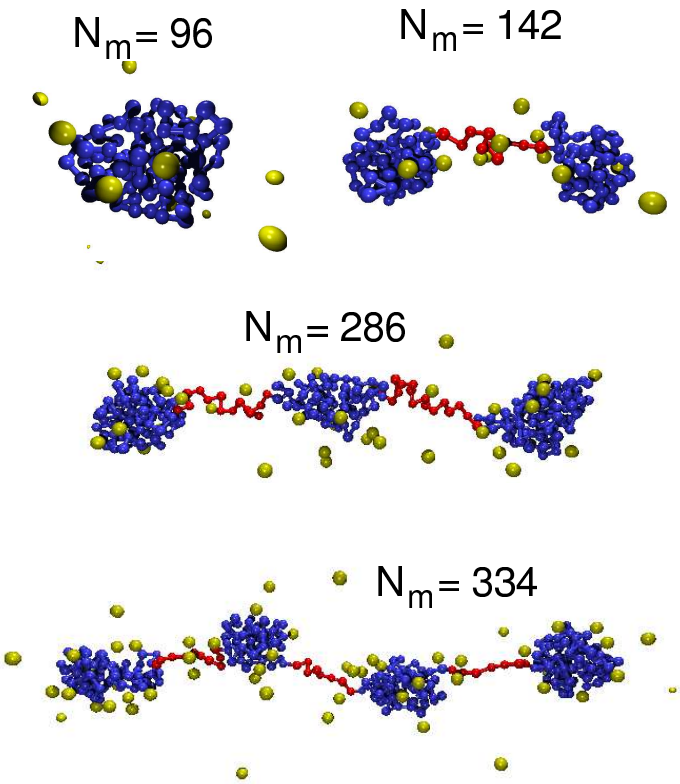

Figure 5.2.: Snapshots of single chain polyelectrolytes from series A1 with different chain lengths N_m in a poor solvent environment where $\epsilon_\mathrm{LJ} = 1.75\,k_\mathrm{B}T$ and $f = 0.3333$, $\ell_\mathrm{B} = 1.5\sigma$ at a density of $\rho_\mathrm{c} = 1 \cdot 10^{-5}\sigma^{-3}$, resulting in different numbers of pearls n_P; the colour coding indicates monomers identified as belonging to one of the clusters in *blue*, the remaining ones on the chain, part of the connecting strings, in *red*, while counterions are given in *yellow* (taken from [54]).

charges. Contrary to chains without charged groups, where the effective attraction between the monomers causes them to collapse into spherical globules, coalescing with each other, and precipitating from solution, the coulombic repulsion between the fN_m repeat units per strand significantly improves the polymer solubility, in the parameter regime of series A1 now leading to the predicted pearl-necklace conformations. From visual inspection it can already be observed that the occurrence of two or more pearls requires a sufficiently long chain, as in the case of $N_\mathrm{m} = 96$ the polyelectrolyte has a merely globular, for $N_\mathrm{m} = 142$ only a dumbbell-shaped appearance. With the number g_P of monomers per pearl remaining constant, *e.g.* $g_\mathrm{P} = 78 \pm 4$ for series A1 and $N_\mathrm{m} > 200$, this observation becomes understandable in terms of the emerging equilibrium between the poor solvent attraction and the electrostatic repulsion, as was discussed in section 5.1.

It is quite apparent that the observables usually employed in polymer physics are not sufficient to characterize these equilibrium states. Neither end-to-end distance R_E nor radius of gyration R_G contain enough information on the *local* structure of the chains to distinguish between *e.g.* conformations with four or five pearls; though the hydrodynamic radius R_H is more sensitive by definition, it is still lacking the necessary precision for particularly larger number of pearls. In many cases the ener-

getic difference between similar structures is so small that several of them may even coexist. Consequently, it is important to be able to analyze individual conformations with respect to occurrence of pearls, their amount and size, because based on this knowledge interpretation of the experimentally accessible observables will then be possible on a more substantiated basis. One very successful approach to this task is the *Cluster Recognition Algorithm* developed in [188] which detects the pearls and strings based on a distance criterion, and which had also been used to colour code the monomers in figure 5.2. Since for a polymer the chain connectivity has to be taken into account as well, the following algorithm emerges:

(CA.1) Define every monomer $i = 1, \ldots, N_\mathrm{m}$ on the chain as an initial cluster $\mathcal{C}_i := \{i\}$ of size $|\mathcal{C}_i| = 1$.

(CA.2) Merge two clusters $\mathcal{C}_m$ and $\mathcal{C}_n$ if they contain a pair (i, j) of monomers $i \in \mathcal{C}_m$ and $j \in \mathcal{C}_n$, $|i-j| > n_\mathrm{c}$ with spatial separation $\vec{r}_{ij} = |\vec{r}_i - \vec{r}_j| < r_\mathrm{c}$.

(CA.3) Repeat (CA.2) for all (m, n) until only non-mergeable clusters remain.

(CA.4) Merge cluster $\mathcal{C}_m$ into $\mathcal{C}_n$ if $\mathcal{C}_m \subsetneq \mathcal{C}_n$; repeat for all (m, n).

(CA.5) Define $\mathcal{C}_m$ to be a *pearl* if $|\mathcal{C}_m| \geq p_\mathrm{c}$.

(CA.6) Define $\mathcal{C}_m$ to be a *string* if $|\mathcal{C}_m| < p_\mathrm{c}$.

(CA.7) Merge all adjacent clusters $\mathcal{C}_m$ and $\mathcal{C}_n$ that are likewise defined.

(CA.8) Remove dangling ends by merging them into the subsequent "pearl".

(CA.9) Output length $|\mathcal{C}_m|$ of all clusters sorted in successive sequence.

Three parameters are hereby necessary, namely the minimum number of monomers p_c a cluster must possess before being regarded as "pearl", the minimum backbone separation n_c between a monomer pair (i, j), *i.e.* the required number of bonds between them, before they are considered for the distance criterion, and the maximum spatial distance r_c between two monomers within the same pearl. The output sequence, alternating the found sizes of pearls, strings, and pearls, can then easily be used to obtain the number of pearls n_P and the average amount of monomers per pearl g_P. Although in [188] and the subsequent publications, where we once again focus on [54] for comparison, a custom implementation of this cluster algorithm was used, it has meanwhile become part of ESPResSo as well, such that the simple call

```
analyze necklace <p_c> <n_c> <r_c> <first_ID> <N_M>
```

is sufficient to invoke analysis of all particles $i =$ `<first_ID>`,...,`<first_ID>+<N_M>`.

Figure 5.3 now shows the dependency of the resulting number of pearls n_P on the Bjerrum length, comparing it to the behaviour of the end-to-end distance R_E.

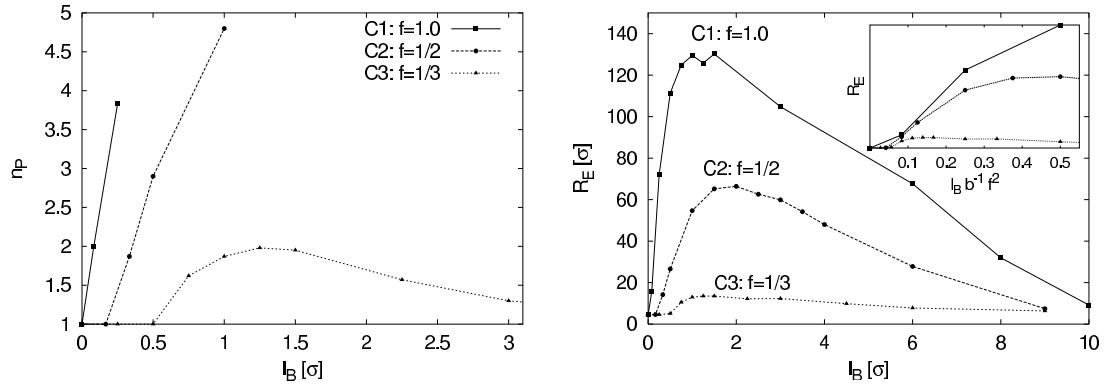

Figure 5.3.: Dependence of n_P (*left*) and R_E (*right*) on the Bjerrum length ℓ_B for series C1, C2, C3; the inset of the latter shows the dependence of the end-to-end distance on the scaling variable $\ell_B b^{-1} f^2$ (taken from [54]).

In the framework of the scaling theory of section 5.1.1, the simulations performed at the same value of $\ell_B b^{-1} f^2$ should be identical, the data should collapse onto a single master curve. In [54] it was however found that this only holds in the low electrostatics limit, as the inset in the *right plot* of figure 5.3 shows. Similarly, the counterions and their interaction with the chain conformation is only of minor importance for very small values of ℓ_B.

The structure diagram in figure 5.4 is now providing an overview of the conformational variety the single chain polyelectrolytes exhibited in series C1, C2, C3 alone. Besides the much discussed pearl-necklace structures, which obviously only occurred for a small range of weak electrostatics, *i.e.* small Bjerrum lengths ℓ_B, other observations included globular states for vanishing coulombic interactions (in agreement with the expectations for neutral cases), which slowly grow for increasing f and/or ℓ_B while the self-energy gets larger, until the Rayleigh instability splits the globule into a dumbbell-like structure and the pearl-necklace regime is entered. In the case of higher charge fractions ≥ 0.5, a cascade of Rayleigh instabilities leads to a stretched conformation of maximum extension for increasing ℓ_B, while for $f = 0.3333$ the conformations directly cross from a dumbbell-like structure into the "sausage"-regime [54], where electrostatics is so high that the resulting counterion condensation partially neutralizes the chains, causing local collapses which appear as elongated cigars or "sausages"; smaller values of f hereby lead to thicker structures. Increasing the coulombic interactions further finally induces enough condensation to effectively neutralize the entire chain, which then collapses *containing* the counterions within its shape (as opposed to the case of very low electrostatics where the entropy of the counterions keeps them in solution, far from the chains).

The plots on the *right* side of figure 5.4 finally connect the findings to experimentally accessible observables, *i.e.* R_G and R_H, by looking at the characteristic ratios $r = \langle R_E^2 \rangle / \langle R_G^2 \rangle$ and $\alpha = \langle R_G^2 \rangle^{1/2} / \langle R_H \rangle$ as a function of the Bjerrum length ℓ_B for the

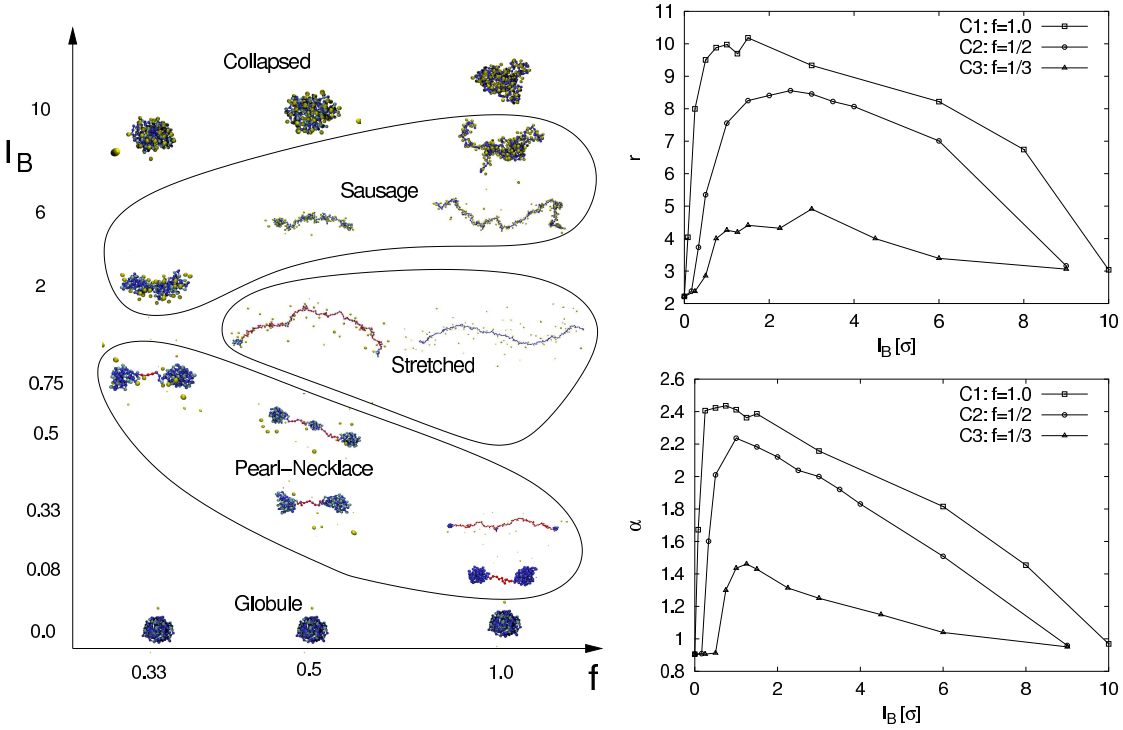

Figure 5.4.: *Left:* Structure diagram of the single chain conformations polyelectrolytes assume in a poor solvent with $\epsilon_{LJ} = 1.75\,k_BT$ for varying charge fraction f and Bjerrum lengths ℓ_B, sketching snapshots from series C1, C2, C3.
Right: Change of the characteristic ratios $r = \langle R_E^2\rangle/\langle R_G^2\rangle$ (*top*) and $\alpha = \langle R_G^2\rangle^{1/2}/\langle R_H\rangle$ (*bottom*) with ℓ_B for series C1, C2, C3 (taken from [54]).

data in series C1, C2, and C3. For the globular conformations at $\ell_B = 0\sigma$ the plots display $r \approx 2.2$ and $\alpha \approx 0.9$, while for the dumbbell-like structures $r \approx 4, \ldots, 4.5$ and $\alpha \approx 1.6$ is found. Further increase of ℓ_B leads to a maximum in both observables at roughly the maximum chain extension, as supported by figure 5.3, after which r and α decrease towards their final collapsed states where $r \approx 3$ and $\alpha \approx 1$. Referring to table 2.2, for a completely elongated object a characteristic ratio of $r = 12$ would be expected, which is not even reached for the polyelectrolytes in the stretched regime, while the lower boundary seems to be consistent with the predictions for compact objects ($r = 2, \ldots, 5/3$). The form of the curves in the plots of figure 5.4 clearly indicates that it is not possible to deduce the type of conformation the chains have from these observables, because the same value of r or α can indicate *e.g.* either a pearl-necklace or a "sausage"-like structure, merely depending on the underlying Bjerrum length ℓ_B. This once again proves the usefulness of computer simulations, since here we have the possibility to look at all microscopic details when in doubt, trying to connect the findings to the macroscopic world.

5.3. Simulations, Snapshots, Structures

There is no apparent reason why a similar variety of structures observed for the single polyelectrolytes in section 5.2 should not be present in our charged hydrogels as well, once they are placed in a poor solvent environment. In fact, for the formation of pearl-necklaces this was already postulated theoretically [40] in section 5.1.2 if one assumes the strands between neighbouring network nodes to be sufficiently long.

To be able to have this comparison as close as possible, avoiding any additional aberrations, we adjusted the parameters to the ones from the single chain study [54] presented in the previous section 5.2 while re-using our diamond-like network model which was discussed extensively in section 4.1. The following modifications were employed in that process: The parameters for the Lennard-Jones interaction between the monomers were changed to $\epsilon_{\mathrm{LJ}} = 1.75\, k_{\mathrm{B}}T$ and $r_{\mathrm{cut}} = 2.5\sigma$, the ones for the FENE bonds to $k_{\mathrm{F}} = 7\frac{k_{\mathrm{B}}T}{\sigma^2}$ and $r_{\mathrm{F}} = 2.0\sigma$, hence matching the reference specifications. We investigated systems with $N_{\mathrm{m}} = 199$ as chain length[2] and charge fraction $f \in \{0.125, 0.25, 0.3333, 0.5, 1.0\}$ for multiple Bjerrum lengths $\ell_{\mathrm{B}} \in \{0\sigma, 0.125\sigma, 0.25\sigma, 0.5\sigma, 0.75\sigma, 1.0\sigma, 2.0\sigma, 3.0\sigma, 5.0\sigma, 6.0\sigma, 9.0\sigma\}$, calling these parameter sets the *C-series* because it covers the regime of C1, C2 and C3 from [54]. We looked at additional systems with $N_{\mathrm{m}} \in \{200, 239, 287, 335, 383, 431, 479\}$ for charge fraction $f = 0.3333$ and Bjerrum length $\ell_{\mathrm{B}} = 1.5\sigma$, corresponding to A1 in [54] and consequently called *A-series*. Then, we also investigated very long chains at $N_{\mathrm{m}} = 479$ for charge fractions $f \in \{0.0625, 0.125, 0.25, 0.3333, 0.5, 1.0\}$ and $\ell_{\mathrm{B}} = 1.5\sigma$, which have no counterpart in the previous study; for better reference it shall be named *E-series*. Table 5.2 now gives a summary of these settings, reflecting the choices from the single chain study in table 5.1.

name	N_{m}	f	ℓ_{B}	ϵ_{LJ}
A-series	$200, \ldots, 479$	0.3333	1.5σ	$1.75 k_{\mathrm{B}}T$
C-series	199 (or 200)	$0.125, \ldots, 1.0$	$0\sigma, \ldots, 9.0\sigma$	$1.75 k_{\mathrm{B}}T$
E-series	479	$0.0625, \ldots, 1.0$	1.5σ	$1.75 k_{\mathrm{B}}T$

Table 5.2.: The parameters used in our simulation study [66].

5.3.1. Finding Equilibrium: Simulation Scripts Revisited

Although we tried hard to get it working, it was not possible to utilize the (N, p, T)-algorithm in the poor solvent regime. As becomes apparent later on when looking at the $p(V)$-diagrams, the fluctuations in the pressure were simply too large and some of the systems simply too close to a volume collapse that no equilibrium

[2] In the case of $f = 0.3333$ the chain length was actually chosen to be $N_{\mathrm{m}} = 200$ to ensure that $N_{\mathrm{CI}} \in \mathbb{N}$.

could be found. This now dramatically increased the required computational effort for this simulation study, because contrary to the single polyelectrolytes where any sufficiently low density would suffice, the charged hydrogels *must* be at $\mathcal{P} \approx 0$ before any evaluation could start, otherwise they are simply not in the thermodynamic equilibrium. Consequently, we had to revert to the safest method laid out in section 4.1, namely the thorough measurement of $p(V)$-diagrams, from which the swelling equilibrium was then determined as the intersection of the plot at $p = 0$. Of course this implied that for *every* single data point in [54] we had to run at least 16 (!) individual simulations in the (N, V, T)-ensemble, measuring the pressure as careful as possible, to cover the required minimum of four decades in the system density. With the parameter regimes we needed to cover, such a procedure totals up to 112 runs for the A-series, 880 runs for the C-series, and 96 runs for the E-series, *summa summarum* a grand total of 1088 runs only for getting the equivalent data to the single chain results. Now considering that the systems in questions were rather large setups with up to 15,344 charged (!) particles[3], the amount of necessary CPU time becomes apparent[4] (*i.e.* between 6 and 14 hours per run on system *s1* from section 1.6, depending on the amount of charges and the range of the electrostatic interactions).

Varying the simulation box volume over orders of magnitude also made it necessary to enhance the warm-up and equilibration sequences of the simulation scripts we used for the case of good solvents. Particularly for very large and very small volumes special care was required, as the former generate strongly elongated chains close to being ruptured due to the periodic network topology, the latter imply a high density where excluded volume effects might become destructive. Hence, we had to reduce the increase of the LJ-cap in the warm-up sequence from section 4.1 to slow down the process of pushing particles apart which were set up too close to each other, because in a very dense system those are usually surrounded by more objects obstructing the intended separation. It was also necessary to add an intermediate step afterwards (*i.e.* with the system still being neutral), where we temporarily fixed the spatial coordinates of all monomers on the chains, using

```
for { set i 0 } { $i < $N_node+$N_P*$MPC } { incr i } { part $i fix }
```

to allow the counterions to relax towards their equilibrium distribution, once electrostatics had been activated, within one possible electric field generated by the chains in their current conformation, without having to worry about unrealisticly high strains on the monomers because of a counterion set up too close to the chains for too high a Bjerrum length. As soon as this was achieved, the constraint could be

[3] The biggest network we investigated under the good solvent conditions of chapter 4 had a chain length of $N_m = 259$, compared to the $N_m = 479$ employed here.

[4] Luckily, at the time the poor solvent investigations started ESPResSo had already evolved to a much more efficient level, with *e.g.* the newly added cell tuning granting a significant speed increase; parallelization and hardware optimization for specific platforms had also been improved.

lifted (using the same loop but merely replacing the keyword `fix` by `unfix`), and the monomers were allowed to adjust their conformation according to the new, and more equilibrated, distribution of surrounding counterions.

These modifications dramatically improved the simulation results, allowing to access all critical values of very large volumes without having the bonds broken on course of the integration, and also enabled to enter the high density limit, even if for very high electrostatics ($\ell_B \to 9.0\sigma$) the counterion condensation caused systems particularly with larger charge fractions to become unstable (which is understandable as we know from the single polyelectrolytes that the effective neutralization induces the desire to collapse).

5.3.2. Finding Equilibrium: Diagrams of Pressure and Volume

Without the possibility to use the (N, p, T)-ensemble, the swelling equilibrium has to be determined from the roots[5] of a $p(V)$-diagram which relates the simulation box volume V to the pressure $\mathcal{P}$ measured according to (4.5) and averaged over uncorrelated network conformations.

For the C-series this is shown in figures 5.5 and 5.6, where the former uses the bulk charge density $\rho_c = 2N_{CI}/V$ as "inverse" volume axis, while the latter normalizes $\mathcal{P}$ with the ideal pressure $\rho_c k_B T$ of the charges, arriving at the equivalent to the osmotic coefficient commonly considered in polyelectrolyte solutions. Each graph thereby contains the results for (N, V, T)-simulations with $N_m = 199$ and $f = 1.0$ (*red lines*), $f = 0.5$ (*green lines*), $f = 0.3333$ (*yellow lines*; here, $N_m = 200$), $f = 0.25$ (*blue lines*), and $f = 0.125$ (*magenta lines*), the used symbol reflects the Bjerrum length employed and corresponds to the ones introduced in the previous chapter 4, ranging from $\ell_B = 0\sigma$ in the *top left* of the respective figure to $\ell_B = 9.0\sigma$ in its *bottom right*. While the data points are connected by simple straight lines in the second figure 5.6, splines were used in case of figure 5.5 to emphasize the general trends over local fluctuations, which may become quite large for high densities and small charge fractions.

There, multiple effects overlap each other at comparable orders of magnitude, as very small volume "freezes" part of the conformation such that shifting particles can greatly change the excluded volume and electrostatic contributions[6]. An increasing box size reduces the impact of local fluctuations, and global mechanisms become more important. Additionally, the network topology constantly reduces the chain's degrees of freedom for larger volumes, because in a more elongated state there are less possible conformations it can assume, which in turn also reduces the possible constraints on the counterions through the electric field the monomers generate.

[5] If there is more than one, we are looking at a phase transition in the volume.

[6] A possible improvement to minimize similar effects would be the creation of multiple, independent start conformations, averaging their respective results at the end.

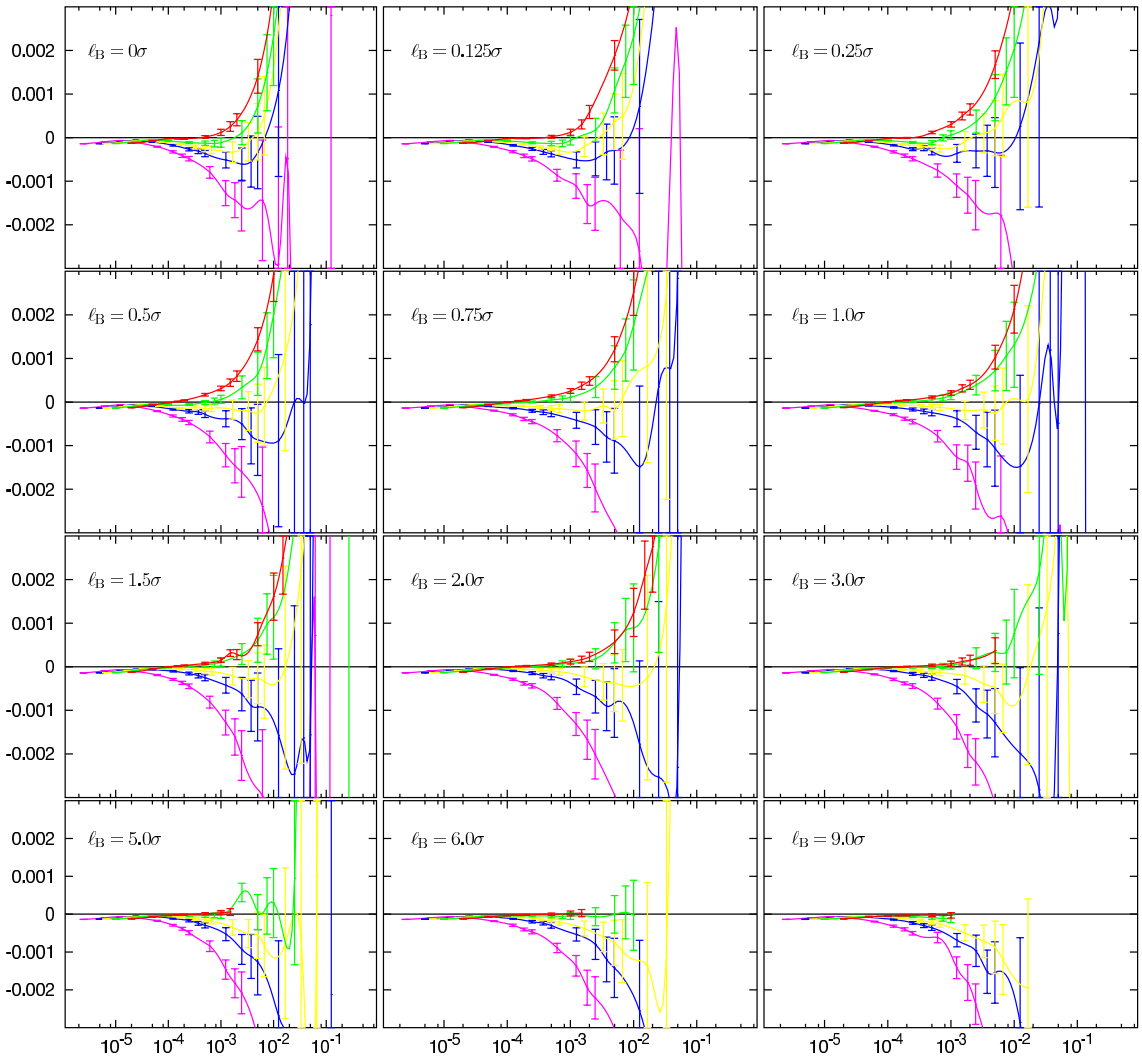

Figure 5.5.: Equilibrium pressure $\mathcal{P}$ as a function of the bulk charge density ρ_c for the C-series with ℓ_B from $\ell_B = 0\sigma$ (*upper left*) through $\ell_B = 9.0\sigma$ (*lower right*); the colour coding corresponds again to table S.1 regarding charge fraction f.

This can be most easily seen in the low density limit of figure 5.5 where all plots approach each other and would also fall on a master curve if not for their different bulk charge densities (despite a same volume, larger f leads to larger N_{CI} leads to larger ρ_c), where the elastic contribution dominates the pressure. Continuing down towards the minimum possible density ρ_{min}, corresponding to a simulation box volume stretching each network chain to $R_E = R_{max} = N_m b$ with $b \to r_F$, $\mathcal{P}_{FENE}$ diverges into the finite extensibility of the FENE potential, taking $\mathcal{P}$ with it, and rendering everything else negligible – hence, clearly

$$\lim_{\rho_c \searrow \rho_{min}} \mathcal{P} = \lim_{V \nearrow V_{max}} \mathcal{P} = -\infty \tag{5.7}$$

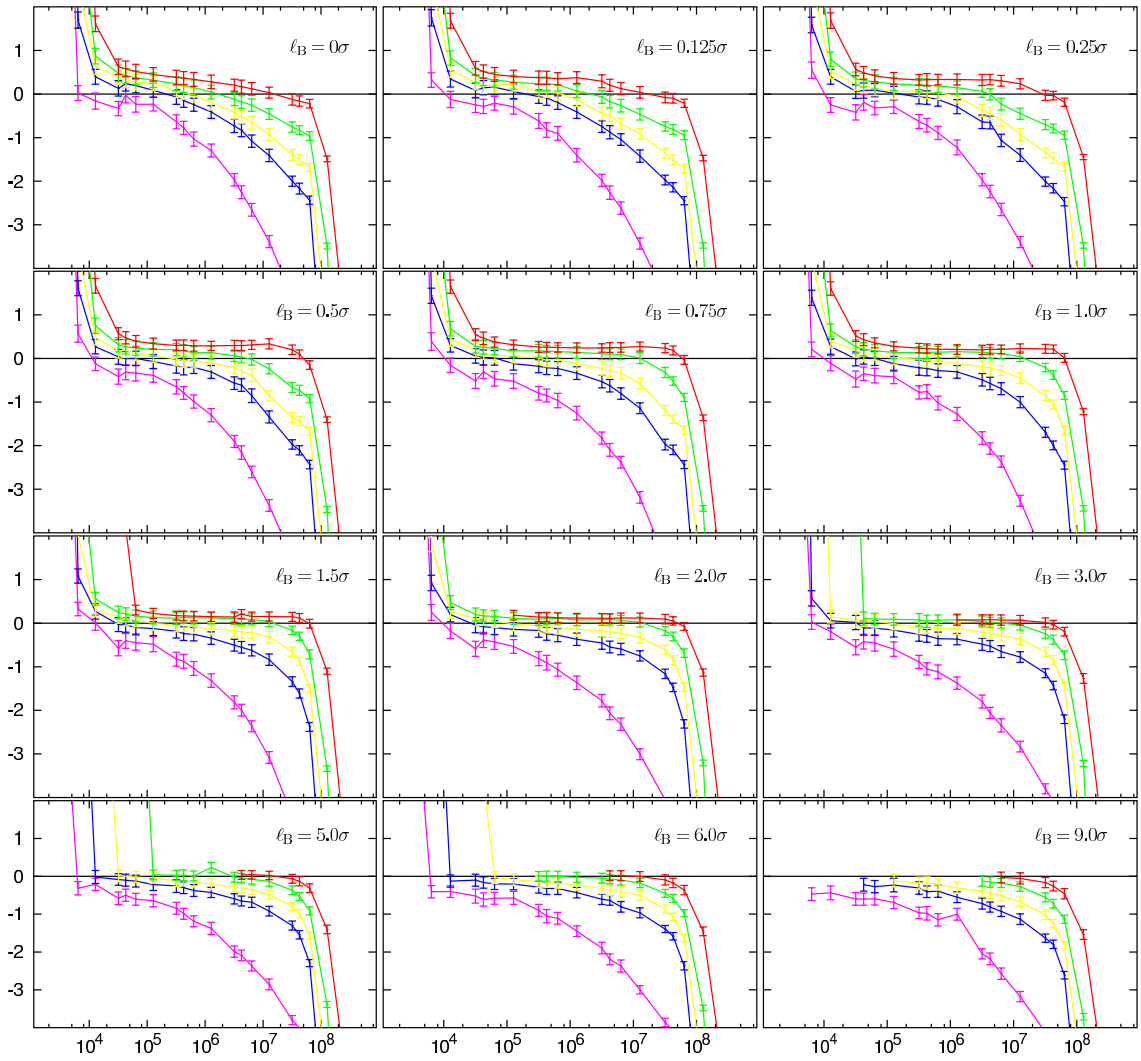

Figure 5.6.: Osmotic coefficient $\mathcal{P}/(\rho_c k_B T)$ as a function of the box volume V for the C-series with ℓ_B from $\ell_B = 0\sigma$ (*upper left*) through $\ell_B = 9.0\sigma$ (*lower right*); the colour coding corresponds again to table S.1 regarding charge fraction f.

is the lower (upper) limit of the pressure; similar to (3.74), the maximum volume is given by $V_{max} = a_{sim}^3 = [(4/\sqrt{3})R_E]^3 = [(4/\sqrt{3})N_m r_F]^3$. For very high densities a similar line of arguments identifies the excluded volume terms $\mathcal{P}_{LJ}^{monomers}$ and $\mathcal{P}_{LJ}^{CI}$ as the dominating ones, because pushing the particles into each other acts against the steep short-range divergence in $U_{LJ}(r)$ with r^{-12}, which will always overcome the r^{-1}-divergence in $U_{\ell_B}(r)$ bearing an opposite sign. The corresponding limit

$$\lim_{\rho_c \nearrow \rho_{max}} \mathcal{P} = \lim_{V \searrow V_{min}} \mathcal{P} = +\infty \tag{5.8}$$

does not seem to be reached for lower charge fractions in figure 5.5; this, however, is

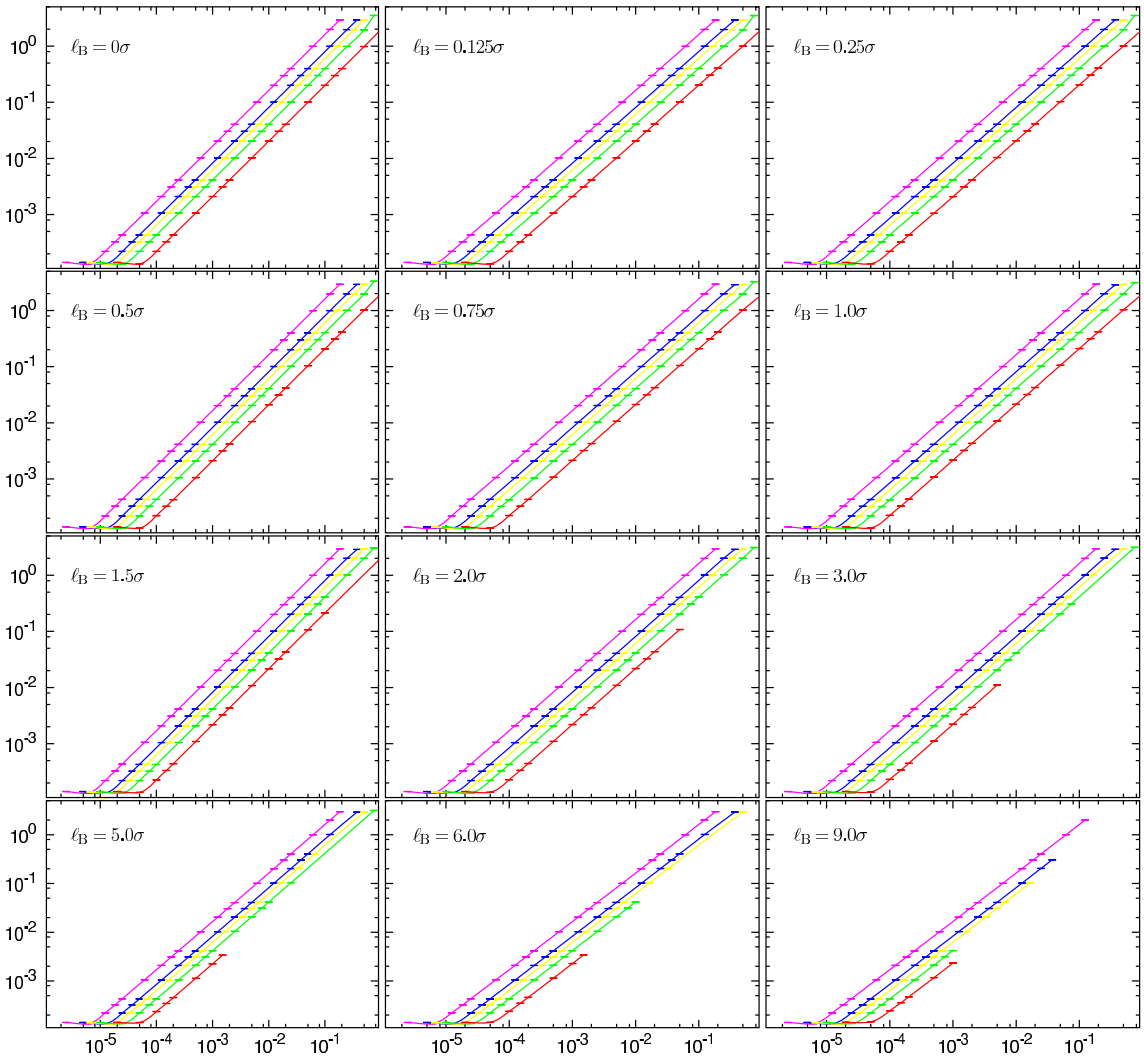

Figure 5.7.: Elastic pressure contribution $-\mathcal{P}_{\mathrm{FENE}}$ as a function of ρ_c as in figure 5.5 for the C-series with ℓ_B from $\ell_B = 0\sigma$ (*upper left*) through $\ell_B = 9.0\sigma$ (*lower right*).

only due to the magnification employed there (to allow inspection of the low density limit). As the plots in figure 5.6 show, the limit in (5.8) is not only found for all parameters where the high density limit could be accessed, but it is approached with a much higher gradient than the other one, *i.e.* the corresponding (non-normalized) values in figure 5.5 are simply off-scale.

There is one striking difference between the pure pressure plots in figure 5.5 and the rescaled ones in figure 5.6, namely that the osmotic coefficient behaves strictly monotonic, whereas the total pressure displays monotonic behaviour only for the highest charge fractions $f = 1.0$ and $f = 0.5$, exhibiting a minimum for the others. The reason is to be found in the volume dependency of all pressure compo-

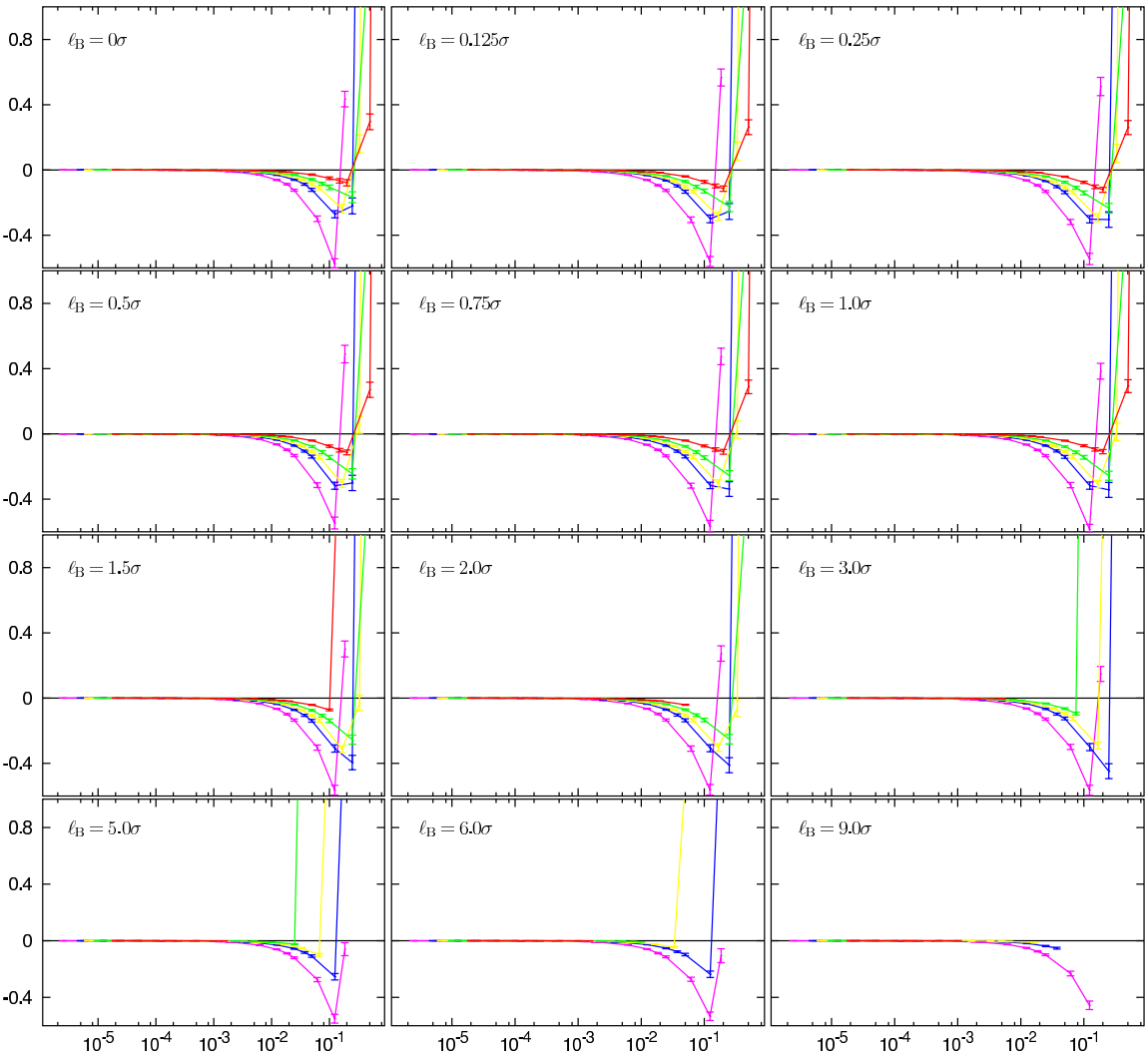

Figure 5.8.: Elasticity and excluded volume pressure $\mathcal{P}_{\text{FENE}} + \mathcal{P}_{\text{LJ}}^{\text{monomers}} + \mathcal{P}_{\text{LJ}}^{\text{CI}}$ as a function of ρ_c as in figure 5.5 for the C-series with $\ell_B \in \{0\sigma, \ldots, 9\sigma\}$.

nents, which is effectively scaled out when looking at the osmotic coefficient. If the volume decreases faster than other effects (such as excluded volume or electrostatics) increase, the resulting $\mathcal{P}$ will naturally be lower. With the chains relaxing and the ideal gas contribution $\rho k_B T$ growing linearly, this is confirmed by figure 5.7 which only shows the FENE-part of the total pressure and clearly decreases further for growing ρ_c (note that $-1 \cdot \mathcal{P}_{\text{FENE}}$ is plotted to be able to use a logarithmic y-scale). Even though this might seem counterintuitive at first, it nevertheless makes sense that while the elastic restoring force decreases linearly (within the harmonic regime, taking up most of figure 5.7), the absolute value of its pressure $\mathcal{P}_{\text{FENE}} \sim -\sum(\mathsf{f}_{\text{FENE}} \cdot b)/(3L^3)$ *grows* quadratically in the box length L.

For low charge fractions f this effect outweighs all others as long as the excluded volume interaction is not too strong. It is compensated mainly by $\mathcal{P}_{\mathrm{LJ}}^{\mathrm{monomers}}$, which turns out to be larger for higher charge fractions f because it contains with $\mathcal{P}_{\mathrm{LJ}}^{\mathrm{CI-monomers}}$ the crossterm between the (fixed amount of) N_{m} monomers per chain and the fN_{m} corresponding counterions, which interact more strongly for increasing ℓ_{B} and decreasing V; as more counterions there are (*i.e.* as higher f becomes), as more likely it is to find a counterion close enough to a chain, increasing $\mathcal{P}_{\mathrm{LJ}}^{\mathrm{monomers}}$ with f. The other part of the excluded volume contribution, $\mathcal{P}_{\mathrm{LJ}}^{\mathrm{CI}}$, becomes noticeable for very high densities $\rho_{\mathrm{c}} \geq 0.5$ only where the box is so small that even the likewise charged counterions are pushed onto each other. Both ideal gas-like pressures

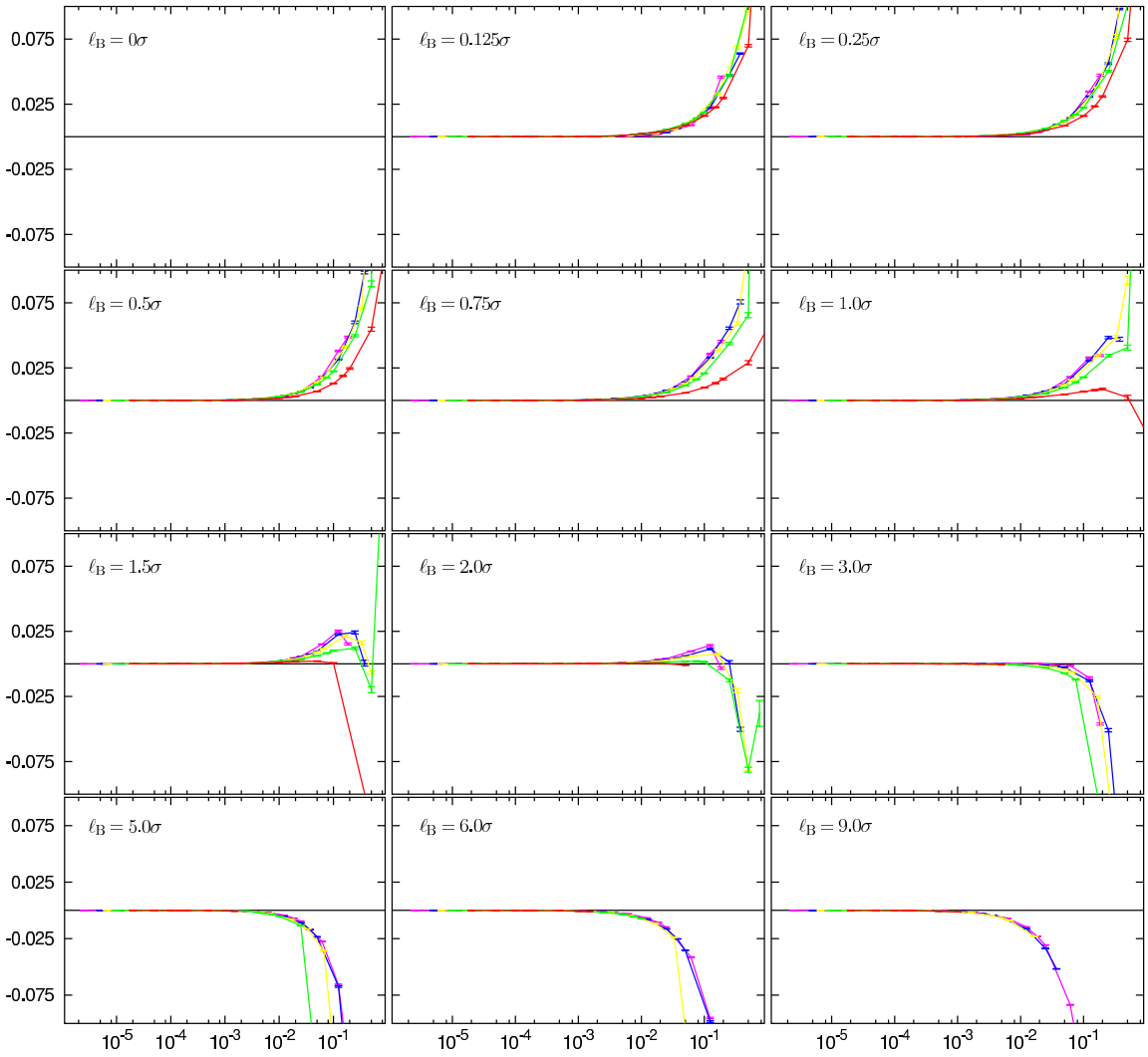

Figure 5.9.: Electrostatic pressure contribution $\mathcal{P}_{\ell_{\mathrm{B}}}^{\mathrm{tot}}$ as a function of ρ_{c} as in figure 5.5 for the C-series with ℓ_{B} from $\ell_{\mathrm{B}} = 0\sigma$ (*upper left*) through $\ell_{\mathrm{B}} = 9.0\sigma$ (*lower right*).

$\mathcal{P}_{\text{ideal}}^{\text{monomers}}$ and $\mathcal{P}_{\text{ideal}}^{\text{CI}}$, growing linearly with the density, merely shift the elastic $\mathcal{P}_{\text{FENE}}$ towards positive values, while the coulombic contribution $\mathcal{P}_{\ell_B}^{\text{tot}}$ is negligible for small Bjerrum lengths, positive for intermediate ones due to the electrostatic self-energy of the network chains, becoming negative for larger electrostatics and higher densities once opposite charges end up close to each other (causing $\mathcal{P}_{\text{LJ}}^{\text{CI-monomers}}$ to increase, too), before finally diverging when the density becomes too high; figure 5.9 thereby also allows to compare the *absolute* impact electrostatics has with respect to *e.g.* the elastic contribution from figure 5.7 or the effective short-range virial from figure 5.8.

All this allows to understand the behaviour of the measured pressure $\mathcal{P}$ as a function of increasing bulk charge density ρ_c in figure 5.5 and its connection to the renormalized depiction as osmotic coefficient in figure 5.6. Without the volume effects the latter is much more convenient to determine the equilibrium swelling volume V_{eq} where $\mathcal{P}(V = V_{\text{eq}}) \approx 0$. Instead of continuing with yet another simulation run at $(N, V = V_{\text{eq}}, T)$, maybe even entering an iterative process similar to the one described in *e.g.* figure 4.3, we decided to use the V_{eq} from figure 5.6 to interpolate the equilibrium results at that volume; since for any observable x we had already obtained its volume dependence $x(V)$ while measuring $\mathcal{P}(V)$, this merely assumes monotonic behaviour close to $V = V_{\text{eq}}$ and a sufficiently fine spacing in V. The equilibrium properties discussed in the following are likewisely determined, while the example conformations or snapshots shown will reflect the actual (N, V, T)-simulation closest to V_{eq}.

5.3.3. Conformations of Charged Hydrogels at Swelling Equilibrium

Now we can finally begin comparing our findings from charged hydrogels in a poor solvent environment to the results of single polyelectrolytes from the previous section 5.2. We begin by looking at some simulation snapshots across the parameter space of charge fraction f and Bjerrum length ℓ_B, keeping *e.g.* the single chain pictures from figure 5.2 in mind. While for full reference the entire C-series is depicted in appendix C, here we will focus on representative examples for the identified shapes.

Starting in the limit of vanishing electrostatics, figure 5.10 shows conformations for $\ell_B = 0\sigma$. For the low charge fraction $f = 0.125$, depicted in the *top left*, we find a clearly collapsed structure. The $\mathcal{P}(\rho)$-diagram in figure 5.5 confirms that the system tries to minimize its density as much as possible, and the snapshot indicates a clear phase separation between the mutually attractive monomers and the counterions with their purely repulsive excluded volume interactions. Due to the periodic network topology, the latter are trapped within the hydrogel, thereby also preventing its total collapse into a space filling globule (note that the seemingly empty space in the lower left of the snapshot is actually taken up by the periodic image of the monomers extending outwards of the simulation box to the lower right

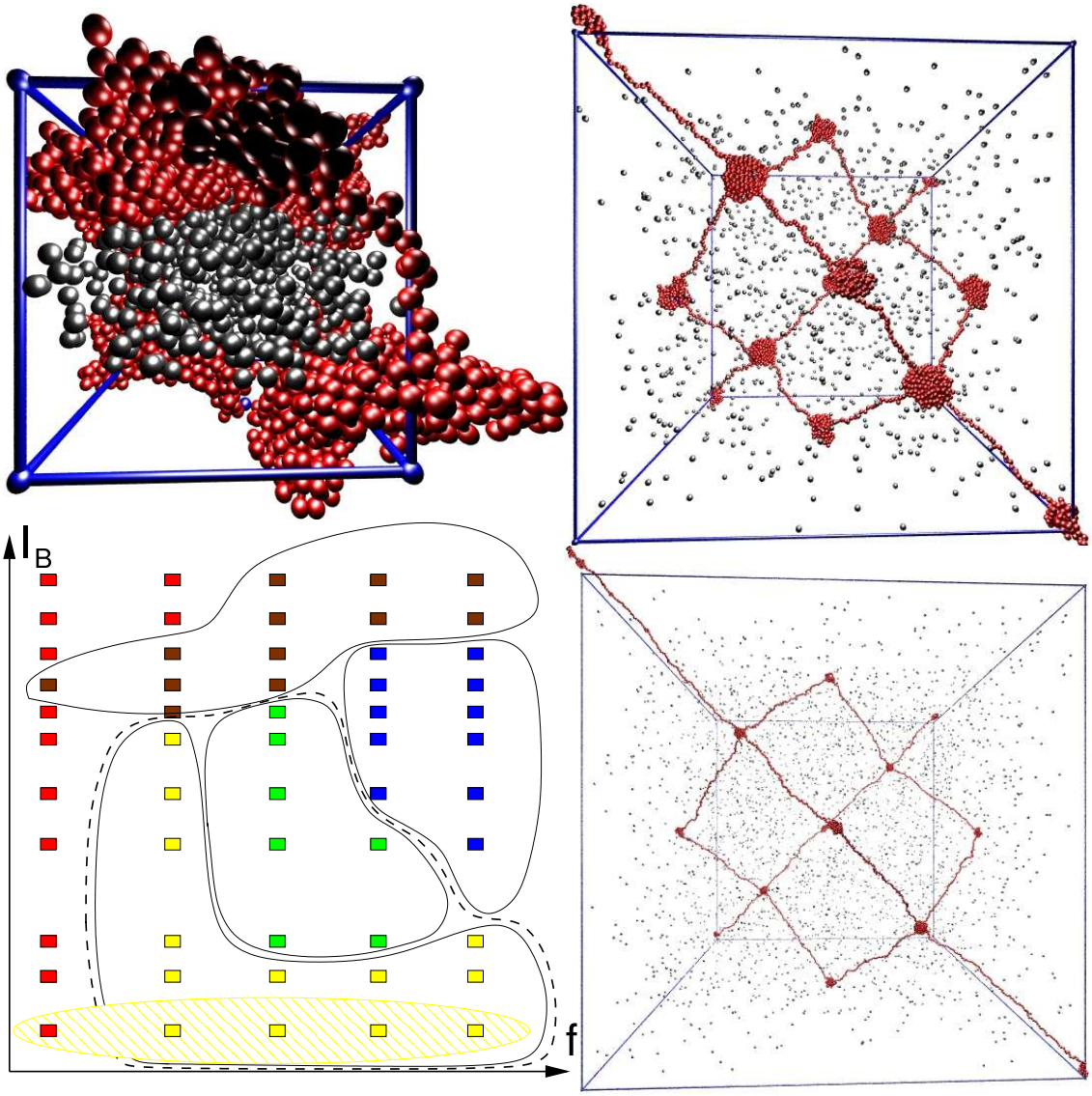

Figure 5.10.: Snapshots of C-series equilibrium conformations at $\ell_B = 0\sigma$ for $f = 0.125$ (*top left*), $f = 0.3333$ (*top right*), and $f = 1.0$ (*bottom right*); its position in the parameter space is illustrated with the yellow-shaded ellipsoid; monomers are *red*, counterions *gray* spheres.

and through the bottom). Consequently, we cannot expect as low a value for R_E and the characteristic ratios r and α as in the previous section 5.2, because there the single polymers neither had external constraints while collapsing nor did they enclose the "counterions" which were free to move away from the emerging globule due to their entropic degrees of freedom.

That is also the reason why for an increasing charge fraction f we no longer observe collapsed structures at all, even for the case of no electrostatics: The growing

amount of $N_{\mathrm{CI}} = N_{\mathrm{nodes}} + N_{\mathrm{p}} \cdot f N_{\mathrm{m}}$ "counterions" exerts a larger, entropy-driven osmotic pressure against the short-range attraction between the monomers on smaller length scales, and enforces swelling of the hydrogel. The two snapshots on the *left* in figure 5.10 illustrate this competition, having the network nodes act as condensation nuclei where, due to the larger monomer density there, onsets of globular collapse remain. Between the intermediate $f = 0.3333$ in the *upper left* and the maximum $f = 1.0$ (*bottom left*), these become as smaller as more counterions enter the system and swell the hydrogel. Quite obviously, without the network connectivity no such swelling mechanisms would exist, allowing the "counterions" to obtain their entropic freedom without stretching the chains into energetically and entropically unfavorable positions. Neutral networks (*i.e.* without additional "counterions") on the other hand would also collapse *despite* their topology, since no counteracting force prevents them to. Therefore, it is once more the unique combination of balancing "counterion" and network chain properties which determines the hydrogel's behaviour, making it distinct from single polyelectrolytes and neutral networks.

The schematic structure diagram in the *lower left* of figure 5.10 already indicated this increased complexity, colour coding simulation runs whose swelling equilibrium was found to be a collapsed state in *red*, the ones with only the nodes acting as condensation nuclei in *yellow*, pearl-necklace structures in *green*, simply stretched networks in *blue*, and snapshots falling into the sausage-regime in *brown*. The transition between the five regimes is smooth and continuous, in good agreement with the results from single polyelectrolytes, but contrary to what scaling theories have predicted there, expecting *e.g.* a collapse of the pearl-necklace structures in a first-order transition with the onset of counterion condensation [164, 184]. Particularly the first four categories cannot be precisely separated while they smoothly cross over from one to the other: Starting out as a collapsed conformation, an increase in the amount of counterions (*i.e.* a larger f) and higher electrostatics (*i.e.* larger ℓ_{B}) slowly pushes the monomers apart and feazes the globules around the network nodes, which separate once the required volume increase (with the corresponding surface tension attached) invokes the Rayleigh instability. The emerging structure, now in the *yellow* regime, has features of the dumbbell-like polyelectrolytes, except that here the "dumbbell's" ends are joined and shared with the three neighbouring network strands. Increasing f and ℓ_{B} further exerts more pressure on the hydrogel and enforces larger box volumes, which in turn causes elongation of the chains and reduces the number of monomers in the globules at the nodes. As this is an external constraint, sufficiently long strands can now form additional pearls, the pear-necklace regime is reached. There, it is the delicate balance between electrostatic repulsion and short-range attraction which dominates the shape of the network strands, as we already know from the investigation of single polyelectrolytes, now competing with the additional osmotic pressure of the counterions which was unimportant before in case of the polyelectrolyte solution. Even stronger electrostatics and counterions shift the balance in favor of the coulombic repulsion, the pearls break down, and

as the short-range attraction becomes less important the network approaches the behaviour of strongly charged hydrogels in good solvent.

From this description, the continuous nature of the transitions between these regimes already becomes apparent. Supplemented by fluctuations and anisotropical effects in the high density limit, no sudden phase transition can be expected here. It nevertheless makes sense to distinguish regimes with similar conformations as good as possible, because they are characterized by intrinsically different physical mechanisms originating in the respectively dominating effect of either short-range attraction, entropic degrees of freedom, electrostatic repulsion, surface tension, or network topology.

Coming back to the pearl-necklace regime, theorists started to suspect its existence for charged hydrogels in poor solvent as well, once the corresponding conformations had been found for the single polyelectrolytes. The inset of figure 5.11 shows such a prediction, taken from [40], and relates it to an actual snapshot from our simulation,

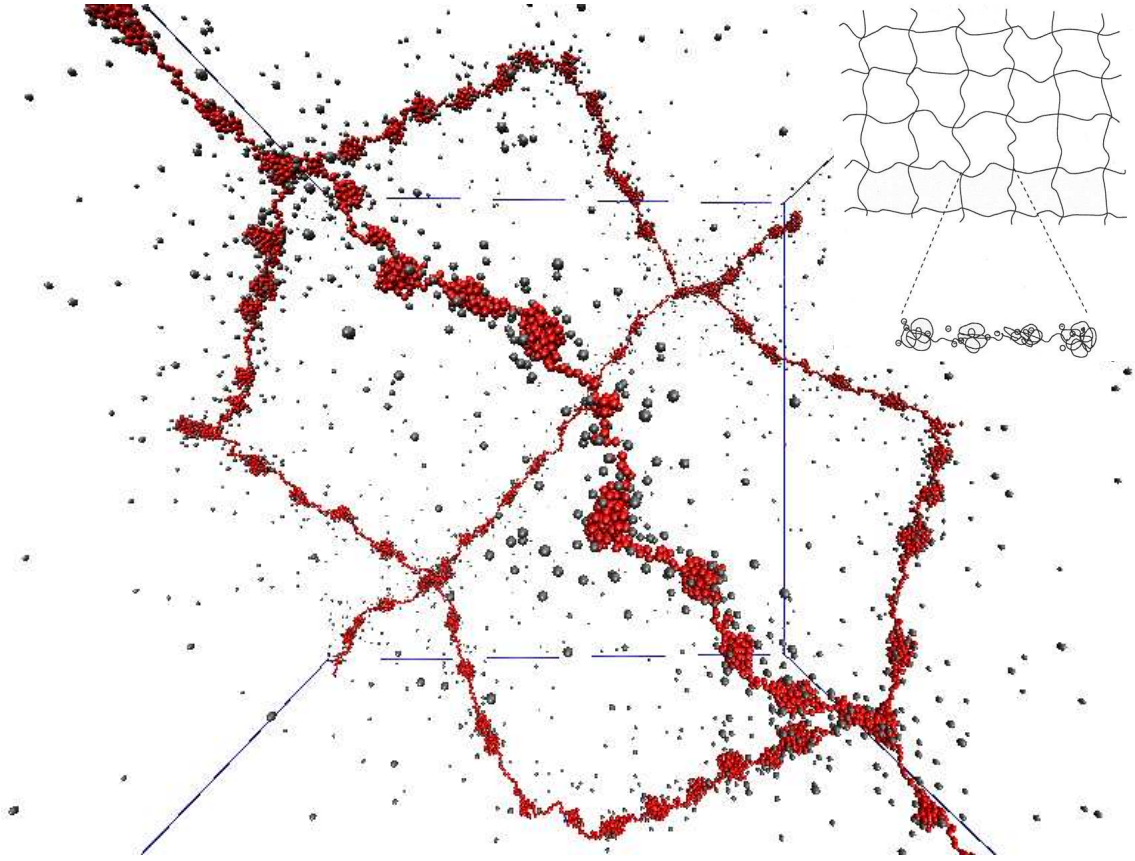

Figure 5.11.: Snapshot of our equilibrium conformation for $N_{\mathrm{m}} = 479$, $f = 0.3333$, and $\ell_{\mathrm{B}} = 1.5\sigma$, nicely depicting the predicted pearl-necklace structure the theoretical sketch in the inset (taken from [40]) envisioned.

for illustration purposes this time not from the C-series we are discussing in this subsection, but from a system with much longer chains ($N_m = 479$) in the otherwise unchanged parameter regime (*i.e.* $f = 0.3333$ and $\ell_B = 1.5\sigma$) to emphasize that formation of more than one pearl is actually possible and is only dependent on the available chain length. We know from figure 5.2 that for $N_m = 200$ more than the

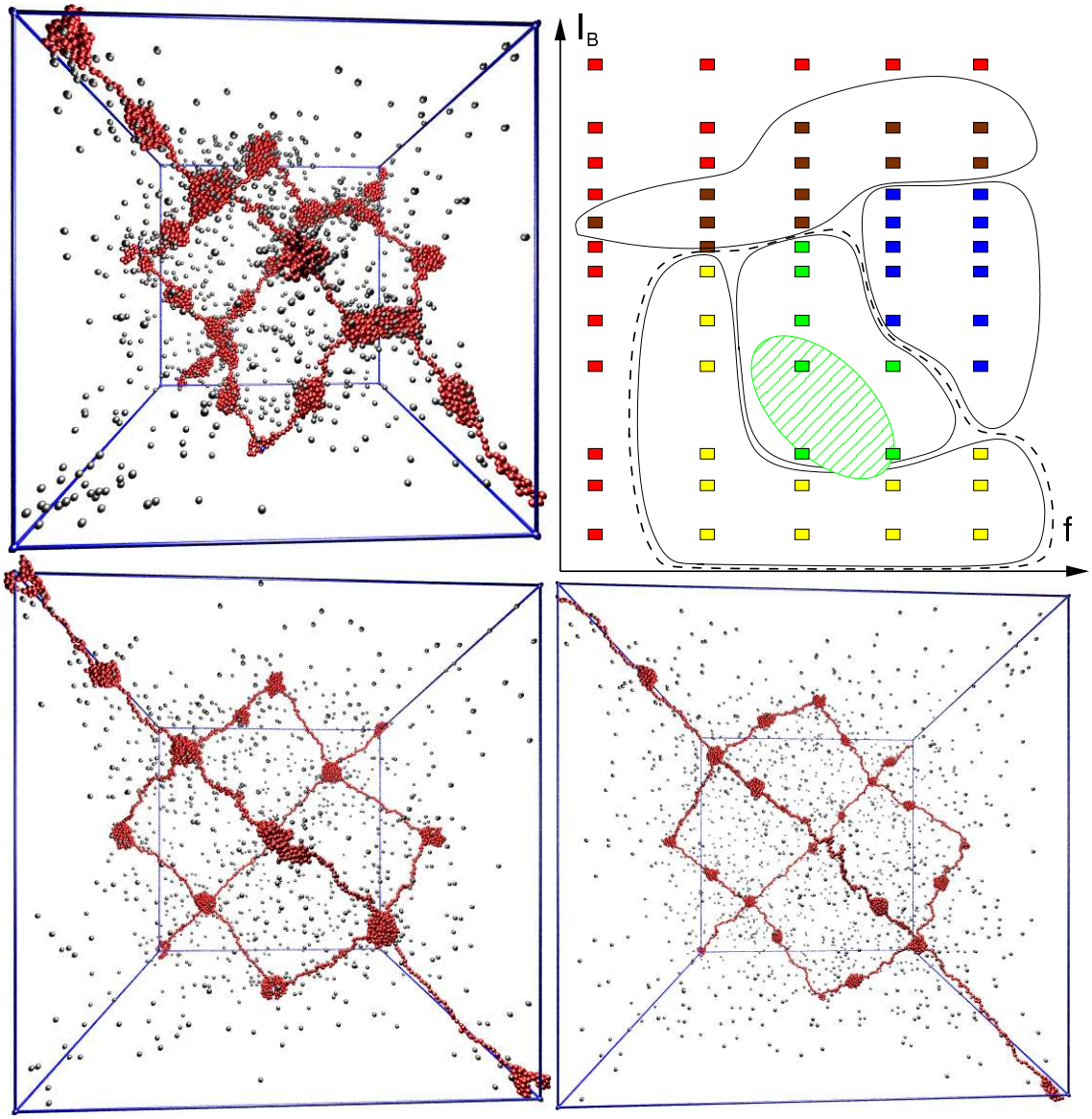

Figure 5.12.: Snapshots of C-series equilibrium conformations at $\ell_B = 0.25\sigma$ and $f = 0.3333$ (*bottom left*), $\ell_B = 0.25\sigma$ and $f = 0.5$ (*bottom right*), $\ell_B = 0.75\sigma$ and $f = 0.3333$ (*top left*); again, their position in the parameter space is illustrated with the green-shaded ellipsoid; the structure diagram in the *upper right* is discussed in the text.

two pearls at the respective ends cannot be expected, particularly since section 5.2 estimated each to contain $g_P = 78 \pm 4$ monomers in the parameter regime we are using. Since in our networks, the ones at the nodes are actually "shared" with the neighbouring chains, only around $\frac{1}{4} \cdot 78$ monomers have to be contributed by each one, such that an intermediate pearl and two adjacent strings of $\sim$40 monomers may exist. Figure 5.12 shows this rough estimate to be correct, as we find the expected number of pearls in the snapshots. Comparing the case of $f = 0.3333$ and $\ell_B = 0.25\sigma$ in the *lower left* to the other two examples depicted, the trends discussed so far can be found again: For a larger charge fraction of $f = 0.5$ but the same strength in the electrostatics, equilibrium is reached at a larger simulation box volume due to the additional osmotic pressure the higher number of counterions caused; as a consequence, the network chains in the snapshot on the *lower right* are elongated further, the pearls became smaller since the stronger strain on the strands pulled some of the monomers out of the globules. Increasing electrostatics to $\ell_B = 0.75\sigma$ instead, while keeping the charge fraction constant at $f = 0.3333$, shifts the equilibrium towards smaller volumes of the box, because the counterions are pulled closer to the chains, as one realizes upon visual inspection of the snapshot in the *upper left* of figure 5.12 where the *gray* spheres depicting the counterions are more commonly found close to the beads in *red*; consequently, the chain extension decreases and more monomers may enter the pearls, hereby favoring the ones at the nodes due to the locally increased concentration there.

Such behaviour already hints to the conformational changes occurring once the strength of the coulombic coupling continues to grow, giving rise to effects which are now less dependent of the charge fraction f but on the Manning parameter ξ_M, a characteristic combination of system properties and indicator for the onset of counterion condensation, as extensively discussed in the previous chapters 3 and 4, *e.g.* sections 3.2.4, 3.2.7, and 4.2.2. Stronger electrostatics pulls the ions towards the chains, decreasing the effective osmotic pressure swelling the network against elasticity and short-range attraction. While this merely allows more monomers to make the globules grow at first, it also screens the electrostatic repulsion separating the pearls, such that the intermediate strings may become shorter until neighbouring clusters of monomers merge, rendering the chains to appear more cigar-like or "sausage"-shaped, and the final regime is entered.

Figure 5.13 displays three example conformations which do no longer have distinct pearls but rather exhibit massive monomeric structures along the network backbone. These are thicker for lower charge fractions, because the larger ratio of monomers to counterions makes the (attractive) contacts between beads more likely, while their repulsive electrostatic interaction is screened by the (almost) completely condensed counterions. In the case of $f = 0.25$ and $\ell_B = 3.0\sigma$ (*lower left* of figure 5.13), the Manning parameter $\xi_M \approx 7.5$ indicates a very strong coulombic coupling, and the *gray* counterions are indeed localized on the chains; the snapshot shows thick cylindrical or "sausage"-like clustering of the monomers, where the radius naturally

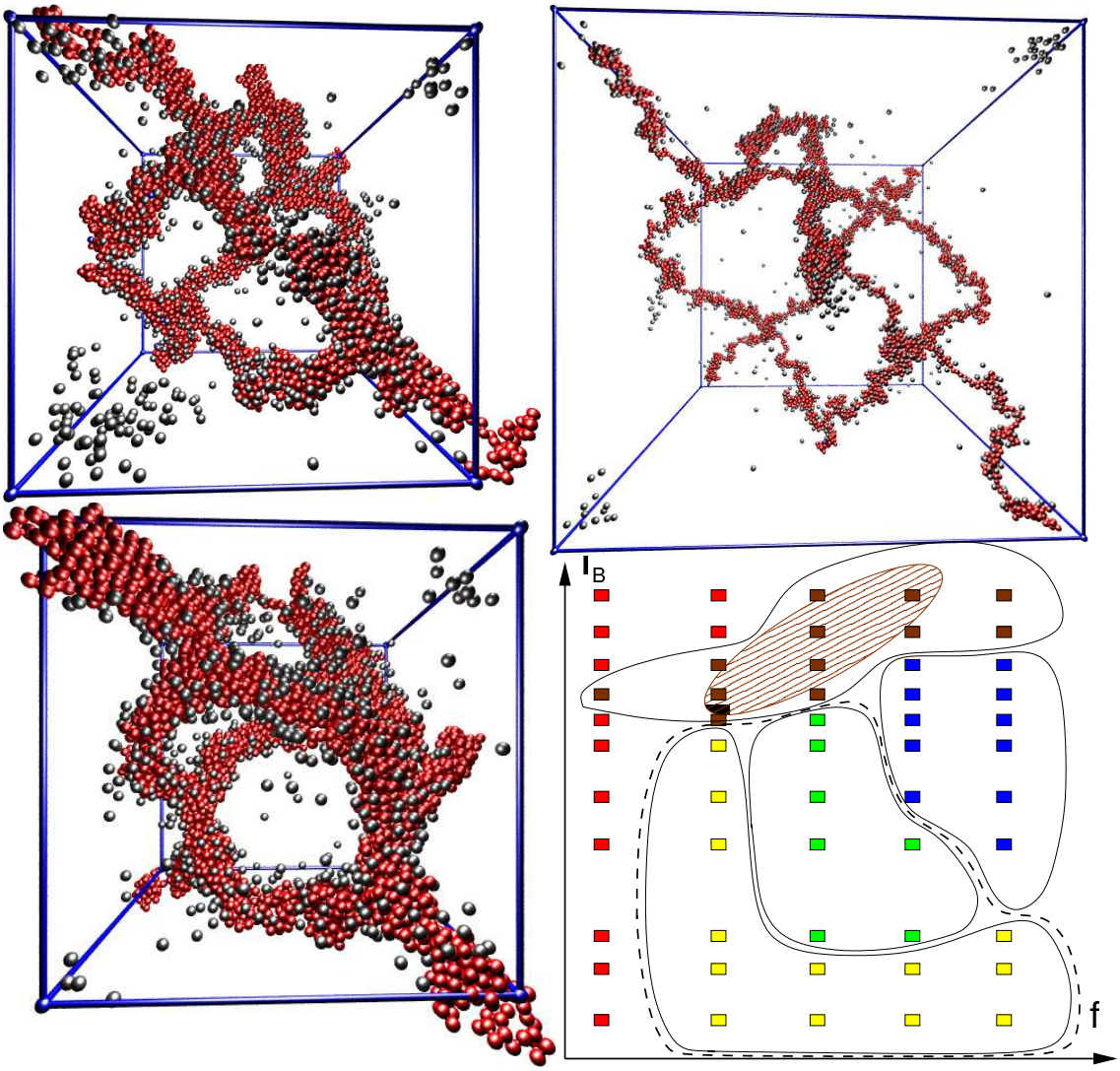

Figure 5.13.: Snapshots of C-series equilibrium conformations at $\ell_B = 3.0\sigma$ and $f = 0.25$ (*bottom left*), $\ell_B = 5.0\sigma$ and $f = 0.3333$ (*top left*), $\ell_B = 6.0\sigma$ and $f = 0.5$ (*top right*); their position in the parameter space is illustrated with the brown-shaded ellipsoid.

varies with the distance from the nodes with their locally increased monomeric density. Even higher electrostatics with $f = 0.3333$, $\ell_B = 5.0\sigma$, and $\xi_M \approx 16.7$ have more condensed counterions in contact with chain monomers, preventing part of their mutual contacts therefore increasing the node-node separation while shrinking the "sausage" size. The uniformity of such structures is disrupted further for larger amounts of counterions firmly bound to the chains due to the coulombic coupling, as in the case of the *upper right* snapshot with $f = 0.5$ and $\ell_B = 6.0\sigma$ where the strand in the center of the picture is still resembling the "sausage"-like clusters from

the other examples, while some of the outer chains, *e.g.* the one in the top left of the simulation box, almost seem to display another pearl-necklace conformation, clearly having a locally varying monomer density profile.

It is now straightforward to see what will happen for another increase in the Bjerrum length, as it will tightly bind the few free counterions left to the chains, completely screening off any remaining repulsion, leaving only the elasticity and the short-range attraction which will then collapse the network. As figure 5.13 inferred, lower charge fractions will aid in this process because monomer-monomer interactions are already stronger there, initiating the transition earlier as compared to systems with many counterions.

Nevertheless, collapsed structures in the strong electrostatics limit are fundamentally different from the ones for vanishing electrostatics, as a direct comparison of their respective snapshots shows (see *e.g.* the complete overview in appendix C). The former see an almost dipolar structure, where pairs of ions and monomers are maximally mixed, while the latter have a clear phase separation between the "gas" of counterions, trapped within the network topology but eager to maximize their respective distance to one another and to the network itself, on the one side, and the monomers, trying to minimize their mutual separation due to the short-range attraction between them, on the other. There is a smooth crossover in between, where the phase separation slowly gives rise to the total mixing of the two particle types for increasing coulombic coupling; this, however, does not change the general trend of being collapsed in the swelling equilibrium.

Figure 5.14 summarizes the entire discussion into a structure diagram of charge fraction f and Bjerrum length ℓ_B, illustrating the small sketch already contained in figures 5.10, 5.12, and 5.13 with even more example conformations taken from the complete overview in appendix C. Similar to the structure diagram found for single polyelectrolytes, which was shown in figure 5.4, we identified regimes of similar structures, *i.e.* collapsed conformations for small charge fractions or very strong electrostatics, pearl-necklaces for moderate to high charge fractions and not too strong coulombic coupling, stretched structures for large f and moderate ℓ_B, and finally the "sausage"-regime for larger Bjerrum lengths; to emphasize the trends discussed earlier, we distinguished between cases where only the nodes act as condensation nuclei, and those with at least one additional pearl along the network strand.

Compared to figure 5.4 we notice that the structure diagram for polyelectrolyte networks contains similar regimes, albeit at shifted positions in the parameter space, despite the fact that we used the very same set of parameters for our simulations. Besides the pearl-necklace regime extending down to the case of vanishing electrostatics ($\ell_\mathrm{B} = 0\sigma$) for not too low charge fractions, we do not (and cannot) find globular conformations, both differences due to the network topology trapping the counterions. Once electrostatics is up and chains are sufficiently long, the charged hydrogels behave similarly to the single polyelectrolytes, including the collapse for very strong coulombic coupling where the remaining dependence on the network

topology becomes negligible. As we have ventured further towards lower charge fractions, also investigating $f = 0.25$ and $f = 0.125$ which were not considered in the single chain study, we are able to conclude on that limit, too, particularly since we find only collapsed conformations for the lowest amount of counterions which are obviously insufficient to generate a strong enough osmotic pressure to push the

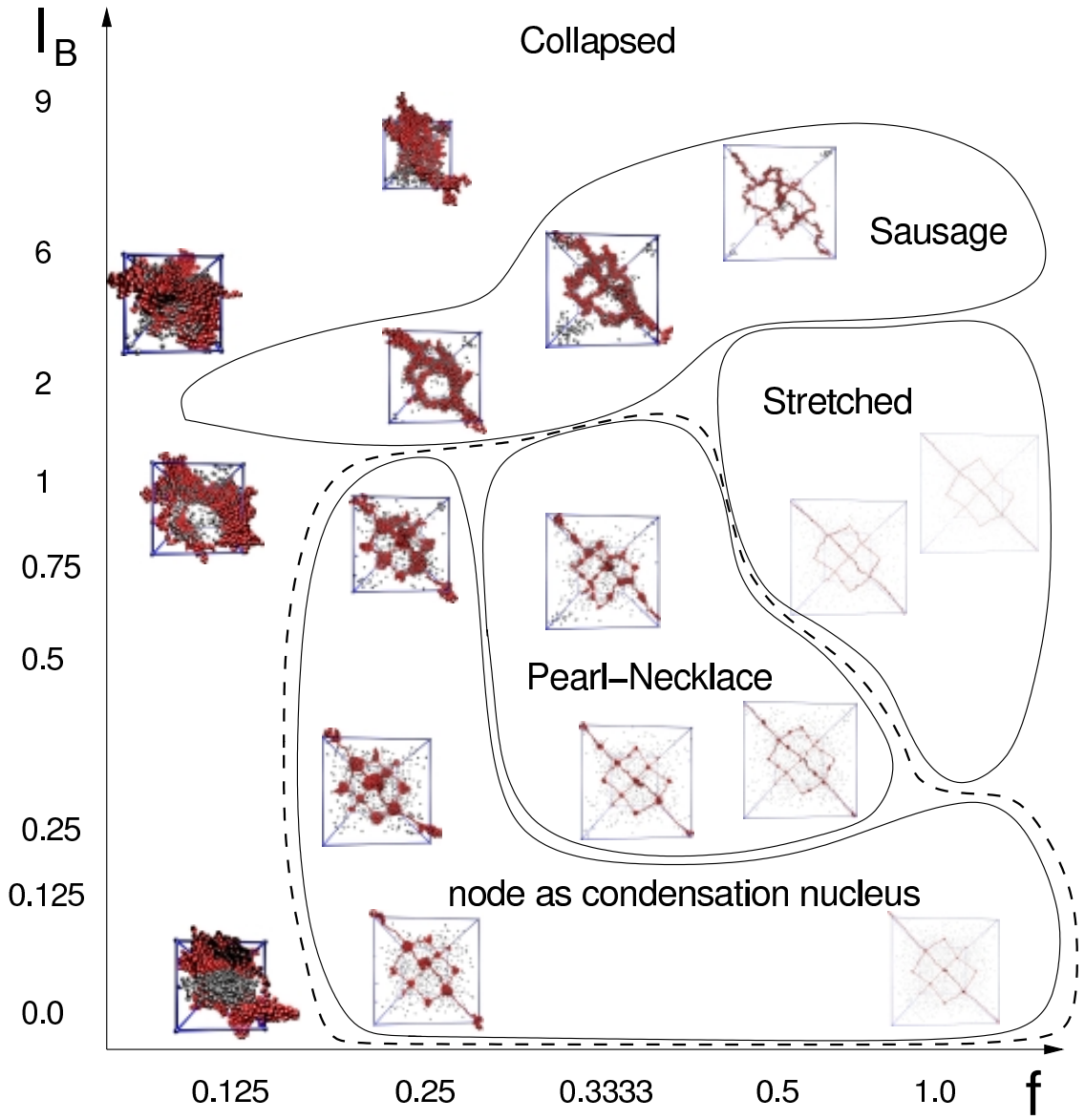

Figure 5.14.: Structure diagram of the equilibrium swelling conformations charged hydrogels assume in a poor solvent with $\epsilon_{\mathrm{LJ}} = 1.75\, k_{\mathrm{B}}T$ for varying charge fraction f and Bjerrum length ℓ_{B}, contrasting the corresponding picture for single polyelectrolytes in figure 5.4 and summarizing the results from the previous figures.

attractive monomers apart. (One would consequently expect single polyelectrolytes with $f = 0.125$ to also form globules for all values of ℓ_B, with an increasing amount of counterion condensation and subsequent mixing between ions and monomers for growing electrostatics, arguing that the few remaining charges on the chain are not sufficient to effectively counteract the collapsing tendencies.)

In general, the parameter space for polyelectrolytes has far more dimensions, such as the solvent quality parameter ϵ_{LJ}, the valency of monomers or counterions, and added salt in the system. As we are focusing on a direct comparison with the single chain results, none of these were examined further; for the future, however, they would provide the next logical steps.

5.3.4. Geometrical Properties

Now that we have identified and discussed the respective regimes of equivalent conformations in the parameter space of charge fraction and Bjerrum length, we can try to find hints to that behaviour in plots of the geometrical properties at swelling equilibrium, as determined from the interpolation of the (N, V, T)-data towards $V = V_{eq}$.

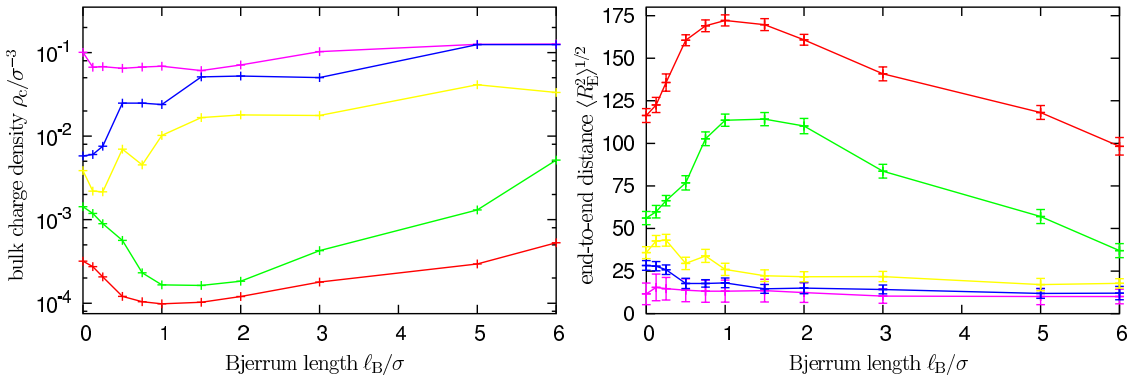

Figure 5.15.: Dependence of ρ_c (*left*) and R_E (*right*) on the Bjerrum length ℓ_B for the C-series (see table 5.2), contrasting the single polyelectrolyte behaviour from figure 5.3 (charge fraction dependent colouring as in table S.1).

Starting with the bulk charge density ρ_c and the node-node separation R_E, we observe largely equivalent dependence on ℓ_B in the plots of figure 5.15, because both are connected via the periodic network topology to the simulation box; contrary to the total particle density $\rho = N_{tot}/V$, however, the bulk charge density depends on the amount of charges only, such that its relation to R_E is different from the usual diamond-lattice prefactor. Where the single polyelectrolytes in figure 5.3 started off at $\ell_B = 0\sigma$ as compact globules with an almost negligible size independent of the charge fraction, uniformly returning to only slightly larger conformations in the high electrostatics limit, the networks have clearly f-dependent sizes in the first

case, because of the osmotic pressure the trapped counterions exert which prevents the total collapse; that is corroborated by the fact that higher densities are possible for $\ell_B \to 0$ if the charge fraction drops. In the other limit, the networks are now following the example of the single polyelectrolytes, as the counterion condensation-induced neutralization removes the constraint of their osmotic pressure and allows the short-range attraction to dominate. Hereby note that our plot only extends up to $\ell_B = 6\sigma$ as higher electrostatics already proved to be so dense that no equilibration was possible (also refer to the $p(V)$-diagrams in figure 5.6); compared to the single chains the cases of $f = 0.5$ and $f = 0.3333$ had already reached similar sizes to their respective counterparts at that point, resulting in a much higher slope in the descent and justifying our statement. Though the general trend in $R_E(\ell_B)$ is the same for both scenarios, with the chain extension exhibiting a broad maximum for $f = 1.0$ and $f = 0.5$, the peak position is shifted from around $\ell_B = 2\sigma$ towards $\ell_B = 1\sigma$, being much larger as well ($R_E \approx 130\sigma$ to $R_E \approx 170\sigma$ for $f = 1.0$), once again due to the presence of the counterions whose osmotic pressure, negligible in the single chain case, exerts an additional swelling effect (increasing R_E) before being decreased by the "removal" of condensed ions (shifting ℓ_B). In case of the lower charge fractions, the chain extension decreases monotonically as the remaining obstructions from gas-like ions are also removed through increasing electrostatics binding them to the chains, maybe with an additional small maximum for $f = 0.3333$ at very low values of the coulombic coupling, which could be explained by the initially larger volume likewise charged counterions require before condensation sets in.

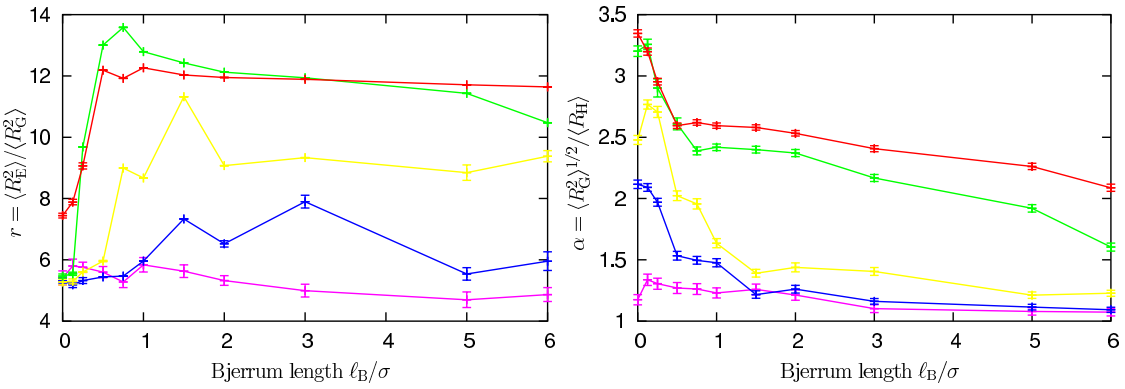

Figure 5.16.: Change of the characteristic ratios $r = \langle R_E^2 \rangle / \langle R_G^2 \rangle$ (*left*) and $\alpha = \langle R_G^2 \rangle^{1/2} / \langle R_H \rangle$ (*right*) with ℓ_B for the C-series, contrasting the single polyelectrolyte behaviour from figure 5.4; colours correspond to their usual f as in table S.1.

The characteristic ratios $r = \langle R_E^2 \rangle / \langle R_G^2 \rangle$ and $\alpha = \langle R_G^2 \rangle^{1/2} / \langle R_H \rangle$ as a function of the Bjerrum length ℓ_B, displayed in figure 5.16, reflect this behaviour of equilibrium density and node-node separation. They do no longer start off at a common value for $\ell_B = 0\sigma$, there is no sharp increase in α for small Bjerrum lengths, although the subsequent monotonic decay can be observed. The values found are also commonly

higher than in the case of single polyelectrolytes, most notably the ratio between end-to-end distance and radius of gyration for *e.g.* $f = 1.0$ and $f = 0.5$ which are indicating through $r \approx 12$ a strongly elongated conformation, much stronger than for the isolated chains because these did not experience the additional swelling contribution from the osmotic pressure of the counterions. Though the intermediate exceeding of the rod-like ratio for $\ell_B \lesssim 1\sigma$, with $f = 0.5$ even reaching values close to $r = 14$ (!), might seem surprising at first, we already mentioned during the discussion of the several model values for r collected in table 2.2 that this merely indicates an increased "mass" (*i.e.* monomer) agglomeration close to the center-of-mass of the chain. Recalling that for the chosen parameters and chain lengths we find one pearl per network strand (plus the shared ones at the nodes) which was located in the middle of that chain due to the electrostatic pear-pearl repulsion, our observation fits perfectly as $r > 12$ now indicates recognition of the locally increased monomer density close to the chain's center. Figure 5.17 visualizes this, emphasizing that since the pearls at the nodes are composed of contributions from all four network chains crosslinked there, the analysis of the radius of gyration R_G for each of them individually only detects the "mass" agglomeration at the chain's center which is four times higher than the (symmetric) increase at its ends.

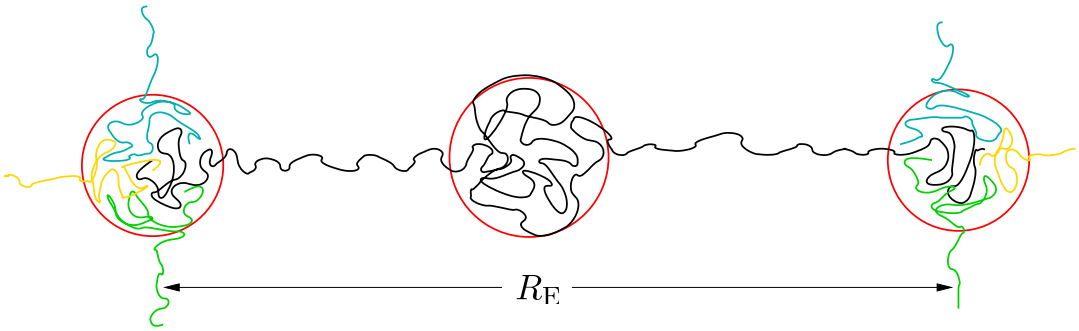

Figure 5.17.: Visualization of a ratio $r > 12$ on our network chains occurring for one central pearl, since the globules at the nodes are composed of contributions from all four strands crosslinked there (the *red circles* indicate the positions of pearls, coloured lines facilitate distinction of different network chains).

For single polyelectrolytes similar findings cannot be expected since it requires the *biggest* pearl to be localized close to the middle of the polymer, which is precisely the opposite of what is usually found as they exhibit an orb-like size profile for the pearls, *i.e.* having their diameter grow with the distance from the chain's center. It would also be futile to try to generalize this observation towards a pearl-recognition criterion, because it is an artefact of the network topology which causes the pearls at the nodes to be "shared" among all neighbouring chains, such that the individual network strand with one centered pearl only sees slightly increased local monomer concentrations at its end, without "knowing" that the latter will eventually add up

to additional pearls. Longer chains with more than one individual pearl along their backbone will decrease the peak in r further, until it can no longer be distinguished if the ratio refers to extended conformations as in the case of good solvents or describes a pearl-necklace structure.

5.3.5. Form Factor Findings

More information about the chain conformation is usually obtainable from the form factor $S(q)$ which we already employed successfully in section 4.2.1 to study the reflection of simple scaling arguments in the structural properties of good solvent hydrogels. For the single polyelectrolytes, the form factor of the chains with $N_\mathrm{m} = 382$ in series A1 is plotted on the *left* of figure 5.18, where it is known that they assume pearl-necklace conformations with $n_\mathrm{P} = 4.5$ pearls per chain; it is compared to the charged hydrogels of the A-series plotted on the *right* for the chain lengths between $N_\mathrm{m} = 335$ and $N_\mathrm{m} = 479$, exhibiting $n_\mathrm{P} = 4.0$, $n_\mathrm{P} = 4.3$, $n_\mathrm{P} = 5.9$, $n_\mathrm{P} = 5.7$ pearls, respectively.

In the Guinnier regime of low scattering angles $qR_\mathrm{G} \ll 1$, the form factor can be expanded [156] into the *Guinnier function*

$$S(q) \approx N_\mathrm{m} \exp\left(-\frac{q^2 R_\mathrm{G}^2}{3}\right) \approx N_\mathrm{m}\left(1 - \frac{q^2 R_\mathrm{G}^2}{3}\right)$$

providing a basis for determining the radius of gyration from small-angle scattering experiments for objects with unknown form factor. This yields $R_\mathrm{G} = 16.8\sigma$ for the single polyelectrolytes, in good agreement with the directly measured $R_\mathrm{G} = 16.9\sigma$ [54], while in case of the charged hydrogels the same approach results in $R_\mathrm{G} = 16.7\sigma$ for the network chains with $N_\mathrm{m} = 383$ monomers, which is also corresponding quite perfectly to the $R_\mathrm{G} = 16.7\sigma$ observed; the other network chains also lead to matching values of $R_\mathrm{G} = 15.8\sigma$ (for $N_\mathrm{m} = 335$), $R_\mathrm{G} = 17.2\sigma$ ($N_\mathrm{m} = 431$), and $R_\mathrm{G} = 17.7\sigma$ ($N_\mathrm{m} = 479$) for both types of derivations.

Small scattering angles between $0.07\sigma^{-1}$ and $0.4\sigma^{-1}$ see the form factor scale as $S(q) \propto q^{-1}$, reminiscent of the strongly elongated structures we observed for good solvent hydrogels; on length scales larger than 15σ the chain conformations are therefore stretched. It should however be noted that for the isolated polyelectrolytes this behaviour is only approximately reached, indicated by the employed fit of $\sim q^{-0.93}$ in the plot, whereas the charged hydrogels clearly exhibit an almost perfect match with $\sim q^{-1.00}$ over the entire range given. This reflects what we already found earlier in the characteristic ratio $r = \langle R_\mathrm{E}^2\rangle / \langle R_\mathrm{G}^2\rangle$ where the single chains could not really reach the rod-like regime of $r = 12$ while the networks even exceeded that threshold locally; it also emphasizes the influence of the node connectivity which is the responsible mechanism.

For wave vectors around $q \approx 0.5\sigma^{-1}$, we observe a weakly pronounced shoulder in

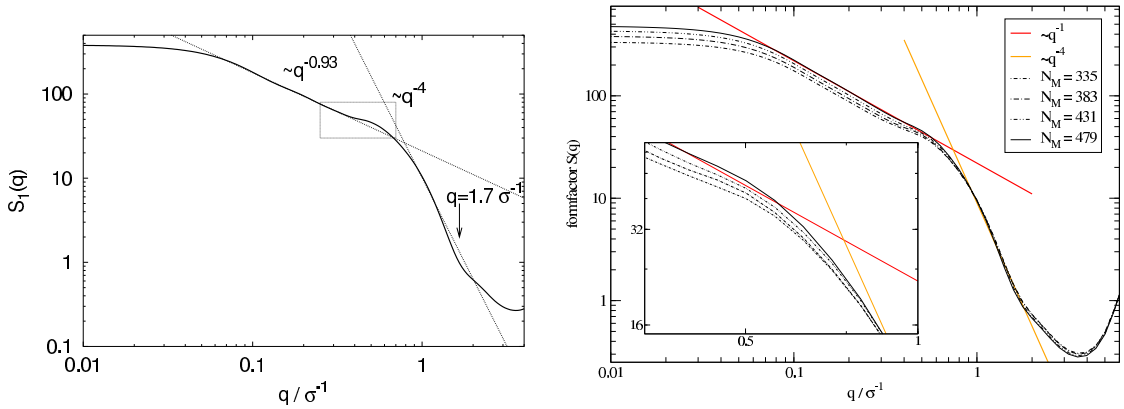

Figure 5.18.: Form factor $S(q)$ for typical pearl-necklace conformations on single polyelectrolytes (*left*, taken from [54]) with $N_\mathrm{m} = 382$, $f = 0.3333$, $\ell_\mathrm{B} = 1.5\sigma$, and for networks (*right*) with the same parameters but different chain lengths; the straight lines are fits to certain q-ranges, the marked region indicates a shoulder in the plots present for both systems which is magnified in case of the hydrogels.

the form factor. Looking closer (see inset of figure 5.18) it is revealed that $S(q)$ has an inflection point there, which could be related to the inter-pearl scattering in [54].

In the limit of large q between $0.9\sigma^{-1}$ and $2.5\sigma^{-1}$, the scaling shifts towards $S(q) \propto q^{-4}$, the typical Porod scattering of strongly collapsed objects. While the single polyelectrolytes exhibit another small dip at $q \approx 1.7\sigma^{-1}$ which relates to the pearl radius, the networks do not seem to distinctly have such a feature because of the external tension exerted through the network topology.

The cooperative effect of fluctuations on overlapping length scales consequently broadens all characteristic signatures that can be revealed by experimental scattering methods. Considering that we have investigated a model system without impurities, irregularities, influences of defects or other obstructions to the leading mechanisms we identified here, pear-necklace structures might indeed be difficult to detect in real world experiments. Nevertheless, our computer simulations allowed to indicate some of the prominent features experimentalists can expect when analyzing their data, which combined with highly regular model networks such as the example of the P*t*BMA introduced in figure I.3 should finally enable experimental observation of the prominent pearl-necklace structures unique to polyelectrolyte networks in poor solvent.

5.3.6. How Pearls might be discovered

When this work was already completed, we learned of some very recent experiments by Combet *et al.* [189] who examined a solution of CsPSS with the help of small angle x-ray scattering (SASX). Using caesium instead of the usual sodium as counterions (compare to *e.g.* figure I.2 or I.4) returns a higher intensity and allows to analyze

spatial structures they might form. As figure 5.19 now shows, rescaling by the many concentration c does not only have all the data fall onto a single master curve for sufficiently large q, but it also reveals the counterions to have a common second maximum (marked by the arrow) in their total scattering function which indicates the existence of a dominant (short-range!) length scale there, at around $q^* \approx 0.2$Å.

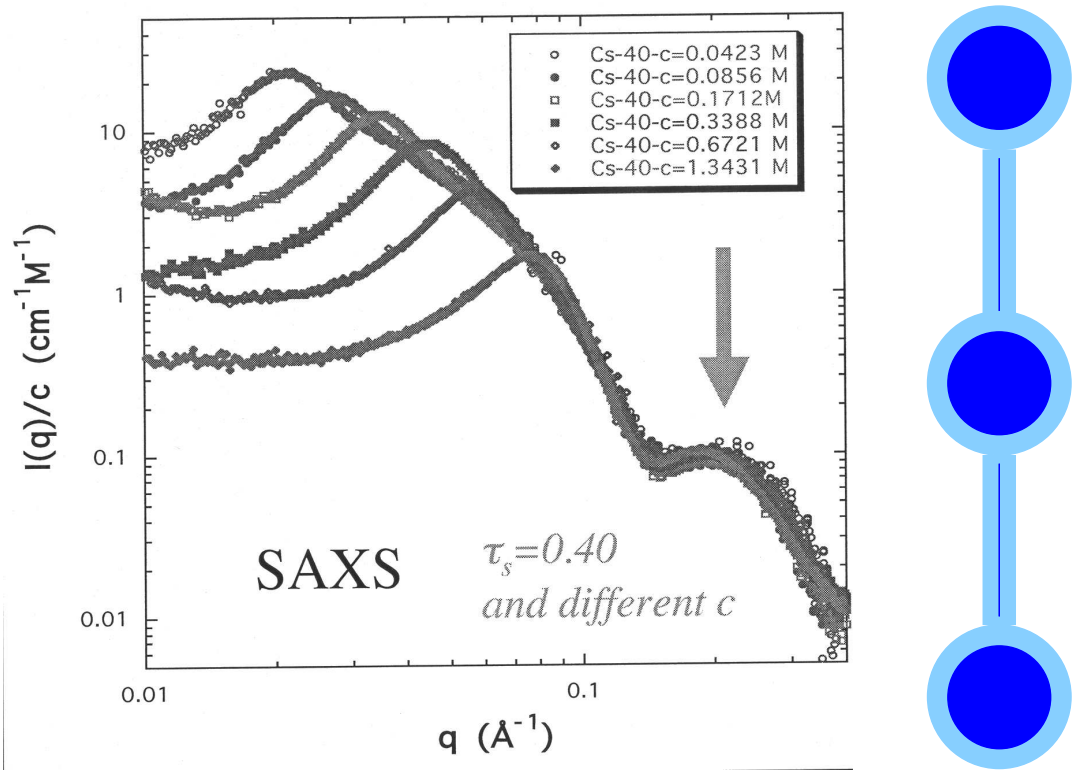

Figure 5.19.: Scattering intensity $I(q)$ obtained from SAXS measurements of CsPSS polyelectrolytes [189]. Normalized by the concentration c all points fall onto the same master curve for large enough q, exhibiting a common maximum for short spatial distances. On the *right* it is sketched how the experimentalists attribute this finding to the polyelectrolyte's geometrical structure, where the darker core represents the polymeric backbone, the lighter shell the condensed counterions; the circles stand for the spherical hydrophobic aggregates (beads), the elongated parts for the cylindrical strings.

A possible explanation is sketched on the *right* of figure 5.19 and tries to connect the findings from the scattering experiment to spatial structures. Claiming that those counterions which are no longer unperturbed by the electrostatic attraction of the chains condense or get very close to them, it is argued that they form a "shell" around the polyelectrolyte's curled shape induced by the hydrophobic interactions with the solvent. Then, the second maximum found is indicating both the regularity of such a structure and its typical spatial extension $\xi^* = 2\pi/q^* \approx 31$Å. Such an

interpretation would be compatible with a pearl-necklace conformation where the counterions would be localized on the surface of the pearls. Although hydrophobic aggregates are easily evidenced by SAXS, non-sulfonated sequences could also form small domains (quenched hydrophobicity) which would be detected in a similar manner; careful preparation of the setup polyelectrolytes can however minimize such anomalies, leaving only globular chain segments to be associated with the findings.

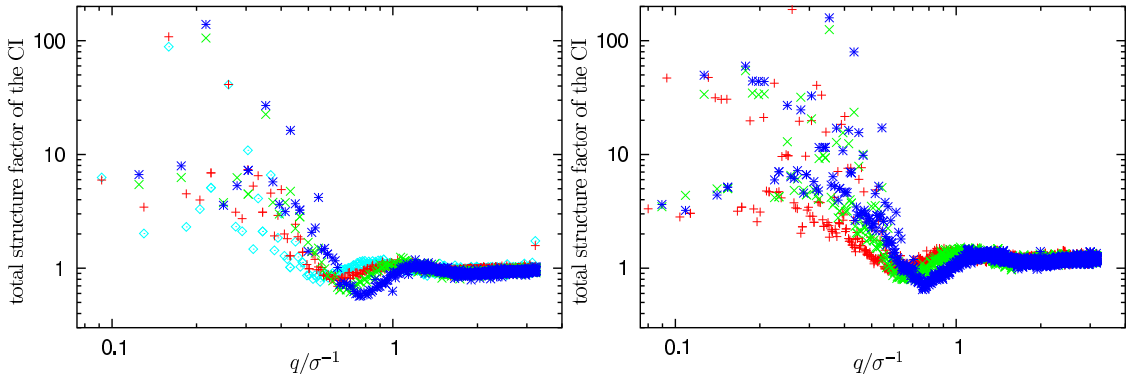

Figure 5.20.: Total structure factor of the counterions for typical pearl-necklace conformations on the strands of a charged hydrogel. While on the *left* equilibrium networks from the C-series have been examined (with $N_\mathrm{m} = 200$, $f = 0.3333$, and $\ell_\mathrm{B} \in \{0.5, 0.75, 1.0, 1.5\}$ plotted in *cyan*, *red*, *green*, and *blue*), with their structure factor averaged over 27 intermediate snapshots, on the *right* the same systems were investigated, but with $N_\mathrm{nodes} = 64$ instead of $N_\mathrm{nodes} = 8$ to evaluate the influence of finite size effects.

Consequently, this could lead to the first direct experimental proof of the pearl-necklace structures on polyelectrolyte chains in poor solvent, and should therefore be observable in our simulations as well, if the arguments are expected to hold at all. So we selected some of the equilibrium conformations within the pearl-necklace regime, and analyzed their total structure factor

$$S(\vec{q}) = (N_\mathrm{p} N_\mathrm{m})^{-2} \sum_{i=1}^{N_\mathrm{p} N_\mathrm{m}} \sum_{j=1}^{N_\mathrm{p} N_\mathrm{m}} \mathrm{e}^{-\mathrm{i}\vec{q}(\vec{r}_i - \vec{r}_j)} \tag{5.9}$$

spherically averaged within the periodic simulation box to [188]

$$S(q) = \left(\sum_{|\vec{q}'|=q-\frac{1}{2}\Delta q}^{|\vec{q}'|=q+\frac{1}{2}\Delta q} S(\vec{q}') \right) \times \left(\sum_{|\vec{q}'|=q-\frac{1}{2}\Delta q}^{|\vec{q}'|=q+\frac{1}{2}\Delta q} 1 \right)^{-1} \tag{5.10}$$

and averaged over all 27 intermediate snapshots. The result, shown in figure 5.20, is very encouraging because it clearly confirms the existence of a second maximum

at large q, even if the finite size of the simulation system prevents from reaching a high enough resolution to cover the entire experimental range. To make sure that the information gained on the position of that second maximum is reliable as well as to estimate the impact of finite size effects on the results, we did not only evaluate our previously obtained systems with $N_{\mathrm{nodes}} = 8$ nodes and $N_{\mathrm{p}} = 16$ chains (*i.e.* a total of 4,272 particles, *left* plot in figure 5.20), but we also analyzed the structures of a diamond-like topology with $N_{\mathrm{nodes}} = 64$ nodes and $N_{\mathrm{p}} = 128$ chains (*i.e.* a total of 34,176 particles, *right* plot in figure 5.20). While none of the main observables previously discussed are affected by the reduction in artificial periodicity (as eight periodic images of the smaller system correspond to the simulation box of the $N_{\mathrm{nodes}} = 64$-system), the resolution of the total structure factor in figure 5.20 improves slightly towards smaller values of q, but it still remains too noisy to identify the main maximum of the scattering function. Further attempts at even larger systems seem inappropriate regarding the disappointing increase in resolution in view of the significant rise of the required computation time, because it would take an estimated factor of 4,096 times the original box size to arrive at a sufficiently large system, extrapolating current CPU consumption to about 11.5 years. However, as we are interested in the limit of large q, it is sufficient to be able to conclude from comparing both systems that even the small one has already resolved the second peak satisfactorily, continuing from there.

With a q^* ranging from $0.8\sigma^-1$ to $1.1\sigma^-1$, the second maximum corresponds to spatial structures of a size between $7.8, \sigma$ and $5.7, \sigma$. This is in nice agreement with the outcome of the cluster algorithm which estimated $n_{\mathrm{P}} = 80, \ldots, 140$ monomers to be in one pearl, putting their extension at around $3.9, \sigma, \ldots, 4.8\sigma$ (close packing assumed), and therefore leads to an average characteristic length scale including the condensed shell of counterions on their surface of $5.9, \sigma, \ldots, 7.3\sigma$.

Hence it seems that experimentalists are now very close to prove the existence of the pearl-necklace structures predicted in theories and seen in simulations for some time, because in our data we can clearly confirm the assumed connection between pearls and the occurrence of a second maximum in the scattering function of the counterions. What needs to be done now is to exclude

5.3.7. Chain Length Dependency

It was already recognized early on that the choice of a sufficiently long chain length plays a more important role in the poor solvent regime, where the dominant effects require a certain minimum amount of monomers to become visible. When looking at the snapshots of figure 5.2 and the corresponding data in [54] from the pearl-necklace regime, a minimum $N_{\mathrm{m}} \gtrsim 190$ is needed to detect pearls also on the chains themselves, preferring $N_{\mathrm{m}} \gtrsim 286$ to clearly characterize these fluctuating structures – for a good solvent, such a chain would already be considered very long, while in poor solvent it seems to rather pose as a lower limit.

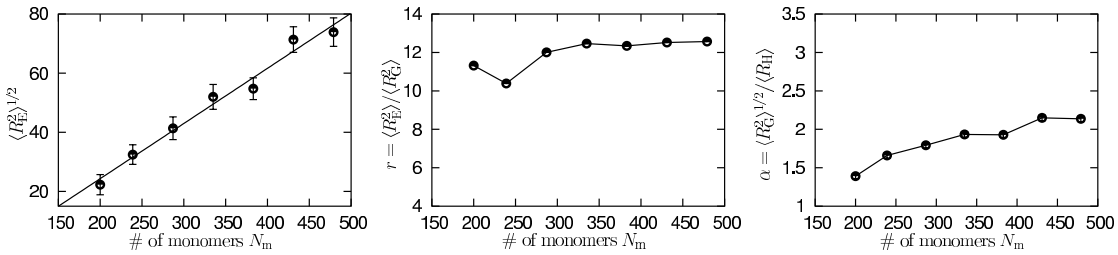

Figure 5.21.: The dependence of node-node separation R_E (*left*) and the characteristic ratios r (*center*) and α (*right*) on the amount of monomers per chain, reflecting figures 5.15 and 5.16 for the A-series ($f = 0.3333$, $\ell_B = 1.5\sigma$).

That is why we also investigated the impact of N_m on our results previously discussed. Looking at the data from the A-series, we do not find dramatic changes once the aforementioned minimum chain length is exceeded. As figure 5.21 illustrates, the equilibrium end-to-end distance for the chosen parameter set of $f = 0.3333$ and $\ell_B = 1.5\sigma$, *i.e.* within the pearl-necklace regime, simply increases linearly with N_m, in agreement with simple scaling predictions [40] expecting the chain extension to behave as $R_E = bN_m (\ell_B f^2/b)^{1/2} \tau^{-1/2}$, where $\tau = (\theta - T)/\theta$ is once again the reduced temperature. The characteristic ratio $r = \langle R_E^2 \rangle / \langle R_G^2 \rangle$ is quite constant for $N_m \geq 287$ at values exceeding the rod-like value $r = 12$ which indicates the aforementioned anisotropic "mass" distribution along the chain. The increase in $\alpha = \langle R_G^2 \rangle^{1/2} / \langle R_H \rangle$ is more pronounced, as the additional pearls allowed on the larger chains become (indirectly) noticeable. This is also the only effect on the snapshots upon visual inspection, with more and more pearls emerging on the network chains in a similar manner the single polyelectrolytes already exhibited in figure 5.2.

If one varies the charge fraction instead, choosing very long chains with $N_m = 479$ monomers at the same $\ell_B = 1.5\sigma$, we can once more observe the transition from collapsed via pearl-necklace towards stretched conformations, as the plots in figure 5.22 show. While the node-node separation $R_E(f)$ grows one order of magnitude, the characteristic ratio r increases from the random walk-like $r = 6$ up to around $r = 12$ of a rod-like, strongly elongated conformation. Similar behaviour is observed for α which mirrors the trends found for the shorter chains in figure 5.16.

It is therefore safe to assume that the chains in the C-series were sufficiently long to exhibit the full range of structures, with longer strands only marginally improving the results (*e.g.* by having more pearls to average over, *etc.*) while at the same time dramatically increasing the required computational effort. Consequently, future studies might also initially focus on the parameter regime we covered here, as it was shown to provide access to the complex behaviour of polyelectrolyte networks in poor solvents.

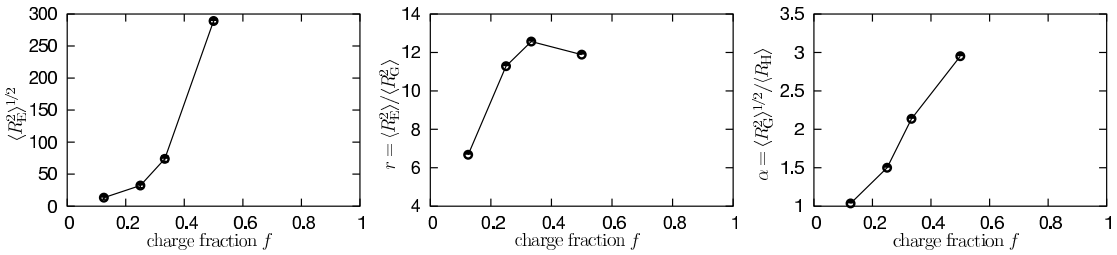

Figure 5.22.: The dependence of node-node separation R_E (*left*) and the characteristic ratios r (*center*) and α (*right*) on the charge fraction f, reflecting figures 5.15 and 5.16 for the E-series ($N_m = 479$, $\ell_B = 1.5\sigma$; see table 5.2).

5.4. Conclusions and Outlook

Macromolecules below the θ-point are no longer easily solvable and favor contacts with themselves over the surrounding solvent molecules. Corresponding to an effective short-range attraction between the repeat units, this additional mechanism gives rise to a variety of new effects in charged hydrogels, as it is competing with the already complex interplay of elasticity, excluded volume, and long-range electrostatics in place.

In this chapter, we therefore expanded further on our results from good solvent systems, investigating the behaviour of polyelectrolyte networks under poor solvent conditions which were taken to mimic previous studies of single polyelectrolyte chains. After introducing these results, we found similar equilibrium swelling conformations in the charged hydrogels, *i.e.* collapsed structures for very low charge fractions or very high electrostatics, local globules of monomers around the nodes and (later on) on the chains forming pearl-necklaces for increasing f and ℓ_B, strongly stretched conformations for large f and intermediate ℓ_B, and "sausage"-like structures for not too low charge fractions and large Bjerrum lengths. Their response to the system environment was comparable to the single chain case, albeit a different structure diagram emerged which arranged them based on the parameters of charge fraction and strength of coulombic coupling. Particularly in the case of vanishing electrostatics systems were no longer dense globules, because the entropy of the counterions confined to the network topology prevented too high densities, increasingly so for larger amounts of mobile ions in the system. The pearl-necklace regime was smaller than theories anticipated, which was consistent with the single chain results where even in dilute solution the delicate interplay between the counterion distribution and the chain conformation for strongly charged chains limited the range of applicability for scaling predictions. We found the point of maximum extension in the network strands to be larger, but shifted towards smaller Bjerrum lengths; the former was attributed to the additional osmotic pressure of the ions, the latter to the onset of condensation effects which effectively remove particles from

the ideal gas-like distribution. The same reason also rendered the network chains to be more elongated, even surpassing rod-like structures for parameters in the pearl-necklace regime. This phenomenon was as extensively discussed as the crossover between the different structures, which was identified to be smooth and continuous. Experimentally accessible observables such as characteristics ratios and form factors were also determined; they may aid in the analyzation of experimental data, although we already revealed that even in the much more homogeneous environment of our simulation box the signatures of *e.g.* pearl-necklace structures are not very pronounced, such that the difficulties in proving the existence of those regimes in real world experiments becomes understandable.

Consequently, including part of their impurities and anisotropies into the simulation model might not be too successful in terms of more clearly distinguishing different regimes, but it would definitely help in understanding the complex scenarios experimentalists are facing, allowing to evaluate promising routes towards a better detection of key observables and structure properties. In that respect, the same suggestions for the good solvent systems hold here as well, *i.e.* introducing random crosslinks with their entanglements and polydisperse polymer distribution, adding salt molecules, or attempting advanced coarse-graining, although the latter might lead to severe difficulties in distinguishing the various structures.

It will also remain an ongoing challenge to connect the findings from such simulations to the theoretical expectations, because the additional layer of complexity through the parameter-dependent short-range attraction induced by the solvent restricts most of their models to a rather small range of applicability, without the possibility to find a quite general description for the majority of the parameter space as this was the case in the good solvent regime from the previous chapters. This, however, is also once more emphasizing the unique contribution computer simulations can offer to the scientific community: Taking up the idealized depiction of reality any theory is based upon, considering it without further assumptions but an appropriate translation onto the techniques developed to handle such systems, and treating it as a real world experiment in terms of observables, implementation, and analysis process; thereby, they are creating a direct link between theory and experiment wherever system complexity formerly prevented it. Until a new generation of experiments will be able to access structural properties in detail, the presented computer simulations may therefore provide a very good template for further expansion upon the achieved relation of the theoretical picture and the single chain studies to the environment of charged hydrogels, the characterization of their equilibrium properties, and the successful identification of the main mechanisms behind the swelling behaviour of polyelectrolyte networks.

A. Equilibrium Swelling Properties

This appendix provides the geometrical and pressure-related data measured for the polyelectrolyte model network, as introduced in section 4.1 and depicted in figure 4.2 with $N_{\mathrm{nodes}} = 8$ nodes and $N_{\mathrm{p}} = 16$ chains carrying N_{m} monomers each, in good solvent or close to the θ-point. Similar to table 4.1 and table 4.3, the observables were determined in the swelling equilibrium where the simulation box volume reached $V = V_{\mathrm{eq}}(\mathcal{P} \approx 0)$, comparing the behaviour for different bare charge fractions f of the network strands and varying strength of the electrostatic interactions, as expressed through the Bjerrum length ℓ_{B}.

While V_{eq} hereby is the direct result of the (N, p, T)-algorithm described in section 4.1, which used an artificial piston mass Q on the simulation box volume to adjust it such that the measured instantaneous pressure $\mathcal{P}$ in the system goes to the given external $P = 0$, everything else was measured in the $(N, V = V_{\mathrm{eq}}, T)$-ensemble. Due to the network's topology, however, most of its geometric properties are directly linked to V_{eq} via the periodic boundary conditions, such that even in swelling equilibrium artifacts of the initial process are unavoidable. Among the observables were the mean-square end-to-end distance $R_{\mathrm{E}} = \langle R_{\mathrm{E}}^2 \rangle^{1/2}$ as in (2.6) and figure 2.4, the swelling ratio $\alpha_\nu = R_{\mathrm{E}}/R_\nu$ from (3.6), and the relative extension $R_{\mathrm{E}}/R_{\mathrm{max}}$ comparing the end-to-end distance to the maximum contour or chain length of N_{m} monomers with average bonds of size $b = \langle b \rangle$ (see figure 4.11 as well); all of which averaged not only over all N_{p} chains of the ensemble, but measured repeatedly at 200 equidistant times on course of the integration for temporal averaging, too. The same holds for the mean-square radius of gyration $R_{\mathrm{G}} = \langle R_{\mathrm{G}}^2 \rangle^{1/2}$ from (2.16) and its characteristic ratio with R_{E}, known since section 2.2 to indicate random walk-like or rod-like behaviour of a chain if $R_{\mathrm{E}}^2/R_{\mathrm{G}}^2 = 6$ (2.17) or $R_{\mathrm{E}}^2/R_{\mathrm{G}}^2 = 12$ (2.18), respectively (refer to table 2.2 for further examples).

As the balance in the pressure components is the crucial mechanism behind the swelling equilibrium of the charged hydrogels, its contributions from the short range excluded volume (LJ) and bond potentials as well as from electrostatic interactions and ideal gas-like behaviour are given, all measured as virial or energetic terms as in (4.5). From the ten partial pressures followed in the simulation, only the subsets attributed to the gas part $\mathcal{P}_{\mathrm{gas}}$ and gel part $\mathcal{P}_{\mathrm{gel}}$ of the system in (4.12) are contained in this appendix; refer to the discussion in section 4.2.3 for more informations. Note, however, the leading impact of excluded volume repulsion for highly charged systems with strong counterion condensation which noticeably shifts the point of equilibrium.

ℓ_B	f	$L = V_{eq}^{1/3}$	$\langle R_E^2 \rangle^{1/2}$	α_ν	$\frac{R_E}{N_m b}$	$\langle R_G^2 \rangle^{1/2}$	$\frac{\langle R_E^2 \rangle}{\langle R_G^2 \rangle}$	R_H
1	0.125	44±1	19±2	2.06	0.46	6±1	10.2±0.3	4.1±0.2
2	0.125	43±1	18±2	2.02	0.45	6±1	10.0±0.4	4.1±0.2
5	0.125	38±2	17±3	1.83	0.41	5±1	9.6±0.4	4.0±0.3
1	0.25	54±1	22±2	2.47	0.548	7±1	10.8±0.3	4.4±0.2
2	0.25	52±1	22±2	2.42	0.537	7±1	10.7±0.3	4.4±0.2
5	0.25	43±2	18±3	2.04	0.455	6±1	9.9±0.4	4.2±0.2
1	0.5	64±1	26±2	2.91	0.645	8±1	11.1±0.2	4.8±0.2
2	0.5	60±1	25±2	2.79	0.619	8±1	11.0±0.2	4.8±0.2
5	0.5	47±2	20±2	2.21	0.493	6±1	10.1±0.3	4.4±0.2
1	1.0	73±1	30±1	3.33	0.738	9±0	11.3±0.1	5.3±0.1
2	1.0	68±1	28±2	3.11	0.689	8±0	11.1±0.2	5.1±0.1
5	1.0	49±2	21±3	2.27	0.506	7±1	10.0±0.4	4.6±0.2

ℓ_B	f	$L = V_{eq}^{1/3}$	$\langle R_E^2 \rangle^{1/2}$	α_ν	$\frac{R_E}{N_m b}$	$\langle R_G^2 \rangle^{1/2}$	$\frac{\langle R_E^2 \rangle}{\langle R_G^2 \rangle}$	R_H
1	0.125	37±1	16±2	2.51	0.406	5±1	9.9±0.4	3.6±0.3
2	0.125	36±2	15±2	2.42	0.392	5±1	9.8±0.4	3.6±0.3
5	0.125	31±2	13±2	2.14	0.348	4±1	9.1±0.4	3.5±0.3
1	0.25	48±1	20±2	3.18	0.512	6±1	10.7±0.3	4.0±0.2
2	0.25	46±2	19±2	3.06	0.492	6±1	10.5±0.3	4.0±0.2
5	0.25	37±2	16±2	2.57	0.416	5±1	9.7±0.4	3.8±0.2
1	0.5	59±1	24±2	3.89	0.624	7±0	11.1±0.2	4.5±0.2
2	0.5	56±1	23±2	3.7	0.594	7±1	11.0±0.2	4.4±0.2
5	0.5	41±2	18±3	2.81	0.455	6±1	9.8±0.4	4.0±0.2
1	1.0	70±1	29±1	4.54	0.728	9±0	11.3±0.1	5.0±0.1
2	1.0	65±1	27±2	4.22	0.677	8±0	11.1±0.2	4.9±0.1
5	1.0	47±2	20±3	3.15	0.509	6±1	10.0±0.3	4.4±0.2

Table A.1.: Selected network properties for a system with $N_m = 39$ monomers per chain in good solvent (*top*) and close to the θ-point (*bottom*) for different values of Bjerrum length ℓ_B and charge fraction f, namely length L of the simulation box after reaching the equilibrium volume V_{eq}, the average chain extension R_E, its swelling ratio α_ν compared to a single neutral chain, its extension relative to the contour length $N_m b$, its radius of gyration R_G, its aspect ratio R_E^2/R_G^2, and its hydrodynamic radius R_H.

ℓ_B	f	$\mathcal{P}^{CI}_{ideal}$	$\mathcal{P}^{CI}_{LJ}$	$\mathcal{P}^{tot}_{\ell_B}$	$\mathcal{P}^{monomers}_{ideal}$	$\mathcal{P}^{monomers}_{LJ}$	$\mathcal{P}_{FENE}$
1	0.125	$8.44{\cdot}10^{-4}$	$2.22{\cdot}10^{-5}$	$9.82{\cdot}10^{-5}$	$7.38{\cdot}10^{-3}$	$4.44{\cdot}10^{-2}$	$-5.31{\cdot}10^{-2}$
2	0.125	$9.03{\cdot}10^{-4}$	$6.17{\cdot}10^{-5}$	$-5.89{\cdot}10^{-5}$	$7.89{\cdot}10^{-3}$	$4.80{\cdot}10^{-2}$	$-5.66{\cdot}10^{-2}$
5	0.125	$1.26{\cdot}10^{-3}$	$4.10{\cdot}10^{-4}$	$-7.00{\cdot}10^{-4}$	$1.12{\cdot}10^{-2}$	$6.73{\cdot}10^{-2}$	$-8.01{\cdot}10^{-2}$
1	0.25	$9.88{\cdot}10^{-4}$	$3.44{\cdot}10^{-5}$	$7.15{\cdot}10^{-5}$	$4.12{\cdot}10^{-3}$	$2.46{\cdot}10^{-2}$	$-2.96{\cdot}10^{-2}$
2	0.25	$1.07{\cdot}10^{-3}$	$8.76{\cdot}10^{-5}$	$-4.65{\cdot}10^{-6}$	$4.46{\cdot}10^{-3}$	$2.63{\cdot}10^{-2}$	$-3.22{\cdot}10^{-2}$
5	0.25	$1.86{\cdot}10^{-3}$	$9.22{\cdot}10^{-4}$	$-1.32{\cdot}10^{-3}$	$7.71{\cdot}10^{-3}$	$4.60{\cdot}10^{-2}$	$-5.55{\cdot}10^{-2}$
1	0.5	$1.21{\cdot}10^{-3}$	$7.20{\cdot}10^{-5}$	$2.37{\cdot}10^{-4}$	$2.46{\cdot}10^{-3}$	$1.39{\cdot}10^{-2}$	$-1.79{\cdot}10^{-2}$
2	0.5	$1.41{\cdot}10^{-3}$	$2.83{\cdot}10^{-4}$	$9.19{\cdot}10^{-5}$	$2.86{\cdot}10^{-3}$	$1.62{\cdot}10^{-2}$	$-2.08{\cdot}10^{-2}$
5	0.5	$2.97{\cdot}10^{-3}$	$3.12{\cdot}10^{-3}$	$-2.79{\cdot}10^{-3}$	$6.02{\cdot}10^{-3}$	$3.46{\cdot}10^{-2}$	$-4.37{\cdot}10^{-2}$
1	1.0	$1.60{\cdot}10^{-3}$	$2.46{\cdot}10^{-4}$	$6.10{\cdot}10^{-4}$	$1.60{\cdot}10^{-3}$	$8.02{\cdot}10^{-3}$	$-1.20{\cdot}10^{-2}$
2	1.0	$1.97{\cdot}10^{-3}$	$1.04{\cdot}10^{-3}$	$3.46{\cdot}10^{-4}$	$1.97{\cdot}10^{-3}$	$9.54{\cdot}10^{-3}$	$-1.49{\cdot}10^{-2}$
5	1.0	$5.22{\cdot}10^{-3}$	$1.14{\cdot}10^{-2}$	$-5.13{\cdot}10^{-3}$	$5.21{\cdot}10^{-3}$	$2.33{\cdot}10^{-2}$	$-4.02{\cdot}10^{-2}$

ℓ_B	f	$\mathcal{P}^{CI}_{ideal}$	$\mathcal{P}^{CI}_{LJ}$	$\mathcal{P}^{tot}_{\ell_B}$	$\mathcal{P}^{monomers}_{ideal}$	$\mathcal{P}^{monomers}_{LJ}$	$\mathcal{P}_{FENE}$
1	0.125	$1.45{\cdot}10^{-3}$	$7.03{\cdot}10^{-5}$	$-7.14{\cdot}10^{-6}$	$1.27{\cdot}10^{-2}$	$6.34{\cdot}10^{-2}$	$-7.72{\cdot}10^{-2}$
2	0.125	$1.60{\cdot}10^{-3}$	$1.49{\cdot}10^{-4}$	$-1.38{\cdot}10^{-4}$	$1.41{\cdot}10^{-2}$	$6.99{\cdot}10^{-2}$	$-8.53{\cdot}10^{-2}$
5	0.125	$2.49{\cdot}10^{-3}$	$1.14{\cdot}10^{-3}$	$-1.63{\cdot}10^{-3}$	$2.19{\cdot}10^{-2}$	$1.08{\cdot}10^{-1}$	$-1.33{\cdot}10^{-1}$
1	0.25	$1.41{\cdot}10^{-3}$	$7.12{\cdot}10^{-5}$	$1.10{\cdot}10^{-4}$	$5.88{\cdot}10^{-3}$	$2.85{\cdot}10^{-2}$	$-3.58{\cdot}10^{-2}$
2	0.25	$1.59{\cdot}10^{-3}$	$1.88{\cdot}10^{-4}$	$-3.02{\cdot}10^{-5}$	$6.64{\cdot}10^{-3}$	$3.21{\cdot}10^{-2}$	$-4.05{\cdot}10^{-2}$
5	0.25	$2.92{\cdot}10^{-3}$	$1.83{\cdot}10^{-3}$	$-2.30{\cdot}10^{-3}$	$1.22{\cdot}10^{-2}$	$5.92{\cdot}10^{-2}$	$-7.41{\cdot}10^{-2}$
1	0.5	$1.54{\cdot}10^{-3}$	$1.20{\cdot}10^{-4}$	$3.05{\cdot}10^{-4}$	$3.11{\cdot}10^{-3}$	$1.41{\cdot}10^{-2}$	$-1.93{\cdot}10^{-2}$
2	0.5	$1.81{\cdot}10^{-3}$	$4.48{\cdot}10^{-4}$	$1.05{\cdot}10^{-4}$	$3.66{\cdot}10^{-3}$	$1.66{\cdot}10^{-2}$	$-2.27{\cdot}10^{-2}$
5	0.5	$4.44{\cdot}10^{-3}$	$5.27{\cdot}10^{-3}$	$-4.33{\cdot}10^{-3}$	$8.95{\cdot}10^{-3}$	$4.10{\cdot}10^{-2}$	$-5.54{\cdot}10^{-2}$
1	1.0	$1.88{\cdot}10^{-3}$	$3.19{\cdot}10^{-4}$	$7.34{\cdot}10^{-4}$	$1.88{\cdot}10^{-3}$	$7.29{\cdot}10^{-3}$	$-1.22{\cdot}10^{-2}$
2	1.0	$2.35{\cdot}10^{-3}$	$1.36{\cdot}10^{-3}$	$4.46{\cdot}10^{-4}$	$2.35{\cdot}10^{-3}$	$8.84{\cdot}10^{-3}$	$-1.54{\cdot}10^{-2}$
5	1.0	$5.94{\cdot}10^{-3}$	$1.37{\cdot}10^{-2}$	$-5.66{\cdot}10^{-3}$	$5.96{\cdot}10^{-3}$	$2.00{\cdot}10^{-2}$	$-4.00{\cdot}10^{-2}$

Table A.2.: Detailed pressure components for a system with $N_m = 39$ monomers per chain in good solvent (*top*) and close to the θ-point (*bottom*) for different values of Bjerrum length ℓ_B and charge fraction f, namely the contributions to the gas-like pressure $\mathcal{P}_{gas}$ (ideal part $\mathcal{P}^{CI}_{ideal}$, excluded volume $\mathcal{P}^{CI}_{LJ} = \mathcal{P}^{CI-CI}_{LJ} + \mathcal{P}^{CI-monomers}_{LJ}$, total electrostatic pressure $\mathcal{P}^{tot}_{\ell_B}$) and to the one of the gel $\mathcal{P}_{gel}$ (ideal part $\mathcal{P}^{monomers}_{ideal}$, excluded volume $\mathcal{P}^{monomers}_{LJ}$, bonded virial $\mathcal{P}_{FENE}$) for the fully charged gel at its swelling equilibrium volume V_{eq}.

ℓ_B	f	$L = V_{eq}^{1/3}$	$\langle R_E^2 \rangle^{1/2}$	α_ν	$\frac{R_E}{N_m b}$	$\langle R_G^2 \rangle^{1/2}$	$\frac{\langle R_E^2 \rangle}{\langle R_G^2 \rangle}$	R_H
1	0.25	80±2	34±2	2.94	0.549	10±1	11.3±0.2	5.9±0.3
2	0.25	77±2	33±2	2.89	0.539	10±1	11.2±0.2	5.8±0.2
5	0.25	66±2	28±3	2.46	0.461	9±1	10.7±0.3	5.5±0.3
1	0.5	96±1	40±2	3.5	0.653	12±1	11.5±0.2	6.5±0.2
2	0.5	91±2	38±2	3.34	0.623	11±1	11.3±0.2	6.4±0.2
5	0.5	72±2	31±3	2.65	0.497	9±1	10.7±0.3	5.8±0.3
1	1.0	111±1	47±1	4.03	0.752	14±0	11.6±0.1	7.1±0.1
2	1.0	103±1	43±2	3.75	0.7	13±1	11.4±0.1	6.9±0.2
5	1.0	76±4	33±3	2.79	0.524	10±1	10.7±0.3	6.1±0.3

ℓ_B	f	$L = V_{eq}^{1/3}$	$\langle R_E^2 \rangle^{1/2}$	α_ν	$\frac{R_E}{N_m b}$	$\langle R_G^2 \rangle^{1/2}$	$\frac{\langle R_E^2 \rangle}{\langle R_G^2 \rangle}$	R_H
1	0.25	72±2	31±2	4.07	0.532	9±1	11.2±0.2	5.4±0.3
2	0.25	69±2	28±3	3.66	0.479	8±1	11.1±0.3	5.2±0.3
5	0.25	55±2	23±3	2.94	0.386	7±1	10.1±0.4	4.8±0.3
1	0.5	89±1	38±2	4.93	0.643	11±1	11.5±0.2	6.1±0.2
2	0.5	84±2	36±2	4.67	0.609	11±1	11.4±0.2	6.0±0.2
5	0.5	63±2	27±3	3.46	0.454	8±1	10.6±0.4	5.3±0.3
1	1.0	105±1	44±2	5.71	0.744	13±0	11.6±0.1	6.8±0.1
2	1.0	98±1	42±2	5.34	0.697	12±1	11.4±0.2	6.6±0.2
5	1.0	70±2	30±3	3.83	0.501	9±1	10.5±0.3	5.8±0.2

Table A.3.: Selected network properties for a system with $N_m = 59$ monomers per chain in good solvent (*top*) and close to the θ-point (*bottom*) for different values of Bjerrum length ℓ_B and charge fraction f, namely length L of the simulation box after reaching the equilibrium volume V_{eq}, the average chain extension R_E, its swelling ratio α_ν compared to a single neutral chain, its extension relative to the contour length $N_m b$, its radius of gyration R_G, its aspect ratio R_E^2/R_G^2, and its hydrodynamic radius R_H.

ℓ_B	f	$\mathcal{P}^{CI}_{ideal}$	$\mathcal{P}^{CI}_{LJ}$	$\mathcal{P}^{tot}_{\ell_B}$	$\mathcal{P}^{monomers}_{ideal}$	$\mathcal{P}^{monomers}_{LJ}$	$\mathcal{P}_{FENE}$
1	0.25	$4.55{\cdot}10^{-4}$	$9.37{\cdot}10^{-6}$	$5.49{\cdot}10^{-5}$	$1.87{\cdot}10^{-3}$	$1.10{\cdot}10^{-2}$	$-1.35{\cdot}10^{-2}$
2	0.25	$4.81{\cdot}10^{-4}$	$3.24{\cdot}10^{-5}$	$3.87{\cdot}10^{-5}$	$1.97{\cdot}10^{-3}$	$1.16{\cdot}10^{-2}$	$-1.42{\cdot}10^{-2}$
5	0.25	$8.01{\cdot}10^{-4}$	$3.79{\cdot}10^{-4}$	$-4.93{\cdot}10^{-4}$	$3.28{\cdot}10^{-3}$	$1.94{\cdot}10^{-2}$	$-2.35{\cdot}10^{-2}$
1	0.5	$5.36{\cdot}10^{-4}$	$2.14{\cdot}10^{-5}$	$1.48{\cdot}10^{-4}$	$1.08{\cdot}10^{-3}$	$6.05{\cdot}10^{-3}$	$-7.85{\cdot}10^{-3}$
2	0.5	$6.20{\cdot}10^{-4}$	$1.06{\cdot}10^{-4}$	$9.63{\cdot}10^{-5}$	$1.25{\cdot}10^{-3}$	$6.97{\cdot}10^{-3}$	$-9.10{\cdot}10^{-3}$
5	0.5	$1.28{\cdot}10^{-3}$	$1.29{\cdot}10^{-3}$	$-1.10{\cdot}10^{-3}$	$2.57{\cdot}10^{-3}$	$1.45{\cdot}10^{-2}$	$-1.86{\cdot}10^{-2}$
1	1.0	$6.90{\cdot}10^{-4}$	$7.89{\cdot}10^{-5}$	$3.26{\cdot}10^{-4}$	$6.90{\cdot}10^{-4}$	$3.39{\cdot}10^{-3}$	$-5.18{\cdot}10^{-3}$
2	1.0	$8.58{\cdot}10^{-4}$	$4.13{\cdot}10^{-4}$	$2.22{\cdot}10^{-4}$	$8.59{\cdot}10^{-4}$	$4.14{\cdot}10^{-3}$	$-6.48{\cdot}10^{-3}$
5	1.0	$2.16{\cdot}10^{-3}$	$4.59{\cdot}10^{-3}$	$-1.64{\cdot}10^{-3}$	$2.17{\cdot}10^{-3}$	$9.67{\cdot}10^{-3}$	$-1.66{\cdot}10^{-2}$

ℓ_B	f	$\mathcal{P}^{CI}_{ideal}$	$\mathcal{P}^{CI}_{LJ}$	$\mathcal{P}^{tot}_{\ell_B}$	$\mathcal{P}^{monomers}_{ideal}$	$\mathcal{P}^{monomers}_{LJ}$	$\mathcal{P}_{FENE}$
1	0.25	$5.70{\cdot}10^{-4}$	$1.48{\cdot}10^{-5}$	$7.44{\cdot}10^{-5}$	$2.34{\cdot}10^{-3}$	$1.12{\cdot}10^{-2}$	$-1.43{\cdot}10^{-2}$
2	0.25	$8.15{\cdot}10^{-4}$	$8.38{\cdot}10^{-5}$	$4.89{\cdot}10^{-5}$	$3.34{\cdot}10^{-3}$	$1.60{\cdot}10^{-2}$	$-2.03{\cdot}10^{-2}$
5	0.25	$1.65{\cdot}10^{-3}$	$1.03{\cdot}10^{-3}$	$-1.20{\cdot}10^{-3}$	$6.78{\cdot}10^{-3}$	$3.29{\cdot}10^{-2}$	$-4.11{\cdot}10^{-2}$
1	0.5	$6.44{\cdot}10^{-4}$	$3.01{\cdot}10^{-5}$	$1.77{\cdot}10^{-4}$	$1.30{\cdot}10^{-3}$	$5.85{\cdot}10^{-3}$	$-8.05{\cdot}10^{-3}$
2	0.5	$7.64{\cdot}10^{-4}$	$1.60{\cdot}10^{-4}$	$1.15{\cdot}10^{-4}$	$1.54{\cdot}10^{-3}$	$6.91{\cdot}10^{-3}$	$-9.52{\cdot}10^{-3}$
5	0.5	$1.98{\cdot}10^{-3}$	$2.27{\cdot}10^{-3}$	$-1.82{\cdot}10^{-3}$	$4.01{\cdot}10^{-3}$	$1.82{\cdot}10^{-2}$	$-2.47{\cdot}10^{-2}$
1	1.0	$8.06{\cdot}10^{-4}$	$1.03{\cdot}10^{-4}$	$3.88{\cdot}10^{-4}$	$8.04{\cdot}10^{-4}$	$3.08{\cdot}10^{-3}$	$-5.20{\cdot}10^{-3}$
2	1.0	$9.88{\cdot}10^{-4}$	$5.20{\cdot}10^{-4}$	$2.67{\cdot}10^{-4}$	$9.89{\cdot}10^{-4}$	$3.64{\cdot}10^{-3}$	$-6.46{\cdot}10^{-3}$
5	1.0	$2.73{\cdot}10^{-3}$	$6.12{\cdot}10^{-3}$	$-2.48{\cdot}10^{-3}$	$2.73{\cdot}10^{-3}$	$9.14{\cdot}10^{-3}$	$-1.82{\cdot}10^{-2}$

Table A.4.: Detailed pressure components for a system with $N_m = 59$ monomers per chain in good solvent (*top*) and close to the θ-point (*bottom*) for different values of Bjerrum length ℓ_B and charge fraction f, namely the contributions to the gas-like pressure $\mathcal{P}_{gas}$ (ideal part $\mathcal{P}^{CI}_{ideal}$, excluded volume $\mathcal{P}^{CI}_{LJ} = \mathcal{P}^{CI-CI}_{LJ} + \mathcal{P}^{CI-monomers}_{LJ}$, total electrostatic pressure $\mathcal{P}^{tot}_{\ell_B}$) and to the one of the gel $\mathcal{P}_{gel}$ (ideal part $\mathcal{P}^{monomers}_{ideal}$, excluded volume $\mathcal{P}^{monomers}_{LJ}$, bonded virial $\mathcal{P}_{FENE}$) for the fully charged gel at its swelling equilibrium volume V_{eq}.

ℓ_B	f	$L = V_{eq}^{1/3}$	$\langle R_E^2 \rangle^{1/2}$	α_ν	$\frac{R_E}{N_m b}$	$\langle R_G^2 \rangle^{1/2}$	$\frac{\langle R_E^2 \rangle}{\langle R_G^2 \rangle}$	R_H
1	0.0625	73±2	31±3	2.3	0.383	10±1	10.6±0.3	6.1±0.4
2	0.0625	72±3	31±4	2.26	0.378	10±1	10.6±0.4	6.0±0.4
5	0.0625	66±3	29±4	2.09	0.35	9±1	10.1±0.4	5.9±0.4
1	0.125	88±2	37±3	2.75	0.457	11±1	11.1±0.3	6.6±0.3
2	0.125	86±2	37±4	2.7	0.448	11±1	11.2±0.3	6.5±0.3
5	0.125	76±3	33±4	2.39	0.398	10±1	10.6±0.3	6.3±0.4
1	0.25	107±2	46±3	3.36	0.556	13±1	11.5±0.2	7.2±0.3
2	0.25	105±2	45±3	3.28	0.543	13±1	11.4±0.2	7.2±0.3
5	0.25	85±3	36±4	2.67	0.444	11±1	10.8±0.3	6.7±0.3
1	0.5	129±2	55±2	4.02	0.664	16±1	11.7±0.1	8.0±0.2
2	0.5	123±2	52±3	3.81	0.631	15±1	11.6±0.2	7.9±0.2
5	0.5	93±3	40±4	2.91	0.483	12±1	10.9±0.3	7.0±0.3
1	1.0	150±1	63±2	4.62	0.765	19±1	11.7±0.1	8.9±0.2
2	1.0	139±2	59±2	4.27	0.707	17±1	11.6±0.1	8.6±0.2
5	1.0	100±3	43±4	3.12	0.517	13±1	10.9±0.3	7.5±0.3

ℓ_B	f	$L = V_{eq}^{1/3}$	$\langle R_E^2 \rangle^{1/2}$	α_ν	$\frac{R_E}{N_m b}$	$\langle R_G^2 \rangle^{1/2}$	$\frac{\langle R_E^2 \rangle}{\langle R_G^2 \rangle}$	R_H
1	0.0625	57±3	25±4	2.81	0.32	8±1	10.2±0.4	5.1±0.4
2	0.0625	55±3	24±4	2.75	0.313	8±1	10.0±0.4	5.1±0.4
5	0.0625	47±3	21±3	2.36	0.27	7±1	9.5±0.4	4.8±0.4
1	0.125	75±2	32±3	3.62	0.409	10±1	10.9±0.3	5.8±0.3
2	0.125	74±2	32±4	3.62	0.41	10±1	11.0±0.3	5.8±0.3
5	0.125	60±3	26±3	2.95	0.334	8±1	10.1±0.4	5.4±0.3
1	0.25	96±2	41±3	4.6	0.519	12±1	11.5±0.2	6.6±0.3
2	0.25	93±2	40±3	4.47	0.504	12±1	11.4±0.2	6.5±0.3
5	0.25	75±3	32±4	3.61	0.409	10±1	10.6±0.3	6.0±0.3
1	0.5	120±2	51±2	5.72	0.644	15±1	11.7±0.1	7.5±0.2
2	0.5	115±2	48±2	5.47	0.616	14±1	11.5±0.2	7.4±0.2
5	0.5	85±3	36±3	4.08	0.461	11±1	10.9±0.3	6.5±0.3
1	1.0	142±1	60±2	6.69	0.753	18±1	11.7±0.1	8.4±0.2
2	1.0	131±2	56±2	6.21	0.699	16±1	11.6±0.1	8.2±0.2
5	1.0	103±15	44±3	4.85	0.547	13±1	11.2±0.2	7.4±0.3

Table A.5.: Selected network properties for a system with $N_m = 79$ monomers per chain in good solvent (*top*) and close to the θ-point (*bottom*) for different values of Bjerrum length ℓ_B and charge fraction f, namely length L of the simulation box after reaching the equilibrium volume V_{eq}, the average chain extension R_E, its swelling ratio α_ν compared to a single neutral chain, its extension relative to the contour length $N_m b$, its radius of gyration R_G, its aspect ratio R_E^2/R_G^2, and its hydrodynamic radius R_H.

ℓ_B	f	$\mathcal{P}_{ideal}^{CI}$	$\mathcal{P}_{LJ}^{CI}$	$\mathcal{P}_{\ell_B}^{tot}$	$\mathcal{P}_{ideal}^{monomers}$	$\mathcal{P}_{LJ}^{monomers}$	$\mathcal{P}_{FENE}$
1	0.0625	$1.86{\cdot}10^{-4}$	$1.96{\cdot}10^{-6}$	$-1.74{\cdot}10^{-6}$	$3.29{\cdot}10^{-3}$	$2.00{\cdot}10^{-2}$	$-2.35{\cdot}10^{-2}$
2	0.0625	$1.96{\cdot}10^{-4}$	$4.11{\cdot}10^{-6}$	$1.05{\cdot}10^{-5}$	$3.47{\cdot}10^{-3}$	$2.10{\cdot}10^{-2}$	$-2.47{\cdot}10^{-2}$
5	0.0625	$2.55{\cdot}10^{-4}$	$3.30{\cdot}10^{-5}$	$-7.18{\cdot}10^{-5}$	$4.50{\cdot}10^{-3}$	$2.72{\cdot}10^{-2}$	$-3.20{\cdot}10^{-2}$
1	0.125	$2.23{\cdot}10^{-4}$	$2.35{\cdot}10^{-6}$	$1.03{\cdot}10^{-5}$	$1.87{\cdot}10^{-3}$	$1.12{\cdot}10^{-2}$	$-1.33{\cdot}10^{-2}$
2	0.125	$2.41{\cdot}10^{-4}$	$7.93{\cdot}10^{-6}$	$9.48{\cdot}10^{-6}$	$2.01{\cdot}10^{-3}$	$1.21{\cdot}10^{-2}$	$-1.43{\cdot}10^{-2}$
5	0.125	$3.51{\cdot}10^{-4}$	$7.29{\cdot}10^{-5}$	$-8.73{\cdot}10^{-6}$	$2.93{\cdot}10^{-3}$	$1.76{\cdot}10^{-2}$	$-2.09{\cdot}10^{-2}$
1	0.25	$2.52{\cdot}10^{-4}$	$3.25{\cdot}10^{-6}$	$4.08{\cdot}10^{-5}$	$1.03{\cdot}10^{-3}$	$6.03{\cdot}10^{-3}$	$-7.35{\cdot}10^{-3}$
2	0.25	$2.69{\cdot}10^{-4}$	$1.42{\cdot}10^{-5}$	$3.67{\cdot}10^{-5}$	$1.09{\cdot}10^{-3}$	$6.40{\cdot}10^{-3}$	$-7.83{\cdot}10^{-3}$
5	0.25	$5.10{\cdot}10^{-4}$	$2.38{\cdot}10^{-4}$	$-2.91{\cdot}10^{-4}$	$2.07{\cdot}10^{-3}$	$1.23{\cdot}10^{-2}$	$-1.48{\cdot}10^{-2}$
1	0.5	$2.92{\cdot}10^{-4}$	$7.03{\cdot}10^{-6}$	$9.48{\cdot}10^{-5}$	$5.88{\cdot}10^{-4}$	$3.29{\cdot}10^{-3}$	$-4.26{\cdot}10^{-3}$
2	0.5	$3.42{\cdot}10^{-4}$	$4.79{\cdot}10^{-5}$	$7.82{\cdot}10^{-5}$	$6.89{\cdot}10^{-4}$	$3.83{\cdot}10^{-3}$	$-4.99{\cdot}10^{-3}$
5	0.5	$7.80{\cdot}10^{-4}$	$7.61{\cdot}10^{-4}$	$-6.52{\cdot}10^{-4}$	$1.57{\cdot}10^{-3}$	$8.88{\cdot}10^{-3}$	$-1.14{\cdot}10^{-2}$
1	1.0	$3.77{\cdot}10^{-4}$	$3.48{\cdot}10^{-5}$	$2.07{\cdot}10^{-4}$	$3.77{\cdot}10^{-4}$	$1.83{\cdot}10^{-3}$	$-2.83{\cdot}10^{-3}$
2	1.0	$4.73{\cdot}10^{-4}$	$2.16{\cdot}10^{-4}$	$1.50{\cdot}10^{-4}$	$4.74{\cdot}10^{-4}$	$2.25{\cdot}10^{-3}$	$-3.58{\cdot}10^{-3}$
5	1.0	$1.26{\cdot}10^{-3}$	$2.65{\cdot}10^{-3}$	$-1.14{\cdot}10^{-3}$	$1.26{\cdot}10^{-3}$	$5.61{\cdot}10^{-3}$	$-9.62{\cdot}10^{-3}$

ℓ_B	f	$\mathcal{P}_{ideal}^{CI}$	$\mathcal{P}_{LJ}^{CI}$	$\mathcal{P}_{\ell_B}^{tot}$	$\mathcal{P}_{ideal}^{monomers}$	$\mathcal{P}_{LJ}^{monomers}$	$\mathcal{P}_{FENE}$
1	0.0625	$3.86{\cdot}10^{-4}$	$1.17{\cdot}10^{-5}$	$-1.38{\cdot}10^{-6}$	$6.84{\cdot}10^{-3}$	$3.37{\cdot}10^{-2}$	$-4.12{\cdot}10^{-2}$
2	0.0625	$4.21{\cdot}10^{-4}$	$1.39{\cdot}10^{-5}$	$-1.43{\cdot}10^{-5}$	$7.46{\cdot}10^{-3}$	$3.69{\cdot}10^{-2}$	$-4.49{\cdot}10^{-2}$
5	0.0625	$6.88{\cdot}10^{-4}$	$1.56{\cdot}10^{-4}$	$-2.78{\cdot}10^{-4}$	$1.22{\cdot}10^{-2}$	$6.04{\cdot}10^{-2}$	$-7.32{\cdot}10^{-2}$
1	0.125	$3.60{\cdot}10^{-4}$	$5.83{\cdot}10^{-6}$	$2.26{\cdot}10^{-5}$	$3.01{\cdot}10^{-3}$	$1.47{\cdot}10^{-2}$	$-1.82{\cdot}10^{-2}$
2	0.125	$3.67{\cdot}10^{-4}$	$1.50{\cdot}10^{-5}$	$1.27{\cdot}10^{-5}$	$3.08{\cdot}10^{-3}$	$1.51{\cdot}10^{-2}$	$-1.86{\cdot}10^{-2}$
5	0.125	$6.96{\cdot}10^{-4}$	$2.14{\cdot}10^{-4}$	$-3.38{\cdot}10^{-4}$	$5.85{\cdot}10^{-3}$	$2.88{\cdot}10^{-2}$	$-3.53{\cdot}10^{-2}$
1	0.25	$3.50{\cdot}10^{-4}$	$6.35{\cdot}10^{-6}$	$5.88{\cdot}10^{-5}$	$1.43{\cdot}10^{-3}$	$6.82{\cdot}10^{-3}$	$-8.67{\cdot}10^{-3}$
2	0.25	$3.87{\cdot}10^{-4}$	$2.99{\cdot}10^{-5}$	$5.17{\cdot}10^{-5}$	$1.58{\cdot}10^{-3}$	$7.55{\cdot}10^{-3}$	$-9.57{\cdot}10^{-3}$
5	0.25	$7.51{\cdot}10^{-4}$	$4.20{\cdot}10^{-4}$	$-4.82{\cdot}10^{-4}$	$3.06{\cdot}10^{-3}$	$1.47{\cdot}10^{-2}$	$-1.86{\cdot}10^{-2}$
1	0.5	$3.64{\cdot}10^{-4}$	$1.38{\cdot}10^{-5}$	$1.21{\cdot}10^{-4}$	$7.33{\cdot}10^{-4}$	$3.26{\cdot}10^{-3}$	$-4.53{\cdot}10^{-3}$
2	0.5	$4.21{\cdot}10^{-4}$	$7.62{\cdot}10^{-5}$	$9.24{\cdot}10^{-5}$	$8.44{\cdot}10^{-4}$	$3.77{\cdot}10^{-3}$	$-5.21{\cdot}10^{-3}$
5	0.5	$1.04{\cdot}10^{-3}$	$1.13{\cdot}10^{-3}$	$-8.95{\cdot}10^{-4}$	$2.09{\cdot}10^{-3}$	$9.49{\cdot}10^{-3}$	$-1.28{\cdot}10^{-2}$
1	1.0	$4.43{\cdot}10^{-4}$	$4.65{\cdot}10^{-5}$	$2.46{\cdot}10^{-4}$	$4.44{\cdot}10^{-4}$	$1.67{\cdot}10^{-3}$	$-2.87{\cdot}10^{-3}$
2	1.0	$5.57{\cdot}10^{-4}$	$2.82{\cdot}10^{-4}$	$1.83{\cdot}10^{-4}$	$5.60{\cdot}10^{-4}$	$2.07{\cdot}10^{-3}$	$-3.65{\cdot}10^{-3}$
5	1.0	$1.18{\cdot}10^{-3}$	$2.55{\cdot}10^{-3}$	$-1.01{\cdot}10^{-3}$	$1.18{\cdot}10^{-3}$	$3.90{\cdot}10^{-3}$	$-7.88{\cdot}10^{-3}$

Table A.6.: Detailed pressure components for a system with $N_m = 79$ monomers per chain in good solvent (*top*) and close to the θ-point (*bottom*) for different values of Bjerrum length ℓ_B and charge fraction f, namely the contributions to the gas-like pressure $\mathcal{P}_{gas}$ (ideal part $\mathcal{P}_{ideal}^{CI}$, excluded volume $\mathcal{P}_{LJ}^{CI} = \mathcal{P}_{LJ}^{CI-CI} + \mathcal{P}_{LJ}^{CI-monomers}$, total electrostatic pressure $\mathcal{P}_{\ell_B}^{tot}$) and to the one of the gel $\mathcal{P}_{gel}$ (ideal part $\mathcal{P}_{ideal}^{monomers}$, excluded volume $\mathcal{P}_{LJ}^{monomers}$, bonded virial $\mathcal{P}_{FENE}$) for the fully charged gel at its swelling equilibrium volume V_{eq}.

ℓ_B	f	$L = V_{eq}^{1/3}$	$\langle R_E^2 \rangle^{1/2}$	α_ν	$\frac{R_E}{N_m b}$	$\langle R_G^2 \rangle^{1/2}$	$\frac{\langle R_E^2 \rangle}{\langle R_G^2 \rangle}$	R_H
1	0.25	135±2	58±3	3.71	0.56	17±1	11.7±0.2	8.5±0.3
2	0.25	132±2	56±3	3.62	0.546	16±1	11.6±0.2	8.5±0.3
5	0.25	106±3	46±5	2.95	0.447	14±1	11.1±0.3	7.8±0.4
1	0.5	163±2	69±2	4.44	0.669	20±1	11.8±0.1	9.5±0.2
2	0.5	154±2	67±3	4.29	0.647	20±1	11.6±0.1	9.4±0.2
5	0.5	119±3	51±4	3.28	0.496	15±1	11.2±0.2	8.4±0.3
1	1.0	189±1	80±2	5.12	0.771	23±1	11.8±0.1	10.6±0.2
2	1.0	174±2	75±2	4.79	0.722	22±1	11.7±0.1	10.2±0.2
5	1.0	124±3	53±4	3.35	0.505	16±1	11.2±0.2	8.7±0.3

ℓ_B	f	$L = V_{eq}^{1/3}$	$\langle R_E^2 \rangle^{1/2}$	α_ν	$\frac{R_E}{N_m b}$	$\langle R_G^2 \rangle^{1/2}$	$\frac{\langle R_E^2 \rangle}{\langle R_G^2 \rangle}$	R_H
1	0.25	121±2	52±3	5.21	0.524	15±1	11.7±0.2	7.7±0.3
2	0.25	118±2	50±3	5.05	0.509	15±1	11.6±0.2	7.7±0.3
5	0.25	92±3	41±4	4.09	0.413	12±1	10.9±0.3	7.0±0.4
1	0.5	150±2	63±2	6.37	0.641	18±1	11.9±0.1	8.8±0.2
2	0.5	144±2	61±3	6.18	0.622	18±1	11.7±0.2	8.8±0.3
5	0.5	108±2	46±4	4.6	0.465	14±1	11.1±0.3	7.7±0.4
1	1.0	179±1	75±2	7.48	0.752	22±1	11.8±0.1	10.0±0.2
2	1.0	160±2	70±3	6.93	0.697	20±1	11.6±0.1	9.7±0.2
5	1.0	120±3	52±4	5.17	0.521	16±1	11.3±0.2	8.5±0.3

Table A.7.: Selected network properties for a system with $N_m = 99$ monomers per chain in good solvent (*top*) and close to the θ-point (*bottom*) for different values of Bjerrum length ℓ_B and charge fraction f, namely length L of the simulation box after reaching the equilibrium volume V_{eq}, the average chain extension R_E, its swelling ratio α_ν compared to a single neutral chain, its extension relative to the contour length $N_m b$, its radius of gyration R_G, its aspect ratio R_E^2/R_G^2, and its hydrodynamic radius R_H.

ℓ_B	f	$\mathcal{P}^{CI}_{ideal}$	$\mathcal{P}^{CI}_{LJ}$	$\mathcal{P}^{tot}_{\ell_B}$	$\mathcal{P}^{monomers}_{ideal}$	$\mathcal{P}^{monomers}_{LJ}$	$\mathcal{P}_{FENE}$
1	0.25	$1.59{\cdot}10^{-4}$	$1.37{\cdot}10^{-6}$	$2.86{\cdot}10^{-5}$	$6.45{\cdot}10^{-4}$	$3.76{\cdot}10^{-3}$	$-4.61{\cdot}10^{-3}$
2	0.25	$1.71{\cdot}10^{-4}$	$8.01{\cdot}10^{-6}$	$3.44{\cdot}10^{-5}$	$6.95{\cdot}10^{-4}$	$4.06{\cdot}10^{-3}$	$-4.98{\cdot}10^{-3}$
5	0.25	$3.26{\cdot}10^{-4}$	$1.41{\cdot}10^{-4}$	$-1.69{\cdot}10^{-4}$	$1.32{\cdot}10^{-3}$	$7.84{\cdot}10^{-3}$	$-9.43{\cdot}10^{-3}$
1	0.5	$1.85{\cdot}10^{-4}$	$4.31{\cdot}10^{-6}$	$6.80{\cdot}10^{-5}$	$3.71{\cdot}10^{-4}$	$2.06{\cdot}10^{-3}$	$-2.68{\cdot}10^{-3}$
2	0.5	$2.08{\cdot}10^{-4}$	$2.63{\cdot}10^{-5}$	$6.08{\cdot}10^{-5}$	$4.18{\cdot}10^{-4}$	$2.30{\cdot}10^{-3}$	$-3.03{\cdot}10^{-3}$
5	0.5	$4.68{\cdot}10^{-4}$	$4.49{\cdot}10^{-4}$	$-3.68{\cdot}10^{-4}$	$9.39{\cdot}10^{-4}$	$5.26{\cdot}10^{-3}$	$-6.78{\cdot}10^{-3}$
1	1.0	$2.35{\cdot}10^{-4}$	$1.81{\cdot}10^{-5}$	$1.45{\cdot}10^{-4}$	$2.35{\cdot}10^{-4}$	$1.13{\cdot}10^{-3}$	$-1.77{\cdot}10^{-3}$
2	1.0	$2.89{\cdot}10^{-4}$	$1.21{\cdot}10^{-4}$	$1.06{\cdot}10^{-4}$	$2.89{\cdot}10^{-4}$	$1.36{\cdot}10^{-3}$	$-2.18{\cdot}10^{-3}$
5	1.0	$8.41{\cdot}10^{-4}$	$1.74{\cdot}10^{-3}$	$-7.50{\cdot}10^{-4}$	$8.41{\cdot}10^{-4}$	$3.73{\cdot}10^{-3}$	$-6.43{\cdot}10^{-3}$

ℓ_B	f	$\mathcal{P}^{CI}_{ideal}$	$\mathcal{P}^{CI}_{LJ}$	$\mathcal{P}^{tot}_{\ell_B}$	$\mathcal{P}^{monomers}_{ideal}$	$\mathcal{P}^{monomers}_{LJ}$	$\mathcal{P}_{FENE}$
1	0.25	$2.23{\cdot}10^{-4}$	$2.97{\cdot}10^{-6}$	$4.17{\cdot}10^{-5}$	$8.99{\cdot}10^{-4}$	$4.27{\cdot}10^{-3}$	$-5.45{\cdot}10^{-3}$
2	0.25	$2.42{\cdot}10^{-4}$	$1.44{\cdot}10^{-5}$	$4.45{\cdot}10^{-5}$	$9.81{\cdot}10^{-4}$	$4.68{\cdot}10^{-3}$	$-5.95{\cdot}10^{-3}$
5	0.25	$4.91{\cdot}10^{-4}$	$2.65{\cdot}10^{-4}$	$-2.92{\cdot}10^{-4}$	$2.00{\cdot}10^{-3}$	$9.64{\cdot}10^{-3}$	$-1.21{\cdot}10^{-2}$
1	0.5	$2.39{\cdot}10^{-4}$	$6.45{\cdot}10^{-6}$	$8.98{\cdot}10^{-5}$	$4.81{\cdot}10^{-4}$	$2.15{\cdot}10^{-3}$	$-2.96{\cdot}10^{-3}$
2	0.5	$2.64{\cdot}10^{-4}$	$4.26{\cdot}10^{-5}$	$7.39{\cdot}10^{-5}$	$5.31{\cdot}10^{-4}$	$2.36{\cdot}10^{-3}$	$-3.28{\cdot}10^{-3}$
5	0.5	$6.49{\cdot}10^{-4}$	$7.09{\cdot}10^{-4}$	$-5.41{\cdot}10^{-4}$	$1.31{\cdot}10^{-3}$	$5.91{\cdot}10^{-3}$	$-8.02{\cdot}10^{-3}$
1	1.0	$2.88{\cdot}10^{-4}$	$2.66{\cdot}10^{-5}$	$1.76{\cdot}10^{-4}$	$2.88{\cdot}10^{-4}$	$1.10{\cdot}10^{-3}$	$-1.86{\cdot}10^{-3}$
2	1.0	$3.68{\cdot}10^{-4}$	$1.77{\cdot}10^{-4}$	$1.34{\cdot}10^{-4}$	$3.69{\cdot}10^{-4}$	$1.36{\cdot}10^{-3}$	$-2.40{\cdot}10^{-3}$
5	1.0	$8.70{\cdot}10^{-4}$	$1.91{\cdot}10^{-3}$	$-7.48{\cdot}10^{-4}$	$8.72{\cdot}10^{-4}$	$2.88{\cdot}10^{-3}$	$-5.83{\cdot}10^{-3}$

Table A.8.: Detailed pressure components for a system with $N_m = 99$ monomers per chain in good solvent (*top*) and close to the θ-point (*bottom*) for different values of Bjerrum length ℓ_B and charge fraction f, namely the contributions to the gas-like pressure $\mathcal{P}_{gas}$ (ideal part $\mathcal{P}^{CI}_{ideal}$, excluded volume $\mathcal{P}^{CI}_{LJ} = \mathcal{P}^{CI-CI}_{LJ} + \mathcal{P}^{CI-monomers}_{LJ}$, total electrostatic pressure $\mathcal{P}^{tot}_{\ell_B}$) and to the one of the gel $\mathcal{P}_{gel}$ (ideal part $\mathcal{P}^{monomers}_{ideal}$, excluded volume $\mathcal{P}^{monomers}_{LJ}$, bonded virial $\mathcal{P}_{FENE}$) for the fully charged gel at its swelling equilibrium volume V_{eq}.

ℓ_B	f	$L = V_{eq}^{1/3}$	$\langle R_E^2 \rangle^{1/2}$	α_ν	$\frac{R_E}{N_m b}$	$\langle R_G^2 \rangle^{1/2}$	$\frac{\langle R_E^2 \rangle}{\langle R_G^2 \rangle}$	R_H
1	0.125	133±3	57±4	3.29	0.461	17±1	11.5±0.3	8.8±0.4
2	0.125	131±3	57±4	3.27	0.458	17±1	11.5±0.3	8.8±0.4
5	0.125	119±4	51±4	2.98	0.417	15±1	11.3±0.3	8.4±0.4
1	0.25	162±2	69±3	4	0.559	20±1	11.8±0.2	9.7±0.3
2	0.25	159±3	68±3	3.92	0.548	20±1	11.8±0.2	9.7±0.3
5	0.25	130±3	56±4	3.22	0.451	17±1	11.3±0.2	8.9±0.3
1	0.5	196±2	83±3	4.82	0.673	24±1	11.9±0.1	11.0±0.2
2	0.5	189±2	80±3	4.64	0.648	23±1	11.8±0.1	10.8±0.2
5	0.5	141±3	61±5	3.49	0.489	18±2	11.4±0.3	9.5±0.4
1	1.0	229±1	97±2	5.57	0.778	28±1	11.9±0.1	12.2±0.2
2	1.0	211±3	90±3	5.15	0.719	26±1	11.7±0.1	11.8±0.2
5	1.0	154±3	66±6	3.74	0.524	20±2	11.4±0.3	10.1±0.4

ℓ_B	f	$L = V_{eq}^{1/3}$	$\langle R_E^2 \rangle^{1/2}$	α_ν	$\frac{R_E}{N_m b}$	$\langle R_G^2 \rangle^{1/2}$	$\frac{\langle R_E^2 \rangle}{\langle R_G^2 \rangle}$	R_H
1	0.125	112±3	48±4	4.44	0.408	14±1	11.4±0.3	7.6±0.4
2	0.125	111±3	48±4	4.4	0.404	14±1	11.5±0.3	7.6±0.4
5	0.125	97±6	42±5	3.88	0.357	13±1	11.1±0.3	7.3±0.4
1	0.25	146±2	62±3	5.75	0.528	18±1	11.8±0.2	8.9±0.3
2	0.25	144±2	61±3	5.66	0.519	18±1	11.8±0.2	8.9±0.3
5	0.25	115±3	49±4	4.54	0.418	15±1	11.2±0.3	8.1±0.4
1	0.5	183±2	78±2	7.15	0.656	23±1	11.9±0.1	10.3±0.2
2	0.5	175±2	74±3	6.83	0.627	22±1	11.8±0.1	10.1±0.2
5	0.5	130±4	56±4	5.16	0.474	17±1	11.3±0.2	8.9±0.3
1	1.0	217±2	92±2	8.37	0.768	27±1	11.9±0.1	11.6±0.2
2	1.0	200±2	85±3	7.71	0.708	25±1	11.8±0.1	11.2±0.2
5	1.0	146±4	63±4	5.62	0.517	19±1	11.3±0.2	9.7±0.4

Table A.9.: Selected network properties for a system with $N_m = 119$ monomers per chain in good solvent (*top*) and close to the θ-point (*bottom*) for different values of Bjerrum length ℓ_B and charge fraction f, namely length L of the simulation box after reaching the equilibrium volume V_{eq}, the average chain extension R_E, its swelling ratio α_ν compared to a single neutral chain, its extension relative to the contour length $N_m b$, its radius of gyration R_G, its aspect ratio R_E^2/R_G^2, and its hydrodynamic radius R_H.

ℓ_B	f	$\mathcal{P}^{CI}_{ideal}$	$\mathcal{P}^{CI}_{LJ}$	$\mathcal{P}^{tot}_{\ell_B}$	$\mathcal{P}^{monomers}_{ideal}$	$\mathcal{P}^{monomers}_{LJ}$	$\mathcal{P}_{FENE}$
1	0.125	$9.90{\cdot}10^{-5}$	$3.63{\cdot}10^{-7}$	$8.10{\cdot}10^{-6}$	$8.17{\cdot}10^{-4}$	$4.88{\cdot}10^{-3}$	$-5.82{\cdot}10^{-3}$
2	0.125	$1.02{\cdot}10^{-4}$	$1.49{\cdot}10^{-6}$	$1.12{\cdot}10^{-5}$	$8.43{\cdot}10^{-4}$	$5.03{\cdot}10^{-3}$	$-6.00{\cdot}10^{-3}$
5	0.125	$1.38{\cdot}10^{-4}$	$2.64{\cdot}10^{-5}$	$-3.31{\cdot}10^{-5}$	$1.14{\cdot}10^{-3}$	$6.82{\cdot}10^{-3}$	$-8.08{\cdot}10^{-3}$
1	0.25	$1.10{\cdot}10^{-4}$	$8.63{\cdot}10^{-7}$	$2.18{\cdot}10^{-5}$	$4.48{\cdot}10^{-4}$	$2.61{\cdot}10^{-3}$	$-3.20{\cdot}10^{-3}$
2	0.25	$1.17{\cdot}10^{-4}$	$4.39{\cdot}10^{-6}$	$2.74{\cdot}10^{-5}$	$4.76{\cdot}10^{-4}$	$2.77{\cdot}10^{-3}$	$-3.40{\cdot}10^{-3}$
5	0.25	$2.13{\cdot}10^{-4}$	$9.03{\cdot}10^{-5}$	$-1.01{\cdot}10^{-4}$	$8.63{\cdot}10^{-4}$	$5.09{\cdot}10^{-3}$	$-6.16{\cdot}10^{-3}$
1	0.5	$1.27{\cdot}10^{-4}$	$2.00{\cdot}10^{-6}$	$4.86{\cdot}10^{-5}$	$2.55{\cdot}10^{-4}$	$1.40{\cdot}10^{-3}$	$-1.84{\cdot}10^{-3}$
2	0.5	$1.42{\cdot}10^{-4}$	$1.74{\cdot}10^{-5}$	$4.89{\cdot}10^{-5}$	$2.85{\cdot}10^{-4}$	$1.57{\cdot}10^{-3}$	$-2.07{\cdot}10^{-3}$
5	0.5	$3.40{\cdot}10^{-4}$	$3.17{\cdot}10^{-4}$	$-2.61{\cdot}10^{-4}$	$6.83{\cdot}10^{-4}$	$3.82{\cdot}10^{-3}$	$-4.93{\cdot}10^{-3}$
1	1.0	$1.60{\cdot}10^{-4}$	$1.02{\cdot}10^{-5}$	$1.07{\cdot}10^{-4}$	$1.60{\cdot}10^{-4}$	$7.63{\cdot}10^{-4}$	$-1.20{\cdot}10^{-3}$
2	1.0	$2.03{\cdot}10^{-4}$	$8.43{\cdot}10^{-5}$	$8.31{\cdot}10^{-5}$	$2.03{\cdot}10^{-4}$	$9.57{\cdot}10^{-4}$	$-1.53{\cdot}10^{-3}$
5	1.0	$5.26{\cdot}10^{-4}$	$1.07{\cdot}10^{-3}$	$-4.54{\cdot}10^{-4}$	$5.25{\cdot}10^{-4}$	$2.32{\cdot}10^{-3}$	$-4.02{\cdot}10^{-3}$

ℓ_B	f	$\mathcal{P}^{CI}_{ideal}$	$\mathcal{P}^{CI}_{LJ}$	$\mathcal{P}^{tot}_{\ell_B}$	$\mathcal{P}^{monomers}_{ideal}$	$\mathcal{P}^{monomers}_{LJ}$	$\mathcal{P}_{FENE}$
1	0.125	$1.64{\cdot}10^{-4}$	$1.87{\cdot}10^{-6}$	$1.56{\cdot}10^{-5}$	$1.35{\cdot}10^{-3}$	$6.58{\cdot}10^{-3}$	$-8.13{\cdot}10^{-3}$
2	0.125	$1.70{\cdot}10^{-4}$	$4.90{\cdot}10^{-6}$	$1.84{\cdot}10^{-5}$	$1.40{\cdot}10^{-3}$	$6.81{\cdot}10^{-3}$	$-8.41{\cdot}10^{-3}$
5	0.125	$2.56{\cdot}10^{-4}$	$6.41{\cdot}10^{-5}$	$-9.04{\cdot}10^{-5}$	$2.12{\cdot}10^{-3}$	$1.03{\cdot}10^{-2}$	$-1.28{\cdot}10^{-2}$
1	0.25	$1.51{\cdot}10^{-4}$	$1.82{\cdot}10^{-6}$	$3.21{\cdot}10^{-5}$	$6.11{\cdot}10^{-4}$	$2.89{\cdot}10^{-3}$	$-3.70{\cdot}10^{-3}$
2	0.25	$1.60{\cdot}10^{-4}$	$8.10{\cdot}10^{-6}$	$3.74{\cdot}10^{-5}$	$6.47{\cdot}10^{-4}$	$3.06{\cdot}10^{-3}$	$-3.92{\cdot}10^{-3}$
5	0.25	$3.12{\cdot}10^{-4}$	$1.67{\cdot}10^{-4}$	$-1.71{\cdot}10^{-4}$	$1.26{\cdot}10^{-3}$	$6.06{\cdot}10^{-3}$	$-7.64{\cdot}10^{-3}$
1	0.5	$1.56{\cdot}10^{-4}$	$3.21{\cdot}10^{-6}$	$6.37{\cdot}10^{-5}$	$3.14{\cdot}10^{-4}$	$1.39{\cdot}10^{-3}$	$-1.93{\cdot}10^{-3}$
2	0.5	$1.78{\cdot}10^{-4}$	$2.52{\cdot}10^{-5}$	$6.02{\cdot}10^{-5}$	$3.59{\cdot}10^{-4}$	$1.59{\cdot}10^{-3}$	$-2.21{\cdot}10^{-3}$
5	0.5	$4.35{\cdot}10^{-4}$	$4.67{\cdot}10^{-4}$	$-3.16{\cdot}10^{-4}$	$8.73{\cdot}10^{-4}$	$3.93{\cdot}10^{-3}$	$-5.36{\cdot}10^{-3}$
1	1.0	$1.88{\cdot}10^{-4}$	$1.40{\cdot}10^{-5}$	$1.27{\cdot}10^{-4}$	$1.88{\cdot}10^{-4}$	$7.02{\cdot}10^{-4}$	$-1.22{\cdot}10^{-3}$
2	1.0	$2.40{\cdot}10^{-4}$	$1.11{\cdot}10^{-4}$	$9.82{\cdot}10^{-5}$	$2.40{\cdot}10^{-4}$	$8.76{\cdot}10^{-4}$	$-1.56{\cdot}10^{-3}$
5	1.0	$6.22{\cdot}10^{-4}$	$1.35{\cdot}10^{-3}$	$-5.21{\cdot}10^{-4}$	$6.21{\cdot}10^{-4}$	$2.06{\cdot}10^{-3}$	$-4.15{\cdot}10^{-3}$

Table A.10.: Detailed pressure components for a system with $N_m = 119$ monomers per chain in good solvent (*top*) and close to the θ-point (*bottom*) for different values of Bjerrum length ℓ_B and charge fraction f, namely the contributions to the gas-like pressure $\mathcal{P}_{gas}$ (ideal part $\mathcal{P}^{CI}_{ideal}$, excluded volume $\mathcal{P}^{CI}_{LJ} = \mathcal{P}^{CI-CI}_{LJ} + \mathcal{P}^{CI-monomers}_{LJ}$, total electrostatic pressure $\mathcal{P}^{tot}_{\ell_B}$) and to the one of the gel $\mathcal{P}_{gel}$ (ideal part $\mathcal{P}^{monomers}_{ideal}$, excluded volume $\mathcal{P}^{monomers}_{LJ}$, bonded virial $\mathcal{P}_{FENE}$) for the fully charged gel at its swelling equilibrium volume V_{eq}.

ℓ_B	f	$L = V_{eq}^{1/3}$	$\langle R_E^2 \rangle^{1/2}$	α_ν	$\frac{R_E}{N_m b}$	$\langle R_G^2 \rangle^{1/2}$	$\frac{\langle R_E^2 \rangle}{\langle R_G^2 \rangle}$	R_H
1	0.25	191±2	82±4	4.32	0.566	24±1	11.8±0.2	11.0±0.3
2	0.25	189±3	83±3	4.38	0.573	24±1	11.8±0.1	11.2±0.3
5	0.25	154±3	67±5	3.51	0.461	20±2	11.3±0.2	10.2±0.4
1	0.5	231±2	99±3	5.19	0.68	28±1	12.0±0.1	12.4±0.2
2	0.5	223±2	95±3	5.01	0.657	28±1	11.9±0.1	12.3±0.2
5	0.5	170±3	73±5	3.85	0.505	22±1	11.4±0.2	10.8±0.3
1	1.0	268±1	114±3	5.98	0.783	33±1	11.9±0.1	13.8±0.2
2	1.0	217±5	101±5	5.3	0.694	30±1	11.5±0.1	13.1±0.3
5	1.0	180±3	77±5	4.01	0.526	23±1	11.5±0.2	11.3±0.4

ℓ_B	f	$L = V_{eq}^{1/3}$	$\langle R_E^2 \rangle^{1/2}$	α_ν	$\frac{R_E}{N_m b}$	$\langle R_G^2 \rangle^{1/2}$	$\frac{\langle R_E^2 \rangle}{\langle R_G^2 \rangle}$	R_H
1	0.25	171±2	73±3	6.23	0.528	21±1	11.9±0.1	10.0±0.3
2	0.25	165±3	73±4	6.22	0.528	21±1	11.8±0.2	10.1±0.4
5	0.25	134±3	58±5	4.98	0.424	17±2	11.4±0.3	9.1±0.4
1	0.5	213±2	92±3	7.86	0.667	27±1	12.0±0.1	11.6±0.3
2	0.5	206±2	88±3	7.45	0.632	26±1	11.8±0.1	11.4±0.2
5	0.5	125±4	58±8	4.91	0.42	18±2	10.7±0.4	9.6±0.5
1	1.0	252±2	108±3	9.08	0.77	31±1	11.9±0.1	13.1±0.2
2	1.0	230±2	99±3	8.3	0.704	29±1	11.8±0.1	12.6±0.2
5	1.0	169±4	76±5	6.29	0.535	22±2	11.5±0.2	11.0±0.4

Table A.11.: Selected network properties for a system with $N_m = 139$ monomers per chain in good solvent (*top*) and close to the θ-point (*bottom*) for different values of Bjerrum length ℓ_B and charge fraction f, namely length L of the simulation box after reaching the equilibrium volume V_{eq}, the average chain extension R_E, its swelling ratio α_ν compared to a single neutral chain, its extension relative to the contour length $N_m b$, its radius of gyration R_G, its aspect ratio R_E^2/R_G^2, and its hydrodynamic radius R_H.

ℓ_B	f	$\mathcal{P}_{ideal}^{CI}$	$\mathcal{P}_{LJ}^{CI}$	$\mathcal{P}_{\ell_B}^{tot}$	$\mathcal{P}_{ideal}^{monomers}$	$\mathcal{P}_{LJ}^{monomers}$	$\mathcal{P}_{FENE}$
1	0.25	$7.92{\cdot}10^{-5}$	$4.19{\cdot}10^{-7}$	$1.64{\cdot}10^{-5}$	$3.19{\cdot}10^{-4}$	$1.86{\cdot}10^{-3}$	$-2.28{\cdot}10^{-3}$
2	0.25	$7.65{\cdot}10^{-5}$	$2.22{\cdot}10^{-6}$	$2.14{\cdot}10^{-5}$	$3.09{\cdot}10^{-4}$	$1.79{\cdot}10^{-3}$	$-2.21{\cdot}10^{-3}$
5	0.25	$1.52{\cdot}10^{-4}$	$5.89{\cdot}10^{-5}$	$-6.46{\cdot}10^{-5}$	$6.13{\cdot}10^{-4}$	$3.61{\cdot}10^{-3}$	$-4.37{\cdot}10^{-3}$
1	0.5	$9.09{\cdot}10^{-5}$	$9.66{\cdot}10^{-7}$	$3.83{\cdot}10^{-5}$	$1.82{\cdot}10^{-4}$	$1.00{\cdot}10^{-3}$	$-1.32{\cdot}10^{-3}$
2	0.5	$1.00{\cdot}10^{-4}$	$1.13{\cdot}10^{-5}$	$3.91{\cdot}10^{-5}$	$2.02{\cdot}10^{-4}$	$1.10{\cdot}10^{-3}$	$-1.46{\cdot}10^{-3}$
5	0.5	$2.27{\cdot}10^{-4}$	$2.11{\cdot}10^{-4}$	$-1.67{\cdot}10^{-4}$	$4.55{\cdot}10^{-4}$	$2.54{\cdot}10^{-3}$	$-3.28{\cdot}10^{-3}$
1	1.0	$1.16{\cdot}10^{-4}$	$5.69{\cdot}10^{-6}$	$8.37{\cdot}10^{-5}$	$1.16{\cdot}10^{-4}$	$5.50{\cdot}10^{-4}$	$-8.73{\cdot}10^{-4}$
2	1.0	$1.92{\cdot}10^{-4}$	$7.96{\cdot}10^{-5}$	$8.09{\cdot}10^{-5}$	$1.92{\cdot}10^{-4}$	$9.05{\cdot}10^{-4}$	$-1.45{\cdot}10^{-3}$
5	1.0	$3.84{\cdot}10^{-4}$	$7.87{\cdot}10^{-4}$	$-3.29{\cdot}10^{-4}$	$3.85{\cdot}10^{-4}$	$1.70{\cdot}10^{-3}$	$-2.94{\cdot}10^{-3}$

ℓ_B	f	$\mathcal{P}_{ideal}^{CI}$	$\mathcal{P}_{LJ}^{CI}$	$\mathcal{P}_{\ell_B}^{tot}$	$\mathcal{P}_{ideal}^{monomers}$	$\mathcal{P}_{LJ}^{monomers}$	$\mathcal{P}_{FENE}$
1	0.25	$1.11{\cdot}10^{-4}$	$8.12{\cdot}10^{-7}$	$2.49{\cdot}10^{-5}$	$4.49{\cdot}10^{-4}$	$2.13{\cdot}10^{-3}$	$-2.72{\cdot}10^{-3}$
2	0.25	$1.14{\cdot}10^{-4}$	$4.88{\cdot}10^{-6}$	$2.96{\cdot}10^{-5}$	$4.61{\cdot}10^{-4}$	$2.17{\cdot}10^{-3}$	$-2.80{\cdot}10^{-3}$
5	0.25	$2.22{\cdot}10^{-4}$	$1.13{\cdot}10^{-4}$	$-1.14{\cdot}10^{-4}$	$8.97{\cdot}10^{-4}$	$4.29{\cdot}10^{-3}$	$-5.42{\cdot}10^{-3}$
1	0.5	$1.10{\cdot}10^{-4}$	$1.82{\cdot}10^{-6}$	$4.65{\cdot}10^{-5}$	$2.20{\cdot}10^{-4}$	$9.74{\cdot}10^{-4}$	$-1.36{\cdot}10^{-3}$
2	0.5	$1.28{\cdot}10^{-4}$	$1.68{\cdot}10^{-5}$	$5.00{\cdot}10^{-5}$	$2.58{\cdot}10^{-4}$	$1.14{\cdot}10^{-3}$	$-1.59{\cdot}10^{-3}$
5	0.5	$5.04{\cdot}10^{-4}$	$5.41{\cdot}10^{-4}$	$-4.13{\cdot}10^{-4}$	$1.01{\cdot}10^{-3}$	$4.54{\cdot}10^{-3}$	$-6.19{\cdot}10^{-3}$
1	1.0	$1.38{\cdot}10^{-4}$	$8.52{\cdot}10^{-6}$	$9.90{\cdot}10^{-5}$	$1.38{\cdot}10^{-4}$	$5.14{\cdot}10^{-4}$	$-8.95{\cdot}10^{-4}$
2	1.0	$1.82{\cdot}10^{-4}$	$8.28{\cdot}10^{-5}$	$7.99{\cdot}10^{-5}$	$1.83{\cdot}10^{-4}$	$6.64{\cdot}10^{-4}$	$-1.19{\cdot}10^{-3}$
5	1.0	$4.11{\cdot}10^{-4}$	$8.88{\cdot}10^{-4}$	$-3.36{\cdot}10^{-4}$	$4.11{\cdot}10^{-4}$	$1.36{\cdot}10^{-3}$	$-2.74{\cdot}10^{-3}$

Table A.12.: Detailed pressure components for a system with $N_m = 139$ monomers per chain in good solvent (*top*) and close to the θ-point (*bottom*) for different values of Bjerrum length ℓ_B and charge fraction f, namely the contributions to the gas-like pressure $\mathcal{P}_{gas}$ (ideal part $\mathcal{P}_{ideal}^{CI}$, excluded volume $\mathcal{P}_{LJ}^{CI} = \mathcal{P}_{LJ}^{CI-CI} + \mathcal{P}_{LJ}^{CI-monomers}$, total electrostatic pressure $\mathcal{P}_{\ell_B}^{tot}$) and to the one of the gel $\mathcal{P}_{gel}$ (ideal part $\mathcal{P}_{ideal}^{monomers}$, excluded volume $\mathcal{P}_{LJ}^{monomers}$, bonded virial $\mathcal{P}_{FENE}$) for the fully charged gel at its swelling equilibrium volume V_{eq}.

ℓ_B	f	$L = V_{eq}^{1/3}$	$\langle R_E^2 \rangle^{1/2}$	α_ν	$\frac{R_E}{N_m b}$	$\langle R_G^2 \rangle^{1/2}$	$\frac{\langle R_E^2 \rangle}{\langle R_G^2 \rangle}$	R_H
1	0.0625	142±4	62±5	3	0.373	18±2	11.1±0.3	9.8±0.5
2	0.0625	143±4	62±6	3.01	0.375	18±2	11.3±0.3	9.8±0.5
5	0.0625	133±4	58±7	2.84	0.355	17±2	11.3±0.4	9.6±0.6
1	0.125	177±3	76±5	3.72	0.462	22±1	11.6±0.2	10.9±0.4
2	0.125	176±3	76±5	3.69	0.458	22±1	11.7±0.2	10.8±0.4
5	0.125	157±4	68±5	3.31	0.411	20±1	11.3±0.2	10.5±0.4
1	0.25	218±3	93±4	4.56	0.566	27±1	12.0±0.2	12.2±0.4
2	0.25	217±3	93±4	4.53	0.562	27±1	11.9±0.2	12.2±0.3
5	0.25	180±4	78±7	3.79	0.471	23±2	11.4±0.3	11.3±0.5
1	0.5	263±2	112±3	5.48	0.679	32±1	12.0±0.1	13.7±0.3
2	0.5	256±2	110±4	5.34	0.662	32±1	11.9±0.1	13.7±0.3
5	0.5	193±4	83±6	4.05	0.503	25±2	11.5±0.2	11.9±0.4
1	1.0	309±2	132±2	6.37	0.789	38±1	11.9±0.1	15.4±0.2
2	1.0	284±2	122±3	5.87	0.728	35±1	11.9±0.1	14.8±0.2
5	1.0	209±3	90±4	4.31	0.534	26±1	11.6±0.2	12.6±0.3

ℓ_B	f	$L = V_{eq}^{1/3}$	$\langle R_E^2 \rangle^{1/2}$	α_ν	$\frac{R_E}{N_m b}$	$\langle R_G^2 \rangle^{1/2}$	$\frac{\langle R_E^2 \rangle}{\langle R_G^2 \rangle}$	R_H
1	0.0625	114±3	49±4	3.94	0.313	15±1	11.0±0.3	8.2±0.5
2	0.0625	114±3	50±5	3.95	0.315	15±2	11.3±0.4	8.2±0.5
5	0.0625	105±4	45±5	3.62	0.289	14±2	11.0±0.4	7.9±0.5
1	0.125	152±3	65±4	5.22	0.415	19±1	11.6±0.2	9.5±0.4
2	0.125	150±3	65±4	5.18	0.411	19±1	11.7±0.2	9.5±0.4
5	0.125	130±3	56±6	4.47	0.356	17±2	11.3±0.3	9.0±0.5
1	0.25	197±3	84±4	6.73	0.534	24±1	11.9±0.2	11.1±0.3
2	0.25	195±3	83±4	6.64	0.527	24±1	11.9±0.2	11.1±0.3
5	0.25	155±4	67±5	5.36	0.426	20±2	11.3±0.3	10.1±0.4
1	0.5	246±2	105±3	8.35	0.663	30±1	12.0±0.1	12.9±0.3
2	0.5	239±2	102±4	8.1	0.643	30±1	11.9±0.1	12.8±0.3
5	0.5	174±4	75±6	5.97	0.475	22±2	11.6±0.3	10.9±0.5
1	1.0	293±2	125±2	9.83	0.78	36±1	12.0±0.1	14.6±0.2
2	1.0	271±2	116±3	9.09	0.721	34±1	11.8±0.1	14.1±0.2
5	1.0	202±14	86±4	6.74	0.535	25±2	11.6±0.2	12.1±0.4

Table A.13.: Selected network properties for a system with $N_m = 159$ monomers per chain in good solvent (*top*) and close to the θ-point (*bottom*) for different values of Bjerrum length ℓ_B and charge fraction f, namely length L of the simulation box after reaching the equilibrium volume V_{eq}, the average chain extension R_E, its swelling ratio α_ν compared to a single neutral chain, its extension relative to the contour length $N_m b$, its radius of gyration R_G, its aspect ratio R_E^2/R_G^2, and its hydrodynamic radius R_H.

ℓ_B	f	$\mathcal{P}^{CI}_{ideal}$	$\mathcal{P}^{CI}_{LJ}$	$\mathcal{P}^{tot}_{\ell_B}$	$\mathcal{P}^{monomers}_{ideal}$	$\mathcal{P}^{monomers}_{LJ}$	$\mathcal{P}_{FENE}$
1	0.0625	$5.30{\cdot}10^{-5}$	$1.20{\cdot}10^{-7}$	$1.19{\cdot}10^{-6}$	$8.93{\cdot}10^{-4}$	$5.36{\cdot}10^{-3}$	$-6.34{\cdot}10^{-3}$
2	0.0625	$5.19{\cdot}10^{-5}$	$3.97{\cdot}10^{-7}$	$2.40{\cdot}10^{-6}$	$8.74{\cdot}10^{-4}$	$5.25{\cdot}10^{-3}$	$-6.20{\cdot}10^{-3}$
5	0.0625	$6.46{\cdot}10^{-5}$	$4.11{\cdot}10^{-6}$	$-6.94{\cdot}10^{-6}$	$1.08{\cdot}10^{-3}$	$6.53{\cdot}10^{-3}$	$-7.70{\cdot}10^{-3}$
1	0.125	$5.62{\cdot}10^{-5}$	$1.60{\cdot}10^{-7}$	$3.91{\cdot}10^{-6}$	$4.58{\cdot}10^{-4}$	$2.72{\cdot}10^{-3}$	$-3.26{\cdot}10^{-3}$
2	0.125	$5.75{\cdot}10^{-5}$	$6.62{\cdot}10^{-7}$	$8.71{\cdot}10^{-6}$	$4.70{\cdot}10^{-4}$	$2.80{\cdot}10^{-3}$	$-3.34{\cdot}10^{-3}$
5	0.125	$8.05{\cdot}10^{-5}$	$1.21{\cdot}10^{-5}$	$-1.40{\cdot}10^{-5}$	$6.58{\cdot}10^{-4}$	$3.93{\cdot}10^{-3}$	$-4.67{\cdot}10^{-3}$
1	0.25	$6.11{\cdot}10^{-5}$	$2.52{\cdot}10^{-7}$	$1.29{\cdot}10^{-5}$	$2.46{\cdot}10^{-4}$	$1.43{\cdot}10^{-3}$	$-1.76{\cdot}10^{-3}$
2	0.25	$6.20{\cdot}10^{-5}$	$1.50{\cdot}10^{-6}$	$2.01{\cdot}10^{-5}$	$2.50{\cdot}10^{-4}$	$1.45{\cdot}10^{-3}$	$-1.79{\cdot}10^{-3}$
5	0.25	$1.09{\cdot}10^{-4}$	$4.18{\cdot}10^{-5}$	$-4.26{\cdot}10^{-5}$	$4.39{\cdot}10^{-4}$	$2.57{\cdot}10^{-3}$	$-3.13{\cdot}10^{-3}$
1	0.5	$7.00{\cdot}10^{-5}$	$5.59{\cdot}10^{-7}$	$3.09{\cdot}10^{-5}$	$1.40{\cdot}10^{-4}$	$7.74{\cdot}10^{-4}$	$-1.01{\cdot}10^{-3}$
2	0.5	$7.56{\cdot}10^{-5}$	$7.41{\cdot}10^{-6}$	$3.35{\cdot}10^{-5}$	$1.52{\cdot}10^{-4}$	$8.32{\cdot}10^{-4}$	$-1.10{\cdot}10^{-3}$
5	0.5	$1.75{\cdot}10^{-4}$	$1.61{\cdot}10^{-4}$	$-1.26{\cdot}10^{-4}$	$3.53{\cdot}10^{-4}$	$1.97{\cdot}10^{-3}$	$-2.54{\cdot}10^{-3}$
1	1.0	$8.67{\cdot}10^{-5}$	$3.29{\cdot}10^{-6}$	$6.51{\cdot}10^{-5}$	$8.67{\cdot}10^{-5}$	$4.07{\cdot}10^{-4}$	$-6.53{\cdot}10^{-4}$
2	1.0	$1.11{\cdot}10^{-4}$	$4.29{\cdot}10^{-5}$	$5.29{\cdot}10^{-5}$	$1.11{\cdot}10^{-4}$	$5.17{\cdot}10^{-4}$	$-8.38{\cdot}10^{-4}$
5	1.0	$2.78{\cdot}10^{-4}$	$5.66{\cdot}10^{-4}$	$-2.33{\cdot}10^{-4}$	$2.78{\cdot}10^{-4}$	$1.23{\cdot}10^{-3}$	$-2.12{\cdot}10^{-3}$

ℓ_B	f	$\mathcal{P}^{CI}_{ideal}$	$\mathcal{P}^{CI}_{LJ}$	$\mathcal{P}^{tot}_{\ell_B}$	$\mathcal{P}^{monomers}_{ideal}$	$\mathcal{P}^{monomers}_{LJ}$	$\mathcal{P}_{FENE}$
1	0.0625	$1.02{\cdot}10^{-4}$	$1.01{\cdot}10^{-6}$	$4.19{\cdot}10^{-6}$	$1.70{\cdot}10^{-3}$	$8.38{\cdot}10^{-3}$	$-1.02{\cdot}10^{-2}$
2	0.0625	$1.03{\cdot}10^{-4}$	$1.97{\cdot}10^{-6}$	$5.57{\cdot}10^{-6}$	$1.73{\cdot}10^{-3}$	$8.53{\cdot}10^{-3}$	$-1.04{\cdot}10^{-2}$
5	0.0625	$1.33{\cdot}10^{-4}$	$1.66{\cdot}10^{-5}$	$-2.37{\cdot}10^{-5}$	$2.23{\cdot}10^{-3}$	$1.10{\cdot}10^{-2}$	$-1.34{\cdot}10^{-2}$
1	0.125	$8.96{\cdot}10^{-5}$	$5.34{\cdot}10^{-7}$	$9.64{\cdot}10^{-6}$	$7.32{\cdot}10^{-4}$	$3.57{\cdot}10^{-3}$	$-4.41{\cdot}10^{-3}$
2	0.125	$9.14{\cdot}10^{-5}$	$1.31{\cdot}10^{-6}$	$1.51{\cdot}10^{-5}$	$7.49{\cdot}10^{-4}$	$3.64{\cdot}10^{-3}$	$-4.51{\cdot}10^{-3}$
5	0.125	$1.44{\cdot}10^{-4}$	$3.36{\cdot}10^{-5}$	$-3.96{\cdot}10^{-5}$	$1.18{\cdot}10^{-3}$	$5.73{\cdot}10^{-3}$	$-7.07{\cdot}10^{-3}$
1	0.25	$8.32{\cdot}10^{-5}$	$4.96{\cdot}10^{-7}$	$1.93{\cdot}10^{-5}$	$3.36{\cdot}10^{-4}$	$1.59{\cdot}10^{-3}$	$-2.04{\cdot}10^{-3}$
2	0.25	$8.59{\cdot}10^{-5}$	$3.23{\cdot}10^{-6}$	$2.57{\cdot}10^{-5}$	$3.47{\cdot}10^{-4}$	$1.64{\cdot}10^{-3}$	$-2.10{\cdot}10^{-3}$
5	0.25	$1.68{\cdot}10^{-4}$	$8.55{\cdot}10^{-5}$	$-8.12{\cdot}10^{-5}$	$6.80{\cdot}10^{-4}$	$3.24{\cdot}10^{-3}$	$-4.11{\cdot}10^{-3}$
1	0.5	$8.58{\cdot}10^{-5}$	$1.12{\cdot}10^{-6}$	$4.08{\cdot}10^{-5}$	$1.72{\cdot}10^{-4}$	$7.62{\cdot}10^{-4}$	$-1.06{\cdot}10^{-3}$
2	0.5	$9.38{\cdot}10^{-5}$	$1.16{\cdot}10^{-5}$	$4.02{\cdot}10^{-5}$	$1.88{\cdot}10^{-4}$	$8.23{\cdot}10^{-4}$	$-1.16{\cdot}10^{-3}$
5	0.5	$2.41{\cdot}10^{-4}$	$2.52{\cdot}10^{-4}$	$-1.83{\cdot}10^{-4}$	$4.82{\cdot}10^{-4}$	$2.16{\cdot}10^{-3}$	$-2.96{\cdot}10^{-3}$
1	1.0	$1.02{\cdot}10^{-4}$	$5.18{\cdot}10^{-6}$	$7.79{\cdot}10^{-5}$	$1.02{\cdot}10^{-4}$	$3.74{\cdot}10^{-4}$	$-6.61{\cdot}10^{-4}$
2	1.0	$1.28{\cdot}10^{-4}$	$5.50{\cdot}10^{-5}$	$6.95{\cdot}10^{-5}$	$1.28{\cdot}10^{-4}$	$4.61{\cdot}10^{-4}$	$-8.36{\cdot}10^{-4}$
5	1.0	$3.11{\cdot}10^{-4}$	$6.71{\cdot}10^{-4}$	$-2.53{\cdot}10^{-4}$	$3.11{\cdot}10^{-4}$	$1.03{\cdot}10^{-3}$	$-2.07{\cdot}10^{-3}$

Table A.14.: Detailed pressure components for a system with $N_m = 159$ monomers per chain in good solvent (*top*) and close to the θ-point (*bottom*) for different values of Bjerrum length ℓ_B and charge fraction f, namely the contributions to the gas-like pressure $\mathcal{P}_{gas}$ (ideal part $\mathcal{P}^{CI}_{ideal}$, excluded volume $\mathcal{P}^{CI}_{LJ} = \mathcal{P}^{CI-CI}_{LJ} + \mathcal{P}^{CI-monomers}_{LJ}$, total electrostatic pressure $\mathcal{P}^{tot}_{\ell_B}$) and to the one of the gel $\mathcal{P}_{gel}$ (ideal part $\mathcal{P}^{monomers}_{ideal}$, excluded volume $\mathcal{P}^{monomers}_{LJ}$, bonded virial $\mathcal{P}_{FENE}$) for the fully charged gel at its swelling equilibrium volume V_{eq}.

ℓ_B	f	$L = V_{eq}^{1/3}$	$\langle R_E^2 \rangle^{1/2}$	α_ν	$\frac{R_E}{N_m b}$	$\langle R_G^2 \rangle^{1/2}$	$\frac{\langle R_E^2 \rangle}{\langle R_G^2 \rangle}$	R_H
1	0.25	245±3	105±4	4.78	0.565	30±1	12.0±0.1	13.3±0.4
2	0.25	245±3	105±4	4.8	0.567	31±1	11.9±0.1	13.4±0.3
5	0.25	201±4	86±5	3.94	0.465	25±2	11.7±0.2	12.3±0.4
1	0.5	297±2	128±4	5.8	0.685	37±1	12.1±0.1	15.1±0.3
2	0.5	290±3	126±3	5.72	0.675	37±1	11.8±0.1	15.2±0.3
5	0.5	222±4	95±5	4.32	0.511	28±1	11.7±0.2	13.1±0.4
1	1.0	349±2	149±3	6.72	0.793	43±1	12.0±0.1	16.9±0.2
2	1.0	288±4	129±8	5.8	0.686	38±2	11.4±0.2	16.0±0.3
5	1.0	233±3	100±6	4.49	0.53	29±2	11.8±0.2	13.7±0.4

ℓ_B	f	$L = V_{eq}^{1/3}$	$\langle R_E^2 \rangle^{1/2}$	α_ν	$\frac{R_E}{N_m b}$	$\langle R_G^2 \rangle^{1/2}$	$\frac{\langle R_E^2 \rangle}{\langle R_G^2 \rangle}$	R_H
1	0.25	221±3	94±4	7.05	0.527	27±1	12.0±0.2	12.0±0.4
2	0.25	219±3	94±4	7.06	0.528	27±1	11.9±0.1	12.2±0.3
5	0.25	164±4	76±8	5.69	0.428	22±2	11.4±0.3	11.0±0.6
1	0.5	259±4	117±5	8.74	0.653	34±1	12.0±0.1	14.0±0.4
2	0.5	269±2	114±4	8.57	0.641	33±1	11.9±0.1	14.0±0.3
5	0.5	179±3	80±8	5.96	0.448	24±2	11.2±0.3	11.8±0.4
1	1.0	298±5	136±4	10	0.75	39±1	11.8±0.1	15.8±0.3
2	1.0	274±6	124±8	9.16	0.686	37±2	11.5±0.2	15.3±0.4
5	1.0	151±9	78±14	5.66	0.43	25±3	10.0±0.5	12.6±0.7

Table A.15.: Selected network properties for a system with $N_m = 179$ monomers per chain in good solvent (*top*) and close to the θ-point (*bottom*) for different values of Bjerrum length ℓ_B and charge fraction f, namely length L of the simulation box after reaching the equilibrium volume V_{eq}, the average chain extension R_E, its swelling ratio α_ν compared to a single neutral chain, its extension relative to the contour length $N_m b$, its radius of gyration R_G, its aspect ratio R_E^2/R_G^2, and its hydrodynamic radius R_H.

ℓ_B	f	$\mathcal{P}_{ideal}^{CI}$	$\mathcal{P}_{LJ}^{CI}$	$\mathcal{P}_{\ell_B}^{tot}$	$\mathcal{P}_{ideal}^{monomers}$	$\mathcal{P}_{LJ}^{monomers}$	$\mathcal{P}_{FENE}$
1	0.25	$4.87{\cdot}10^{-5}$	$1.12{\cdot}10^{-7}$	$1.01{\cdot}10^{-5}$	$1.96{\cdot}10^{-4}$	$1.14{\cdot}10^{-3}$	$-1.40{\cdot}10^{-3}$
2	0.25	$4.79{\cdot}10^{-5}$	$9.74{\cdot}10^{-7}$	$1.53{\cdot}10^{-5}$	$1.93{\cdot}10^{-4}$	$1.12{\cdot}10^{-3}$	$-1.38{\cdot}10^{-3}$
5	0.25	$8.82{\cdot}10^{-5}$	$3.38{\cdot}10^{-5}$	$-3.35{\cdot}10^{-5}$	$3.55{\cdot}10^{-4}$	$2.09{\cdot}10^{-3}$	$-2.53{\cdot}10^{-3}$
1	0.5	$5.45{\cdot}10^{-5}$	$3.40{\cdot}10^{-7}$	$2.30{\cdot}10^{-5}$	$1.09{\cdot}10^{-4}$	$6.00{\cdot}10^{-4}$	$-7.90{\cdot}10^{-4}$
2	0.5	$5.65{\cdot}10^{-5}$	$4.70{\cdot}10^{-6}$	$2.72{\cdot}10^{-5}$	$1.13{\cdot}10^{-4}$	$6.14{\cdot}10^{-4}$	$-8.22{\cdot}10^{-4}$
5	0.5	$1.31{\cdot}10^{-4}$	$1.20{\cdot}10^{-4}$	$-9.17{\cdot}10^{-5}$	$2.64{\cdot}10^{-4}$	$1.47{\cdot}10^{-3}$	$-1.90{\cdot}10^{-3}$
1	1.0	$6.76{\cdot}10^{-5}$	$2.31{\cdot}10^{-6}$	$5.48{\cdot}10^{-5}$	$6.77{\cdot}10^{-5}$	$3.17{\cdot}10^{-4}$	$-5.11{\cdot}10^{-4}$
2	1.0	$1.15{\cdot}10^{-4}$	$4.51{\cdot}10^{-5}$	$5.56{\cdot}10^{-5}$	$1.16{\cdot}10^{-4}$	$5.43{\cdot}10^{-4}$	$-8.70{\cdot}10^{-4}$
5	1.0	$2.26{\cdot}10^{-4}$	$4.59{\cdot}10^{-4}$	$-1.88{\cdot}10^{-4}$	$2.26{\cdot}10^{-4}$	$1.00{\cdot}10^{-3}$	$-1.73{\cdot}10^{-3}$

ℓ_B	f	$\mathcal{P}_{ideal}^{CI}$	$\mathcal{P}_{LJ}^{CI}$	$\mathcal{P}_{\ell_B}^{tot}$	$\mathcal{P}_{ideal}^{monomers}$	$\mathcal{P}_{LJ}^{monomers}$	$\mathcal{P}_{FENE}$
1	0.25	$6.88{\cdot}10^{-5}$	$3.24{\cdot}10^{-7}$	$1.56{\cdot}10^{-5}$	$2.78{\cdot}10^{-4}$	$1.32{\cdot}10^{-3}$	$-1.68{\cdot}10^{-3}$
2	0.25	$6.83{\cdot}10^{-5}$	$2.26{\cdot}10^{-6}$	$2.26{\cdot}10^{-5}$	$2.77{\cdot}10^{-4}$	$1.30{\cdot}10^{-3}$	$-1.68{\cdot}10^{-3}$
5	0.25	$1.47{\cdot}10^{-4}$	$7.02{\cdot}10^{-5}$	$-6.78{\cdot}10^{-5}$	$5.92{\cdot}10^{-4}$	$2.82{\cdot}10^{-3}$	$-3.58{\cdot}10^{-3}$
1	0.5	$7.62{\cdot}10^{-5}$	$6.10{\cdot}10^{-7}$	$3.55{\cdot}10^{-5}$	$1.53{\cdot}10^{-4}$	$6.76{\cdot}10^{-4}$	$-9.42{\cdot}10^{-4}$
2	0.5	$7.52{\cdot}10^{-5}$	$8.33{\cdot}10^{-6}$	$3.53{\cdot}10^{-5}$	$1.51{\cdot}10^{-4}$	$6.64{\cdot}10^{-4}$	$-9.31{\cdot}10^{-4}$
5	0.5	$2.39{\cdot}10^{-4}$	$2.50{\cdot}10^{-4}$	$-1.80{\cdot}10^{-4}$	$4.80{\cdot}10^{-4}$	$2.16{\cdot}10^{-3}$	$-2.94{\cdot}10^{-3}$
1	1.0	$1.01{\cdot}10^{-4}$	$5.04{\cdot}10^{-6}$	$8.16{\cdot}10^{-5}$	$1.01{\cdot}10^{-4}$	$3.80{\cdot}10^{-4}$	$-6.57{\cdot}10^{-4}$
2	1.0	$1.27{\cdot}10^{-4}$	$5.45{\cdot}10^{-5}$	$6.22{\cdot}10^{-5}$	$1.27{\cdot}10^{-4}$	$4.62{\cdot}10^{-4}$	$-8.29{\cdot}10^{-4}$
5	1.0	$6.73{\cdot}10^{-4}$	$1.46{\cdot}10^{-3}$	$-5.66{\cdot}10^{-4}$	$6.73{\cdot}10^{-4}$	$2.23{\cdot}10^{-3}$	$-4.48{\cdot}10^{-3}$

Table A.16.: Detailed pressure components for a system with $N_m = 179$ monomers per chain in good solvent (*top*) and close to the θ-point (*bottom*) for different values of Bjerrum length ℓ_B and charge fraction f, namely the contributions to the gas-like pressure $\mathcal{P}_{gas}$ (ideal part $\mathcal{P}_{ideal}^{CI}$, excluded volume $\mathcal{P}_{LJ}^{CI} = \mathcal{P}_{LJ}^{CI-CI} + \mathcal{P}_{LJ}^{CI-monomers}$, total electrostatic pressure $\mathcal{P}_{\ell_B}^{tot}$) and to the one of the gel $\mathcal{P}_{gel}$ (ideal part $\mathcal{P}_{ideal}^{monomers}$, excluded volume $\mathcal{P}_{LJ}^{monomers}$, bonded virial $\mathcal{P}_{FENE}$) for the fully charged gel at its swelling equilibrium volume V_{eq}.

ℓ_B	f	$L = V_{eq}^{1/3}$	$\langle R_E^2 \rangle^{1/2}$	α_ν	$\frac{R_E}{N_m b}$	$\langle R_G^2 \rangle^{1/2}$	$\frac{\langle R_E^2 \rangle}{\langle R_G^2 \rangle}$	R_H
1	0.125	221±3	95±6	4.07	0.461	28±2	12.0±0.2	12.7±0.5
2	0.125	221±3	95±5	4.07	0.46	28±2	11.8±0.2	12.9±0.4
5	0.125	201±4	87±5	3.72	0.42	26±2	11.5±0.2	12.4±0.4
1	0.25	270±3	116±5	4.96	0.561	33±2	12.0±0.2	14.3±0.4
2	0.25	270±4	116±5	4.96	0.56	34±1	11.9±0.1	14.5±0.4
5	0.25	224±4	97±7	4.13	0.468	29±2	11.5±0.2	13.3±0.5
1	0.5	327±2	141±4	6.01	0.679	40±1	12.1±0.1	16.2±0.3
2	0.5	325±2	139±4	5.94	0.671	40±1	11.9±0.1	16.4±0.3
5	0.5	249±5	107±4	4.56	0.515	31±1	11.8±0.1	14.3±0.3
1	1.0	388±2	166±3	7.04	0.795	48±1	12.1±0.1	18.3±0.2
2	1.0	360±2	155±4	6.53	0.738	45±1	11.8±0.1	17.8±0.3
5	1.0	260±3	112±6	4.71	0.533	33±2	11.7±0.2	14.8±0.4

ℓ_B	f	$L = V_{eq}^{1/3}$	$\langle R_E^2 \rangle^{1/2}$	α_ν	$\frac{R_E}{N_m b}$	$\langle R_G^2 \rangle^{1/2}$	$\frac{\langle R_E^2 \rangle}{\langle R_G^2 \rangle}$	R_H
1	0.125	191±3	83±6	5.89	0.419	24±2	11.7±0.2	11.3±0.5
2	0.125	191±3	82±5	5.87	0.417	24±2	11.9±0.2	11.3±0.4
5	0.125	165±4	71±5	5.09	0.362	21±2	11.3±0.2	10.7±0.5
1	0.25	245±3	105±5	7.49	0.532	30±1	12.0±0.2	13.1±0.4
2	0.25	243±3	104±4	7.44	0.528	30±1	12.0±0.2	13.2±0.4
5	0.25	192±4	83±6	5.92	0.42	24±2	11.6±0.2	11.8±0.4
1	0.5	308±2	132±4	9.39	0.666	38±1	12.1±0.1	15.3±0.3
2	0.5	302±3	130±5	9.22	0.654	38±1	11.9±0.1	15.4±0.4
5	0.5	225±4	97±5	6.86	0.487	28±2	11.7±0.2	13.1±0.4
1	1.0	369±2	158±3	11.1	0.787	46±1	12.0±0.1	17.5±0.2
2	1.0	344±2	148±4	10.3	0.733	43±1	11.9±0.1	17.0±0.3
5	1.0	264±24	113±5	7.89	0.56	33±2	11.5±0.2	14.7±0.4

Table A.17.: Selected network properties for a system with $N_m = 199$ monomers per chain in good solvent (*top*) and close to the θ-point (*bottom*) for different values of Bjerrum length ℓ_B and charge fraction f, namely length L of the simulation box after reaching the equilibrium volume V_{eq}, the average chain extension R_E, its swelling ratio α_ν compared to a single neutral chain, its extension relative to the contour length $N_m b$, its radius of gyration R_G, its aspect ratio R_E^2/R_G^2, and its hydrodynamic radius R_H.

ℓ_B	f	$\mathcal{P}^{CI}_{ideal}$	$\mathcal{P}^{CI}_{LJ}$	$\mathcal{P}^{tot}_{\ell_B}$	$\mathcal{P}^{monomers}_{ideal}$	$\mathcal{P}^{monomers}_{LJ}$	$\mathcal{P}_{FENE}$
1	0.125	$3.62{\cdot}10^{-5}$	$5.96{\cdot}10^{-8}$	$3.27{\cdot}10^{-6}$	$2.94{\cdot}10^{-4}$	$1.75{\cdot}10^{-3}$	$-2.09{\cdot}10^{-3}$
2	0.125	$3.65{\cdot}10^{-5}$	$2.75{\cdot}10^{-7}$	$8.26{\cdot}10^{-6}$	$2.97{\cdot}10^{-4}$	$1.77{\cdot}10^{-3}$	$-2.11{\cdot}10^{-3}$
5	0.125	$4.82{\cdot}10^{-5}$	$6.13{\cdot}10^{-6}$	$-5.33{\cdot}10^{-6}$	$3.94{\cdot}10^{-4}$	$2.35{\cdot}10^{-3}$	$-2.80{\cdot}10^{-3}$
1	0.25	$4.01{\cdot}10^{-5}$	$1.03{\cdot}10^{-7}$	$8.16{\cdot}10^{-6}$	$1.62{\cdot}10^{-4}$	$9.40{\cdot}10^{-4}$	$-1.15{\cdot}10^{-3}$
2	0.25	$4.01{\cdot}10^{-5}$	$8.05{\cdot}10^{-7}$	$1.40{\cdot}10^{-5}$	$1.62{\cdot}10^{-4}$	$9.33{\cdot}10^{-4}$	$-1.16{\cdot}10^{-3}$
5	0.25	$7.07{\cdot}10^{-5}$	$2.64{\cdot}10^{-5}$	$-2.52{\cdot}10^{-5}$	$2.85{\cdot}10^{-4}$	$1.67{\cdot}10^{-3}$	$-2.03{\cdot}10^{-3}$
1	0.5	$4.53{\cdot}10^{-5}$	$1.10{\cdot}10^{-7}$	$1.81{\cdot}10^{-5}$	$9.09{\cdot}10^{-5}$	$5.01{\cdot}10^{-4}$	$-6.56{\cdot}10^{-4}$
2	0.5	$4.66{\cdot}10^{-5}$	$3.52{\cdot}10^{-6}$	$2.46{\cdot}10^{-5}$	$9.33{\cdot}10^{-5}$	$5.06{\cdot}10^{-4}$	$-6.77{\cdot}10^{-4}$
5	0.5	$1.04{\cdot}10^{-4}$	$9.28{\cdot}10^{-5}$	$-6.91{\cdot}10^{-5}$	$2.08{\cdot}10^{-4}$	$1.16{\cdot}10^{-3}$	$-1.50{\cdot}10^{-3}$
1	1.0	$5.45{\cdot}10^{-5}$	$1.11{\cdot}10^{-6}$	$4.48{\cdot}10^{-5}$	$5.45{\cdot}10^{-5}$	$2.56{\cdot}10^{-4}$	$-4.11{\cdot}10^{-4}$
2	1.0	$6.82{\cdot}10^{-5}$	$2.45{\cdot}10^{-5}$	$3.95{\cdot}10^{-5}$	$6.83{\cdot}10^{-5}$	$3.15{\cdot}10^{-4}$	$-5.17{\cdot}10^{-4}$
5	1.0	$1.81{\cdot}10^{-4}$	$3.68{\cdot}10^{-4}$	$-1.50{\cdot}10^{-4}$	$1.81{\cdot}10^{-4}$	$8.02{\cdot}10^{-4}$	$-1.38{\cdot}10^{-3}$

ℓ_B	f	$\mathcal{P}^{CI}_{ideal}$	$\mathcal{P}^{CI}_{LJ}$	$\mathcal{P}^{tot}_{\ell_B}$	$\mathcal{P}^{monomers}_{ideal}$	$\mathcal{P}^{monomers}_{LJ}$	$\mathcal{P}_{FENE}$
1	0.125	$5.62{\cdot}10^{-5}$	$1.81{\cdot}10^{-7}$	$6.70{\cdot}10^{-6}$	$4.58{\cdot}10^{-4}$	$2.23{\cdot}10^{-3}$	$-2.76{\cdot}10^{-3}$
2	0.125	$5.60{\cdot}10^{-5}$	$7.26{\cdot}10^{-7}$	$1.05{\cdot}10^{-5}$	$4.56{\cdot}10^{-4}$	$2.21{\cdot}10^{-3}$	$-2.74{\cdot}10^{-3}$
5	0.125	$8.76{\cdot}10^{-5}$	$1.89{\cdot}10^{-5}$	$-1.83{\cdot}10^{-5}$	$7.12{\cdot}10^{-4}$	$3.47{\cdot}10^{-3}$	$-4.29{\cdot}10^{-3}$
1	0.25	$5.40{\cdot}10^{-5}$	$2.04{\cdot}10^{-7}$	$1.36{\cdot}10^{-5}$	$2.18{\cdot}10^{-4}$	$1.03{\cdot}10^{-3}$	$-1.32{\cdot}10^{-3}$
2	0.25	$5.55{\cdot}10^{-5}$	$1.71{\cdot}10^{-6}$	$1.98{\cdot}10^{-5}$	$2.24{\cdot}10^{-4}$	$1.05{\cdot}10^{-3}$	$-1.36{\cdot}10^{-3}$
5	0.25	$1.12{\cdot}10^{-4}$	$5.45{\cdot}10^{-5}$	$-3.93{\cdot}10^{-5}$	$4.53{\cdot}10^{-4}$	$2.17{\cdot}10^{-3}$	$-2.74{\cdot}10^{-3}$
1	0.5	$5.43{\cdot}10^{-5}$	$2.31{\cdot}10^{-7}$	$2.40{\cdot}10^{-5}$	$1.09{\cdot}10^{-4}$	$4.82{\cdot}10^{-4}$	$-6.72{\cdot}10^{-4}$
2	0.5	$5.78{\cdot}10^{-5}$	$5.88{\cdot}10^{-6}$	$2.95{\cdot}10^{-5}$	$1.16{\cdot}10^{-4}$	$5.06{\cdot}10^{-4}$	$-7.19{\cdot}10^{-4}$
5	0.5	$1.41{\cdot}10^{-4}$	$1.44{\cdot}10^{-4}$	$-9.01{\cdot}10^{-5}$	$2.82{\cdot}10^{-4}$	$1.26{\cdot}10^{-3}$	$-1.73{\cdot}10^{-3}$
1	1.0	$6.33{\cdot}10^{-5}$	$2.06{\cdot}10^{-6}$	$5.28{\cdot}10^{-5}$	$6.33{\cdot}10^{-5}$	$2.32{\cdot}10^{-4}$	$-4.13{\cdot}10^{-4}$
2	1.0	$7.84{\cdot}10^{-5}$	$3.13{\cdot}10^{-5}$	$4.34{\cdot}10^{-5}$	$7.83{\cdot}10^{-5}$	$2.80{\cdot}10^{-4}$	$-5.13{\cdot}10^{-4}$
5	1.0	$1.74{\cdot}10^{-4}$	$3.68{\cdot}10^{-4}$	$-1.35{\cdot}10^{-4}$	$1.74{\cdot}10^{-4}$	$5.71{\cdot}10^{-4}$	$-1.16{\cdot}10^{-3}$

Table A.18.: Detailed pressure components for a system with $N_m = 199$ monomers per chain in good solvent (*top*) and close to the θ-point (*bottom*) for different values of Bjerrum length ℓ_B and charge fraction f, namely the contributions to the gas-like pressure $\mathcal{P}_{gas}$ (ideal part $\mathcal{P}^{CI}_{ideal}$, excluded volume $\mathcal{P}^{CI}_{LJ} = \mathcal{P}^{CI-CI}_{LJ} + \mathcal{P}^{CI-monomers}_{LJ}$, total electrostatic pressure $\mathcal{P}^{tot}_{\ell_B}$) and to the one of the gel $\mathcal{P}_{gel}$ (ideal part $\mathcal{P}^{monomers}_{ideal}$, excluded volume $\mathcal{P}^{monomers}_{LJ}$, bonded virial $\mathcal{P}_{FENE}$) for the fully charged gel at its swelling equilibrium volume V_{eq}.

ℓ_B	f	$L = V_{eq}^{1/3}$	$\langle R_E^2 \rangle^{1/2}$	α_ν	$\frac{R_E}{N_m b}$	$\langle R_G^2 \rangle^{1/2}$	$\frac{\langle R_E^2 \rangle}{\langle R_G^2 \rangle}$	R_H
1	0.25	301±3	129±5	5.24	0.569	37±2	12.0±0.1	15.5±0.4
2	0.25	304±3	130±4	5.27	0.573	38±1	11.9±0.1	15.8±0.3
5	0.25	252±5	109±6	4.4	0.478	32±2	11.5±0.2	14.5±0.4
1	0.5	362±2	155±4	6.27	0.681	45±1	12.2±0.1	17.6±0.3
2	0.5	364±3	158±5	6.38	0.693	46±2	12.1±0.1	17.9±0.4
5	0.5	275±4	118±6	4.77	0.518	34±2	11.8±0.2	15.3±0.4
1	1.0	430±2	184±3	7.37	0.801	53±1	12.1±0.1	19.8±0.2
2	1.0	390±2	170±5	6.77	0.735	49±1	11.8±0.1	19.2±0.3
5	1.0	291±4	125±6	4.98	0.542	37±2	11.7±0.2	16.2±0.4

ℓ_B	f	$L = V_{eq}^{1/3}$	$\langle R_E^2 \rangle^{1/2}$	α_ν	$\frac{R_E}{N_m b}$	$\langle R_G^2 \rangle^{1/2}$	$\frac{\langle R_E^2 \rangle}{\langle R_G^2 \rangle}$	R_H
1	0.25	253±4	115±7	7.81	0.529	33±2	11.8±0.2	14.1±0.6
2	0.25	272±4	116±5	7.9	0.534	34±2	12.0±0.1	14.3±0.4
5	0.25	186±4	86±9	5.85	0.398	26±2	11.2±0.3	12.6±0.5
1	0.5	337±3	146±4	9.91	0.67	42±1	12.0±0.1	16.6±0.3
2	0.5	334±3	144±4	9.75	0.659	42±1	12.0±0.1	16.6±0.3
5	0.5	221±4	101±10	6.83	0.464	30±3	11.3±0.3	13.9±0.6
1	1.0	350±7	164±6	11	0.742	48±2	11.8±0.1	18.4±0.3
2	1.0	270±11	135±18	8.92	0.608	41±4	10.8±0.4	17.4±0.6
5	1.0	193±8	98±17	6.4	0.441	30±4	10.6±0.5	14.7±0.9

Table A.19.: Selected network properties for a system with $N_m = 219$ monomers per chain in good solvent (*top*) and close to the θ-point (*bottom*) for different values of Bjerrum length ℓ_B and charge fraction f, namely length L of the simulation box after reaching the equilibrium volume V_{eq}, the average chain extension R_E, its swelling ratio α_ν compared to a single neutral chain, its extension relative to the contour length $N_m b$, its radius of gyration R_G, its aspect ratio R_E^2/R_G^2, and its hydrodynamic radius R_H.

ℓ_B	f	$\mathcal{P}_{ideal}^{CI}$	$\mathcal{P}_{LJ}^{CI}$	$\mathcal{P}_{\ell_B}^{tot}$	$\mathcal{P}_{ideal}^{monomers}$	$\mathcal{P}_{LJ}^{monomers}$	$\mathcal{P}_{FENE}$
1	0.25	$3.18{\cdot}10^{-5}$	$2.45{\cdot}10^{-8}$	$4.92{\cdot}10^{-6}$	$1.28{\cdot}10^{-4}$	$7.49{\cdot}10^{-4}$	$-9.16{\cdot}10^{-4}$
2	0.25	$3.10{\cdot}10^{-5}$	$3.97{\cdot}10^{-7}$	$1.24{\cdot}10^{-5}$	$1.25{\cdot}10^{-4}$	$7.23{\cdot}10^{-4}$	$-8.93{\cdot}10^{-4}$
5	0.25	$5.42{\cdot}10^{-5}$	$1.94{\cdot}10^{-5}$	$-1.66{\cdot}10^{-5}$	$2.19{\cdot}10^{-4}$	$1.28{\cdot}10^{-3}$	$-1.56{\cdot}10^{-3}$
1	0.5	$3.69{\cdot}10^{-5}$	$1.28{\cdot}10^{-7}$	$1.51{\cdot}10^{-5}$	$7.39{\cdot}10^{-5}$	$4.07{\cdot}10^{-4}$	$-5.34{\cdot}10^{-4}$
2	0.5	$3.52{\cdot}10^{-5}$	$2.03{\cdot}10^{-6}$	$2.07{\cdot}10^{-5}$	$7.05{\cdot}10^{-5}$	$3.79{\cdot}10^{-4}$	$-5.12{\cdot}10^{-4}$
5	0.5	$8.40{\cdot}10^{-5}$	$7.54{\cdot}10^{-5}$	$-5.48{\cdot}10^{-5}$	$1.68{\cdot}10^{-4}$	$9.39{\cdot}10^{-4}$	$-1.21{\cdot}10^{-3}$
1	1.0	$4.42{\cdot}10^{-5}$	$6.12{\cdot}10^{-7}$	$3.80{\cdot}10^{-5}$	$4.41{\cdot}10^{-5}$	$2.05{\cdot}10^{-4}$	$-3.33{\cdot}10^{-4}$
2	1.0	$5.99{\cdot}10^{-5}$	$2.08{\cdot}10^{-5}$	$3.68{\cdot}10^{-5}$	$5.99{\cdot}10^{-5}$	$2.76{\cdot}10^{-4}$	$-4.53{\cdot}10^{-4}$
5	1.0	$1.42{\cdot}10^{-4}$	$2.85{\cdot}10^{-4}$	$-1.15{\cdot}10^{-4}$	$1.42{\cdot}10^{-4}$	$6.26{\cdot}10^{-4}$	$-1.08{\cdot}10^{-3}$

ℓ_B	f	$\mathcal{P}_{ideal}^{CI}$	$\mathcal{P}_{LJ}^{CI}$	$\mathcal{P}_{\ell_B}^{tot}$	$\mathcal{P}_{ideal}^{monomers}$	$\mathcal{P}_{LJ}^{monomers}$	$\mathcal{P}_{FENE}$
1	0.25	$4.97{\cdot}10^{-5}$	$8.86{\cdot}10^{-8}$	$1.04{\cdot}10^{-5}$	$2.00{\cdot}10^{-4}$	$9.49{\cdot}10^{-4}$	$-1.21{\cdot}10^{-3}$
2	0.25	$4.42{\cdot}10^{-5}$	$1.04{\cdot}10^{-6}$	$1.62{\cdot}10^{-5}$	$1.77{\cdot}10^{-4}$	$8.35{\cdot}10^{-4}$	$-1.08{\cdot}10^{-3}$
5	0.25	$1.28{\cdot}10^{-4}$	$6.09{\cdot}10^{-5}$	$-5.75{\cdot}10^{-5}$	$5.15{\cdot}10^{-4}$	$2.46{\cdot}10^{-3}$	$-3.11{\cdot}10^{-3}$
1	0.5	$4.51{\cdot}10^{-5}$	$1.67{\cdot}10^{-7}$	$2.24{\cdot}10^{-5}$	$9.02{\cdot}10^{-5}$	$3.98{\cdot}10^{-4}$	$-5.57{\cdot}10^{-4}$
2	0.5	$4.63{\cdot}10^{-5}$	$4.13{\cdot}10^{-6}$	$2.58{\cdot}10^{-5}$	$9.28{\cdot}10^{-5}$	$4.05{\cdot}10^{-4}$	$-5.74{\cdot}10^{-4}$
5	0.5	$1.62{\cdot}10^{-4}$	$1.65{\cdot}10^{-4}$	$-1.17{\cdot}10^{-4}$	$3.24{\cdot}10^{-4}$	$1.45{\cdot}10^{-3}$	$-1.99{\cdot}10^{-3}$
1	1.0	$7.55{\cdot}10^{-5}$	$3.03{\cdot}10^{-6}$	$6.57{\cdot}10^{-5}$	$7.55{\cdot}10^{-5}$	$2.82{\cdot}10^{-4}$	$-4.89{\cdot}10^{-4}$
2	1.0	$1.48{\cdot}10^{-4}$	$6.53{\cdot}10^{-5}$	$6.98{\cdot}10^{-5}$	$1.48{\cdot}10^{-4}$	$5.42{\cdot}10^{-4}$	$-9.60{\cdot}10^{-4}$
5	1.0	$3.89{\cdot}10^{-4}$	$8.41{\cdot}10^{-4}$	$-3.20{\cdot}10^{-4}$	$3.89{\cdot}10^{-4}$	$1.29{\cdot}10^{-3}$	$-2.59{\cdot}10^{-3}$

Table A.20.: Detailed pressure components for a system with $N_m = 219$ monomers per chain in good solvent (*top*) and close to the θ-point (*bottom*) for different values of Bjerrum length ℓ_B and charge fraction f, namely the contributions to the gas-like pressure $\mathcal{P}_{gas}$ (ideal part $\mathcal{P}_{ideal}^{CI}$, excluded volume $\mathcal{P}_{LJ}^{CI} = \mathcal{P}_{LJ}^{CI-CI} + \mathcal{P}_{LJ}^{CI-monomers}$, total electrostatic pressure $\mathcal{P}_{\ell_B}^{tot}$) and to the one of the gel $\mathcal{P}_{gel}$ (ideal part $\mathcal{P}_{ideal}^{monomers}$, excluded volume $\mathcal{P}_{LJ}^{monomers}$, bonded virial $\mathcal{P}_{FENE}$) for the fully charged gel at its swelling equilibrium volume V_{eq}.

ℓ_B	f	$L = V_{eq}^{1/3}$	$\langle R_E^2 \rangle^{1/2}$	α_ν	$\frac{R_E}{N_m b}$	$\langle R_G^2 \rangle^{1/2}$	$\frac{\langle R_E^2 \rangle}{\langle R_G^2 \rangle}$	R_H
1	0.25	364±3	156±5	5.73	0.581	45±2	12.0±0.1	18.0±0.4
2	0.25	359±4	155±5	5.67	0.575	45±1	12.1±0.1	18.0±0.4
5	0.25	304±4	131±5	4.81	0.488	38±2	11.8±0.1	16.6±0.4
1	0.5	433±3	186±4	6.8	0.69	53±1	12.2±0.1	20.1±0.3
2	0.5	434±3	186±4	6.8	0.689	54±1	12.0±0.1	20.4±0.3
5	0.5	325±4	140±7	5.13	0.521	41±2	11.6±0.2	17.6±0.5
1	1.0	507±2	218±4	7.88	0.799	62±1	12.2±0.1	22.6±0.3
2	1.0	481±3	207±4	7.48	0.758	60±1	11.9±0.1	22.2±0.3
5	1.0	352±4	151±6	5.46	0.553	44±2	11.8±0.1	18.6±0.5

ℓ_B	f	$L = V_{eq}^{1/3}$	$\langle R_E^2 \rangle^{1/2}$	α_ν	$\frac{R_E}{N_m b}$	$\langle R_G^2 \rangle^{1/2}$	$\frac{\langle R_E^2 \rangle}{\langle R_G^2 \rangle}$	R_H
1	0.25	320±3	138±5	8.63	0.536	40±2	12.2±0.1	16.1±0.4
2	0.25	326±4	140±5	8.77	0.545	40±2	12.1±0.1	16.4±0.4
5	0.25	261±4	113±7	7.05	0.439	33±2	11.6±0.2	14.8±0.5
1	0.5	406±3	174±3	10.9	0.675	50±1	12.2±0.1	18.9±0.3
2	0.5	406±3	175±4	10.9	0.675	50±1	12.0±0.1	19.2±0.3
5	0.5	298±5	128±7	7.99	0.497	38±2	11.7±0.2	16.2±0.5
1	1.0	482±2	207±3	12.7	0.791	59±1	12.2±0.1	21.6±0.3
2	1.0	456±2	196±4	12	0.746	57±1	11.9±0.1	21.1±0.3
5	1.0	342±16	147±7	8.97	0.558	43±2	11.8±0.2	18.0±0.4

Table A.21.: Selected network properties for a system with $N_m = 259$ monomers per chain in good solvent (*top*) and close to the θ-point (*bottom*) for different values of Bjerrum length ℓ_B and charge fraction f, namely length L of the simulation box after reaching the equilibrium volume V_{eq}, the average chain extension R_E, its swelling ratio α_ν compared to a single neutral chain, its extension relative to the contour length $N_m b$, its radius of gyration R_G, its aspect ratio R_E^2/R_G^2, and its hydrodynamic radius R_H.

ℓ_B	f	$\mathcal{P}_{ideal}^{CI}$	$\mathcal{P}_{LJ}^{CI}$	$\mathcal{P}_{\ell_B}^{tot}$	$\mathcal{P}_{ideal}^{monomers}$	$\mathcal{P}_{LJ}^{monomers}$	$\mathcal{P}_{FENE}$
1	0.25	$2.14{\cdot}10^{-5}$	$4.29{\cdot}10^{-8}$	$7.30{\cdot}10^{-6}$	$8.63{\cdot}10^{-5}$	$4.99{\cdot}10^{-4}$	$-6.16{\cdot}10^{-4}$
2	0.25	$2.22{\cdot}10^{-5}$	$2.60{\cdot}10^{-7}$	$8.16{\cdot}10^{-6}$	$8.94{\cdot}10^{-5}$	$5.16{\cdot}10^{-4}$	$-6.39{\cdot}10^{-4}$
5	0.25	$3.66{\cdot}10^{-5}$	$1.23{\cdot}10^{-5}$	$-9.08{\cdot}10^{-6}$	$1.47{\cdot}10^{-4}$	$8.58{\cdot}10^{-4}$	$-1.05{\cdot}10^{-3}$
1	0.5	$2.55{\cdot}10^{-5}$	$4.18{\cdot}10^{-8}$	$9.78{\cdot}10^{-6}$	$5.11{\cdot}10^{-5}$	$2.81{\cdot}10^{-4}$	$-3.69{\cdot}10^{-4}$
2	0.5	$2.55{\cdot}10^{-5}$	$1.23{\cdot}10^{-6}$	$1.72{\cdot}10^{-5}$	$5.10{\cdot}10^{-5}$	$2.74{\cdot}10^{-4}$	$-3.70{\cdot}10^{-4}$
5	0.5	$6.07{\cdot}10^{-5}$	$5.43{\cdot}10^{-5}$	$-3.81{\cdot}10^{-5}$	$1.21{\cdot}10^{-4}$	$6.73{\cdot}10^{-4}$	$-8.74{\cdot}10^{-4}$
1	1.0	$3.19{\cdot}10^{-5}$	$2.14{\cdot}10^{-7}$	$2.56{\cdot}10^{-5}$	$3.19{\cdot}10^{-5}$	$1.50{\cdot}10^{-4}$	$-2.41{\cdot}10^{-4}$
2	1.0	$3.73{\cdot}10^{-5}$	$1.14{\cdot}10^{-5}$	$2.54{\cdot}10^{-5}$	$3.72{\cdot}10^{-5}$	$1.70{\cdot}10^{-4}$	$-2.82{\cdot}10^{-4}$
5	1.0	$9.53{\cdot}10^{-5}$	$1.91{\cdot}10^{-4}$	$-7.53{\cdot}10^{-5}$	$9.53{\cdot}10^{-5}$	$4.20{\cdot}10^{-4}$	$-7.28{\cdot}10^{-4}$

ℓ_B	f	$\mathcal{P}_{ideal}^{CI}$	$\mathcal{P}_{LJ}^{CI}$	$\mathcal{P}_{\ell_B}^{tot}$	$\mathcal{P}_{ideal}^{monomers}$	$\mathcal{P}_{LJ}^{monomers}$	$\mathcal{P}_{FENE}$
1	0.25	$3.14{\cdot}10^{-5}$	$6.46{\cdot}10^{-8}$	$7.03{\cdot}10^{-6}$	$1.26{\cdot}10^{-4}$	$5.99{\cdot}10^{-4}$	$-7.65{\cdot}10^{-4}$
2	0.25	$2.98{\cdot}10^{-5}$	$4.55{\cdot}10^{-7}$	$1.21{\cdot}10^{-5}$	$1.20{\cdot}10^{-4}$	$5.63{\cdot}10^{-4}$	$-7.28{\cdot}10^{-4}$
5	0.25	$5.82{\cdot}10^{-5}$	$2.62{\cdot}10^{-5}$	$-2.10{\cdot}10^{-5}$	$2.35{\cdot}10^{-4}$	$1.12{\cdot}10^{-3}$	$-1.42{\cdot}10^{-3}$
1	0.5	$3.10{\cdot}10^{-5}$	$9.33{\cdot}10^{-8}$	$1.30{\cdot}10^{-5}$	$6.21{\cdot}10^{-5}$	$2.74{\cdot}10^{-4}$	$-3.83{\cdot}10^{-4}$
2	0.5	$3.09{\cdot}10^{-5}$	$2.14{\cdot}10^{-6}$	$1.98{\cdot}10^{-5}$	$6.20{\cdot}10^{-5}$	$2.68{\cdot}10^{-4}$	$-3.84{\cdot}10^{-4}$
5	0.5	$7.84{\cdot}10^{-5}$	$7.87{\cdot}10^{-5}$	$-5.28{\cdot}10^{-5}$	$1.57{\cdot}10^{-4}$	$6.98{\cdot}10^{-4}$	$-9.63{\cdot}10^{-4}$
1	1.0	$3.71{\cdot}10^{-5}$	$4.00{\cdot}10^{-7}$	$3.19{\cdot}10^{-5}$	$3.71{\cdot}10^{-5}$	$1.36{\cdot}10^{-4}$	$-2.42{\cdot}10^{-4}$
2	1.0	$4.39{\cdot}10^{-5}$	$1.55{\cdot}10^{-5}$	$2.92{\cdot}10^{-5}$	$4.39{\cdot}10^{-5}$	$1.55{\cdot}10^{-4}$	$-2.88{\cdot}10^{-4}$
5	1.0	$1.04{\cdot}10^{-4}$	$2.19{\cdot}10^{-4}$	$-7.85{\cdot}10^{-5}$	$1.04{\cdot}10^{-4}$	$3.41{\cdot}10^{-4}$	$-6.94{\cdot}10^{-4}$

Table A.22.: Detailed pressure components for a system with $N_m = 259$ monomers per chain in good solvent (*top*) and close to the θ-point (*bottom*) for different values of Bjerrum length ℓ_B and charge fraction f, namely the contributions to the gas-like pressure $\mathcal{P}_{gas}$ (ideal part $\mathcal{P}_{ideal}^{CI}$, excluded volume $\mathcal{P}_{LJ}^{CI} = \mathcal{P}_{LJ}^{CI-CI} + \mathcal{P}_{LJ}^{CI-monomers}$, total electrostatic pressure $\mathcal{P}_{\ell_B}^{tot}$) and to the one of the gel $\mathcal{P}_{gel}$ (ideal part $\mathcal{P}_{ideal}^{monomers}$, excluded volume $\mathcal{P}_{LJ}^{monomers}$, bonded virial $\mathcal{P}_{FENE}$) for the fully charged gel at its swelling equilibrium volume V_{eq}.

B. Integrated Counterion Distributions

In this appendix, the integrated counterion distributions are shown for all the polyelectrolyte networks we investigated in good solvent and close to the θ-point. They are presented along increasing chain length N_m and charge fraction f, grouped into quad panels comparing the three investigated Bjerrum lengths ℓ_B and both solvents with each other.

While the colours and symbols chosen for the respective plots correspond to the scheme used throughout this entire thesis (*i.e.* same colour refers to same f, same symbol to same ℓ_B-/solvent-combination), it is distinguished between the integrated counterion distributions around the monomers on the network chains (*mere coloured symbols*) and those around the node monomers (*line-connected coloured symbols*) to emphasize the different "perspectives" of the strands, onto which condensation and charge renormalization takes place, and the network nodes, to which the counterions always appear as an ideal gas. Obtained from counting the number of counterions within binned distances from the nearest network monomers, the plots have been normalized onto the unit interval, such that a functional value of *e.g.* 0.63 for $|r| = 24\sigma$ corresponds to "63 % of all counterions can be found within a radius of 24σ around the reference monomers (*i.e.* network strands or node monomers)".

In case of the good solvent plots, some additional geometrical properties are given to allow better estimation of the counterion distributions relative to the system size: For one, the spatial distance $|r|$ from a chain corresponding to its average length $\langle R_\mathrm{E}^2 \rangle^{1/2}$ is indicated by a *straight line*, while the model representations $R_\mathrm{cyl}^\mathrm{Blob}$ (*dashed line*) and $R_\mathrm{cyl}^\mathrm{Rod}$ (*dotted line*) provide the idealized length of a network strand in the blob-like and rod-like representation of the cylindrical cell model, respectively.

For strongly charged systems with counterion condensation taking place, the analogy to single polyelectrolytes suggests that the inflection point of the integrated counterion distribution corresponds to $(R_\mathrm{M}, 1/\xi_\mathrm{M})$. On course of the investigation of effective charge fractions, however, it was found that this criterion does not provide suitable results in case of networks. To assert that statement, the good solvent plots also contain the $(2,2)$-Padé-fit of the integrated distribution functions in the vicinity of the point of inflection with an arrow indicating the point itself (if multiple points exists, more than one arrow is given), adding additional arrows corresponding to the f_eff required from the various theoretical predictions for R_E.

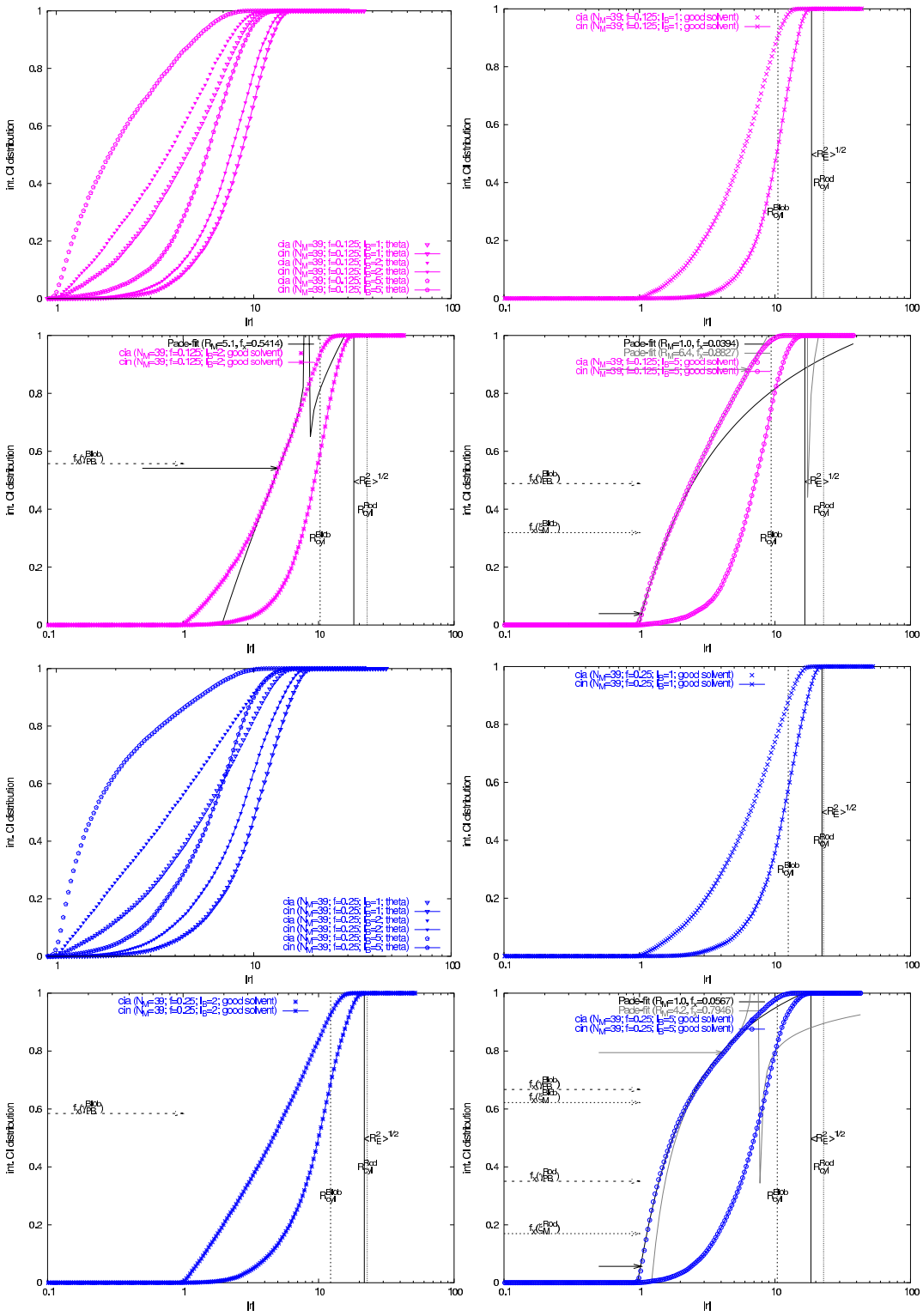

Figure B.1.: $N_\mathrm{m} \in \{39\}$, $f \in \{\frac{1}{8}, \frac{1}{4}\}$, $\ell_\mathrm{B} \in \{1\sigma, 2\sigma, 5\sigma\}$, in both solvents.

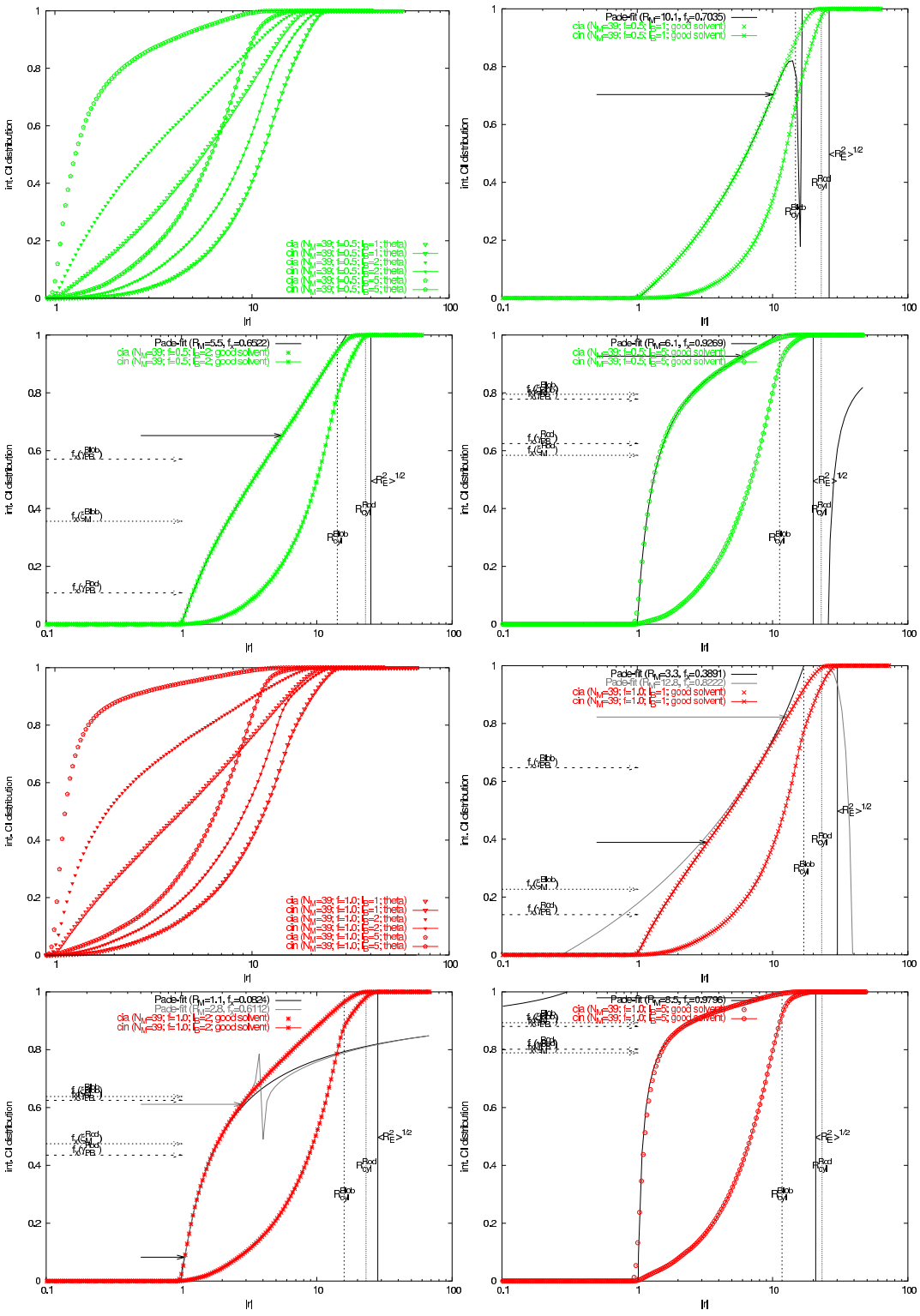

Figure B.2.: $N_{\mathrm{m}} \in \{39\}$, $f \in \{\frac{1}{2}, \frac{1}{1}\}$, $\ell_{\mathrm{B}} \in \{1\sigma, 2\sigma, 5\sigma\}$, in both solvents.

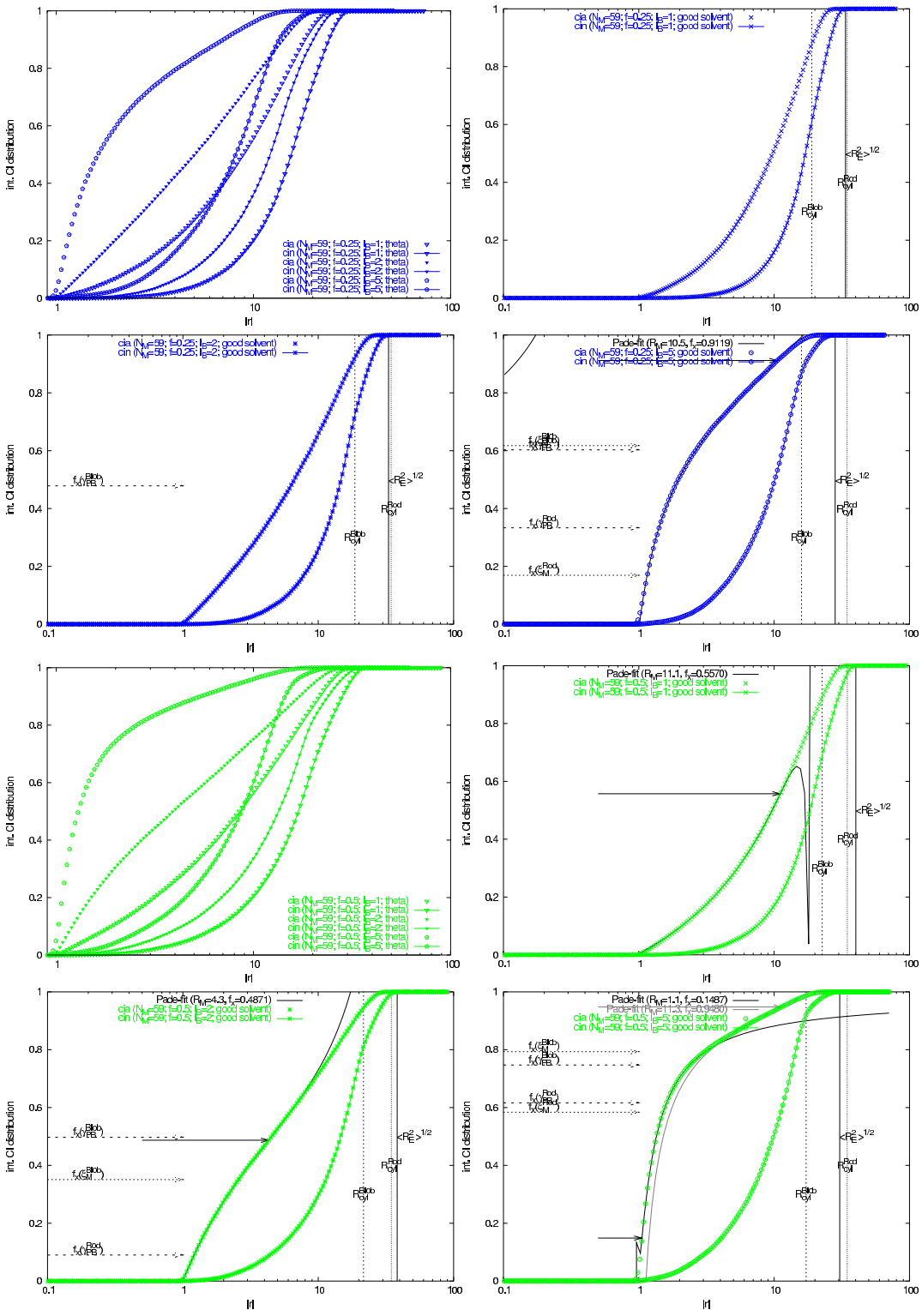

Figure B.3.: $N_\mathrm{m} \in \{59\}$, $f \in \{\frac{1}{4}, \frac{1}{2}\}$, $\ell_\mathrm{B} \in \{1\sigma, 2\sigma, 5\sigma\}$, in both solvents.

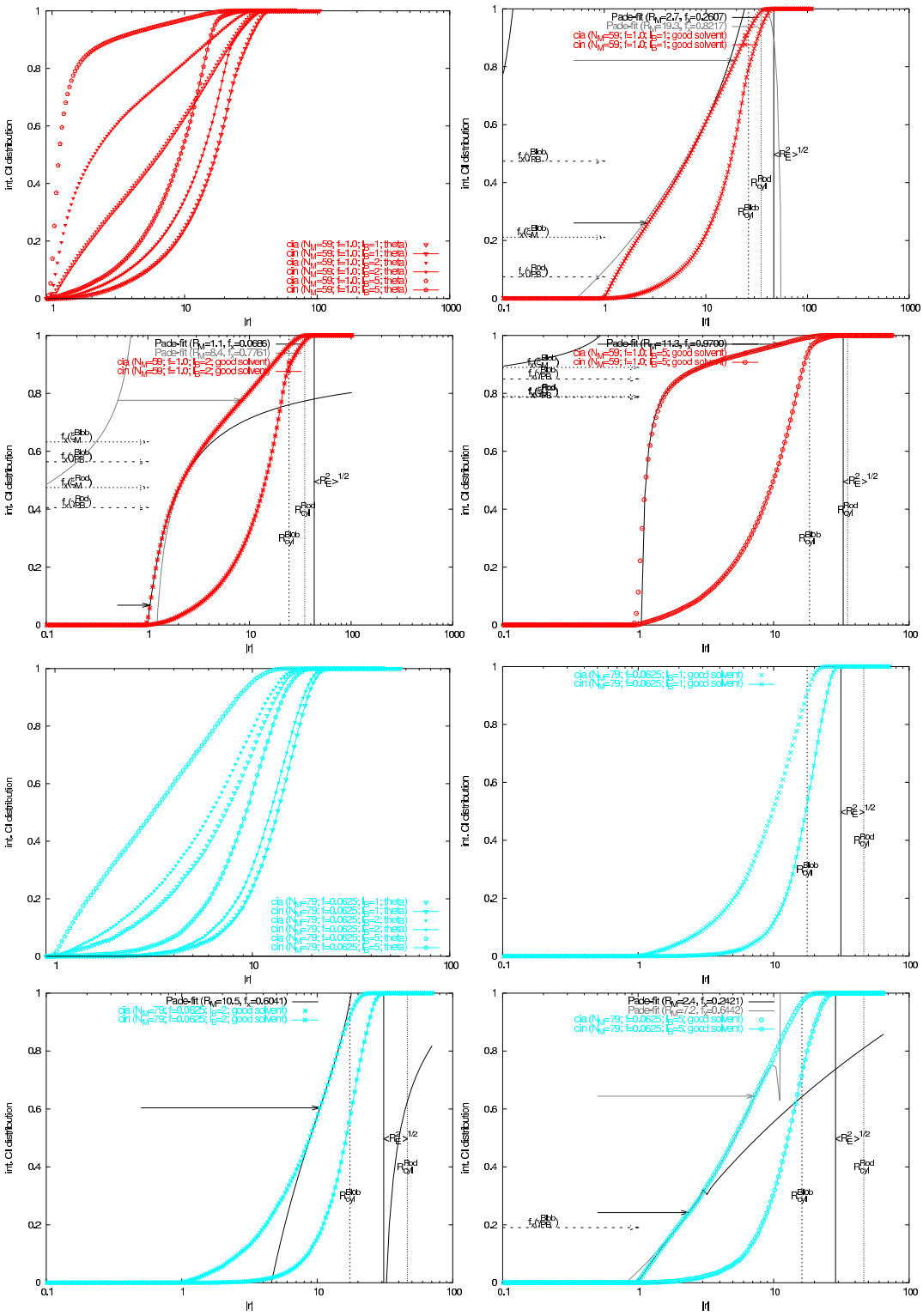

Figure B.4.: $N_{\mathrm{m}} \in \{59, 79\}$, $f \in \{\frac{1}{1}, \frac{1}{16}\}$, $\ell_{\mathrm{B}} \in \{1\sigma, 2\sigma, 5\sigma\}$, in both solvents.

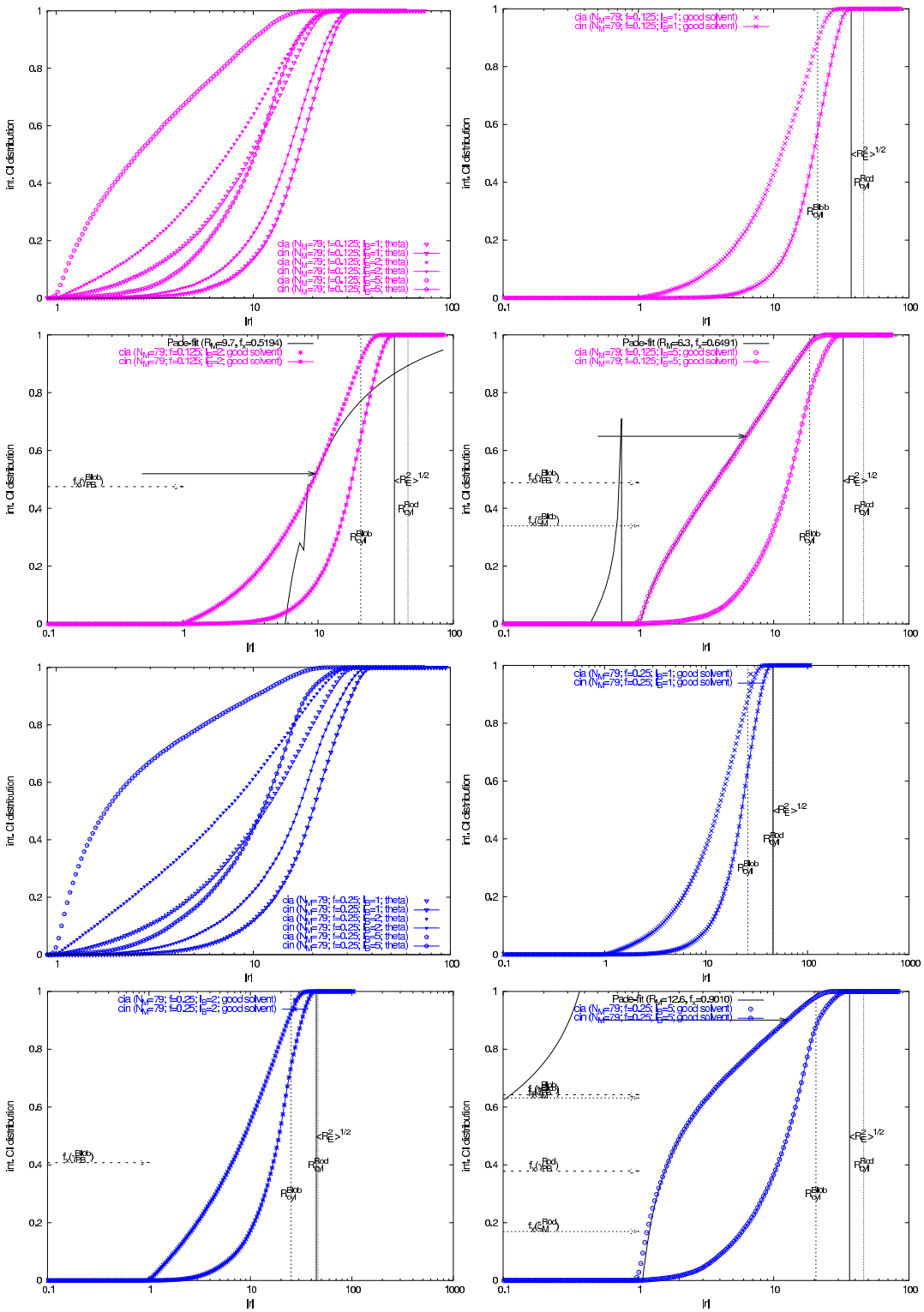

Figure B.5.: $N_\mathrm{m} \in \{79\}$, $f \in \{\frac{1}{8}, \frac{1}{4}\}$, $\ell_\mathrm{B} \in \{1\sigma, 2\sigma, 5\sigma\}$, in both solvents.

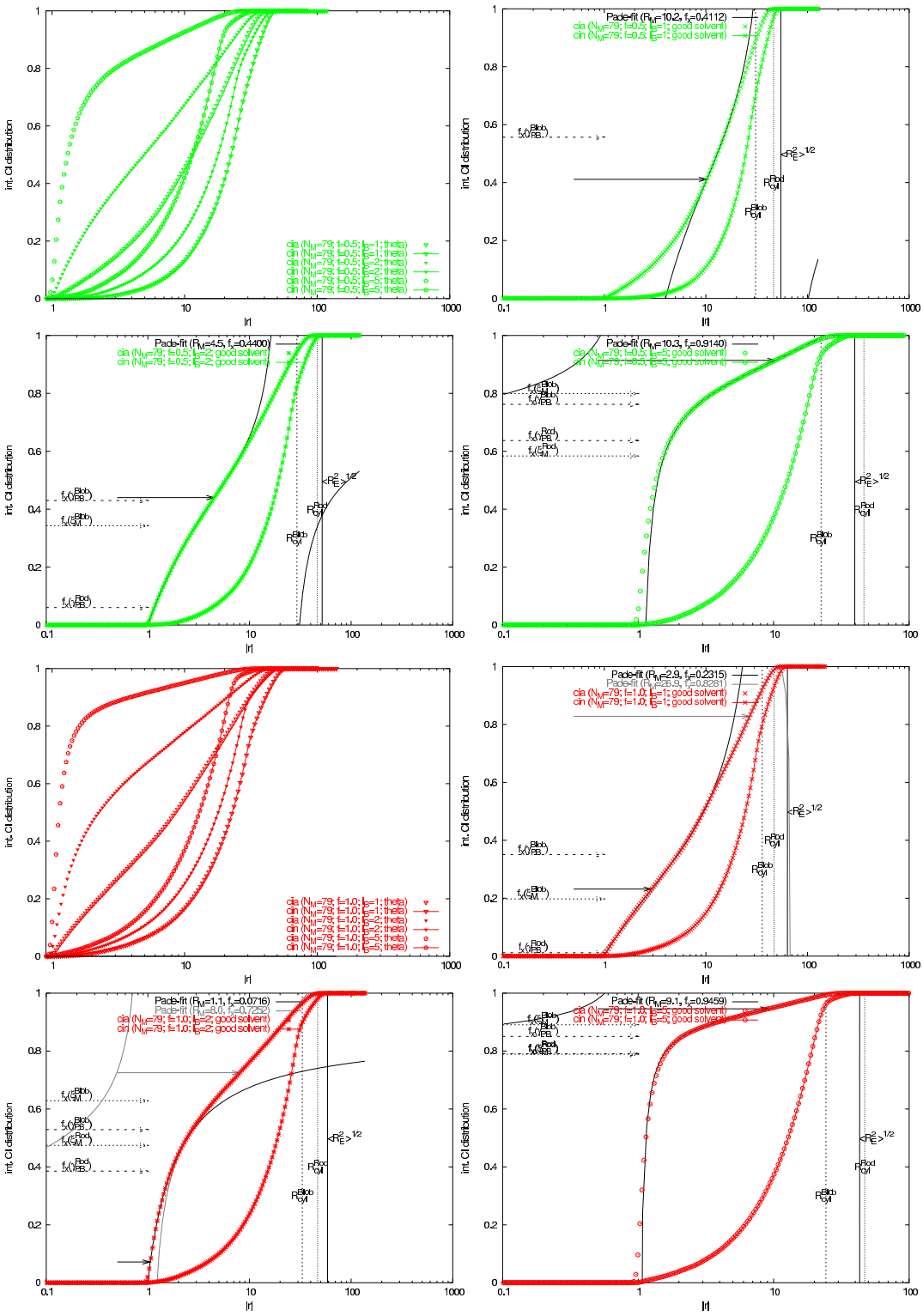

Figure B.6.: $N_\mathrm{m} \in \{79\}$, $f \in \{\frac{1}{2}, \frac{1}{1}\}$, $\ell_\mathrm{B} \in \{1\sigma, 2\sigma, 5\sigma\}$, in both solvents.

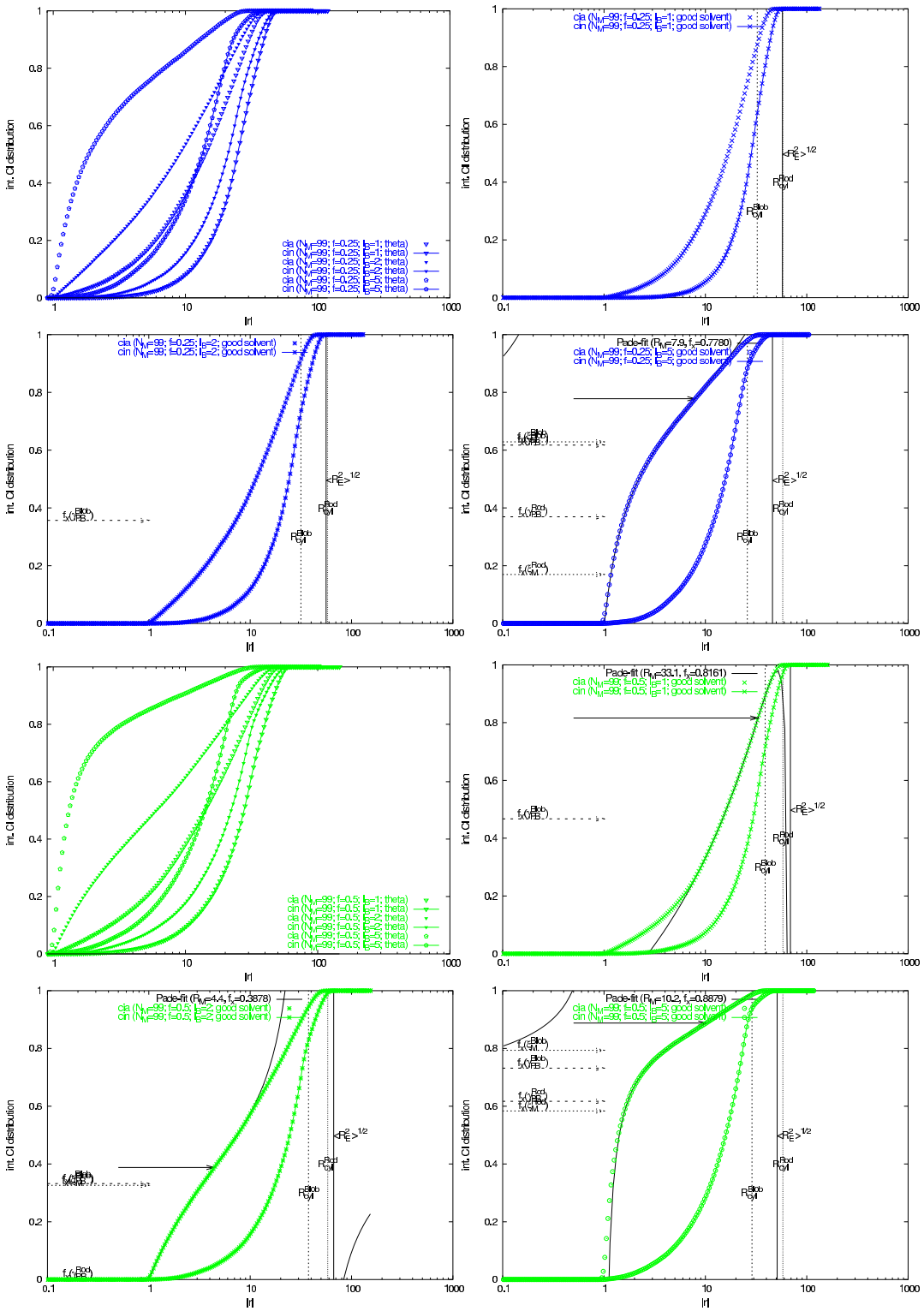

Figure B.7.: $N_\mathrm{m} \in \{99\}$, $f \in \{\frac{1}{4}, \frac{1}{2}\}$, $\ell_\mathrm{B} \in \{1\sigma, 2\sigma, 5\sigma\}$, in both solvents.

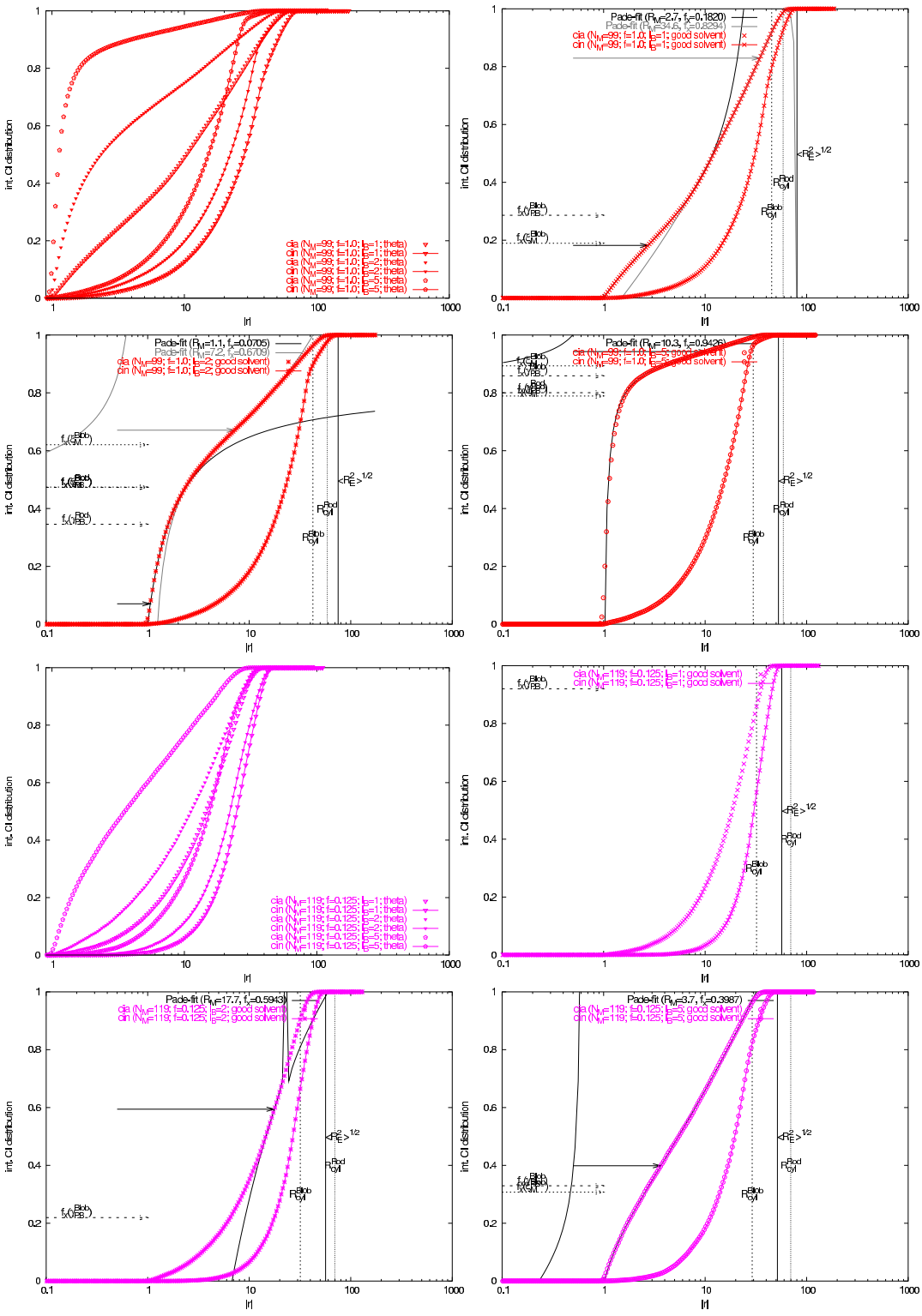

Figure B.8.: $N_{\mathrm{m}} \in \{99, 119\}$, $f \in \{\frac{1}{1}, \frac{1}{8}\}$, $\ell_{\mathrm{B}} \in \{1\sigma, 2\sigma, 5\sigma\}$, in both solvents.

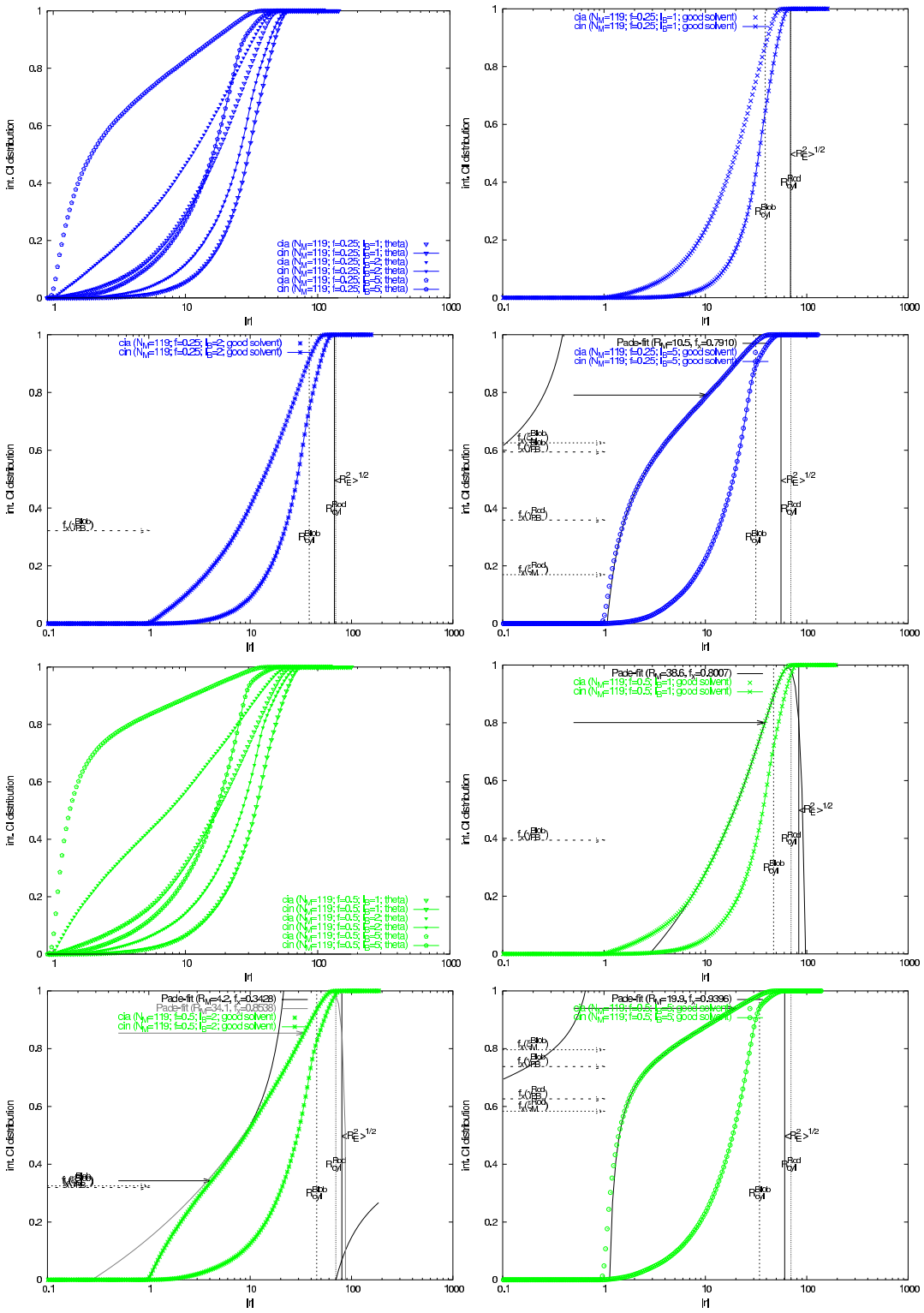

Figure B.9.: $N_\mathrm{m} \in \{119\}$, $f \in \{\frac{1}{4}, \frac{1}{2}\}$, $\ell_\mathrm{B} \in \{1\sigma, 2\sigma, 5\sigma\}$, in both solvents.

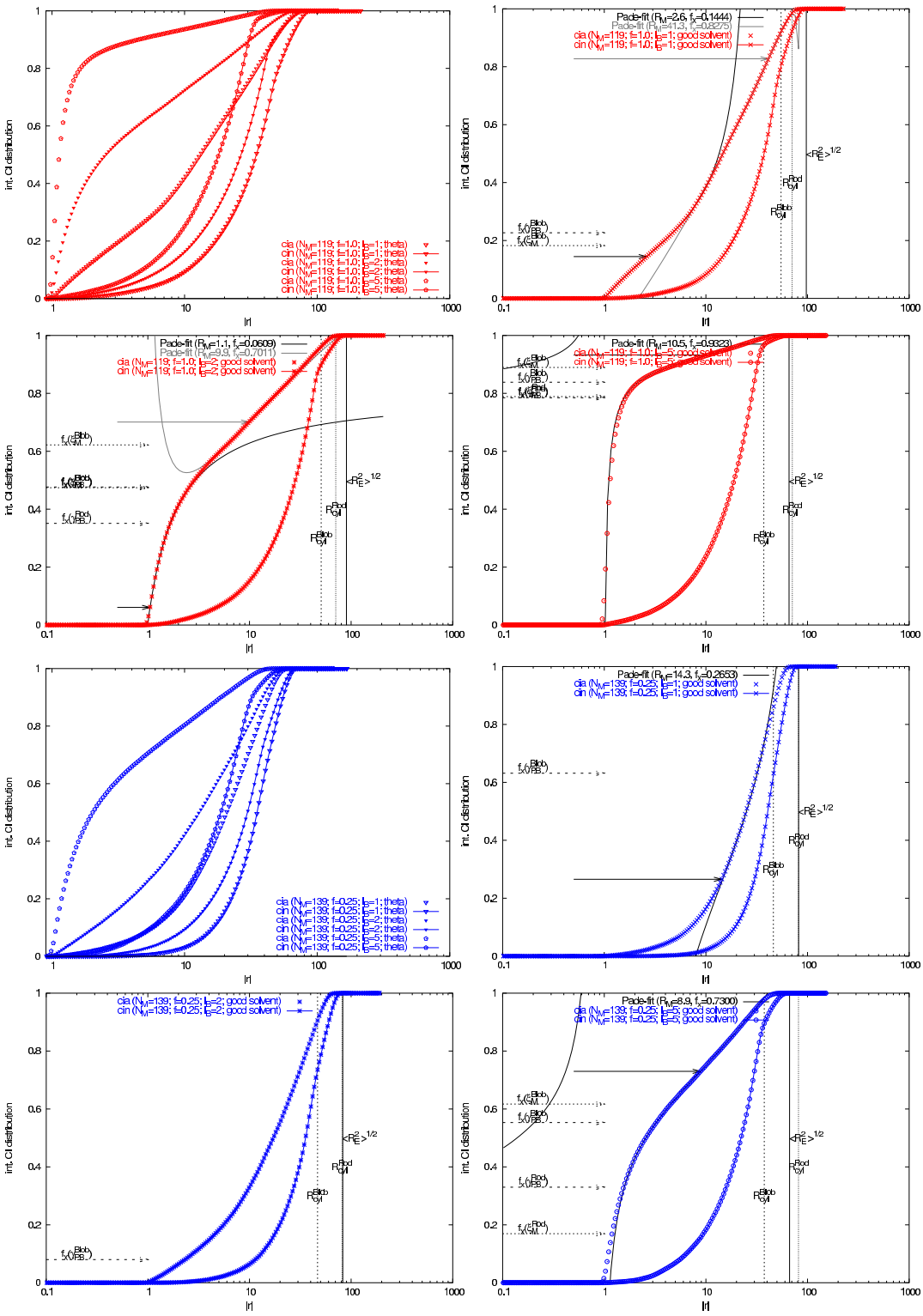

Figure B.10.: $N_\mathrm{m} \in \{119, 139\}$, $f \in \{\frac{1}{1}, \frac{1}{4}\}$, $\ell_\mathrm{B} \in \{1\sigma, 2\sigma, 5\sigma\}$, in both solvents.

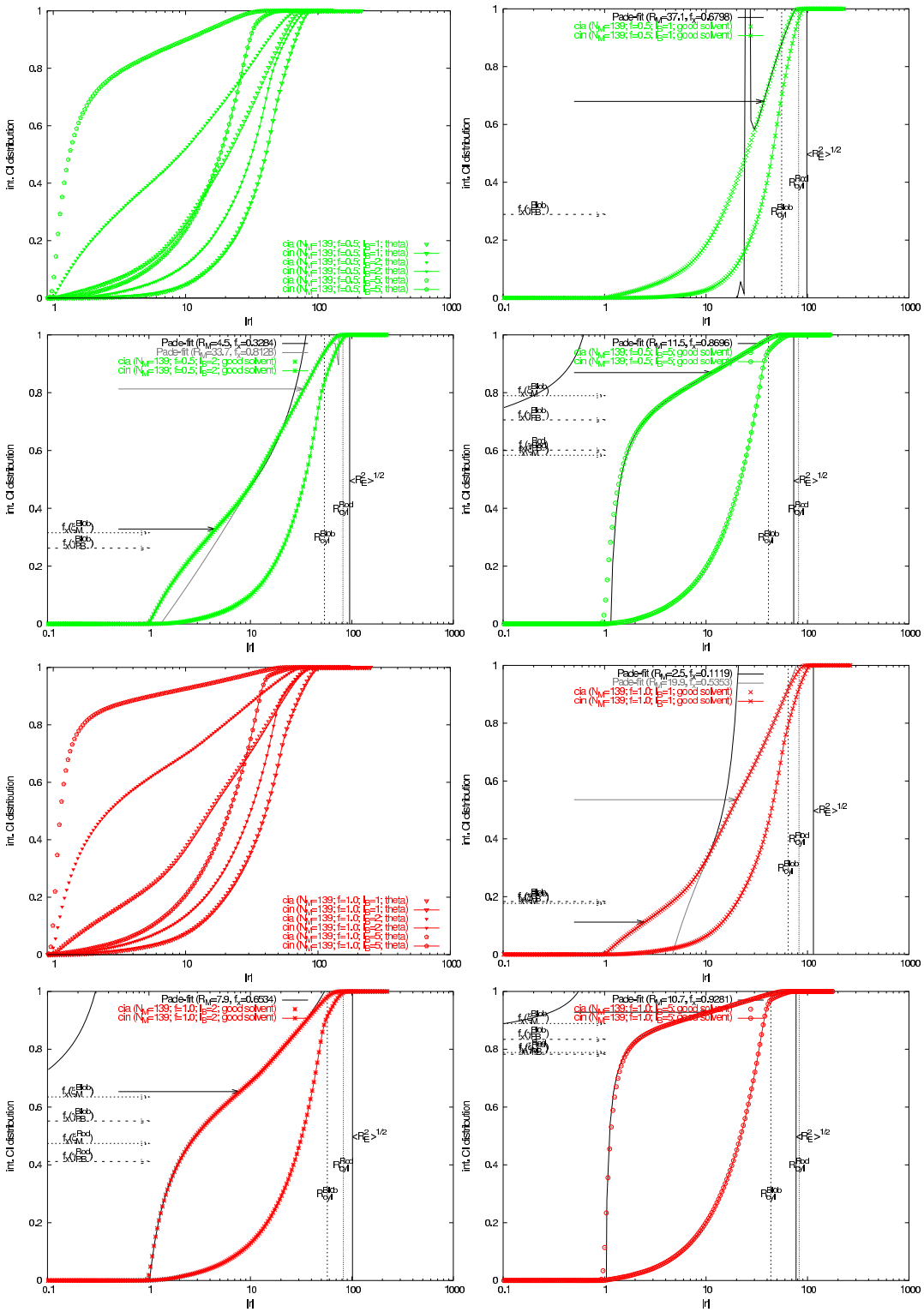

Figure B.11.: $N_\mathrm{m} \in \{139\}$, $f \in \{\frac{1}{2}, \frac{1}{1}\}$, $\ell_\mathrm{B} \in \{1\sigma, 2\sigma, 5\sigma\}$, in both solvents.

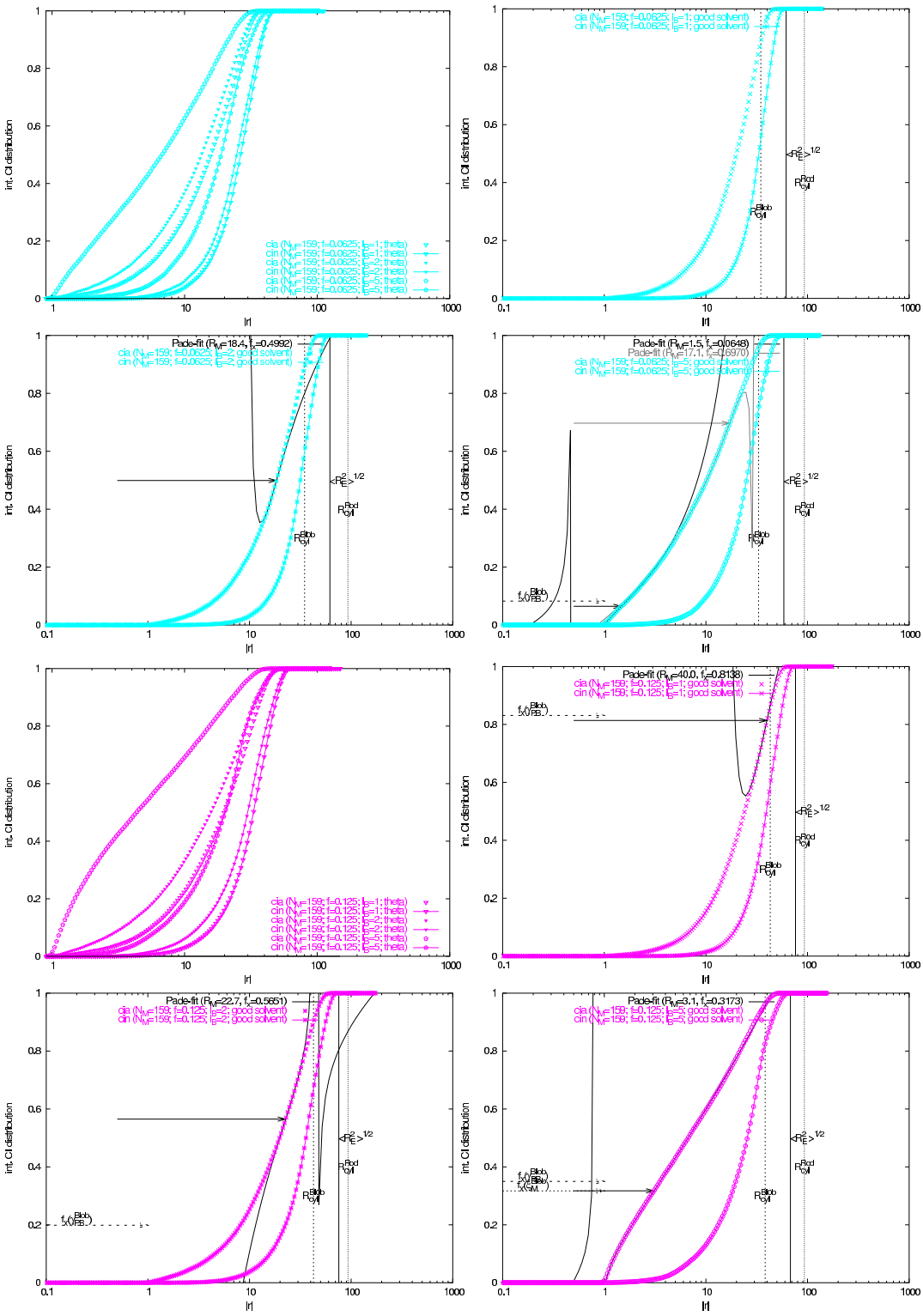

Figure B.12.: $N_\mathrm{m} \in \{159\}$, $f \in \{\frac{1}{16}, \frac{1}{8}\}$, $\ell_\mathrm{B} \in \{1\sigma, 2\sigma, 5\sigma\}$, in both solvents.

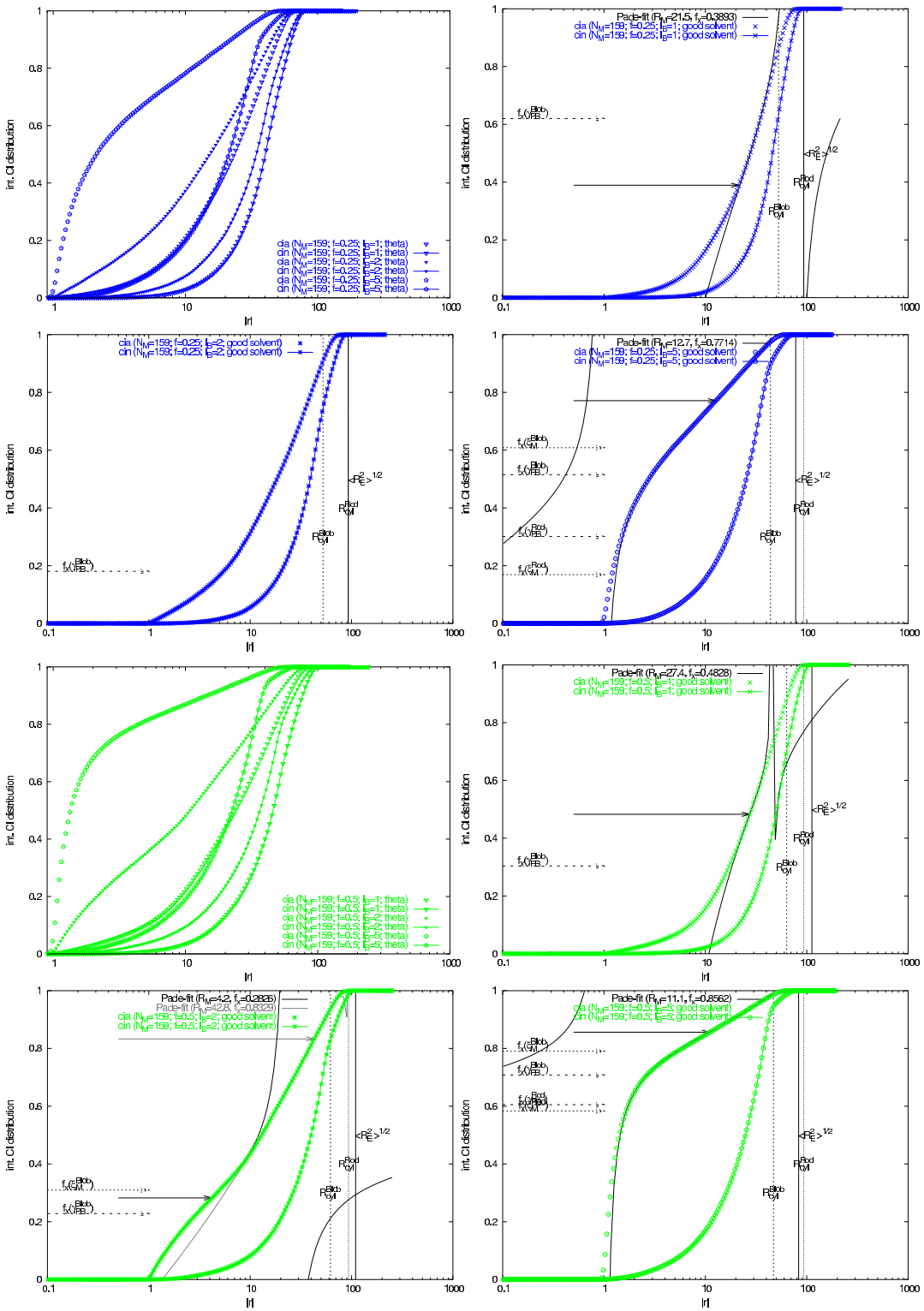

Figure B.13.: $N_{\mathrm{m}} \in \{159\}$, $f \in \{\frac{1}{4}, \frac{1}{2}\}$, $\ell_{\mathrm{B}} \in \{1\sigma, 2\sigma, 5\sigma\}$, in both solvents.

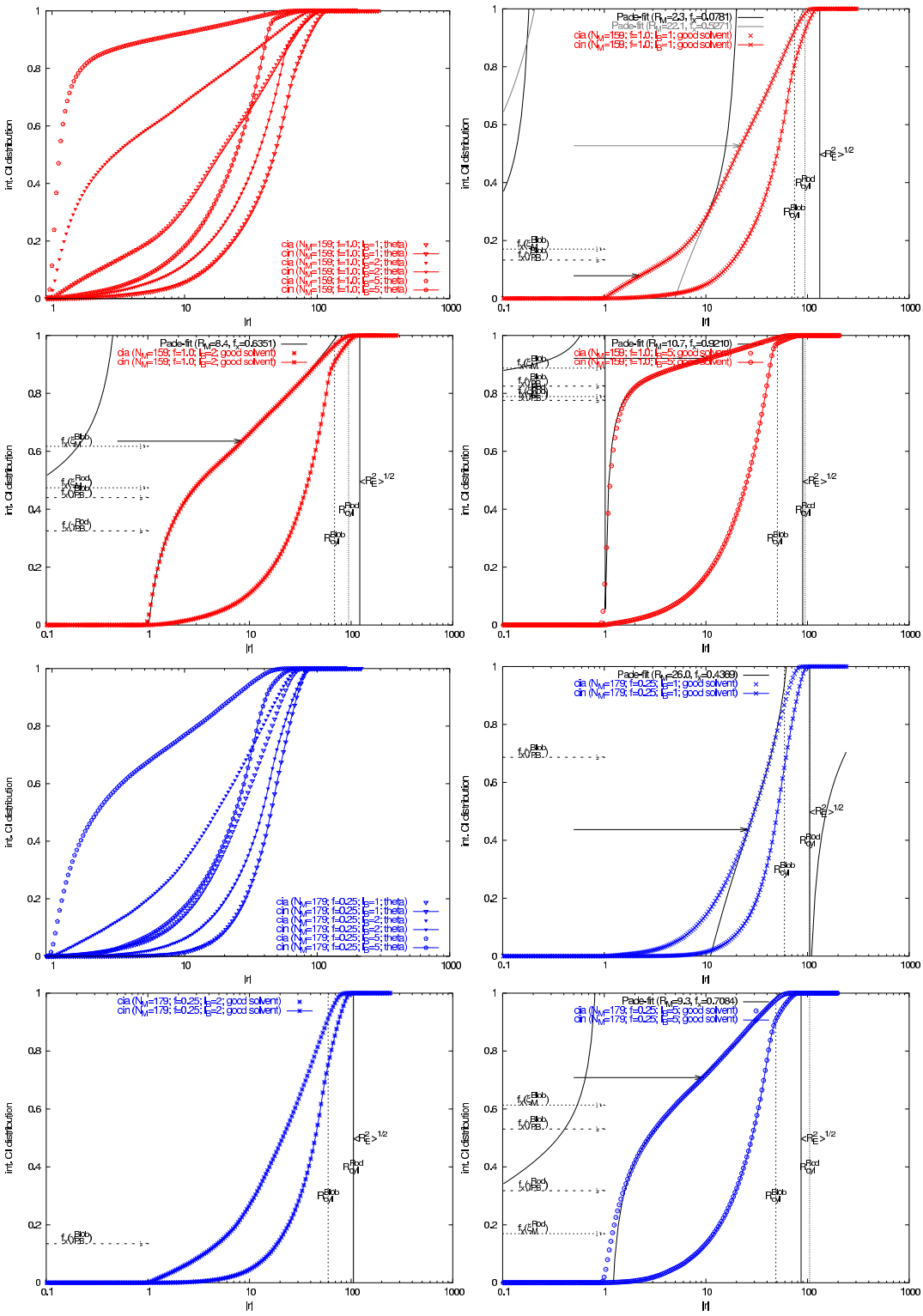

Figure B.14.: $N_\mathrm{m} \in \{159, 179\}$, $f \in \{\frac{1}{1}, \frac{1}{4}\}$, $\ell_\mathrm{B} \in \{1\sigma, 2\sigma, 5\sigma\}$, in both solvents.

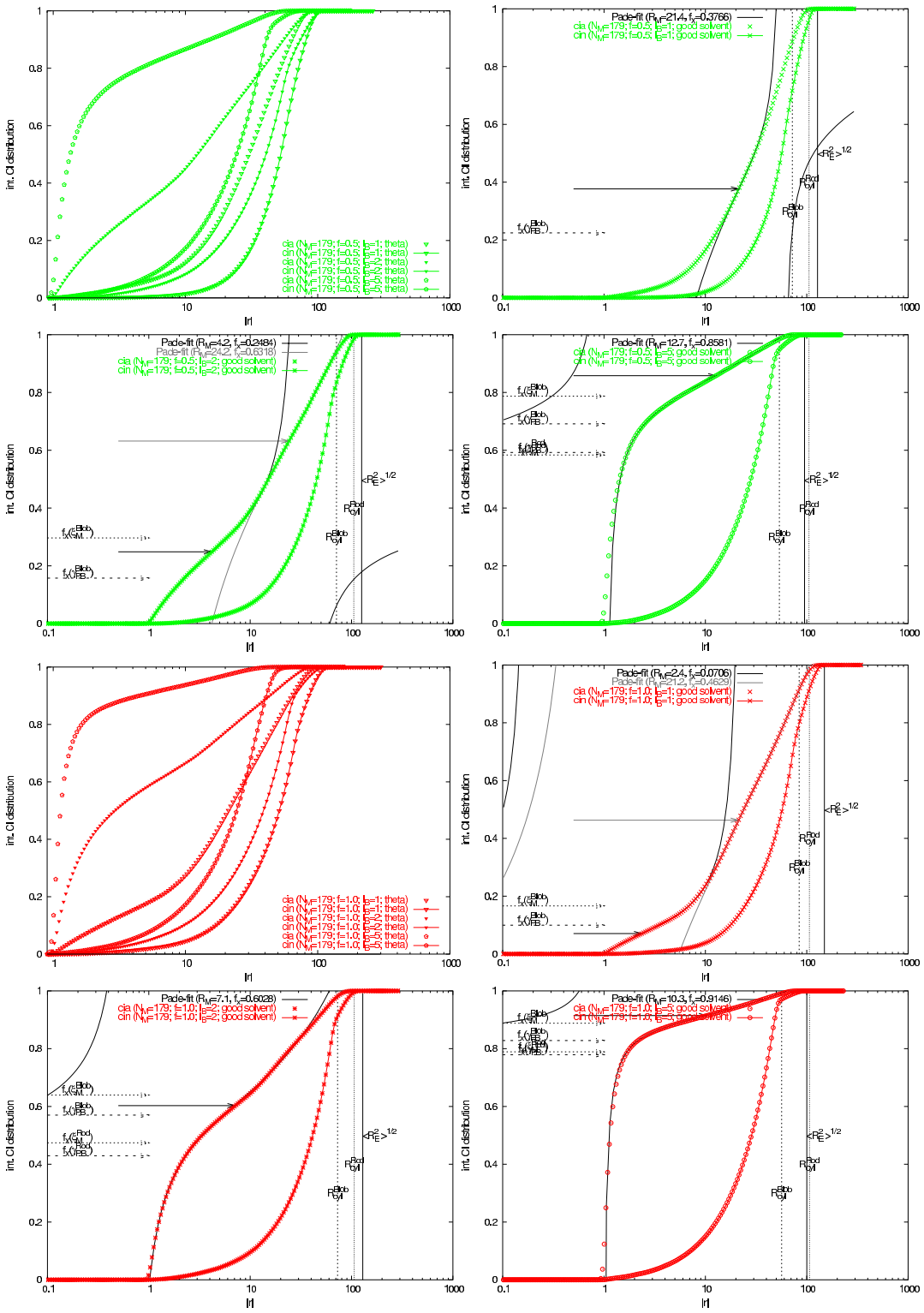

Figure B.15.: $N_{\mathrm{m}} \in \{179\}$, $f \in \{\frac{1}{2}, \frac{1}{1}\}$, $\ell_{\mathrm{B}} \in \{1\sigma, 2\sigma, 5\sigma\}$, in both solvents.

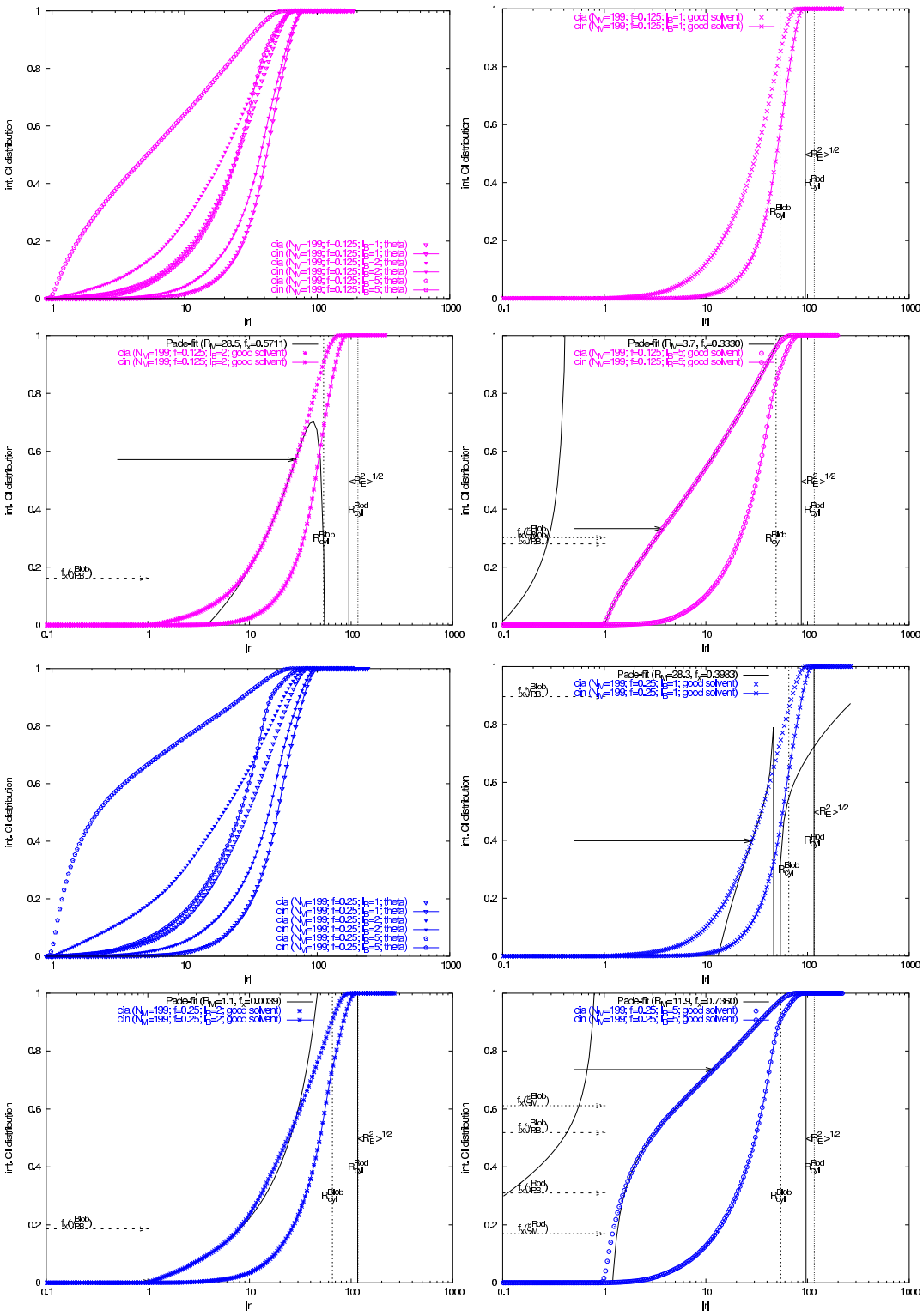

Figure B.16.: $N_{\mathrm{m}} \in \{199\}$, $f \in \{\frac{1}{8}, \frac{1}{4}\}$, $\ell_{\mathrm{B}} \in \{1\sigma, 2\sigma, 5\sigma\}$, in both solvents.

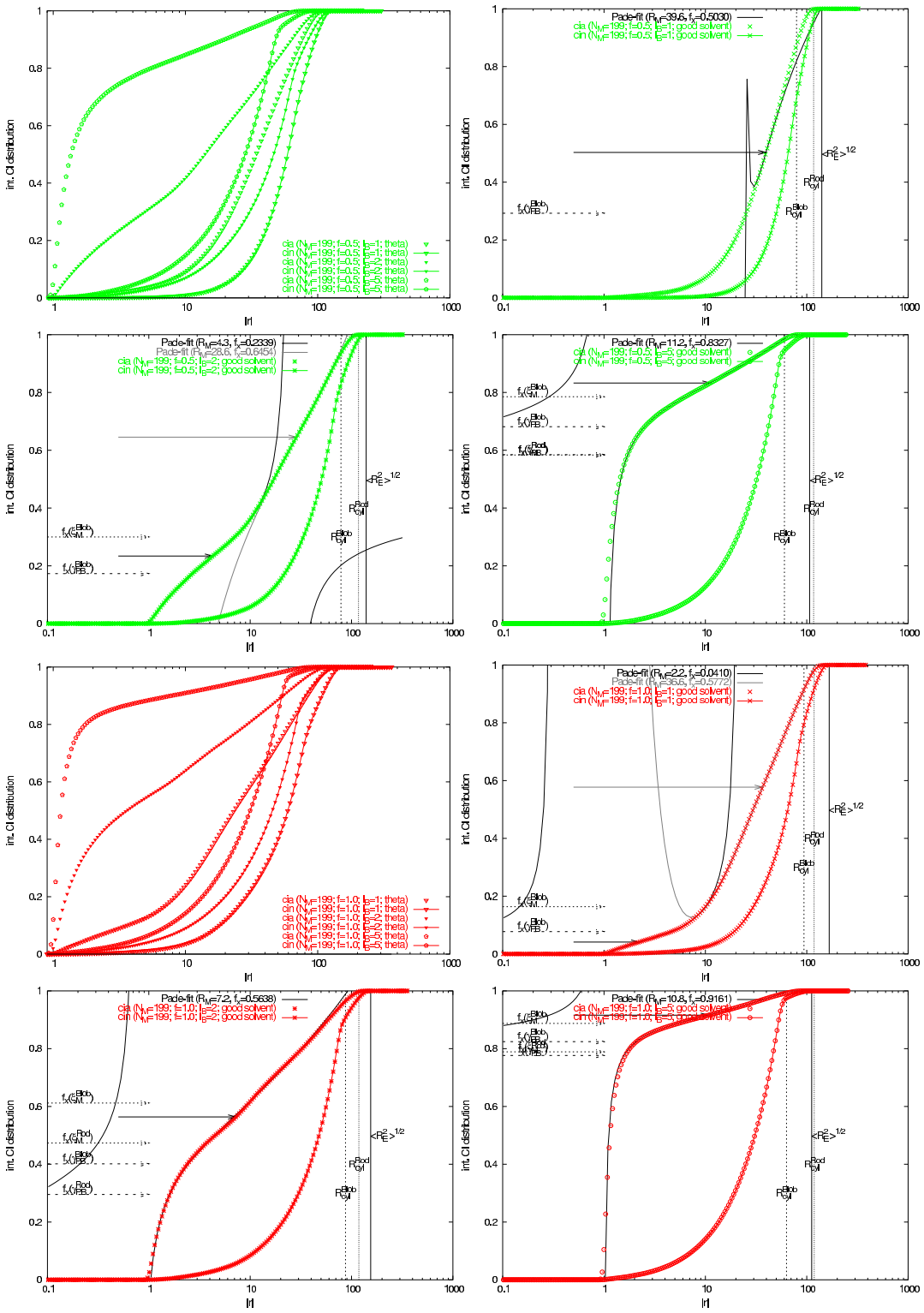

Figure B.17.: $N_\mathrm{m} \in \{199\}$, $f \in \{\frac{1}{2}, \frac{1}{1}\}$, $\ell_\mathrm{B} \in \{1\sigma, 2\sigma, 5\sigma\}$, in both solvents.

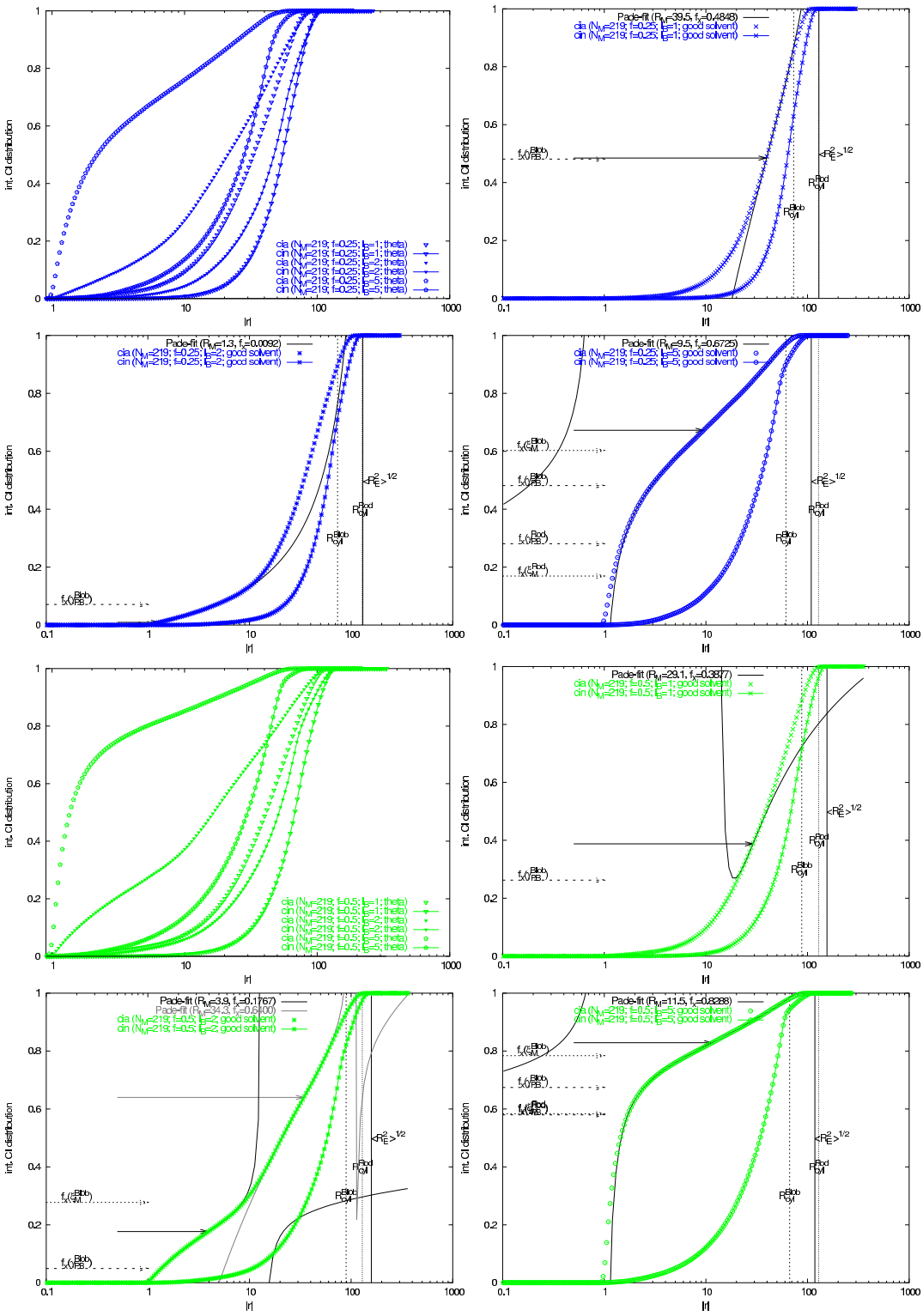

Figure B.18.: $N_{\mathrm{m}} \in \{219\}$, $f \in \{\frac{1}{4}, \frac{1}{2}\}$, $\ell_{\mathrm{B}} \in \{1\sigma, 2\sigma, 5\sigma\}$, in both solvents.

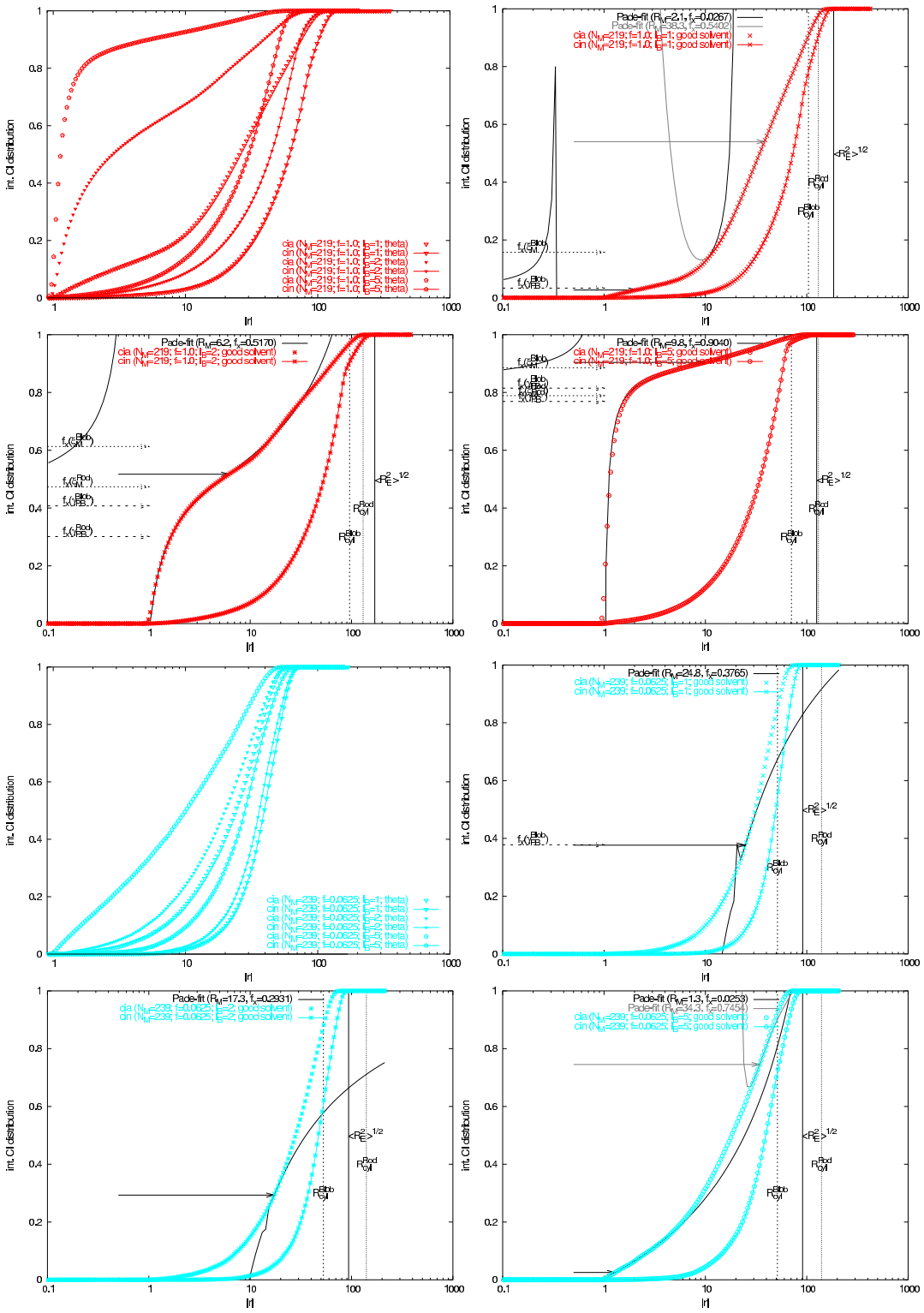

Figure B.19.: $N_\mathrm{m} \in \{219, 239\}$, $f \in \{\frac{1}{1}, \frac{1}{16}\}$, $\ell_\mathrm{B} \in \{1\sigma, 2\sigma, 5\sigma\}$, in both solvents.

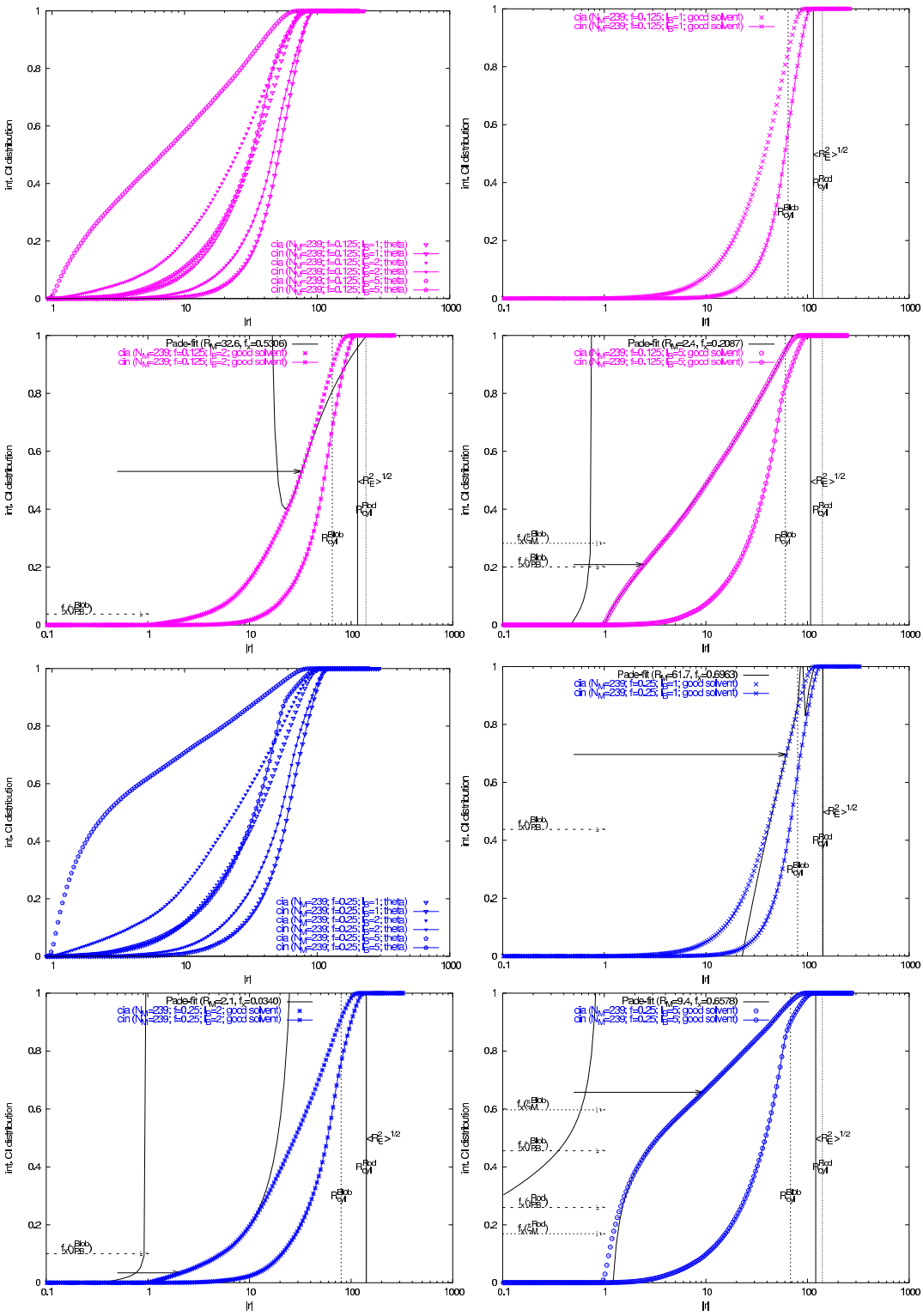

Figure B.20.: $N_{\mathrm{m}} \in \{239\}$, $f \in \{\frac{1}{8}, \frac{1}{4}\}$, $\ell_{\mathrm{B}} \in \{1\sigma, 2\sigma, 5\sigma\}$, in both solvents.

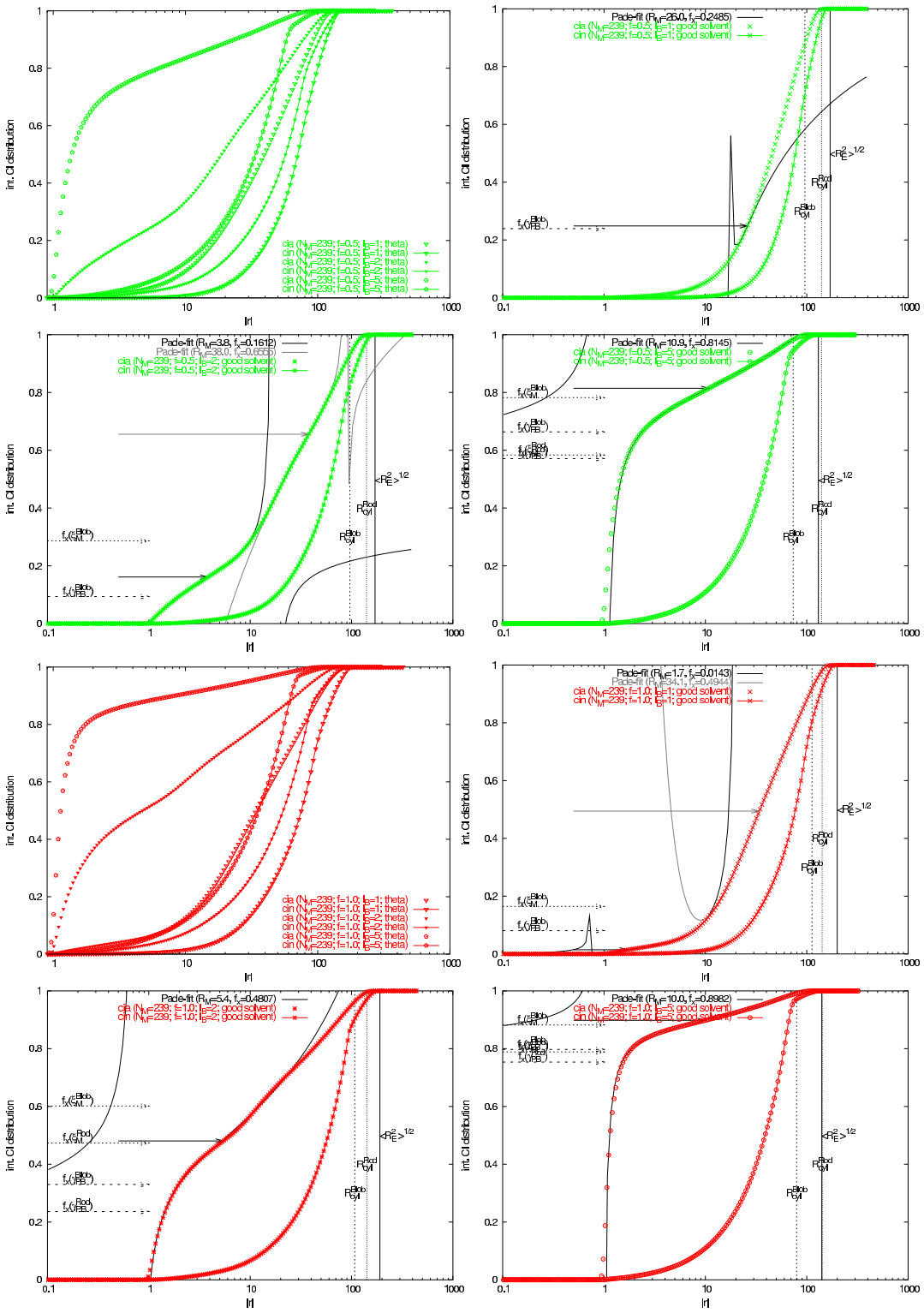

Figure B.21.: $N_\mathrm{m} \in \{239\}$, $f \in \{\frac{1}{2}, \frac{1}{1}\}$, $\ell_\mathrm{B} \in \{1\sigma, 2\sigma, 5\sigma\}$, in both solvents.

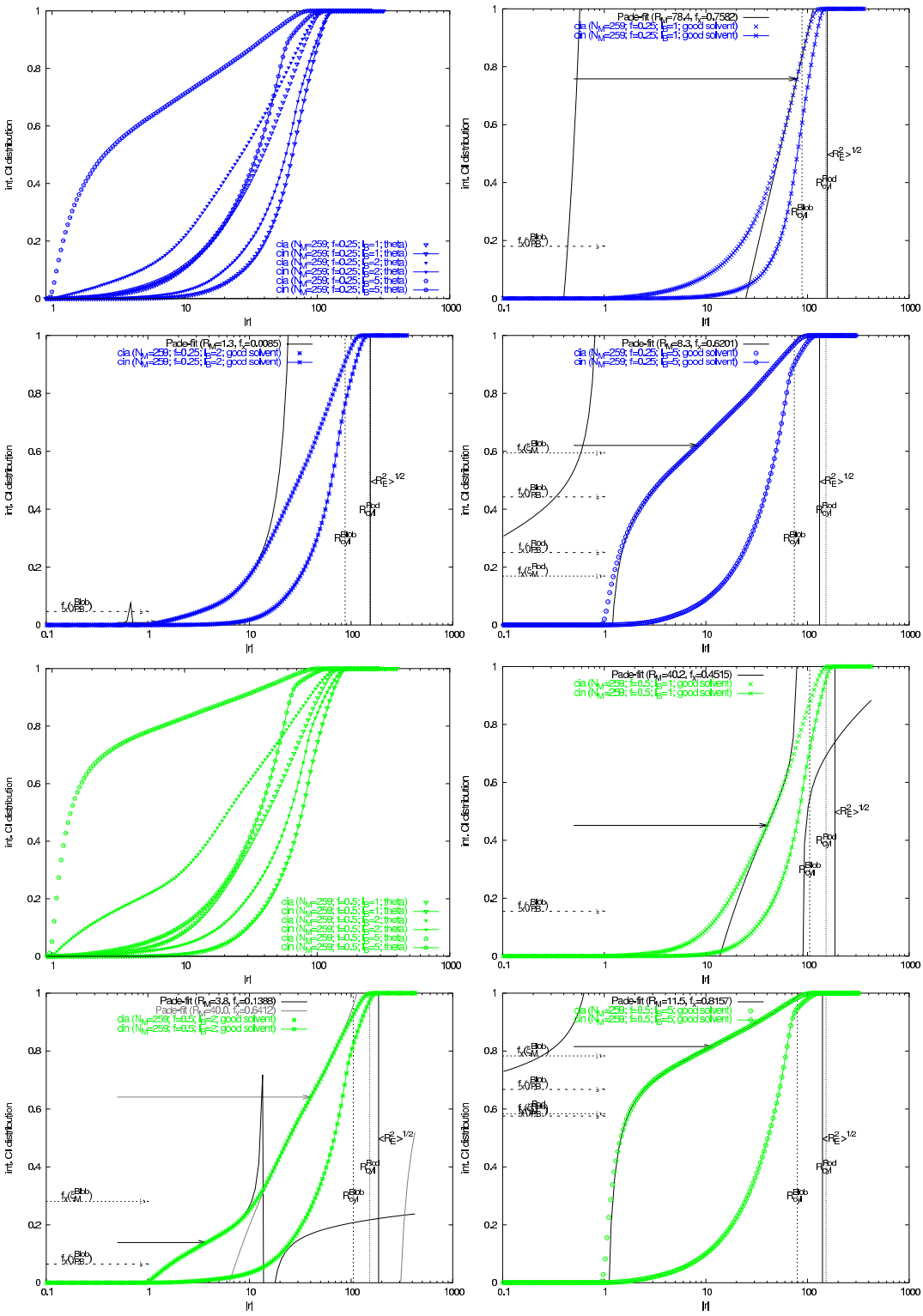

Figure B.22.: $N_{\mathrm{m}} \in \{259\}$, $f \in \{\frac{1}{4}, \frac{1}{2}\}$, $\ell_{\mathrm{B}} \in \{1\sigma, 2\sigma, 5\sigma\}$, in both solvents.

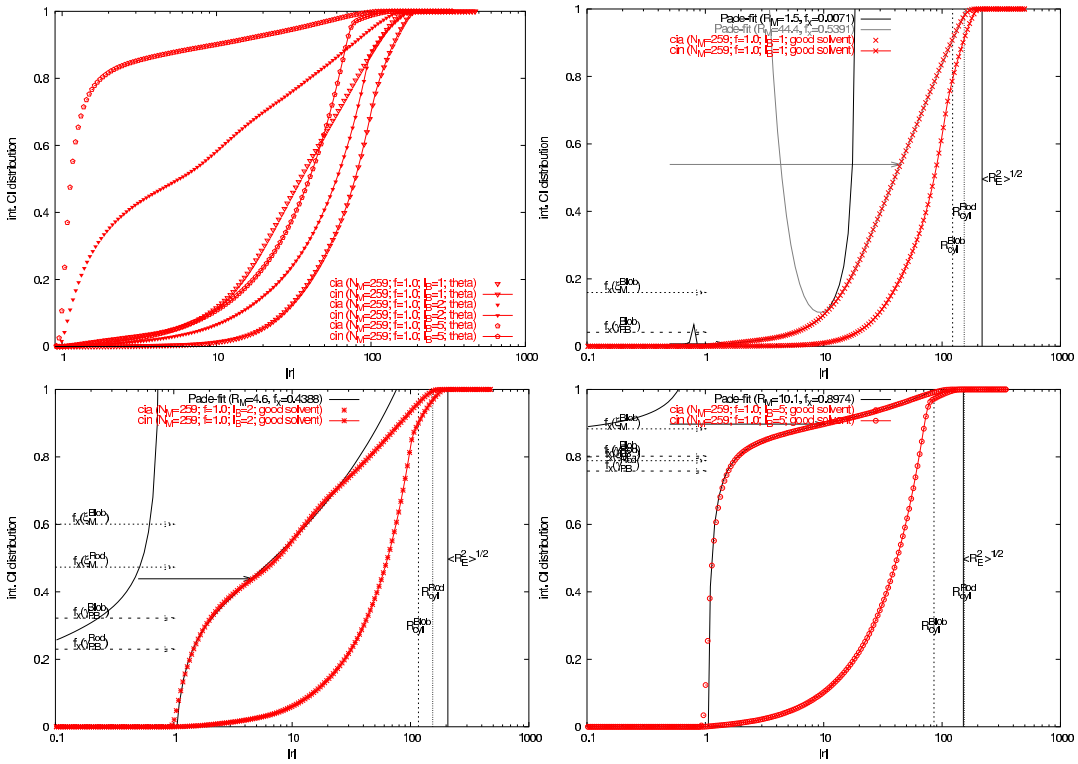

Figure B.23.: $N_\mathrm{m} \in \{259\}$, $f \in \{\frac{1}{1}\}$, $\ell_\mathrm{B} \in \{1\sigma, 2\sigma, 5\sigma\}$, in both solvents.

C. Snapshots of Poor Hydrogels

To illustrate the different regimes introduced in the phase diagram, this appendix displays simulation box snapshots of polyelectrolyte networks in a poor solvent environment close to their swelling equilibrium. As discussed in chapter 5, this will occur at different system densities, depending on the chosen charge fraction f (determining the amount of counterions $N_{\mathrm{CI}} = N_{\mathrm{nodes}} + N_{\mathrm{p}} \cdot [f(N_{\mathrm{m}}+1) - 1]$ around the N_{p} chains of length N_{m}, interconnected at N_{nodes} charged nodes) and the strength of the electrostatics as characterized through the Bjerrum length $\ell_{\mathrm{B}} = \frac{e_0^2}{4\pi\epsilon_0\epsilon_{\mathrm{S}}k_{\mathrm{B}}T}$ (which is $\ell_{\mathrm{B}} \approx 7.14\text{Å}$ in water at room temperature, and represents the distance two elementary charges e_0 will have when interacting with an electrostatic energy of $k_{\mathrm{B}}T$). Hence, in the following panels the indicated box frame usually sets a different length scale for different parameters; the relative sphere radius of monomers and counterions, however, remains the same in all pictures, and might therefore pose as a reference for comparisons.

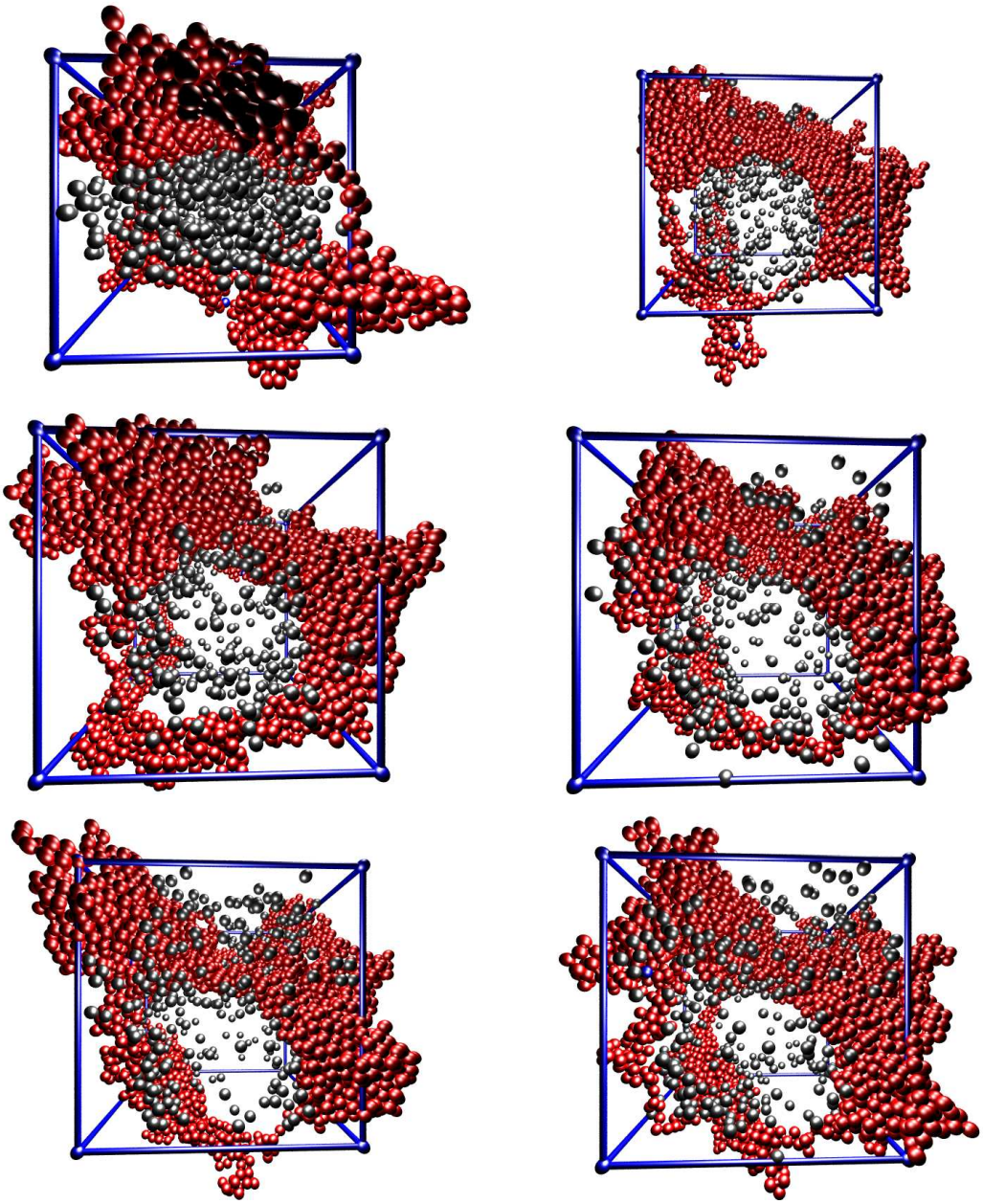

Figure C.1.: Simulation box snapshots for $N_\mathrm{m} = 199$, $f = 0.125$ ($\Rightarrow N_\mathrm{CI} = 392$, $N_\mathrm{tot} = 3584$) and $\ell_\mathrm{B} = 0\sigma$, $\rho = 0.56\sigma^{-3}$, $\rho_\mathrm{c} = 0.012\sigma^{-3}$ (*top left*), $\ell_\mathrm{B} = 0.125\sigma$, $\rho = 0.28\sigma^{-3}$, $\rho_\mathrm{c} = 0.062\sigma^{-3}$ (*top right*), $\ell_\mathrm{B} = 0.25\sigma$, $\rho = 0.28\sigma^{-3}$, $\rho_\mathrm{c} = 0.062\sigma^{-3}$ (*center left*), $\ell_\mathrm{B} = 0.5\sigma$, $\rho = 0.28\sigma^{-3}$, $\rho_\mathrm{c} = 0.062\sigma^{-3}$ (*center right*), $\ell_\mathrm{B} = 0.75\sigma$, $\rho = 0.28\sigma^{-3}$, $\rho_\mathrm{c} = 0.062\sigma^{-3}$ (*bottom left*), $\ell_\mathrm{B} = 1.0\sigma$, $\rho = 0.28\sigma^{-3}$, $\rho_\mathrm{c} = 0.062\sigma^{-3}$ (*bottom right*), in a poor solvent environment with $\epsilon_\mathrm{LJ} = 1.75\sigma$ and $r_c = 2.5\sigma$ as LJ-parameters.

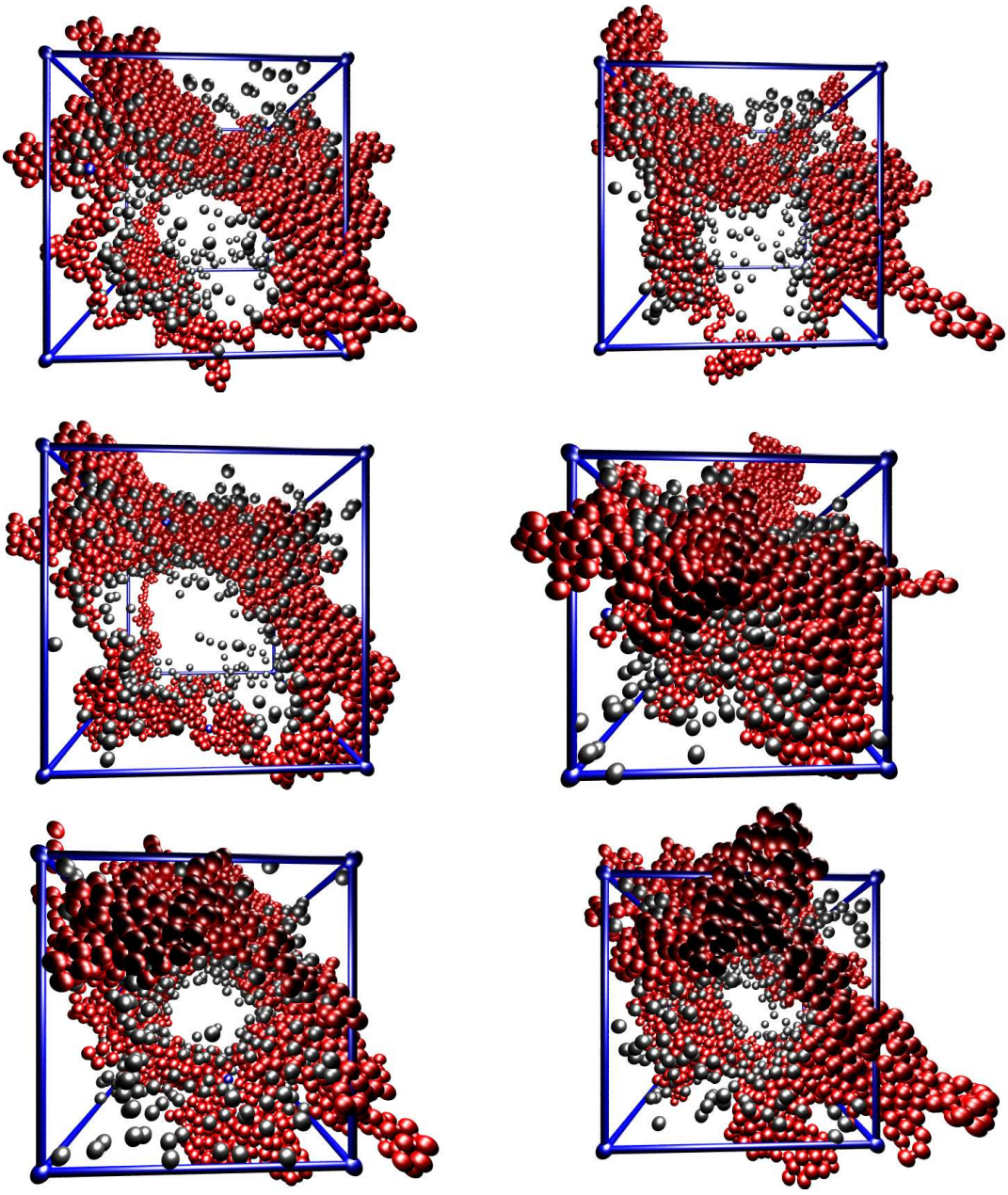

Figure C.2.: Simulation box snapshots for $N_{\mathrm{m}} = 199$, $f = 0.125$ ($\Rightarrow N_{\mathrm{CI}} = 392$, $N_{\mathrm{tot}} = 3584$) and $\ell_{\mathrm{B}} = 1.0\sigma$, $\rho = 0.28\sigma^{-3}$, $\rho_{\mathrm{c}} = 0.062\sigma^{-3}$ (*top left*), $\ell_{\mathrm{B}} = 1.5\sigma$, $\rho = 0.28\sigma^{-3}$, $\rho_{\mathrm{c}} = 0.062\sigma^{-3}$ (*top right*), $\ell_{\mathrm{B}} = 2.0\sigma$, $\rho = 0.28\sigma^{-3}$, $\rho_{\mathrm{c}} = 0.062\sigma^{-3}$ (*center left*), $\ell_{\mathrm{B}} = 3.0\sigma$, $\rho = 0.56\sigma^{-3}$, $\rho_{\mathrm{c}} = 0.012\sigma^{-3}$ (*center right*), $\ell_{\mathrm{B}} = 5.0\sigma$, $\rho = 0.56\sigma^{-3}$, $\rho_{\mathrm{c}} = 0.012\sigma^{-3}$ (*bottom left*), $\ell_{\mathrm{B}} = 6.0\sigma$, $\rho = 0.56\sigma^{-3}$, $\rho_{\mathrm{c}} = 0.012\sigma^{-3}$ (*bottom right*), in a poor solvent environment with $\epsilon_{\mathrm{LJ}} = 1.75\sigma$ and $r_c = 2.5\sigma$ as LJ-parameters.

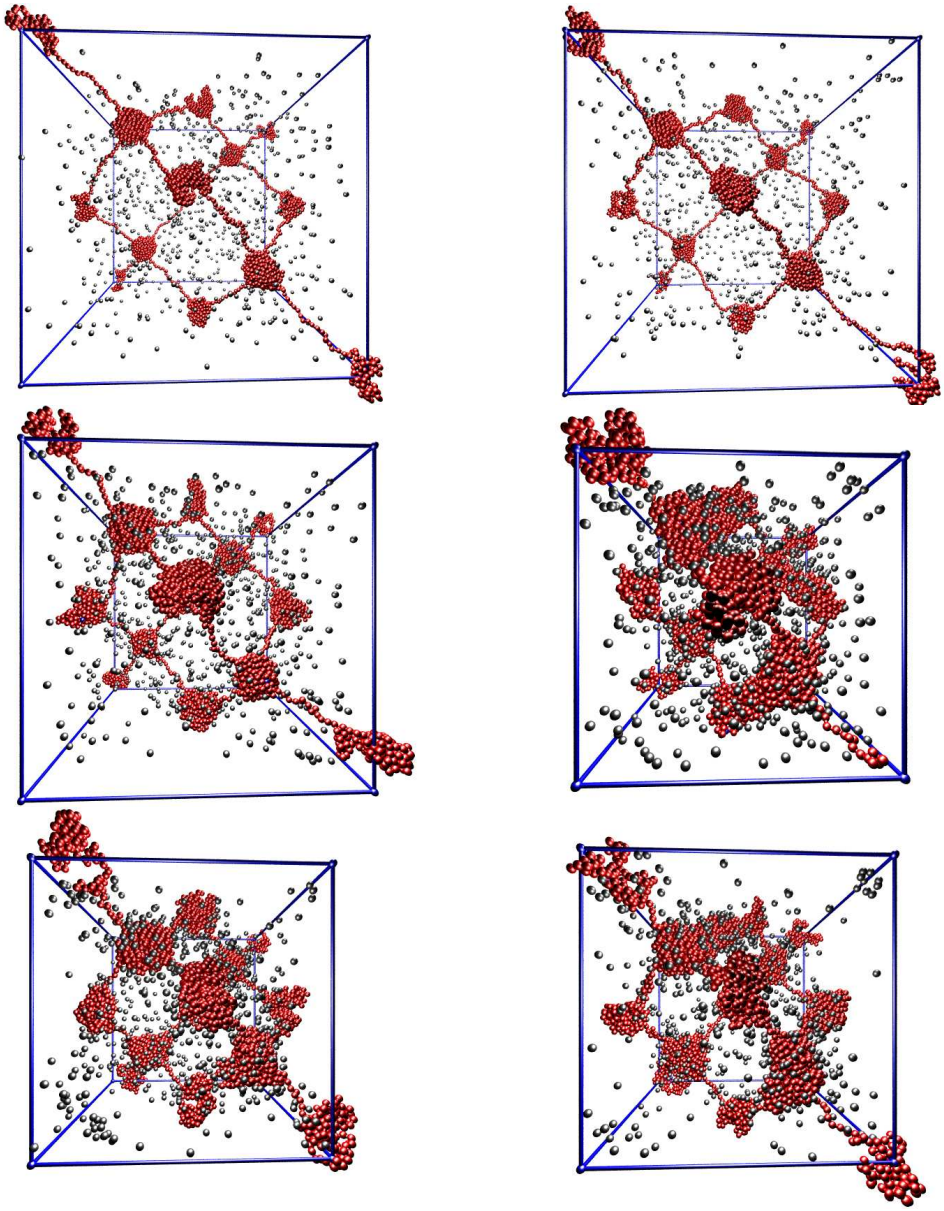

Figure C.3.: Simulation box snapshots for $N_{\mathrm{m}} = 199$, $f = 0.25$ ($\Rightarrow N_{\mathrm{CI}} = 792$, $N_{\mathrm{tot}} = 3984$) and $\ell_{\mathrm{B}} = 0\sigma$, $\rho = 0.013\sigma^{-3}$, $\rho_{\mathrm{c}} = 0.0050\sigma^{-3}$ (*top left*), $\ell_{\mathrm{B}} = 0.125\sigma$, $\rho = 0.013\sigma^{-3}$, $\rho_{\mathrm{c}} = 0.0050\sigma^{-3}$ (*top right*), $\ell_{\mathrm{B}} = 0.25\sigma$, $\rho = 0.031\sigma^{-3}$, $\rho_{\mathrm{c}} = 0.012\sigma^{-3}$ (*center left*), $\ell_{\mathrm{B}} = 0.5\sigma$, $\rho = 0.093\sigma^{-3}$, $\rho_{\mathrm{c}} = 0.037\sigma^{-3}$ (*center right*), $\ell_{\mathrm{B}} = 0.75\sigma$, $\rho = 0.063\sigma^{-3}$, $\rho_{\mathrm{c}} = 0.025\sigma^{-3}$ (*bottom left*), $\ell_{\mathrm{B}} = 1.0\sigma$, $\rho = 0.063\sigma^{-3}$, $\rho_{\mathrm{c}} = 0.025\sigma^{-3}$ (*bottom right*), in a poor solvent environment with $\epsilon_{\mathrm{LJ}} = 1.75\sigma$ and $r_c = 2.5\sigma$ as LJ-parameters.

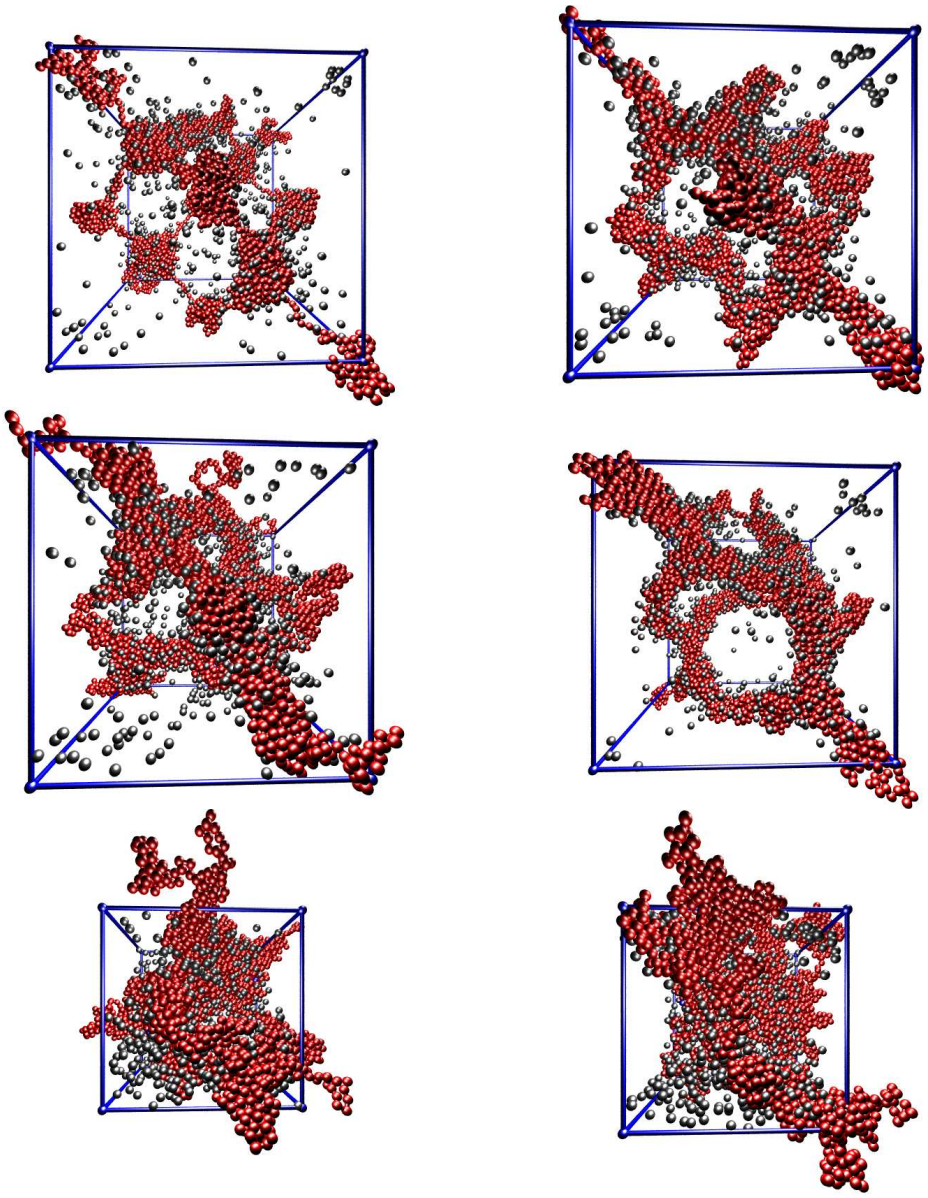

Figure C.4.: Simulation box snapshots for $N_\mathrm{m} = 199$, $f = 0.25$ ($\Rightarrow N_\mathrm{CI} = 792$, $N_\mathrm{tot} = 3984$) and $\ell_\mathrm{B} = 1.0\sigma$, $\rho = 0.063\sigma^{-3}$, $\rho_\mathrm{c} = 0.025\sigma^{-3}$ (*top left*), $\ell_\mathrm{B} = 1.5\sigma$, $\rho = 0.13\sigma^{-3}$, $\rho_\mathrm{c} = 0.050\sigma^{-3}$ (*top right*), $\ell_\mathrm{B} = 2.0\sigma$, $\rho = 0.13\sigma^{-3}$, $\rho_\mathrm{c} = 0.050\sigma^{-3}$ (*center left*), $\ell_\mathrm{B} = 3.0\sigma$, $\rho = 0.094\sigma^{-3}$, $\rho_\mathrm{c} = 0.037\sigma^{-3}$ (*center right*), $\ell_\mathrm{B} = 5.0\sigma$, $\rho = 0.31\sigma^{-3}$, $\rho_\mathrm{c} = 0.12\sigma^{-3}$ (*bottom left*), $\ell_\mathrm{B} = 6.0\sigma$, $\rho = 0.31\sigma^{-3}$, $\rho_\mathrm{c} = 0.12\sigma^{-3}$ (*bottom right*), in a poor solvent environment with $\epsilon_\mathrm{LJ} = 1.75\sigma$ and $r_c = 2.5\sigma$ as LJ-parameters.

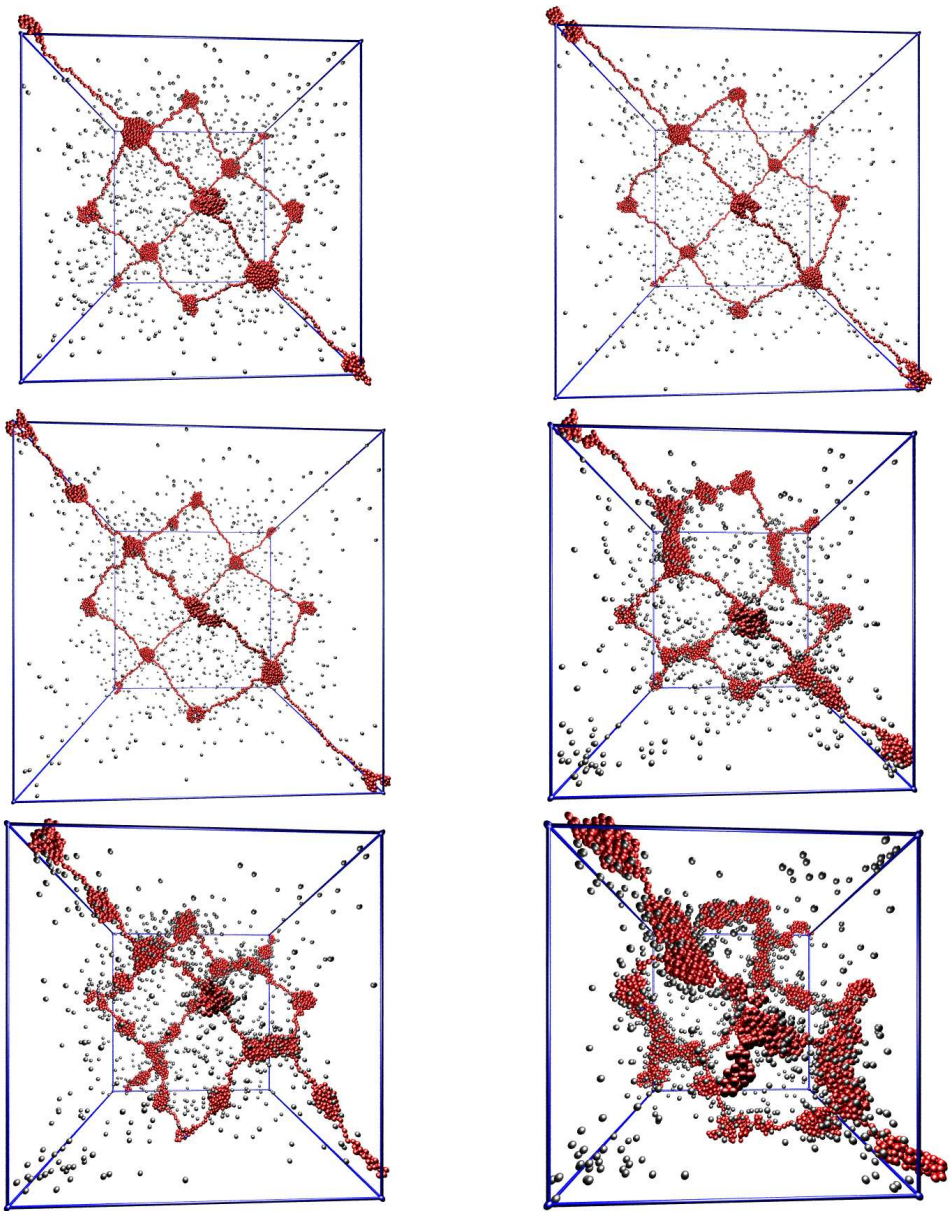

Figure C.5.: Simulation box snapshots for $N_\mathrm{m} = 200$, $f = 0.3333$ ($\Rightarrow N_\mathrm{CI} = 1064$, $N_\mathrm{tot} = 4272$) and $\ell_\mathrm{B} = 0\sigma$, $\rho = 0.0067\sigma^{-3}$, $\rho_\mathrm{c} = 0.0033\sigma^{-3}$ (*top left*), $\ell_\mathrm{B} = 0.125\sigma$, $\rho = 0.0033\sigma^{-3}$, $\rho_\mathrm{c} = 0.0017\sigma^{-3}$ (*top right*), $\ell_\mathrm{B} = 0.25\sigma$, $\rho = 0.0033\sigma^{-3}$, $\rho_\mathrm{c} = 0.0017\sigma^{-3}$ (*center left*), $\ell_\mathrm{B} = 0.5\sigma$, $\rho = 0.013\sigma^{-3}$, $\rho_\mathrm{c} = 0.0066\sigma^{-3}$ (*center right*), $\ell_\mathrm{B} = 0.75\sigma$, $\rho = 0.013\sigma^{-3}$, $\rho_\mathrm{c} = 0.0066\sigma^{-3}$ (*bottom left*), $\ell_\mathrm{B} = 1.0\sigma$, $\rho = 0.033\sigma^{-3}$, $\rho_\mathrm{c} = 0.017\sigma^{-3}$ (*bottom right*), in a poor solvent environment with $\epsilon_\mathrm{LJ} = 1.75\sigma$ and $r_\mathrm{c} = 2.5\sigma$ as LJ-parameters.

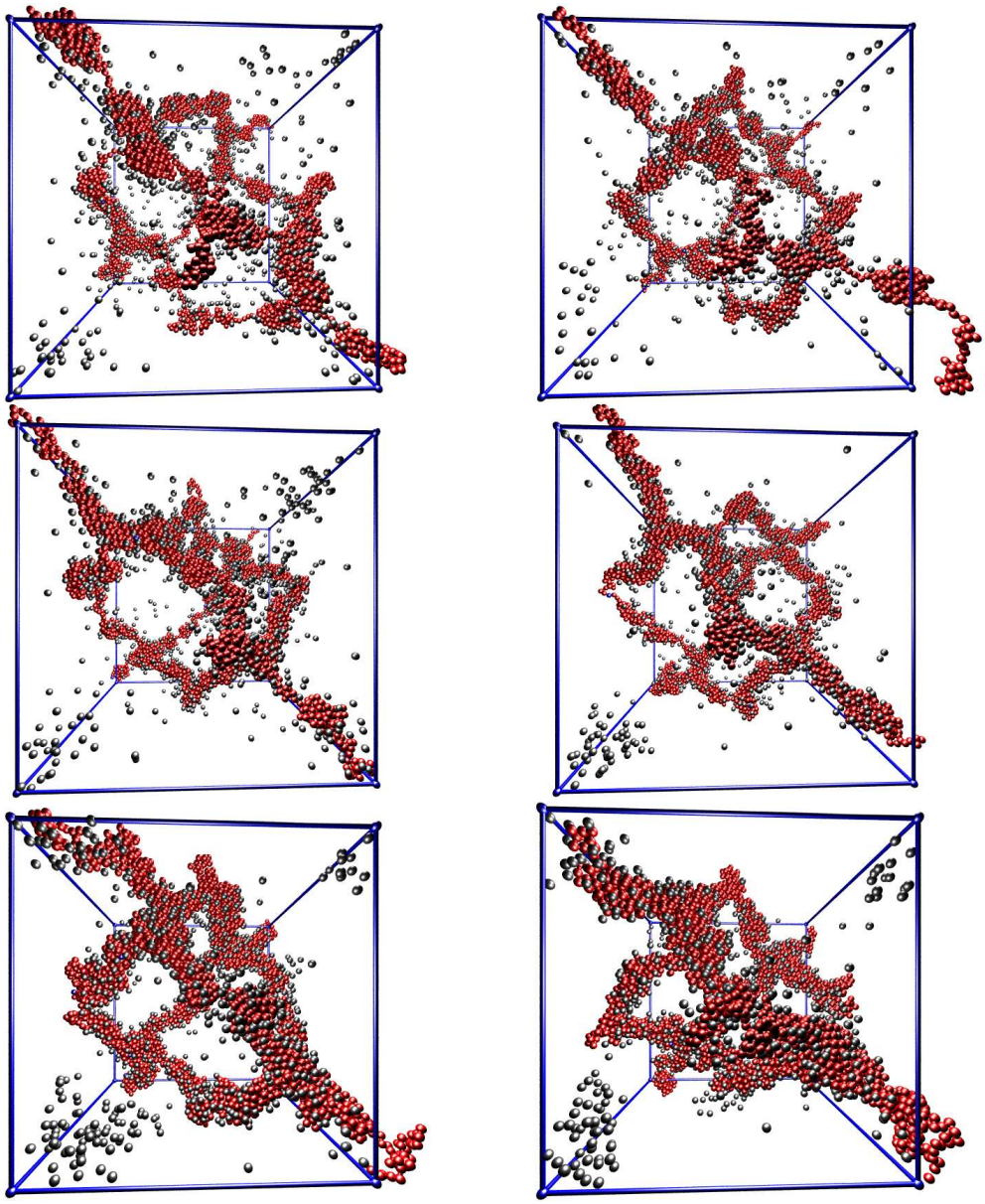

Figure C.6.: Simulation box snapshots for $N_\mathrm{m} = 200$, $f = 0.3333$ ($\Rightarrow N_\mathrm{CI} = 1064$, $N_\mathrm{tot} = 4272$) and $\ell_\mathrm{B} = 1.0\sigma$, $\rho = 0.033\sigma^{-3}$, $\rho_\mathrm{c} = 0.017\sigma^{-3}$ (*top left*), $\ell_\mathrm{B} = 1.5\sigma$, $\rho = 0.033\sigma^{-3}$, $\rho_\mathrm{c} = 0.017\sigma^{-3}$ (*top right*), $\ell_\mathrm{B} = 2.0\sigma$, $\rho = 0.033\sigma^{-3}$, $\rho_\mathrm{c} = 0.017\sigma^{-3}$ (*center left*), $\ell_\mathrm{B} = 3.0\sigma$, $\rho = 0.033\sigma^{-3}$, $\rho_\mathrm{c} = 0.017\sigma^{-3}$ (*center right*), $\ell_\mathrm{B} = 5.0\sigma$, $\rho = 0.066\sigma^{-3}$, $\rho_\mathrm{c} = 0.033\sigma^{-3}$ (*bottom left*), $\ell_\mathrm{B} = 6.0\sigma$, $\rho = 0.066\sigma^{-3}$, $\rho_\mathrm{c} = 0.033\sigma^{-3}$ (*bottom right*), in a poor solvent environment with $\epsilon_\mathrm{LJ} = 1.75\sigma$ and $r_c = 2.5\sigma$ as LJ-parameters.

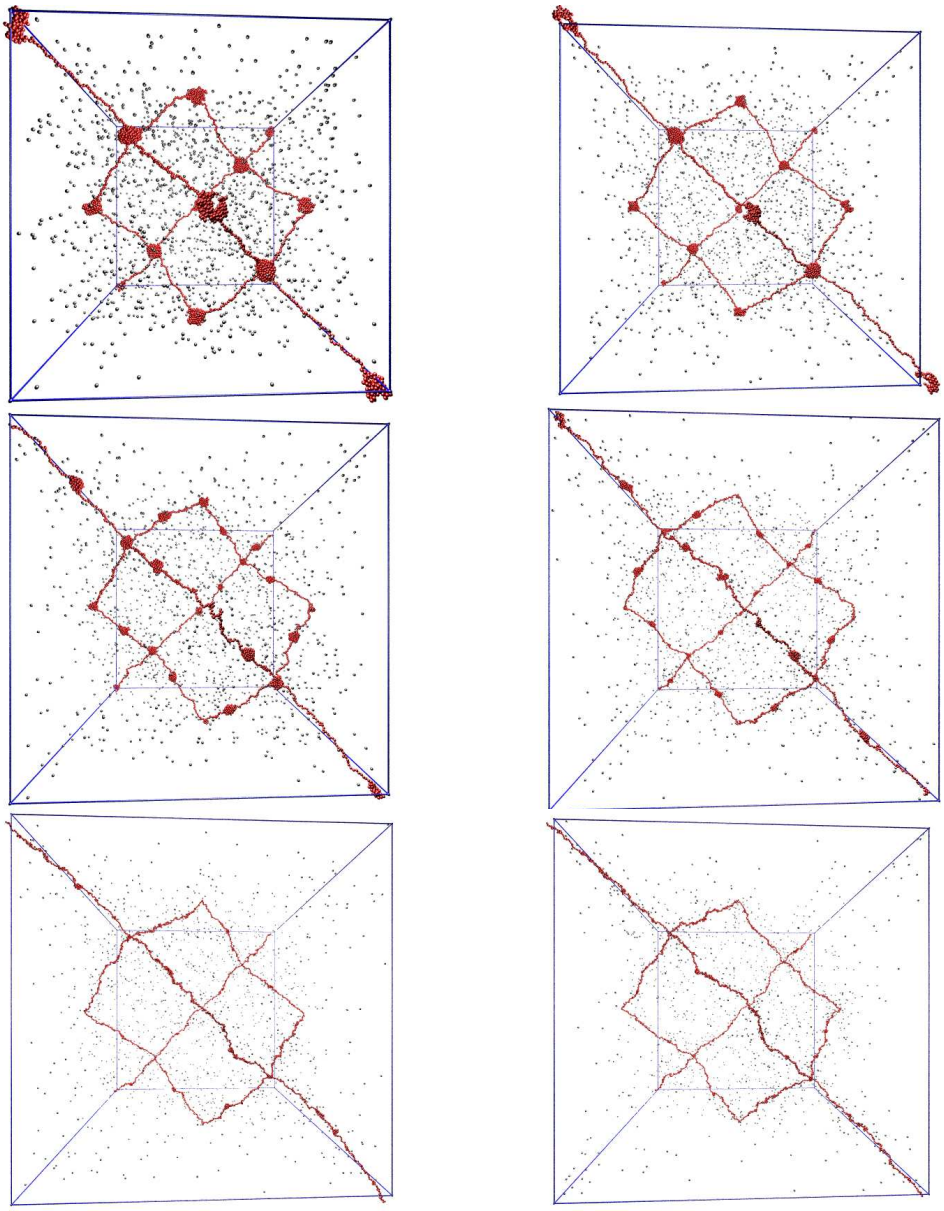

Figure C.7.: Simulation box snapshots for $N_\mathrm{m} = 199$, $f = 0.5$ ($\Rightarrow N_\mathrm{CI} = 1592$, $N_\mathrm{tot} = 4784$) and $\ell_\mathrm{B} = 0\sigma$, $\rho = 0.0038\sigma^{-3}$, $\rho_\mathrm{c} = 0.0025\sigma^{-3}$ (*top left*), $\ell_\mathrm{B} = 0.125\sigma$, $\rho = 0.0015\sigma^{-3}$, $\rho_\mathrm{c} = 0.001\sigma^{-3}$ (*top right*), $\ell_\mathrm{B} = 0.25\sigma$, $\rho = 0.0015\sigma^{-3}$, $\rho_\mathrm{c} = 0.001\sigma^{-3}$ (*center left*), $\ell_\mathrm{B} = 0.5\sigma$, $\rho = 0.00075\sigma^{-3}$, $\rho_\mathrm{c} = 0.0005\sigma^{-3}$ (*center right*), $\ell_\mathrm{B} = 0.75\sigma$, $\rho = 0.00038\sigma^{-3}$, $\rho_\mathrm{c} = 0.00025\sigma^{-3}$ (*bottom left*), $\ell_\mathrm{B} = 1.0\sigma$, $\rho = 0.00038\sigma^{-3}$, $\rho_\mathrm{c} = 0.00025\sigma^{-3}$ (*bottom right*), in a poor solvent environment with $\epsilon_\mathrm{LJ} = 1.75\sigma$ and $r_\mathrm{c} = 2.5\sigma$ as LJ-parameters.

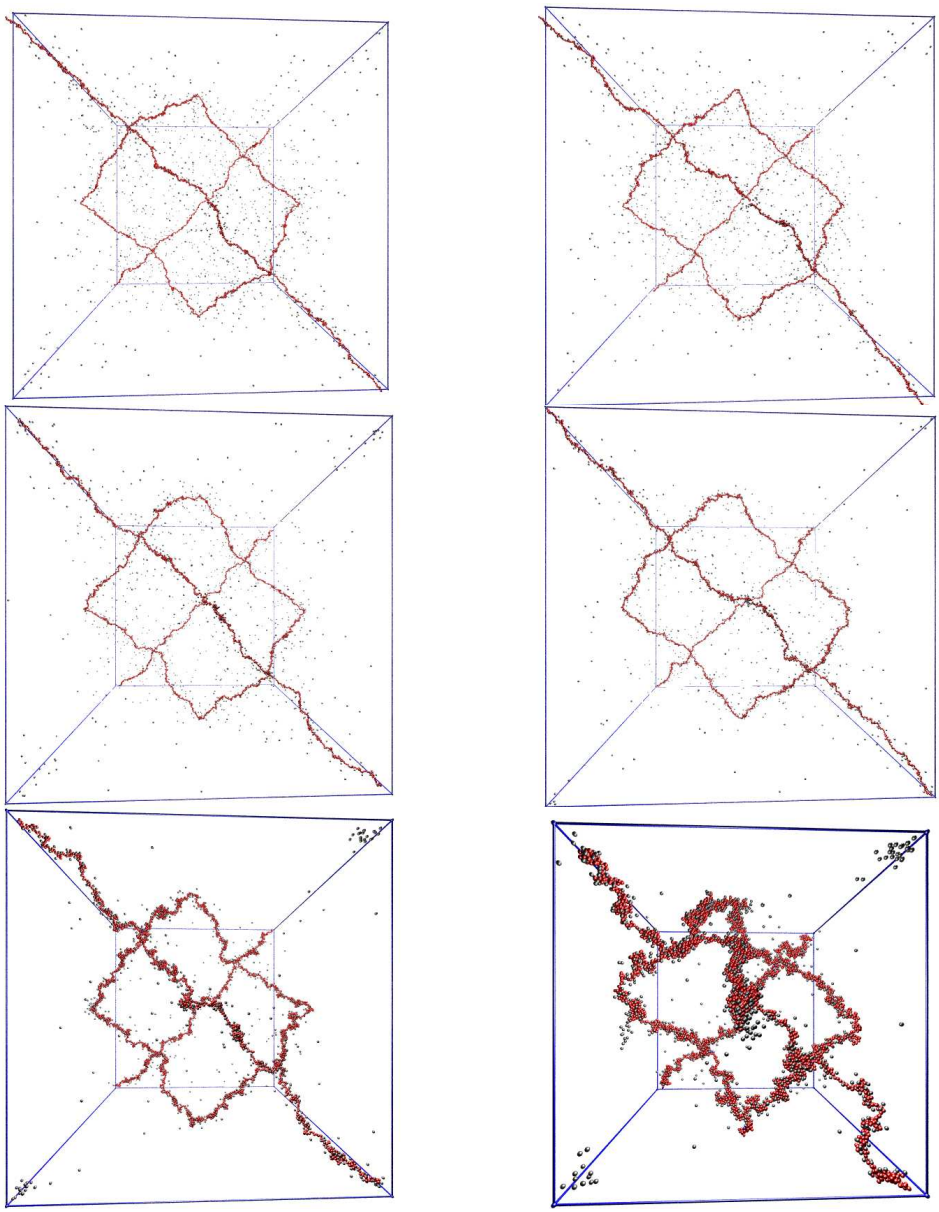

Figure C.8.: Simulation box snapshots for $N_\mathrm{m} = 199$, $f = 0.5$ ($\Rightarrow N_\mathrm{CI} = 1592$, $N_\mathrm{tot} = 4784$) and $\ell_\mathrm{B} = 1.0\sigma$, $\rho = 0.00038\sigma^{-3}$, $\rho_\mathrm{c} = 0.00025\sigma^{-3}$ (*top left*), $\ell_\mathrm{B} = 1.5\sigma$, $\rho = 0.00038\sigma^{-3}$, $\rho_\mathrm{c} = 0.00025\sigma^{-3}$ (*top right*), $\ell_\mathrm{B} = 2.0\sigma$, $\rho = 0.00038\sigma^{-3}$, $\rho_\mathrm{c} = 0.00025\sigma^{-3}$ (*center left*), $\ell_\mathrm{B} = 3.0\sigma$, $\rho = 0.00038\sigma^{-3}$, $\rho_\mathrm{c} = 0.00025\sigma^{-3}$ (*center right*), $\ell_\mathrm{B} = 5.0\sigma$, $\rho = 0.0015\sigma^{-3}$, $\rho_\mathrm{c} = 0.001\sigma^{-3}$ (*bottom left*), $\ell_\mathrm{B} = 6.0\sigma$, $\rho = 0.0075\sigma^{-3}$, $\rho_\mathrm{c} = 0.005\sigma^{-3}$ (*bottom right*), in a poor solvent environment with $\epsilon_\mathrm{LJ} = 1.75\sigma$ and $r_c = 2.5\sigma$ as LJ-parameters.

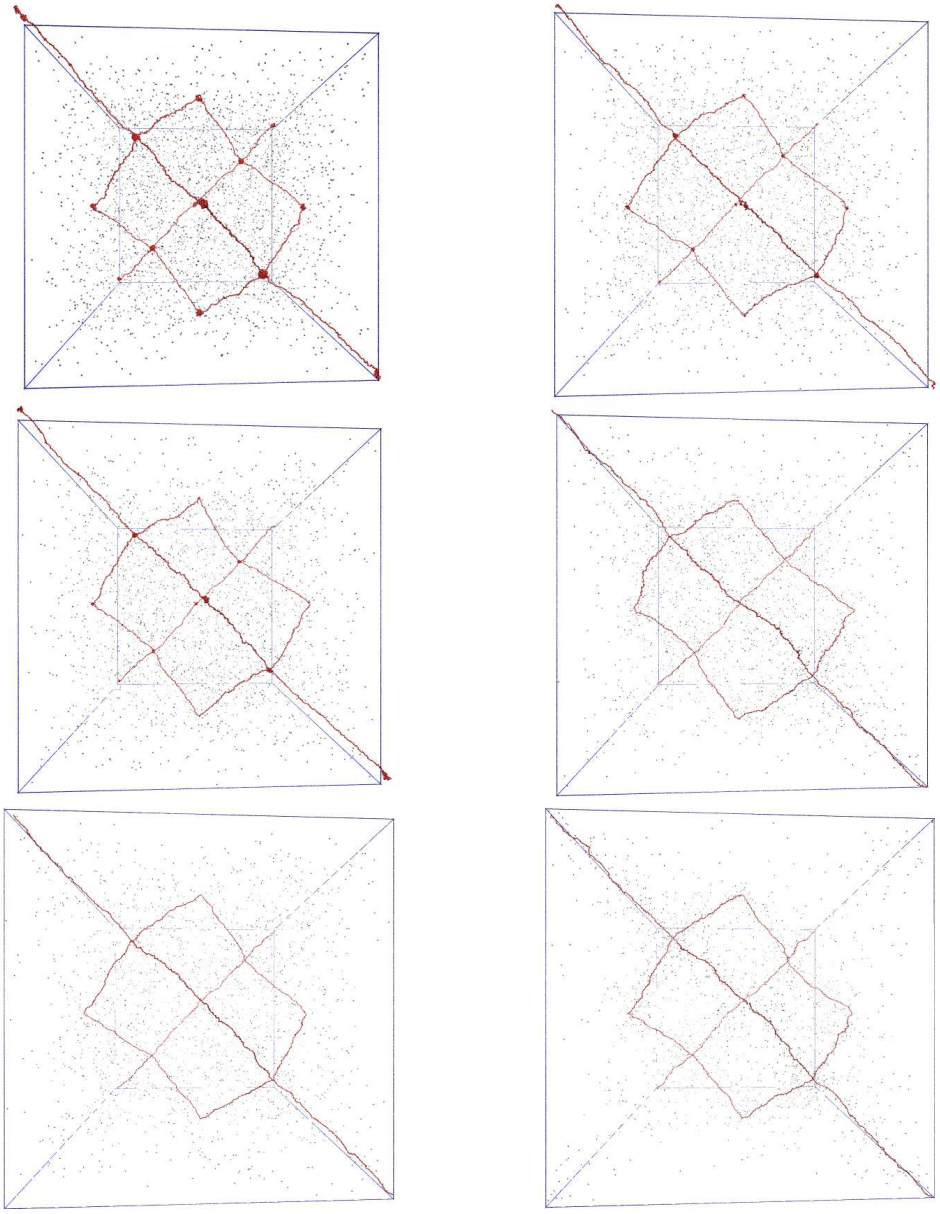

Figure C.9.: Simulation box snapshots for $N_\mathrm{m} = 199$, $f = 1.0$ ($\Rightarrow N_\mathrm{CI} = 3192$, $N_\mathrm{tot} = 6384$) and $\ell_\mathrm{B} = 0\sigma$, $\rho = 0.00050\sigma^{-3}$, $\rho_\mathrm{c} = 0.00050\sigma^{-3}$ (*top left*), $\ell_\mathrm{B} = 0.125\sigma$, $\rho = 0.00020\sigma^{-3}$, $\rho_\mathrm{c} = 0.00020\sigma^{-3}$ (*top right*), $\ell_\mathrm{B} = 0.25\sigma$, $\rho = 0.00020\sigma^{-3}$, $\rho_\mathrm{c} = 0.00020\sigma^{-3}$ (*center left*), $\ell_\mathrm{B} = 0.5\sigma$, $\rho = 0.00015\sigma^{-3}$, $\rho_\mathrm{c} = 0.00015\sigma^{-3}$ (*center right*), $\ell_\mathrm{B} = 0.75\sigma$, $\rho = 0.00010\sigma^{-3}$, $\rho_\mathrm{c} = 0.00010\sigma^{-3}$ (*bottom left*), $\ell_\mathrm{B} = 1.0\sigma$, $\rho = 0.00010\sigma^{-3}$, $\rho_\mathrm{c} = 0.00010\sigma^{-3}$ (*bottom right*), in a poor solvent environment with $\epsilon_\mathrm{LJ} = 1.75\sigma$ and $r_c = 2.5\sigma$ as LJ-parameters.

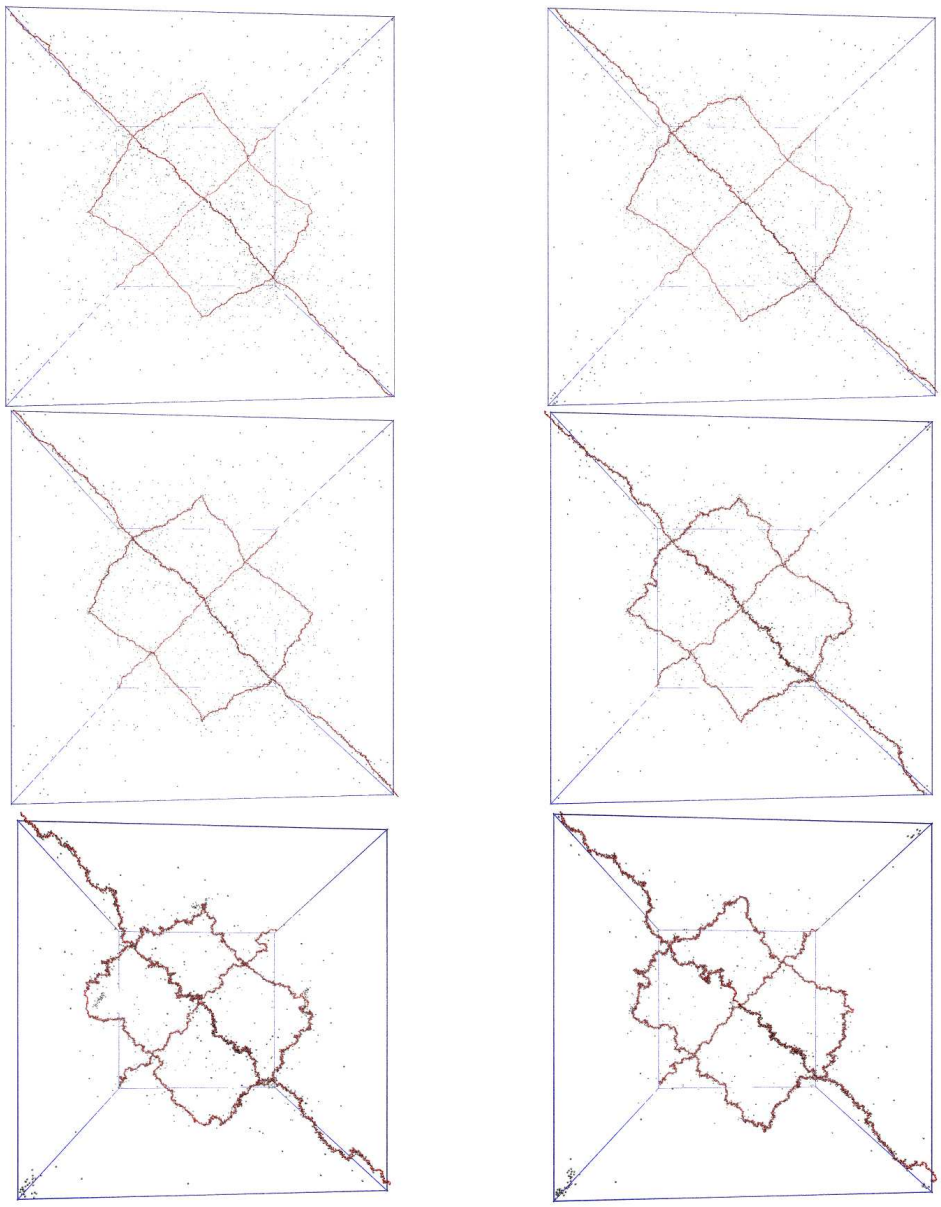

Figure C.10.: Simulation box snapshots for $N_{\mathrm{m}} = 199$, $f = 1.0$ ($\Rightarrow N_{\mathrm{CI}} = 3192$, $N_{\mathrm{tot}} = 6384$) and $\ell_{\mathrm{B}} = 1.0\sigma$, $\rho = 0.00010\sigma^{-3}$, $\rho_{\mathrm{c}} = 0.00010\sigma^{-3}$ (*top left*), $\ell_{\mathrm{B}} = 1.5\sigma$, $\rho = 0.00010\sigma^{-3}$, $\rho_{\mathrm{c}} = 0.00010\sigma^{-3}$ (*top right*), $\ell_{\mathrm{B}} = 2.0\sigma$, $\rho = 0.00010\sigma^{-3}$, $\rho_{\mathrm{c}} = 0.00010\sigma^{-3}$ (*center left*), $\ell_{\mathrm{B}} = 3.0\sigma$, $\rho = 0.00020\sigma^{-3}$, $\rho_{\mathrm{c}} = 0.00020\sigma^{-3}$ (*center right*), $\ell_{\mathrm{B}} = 5.0\sigma$, $\rho = 0.00050\sigma^{-3}$, $\rho_{\mathrm{c}} = 0.00050\sigma^{-3}$ (*bottom left*), $\ell_{\mathrm{B}} = 6.0\sigma$, $\rho = 0.00050\sigma^{-3}$, $\rho_{\mathrm{c}} = 0.00050\sigma^{-3}$ (*bottom right*), in a poor solvent environment with $\epsilon_{\mathrm{LJ}} = 1.75\sigma$ and $r_c = 2.5\sigma$ as LJ-parameters.

List of Figures

List of Tables

List of Used Symbols

The 52 lower and upper case characters seem to be insufficient when physicists try to map nature onto mathematical expressions, even when also adding the 48 Greek characters. The invention of indices at least allowed to group variables with a similar meaning, as did the onset of computerized word processing which introduced the possibility of having varying font sets instead of additional alphabets like old German, Hebrew, Cyrillic, and so forth. Tradition and convention however limit this choices again, as certain characters have obtained a specific (unfortunately sometimes ambiguous) meaning over the years.

In this work we nevertheless tried to use a self-consistent notation which is primarily based on the following guidelines: Characters with a special mathematical meaning are set in a blackboard font, *e.g.* $\mathbb{i}$, $\mathbb{R}$, $\mathbb{C}$, except for the Euler number e as it also stands for the exponential function $\exp(x) := \mathrm{e}^x$. Free energies are given as capitalized script letters, *e.g.* $\mathcal{F}$, as are pressures measured in the simulation, *i.e.* $\mathcal{P}$. Capital Greek letters like Π are used if predicted pressures from a theoretical model are inferred, the Latin letter P indicates prescripted pressures such as the input parameter P_{ext} to the (N, p, T)-algorithm. Unfortunately, this concept could not be transferred to the forces investigated due to the many meanings the literature came to assign the traditional letter used there. Hence, f or $\vec{\mathsf{f}}$ now refer to a scalar force or force vector, respectively, while f is reserved for the charge fraction of the chain and f_{f} for the functionality of the monomer.

The remaining conventions are (hopefully) straightforward, as should become clear in the following list. There, symbols are assorted alphabetically with Roman letters and lower case characters first, followed by miscellaneous symbols and Greek letters, while same letters are ordered by different fonts first, then by their indices.

a_{sim}	edge length of a diamond lattice unit cell
b	bond length between neighbouring monomers; Kuhn length
c	concentration
c_{blob}	scaling factor in the blob extension relation, see section 3.2.6
c_{id}	scaling factor in the ideal gas expression Π_{C}, see section 3.2.6
c_{PE}	scaling factor in the electrostatic self-energy, see section 3.2.8
e_0	unit charge $e_0 = 1.60217646 \cdot 10^{-19}\,\mathrm{C}$

f	charge fraction $f \in \mathbb{Q}$ of the polyelectrolytes
f_{eff}	effective charge fraction
f_{f}	functionality of the monomer
$f_{\max}$	maximum charge fraction due to counterion condensation
$f_{\max}^{\mathrm{blob}}$	maximum charge fraction in the blob-like description
$f_{\max}^{\mathrm{rod}}$	maximum charge fraction in the rod-like description
f_x	fraction of condensed counterions at the point of inflection (R_{M}, f_x) in the integrated counterion distribution plot (see appendix B); for infinitely long, charged rods it is related to the Manning parameter ξ_{M} via $f_x = 1 - \frac{1}{\xi_{\mathrm{M}}}$
f_{DoF}	number of the degrees of freedom in a system (*e.g.* 3 translative and 3 rotatory ones for a solid, macroscopic object)
f_{E}	measured restoring force of the polymer chain
$\mathring{f}_{\mathrm{E}}$	measured restoring force without electrostatics
g_{P}	monomers per pearl on a polyelectrolyte chain in poor solvent
g_{PE}	number of monomers in a polyelectrolyte blob
$g_{\mathrm{PE}}^{\mathrm{blob}}$	number g_{PE} including Manning condensation on a blob-like chain
$g_{\mathrm{PE}}^{\mathrm{rod}}$	number g_{PE} including Manning condensation on a rod-like chain
g_{T}	number of monomers in a tension blob
k_{h}	spring constant parameter of the harmonic potential
k_{B}	Boltzmann constant $k_{\mathrm{B}} = 1.380650 \cdot 10^{-23}\,\mathrm{J\,K^{-1}}$
$k_{\mathrm{B}}T$	Boltzmann factor ("*thermal energy*") used to rescale the energy
k_{F}	spring constant parameter of the FENE potential
l_g	contour length per blob size ξ, see (3.77)
l_p	persistence length, see (2.15)
$n(r)$	counterion (number) density in the framework of Poisson-Boltzmann theory
$\bar{n}_{\mathrm{avg}}$	average counterion (number) density in the cylindrical cell
n_{c}	minimum monomer separation between clusters $\mathcal{C}$
$n_{\mathrm{f}}(r)$	(number) density of the fixed charges on the center rod
n_{tot}	total charge (number) density in the cylindrical cell model
n_{P}	number of pearls on a polyelectrolyte chain in poor solvent
p_{c}	minimum spatial extension of a cluster $\mathcal{C}$
$p_{\min}$	pressure limit for the (N, p, T)-algorithm
q	scalar scattering number $q = \lvert\vec{q}\rvert = 2\pi/\lambda \sin(\theta/2)$ where λ is the wave length and θ is the scattering angle

$\vec{q}$	scattering vector of the employed scattered waves, *e.g.* x-rays for SAXS or neutrons for SANS
r_0	inner radius of the cylindrical cell model
$\tilde{r}_0$	modified inner radius r_0, see section 3.3.3
$\check{r}_0$	modified inner radius set to 1.0σ, see section 3.3.3
r_c	maximum spatial separation between clusters $\mathcal{C}$
r_cut	cut-off parameter of the Lennard-Jones potential
r_h	cut-off parameter of the harmonic potential
r_F	cut-off parameter of the FENE potential
$\vec{r}_\mathrm{old}$	former spatial position of a particle
r_skin	skin distance
v_ex	excluded volume of a monomer, see (2.37)
v_CI	valency of the counterions
$y(r)$	reduced electrostatic potential of the counterions in the framework of Poisson-Boltzmann theory
$y_\mathrm{f}(r)$	reduced electrostatic potential of the fixed charges (*i.e.* monomers) in the framework of Poisson-Boltzmann theory
$\vec{F}_{ij}^\mathrm{sr}$	sum of all short-range forces between particles i and j, see section 4.1
E_r	radial electric field of the fixed charges, see (3.98a)
E_C	coulombic contributions to the energy, see section 4.1; also used as average $\langle E_\mathrm{C}\rangle$ for the measured pressure $\mathcal{P}_{\ell_\mathrm{B}}^\mathrm{tot}$
L_cyl	lateral length of the cylindrical cell model
L_eq	edge length of the (cubic) simulation box at equilibrium, corresponding to $V_\mathrm{eq} = L_\mathrm{eq}^{1/3}$
$\overline{M}_n$	number average of the molecular weight, see (2.1)
$\overline{M}_w$	weight average of the molecular weight, see (2.2)
$\overline{M}_z$	higher order average of the molecular weight
N_m	number of monomers on each chain, *i.e.* length of a chain
N_nodes	number of network nodes
N_p	number of polymer chains between the network nodes
N_tot	total number of particles in the simulation box
N_CI	number of counterions in the simulation box
P_ext	externally imposed pressure for the (N,p,T)-algorithm
P_n	degree of polymerization

Q	artificial piston mass of the (N,p,T)-integrator, see section 4.1
Q_{eff}	effective charge in a system with counterion condensation, see (3.17) in section 3.2.4
Q_{in}	total charge within a certain spatial area, *e.g.* monomers within the central cylinder of the cylindrical cell model
Q_{Gauss}	charge prefactor of Gaussian-like distributed charges, see (3.106)
R_0	integration constant replacing a $R_{\text{M}} \in \mathbb{C}$, see section 3.3.2
R_{cyl}	outer radius of the cylindrical cell model
$\tilde{R}_{\text{cyl}}$	modified outer radius $R_{\text{cyl}}(r_0 = \tilde{r}_0)$, see section 3.3.3
$\check{R}_{\text{cyl}}$	modified outer radius $R_{\text{cyl}}(r_0 = \check{r}_0)$, see section 3.3.3
R_{max}	contour length $R_{\text{max}} = N_{\text{m}}b$ of a chain with N_{m} monomers and a bond length b
R_{x}	length of vector $\vec{R}_{\text{x}}$, *i.e.* $\lvert\vec{R}_{\text{x}}\rvert = R_{\text{x}}$
$\vec{R}_{\text{x}}$	extension vector, usually associated with extending a polymer chain along a specific coordinate axis
R_{CM}	length of the center-of-mass vector $\vec{R}_{\text{CM}}$
$\vec{R}_{\text{CM}}$	vector pointing to the center-of-mass
R_{E}	spatial size (extension) of the polymer chain
$\vec{R}_{\text{E}}$	end-to-end vector of the chain with $\lvert\vec{R}_{\text{E}}\rvert = R_{\text{E}}$
R_{F}	Flory radius, see (2.46)
R_{G}	radius of gyration, see (2.16)
R_{G}	extension of a Gaussian chain, see (2.7)
R_{H}	hydrodynamic radius, see (2.19)
R_{M}	Manning radius of counterion condensation
$S(q)$	structure factor, *e.g.* as single chain form factor
T	temperature, usually measured in reduced units such as $k_{\text{B}}T$
U_{harm}	harmonic potential
U_{FENE}	FENE potential, see (4.1)
U_{FESAW}	interaction potential of a self-avoiding walk-like polymer with FENE bonds, see (3.30)
$U_{\text{FE/fit}}$	interaction potential of a self-avoiding walk-like polymer with an effective bond potential as in the simulations, see (3.104)
$U_{\text{Gauß}}$	interaction potential of a Gaussian chain, see (3.28)
U_{LJ}	Lennard-Jones potential, see (4.2)
U_{PE}	electrostatic self-energy of a blob chain, see (3.69)

U_{SAW}	interaction potential of a self-avoiding walk-like polymer with harmonic bonds, see (3.29)
$U_{\ell_{\mathrm{B}}}$	electrostatic self-energy of likewisely charged monomers, see (3.65)
$U_{\ell_{\mathrm{B}}}^{\ominus}$	electrostatic self-energy of an elliptical, charged object, see (3.102)
V	(current) simulation box volume
V_{eq}	simulation box volume at the end of equilibration, *i.e.* with a measured pressure of $\mathcal{P} = 0$
V_{max}	maximum volume of the simulation box
V_{min}	minimum volume of the simulation box
f	plain force (not necessarily a scalar)
$\vec{\mathsf{f}}$	plain force vector
f_{x}	force along one of the spatial axes
$\vec{\mathsf{f}}_{\mathrm{x}}$	force vector, usually along one of the spatial axes
f_{DH}	force corresponding to the pressure Π_{DH}
f_{E}	restoring force of the polymer chain if extended, see (4.16a)
$\vec{\mathsf{f}}_{\mathrm{E}}$	vector of the restoring force f_{E}
$\mathsf{f}_{\mathrm{E}}^{\mathrm{real}}$	real restoring force, includes a divergence due to the chains' finite extensibility
$\mathsf{f}_{\mathrm{E}}^{\mathrm{tot}}$	total restoring force for $\Pi_{\mathrm{tot}} \neq 0$, see section 3.2.9
$\mathsf{f}_{\mathrm{FENE}}$	force corresponding to the potential U_{FENE}
$\mathsf{f}_{\mathrm{FESAW}}$	force corresponding to the potential U_{FESAW}
$\mathsf{f}_{\mathrm{FE/fit}}$	force corresponding to the potential $U_{\mathrm{FE/fit}}$
f_{PE}	force corresponding to the potential U_{PE}
$\mathsf{f}_{\ell_{\mathrm{B}}}$	force corresponding to the potential $U_{\ell_{\mathrm{B}}}$
ℓ	real bond length between two repeat units
$\vec{\ell}$	real bond length vector with $\lvert\vec{\ell}\rvert = \ell$
ℓ_{B}	Bjerrum length $\ell_{\mathrm{B}} = e_0^2/(4\pi\epsilon_0\epsilon_{\mathrm{S}}k_{\mathrm{B}}T)$, indicating the strength of the coulombic potential by representing the distance at which two elementary charges e_0 have an electrostatic interaction energy of $k_{\mathrm{B}}T$; also allows to map the simulation length scale σ onto SI-units, as $\ell_{\mathrm{B}} \approx 7.14\text{Å}$ in water at room temperature
ℓ_{P}	electrostatic persistence length, see (3.26)
$\langle p \rangle$	average pressure, measured in equilibrium

$\langle E_{\mathrm{C}} \rangle$	average of the coulombic contributions to the energy in the (N,p,T)-integrator, see section 4.1
e	Euler number $\mathrm{e} = 2.718281828\ldots$
$\mathbb{i}$	imaginary unit $\mathbb{i}^2 := -1$
$\mathbb{C}$	set of complex numbers
$\mathbb{N}$	set of non-negative integers
$\mathbb{Q}$	set of rational numbers
$\mathbb{R}$	set of real numbers
$\mathbb{Z}$	set of integers
$\mathcal{C}$	a cluster on a polyelectrolyte chain in poor solvent
$\mathcal{F}_{\mathrm{se-rod}}$	self-energy of the rod-like polymer, see (3.100)
$\mathcal{F}_{\mathrm{tot}}$	total free energy of the "cell under tension"-model, see (3.105)
$\mathcal{F}_{\mathrm{PB}}$	free energy of the cell model in the framework of Poisson-Boltzmann theory, see (3.94)
$\mathcal{F}_{\mathrm{PB-E}}$	energetic part of $\mathcal{F}_{\mathrm{PB}}$, see (3.95a)
$\mathcal{F}_{\mathrm{PB-S}}$	entropic part of $\mathcal{F}_{\mathrm{PB}}$, see (3.95b)
$\mathcal{F}_{\mathrm{PB-V}}$	excluded-volume contribution to $\mathcal{F}_{\mathrm{PB}}$, see (3.95c)
$\mathcal{F}_{\mathrm{PB-tot}}$	total free energy of the cell model, see (3.99)
$\mathcal{F}_{\mathrm{PB}}^{\mathrm{FV}}$	free energy $\mathcal{F}_{\mathrm{PB}}$ of the cell model including the free volume term
$\mathcal{L}$	Langevin function, see (2.32)
$\mathcal{L}^{-1}$	inverse of the Langevin function
$\mathcal{P}$	pressure measured according to (4.5)
$\mathcal{P}_{\mathrm{gas}}$	measured pressure of the gas, see (4.12a)
$\mathcal{P}_{\mathrm{gel}}$	measured pressure of the gel, see (4.12b)
$\mathcal{P}_{\mathrm{ideal}}^{\mathrm{CI}}$	measured ideal pressure of the counterions
$\mathcal{P}_{\mathrm{ideal}}^{\mathrm{monomers}}$	measured ideal pressure of the monomers
$\mathcal{P}_{\mathrm{osm}}$	measured osmotic pressure $\mathcal{P}/(\rho k_{\mathrm{B}} T)$
$\mathcal{P}_{\mathrm{FENE}}$	measured pressure due to the elastic bonds
$\mathcal{P}_{\mathrm{LJ}}^{\mathrm{CI}}$	measured excluded volume pressure of counterions, combining $\mathcal{P}_{\mathrm{LJ}}^{\mathrm{CI}} = \mathcal{P}_{\mathrm{LJ}}^{\mathrm{CI-CI}} + \mathcal{P}_{\mathrm{LJ}}^{\mathrm{CI-monomers}}$
$\mathcal{P}_{\mathrm{LJ}}^{\mathrm{CI-CI}}$	measured excluded volume pressure between counterions and counterions
$\mathcal{P}_{\mathrm{LJ}}^{\mathrm{CI-monomers}}$	measured excluded volume pressure between counterions and monomers

$\mathcal{P}_{\mathrm{LJ}}^{\mathrm{monomers}}$	measured excluded volume pressure between monomers and monomers
$\mathcal{P}_{\ell_{\mathrm{B}}}^{\mathrm{tot}}$	measured total electrostatic pressure
$\mathcal{P}_{\ell_{\mathrm{B}}}^{\Delta}$	deviation in the electrostatic pressure
$\mathring{\mathcal{P}}$	total pressure measured without electrostatics
$\mathring{\mathcal{P}}_{\mathrm{gas}}$	pressure $\mathcal{P}_{\mathrm{gas}}$ measured without electrostatics
$\mathring{\mathcal{P}}_{\mathrm{gel}}$	pressure $\mathcal{P}_{\mathrm{gel}}$ measured without electrostatics
$\mathring{\mathcal{P}}_{\mathrm{LJ}}^{\mathrm{CI}}$	pressure $\mathcal{P}_{\mathrm{LJ}}^{\mathrm{CI}}$ measured without electrostatics
$\mathcal{W}_{\sigma_{\mathrm{Gauss}}}^{\mu_{\mathrm{Gauss}}}(r)$	Gaussian probability distribution with mean value μ_{Gauss} and profile width σ_{Gauss}
$\Delta\mathsf{f}_{\mathrm{E}}$	difference between $\mathsf{f}_{\mathrm{E}}^{\mathrm{tot}}$ and f_{E}, see section 3.2.9
$\mathring{\Delta} f_{\mathrm{E}}$	difference between the measured forces, *i.e.* $\mathring{\Delta} f_{\mathrm{E}} = f_{\mathrm{E}} - \mathring{f}_{\mathrm{E}}$
$\mathring{\Delta}\mathcal{P}_{\mathrm{gas}}$	difference between the measured gas-like pressures, *i.e.* $\mathring{\Delta}\mathcal{P}_{\mathrm{gas}} = \mathcal{P}_{\mathrm{gas}} - \mathring{\mathcal{P}}_{\mathrm{gas}}$
$\mathring{\Delta}\mathcal{P}_{\mathrm{gel}}$	difference between the measured gel-like pressures, *i.e.* $\mathring{\Delta}\mathcal{P}_{\mathrm{gel}} = \mathcal{P}_{\mathrm{gel}} - \mathring{\mathcal{P}}_{\mathrm{gel}}$
γ_0	molecular dampening in the (N,p,T)-integrator, see section 4.1
γ_{PB}	integration constant for solving the Poisson-Boltzmann equation, see section 3.2.7 and 3.3.2
γ_{PB}	imaginary integration constant $-\mathbb{i}\gamma_{\mathrm{PB}}$, see section 3.2.7 and 3.3.2
γ_V	piston dampening in the (N,p,T)-integrator, see section 4.1
ϵ	Lennard-Jones unit ϵ used as basic energy scale
ϵ_0	permittivity of the vacuum
ϵ_{LJ}	energy parameter of the Lennard-Jones potential
$\epsilon_{\mathrm{LJ}}^{\theta}$	energy parameter ϵ_{LJ} at the θ-point
ϵ_{S}	permittivity of the solvent
θ	temperature T at the θ-point
κ_T	isothermal compressibility in the (N,p,T)-integrator, see section 4.1
λ	scattering wave vector
μ_{Gauss}	mean of the Gaussian charge distribution $n_{\mathrm{f}}(r)$
ξ	spatial extension of a blob
ξ_{M}	Manning parameter, indicating the effective strength of the electrostatic interactions
$\xi_{\mathrm{M}}^{\mathrm{min}}$	Manning minimum parameter

$\xi_{\mathrm{M}}^{\mathrm{CuT}}$	Manning parameter from the "cell under tension"-model
ξ_{PE}	polyelectrolyte blob size
ξ_{T}	tension blob size
$\xi_{\perp}$	vertical extension of a blob, see section 3.3.1
$\xi_{\parallel}$	horizontal extension of a blob, see section 3.3.1
π	ratio of a circle's circumference to its diameter, *i.e.* 3.141593...
ρ	system density of particles, *i.e.* a number density
ρ_{c}	bulk charge density, *i.e.* $\rho_{\mathrm{c}} = 2N_{\mathrm{CI}}/V$
ρ_{m}	monomer density, *i.e.* $\rho_{\mathrm{m}} = N_{\mathrm{p}}N_{\mathrm{m}}/V$
$\rho_{\max}$	maximum system density
$\rho_{\min}$	minimum system density
ρ_{CI}	density of the counterions, *i.e.* $\rho_{\mathrm{CI}} = N_{\mathrm{CI}}/V$
σ	Lennard-Jones unit σ used as basic length scale
σ_{Gauss}	width of the Gaussian charge distribution $n_{\mathrm{f}}(r)$
τ	Lennard-Jones unit τ used as basic time scale; *or:* reduced temperature $\tau = (\theta - T)/\theta$ in a poor solvent
ψ	electrostatic potential of the counterions
ψ_{f}	electrostatic potential of the fixed charges (*i.e.* monomers)
ψ_{tot}	total electrostatic potential $\psi_{\mathrm{tot}} = \psi + \psi_{\mathrm{f}}$
ω_0	molecular frequency in the (N, p, T)-integrator, see section 4.1
Π	theoretically predicted pressure
$\Pi_V = Q\dot{V}$	canonically conjugate momentum of an artificial piston of mass Q in the (N, p, T)-integrator, see section 4.1
$\mathring{\Pi}$	theoretical pressure without electrostatics
Π_{C}	theoretical pressure of the (supposedly ideal) gas
$\Pi_{\mathrm{C}}^{\mathrm{eff}}$	theoretical pressure Π_{C} including counterion condensation
$\Pi_{\mathrm{C}}^{\mathrm{PB}}$	theoretical pressure Π_{C} in the framework of Poisson-Boltzmann
Π_{DH}	theoretical pressure due to Debye-Hückel-like screening
Π_{E}	theoretical pressure of the gel, *i.e.* of the elastic response of the network chains
$\Pi_{\mathrm{E}}^{\mathrm{real}}$	theoretical pressure of the gel including a divergence due to the chains' finite extensibility
$\Pi_{\mathrm{E}}^{\mathrm{FESAW}}$	same as $\Pi_{\mathrm{E}}^{\mathrm{real}}$, but using $\mathsf{f}_{\mathrm{FESAW}}$ to model the (diverging) restoring force

Π_{tot}	total theoretical pressure
$\Pi_{\ell_{\mathrm{B}}}$	theoretical pressure of the electrostatic self-energy
Ω_0	frequency of the fluctuating box walls in the (N,p,T)-integrator, see section 4.1

In chapter 4 we are comparing the results of computer simulations for various parameters to the theoretical predictions, namely two kind of solvents (good solvent with $\nu = 0.5$ and close to the θ-point where $\nu = 0.588$), twelve chain lengths $N_{\mathrm{m}} = 39, \ldots, 259$, five charge fractions $f = 0.0625, \ldots, 1.0$, and four Bjerrum lengths $\ell_{\mathrm{B}} = 0\sigma, \ldots, 5\sigma$ for systems with full electrostatics and those termed "neutral" where the coulombic coupling is deactivated while the volume is kept at the equilibrium value $V = V_{\mathrm{eq}}$ obtained for all interactions present. To be able to distinguish this multitude of information, we used the following coding scheme in all related plots to allow easy identification of the respective underlying parameter set:

f	0.0625	0.125	0.25	0.3333	0.5	1.0
colour	cyan	purple	blue	yellow	green	red

	good solvent ($\nu = 0.588$)		θ-solvent ($\nu = 0.50$)	
ℓ_{B}	full electrostatics	"neutral"	full electrostatics	"neutral"
0	+	−	×	−
1	△	▲	▽	▼
2	◇	◆	□	■
5	⬠	⬟	○	●

Table S.1.: The colour coding scheme used for all data plots presenting results of our computer simulation study, illustrating our principle "same colour refers to same charge fraction, same symbol to same Bjerrum length".

Bibliography

[1] Information obtained from the manufacturer's homepage, *ConvaTec*, 2002, `http://www.convatec.com/de_DE/products/information/woundcare/... ...varihesive_hydrogel.html`.

[2] J. Daniels, Hydrogel – A Management Tool for Droughty Conditions with Roadside Flowers, 2002, `http://filebox.vt.edu/users/jodaniel/hydrogel.html`.

[3] K. S. Kazanskii and S. A. Dubrovskii, Adv. Polym. Sci. **104**, 97 (1992).

[4] F. Buchholz and N. Peppas, in *ACS Symposium Series*, American Chemical Society, edited by M. Comstock (American Chemical Society, Washington, D.C., 1994), Vol. 573.

[5] G. M. Eichenbaum *et al.*, Macromolecules **32**, 4867 (1999).

[6] N. A. Peppas, P. Bures, W. Leobandung, and H. Ichikawa, Biopharm. **50**, 27 (2000).

[7] *Physical Chemistry of Polyelectrolytes*, Vol. 99 of *Surfactant Science Series* (Marcel Dekker Inc., New York, 2001).

[8] W. E. Rudzinski *et al.*, Design Monom. Polym. **5**, 39 (2002).

[9] R. Harland and R. Prud'homme, *Polyelectrolyte Gels* (American Chemical Society, Washington DC, 1992).

[10] J. Rädler, I. Koltover, T. Salditt, and C. Safinya, Science **275**, 810 (1997).

[11] M. Deserno, C. Holm, and K. Kremer, in *Physical Chemistry of Polyelectrolytes*, Vol. 99 of *Surfactant science series*, edited by T. Radeva (Marcel Decker, New York, 2001), Chap. 2, pp. 59–110.

[12] J.-L. Barrat and J.-F. Joanny, Advances in Chemical Physics **94**, 1 (1996).

[13] A. Khokhlov, S. G. Starodubtzev, and V. V. Vasilevskaya, in *Conformational transitions in polymer gels: theory and experiment*, Vol. 109 of *Adv. Polym. Sci.*, edited by K. Dusek (Springer Verlag, New York, 1993), p. 123.

[14] C. Mengel, W. H. Meyer, and G. Wegner, Macromol. Chem. Phys. **202**, 1138 (2001).

[15] O. Okay and S. B. Sariisik, Eur. Phys. J. E **36**, 393 (2000).

[16] A. R. Khokhlov, E. Y. Kramarenko, E. E. Makhaeva, and S. G. Starodubtzev, Macromolecules **25**, 4779 (1992).

[17] P. Hansson, Langmuir **14**, 4059 (1998).

[18] C. Holm, K. Kremer, and T. Vilgis, Physikalische Blätter **54**, 1013 (1998).

[19] W. Kuhn, B. Hargitay, A. Katchalsky, and H. Eisenberg, Nature **165**, 514 (1950).

[20] T. Tanaka, Phys. Rev. Lett. **40**, 820 (1978).

[21] K. Dusek, *Advances in Polymer Sciences* (Springer-Verlag, New York, 1993), Vol. 109 and 110.

[22] A. Katchalsky and I. Michaeli, J. Polym. Sci. **15**, 69 (1955).

[23] I. Michaeli and A. Katchalsky, J. Polym. Sci. **23**, 683 (1957).

[24] P. Hansson, Langmuir **14**, 2269 (1998).

[25] H. S. Ashbaugh, L. Piculell, and B. Lindman, Langmuir **16**, 2529 (2000).

[26] J. Sjöström and L. Piculell, Colloids Surf. A **183–185**, 429 (2001).

[27] P. Hansson, S. Schneider, and B. Lindman, Prog. Colloid Polym. Sci. **115**, 342 (2000).

[28] P. Hansson, S. Schneider, and B. Lindman, J. Phys. Chem. B **106**, 9777 (2002).

[29] A. Fernandez-Nieves, A. Fernandez-Barbero, B. Vincent, and F. J. de las Nieves, Macromolecules **33**, 2114 (2000).

[30] A. Fernandez-Nieves, A. Fernandez-Barbero, B. Vincent, and F. J. de las Nieves, Prog. Colloid Polym. Sci. **115**, 134 (2000).

[31] P. Flory, *Principles of Polymer Chemistry* (Cornell University Press, Ithaca, NY, 1953).

[32] P. de Gennes, *Scaling Concepts in Polymer Physics* (Cornell University Press, Ithaca, NY, 1979).

[33] H. Schiessel, Macromolecules **32**, 5673 (1999).

[34] K. Kremer and G. Grest, J. Chem. Phys. **92**, 5057 (1990).

[35] M. J. Stevens and K. Kremer, J. Chem. Phys. **103**, 1669 (1995).

[36] R. Everaers, New J. Phys. **1**, 1 (1999).

[37] M. Pütz, K. Kremer, and R. Everaers, Phys. Rev. Lett. **84**, 298 (2000).

[38] R. Everaers, A. Milchev, and V. Yamakov, Eur. Phys. J. E **8**, 3 (2002).

[39] J.-L. Barrat, J.-F. Joanny, and P. Pincus, J. Phys. II France **2**, 1531 (1992).

[40] T. A. Vilgis, A. Johner, and J.-F. Joanny, Eur. Phys. J. E **3**, 237 (2000).

[41] A. Khokhlov, K. Zeldovich, and E. Kramarenko, in *Electrostatic Effects in Soft Matter and Biophysics*, Vol. 46 of *NATO Science Series II - Mathematics, Physics and Chemistry*, edited by C. Holm, P. Kékicheff, and R. Podgornik (Kluwer Academic Publishers, Dordrecht, Nl, 2001), pp. 283–317.

[42] J. P. Flory and J. Rehner, J. Chem. Phys. **11**, 512 (1943).

[43] R. C. Ball and S. F. Edwards, Macromolecules **13**, 748 (1980).

[44] J. U. Sommer, T. A. Vilgis, and G. Heinrich, J. Chem. Phys. **100**, 9181 (1994).

[45] T. A. Vilgis and J. Wilder, Comp. and Theor. Polymer Science **8**, 61 (1998).

[46] H. Frusawa and R. Hayakawa, Phys. Rev. E **58**, 6145 (1998).

[47] M. P. Allen and D. J. Tildesley, *Computer Simulation of Liquids*, *Oxford Science Publications*, 1 ed. (Clarendon Press, Oxford, 1987).

[48] K. Kremer, in *Computer Simulation in Chemical Physics*, edited by A. D. Tildesley and M. P. Allen (Kluwer Academic, Dodrecht, 1993), pp. 173–209.

[49] K. Kremer, in *Computer Simulation in Chemical Physics*, edited by M. P. Allen and D. J. Tildesley (Kluwer Academic Publishers, Amsterdam, 1993), pp. 397–459.

[50] K. Kremer and G. S. Grest, in *Monte Carlo and Molecular Dynamics Simulations in Polymer Science*, edited by K. Binder (Clarendon Press, Oxford, 1994).

[51] D. Frenkel and B. Smit, *Understanding Molecular Simulation*, 2nd ed. (Academic Press, San Diego, 2002).

[52] H. J. Limbach and C. Holm, Comp. Phys. Comp. **147**, 321 (2002).

[53] H. J. Limbach, C. Holm, and K. Kremer, Europhys. Lett. **60**, 566 (2002).

[54] H. J. Limbach and C. Holm, J. Phys. Chem. B **107**, 8041 (2003).

[55] D. Hinderberger, 2004, private communication.

[56] A. W. Arnold, B. A. Mann, H. J. Limbach, and C. Holm, *ESPResSo – An Extensible Simulation Package for Research on Soft Matter Systems*, entry for the Heinz-Billing-Competition for the Advancement of Scientific Computation, 2003 (unpublished).

[57] A. Arnold, B. A. Mann, H.-J. Limbach, and C. Holm, in *Forschung und wissenschaftliches Rechnen 2003*, Vol. 63 of *GWDG-Bericht*, edited by K. Kremer and V. Macho (Gesellschaft für wissenschaftliche Datenverarbeitung mbh, Göttingen, Germany, 2004), pp. 43–59.

[58] S. Schneider and P. Linse, Eur. Phys. J. E **8**, 457 (2002).

[59] Z.-Y. Lu and R. Hentschke, Phys. Rev. E **67**, 061807 (2003).

[60] Q. Yan and J. J. de Pablo, Phys. Rev. Lett. **91**, 018301 (2003).

[61] S. Schneider and P. Linse, J. Phys. Chem. B **107**, 8030 (2003).

[62] B. A. Mann, R. Everaers, C. Holm, and K. Kremer, Europhys. Lett. **67**, 786 (2004).

[63] B. A. Mann, C. Holm, and K. Kremer, J. Chem. Phys. **122**, 154903 (2005).

[64] H.-J. Limbach, A. Arnold, B. A. Mann, and C. Holm, Comp. Phys. Comm., in press (2005).

[65] B. A. Mann and R. Everaers, in preparation (2005).

[66] B. A. Mann, C. Holm, and K. Kremer, in preparation (2005).

[67] I. Newton, *Philosophiae Naturalis Principia Mathematica* (apud Sa. Smith, London, 1687).

[68] R. A. L. Jones, *Soft Condensed Matter* (Oxford University Press, Great Clarendon Street, Oxford OX2 6DP, 2002).

[69] L. Treloar, *The Physics of Rubber Elasticity* (Clarendon Press, Oxford, 1986).

[70] *Electrostatic Effects in Soft Matter and Biophysics*, Vol. 46 of *NATO Science Series II - Mathematics, Physics and Chemistry*, edited by C. Holm, P. Kékicheff, and R. Podgornik (Kluwer Academic Publishers, Dordrecht, Nl, 2001).

[71] C. Holm, in *Computational Soft Matter: From Synthetic Polymers to Proteins*, Vol. 23 of *NIC series*, edited by N. Attig, K. Binder, H. Grubmüller, and K. Kremer (Research Centre Jülich, ADDRESS, 2004).

[72] A. Arnold and C. Holm, in *Advanced Computer Simulation Approaches for Soft Matter Sciences*, Vol. II of *Advances in Polymer Sciences*, edited by C. Holm and K. Kremer (Springer, ADDRESS, 2005, in press).

[73] J. Norberg and L. Nilsson, Quarterly Reviews of Biophysics **36**, 257 (2003).

[74] M. Deserno and C. Holm, J. Chem. Phys. **109**, 7678 (1998).

[75] M. Deserno and C. Holm, J. Chem. Phys. **109**, 7694 (1998).

[76] A. Arnold and C. Holm, Comp. Phys. Comm. **148**, 327 (2002).

[77] A. Arnold, J. de Joannis, and C. Holm, J. Chem. Phys. **117**, 2496 (2002).

[78] J. de Joannis, A. Arnold, and C. Holm, J. Chem. Phys. **117**, 2503 (2002).

[79] W. Tschöp *et al.*, Acta Polymer. **49**, 61 (1998).

[80] W. Tschöp *et al.*, Acta Polymer. **49**, 75 (1998).

[81] K. Kremer and F. Müller-Plathe, Mol. Sim. **28**, 729 (2002).

[82] N. Boghossian, O. Kohlbacher, and H.-P. Lenhof, Research report, Max-Planck-Institut für Informatik, Saarbrücken (unpublished).

[83] C. J. Lejdfors, GISMOS: Graphics and Interactive Steering of MOlecular Simulations – Homepage, 1998.

[84] W. F. van Gunsteren, GROMOS96: GROningen MOlecular Simulation computer program package – Homepage, 1996.

[85] E. Lindahl, B. Hess, and D. van der Spoel, J. Mol. Mod. **7**, 306 (2001).

[86] S. J. Plimpton, J. Comp. Phys. **117**, 1 (1995).

[87] M. Nelson *et al.*, Int. J. Supercomput. Ap. **10**, 251 (1996).

[88] L. Kalé *et al.*, J. Comp. Phys. **151**, 283 (1999).

[89] M. Pütz and A. Kolb, Comp. Phys. Comm. **113**, 145 (1998).

[90] D. Pearlman *et al.*, Comp. Phys. Comm. **91**, 1 (1995).

[91] T. Straatsma *et al.*, *NWChem, A Computational Chemistry Package for Parallel Computers, Version 4.6*, Pacific Northwest National Laboratory, Richland, Washington 99352-0999, USA, 2004.

[92] W. Smith and T. Forester, J. Molec. Graphics **14**, 136 (1996).

[93] M. Doi, OCTA: Growth for the Future – Homepage, 2003.

[94] INFM Democritos, Quantum-Espresso — Homepage, 2005.

[95] GPL, GNU General Public License – Homepage, 2004.

[96] J. Rottler and A. Maggs, Phys. Rev. Lett. **93**, 170201 (2004).

[97] I. Pasichnyk and B. Dünweg, Journal of Physics: Cond. Mat. **16**, 3999 (2004).

[98] Tcl/Tk, Tool Command Language / ToolKit – Homepage, 2003.

[99] A. Bunker and B. Dünweg, Phys. Rev. E **63**, (2001).

[100] FFTW, Fastest Fourier Transform in the West – Homepage, 2003.

[101] LAM/MPI, Local Area Multicomputer Message Passing Interface – Homepage, 2004.

[102] MPICH, Message Passing Interface CHameleon – Homepage, 2004.

[103] D. C. Rapaport, *The Art of Molecular Dynamics Simulation*, 2nd ed. (Cambridge University Press, ADDRESS, 2004).

[104] N. Martys and R. Mountain, Phys. Rev. E **59**, 3733 (1999).

[105] F. Müller-Plathe, Phys. Rev. E; **59**, 4894 (1999).

[106] T. Soddemann, B. Dünweg, and K. Kremer, Phys. Rev. E **68**, 046702 (2003).

[107] H. J. C. Berendsen *et al.*, J. Chem. Phys. **81**, 3684 (1984).

[108] P. Español and P. Warren, Europhys. Lett. **30**, 191 (1995).

[109] A. Kolb and B. Dünweg, J. Chem. Phys. **111**, 4453 (1999).

[110] I. R. Cooke, K. Kremer, and M. Deserno, Phys. Rev. E **72**, 011506 (2005).

[111] J. D. Weeks, D. Chandler, and H. C. Andersen, J. Chem. Phys. **54**, 5237 (1971).

[112] T. Soddemann, B. Dünweg, and K. Kremer, Eur. Phys. J. E **6**, 409 (2001).

[113] A. D. Buckingham and P. W. Fowler, Canad. J. Chem **63**, 2018 (1985).

[114] J. G. Gay and B. J. BERNE, J. Chem. Phys. **74**, 3316 (1981).

[115] P. Debye and E. Hückel, Phys. Z. **24**, 185 (1923).

[116] R. W. Hockney and J. W. Eastwood, *Computer Simulation Using Particles* (IOP, London, 1988).

[117] T. Darden, D. York, and L. Pedersen, J. Chem. Phys. **98**, 10089 (1993).

[118] U. Essmann *et al.*, J. Chem. Phys. **103**, 8577 (1995).

[119] A. Arnold and C. Holm, Chemical Physical Letters **354**, 324 (2002).

[120] A. Arnold and C. Holm, in preparation (unpublished).

[121] J. Lekner, Physica A **176**, 485 (1991).

[122] A. Arnold, Diploma thesis, Johannes Gutenberg–Universität, 2001.

[123] A. Arnold, Ph.D. thesis, Johannes Gutenberg-Universität, Mainz, Germany, 2004.

[124] E. R. Smith, Proc. R. Soc. Lond. A **375**, 475 (1981).

[125] A. Maggs and V. Rosseto, Phys. Rev. Lett. **88**, 196402 (2002).

[126] D. Nykypanchuk, H. Strey, and D. Hoagland, Science **297**, 987 (2002).

[127] VMD, Visual Molecular Dynamics – Homepage, 2003.

[128] F. Oded, J. Chem. Phys. **119**, 596 (2003).

[129] U. Wolff, Comput. Phys. Commun. **156**, 143 (2004).

[130] R. W. Hockney and J. W. Eastwood, *Computer Simulations using Particles* (McGraw-Hill, New York, 1981).

[131] G. S. Grest, B. Dünweg, and K. Kremer, Comp. Phys. Comm. **55**, 269 (1989).

[132] M. Rubinstein and S. Panyukov, Macromolecules **30**, 8036 (1997).

[133] R. Everaers, Eur. Phys. J B **4**, 341 (1998).

[134] Doxygen, Doxygen – A documentation generation system, 2005.

[135] CVS, Concurrent Versions System – Homepage, 2003.

[136] LAMMPS, Benchmarks of the LAMMPS Molecular Dynamics Simulator, 2005.

[137] gcc, GNU compiler suite, 2002-2004.

[138] icc, Intel C/C++ compiler for Linux, 2003-2004.

[139] H. J. Limbach, M. Sayar, and C. Holm, J. Phys.: Condensed Matter **16**, S2135 (2004).

[140] H. J. Limbach, C. Holm, and K. Kremer, Macromolecular Chemistry and Physics **206**, 77 (2005).

[141] A. Naji, A. Arnold, C. Holm, and R. R. Netz, Europhys. Lett. **67**, 130 (2004).

[142] R. Everaers *et al.*, Science **303**, 823 (2004).

[143] S. K. Sukumaran, G. S. Grest, K. Kremer, and R. Everaers, J. Polym. Sci. B: Pol. Phys. **in press**, (2005).

[144] Z. W. Wang and C. Holm, J. Chem. Phys. **115**, 6277 (2001).

[145] P. Ahlrichs and B. Dünweg, Int. J. Mod. Phys. C **9**, 1429 (1998).

[146] P. Ahlrichs and B. Dünweg, J. Chem. Phys. **111**, 8225 (1999).

[147] V. Lobaskin and B. Dünweg, New J. Phys. **6**, 54 (2004).

[148] V. Lobaskin, B. Dünweg, and C. Holm, J. Phys.: Condens. Matter **16**, S4063 (2004).

[149] S. Duane, A. D. Kennedy, B. J. Pendleton, and D. Roweth, Phys. Lett. B **195**, 216 (1987).

[150] M. Sayar and C. Holm, unpublished (unpublished).

[151] M. Doi and S. F. Edwards, *The theory of polymer dynamics* (Oxford Science Publications, ADDRESS, 1986).

[152] J. des Cloizeaux and G. Jannink, *Polymers in Solution, their Modelling and Structure*, *Oxford Science Publications* (Clarendon Press, Oxford, 1990).

[153] J. Zinn-Justin, *Quantum Field Theory and Critical Phenomena*, 2nd ed. (Clarendon Press / Oxford Science Publications, Oxford, 1993).

[154] B. Tieke, *Makromolekulare Chemie* (VCH Verlagsgesellschaft mbH, Weinheim, 1997).

[155] W. Nolting, *Statistische Physik*, Vol. 6 of *Grundkurs Theoretische Physik*, 3*rd* ed. (vieweg Lehrbuch, Braunschweig/Wiesbaden, Germany, 1998).

[156] M. Rubinstein and R. H. Colby, *Polymer Physics* (Oxford University Press, Oxford, UK, 2003).

[157] M. Deserno, Ph.D. thesis, Universität Mainz, 2000.

[158] M. Doi, *Introduction do Polymer Physics* (Clarendon Press, Oxford, 1996).

[159] M. Fisher, J. Phys. Soc. Japan **26**, 44 (1969).

[160] B. Li, N. Madras, and A. Sokal, J. Stat. Phys. **80**, 661 (1995).

[161] A. Sokal, in *Monte Carlo and Molecular Dynamics Simulations in Polymer Science*, edited by K. Binder (Oxford University Press, New York / Oxford, 1995).

[162] P. Pincus, Macromolecules **9**, 386 (1976).

[163] P. de Gennes, P. Pincus, and R. Velasco, J. Physique **37**, 1461 (1976).

[164] H. Schiessel and P. Pincus, Macromolecules **31**, 7953 (1998).

[165] G. Manning, J. Chem. Phys. **51**, 924 (1969).

[166] M. Deserno, C. Holm, and S. May, Macromolecules **33**, 199 (2000).

[167] M. Deserno and C. Holm, in *Electrostatic Effects in Soft Matter and Biophysics*, Vol. 46 of *NATO Science Series II - Mathematics, Physics and Chemistry*, edited by C. Holm, P. Kékicheff, and R. Podgornik (Kluwer Academic Publishers, Dordrecht, Nl, 2001).

[168] H. Wennerström, B. Jönsson, and P. Linse, J. Chem. Phys. **76**, 4665 (1982).

[169] R. M. Fuoss, A. Katchalsky, and S. Lifson, Proc. Natl. Acad. Sci. USA **37**, 579 (1951).

[170] T. Alfrey, P. W. Berg, and H. J. Morawetz, J. Polym. Sci. **7**, 543 (1951).

[171] S. Safran, P. Pincus, M. Cates, and F. MacKintosh, Phys. France **51**, 503 (1990).

[172] M. Deserno, Physica A **278**, 405 (2000).

[173] M. Le Bret and B. Zimm, Biopolymers **23**, 287 (1984).

[174] P. A. Tipler, *Physik*, revised 1*st* ed. (Spektrum Akademischer Verlag GmbH, Heidelberg, 1995).

[175] W. Nolting, *Elektrodynamik*, Vol. 3 of *Grundkurs Theoretische Physik*, 5*th* ed. (vieweg Lehrbuch, Braunschweig/Wiesbaden, Germany, 1997).

[176] G. Wendt, *Encyclopedia of Physics*, edited by S. Flügge (Springer-Verlag, Berlin, 1958), Vol. 26.

[177] A. V. Lyulin, B. Dünweg, O. V. Borisov, and A. A. Darinskii, Macromolecules **32**, 3264 (1999).

[178] U. Micka, C. Holm, and K. Kremer, Langmuir **15**, 4033 (1999).

[179] U. Micka and K. Kremer, Europhys. Lett. **49**, 189 (2000).

[180] G. S. Grest and K. Kremer, Phys. Rev. A **33**, 3628 (1986).

[181] S. F. Edwards and T. A. Vilgis, Rep. Prog. Phys. **51**, 247 (1988).

[182] Y. Kantor, M. Kardar, and H. Li, Phys. Rev. E **49**, 1383 (1994).

[183] Y. Kantor and M. Kardar, Phys. Rev. E **51**, 1299 (1995).

[184] A. V. Dobrynin, M. Rubinstein, and S. P. Obukhov, Macromolecules **29**, 2974 (1996).

[185] A. V. Dobrynin and M. Rubinstein, Macromolecules **32**, 915 (1999).

[186] L. Rayleigh, Philos. Mag. **14**, 182 (1882).

[187] M. Deserno, Eur. Phys. J. E **6**, 163 (2001).

[188] H. J. Limbach, Ph.D. thesis, Johannes Gutenberg–Universität, Mainz, Germany, 2001.

[189] J. Combet, M. Rawiso, and F. Boué, 2005, in preparation.